Entwicklung neuartiger Kupferkomplexe für die Cu-vermittelte Radiofluorierung und deren Anwendung für die Herstellung von Radiotracern

Inaugural-Dissertation

Zur

Erlangung des Doktorgrades

Der mathematischen-Naturwissenschaftlichen Fakultät

Der Universität zu Köln

Vorgelegt von

Chris Michael Hoffmann

Aus Krefeld

Köln, 2024

Berichterstatter: Prof. Dr. Boris D. Zlatopolskiy
Prof. Dr. Axel Griesbeck

Tag der mündlichen Prüfung: 08.07.2024

Danksagung

Zunächst möchte ich mich beim Institutsleiter Prof. Dr. Bernd Neumaier für seine stetige Unterstützung und Anregungen zu den Projekten bedanken, die meine Promotion stetig vorangetrieben und meine Arbeit qualitativ verbessert haben.

Mein großer Dank geht an meinem Doktorvater Prof. Dr. Boris Zlatopolskiy für die Aufnahme in seine Arbeitsgruppe und Möglichkeit meine Promotion unter seiner Obhut durchführen zu können. Durch unsere stetigen Diskussionen hast du mir den Einstieg in die Radiochemie erleichtert, wodurch ich auch meinen Horizont in den letzten vier Jahren ununterbrochen erweitern konnte.

Ich möchte mich auch bei Prof. Dr. Axel Griesbeck und Prof. Dr. Mathias Wickleder bedanken, die die Rollen des Zweitgutachters und Vorsitz im Prüfungskomitee übernommen haben.

Mein nächster Dank geht an die Teams von Prof. Dr. Heike Endepols und Dr. Dirk Bier, die die biologische Evaluation meiner hergestellten Radiotracer durchgeführt und ausgewertet haben.

Mein besonderer Dank geht an Dr. Swen Humpert. Durch ihn konnte ich mein Wissen in der HPLC-Analytik und Radiochemie weiter vertiefen und selbst bei der 1000. Frage hat er mir geduldig und besonnen geantwortet.

Ebenso möchte ich mir bei Dr. Felix Neumaier für seine Unterstützung bei der Korrektur der Texte bedanken und die Hilfestellung wissenschaftliche Texte besser verfassen zu können.

Zu guter Letzt möchte ich mich beim restlichen INM-5 und IREMB-Team für ihre Unterstützung während meiner Promotion bedanken, aber auch bei all meinen Doktorandenkollegen für die großartige und lustige Zeit.

Den allerletzten Dank möchte ich meiner Familie und meinem Photon widmen. Drei Abschlussarbeiten und drei Zeiträume, in denen ich einfach nur unausstehlich war. Danke, dass ihr mir zur Seite standet. Diese Arbeit widme ich Euch.

„Ich habe keine besondere Begabung, sondern bin nur leidenschaftlich neugierig.“

Albert Einstein

Kurzzusammenfassung

Die („Alkohol-verstärkte“) Cu-vermittelte Radiofluorierung (CVRF) ist eine einfache und vielfältig anwendbare Methode für die Herstellung von [^{18}F](Hetero)Arylfluoriden aus leicht zugänglichen Boronsäure- [$B(OH)_2$], Boronsäurepinakolester- (BPin) und Trimethylstannylvorläufern ($SnMe_3$). Sie bietet die Möglichkeit, hohe und reproduzierbare radiochemische Umsätze (RCUs) mit Tetrakispyridinkupfer(II)triflat [$Cu(Py)_4(OTf)_2$] als Vermittler zu erzielen und ermöglicht die Herstellung von Radiotracern, die über konventionelle Methoden nur schwer zugänglich sind. Trotz intensiver Optimierung der Methode sind jedoch nach wie vor große Vorläufermengen (≥10 µmol) für hohe und reproduzierbare RCUs notwendig. Daher war das übergeordnete Ziel dieser Promotionsarbeit, die CVRF durch die Identifizierung effizienterer Cu(II)-Komplexe in dieser Hinsicht weiter zu optimieren und das optimierte Protokoll für die Herstellung verschiedener Radiotracer einzusetzen. Das erste Themengebiet umfasste die Synthese und Evaluation neuartiger Cu(II)-Komplexe für die CVRF unter Verwendung verschiedener Modellsubstrate. Im Rahmen einer umfassenden Studie wurden insgesamt 36 Cu(II)-Komplexe mit insgesamt 15 substituierten *N*-heterozyklischen Liganden und neun Gegenionen hergestellt und ihr Einsatz als Vermittler für die CVRF untersucht. Die Eignung und Effizienz der einzelnen Cu(II)-Komplexe wurde durch Radiosynthesen mit elektronenarmen und -neutralen aromatischen Substraten evaluiert, die eine $B(OH)_2$ oder BPin Abgangsgruppe trugen. Im Anschluss wurden „Ein-Parameter“-Optimierungen der Reaktionsbedingungen in Hinblick auf Temperatur, Reaktionszeit, Lösungsmittel und weitere Parameter durchgeführt. In diesem Rahmen konnten drei Cu-Komplexe [$Cu(4\text{-}PhPy)_4(ClO_4)_2$, $Cu(3,4\text{-}Me_2Py)_4(OTf)_2$ und $Cu(3,4\text{-}Me_2Py)_4(ClO_4)_2$] identifiziert werden, die eine erhebliche Verbesserung der RCUs in DMI/*n*BuOH oder reinem DMI ermöglichten [≥47% vs. 2–30% mit dem Standard-Protokoll]. Zusätzlich ergaben Radiosynthesen hohe und reproduzierbare RCUs in einem breiten Temperaturbereich (80–130 °C) bei kurzen Reaktionszeiten (5–20 min). Bemerkenswert war, dass auch bei Temperaturen von 60 bzw. 70 °C und längerer Reaktionszeit (bis zu 40 min) gute RCUs erzielten werden konnten. Zuletzt wurde das optimierte Protokoll für die CVRF von insgesamt 21 substituierten Aryl-$B(OH)_2$/-BPin/Bneo/$SnMe_3$ Substraten bei reduzierter Vorläufermenge (2,5 µmol) angewendet und RCUs von bis zu 76% erzielt. Im zweiten Themengebiet wurde die Praktikabilität und Effizienz des optimierten Protokolls in Rahmen der Herstellung von vier klinisch relevanten PET-Tracern und

fünf Radiotracer-Kandidaten überprüft. Für die PET-Tracer (*R*)-/(*S*)-3-[^{18}F]Fluorphenylalanin, (*S*)-αMe-3-[^{18}F]Fluorphenylalanin und [^{18}F]FDOPA konnten dabei ausgehend von 10 oder 2,5 µmol Vorläufermenge isolierte Aktivitätsausbeuten (AAs) von 23–41% (Lit.: 10–17%) erhalten werden. Im Falle der Radiosynthese von [^{18}F]MNI1126 konnte die RCU auf 47 ± 5% (Standard-Protokoll: 6 ± 2%) verbessert werden. Durch Anwendung des optimierten Protokolls konnten zudem die Radiotracer-Kandidaten [^{18}F]ALX5407, [^{18}F]R91150 und 6-[^{18}F]F-FAPI mit AAs von 30 ± 5%, 24 ± 2% und 19 ± 2% (Lit.: 14 ± 6%, 10–15% und 16–43%) hergestellt und anschließend präklinisch in Nagetieren evaluiert werden. Außerdem konnte der Radiotracer-Kandidat 5-[^{18}F]FMT mit guten AAs von 30 ± 2% ausgehend von nur 2,5 µmol Vorläufer hergestellt werden.

Da sich der Glyzin-Transporter Typ 1 (GlyT1) Radioligand [^{18}F]ALX5407 bei der biologischen Evaluation als unzureichend hirngängig erwies, wurde eine Prodrug-Strategie zur GlyT1-Bildgebung im Gehirn mit dem entsprechenden Methylester [^{18}F]ALX5406 entwickelt. Das Radioaktivitätsverteilungsmuster in µPET-Scans mit [^{18}F]ALX5406 stimmte mit dem In-vitro-Verteilungsmuster von [^{18}F]ALX5407 in Rattenhirnschnitten überein.

Mit dem Radioligand [^{18}F]R91150 konnte die 5-HT$_{2A}$-Rezeptorverteilung im Gehirn von Nagetieren erfolgreich dargestellt und durch erste Blockierungs- bzw. Verdrängungsstudien eine weitgehend 5-HT$_{2A}$-selektive Rezeptorbindung im Kortex nachgewiesen werden.

Der letzte Radiotracer 6-[^{18}F]F-FAPI ermöglichte in verschiedenen Tiermodellen eine gute Darstellung von FAP-positiven Zellen und Tumoren mit schneller Anreicherung und einem guten Tumor-zu-Hintergrund-Verhältnis.

Zusammenfassend wurden in dieser Promotionsarbeit verschiedene neue Cu(II)-Komplexe identifiziert, welche die Herstellung von [^{18}F]Arylfluoriden mittels CVRF in verbesserten Ausbeuten trotz verringerter Vorläufermengen ermöglichen. Neben verschiedenen klinisch relevanten PET-Tracern konnte mit dem optimierten Protokoll eine Reihe von Tracer-Kandidaten in den für präklinische Evaluationen ausreichenden Mengen hergestellt werden.

Abstract

The ("alcohol-enhanced") Cu-mediated radiofluorination (CMRF) is a versatile and simple method for the preparation of [^{18}F](hetero)aryl fluorides from readily accessible boronic acid [B(OH)$_2$], boronic acid pinacol ester (Bpin) and trimethylstannyl (SnMe$_3$) precursors. Using tetrakispyridine copper(II) triflate [Cu(Py)$_4$(OTf)$_2$] as the mediator, this method offers high and reproducible radiochemical conversions (RCCs) and provides access to radiotracers which are difficult to prepare by conventional methods. However, despite intensive optimizations, the method still requires large precursor amounts (≥10 µmol) to achieve high and reproducible RCUs. Therefore, the overall aim of this PhD thesis was to further optimize the CMRF by the identification of more efficient Cu(II) complexes and to apply the developed protocol for the preparation of various radiotracers. In the first topic, a series of novel Cu(II) complexes were prepared and evaluated as mediators of radiofluorination of various model substrates. As part of a comprehensive study, a total of 36 Cu(II) complexes with 15 different substituted *N*-heterocyclic ligands and nine different counterions were prepared and investigated. Subsequently, "one-parameter" optimizations were carried out to optimize the reaction conditions with regard to temperature, reaction time, solvent and further parameters. This led to the identification of three Cu-complexes [Cu(4-PhPy)$_4$(ClO$_4$)$_2$, Cu(3,4-Me$_2$Py)$_4$(OTf)$_2$ and Cu(3,4-Me$_2$Py)$_4$(ClO$_4$)$_2$] that enabled significant improvements of the RCCs in DMI/*n*BuOH or pure DMI [≥47% vs. 2–30% with the standard protocol]. In addition, the developed protocol afforded high and reproducible RCCs over a broad temperature range (80–130 °C) within short reaction times (5-20 min). Remarkably, good RCCs were also obtained at temperatures of 60 and 70 °C with longer reaction times (up to 40 min). Finally, the optimized protocol was applied to a total of 21 substituted aryl-B(OH)$_2$/-Bpin/Bneo/SnMe$_3$ substrats which furnished RCCs of up to 76% using reduced precursor amounts (2.5 µmol).

In the second topic, the practicability and efficiency of the optimized protocol was confirmed by the preparation of four clinically relevant PET tracers and five radiotracer candidates. Using 10 or 2.5 µmol precursor, the PET tracers (*R*)-/(*S*)-3-[^{18}F]fluorophenylalanine, (*S*)-αMe-3-[^{18}F]fluorophenylalanine and [^{18}F]FDOPA could be prepared in isolated activity yields (AYs) of 23–41% (Lit.: 10–17%). In the case of [^{18}F]MNI1126, the RCCs could be improved to 47 ± 5% (standard protocol: 6 ± 2%). Additionally, application of the optimized protocol afforded the radiotracer candidates [^{18}F]ALX5407, [^{18}F]R91150 and 6-[^{18}F]F-FAPI in AAs of 30 ± 5%, 24 ± 2% and

19 ± 2% (Lit.: 14 ± 6%, 10-15% and 16-43%, respectively), enabling their preclinical evaluation. Finally, the radiotracer candidate 5-[^{18}F]FMT could be produced in good AYs of 30 ± 2 using only 2.5 µmol precursor.

In vivo biodistribution studies with the glycine transporter type 1 (GlyT1) specific radioligand [^{18}F]ALX5407 revealed insufficient brain penetration, which could be overcome by development of a prodrug strategy with the corresponding methyl ester [^{18}F]ALX5406. The brain distribution of radioactivity in µPET scans with [^{18}F]ALX5406 was consistent with the distribution of [^{18}F]ALX5407 observed in brain slices.

The radioligand [^{18}F]R91150 enabled visualization of 5-HT$_{2A}$ receptor in the rodent brain. Furthermore, blocking/displacement studies confirmed 5-HT$_{2A}$ receptor-selective binding in the cortex.

The last radiotracer 6-[^{18}F]F-FAPI demonstrated high and rapid accumulation in FAP-positive cells and tumors and a good tumor-to-background ratio in various *in vivo* rat models.

In summary, this doctoral thesis identified several novel CMRF-promotors that enabled the production of [^{18}F]aryl fluorides in improved yields applying reduced precursor amounts. In addition to various clinically relevant PET tracers, application of the optimized protocol enabled the production of several tracer candidates in amounts sufficient for their preclinical evaluation.

Inhaltsverzeichnis

1 Einleitung

Die Anwendung von Radionukliden zur Verfolgung von Prozessen in biologischen Systemen geht auf George Charles de Hevesy zurück. Im Jahr 1923 veröffentlichte er eine Abhandlung über die Verteilung von ^{212}Pb in Pflanzen und legte somit das Fundament für die *in vivo* Anwendung von Radionukliden und des Tracer-Prinzips.[1] Durch den praktischen Ansatz dieses Prinzips wurde es schließlich möglich, biochemische Prozesse *in vivo* zu beobachten und darzustellen. Hevesys Definition des Tracer-Prinzips basiert auf dem Schlüssel-Schloss-Prinzip und ist mit zwei Bedingungen verknüpft, die erfüllt sein müssen:

1. Der Tracer darf das zu beobachtende Target nicht beeinflussen.
2. Der Tracer muss von außerhalb des Körpers ohne invasive Eingriffe detektierbar sein.

Basierend auf diesem Prinzip besteht ein Radiotracer aus einem Pharmakophor (=Schlüssel), welches mit einem Radionuklid verbunden ist und im Idealfall ausschließlich mit dem Prozess bzw. Struktur von Interesse (=Schloss) interagiert (**Abbildung 1**).

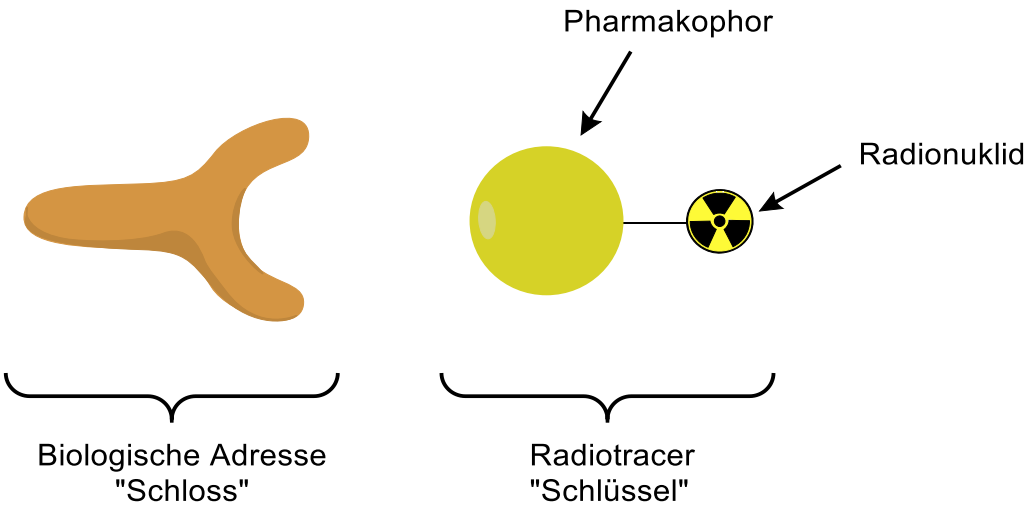

Abbildung 1: Das (Radio)tracer-Prinzip.

Klinisch gesehen ermöglichen Tracer, die mit einem geeigneten Radionuklid markiert sind, die frühzeitige Diagnose und oftmals eine verbesserte Therapie von pathologischen Veränderungen wie etwa Tumoren oder neurologische Erkrankungen.

Für die betroffenen Patienten kann dies wiederrum zu einer erhöhten Überlebensrate und auch zu einer verbesserten Lebensqualität führen.

1.1 Positronen-Emissions-Tomographie – PET

Die Auswahl eines geeigneten Radionuklids spielt für die Radiopharmaka-Entwicklung in der Nuklearmedizin eine entscheidende Rolle und hängt maßgeblich vom jeweiligen Anwendungsgebiet ab. So können Radionuklide, die einem α- oder β^--Zerfall unterliegen, für therapeutische Zwecke verwendet werden, während γ- bzw. β^+-Emitter für die bildgebende Diagnostik im Rahmen von Single-Photon-Emission-Computer-Tomographie (SPECT) bzw. Positronen-Emissions-Tomographie (PET) verwendet werden.

Die PET-Bildgebung basiert auf der Detektion von Vernichtungsstrahlung, die bei der Positron-Elektron-Annihilation entsteht. Das Positron resultiert aus dem β^+-Zerfall eines Radionuklids (β^+-Emitters), bei dem ein Proton (^1_1p) des Kerns unter Emission eines Positrons (e^+) und eines Neutrinos (ν_e) in ein Neutron (^1_0n) umwandelt wird (**Abbildung 2**).

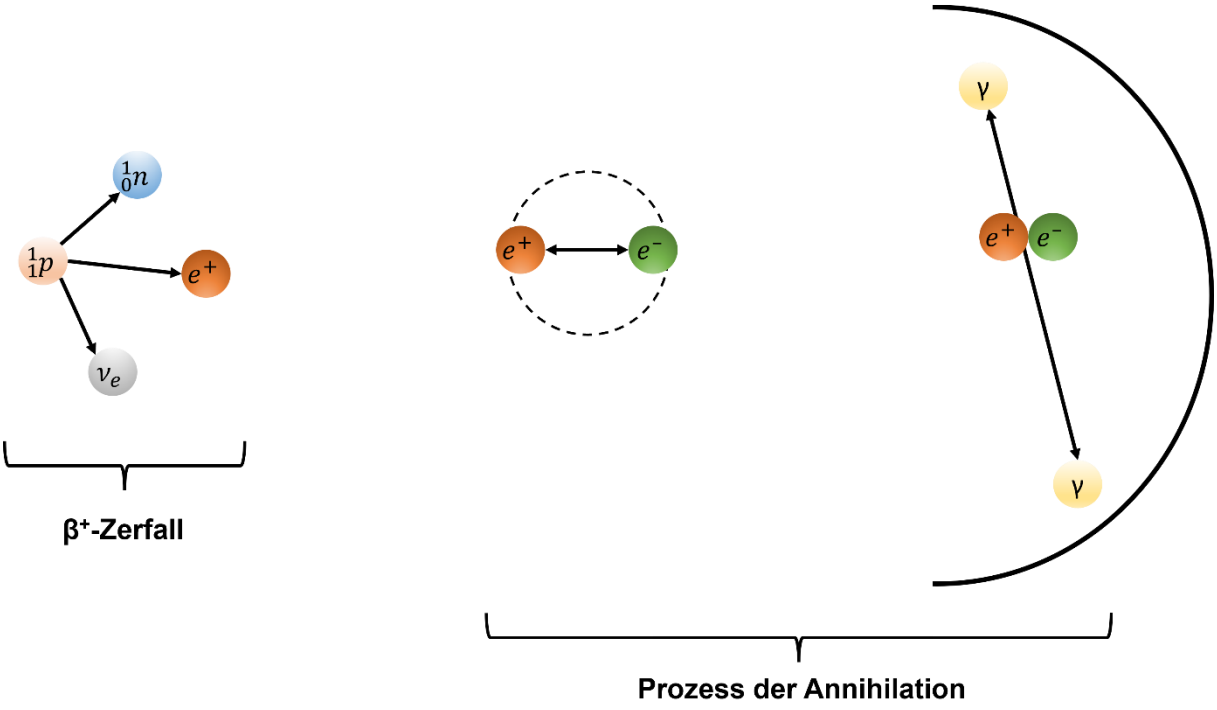

Abbildung 2: Schematische Darstellung des β^+-Zerfalls und der anschließenden Annihilation unter Emission zweier γ-Quanten, welche die Grundlage für die PET-Bildgebung darstellt.

Da die Wechselwirkung des Neutrinos mit Materie sehr schwach ist, kann es für die PET-Bildgebung vernachlässigt werden. Das Positron durchläuft nach seiner Emission dagegen eine Kaskade an elastischen Stößen mit der Materie in seiner Umgebung, wobei es seine kinetische Energie abgibt und so abgebremst wird. Erreicht es eine Energie von 511 keV, was der Ruheenergie eines Elektrons entspricht (Äquivalenz von Energie und Masse nach Einstein), kommt es zu einem Vernichtungsprozess (Annihilation) mit einem nahliegenden Elektron. Die bis dahin zurückgelegte Wegstrecke im Gewebe ist dabei abhängig von der Positronen-Energie, die für jeden β^+- Emitter charakteristische Maximal- und Durchschnittswerte aufweist.

In ca. 60% der Fälle annihiliert das Positron direkt mit einem Elektron zu zwei γ-Quanten, welche in einem Winkel von nahezu 180° zueinander ausgesendet werden. Im Rest der Fälle bilden die emittierten Positronen dagegen mit dem Elektron zunächst ein *para*-Positronium (10%) oder *ortho*-Positronium (30%), bei denen es sich um Wasserstoff-ähnliche Systeme handelt, in denen das Positron formal die Rolle des Kerns ersetzt. Nach einer durchschnittlichen Lebensdauer von 0,12 ns (*para*-Positronium) bis einigen ns (*ortho*-Positronium) annihilieren diese Spezies spontan (*para*-Positronium) bzw. mit einem weiteren Elektron (*ortho*-Positronium) zu zwei γ-Quanten. Beim *ortho*-Positronium kommt es zusätzlich in 0,5% der Fälle nach einer durchschnittlichen Lebensdauer von ca. 140 ns zu einer spontanen Annihilation, wobei drei γ-Quanten ausgesendet werden.[2–5] Dieser Prozess ist jedoch aufgrund seiner sehr geringen Wahrscheinlichkeit vernachlässigbar. Die als Vernichtungsstrahlung bezeichneten γ-Quanten können dann mittels Detektorblöcken im Positron-Emissions-Tomographen detektiert werden und liefern Informationen über die Verteilung des Radiotracers im Körper.[2][5] Im PET-Scanner sind die einzelnen Detektorblöcke ringförmig in gegenüberliegenden Paaren angeordnet, um die γ-Quantenpaare detektieren zu können (**Abbildung 3**).

Es kann aber auch vorkommen, dass fälschlicherweise zwei γ-Quanten detektiert werden, die nicht aus dem gleichen Zerfallsereignis stammen, sondern zufällig auf gegenüberliegende Detektoren treffen. Um dies zu verhindern, werden die gegenüberliegenden Detektoren in Koinzidenz geschaltet. Das bedeutet, dass ein Zerfallsereignis nur dann erkannt und detektiert wird, wenn zwei γ-Quanten in einem bestimmten Zeitfenster (im Regelfall: 8–15 ns) gleichzeitig registriert werden. Aus den mehreren Millionen erfassten Zerfallsereignissen kann schließlich mit einer geeigneten

Software ein 3-dimensionales Abbild (PET-Bild) der Radioaktivitätsverteilung im Körper rekonstruiert werden.

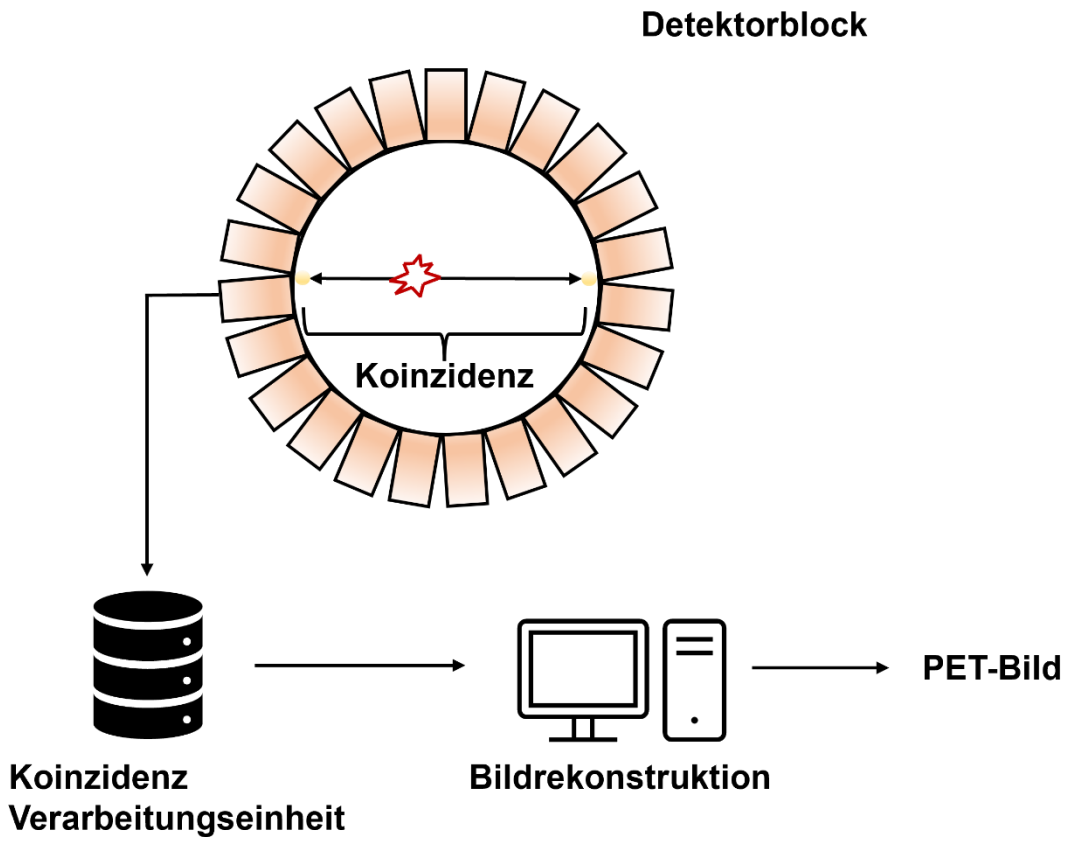

Abbildung 3: Schematischer Aufbau eines Positron-Emissions-Tomographen zur Detektion zweier γ-Quanten in Koinzidenz.

1.2 Standard PET-Nuklide

Neben der technischen Herausforderung ist die Wahl eines geeigneten PET-Nuklids entscheidend für den Erhalt qualitativ guter und aussagekräftiger PET-Bilder. Zunächst muss die Halbwertszeit des PET-Nuklids mit der In-vivo-Halbwertszeit des Pharmakophors im Radiotracer kompatibel sein. Benötigt das Pharmakophor etwa aufgrund einer langsamen Pharmakokinetik für das Erreichen des biologischen Targets lange, sollte die Wahl auf ein PET-Nuklid mit entsprechend langer Halbwertszeit fallen.

Des Weiteren sollte das Radionuklid auch passende Zerfallseigenschaften besitzen. Es sollte einen hohen Anteil an β^+Zerfall für die Detektion aufweisen und im optimalen Fall in ein stabiles Isotop zerfallen. Sofern in der Zerfallsreihe doch ein radioaktives Tochternuklid entsteht, sollte es keine lange Halbwertszeit oder Radiotoxizität aufweisen, um weitere Strahlenbelastung des Patienten zu verhindern.

Die meisten bioaktiven Moleküle sind, unter anderem, aus den Bausteinen Kohlenstoff, Sauerstoff und Stickstoff aufgebaut. Daher ermöglichen Radionuklide wie ^{11}C, ^{13}N und ^{15}O eine Radiomarkierung ohne strukturelle Modifikation der Leitstruktur, wodurch Veränderungen in den physikochemischen oder pharmakologischen Eigenschaften der radiomarkierten Verbindung ausgeschlossen werden können. Entsprechend ergibt sich grundsätzlich ein breitestes Spektrum an Zielmolekülen, welche für die Markierung mit diesen Radionukliden infrage kommen (**Tabelle 1**).

Tabelle 1: Übersicht der Standard PET-Nuklide.

Radionuklid	**$T_{1/2}$ [min]**	**$E_{\beta+,\,max}$ [keV]**	**Kernreaktion**
^{11}C	20,4	960	$^{14}N(p,\alpha)^{11}C$
^{13}N	10,0	1198	$^{16}O(p,\alpha)^{13}N$
^{15}O	2,0	1732	$^{14}N(p,n)^{15}O$
			$^{15}N(p,n)^{15}O$
^{18}F	109,8	634	$^{20}Ne(d,\alpha)^{18}F$[a]
			$^{18}O(p,n)^{18}F$[b]
^{68}Ga	67,6	1899	$^{nat.}Ga(p,xn)^{68}Ge \rightarrow {}^{68}Ga$
			$^{68}Zn(p,n)^{68}Ga$
^{89}Zr	78,4	897	$^{89}Y(p,n)^{89}Zr$
^{124}I	6019,2	687	$^{124}Te(p,n)^{124}I$

[a] als $[^{18}F]F_2$. [b] als $[^{18}F]F^-$

Mit den Radionukliden ^{13}N und ^{15}O können aufgrund sehr kurzer Halbwertszeiten allerdings nur einfache Moleküle synthetisieren werden, was ihre praktische Verwendbarkeit stark einschränkt. Beispiele für ^{15}O-markierte Radiopharmaka sind etwa $[^{15}O]H_2O$,[6] $[^{15}O]N_2O$[7] und [^{15}O]Butanol[8] für die Darstellung des Blutstroms oder $[^{15}O]H_2O_2$ zur Verfolgung des Sauerstoffmetabolismus[9]. Das Radionuklid ^{13}N weist im Vergleich zu ^{15}O eine etwas längere Halbwertszeit auf, seine Verwendung ist jedoch

ebenfalls auf einfache Tracermoleküle begrenzt. Beispiele dafür sind [^{13}N]NH_3[10,11] und das Opioidpeptid [^{13}N]SD-62[12,13], die für die Bildgebung der Durchblutung des Herzens (Myokardperfussionsszintigraphie) bzw. von Opioid-Rezeptoren eingesetzt werden.

Aufgrund seiner längeren Halbwertszeit ermöglicht ^{11}C dagegen auch die Synthese komplexerer Radiotracer. Seit den 1960er wurden ausgehend von [^{11}C]CO_2[14–17] und [^{11}C]CH_4 verschiedene Bausteine für die ^{11}C-Markierung, wie etwa [^{11}C]CH_2O[18–20], [^{11}C]CHF_3[21,22], [^{11}C]HCN[15,23–25] und NH_4[^{11}C]SCN[26] entwickelt (**Abbildung 4**).

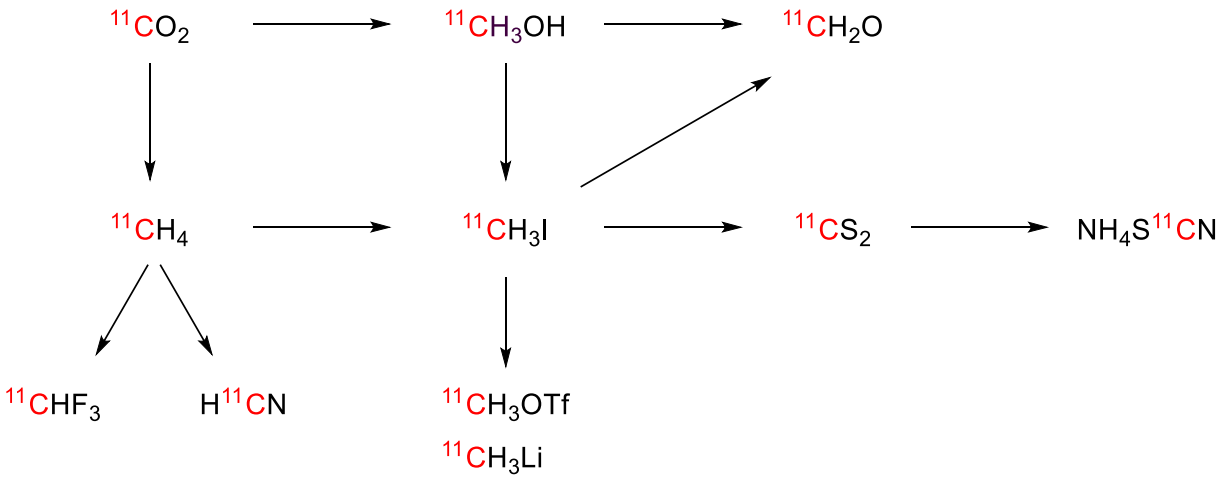

Abbildung 4: Übersicht verschiedener ^{11}C-Radiomakrierungsreagenzien.

Jedoch hat sich die Verwendung von [^{11}C]CH_3I[27–30] und [^{11}C]CH_3OTf[31,32] als Alkylierungsreagenzien durchgesetzt und deckt ein großes Feld relevanter Radiotracer ab, die auch heutzutage für die PET-Bildgebung noch verwendet werden (**Abbildung 5**).[33–39]

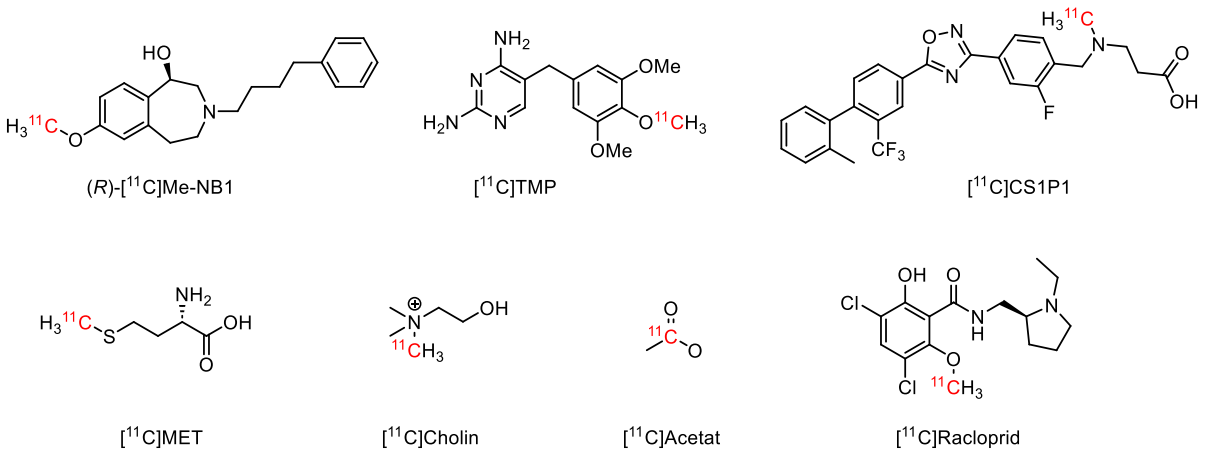

Abbildung 5: Beispiele klinisch relevanter ^{11}C-markierter Radiotracer für die PET-Bildgebung.

Im Vergleich zu den bisher vorgestellten Vertretern zeichnet sich ^{18}F durch seine herausragenden Zerfallseigenschaften und sehr gute Zugänglichkeit aus, was es zu einem der wichtigsten Radionuklide für die PET-Bildgebung macht. So weist dieser (fast) reiner β^+-Emitter mit 109,8 min eine optimale Halbwertszeit für die Herstellung und Anwendung von PET-Tracern auf. Ein weiterer Vorteil von ^{18}F ist seine geringere β^+-Energie im Vergleich zu den anderen β^+-Emittern. Infolgedessen legt das β^+-Teilchen eine kürze Wegstrecke in Geweben zurück, was zu einer Annihilation in unmittelbarer Nähe des Zerfallsereignisses und somit zu besser aufgelösten PET-Bildern führt.[40] Trotz der längeren Halbwertszeit ist die Strahlenbelastung für den Patienten aufgrund der geringeren β^+-Energie im Vergleich zu andere PET-Nukliden zudem deutlich geringer.

^{18}F lässt sich als elektrophiles $[^{18}F]F_2$ oder als nukleophiles $[^{18}F]F^-$ für Radiosynthesen einsetzen. Letzteres bietet den Vorteil, dass es durch Bestrahlung von angereicherten $[^{18}O]H_2O$ leicht zugänglich ist und bessere spezifische Aktivitäten (bis zu 4×10^4 GBq/µmol) erhalten werden können, weil bei der Produktion kein Träger zugesetzt wird („*no carrier added*“). Bei der Produktion von $[^{18}F]F_2$ müssen dem ^{20}Ne Target hingegen geringe Mengen F_2 beigemischt werden, um eine Adsorption an der Targetwand zu verhindern ("*carrier added*“). Dabei verringert sich die spezifische Aktivität auf 100–600 MBq/µmol. Darüber hinaus kann für $[^{18}F]F^-$ das Satellitenkonzept angewendet werden, bei dem die Produktion des Radionuklids (oder des ^{18}F-markierten Radiotracers) an einem zentralen Ort durchgeführt und dieses im Anschluss zu der jeweiligen Forschungseinrichtung oder Klinik transportiert wird.[41] Dieses Konzept ist bei Radionukliden mit kürzeren Halbwertszeiten nicht möglich. [36]

1.3 Radiomarkierungsmethoden mit Fluor-18

Chemisch verhält sich das Radionuklid ^{18}F identisch zu seinem stabilen Analogon Fluor-19 (^{19}F). So lässt sich $[^{18}F]F_2$ beispielsweise analog zu F_2 für elektrophile Additionsreaktionen einsetzen, während $[^{18}F]F^-$ für nukleophile Substitutionsreaktionen verwendet werden kann. Zudem ähnelt der Van-der-Waals-Radius von ^{18}F (1,35 Å) dem von Wasserstoff (1,20 Å), wodurch sich die pharmakologischen Eigenschaften radiofluorierter Tracer im Vergleich zu den entsprechenden nicht-fluorierten Leitstrukturen häufig nur geringfügig ändern. Jedoch kann Fluor als elektronegativstes Element des Periodensystems einen großen Einfluss

auf die elektronische Struktur des radiomarkierten Moleküls nehmen. Als Folge kann eine Radiofluorierung Auswirkungen auf den pKs oder die Lipophilie haben und auch weitere pharmakologisch relevante Eigenschaften wie etwa die metabolische Stabilität beeinflussen. Jedoch können die Reaktionsbedingungen aus der präparativen Synthesechemie aufgrund des starken Unterschusses von ^{18}F und der damit verbundenen langsamen Reaktionskinetik nicht 1:1 auf Radiosynthesen übertragen werden. Um dieses Hindernis zu überwinden, muss nicht nur das Volumen der Reaktionslösung klein gehalten, sondern meist auch vergleichsweise große Mengen an Vorläufer zur Beschleunigung der Reaktionskinetik verwendet werden. Eine Erhöhung der Temperatur wirkt sich ebenfalls positiv auf die Reaktionskinetik aus, kann jedoch einen limitierenden Faktor bei der Auswahl der Vorläufermoleküle darstellen. Aus diesem Grund kann, je nach Vorläufermolekül, auf zwei verschiedene Radiomarkierungsstrategien zurückgegriffen werden.

Bei der „Direkten Radiomarkierung“, welche im Allgemeinen die bevorzugte ^{18}F-Radiomarkierungsstrategie darstellt, erfolgt die Bindung des ^{18}F direkt an das Zielmolekül (**Abbildung 6**).

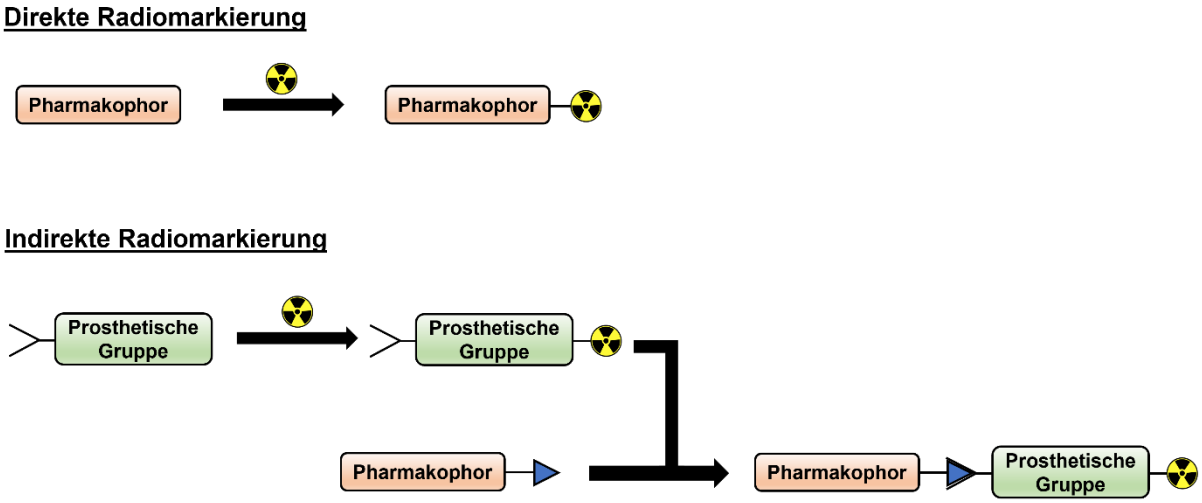

Abbildung 6: Direkte und indirekte Radiomarkierung.

Diese Methode ist zwar mit kürzeren Synthesezeiten und höheren Ausbeuten verbunden, kann jedoch aufgrund der erforderlichen harschen Reaktionsbedingungen und oft verwendeten organischen Lösungsmitteln nicht für empfindliche Moleküle und Biopolymere wie Peptide oder Proteine eingesetzt werden. Daher muss in diesen Fällen meist auf die „Indirekte Radiomarkierung“ zurückgegriffen werden, bei der zunächst eine prosthetische Gruppe ^{18}F-markiert und anschließend mit dem

Zielmolekül konjugiert wird. Für eine praktische Anwendung muss die prosthetische Gruppe dabei einige Voraussetzungen erfüllen. So muss sie eine gute Stabilität unter den Radiomarkierungsbedingungen aufweisen und eine reaktive funktionelle Gruppe für die Konjugation besitzen, welche die Radiomarkierungsreaktion nicht stört. Nimmt die funktionelle Gruppe doch einen erheblichen Einfluss auf die Radiomarkierung, kann sie mit einer Schutzgruppe versehen werden, welche nach der Radiosynthese wieder entfernt wird. Zusätzlich sollte die Konjugation mit dem Zielmolekül schnell und unter milden Bedingungen durchführbar sein und eine möglichst hohe Chemo- bzw. Regioselektivität aufweisen. Des Weiteren darf die prosthetische Gruppe nach der Konjugation die pharmakologischen Eigenschaften des Zielmoleküls nicht wesentlich negativ beeinflussen und der dabei erhaltene Radiotracer sollte eine gute In-vivo-Stabilität aufweisen. Zu guter Letzt sollte die prosthetische Gruppe aus leicht zugänglichen und lagerungsfähigen Vorläufern produzierbar sein und sich idealerweise ohne aufwendige Reinigungsschritte für die Konjugation einsetzen lassen.

Eines der ersten indirekten Radiomarkierungverfahren mit ^{18}F wurde von Müller-Platz et al. (1982) durchgeführt. Zur Radiosynthese von ^{18}F-markierter Urokinase wurde dabei als prosthetische Gruppe [^{18}F]Fluoressigsäure verwendet und durch Konjugation mit einer freien Aminogruppe in das Enzym eingebracht.[42] Zu den seitdem entwickelten, gängigsten prosthetischen Gruppen gehören *p*-[^{18}F]Fluorbenzoesäure ([^{18}F]FBS), *N*-Succinimidyl-4-[^{18}F]fluorbenzoesäureester ([^{18}F]SFB), *N*-[2-(4-[^{18}F]Fluorbenzamido)ethyl]maleimid ([^{18}F]FBEM) und *N*-[6-(4-[^{18}F]Fluorbenzyldin)aminooxyhexyl]maleimid ([^{18}F]FBAM) (**Abbildung 7**).

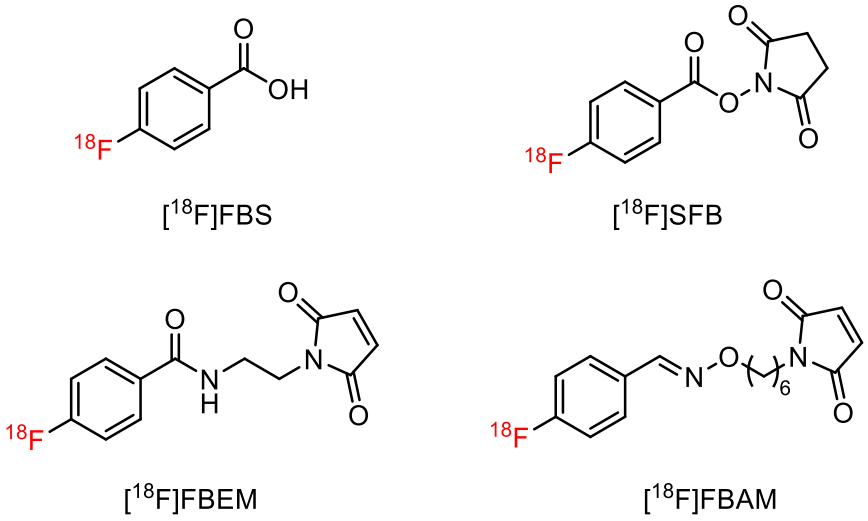

Abbildung 7: Übersicht von prosthetischen Gruppen für die „Indirekte Radiomarkierung“.

1.3.1 Radiofluorierung mittels elektrophiler Addition

Seit den 1970er Jahren ist es gängige Praxis, $[^{18}F]F_2$ für elektrophile Additionen an Alkenen[43] oder Alkinen[44] zu verwenden. Trotz der hohen Reaktionsfreudigkeit von $[^{18}F]F_2$ kann aufgrund des bei der Radionuklidproduktion zugesetzten Trägers so jedoch nur eine theoretische radiochemische Ausbeute (RCA) von maximal 50% erreicht werden. Hinzu kommt die geringe Regioselektivität der Reaktion. Diese führt zur Bildung von radiochemischen Nebenprodukten, welche häufig durch aufwendige Reinigungsschritte abgetrennt werden müssen. Die Herstellung des PET-Tracers 2-Desoxy-2-[^{18}F]fluor-D-glucose ([^{18}F]FDG) aus 3,4,6-Tri-O-acetyl-D-glucal verdeutlicht diese Problematik (**Schema 1**).[45]

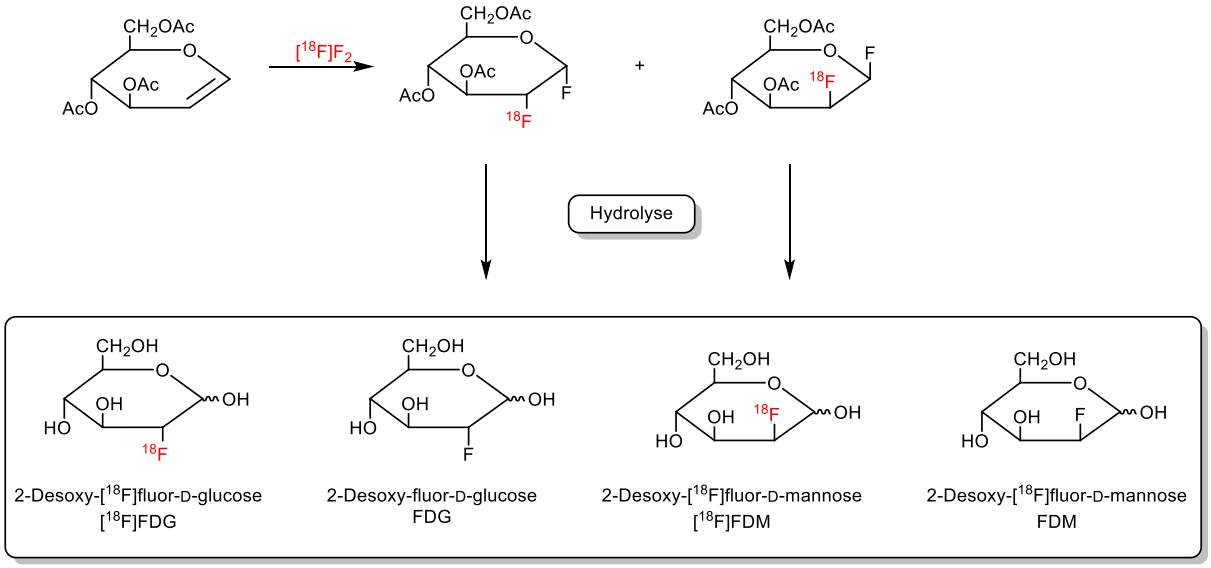

Schema 1: Radiosynthese von [^{18}F]FGD mittels elektrophiler Addition mit $[^{18}F]F_2$ unter Bildung des Radionebenproduktes [^{18}F]FDM.

Der elektrophile Angriff von $[^{18}F]F_2$ kann sowohl von oben als auch von unten an der Doppelbindung erfolgen, so dass nach der Hydrolyse mit HCl auch das Radionebenprodukt 2-Desoxy-[^{18}F]fluor-D-mannose ([^{18}F]FDM) entsteht. Wird noch in Betracht gezogen, dass $[^{18}F]F_2$ zur Hälfte aus nicht radioaktivem ^{19}F besteht, ergibt sich eine statistische Wahrscheinlichkeit von 50%, dass eine Addition mit ^{19}F erfolgt. Im Endeffekt führt dies nicht nur zu geringeren RCAs, sondern es kann auch maximal eine molare Aktivität (A_M) von 100 MBq/µmol erreicht werden. Für Tracer wie [^{18}F]FDG, welches sich durch hoch regulierte Transportprozesse in den Zielzellen anreichert, ist diese A_m ausreichend. Bei der Bildgebung von Rezeptoren kann eine unzureichende

A_m des Radioliganden infolge einer Übersättigung der Rezeptoren durch die nicht radioaktive Verbindung allerdings zu unzureichenden PET-Bildern führen.

Durch die Nutzung verschiedener über $[^{18}F]F_2$ zugänglicher elektrophiler ^{18}F-Reagenzien (**Abbildung 8**)[46] kann zwar die Regioselektivität verbessert werden, aber die A_M bleibt dennoch durch die Radionuklidproduktion begrenzt.

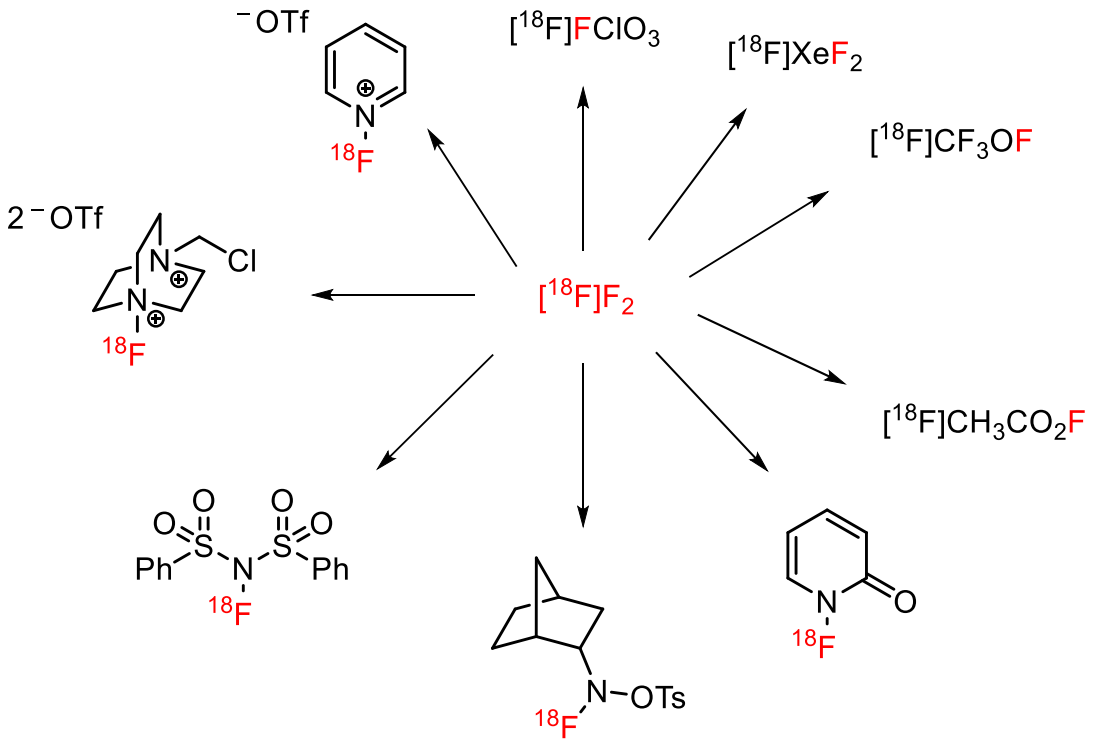

Abbildung 8: Übersicht elektrophiler ^{18}F-Reagenzien.

1.3.2 Radiofluorierung mittels nukleophiler Substitution

Als Alternative zu $[^{18}F]F_2$ hat sich die Verwendung von nukleophilem $[^{18}F]F^-$ etabliert, wodurch bessere RCAs und eine höhere A_M erzielt werden können. Produktionsbedingt liegt $[^{18}F]F^-$ nach dem Bestrahlen als solvatisiertes Anion im angereicherten $[^{18}O]H_2O$ vor und ist nicht direkt für nukleophile Substitutionsreaktionen geeignet. Grund dafür ist die sehr starke H–F-Wechselwirkung[47], welche zu einem Verlust des nukleophilen Charakters von $[^{18}F]F^-$ führt.[48,49] Daher wird vor der Verwendung von $[^{18}F]F^-$ die Solvatationshülle typischerweise durch azeotrope Trocknungsschritte entfernt (**Abbildung 9**).

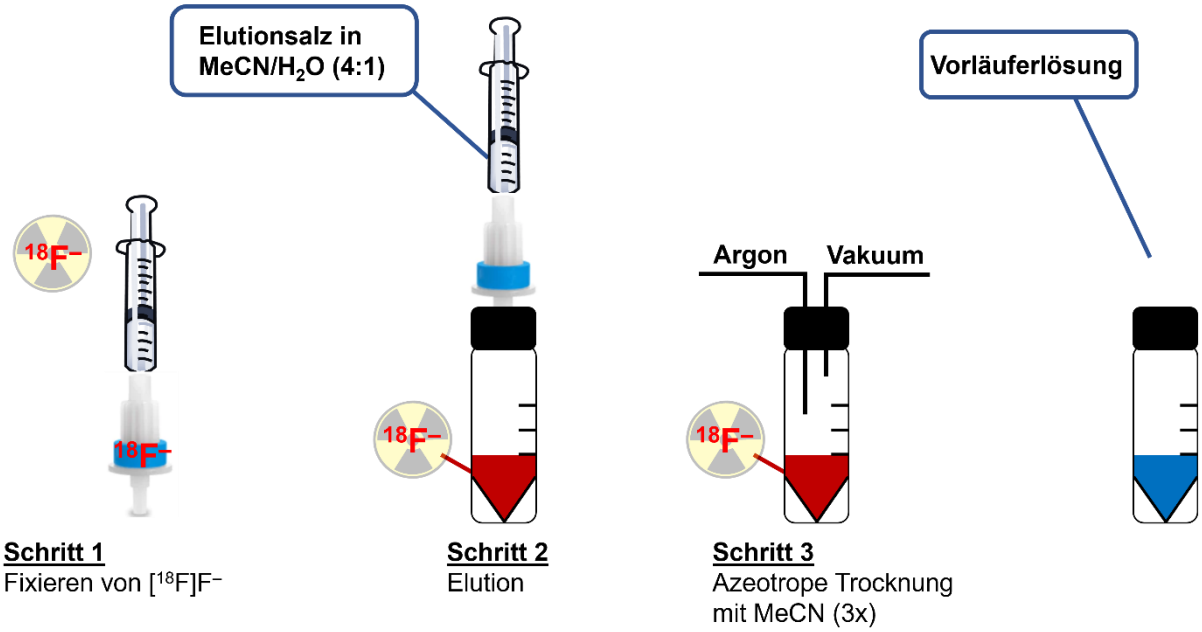

Abbildung 9: Konventionelle Trocknungsprozedur von $[^{18}F]F^-$ für die nukleophile Substitution.

In der Regel wird das wässrige $[^{18}F]F^-$ dafür zunächst auf einer Anionenaustauscher-Kartusche fixiert, um $[^{18}O]H_2O$ zu recyceln. Im Anschluss erfolgt die Elution von der Kartusche mit einer Lösung eines Elutionssalzes wie K_2CO_3, Cs_2CO_3 oder einem Tetraalkylammoniumsalz in H_2O oder MeCN/H_2O (4:1). Das wässrige Lösungsmittel wird dann in Anwesenheit von Kryptofix oder 18-Krone-6 bei Temperaturen von 80–100 °C unter verminderten Druck und im Argonstrom entfernt. Der Abdampfschritt wird noch zwei Mal mit trockenem MeCN wiederholt, wodurch $[^{18}F]F^-$ in „nackter" Form als reaktives Nukleophil erhalten wird. Der Kryptand dient als Phasentransferkatalysator, um das $[^{18}F]F^-$ in ein organisches Lösungsmittel zu überführen und die Reaktivität zu steigern (**Schema 2**)

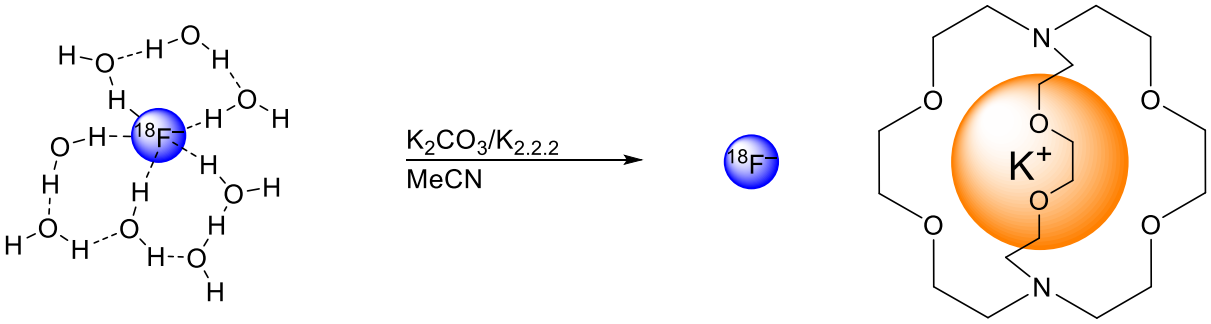

Schema 2: Azeotrope Trocknung von $[^{18}F]F^-$ über K_2CO_3 und $K_{2.2.2}$ in trockenem MeCN.

Die zugegebene Base verhindert, dass während der Trocknungsprozedur das leicht flüchtige [^{18}F]HF entsteht und beim Abdampfschritt ebenfalls entfernt wird. Insgesamt ist die azeotrope Trocknung zwar mit einem relativ großen Zeitaufwand verbunden (15–20 min pro Trocknung), hat sich jedoch als gängigste Methode für viele Radiomarkierungsverfahren mit [^{18}F]F$^-$ etabliert.

Als eine weitere Trocknungsprozedur für [^{18}F]F$^-$ wurde von Richarz et al. der „Minimalistische Ansatz“ entwickelt.[50] Statt der aufwendigen azeotrope Trocknung unter stark basischen Bedingungen kann das dabei [^{18}F]F$^-$ gezielt auf einer Kartusche und mit minimalen Aufwand getrocknet werden. Hierzu wird das [^{18}F]F$^-$ ebenfalls auf einer Anionenaustauscher-Kartusche fixiert. Das Restwasser wird durch Spülen mit trockenem MeOH entfernt und die Kartusche anschließend mit Luft getrocknet. Danach kann die Elution des [^{18}F]F$^-$ mit einem Onium-Vorläufer in MeOH ohne zusätzlichen Einsatz einer Base durchgeführt werden. Nach Entfernen des MeOH bei 60 °C und unter verminderten Druck ist jegliches Wasser innerhalb von 5 min entfernt. Nach Zugabe eines polaren aprotischen Lösungsmittels (DMF oder DMSO) kann die Radiosynthese bei entsprechender Temperatur und Zeit durchgeführt werden. (**Abbildung 10**)

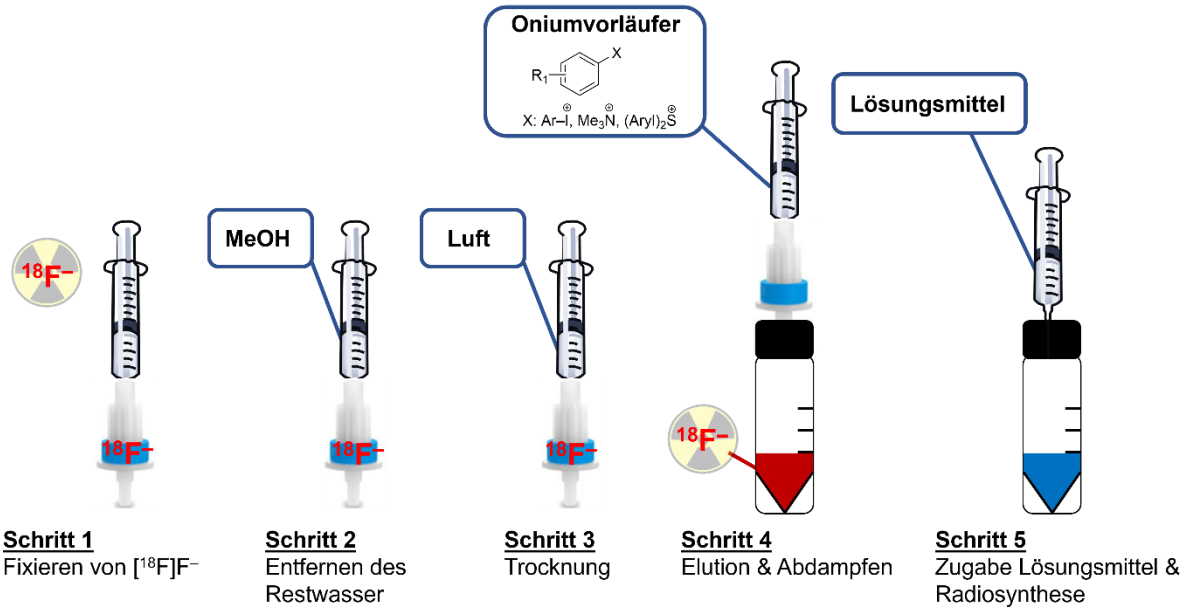

Abbildung 10: Ablauf des „Minimalistischen Ansatzes“ am Beispiel der Radiofluorierung von Oniumsalzen mit [^{18}F]F$^-$.

Alternativ kann diese Trocknungsprozedur auch für andere Vorläufermoleküle durchgeführt werden. Dabei wird wie beschrieben das $[^{18}F]F^-$ auf der Kartusche getrocknet und danach mit einem Tetraalkylammoniumsalz in MeOH eluiert und das MeOH entfernt. Anschließend kann die Vorläuferlösung hinzugegeben und die Radiosynthese durchgeführt werden. Diese alternative Trocknungsmethode führt nicht nur zu einem Zeitersparnis bei der Radiosynthese („Minimalist“: 5 min *vs*. Azeotrope Trocknung: 15–20 min), sondern ermöglicht auch die Radiofluorierung von basenempfindlichen Substraten.

Radiofluorierung an aliphatische Kohlenstoffketten

Durch die nukleophile Radiofluorierung lassen sich Kohlenstoffketten unter Verwendung geeigneter Abgangsgruppen (AG) wie Halogeniden (Cl^-, Br^- oder I^-) oder Sulfonaten (TfO^-, TsO^- oder MsO^-) radiofluorieren. Mechanistisch verläuft diese Reaktion über eine S_N2 ab (**Schema 3**). Dabei greift das nukleophile $[^{18}F]F^-$ das antibindende σ*-Orbital des Moleküls an, gefolgt von einer Eliminierung der vorliegende Abgangsgruppe. Bei einer Radiofluorierung an einem Stereozentrum kommt es im Rahmen der Reaktion zu einer Inversion der Konfiguration (Walden-Umkehr).

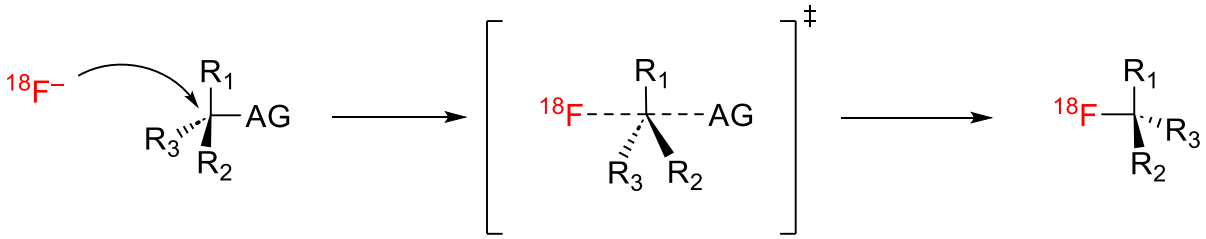

Schema 3: Nukleophile Radiofluorierung über S_N2-Mechanismus unter Inversion der Stereokonfiguration.

Dabei ist zu beachten, dass nukleophile und CH-azide funktionelle Gruppen wie Carbonsäuren, Amine und Alkohole die Radiomarkierung stören können und in der Regel mit einer entsprechenden Schutzgruppe versehen werden müssen. Aufgrund der stark basischen Bedingungen der Radiosynthese und da $[^{18}F]F^-$ neben seiner guten Nukleophilie auch eine sehr starke Base ist, kann es zur Deprotonierung von protischen funktionellen Gruppen kommen. Zusätzlich ist auch die Wahl des Lösungsmittels für die Effizienz der nukleophilen aliphatischen Radiofluorierung entscheidet. Koordinierende Lösungsmittel verringern die Basizität von $[^{18}F]F^-$ und

verhindern nicht erwünschte Nebenreaktionen wie β-Eliminierungen.[51] Zu den bekanntesten klinisch relevanten PET-Tracern, die über die aliphatische nukleophile Radiofluorierung hergestellt werden können, zählen etwa [^{18}F]FDG[52], O-(2-[^{18}F]Fluorethyl)-L-tyrosin ([^{18}F]FET)[53], [^{18}F]Fluor-3-desoxy-L-thymidin ([^{18}F]FLT)[54,55], [^{18}F]Fluorestradiol ([^{18}F]FES)[56,57] und [^{18}F]Fallypride[58] (**Abbildung 11**).

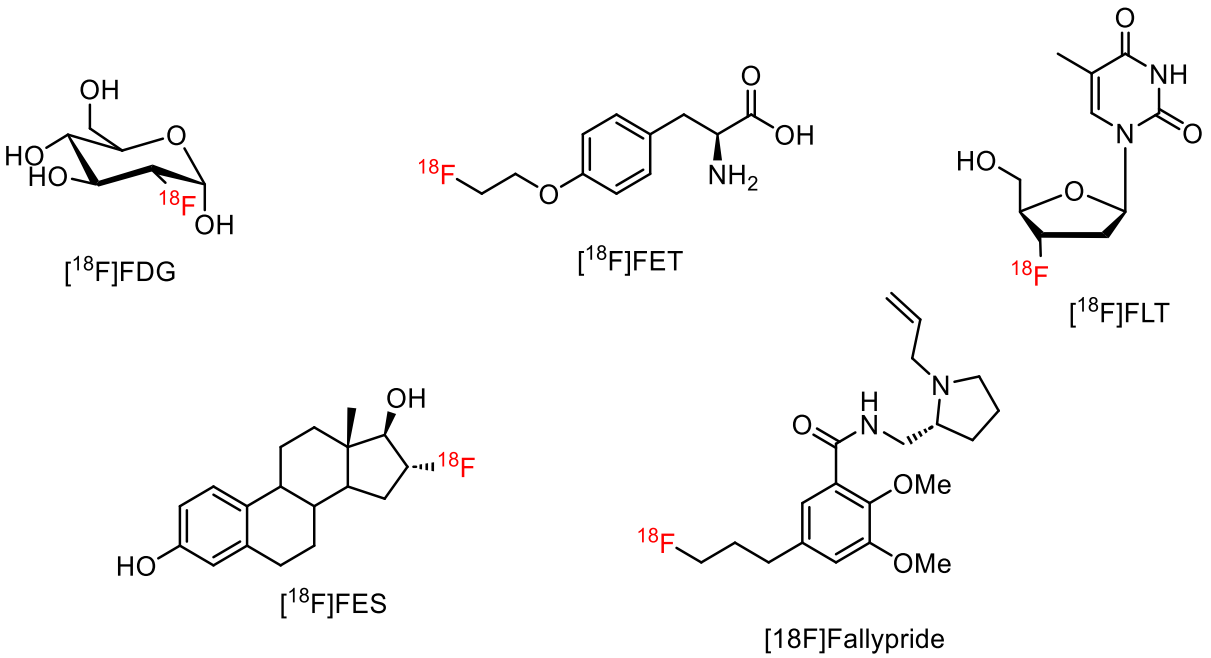

Abbildung 11: Beispiele für klinisch relevante PET-Tracer die mittels Radiofluorierung über S_N2 am aliphatischen Kohlenstoffatom hergestellt werden können.

Im Zuge weiterer Optimierungen zur Steigerung der Effizienz der Radiofluorierung über S_N2 wurden verschiedene weniger basische Salze verwendet, um die Gesamtbasizität der Reaktionslösung herabzusetzen. Zusätzlich findet auch der Einsatz von sterisch anspruchsvollen Alkoholen als Kolösungsmittel Verwendung. Unter Bildung von Wasserstoff-Brücken zum [^{18}F]F$^-$, die schwächer sind als die mit Wasser, kann so die Basizität des Radionuklids ohne Einbußen in der Nukleophilie reduziert werden.[59,60] Dabei hat sich besonders die Verwendung von *tert*-Amylalkohol oder *tert*-BuOH für die Herstellung von Radiotracern mit verbesserten RCAs als praktikabel erwiesen.

Eine alternative Einsatzmöglichkeit von [^{18}F]F$^-$besteht in seiner Verwendung zur Herstellung eines elektrophilen ^{18}F-markierten Synthons durch eine Umpolungsreaktion. Formal betrachtet ist diese Reaktionsklasse der elektrophilen Radiofluorierung zuzuordnen. Da für die Herstellung des Synthons aber [^{18}F]F$^-$

verwendet wird und die Übergangsmetall-vermittelten Radiofluorierungen ebenfalls über eine Umpolungsreaktion ablaufen (siehe **Kapitel 1.3.5**), lässt sie sich besser hier einordnen. Mit diesem Radiofluorierungsprotokoll wurden etwa $[^{18}F]F^-$ (in Form von $[^{18}F]Bu_4NF$) und Tosylbenziodoxol mit einem radiochemischen Umsatz (RCU) von 42% zu [^{18}F]Fluorbenziodoxol umgesetzt (**Schema 4**).[61]

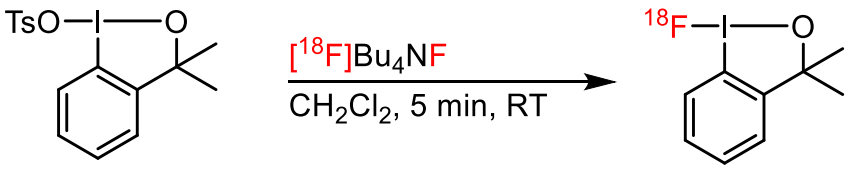

Schema 4: Herstellung von [^{18}F]Fluorbenziodoxol mit [^{18}F]Bu_4NF als elektrophiles Synthon für die elektrophile Radiofluorierung.

Anschließend konnte das elektrophile ^{18}F-Reagenz mit einem nukleophilen Vorläufer über eine Zyklisierungsreaktion umgesetzt werden (**Schema 5**).

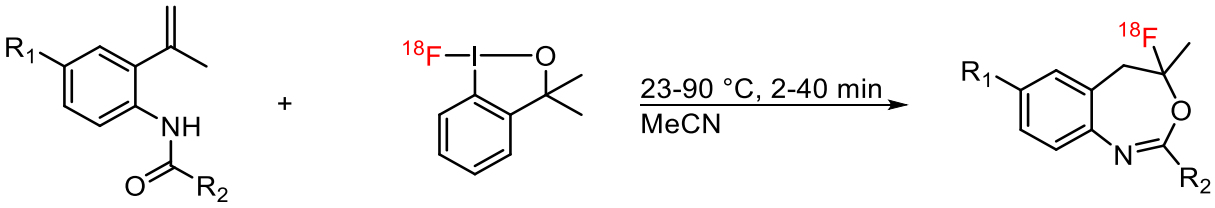

R_1 = Cl, Br, Me
R_2 = Ph, ^{t}Bu, 4-Cl-Ph, 4-Me-Ph

Schema 5: Herstellung von radiomarkierten [^{18}F]Fluorbenzoxazepinen über eine Zyklisierungsreaktion mit [^{18}F]Fluorbenziodoxol.

Obwohl einige Ansätze unter Verwendung dieser Methode veröffentlicht wurden, hat sie bisher keine breite Anwendung gefunden, da die häufig komplexen Synthesen und Selektivitätsprobleme ihren Anwendungsbereich für die Herstellung von Radiotracern stark limitieren.

Nukleophile aromatische Radiofluorierung

Für die Einführung von $[^{18}F]F^-$ in (hetero)aromatische Systeme bietet sich die aromatische nukleophile Substitution an, die typischerweise über den SNAr (Addition-Eliminierung) Mechanismus abläuft. Allerdings können solche Radiofluorierungen nur bei elektronenarmen (Hetero)Aromaten mit einer elektronziehenden Abgangsgruppe durchgeführt werden (**Schema 6**), wodurch ihr Anwendungsbereich erheblich begrenzt wird.

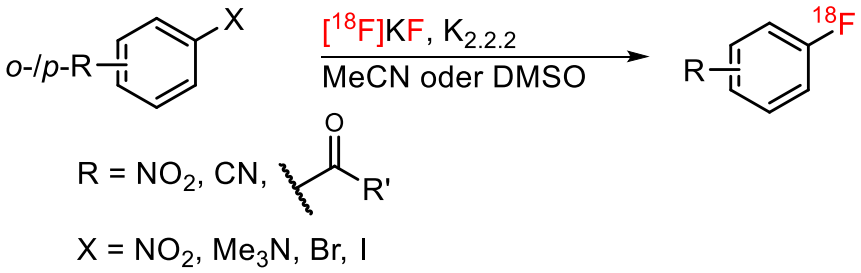

Schema 6: Nukleophile aromatische Radiofluorierung. R: aktivierende Gruppen. X: Abgangsgruppen.

Aus der klassischen organischen Synthesechemie ist bekannt, dass elektronenziehende Substituenten am Aromaten einen –M- und/oder –I-Effekt ausüben und somit die Elektronendichte des Aromaten herabsenken. Dies begünstigt die Zweitsubstitution mit $[^{18}F]F^-$ in der *ortho*- oder *para*-Position über den SNAr-Mechanismus unter Eliminierung der Abgangsgruppe (**Schema 7**). Als klassische Abgangsgruppen zählen Halogenide, Trialkylamine oder NO_2.[48]

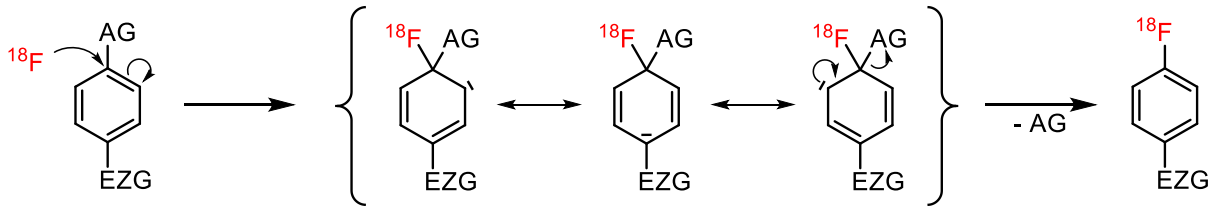

Schema 7: Radiofluorierung von (hetero)Aromaten über den SNAr-Mechanismus. Abkürzungen: AG – Abgangsgruppe, EZG – Elektronenziehende Gruppe.

Um auch elektronenreichere Aromaten radiofluorieren zu können, wurden Protokolle für die ^{18}F-Markierung von Diaryliodoniumsalzen, Aryliodoniumyliden und Triarylsulfoniumsalzen entwickelt (**Abbildung 12**).[62–66]

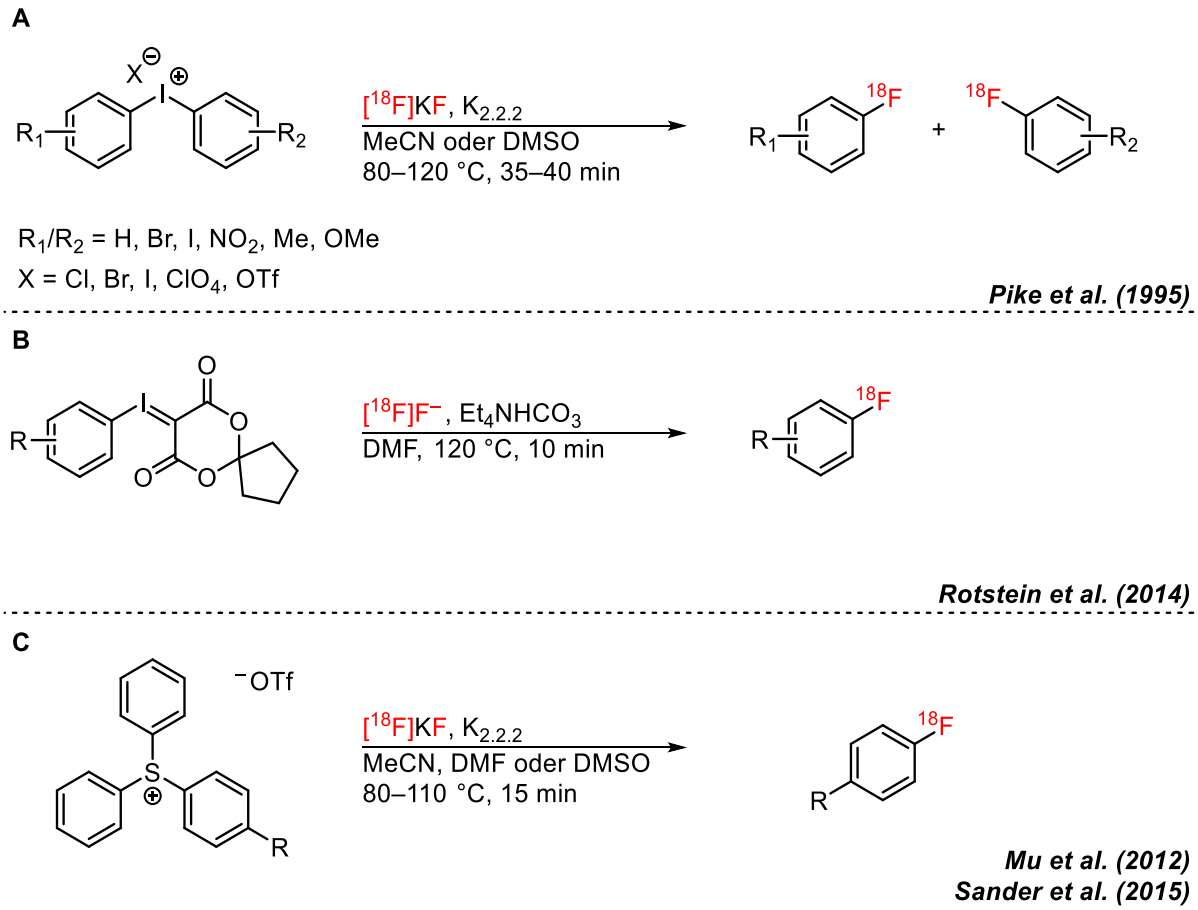

Abbildung 12: Nukleophile aromatische Radiofluorierung über Onium-Vorläufer. A: Diaryliodonium-Salz. B: Spirozyklische hypervalente Aryliodonium(III)-Vorläufer. C: Triarylsulfonium-Salz.

Ein denkbarer Mechanismus für die (Radio)Fluorierung von Iodonium-Salzen wurde von Carroll et al. vorgeschlagen (**Schema 8**).[48,67] [^{18}F]F$^-$ bildet mit dem Iodonium-Salz eine trigonal bipyramidale Struktur, wodurch der nukleophile Angriff von [^{18}F]F$^-$ am äquatorial liegenden Aromaten vonstattengeht und sich das entsprechende Radioprodukt bildet. Unter anderem haben auch quantenchemische Berechnungen ergeben, dass eine Interkonversion des Komplexes stattfindet. Hier tauschen beiden Aromaten die axiale und äquatoriale Position beim Überschreiten der Energiebarriere für einen Konformationswechsel. Dies hat zur Folge, dass bei unsymmetrischen Diaryliodonium-Salzen ein Produktgemisch von zwei Radioprodukten entstehen kann.

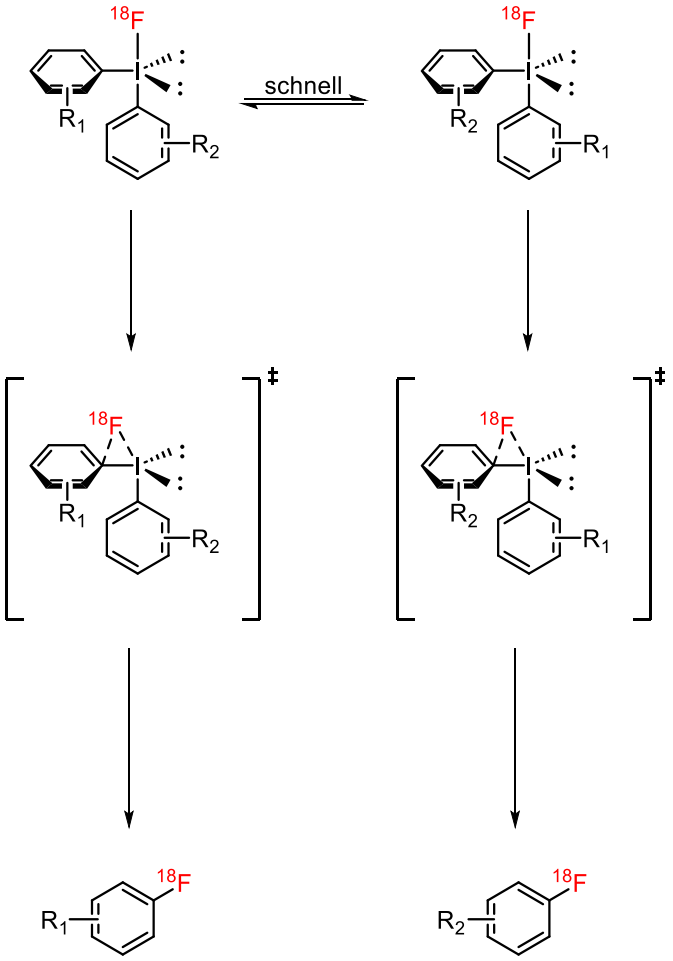

Schema 8: Vorgeschlagener Mechanismus zur Radiofluorierung von Diaryliodoniumsalzen angelehnt an Carroll et al.[67]

Welches Radioprodukt bei asymmetrischen Iodonium-Salzen vorwiegend gebildet wird, hängt von den jeweiligen Substituenten des Aromaten ab. Bei sterisch anspruchsvollen Substituenten ist die äquatoriale Position aufgrund geringerer repulsiver Wechselwirkung bevorzugt. Symmetrische Iodonium-Salze hingegen liefern nur ein einziges Radioprodukt.

1.3.3 Photokatalysierte Radiofluorierung

Bei der photokatalysierten Radiofluorierung werden C–F-Bindungen durch Einsatz von Photokatalysatoren gebildet. Chen et al. entwickelten eine Methode für die ^{18}F-Markierung von substituierten Aromaten durch Verwendung eines Photooxidanten und [^{18}F]Tetrabutylammoniumfluorid ([^{18}F]Bu_4NF als ^{18}F-Quelle (**Schema 9**).

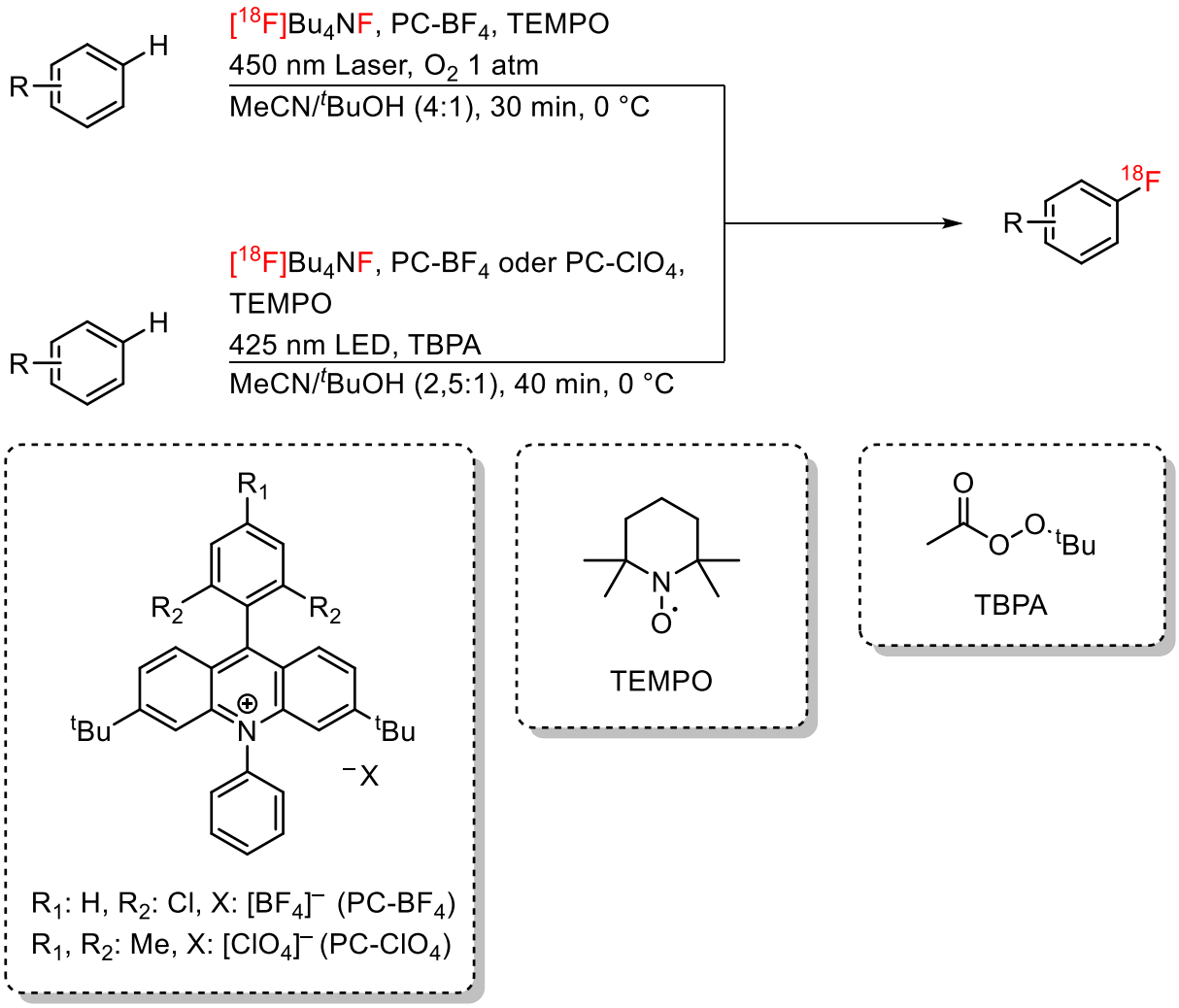

Schema 9: Photokatalysierte Radiofluorierung von Aromaten.

Als Photooxidanten fanden Acridinium-basierte organische Salze Verwendung. Allerdings zeigte sich bei dieser Methode, dass bei Durchführung der Reaktion unter Sauerstoff ein Laser notwendig ist, um das Radioprodukt zu erhalten.[68] Eine spätere Modifikation des Protokolls durch den Einsatz von Peroxoverbindungen wie *tert*-Butylperoxyacetat (TBPA) ermöglichte es, den kostenintensiven Laser durch einfache LEDs zu ersetzen und die Radiosynthesen mit akzeptablen RCAs von bis zu 34% durchzuführen.[69] Die Zugabe on 2,2,6,6-Tetramethylpiperidinyloxyl war notwendig,

um Radikale abzufangen, die potenziell zur Bildung von Nebenprodukten führen könnten. Die Autoren schlugen einen plausiblen Mechanismus über die Bildung eines aromatischen Radikalkations vor, an welches das [^{18}F]F$^-$ nukleophil angreift (**Schema 10**).

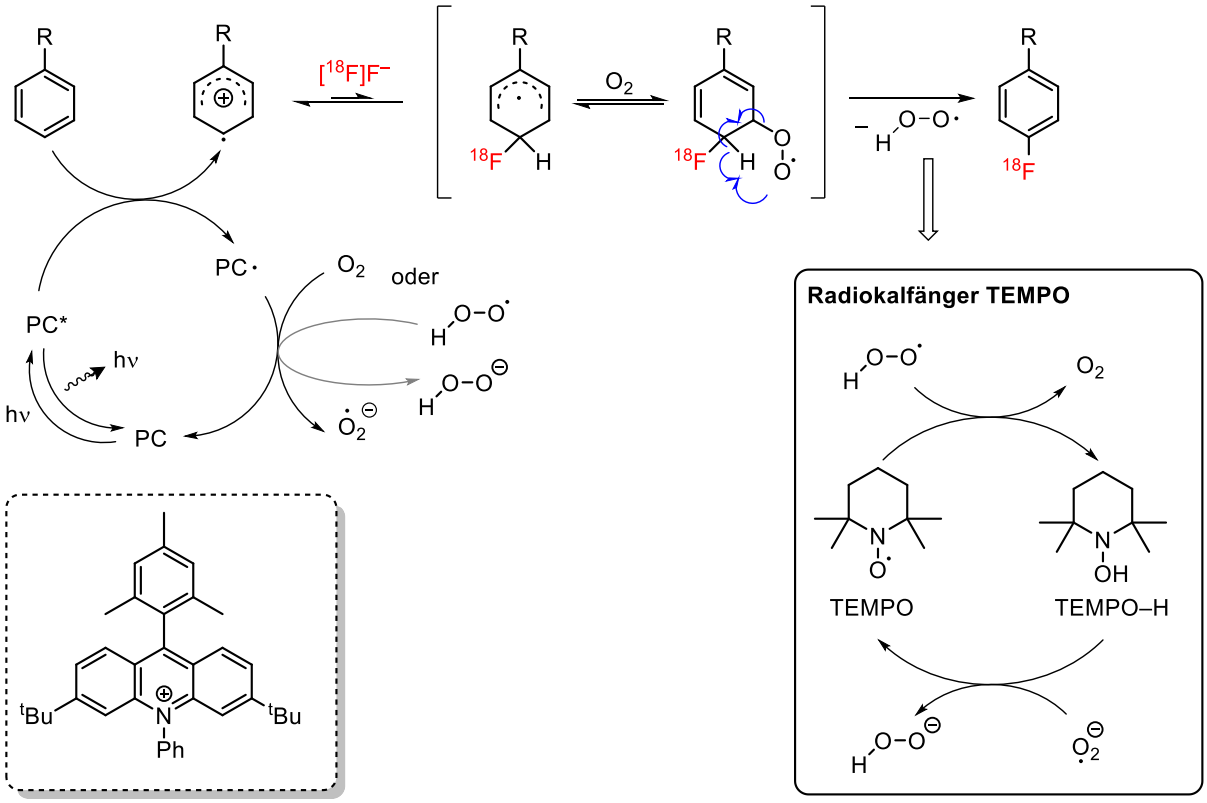

Schema 10: Mechanismus der photokatalysierten Radiofluorierung nach Chen et al.[68]

Die Aktivierung des Photokatalysators erfolgt durch die Absorption eines Photons, wodurch ein Elektron angeregt und in den LUMO-Zustand angehoben wird. Dieser begünstigt eine Ein-Elektronen-Übertragung (engl. „*single electron transfer*“, SET) vom Aromaten, wodurch ein Radikalkation gebildet wird. Danach erfolgt der nukleophile Angriff von [^{18}F]F$^-$ am Aromaten und das freie Radikal kann im Ring mesomer stabilisiert werden. Im Anschluss findet eine Rekombination mit einem Sauerstoffradikal in Orthoposition zum ^{18}F-Substituenten statt, so dass unter Abspaltung eines Hydroperoxoradikals das Radioprodukt entsteht und die Aromatizität wiederhergestellt wird. Die bei der Reaktion entstehenden Radikale werden dann mit TEMPO bzw. TEMPO–H abgefangen.

1.3.4 Heteroatomare Radiofluorierung

^{18}F-Markierung kann nicht nur an Kohlenstoffatomen sondern auch an Heteroatomen durchgeführt werden. Ein Vergleich der Bindungsenergien (**Tabelle 2**) zeigt, dass Fluor mit einigen Heteroatomen ebenso stabile oder stabilere Bindungen als mit Kohlenstoffatomen bilden kann.[49]

Tabelle 2: Bindungsenergien von Heteroatom-Fluor-Bindungen.

X–F-Bindung	Bindungsenergie [kJ/mol]
C–F	536
B–F	766
Al–F	664
Si–F	540
P–F	439
S–F	343

Die Reaktionen zur Bildung heteroatomarer Fluoride weisen in der Regel eine geringere Aktivierungsenergie auf als die Knüpfung von C–F-Bindungen, was mildere Reaktionsbedingungen ermöglicht. Demnach wurden unterschiedliche an einem Heteroatom radiofluorierte Moleküle hergestellt und in Hinblick auf ihre Tauglichkeit als PET-Tracer evaluiert. Einige davon wiesen eine hohe *in vivo*-Stabilität sowie günstige Bildgebungseigenschaften auf und werden heute in der klinischen Diagnostik verwendet. Als die gängigsten und praktikabelsten Methoden für die heteroatomare Radiofluorierung haben sich der ^{19}F/^{18}F-Isotopenaustausch und die Komplexierung von ^{18}F-markierten Metallfluoriden erwiesen.

^{18}F-Markierung am Bor

Eine der ersten Anwendungen von ^{18}F-markierten Fluorboraten wurde in den 60er Jahren von Entzian et al. in einer Arbeit über die Radiosynthese von [^{18}F]Tetrafluorborat und dessen präklinische Evaluation beschrieben.[70] Dennoch fand bis in die 2000er Jahre keine signifikante Weiterentwicklung von Methoden zur Radiosynthese solcher Tracer statt. Erst im Jahr 2005 beschrieben Ting et al. die Radiosynthese von einem [^{18}F]Biotinylarylfluorborat aus dem entsprechenden Arylboronsäurepinakolester (**Schema 11**).[71]

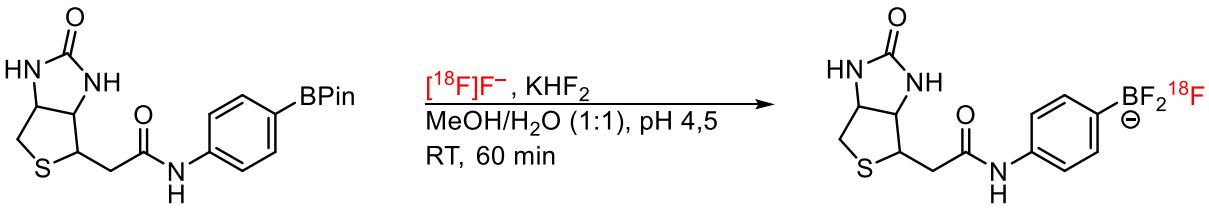

Schema 11: Radiosynthese von Biotinoyl-*p*-aminopenyl-[^{18}F]trifluorborat.

Der Radiotracer konnte unter milden Reaktionsbedingungen und in guten RCAs erhalten werden. Allerding war die A_M durch die Verwendung von KHF_2 und den damit einhergehenden erhöhten Trägergehalt der Reaktionslösung gering. Ein weiterer Aspekt ist die Hydrolysestabilität von Aryltrifluorborate für die Entwicklung weiterer geeigneter Aryl-[^{18}F]BF_3, die in einer Folgepublikation von Ting et al. veröffentlich wurde. Das Resultat der Studie zeigte, dass die Hydrolysestabilität durch elektronenziehenden Substituenten gesteuert und somit längerer Halbwertszeiten im wässrigen Medium erzielt werden konnten.[72]

In den darauffolgenden Jahren wurden weitere Methoden zur Synthese von radiomarkierten Trifluorboraten entwickelt, die eine akzeptable Stabilität und höhere A_M zeigten (**Schema 12**). *Ortho*-phosphonium substituierte Aryl-[^{18}F]Trifluorborate zeigen eine gute Stabilität gegenüber Defluorierung in-vivo und konnten ohne den Einsatz zusätzlicher Träger über ^{19}F/^{18}F-Isotopenaustausch in wässrigem MeCN produziert werden (**Schema 12A**). Nach einer Kristallstrukturanalyse postulierten die Autoren, dass der zwitterionische Charakter durch eine starke Coulomb-Stabilisierung die hydrolytische Stabilität verstärkt.[73] Li et al. und Liu et al. beschrieben ^{18}F-markierte Trifluorborate, die als prosthetische Gruppe für die indirekte Radiofluorierung von Peptiden über Cu(II)-vermittelter [2+3]-Cycloaddition („*Click*“-Reaktion) verwendet werden können (**Schema 12B** und **C**).[74,75]

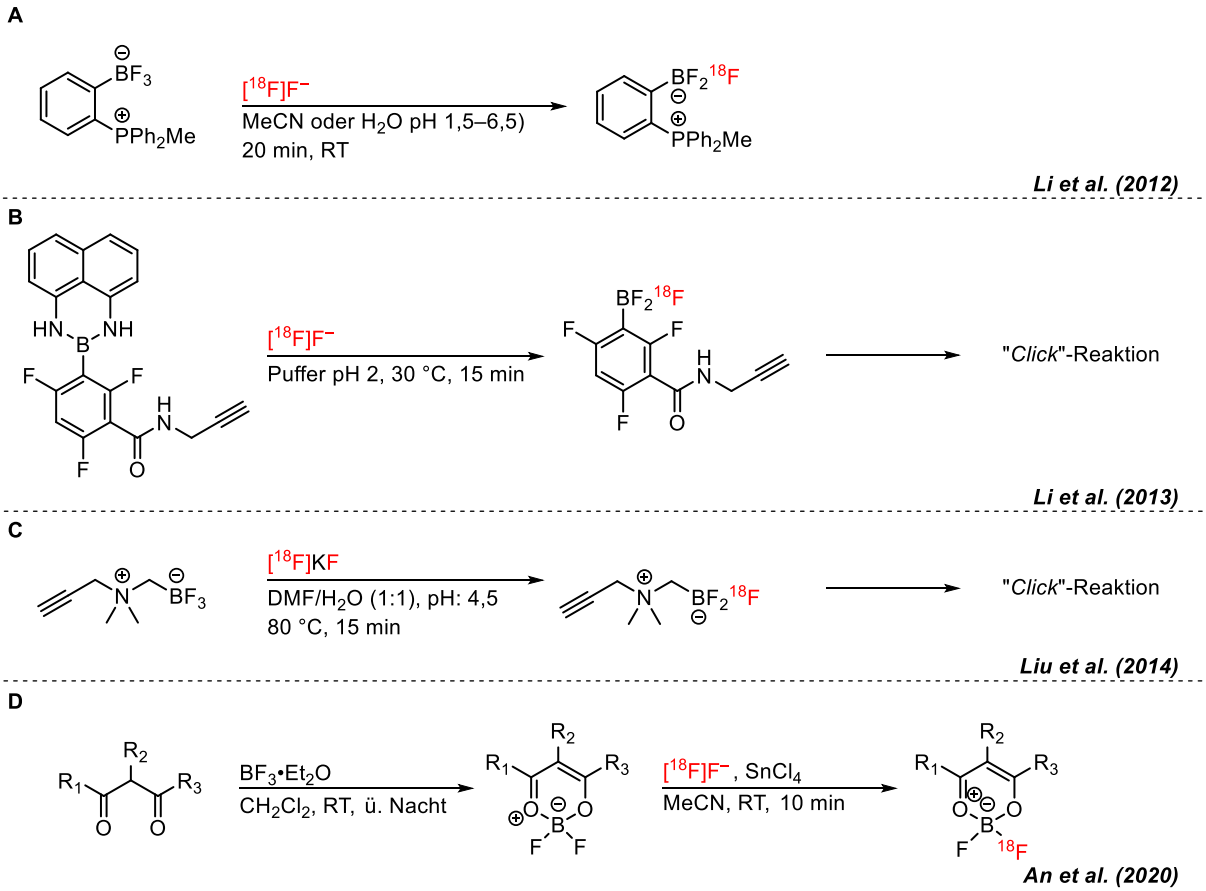

Schema 12: Herstellung von [^{18}F]Trifluorboraten über ^{19}F/^{18}F-Isotopenaustausch.

Eine weitere interessante Vorläuferklasse bilden die 1,3-Diketonderivate, die in vielen Antikrebsmedikamenten und Antibiotika zu finden sind. Diese lassen sich mittels Trifluorborat zum entsprechenden Difluoroxaborin überführen und anschließend mittels ^{19}F/^{18}F-Isotopenaustausch radiomarkieren (**Schema 12D**).[76]

[^{18}F]Metallfluoridkomplexe am Beispiel von [^{18}F]AlF

^{18}F-markierte Metallfluorid-Komplexe ([^{18}F]MF-Komplexe) werden für die Herstellung von radiofluorierten Peptiden häufig benutzt. Diese werden über einen Linker mit einem Chelator verknüpft, durch welchen das [^{18}F]MF bei der Radiosynthese komplexiert wird. Einen wichtigen Vertreter der [^{18}F]MF stellt aufgrund der starken Het–F-Bindungsenergie (**Tabelle 2**) das [^{18}F]AlF dar, welches mit pentadentaten Chelatoren thermodynamisch stabile und kinetisch inerte Komplexe bildet. McBride et al. veröffentlichten 2009 erstmalig ein Protokoll zur Verwendung von [^{18}F]AlF für die Herstellung von [^{18}F]AlF-1,4,7-Triazacyclononan-1,4,7-triessigsäure (NOTA)-Peptid-Konjugaten.[89] Aber auch andere Chelatoren wie 1,4,7-Triazacyclononan-1,4,7-diessigsäure (NODA) und 2-[1,4,7-Triazacyclononan-1-yl-4,7-diessigsäure]-1,5-

pentandiessigsäure (NODAGA) bilden mit [^{18}F]AlF stabile Komplexe, welche Verwendung für die Herstellung von Radiotracern fanden (**Abbildung 13**).[89–94]

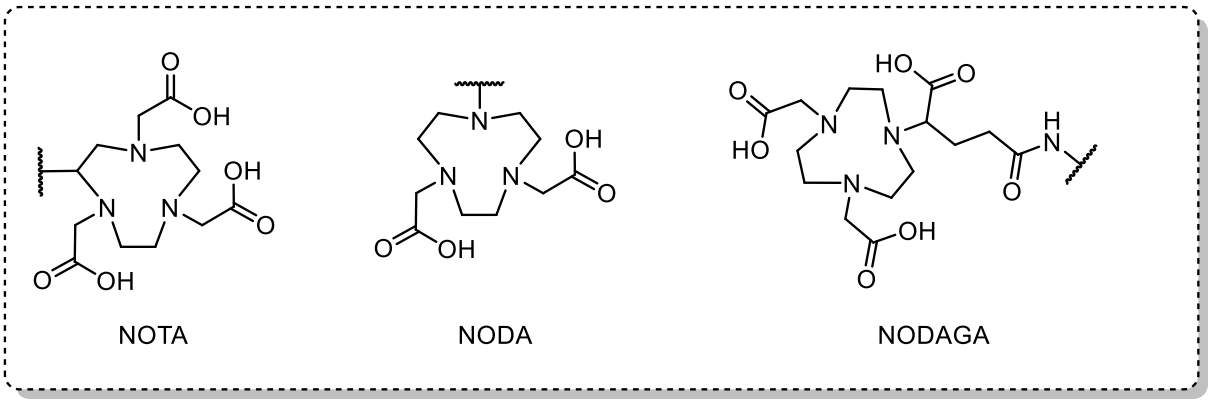

Abbildung 13: Beispiele von Chelatoren für die Komplexierung von [^{18}F]AlF.

Die Synthese von [^{18}F]AlF-Komplexen wird in wässrigen oder organisch-wässrigen Medien bei Temperaturen von bis zu 120 °C durchgeführt. Als organische Lösungsmittel werden aufgrund einer guten Löslichkeit der eingesetzten Substrate meist EtOH und DMSO verwendet[93], während das wässrige Medium aus Puffern mit einem pH-Wert zwischen 4–5 besteht. Letzteres ist entscheidend für den Erhalt von hohen und reproduzierbaren RCAs, da es bei zu sauren Reaktionslösungen (pH<4) zur Bildung von leicht flüchtigem [^{18}F]HF kommen kann, während ein zu basischer pH-Wert (pH>5) zur Bildung von Aluminiumhydroxiden führt (**Abbildung 14**).[95,96]

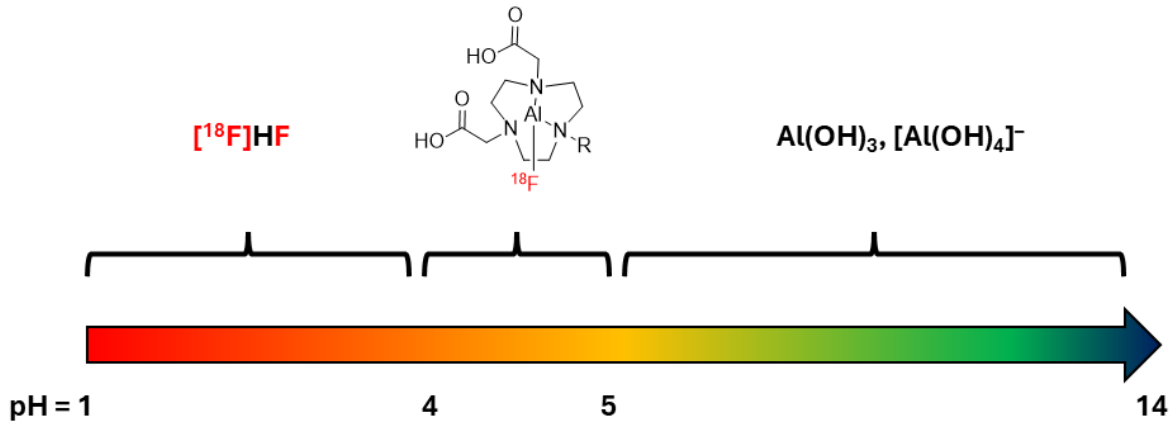

Abbildung 14: pH-Abhängigkeit der Komplexbildung von [^{18}F]AlF durch Chelatoren und der Bildung von [^{18}F]HF und Aluminiumhydroxiden.

Als ^{18}F-Quelle kann sowohl [^{18}F]NaF als auch das Targetwasser mit [^{18}F]F$^-$ direkt nach der Bestrahlung verwendet werden. Letzteres hat allerdings den Nachteil, dass Spuren andere Metallionen, die als Verunreinigung im Targetwasser vorhanden sind, vom Chelator komplexiert werden können, wodurch weniger Vorläufer für die Radiosynthese zur Verfügung steht. Daher wird das [^{18}F]F$^-$ vor der Radiosynthese auf einem Anionenaustauscher-Harz fixiert und so von Metallverunreinigungen befreit. Die darauffolgende Elution kann dann im Anschluss mit 0,9% NaCl oder einem Puffer bei pH 4–5 erfolgen, welcher auch als Lösungsmittel für die Radiosynthese dient. Anschließend erfolgt die Zugabe von $AlCl_3$ und Vorläufer, und nach Erhitzen der Reaktionslösung wird der entsprechende Radiotracer erhalten. Mit diesem Protokoll konnten Radiotracer für die Bildgebung von neuroendokrinen Tumoren ([^{18}F]AlF-NOTA-Octreoid), Prostata-Tumoren ([^{18}F]AlF-NOTA-PSMA) und Tumor-assoziierten Fibroblasten ([^{18}F]AlF-FAPI-42) hergestellt werden.[97–99]

Dennoch bleibt die hohe Temperatur bei der Radiosynthese ein Flaschenhals, da nicht alle Peptide oder Proteine eine gute Temperaturstabilität aufweisen. Somit spielt die Entwicklung neuer Chelatoren, welche eine [^{18}F]MF-Komplexierung bei geringeren Temperaturen ermöglichen, eine wichtige Rolle für die ^{18}F-Markierung von temperatursensitiven Peptiden. In dieser Hinsicht gehören die Chelatoren H_3RESCA, 2-AMPTA und 2-AMPDA-HB zu den vielversprechendsten Kandidaten (**Abbildung 15**).

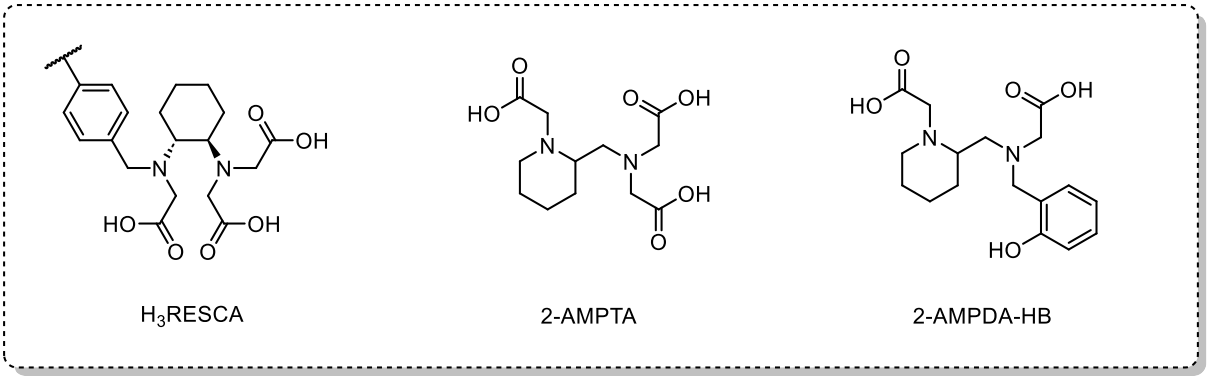

Abbildung 15: Beispiele für Chelatoren für die Komplexierung von [^{18}F]AlF bei Temperaturen von 23–40 °C.

Während [^{18}F]AlF-2-AMPTA-Konjugate nur geringe Blutserumstabilität aufwiesen, konnte für [^{18}F]AlF-2-AMPDA-HB- und [^{18}F]AlF-RESCA-Konjugate eine gute Stabilität mit bis zu 87% intaktem Radiotracer nach 4 stündiger Inkubation in Humanblut gezeigt werden.[100,101]

^{18}F-Markierung am Silizium

Kaliumfluorid, Tetrabutylammoniumfluorid (Bu_4NF) und Fluorwasserstoffsäure sind beliebte Reagenzien zum Entfernen von Silylschutzgruppen, wobei letztere eher selten verwendet wird. Grund dafür ist die hohe Affinität des Siliziums zum Fluor, wodurch Trialkylsilyl-Gruppen eine interessanten Substanzklasse für die ^{18}F-Markierung darstellen. Im Jahr 1985 beschrieben Rosenthal et al. die erste ^{18}F-Markierung von Trimethylchlorsilan mit [^{18}F]Bu_4NF über ein Halogen-Halogen-Austausch zu [^{18}F]Fluortrimethylsilan ([^{18}F]FTMS). Die Reaktion wurde in 65% MeCN in H_2O durchgeführt, wobei gute RCUs von bis zu 80% erreicht wurden.[79] Allerdings wies die Verbindung sowohl eine geringe Hydrolysestabilität ($T_{1/2}$<1,5 min, 20 °C) als auch eine unzureichende In-vivo-Stabilität auf, was sich in einer Anreicherung von [^{18}F]F^- im Knochen wiederspiegelte.[77] Ähnliche Beobachtungen wurden auch von Ting et al. für die Radiosynthese von Biotin-Konjugaten über [^{18}F]Fluortriethylsilylether gemacht. Diese wiesen im Vergleich zu [^{18}F]FTMS eine verbesserte aber dennoch nur moderate Hydrolysestabilität ($T_{1/2}$ ~ 20 min) auf.[78] So folgten weitere Optimierungen durch verschiedene sterisch anspruchsvolle Arylalkyl-Substituenten (**Abbildung 16**).[49]

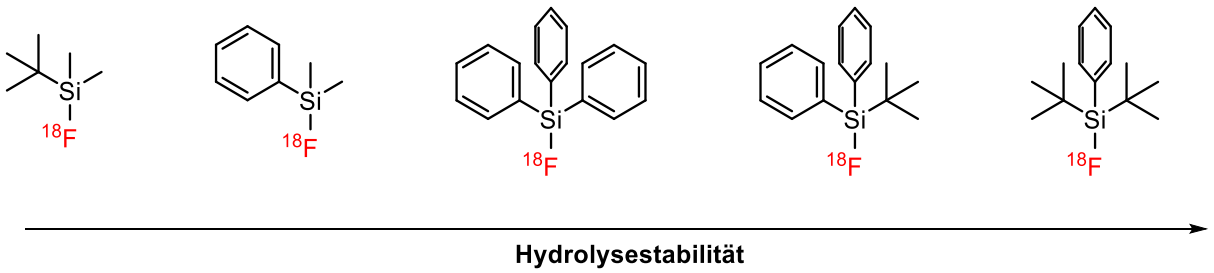

Abbildung 16: Hydrolysestabilität von ^{18}F-markierten Alkyl- und Arylsilanen.

Dabei zeigte sich, dass [^{18}F]Fluorid-*tert*-butyl(het)arylsilane, auch bekannt als Silikonfluorid-Akzeptor (engl. „*silicon-fluoride acceptor*“ – [^{18}F]SiFA) eine ausreichende Stabilität gegenüber Hydrolyse hatten.[79] In der Anwendung wurden diese verwendet, um, z.B., die entsprechende Konjgate mit dem Nukleosid 3-Desoxythimidin, der Aminosäure L-Lysin und dem Octreotid über S_NHet mit *N*-Methylimidazol als Abgangsgruppe direkt zu radiofluorieren.[80] Ebenso lassen sich [^{18}F]SiFA-Tracer über ^{19}F/^{18}F-Isotopenaustausch herstellen (**Abbildung 17**).[81]

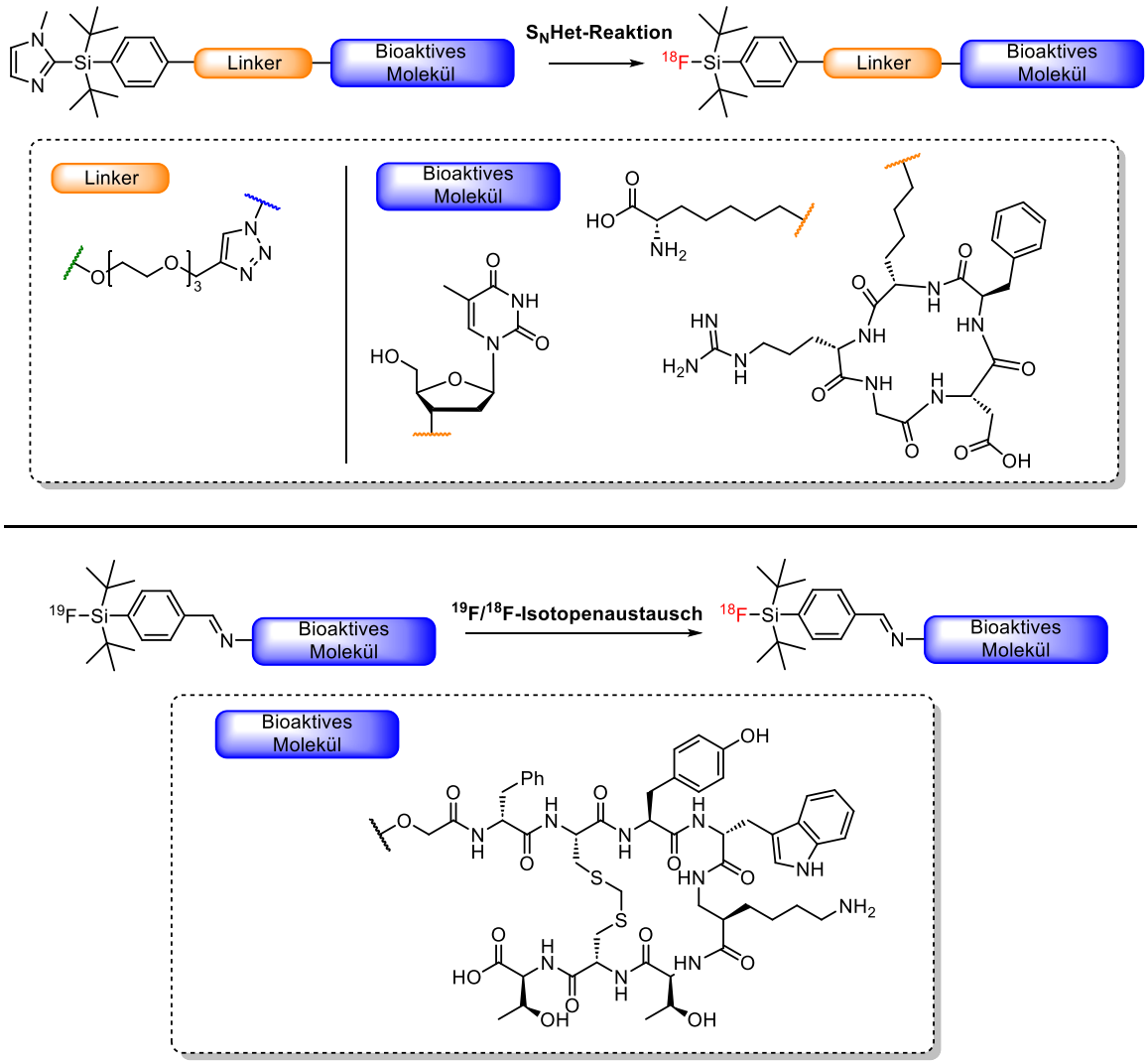

Abbildung 17: Beispiele für die Radiotracersynthesen über S_NHet mit *N*-Methylimidazol als Abgangsgruppe und $^{19}F/^{18}F$-Isotopenaustausch auf dem Si-Atom.

^{18}F-Markierung am Schwefel

Die Radiofluorierung am S(VI)-Atom ergibt [^{18}F]SO_2F-subsituierte Verbindungen, die trotz ihrer schwächeren Bindungsenergie eine gute Stabilität und Reaktivität aufweisen können. Dabei finden die [^{18}F]Sulfonylfluoride, [^{18}F]Fluorsulfate und [^{18}F]Sulfamoylfluoride ihren Einsatz nicht nur als gute prosthetische Gruppen, sondern zeigen auch sehr gute Eigenschaften für die direkte ^{18}F-Markierung unter milden Reaktionsbedingungen. Die Radiosynthese von [^{18}F]Sulfonylfluoriden kann entweder über einen Cl/^{18}F-Austausch oder über die Substitution von Diazoniumsalzen mittels 1,4-Diazabicyclo[2.2.2]octan-1,4-diium-1,4-disulfinat (DABSO) als SO_2-Reagenz durchgeführt werden (**Schema 13**).[82,83]

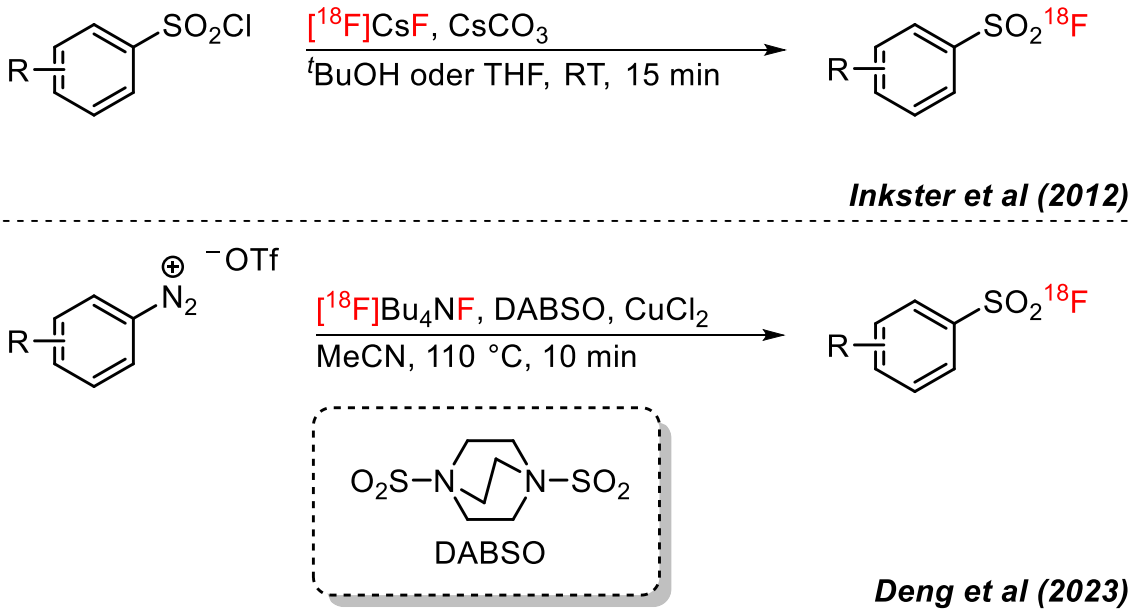

Schema 13: Radiofluorierung von Arylchlorsulfonaten über Cl/^{18}F-Halogenaustausch und Aryldiazoniumsalzen über Substitution mit DABSO.

Obwohl [^{18}F]Sulfonylfluoride eine geringe Hydrolyse- und In-vivo-Stabilität aufweisen und sich somit eine praktische Anwendung als Tracer schwierig erweist, sind sie aufgrund ihrer hohen Reaktivität als ^{18}F-Reagenzien für die Radiofluorierung von Interesse. Nielsen et al (2015) entwickelten eine Methode für eine Desoxyfluorierung von primären und sekundären Alkoholen mit 2-Pyridinylsulfonyfluorid (PyFluor) und übertrugen sie anschließend in die Radiochemie. [^{18}F]PyFluor wurde ausgehen von 2-Pyridinylsulfonylchlorid über einen Cl/^{18}F-Austausch mit gutem RCU von 88% hergestellt und anschließend mit 2,3,4,6-Tetra-*O*-benzyl-D-glucopyranose zur entsprechenden ^{18}F-markierten 5-Desoxylfuorpyranose umgesetzt (**Schema 14**).[84]

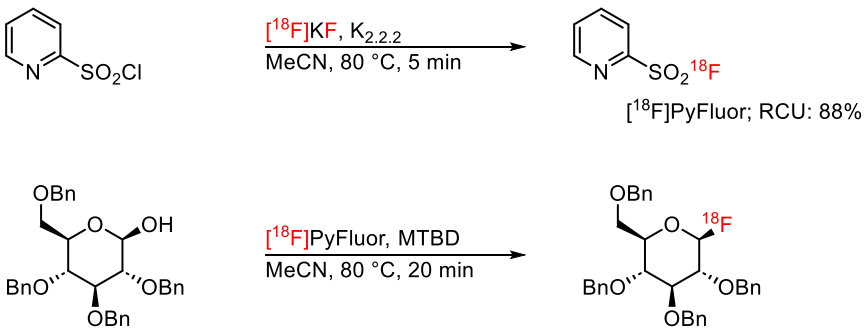

Schema 14: Herstellung von [^{18}F]PyFluor und seine Anwendung zur Synthese von einer ^{18}F-markierten 5-Desxoxyfluorpyranose.

Eine Weiterentwicklung der [^{18}F]Sulfonylfluoride sind die [^{18}F]Arylfluorsulfate, welche eine besser Stabilität und In-vivo-Halbwertszeit besitzen und über ^{19}F/^{18}F-Isotopenaustausch zugänglich sind (**Schema 15A**).[86,87]

A: [^{18}F]Fluorsulfat

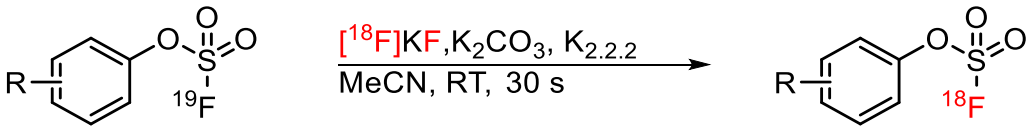

B: [^{18}F]Sulfamoylfluorid

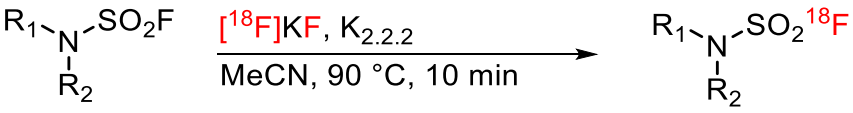

R_1, R_2: H, Alkyl, Aryl

Schema 15: ^{19}F/^{18}F-Isotopenaustausch von: (A) Arylfluorsulfaten zu [^{18}F]Arylfluorsulfate; (B) primären/sekundären Aminen zu [^{18}F]Sulfamoylfluoriden.

Bei der ^{18}F-Markierungsmethode nach Zheng et al erfolgte der ^{19}F/^{18}F-Isotopenaustausch klassisch über K_2CO_3 und $K_{2.2.2}$ nach azeotroper Trocknung. Nach 30 s bei Raumtemperatur konnten die [^{18}F]Arylfluorsulfate mit quantitativen RCUs erhalten werden. Auf diese Weise konnten nicht nur ^{18}F-markierte prosthetische Gruppen für die indirekte Radiomarkierung hergestellt werden, sondern das Protokoll konnte auch für die direkte Radiomarkierung von bioaktiven Molekülen angewendet werden.[86] Walter et al modifizierten das Protokoll durch die Verwendung des „Minimalistischen Ansatzes“ und führten Studien mit verschiedenen Elutionssalzen, Reaktionstemperaturen und Reaktionszeiten zur weiteren Optimierung durch. Unter optimierten Reaktionsbedingungen konnte so eine Vielzahl von Substraten mit RCUs von bis zu 93% ^{18}F-markiert werden.[87]

Ein jüngeres Feld, welches derzeit erforscht und evaluiert wird, sind die [^{18}F]Sulfamoylfluoride (**Schema 15B**), die im Vergleich zu [^{18}F]Fluorsulfaten eine verbesserte In-vivo-Stabilität aufweisen sollen. Die Radiosynthese erfolgt ebenfalls über ^{19}F/^{18}F-Isotopenaustausch an der Sulfonyl-Gruppe, wobei diese nicht am Kohlenstoff, sondern am Stickstoff gebunden ist. Jeon et al (2021) wendeten ihr

Protokoll zum $^{19}F/^{18}F$-Isotopenaustausch auf aromatische und aliphatische primäre bzw. sekundäre Amine (30 Substrate) an, wodurch sie die entsprechenden ^{18}F-markierten Verbindungen mit RCUs von bis zu 97% erhielten. Auch die Anwendung für die ^{18}F-Markierung eines Amoxapin-basierten D_2-Rezeptorantagonisten ergab das gewünschte Radioprodukt in einer guten RCA von 53%.[88]

1.3.5 Übergangsmetall-vermittelte Radiofluorierung

Wie im vorherigen Kapitel erwähnt, stellt die Herstellung von ^{18}F-markierten (Hetero)aromaten unter Verwendung von konventionellen Radiofluorierungsmethoden in vielen Fällen eine große Herausforderung dar. Eine Möglichkeit dieses Problem zu überwinden, ist die Verwendung von Diaryliodoniumsalzen, Iodoniumyliden oder Triarylsulfoniumsalzen. Alternativ können für diesen Zweck Übergangsmetall-vermittelte Radiofluorierungsverfahren verwendet werden. Die erste Methode wurde im Jahr 2011 von Ritter et al. beschrieben. Die Autoren verwendeten zur Radiofluorierung von Aryl-substituierten Pd(II)-Komplexen einen hypervalenten ^{18}F-markierten Pd(IV)-Komplex, der aus $[^{18}F]F^-$ über einen Ligandenaustausch produziert wurde (**Schema 16**).[102]

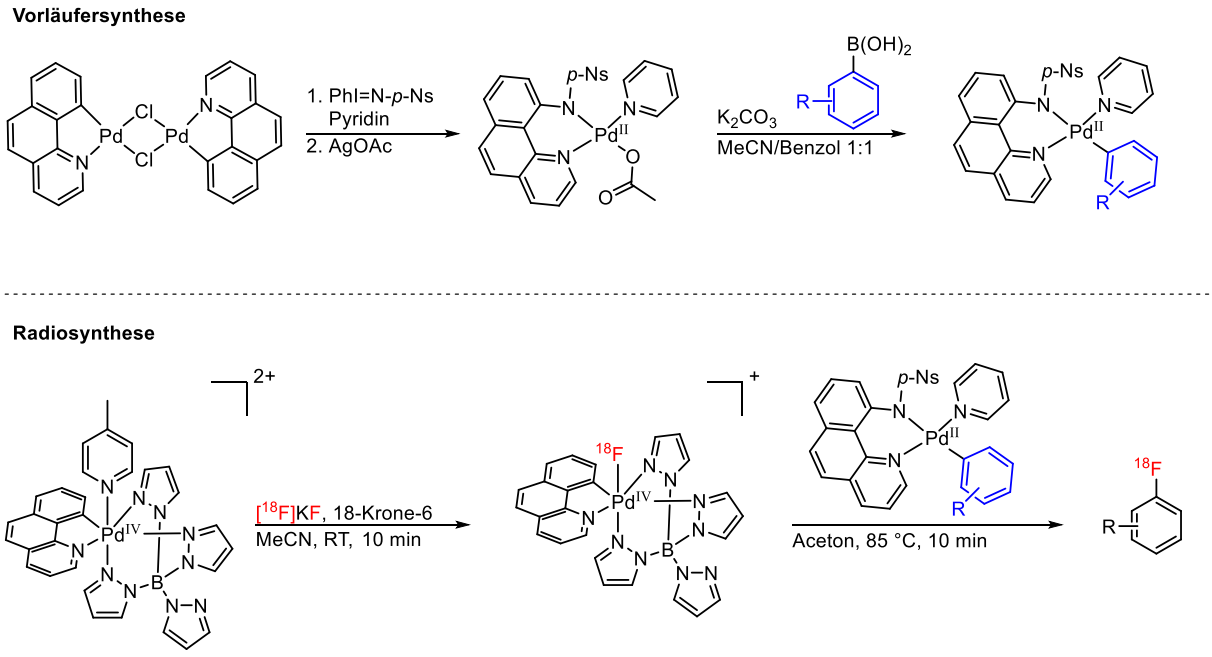

Schema 16: Pd-vermittelte Radiofluorierung von Aryl-Pd(II)-Komplexen mit hypervalenten $[^{18}F]$Pd(IV)-Komplex als elektrophile ^{18}F-Quelle.

Aufgrund der hohen Oxidationszahl des Palladiums erfolgt dabei eine Umpolung des [^{18}F]F^{-}, welches nun einen elektrophilen Charakter besitzt. Bei der anschließenden Reaktion mit einem Pd(II)-Komplex, der das zu radiomarkierende aromatische System trägt, erfolgt eine SET. Dabei wird ein Elektron vom hypervalenten Pd(IV)-Komplex auf den Pd(II)-Komplex übertragen, wodurch zwei Pd(III)-Spezies entstehen. Die darauffolgende Transmetallierung des ^{18}F erfolgt anschließend auf den Pd(III)-Komplex mit dem zu radiomarkierenden Aromaten. Nach einem weiteren SET besitzt dieser Komplex die Oxidationsstufe +IV, woraufhin eine reduktive Eliminierung zum Pd(II)-Komplex erfolgt und dabei die C–F-Bindung geknüpft wird.

Bei der Anwendung dieser Methode wurden Radiotracer mit RCAs von 10–33% erhalten, was einen signifikanten Fortschritt für die Herstellung von ^{18}F-markierten elektronenreichen Aromaten darstellte. Sowohl die Herstellung des Vorläufers als auch die Radiosynthese selbst sind jedoch verhältnismäßig aufwendig. So müssen die zu verwendenden Vorläufer zunächst in einen Pd(II)-Komplex eingebaut werden, dessen Synthese sich nicht immer einfach gestaltet. Ebenso sind die entsprechende Pd(II) und Pd(IV)-Komplexe gegenüber Luft und Feuchtigkeit sehr empfindlich, was ihre Anwendbarkeit für die Tracer-Herstellung stark beeinträchtigt.

Als eine für praktische Anwendungen besser taugliche Alternative zu der Pd-vermittelten Radiofluorierung wurde von Ritter et al. ein Protokoll für die Ni-vermittelte ^{18}F-Markierung vorgeschlagen.[103] Bei diesem Ansatz wird die Herstellung der elektrophilen ^{18}F-Quelle über den Pd(IV)-Komplex durch den Einsatz einer hypervalenten Iodverbindung als Oxidationsmittels umgangen. Die Reaktion kann somit in Anwesenheit des Ni(II)-Komplexes, welcher den Aromaten zur Radiofluorierung enthält, als Eintopf-Reaktion durchgeführt werden (**Schema 17**).

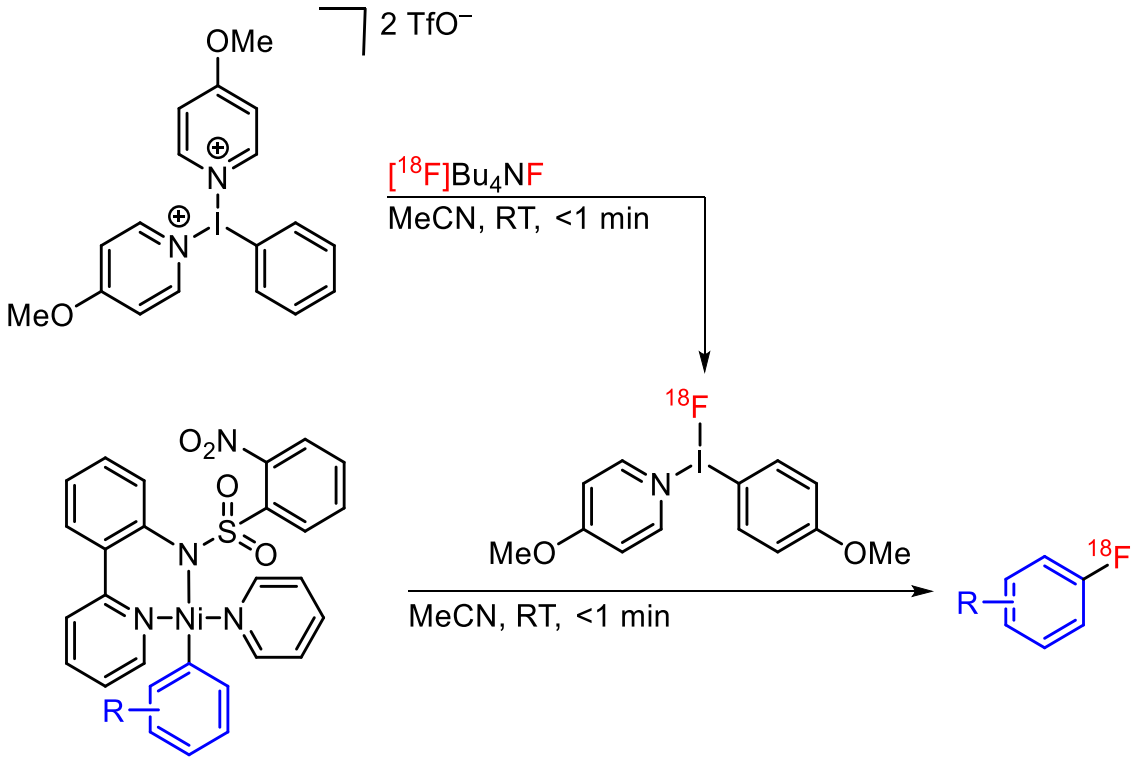

Schema 17: Ni-vermittelte Radiofluorierung.

Die Reaktion verläuft über einen Ni(II)/Ni(IV)-Mechanismus, bei dem nach Umsetzung des Oxidants zur hypervalenten Iod-Verbindung das elektrophile ^{18}F aus dieser in den Ni(II)-Komplex (unter Oxidation zum Ni(IV)-Komplex) übertragen wird. Nach der darauffolgenden reduktiven Eliminierung wird schließlich das [^{18}F]Arylfluorid erhalten. Aufgrund der geringen thermischen und Hydrolysestabilität des Iod-Oxidants erwies sich diese Methode für die ^{18}F-Markierung jedoch als nicht praktikabel. So blieben auch nach weiterer Optimierung der Reaktionsbedingungen die erhaltenen RCAs eher niedrig oder bestenfalls moderat.[48]

1.4 Cu-vermittelte Radiofluorierung

Im Gegensatz zu Ni- oder Pd-vermittelten Radiomarkierungsverfahren, die keine Rolle für die praktische Radiochemie spielen, stellen Cu-vermittelte aromatische Radiofluorierungen einen wichtigen Ansatz für die Tracersynthese dar. Cu-vermittelte Fluorierungen von Aryliodiden[104] und -boronsäureestern[105] sind bereits lange bekannt und wurden schließlich auch in die Radiochemie übertragen.

Die ersten Methoden der Cu-vermittelten Radiofluorierung (CVRF) sind auf Arbeiten von Ichishii et al.[106] und Tredwell et al.[107] zurückzuführen, in denen Cu(I)- bzw. Cu(II)-Komplexe für die Radiofluorierung von (Aryl)(mesityl)iodoniumsalzen bzw.

Arylpinakolboronaten (BPin) unabhängig von der Elektronendichte im Aromaten (**Schema 18A** & **B**) verwendet wurden. Kurze Zeit später wurden Protokolle für die CVRF von Boronsäuren[108] [$B(OH)_2$] und Trimethylstannanen[109] ($SnMe_3$) veröffentlicht (**Schema 18C**).

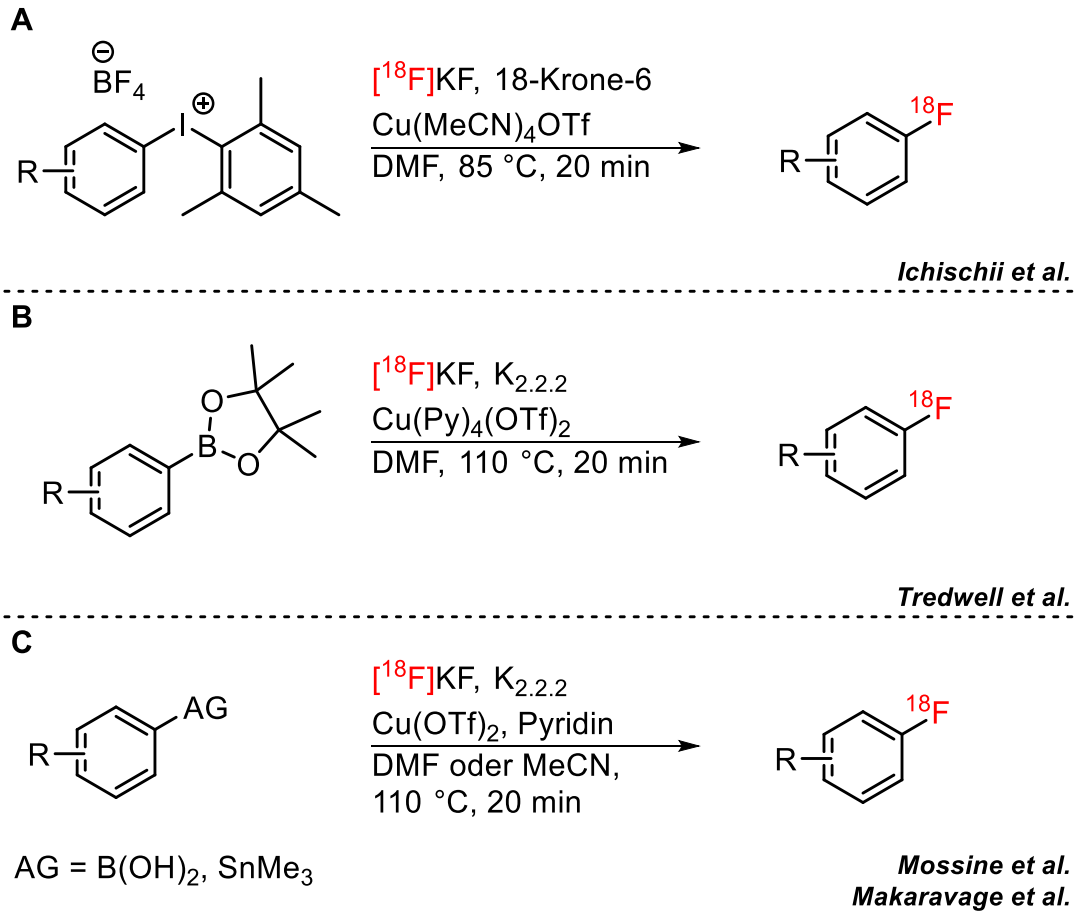

Schema 18: Cu-vermittelte Radiofluorierung von (Aryl)(mesityl)iodoniumsalzen, Aryl-$B(OH)_2$, -BPin und -$SnMe_3$.

Cu-vermittelte Radiofluorierung von (Aryl)(mesityl)iodoniumsalzen

Ichishii et al. beschrieben in ihrer Arbeit den Einsatz von $Cu(MeCN)_4OTf$ als Vermittler für die Radiofluorierung von (Aryl)(mesityl)iodonium-Salzen mit [^{18}F]KF zu den entsprechenden [^{18}F]Arylfluoriden. Das sterisch anspruchsvolle Mesityl fungiert hierbei als gute Abgangsgruppe, wodurch weniger sterisch anspruchsvolle Aromaten ^{18}F-markiert werden können. Die dabei erhaltenen hohen und reproduzierbaren RCUs belegen die gegenüber Pd- oder Ni-vermittelten Protokollen verbesserte Anwendbarkeit von Cu-vermittelten Ansätzen.

Als zugrunde liegender Mechanismus für das sowohl mit Cu(I)- als auch mit Cu(II)-Salzen durchführbare Radiofluorierungsprotokoll wurde von Ichishii et al. ein Cu(I)/(III)-Mechanismus vorgeschlagen. Entscheidet für den Katalysekreislauf ist gemäß des vorgeschlagenen Mechanismus eine Cu(I)-Spezies, welche bei Verwendung von Cu(II)-Salzen zunächst im Rahmen einer Reduktion durch das Lösungsmittel DMF gebildet wird (**Schema 19**).[110]

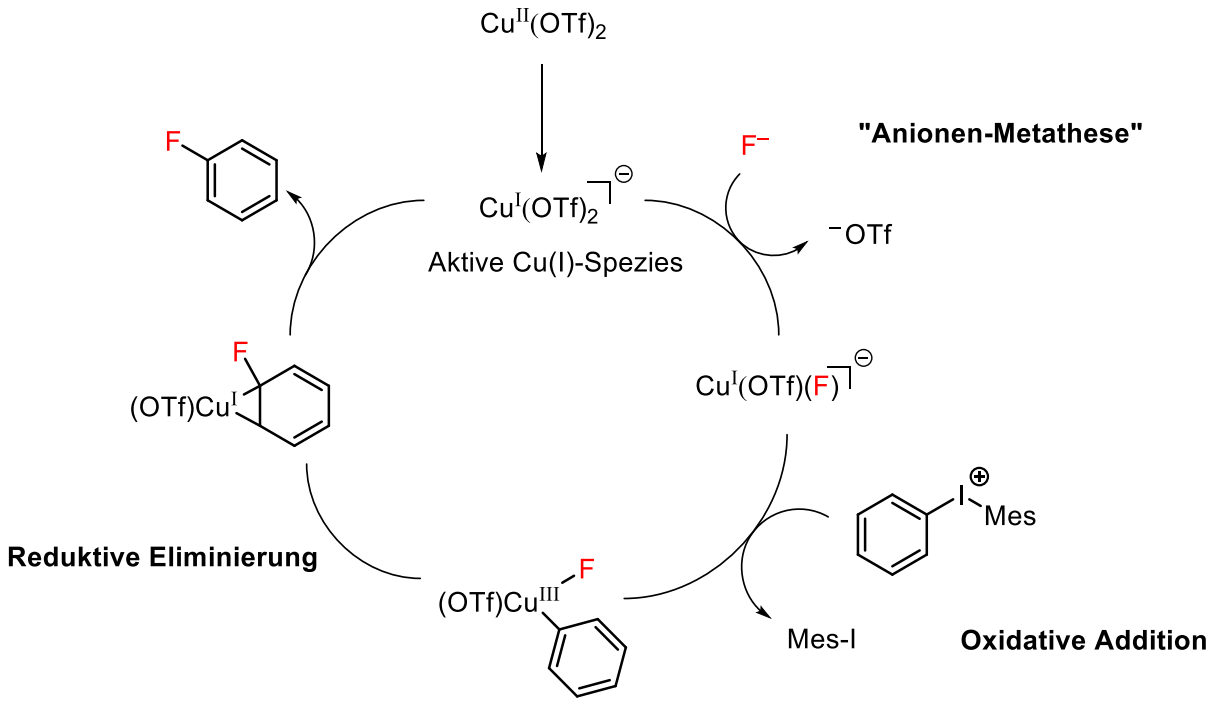

Schema 19: Postulierter Cu(I)/(III)-Mechanismus für die Synthese von Arylfluorid mittels Cu-vermittelte Fluorierung über ein Arylmesityliodoniumsalz nach Ichishii et al.[111]

Durch eine Anionen-Metathese wird aus dieser das Kuprat $[Cu^{I}(OTf)(F)]^{-}$ gebildet, in welches anschließend (unter Wechsel der Oxidationsstufe des Cu von +I zu +III) der Arylrest durch oxidative Addition mit dem Iodoniumsalz eingeführt wird. Im Anschluss folgt die reduktive Eliminierung unter Bildung einer sp^2-C–F-Bindung zum entsprechenden Arylfluorid.[111,112] Als Optimierungsmaßname konnte auch der „Minimalistische“-Ansatz ohne zusätzliche Base auf die Methodik übertragen und angewendet werden. Nach Elution des $[^{18}F]F^{-}$ von der Kartusche und Entfernen von MeOH wurde eine Lösung des Cu(I)-Komplex in DMF zugegeben und die Reaktionsmischung anschließend erhitzt. Dies ermöglichte nicht nur den Einsatz von Basen-sensitiven Cu(II)-Komplexen, sondern führte auch zu einer Erhöhung der RCUs.[113]

Cu-vermittelte Radiofluorierung von $B(OH)_2$-, BPin- und $SnMe_3$-Vorläufer

Mit der Einführung von BPin-Vorläufern durch Tredwell et al. konnte das Spektrum an Vorläufermolekülen für die CVRF erweitert werden. BPin-Vorläufer sind durch einfache Miyaura Borylierungen[114] leicht zugänglich und zeigen meist eine gute Stabilität gegenüber Luftsauerstoff. Des Weiteren lassen sie sich bei niedrigen Temperaturen unter Argon lange lagern. Die mit dem Radiomarkierungsprotokoll nach Tredwell et al. erhaltenen RCUs von 11–83% waren mit den Ergebnissen von Ichishii et al. vergleichbar.[107] Zusätzlich ist der verwendete Cu(II)-Komplex, $Cu(Py)_4(OTf)_2$, unter Normalbedingungen stabil und weniger hygroskopisch als das von Ichishii et al. verwendete $Cu(MeCN)_4OTf$.

Mit der Einführung von $B(OH)_2$ und $SnMe_3$ als weitere Abgangsgruppen für die CVRF durch Mossini et al. und Makaravage et al. konnte der Anwendungsbereich des Verfahrens noch einmal erweitert werden. Im Gegensatz zum Tredwell-Protokoll setzten diese Autoren $Cu(Py)_4(OTf)_2$ nicht direkt ein, sondern griffen auf $Cu(OTf)_2$ und Zugabe von Pyridin in Überschuss zur „*in-situ*“ Generierung von $Cu(Py)_4(OTf)_2$ zurück.

Der genaue Mechanismus, über den die CVRF von $B(OH)_2$-, BPin- und $SnMe_3$-Vorläufern abläuft, ist nicht explizit geklärt. Es ist jedoch festzuhalten, dass alle Autoren gemeinsam einen Cu(II)/Cu(III)-Mechanismus vorschlagen, der auf bekannten Cu-katalysierten Arylierungs- oder Aminierungs-Reaktionen basiert.[115,116] Ye et al. haben einen Mechanismus für die Fluorierung von Aryl-BF_3, -$B(OH)_2$ oder -BPin mit KF und $Cu(OTf)_2$ vorgeschlagen, der möglicherweise bei der CVRF ablaufen könnte (**Schema 20**).[117]

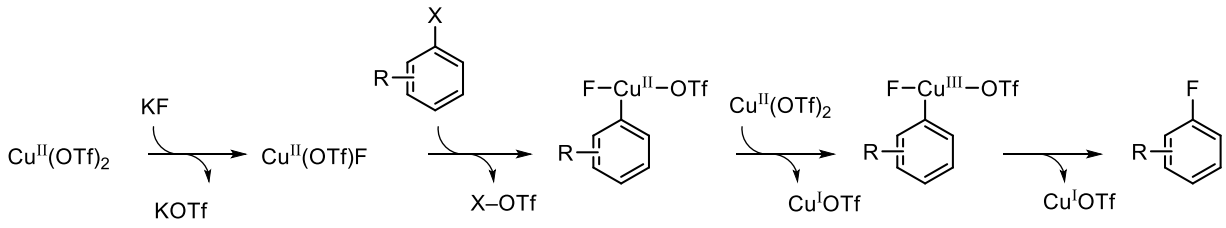

X = BF_3, $B(OH)_2$, BPin

Schema 20: Vorgeschlagener Cu(II)/Cu(III)-Mechanismus für die Cu-vermittelte Fluorierung von Aromaten mit BF_3, $B(OH)_2$ oder BPin als Abgangsgruppe nach Ye et al.[117]

Nach einem Anionenaustausch des Triflats (TfO^-) gegen F^- erfolgt die Transmetallierung des Aromaten zu einem $Cu^{II}(Ar)(OTf)(F)$-Addukt unter Eliminierung der Abgangsgruppe X–OTf. Anschließend findet eine Disproportionierung mit einem weiteren Äquivalent $Cu(OTf)_2$ zum Kuprat $Cu^{III}(Ar)(OTf)(F)$, gefolgt von einer reduktiven Eliminierung zum entsprechenden Arylfluorid statt.

Auch der vorgeschlagene Mechanismus von Zarrad et al. verläuft über einen Anionenaustausch, gefolgt von der Transmetallierung des Aryl-$B(OH)_2$/-BPin bis hin zur reduktiven Eliminierung (**Schema 21**). Der markante Unterschied zum zuvor vorgestellten Mechanismus liegt beim Wechsel der Oxidationsstufe des Cu von +II zu +III. Die Autoren schlugen vor, dass die Oxidation von Cu^{II} zu Cu^{III} durch den während der Radiosynthese vorhandenen Luftsauerstoff erfolgt.[118]

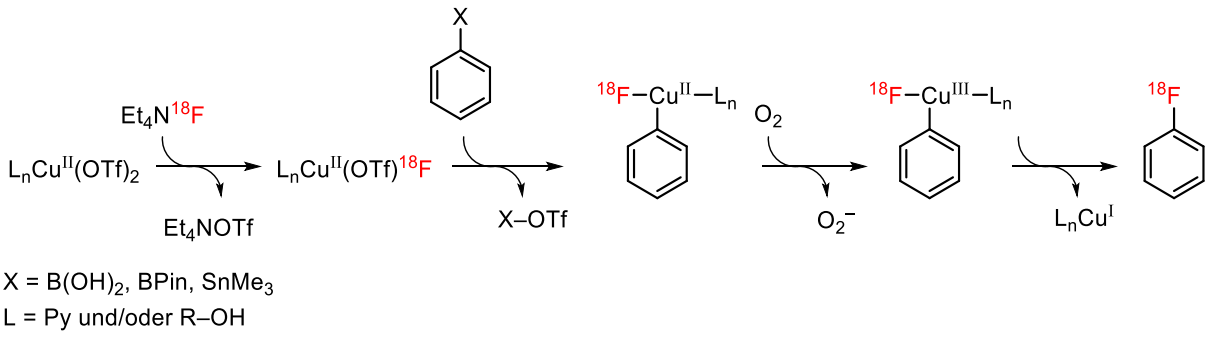

Schema 21: Vorgeschlagener Mechanismus für die Cu-vermittelte Radiofluorierung von Aromaten mit $B(OH)_2$, BPin und $SnMe_3$ als Abgangsgruppe nach Zarrad et al.[118]

Cu-vermittelte Radiofluorierung von Arylhalogeniden

Als weitere potenzielle und interessante Vorläufergruppe für die CVRF dienen die Arylhalogenide, welche neben ihrer guten Stabilität auch kommerziell günstig erhältlich sind. In diesem Fall brachte die Anwendung von konventionellen Cu(I)-Radiomarkierungsvermittlern keinen Erfolg. Erst nach Anwendung von Cu(I)-Komplexen mit einem *N*-heterozyklischen Carben (NHC) als Ligand war die Vorläuferklasse für ein CVRF-Protokoll zugänglich.

Sharninghausen et al. veröffentlichten eine Methode für die Radiofluorierung von Pyridinyl-, Oxazolinyl-, Pyrazolyl- und Cyclohexyl-/Mesitylimin-substituierten Arylhalogeniden über Cu(NHC)OTf mit [^{18}F]KF (**Schema 22**).[119]

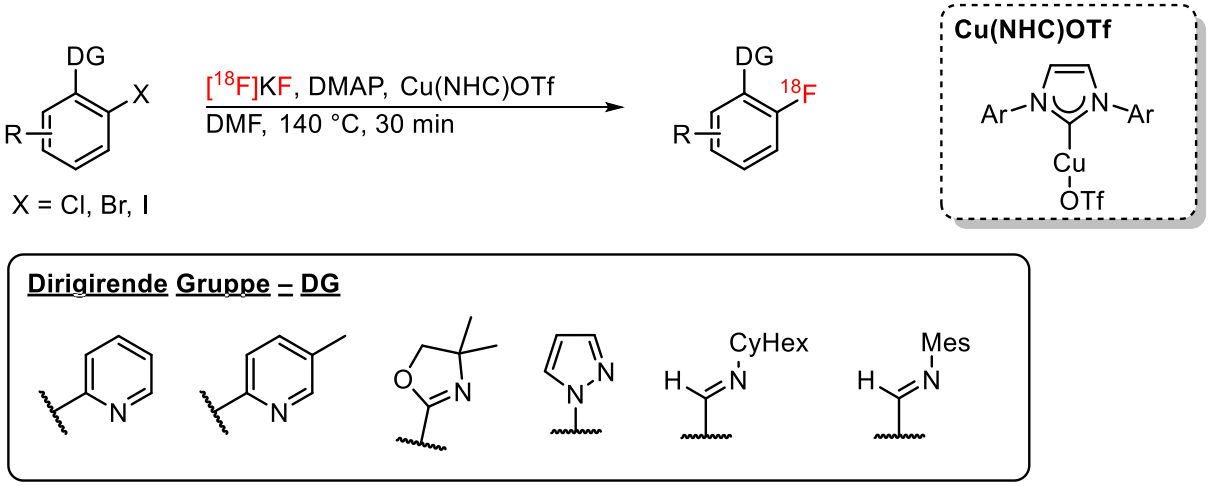

Schema 22: Cu-vermittelte Radiofluorierung von Arylhalogeniden über Cu(NHC)OTf in DMF mit verschiedenen dirigierenden Gruppen.

Die Autoren schlugen einen Cu(I)/Cu(III)-Mechanismus vor, in welchem zunächst $[^{18}F]F^-$ über eine Anionen-Metathese in den Cu(I)-Komplex eingeführt wird. Über eine oxidative Addition des Arylhalogenids entsteht dann das Kuprat $(NHC)Cu^{III}(Aryl)(^{18}F)$ und nach anschließender reduktiver Eliminierung wird das entsprechende $[^{18}F]$Arylfluorid erhalten. Erste mechanistische Untersuchungen durch quantenchemische Rechnungen stützten den vorgeschlagenen Mechanismus.[120] Die besten Ergebnisse mit dieser Methode (RCUs von bis zu 84%) konnten mit Brom oder Iod als Abgangsgruppe erzielt werden, wohingegen Chlor-substituierte Aromaten sich als weniger geeignet erwiesen.

Obwohl dieser neu erschlossene Reaktionsweg die Herstellung ^{18}F-markierter Aromaten ausgehend von den entsprechenden Arylhalogeniden ermöglicht, wird dabei stets eine dirigierende Gruppe benötigt, um die Cu(III)-Spezies vor Disproportionierung zu schützen. Bei der Herstellung von Radiotracern könnte eine solche dirigierende Gruppe jedoch die Affinität oder Selektivität für das biologische Target negativ beeinflussen, so dass ihre Abspaltung nach der Radiosynthese notwendig ist.

Cu-vermittelte Radiolfluorierung über CH-Aktivierung

Während die ^{18}F-Markierung mittels Abgangsgruppen wie Boron-, Stannyl- oder Halogenarylen sehr gut etabliert ist, stellt die Direktmarkierung über CH-Aktivierung eine größere Herausforderung dar. Hierbei ist keine Einführung von Abgangsgruppen in die zu markierenden Aromaten oder aliphatischen Kohlenstoffketten erforderlich, was die Herstellung der Vorläufer erleichtern bzw. verkürzen kann. Zwar sind Strategien der CH-Aktivierung über *N*-[^{18}F]Fluorbenzolsulfonimid beschrieben,[121,122] doch besitzt dieser Ansatz eine geringe Chemoselektivität und führt zu einer geringen A_M des gewünschten Radioproduktes (siehe **Kapitel 1.3.1**). Die Verwendung von nukleophilem [^{18}F]F$^-$ gleicht diese Nachteile aus, erfordert jedoch harsche Reaktionsbedingungen, welche wiederrum die Wahl der Vorläufer stark limitieren. Eine Lösung ist die Verwendung einer Übergangsmetall-vermittelten Methode, um die ^{18}F-Markierung unter milderen Reaktionsbedingungen durchzuführen. Basierend auf den Arbeiten von Daugulis[123] entwickelten Lee et al. eine Cu-vermittelte Methode für die *ortho*-^{18}F-Markierung von 8-Aminochinolin-substituierten Aromaten mit nukleophilem [^{18}F]F$^-$ (**Schema 23**).[124]

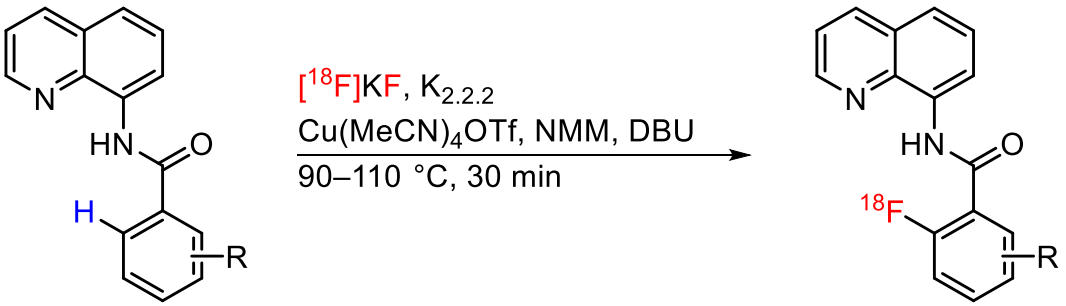

Schema 23: Cu-vermittelte Radiofluorierung von Aromaten über CH-Aktivierung. Abkürzungen: NMM – *N*-Methylmorpholin, DBU – Diazabicycloundecen.

Mit dieser Methode ließen sich elektronenarme, -neutrale und -reiche Aromaten mit guten RCUs von 13–62% radiofluorieren. Ausschlaggebend für den Erfolg der Radiofluorierung war der Substituent des 8-Aminochinolin, welcher als Auxiliar bei der Radiosynthese fungiert. Es wird spekuliert, dass der Mechanismus über Cu(III) abläuft und das Auxiliar die hohe Oxidationsstufe von Cu stabilisiert.[123] Ähnliche Beobachtungen wurden auch bei Pd-katalysierten CH-Aktivierungen gemacht.[125]

„Alkohol-verstärkte“ Cu-vermittelte Radiofluorierung

Das Radiomarkierungsprotokoll für die Einführung von ^{18}F in Aromaten über Cu(II)-Komplexe wurde von Zischler et al. durch den Einsatz protischer Lösungsmittel modifiziert, um die RCAs weiter zu verbessern. Anders als beim „Minimalistischen Ansatz“ unter „*low base*“-Bedingungen erfolgt die Elution beim „Alkohol-verstärkten“ Ansatz direkt in die Reaktionslösung von Vorläufer und Cu(II)-Komplex. In dieser Studie wurden verschiedene Alkohole hinsichtlich ihrer ^{18}F-Elutionseffizienz sowie der RCUs in Beispielradiosynthesen mit verschiedenen Aryl-$B(OH)_2$ und -BPin Vorläufern evaluiert (**Schema 24**). Dabei stellte sich heraus, dass die Verwendung von *n*BuOH in DMA (Verhältnis 1:2) die besten Ergebnisse lieferte.

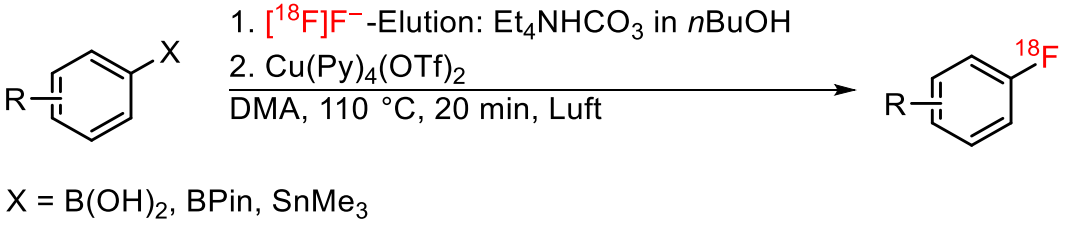

Schema 24: „Alkohol-verstärkte“ Cu-vermittelte Radiofluorierung von Arylboronäuren, -pinakolestern und -trimethylstannanen in DMA/*n*BuOH.

Das modifizierte Radiomarkierungsprotokoll wurde erfolgreich für die Herstellung verschiedener substituierter [^{18}F]Fluoraryle und [^{18}F]Fluorindole mit quantitativen RCUs angewendet. Zusätzlich gelang auch die Herstellung der Radiotracer 6-[^{18}F]Fluor-3,4-dihydroxyphenethylamin (6-[^{18}F]FDA), 6-[^{18}F]Fluor-L-3,4-dihydroxyphenylalanin (6-[^{18}F]FDOPA) und *N*-[(2,5-dimethoxyphenyl)methyl]-*N*-(5-[^{18}F]fluor-2-phenoxyphenyl)acetamid ([^{18}F]FDAA) mit guten RCAs von bis zu 40%. [126] Die Autoren schlugen als mögliche Erklärung für den positiven Effekt des Alkohols vor, dass die Bildung von Wasserstoffbrücken mit der $B(OH)_2$- bzw. BPin-Abgangsgruppe die Transmetallierung in den Cu(II)-Komplex begünstigen könnte.

Neben dem positiven Effekt auf die RCUs ermöglicht die Vermeidung jeglicher Abdampfschritte beim „Alkohol-verstärkten“-Ansatz auch eine kürzere Gesamtsynthesezeit. Allerdings sind für reproduzierbar gute RCUs auch hohe Mengen an Vorläufer (>20 µmol) erforderlich, was durch verstärkte Bildung von chemischen Nebenprodukten die Isolierung der Radioprodukte erschweren kann.

2 Zielsetzung

Das ursprüngliche Protokoll der („Alkohol-verstärkten“) Cu-vermittelten Radiofluorierung (CVRF) ermöglicht einen effizienten und unkomplizierten Zugang zu unterschiedlichen ^{18}F-markierten (Hetero)Aromaten ausgehend von leicht zugänglichen Boronyl- und Stannyl-Vorläufern. Allerdings erfordert die Methode relativ große Vorläufermengen (≥20 µmol), um gute und reproduzierbare radiochemische Umsätze bzw. Ausbeuten zu erhalten. Die damit verbundene Bildung von großen Mengen unerwünschter Nebenprodukte kann zudem die Isolierung der Radioprodukte mittels semipräparativer HPLC erschweren.

Im Rahmen dieser Arbeit sollte eine Reihe neuer Cu(II)-Komplexe aus verschiedenen *N*-heterozyklischen Liganden und Gegenionen hergestellt und ihr Einsatz als Vermittler für die CVRF untersucht werden. Dafür sollte deren Eignung und Effizienz zunächst in Radiosynthesen mit elektronenarmen und -neutralen aromatischen Modellsubstraten evaluiert werden. Anschließend sollten mit den aussichtsreichsten Kandidaten „Ein-Parameter“-Optimierungen der Reaktionsbedingungen in Hinblick auf Temperatur, Reaktionszeit, -Lösungsmittel und weitere Parameter durchgeführt werden.

Schließlich sollte das neue Radiomarkierungsprotokoll für die Herstellung verschiedener klinisch und präklinisch relevanter Radiotracer bei reduzierter Substratmenge eingesetzt werden. Dabei sollte unter anderem ermittelt werden, ob die neue Methode sich auf ein automatisiertes Synthesemodul übertragen lässt. Zuletzt sollte eine Reihe von Radiotracer-Kandidaten, die bei Verwendung des Standard-CMRV-Protokolls nur schwer zugänglich sind, in für eine biologische Evaluation ausreichenden Mengen hergestellt werden.

3 Ergebnisse und Diskussion

3.1 Abdrucke von Publikationen und Manuskripten

3.1.1 [^{18}F]ALX5406: A Brain-Penetrating Prodrug for GlyT1-Specific PET Imaging

Die Aminosäure Glyzin spielt eine entscheidende Rolle in der glutamatergen Neurotransmission des zentralen und peripheren Nervensystems, da sie als obligater Ko-Agonist an der Aktivierung von *N*-Methyl-D-Aspartat-Rezeptoren (NMDARs) beteiligt ist. NMDARs sind hauptsächlich im Kortex und anderen Vorderhinstrukturen stark exprimiert und verantwortlich für kognitive Prozesse, Lernen und Erinnerungsprozesse.[127]

Kognitive Defizite und Schizophrenie-ähnliche Symptomatiken sind mit einer NMDAR-Unterfunktion assoziiert[128–130] und lassen sich auch nach Gabe von NMDAR-Antagonisten wie Phenylcyclidin oder Ketamin beobachten.[131,132] Als pharmakologische Strategien zur Erhöhung der Aktivität von NMDARs kommen neben Agonisten zur direkten Aktivierung der Rezeptoren auch Inhibitoren des Glyzintransporters Typ 1 (GlyT1) in Frage, welcher die Glyzinkonzentration im synaptischen Spalt reguliert. Durch Inhibition dieses Transporters kann daher über eine Erhöhung der Glyzinkonzentration die Aktivität von NMDARs indirekt gesteigert werden. Während die Gabe von NMDAR-Agonisten aufgrund ihrer geringen Selektivität gegenüber anderen Glutamat-Rezeptoren und der damit einhergehenden Neurotoxizität für therapeutische Zwecke ungeeignet ist,[133] sind GlyT1-Inhibitoren ein aussichtsreicher Ansatz für die selektive Steigerung der Aktivität von NMDARs. Obwohl auch die therapeutische Anwendung von GlyT1-Inhibitoren der ersten Generation durch erhebliche Nebenwirkungen erschwert wird[134], sind sie vielversprechende Radiotracer-Kandidaten für die Visualisierung von GlyT1, da die verabreichte Dosis bei der PET-Bildgebung deutlich geringer ist. Ein wichtiger Vertreter ist ALX5407, welches zuvor schon mit ^{11}C radiomarkiert wurde,[135] obwohl bis heute keine präklinischen Studien mit der ^{11}C-markierten Verbindung veröffentlich wurden.

In diesem Projekt wurde [^{18}F]ALX5407 und zusätzlich im Rahmen einer Prodrug-Strategie [^{18}F]ALX5406 über die „Alkohol-verstärkte“ CVRF hergestellt und präklinisch in gesunden Ratten evaluiert.

Das Konzept der Publikation wurde gemeinschaftlich von C. Hoffmann, S. Evcüman und Prof. Dr. B. D. Zlatopolskiy mit Unterstützung von Prof. Dr. B. Neumaier entwickelt. Die organischen Synthesen wurden von C. Hoffmann und S. Evcüman durchgeführt. Die Radiosynthesen wurden von C. Hoffmann und S. Evcüman durchgeführt. Die Optimierung der Radiosynthesen wurden von C. Hoffmann durchgeführt. Die In-vitro-Autoradiographie wurden von A. Schulze und Dr. D. Bier durchgeführt. Die In-vivo-PET-Messungen wurden von Prof. Dr. H. Endepols durchgeführt. Die Ex-vivo-Metabolitenstudie wurde von Dr. S. Humpert durchgeführt. Der Artikel wurde gemeinschaftlich von C. Hoffmann, S. Evcüman, Dr. F. Neumaier, Prof. Dr. B. D. Zlatopolskiy und Prof. Dr. B. Neumaier verfasst.

Im Rahmen dieser Dissertation wurde der Artikel mit allen erhobenen experimentellen und analytischen Daten als Kapitel eingefügt und die dazugehörige „Supporting Information“ im Anhang B hinterlegt.[136]

Copyright

ACS Chemical Neuroscience

pubs.acs.org/chemneuro Research Article

[^{18}F]ALX5406: A Brain-Penetrating Prodrug for GlyT1-Specific PET Imaging

Chris Hoffmann,[⊥] Sibel Evcüman,[⊥] Felix Neumaier, Boris D. Zlatopolskiy, Swen Humpert, Dirk Bier, Marcus Holschbach, Annette Schulze, Heike Endepols, and Bernd Neumaier*

Cite This: *ACS Chem. Neurosci.* 2021, 12, 3335−3346 Read Online

ACCESS | Metrics & More | Article Recommendations | Supporting Information

ABSTRACT: Selective inhibition of glycine transporter 1 (GlyT1) has emerged as a potential approach to alleviate *N*-methyl-D-aspartate receptor (NMDAR) hypofunction in patients with schizophrenia and cognitive decline. ALX5407 is a potent and selective inhibitor of GlyT1 derived from the metabolic intermediate sarcosine (*N*-methylglycine) that showed antipsychotic potential in a number of animal models. Whereas clinical application of ALX5407 is limited by adverse effects on motor performance and respiratory function, a suitably radiolabeled drug could represent a promising PET tracer for the visualization of GlyT1 in the brain. Herein, [^{18}F]ALX5407 and the corresponding methyl ester, [^{18}F]ALX5406, were prepared by alcohol-enhanced copper mediated radiofluorination and studied *in vitro* in rat brain slices and *in vivo* in normal rats. [^{18}F]ALX5407 demonstrated accumulation consistent with the distribution of GlyT1 in *in vitro* autoradiographic studies but no brain uptake in μPET experiments in naïve rats. In contrast, the methyl ester [^{18}F]ALX5406 rapidly entered the brain and was enzymatically transformed into [^{18}F]ALX5407, resulting in a regional accumulation pattern consistent with GlyT1 specific binding. We conclude that [^{18}F]ALX5406 is a promising and easily accessible PET probe for preclinical *in vivo* imaging of GlyT1 in the brain.

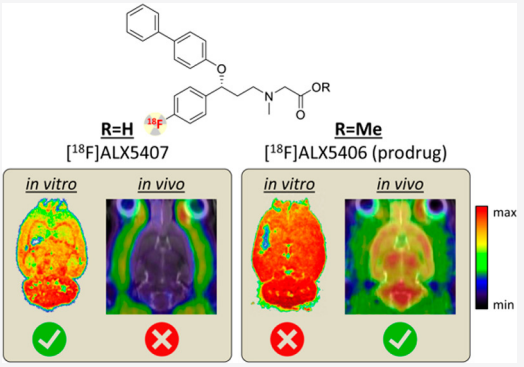

KEYWORDS: *Glycine transporter type 1 (GlyT1), PET imaging, Cu-mediated radiofluorination, microPET, fluorine-18, prodrug*

INTRODUCTION

Glycine is an important neurotransmitter in the central and peripheral nervous system that participates in inhibitory and excitatory neurotransmission. Following its release, glycine can act as an inhibitory neurotransmitter at strychnine-sensitive glycine A receptors, which are mainly located in the spinal cord, cerebellum, and brainstem and involved in motor and respiratory function.[1,2] In addition, glycine can enhance glutamatergic neurotransmission by acting at a strychnine-insensitive glycine B receptor site located on excitatory *N*-methyl-D-aspartate receptors (NMDARs).[3,4] These highly Ca^{2+} permeable ionotropic glutamate receptors are unique in that both glutamate and an obligate coagonist like glycine or D-serine are required for activation, which must be accompanied by membrane depolarization to relieve Mg^{2+}-induced voltage-dependent block of the pore. NMDARs are widely expressed throughout the forebrain and cerebral cortex, where they function as molecular coincidence detectors and are involved in cognition, learning, and memory.[5] NMDAR antagonists like phencyclidine (PCP) or ketamine are well-known to produce schizophrenia-like effects and cognitive deficits,[6,7] and NMDAR hypofunction is thought to contribute to the symptoms associated with schizophrenia.[8−11] As such, enhancement of NMDAR function is regarded as a promising approach for antipsychotic treatment, but glutamate receptor agonists have a high propensity to induce excessive activation, seizures, and excitotoxicity.[12] An alternative, indirect approach to enhance NMDAR function is to increase activation of the glycine B receptor site by high dose treatment with agonists like glycine[13−17] or by inhibition of glycine reuptake in the vicinity of NMDARs. The latter is thought to depend on type-1 glycine transporters (GlyT1), which belong to the family of sodium-dependent solute carrier family 6 (SLC6) transporters and are highly colocalized with NMDARs in neurons and glial cells.[18−20] A number of selective GlyT1 inhibitors, including the metabolic intermediate sarcosine (*N*-methylglycine) and its more potent synthetic analogs like AMG 747, ORG 25935, NFPS, and ALX5407, demonstrated antipsychotic potential in animal models.[21−27] Some of them were also introduced in clinical trials.[28−31] However, the clinical utility of such inhibitors is often limited by adverse effects on motor

Received: April 30, 2021
Accepted: August 13, 2021
Published: August 27, 2021

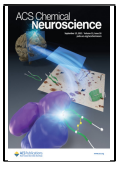

performance and respiratory function produced by moderate to high doses.[22] These side effects have been proposed to result from sustained suppression of GlyT1 in caudal areas of the brain, where increased glycine levels could activate inhibitory glycine A receptors.[22,32,33]

Positron emission tomography (PET) is an important tool for *in vivo* biodistribution and target engagement studies and could aid to elucidate the target occupancy required for clinical efficiency vs potential side effects. As such, sarcosine-based inhibitors like ALX5407 remain potential candidates for *in vivo* imaging of GlyT1. However, while ALX5407 was previously radiolabeled with carbon-11,[34] no biological studies with this tracer have been published so far. Since ALX5407 already contains a fluorine substituent, we focused on radiolabeling with fluorine-18. Besides favorable decay properties, this PET nuclide has a longer half-life, making it well suitable for extended biological studies. In the present work, we describe the preparation of [^{18}F]ALX5407 and its methyl ester [^{18}F]ALX5406 by alcohol-enhanced copper mediated radiofluorination and present the results of *in vitro*, *ex vivo*, and *in vivo* evaluation of both compounds.

RESULTS AND DISCUSSION

Synthesis of the Radiolabeling Precursor 4. The precursor for radiolabeling of the chiral GlyT1 inhibitor (*R*)-*N*-[3-(4′-fluorophenyl)-3-(4′-phenylphenoxy)propyl]sarcosine (ALX5407) was prepared in four steps starting from 4′-bromo-3-chloropropiophenone as follows (Scheme 1). Asymmetric

Scheme 1. Synthesis of the Radiolabeling Precursor 4[a]

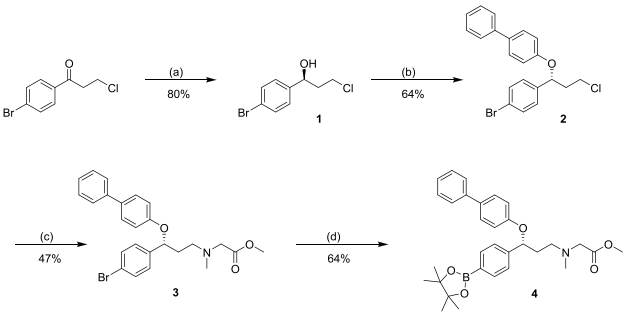

[a]Conditions: (a) $Cu(OAc)_2 \cdot H_2O$, (*S*)-P-Phos, $PhSiH_3$, toluene, 0 °C, 24 h; (b) DIAD, Ph_3P, 4-phenylphenol, THF, 15 h; (c) sarcosine methyl ester, K_2CO_3, KI, MeCN, reflux, 24 h; (d) Pd(dppf)Cl_2, bis(pinacolato)diboron, KOAc, 1,4-dioxane, reflux, 6 h. For the preparation of [^{18}F]ALX5406 and [^{18}F]ALX5407 from **4**, see Scheme 2.

hydrosilylation[35] of this ketone afforded 1-(4-bromophenyl)-3-chloropropan-1-ol (**1**) as a single (*S*)-isomer[36] with an enantiomeric excess (*ee*) of 96.5%. Introduction of the biphenyl moiety via Mitsunobu reaction led to complete inversion of the configuration and resulted in the desired (*R*)-enantiomer **2** (*ee* > 95%). Finally, alkylation of sarcosine methyl ester with **2** followed by Miyaura borylation afforded the radiolabeling precursor **4** in 15% yield over four steps.

Preparation of [^{18}F]ALX5406 and [^{18}F]ALX5407. **4** was radiolabeled using the protocol for copper mediated alcohol-enhanced ^{18}F-fluorination previously developed in our group (Scheme 2).[37−39] Accordingly, [^{18}F]fluoride trapped on an anion exchange resin was eluted with a solution of Et_4NHCO_3 in *n*-BuOH directly into a solution of the radiolabeling

Scheme 2. Synthesis of [^{18}F]ALX5406 and [^{18}F]ALX5407[a]

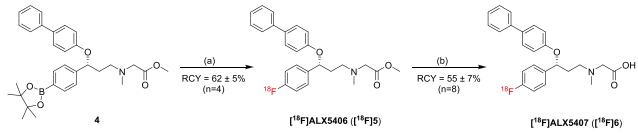

[a]Conditions: (a) elution of $^{18}F^-$ with Et_4NHCO_3 in *n*-BuOH into a solution of **4** and $[Cu(OTf)_2(py)_4]$ in dimethylacetamide (DMA), then 110 °C, 10 min; (b) 6 N NaOH, 110 °C, 10 min. Isolated radiochemical yields (RCYs) after HPLC purification are provided.

precursor **4** and $[Cu(OTf)_2(py)_4]$ in DMA. The reaction mixture was heated for 10 min at 110 °C, furnishing the corresponding radiolabeled ester [^{18}F]ALX5406. The latter was directly hydrolyzed with NaOH at 110 °C for 10 min to afford [^{18}F]ALX5407. After cooling to room temperature, the crude tracer was purified by HPLC and formulated as a ready-to-inject solution. [^{18}F]ALX5407 was obtained in a radiochemical yield (RCY) of 55 ± 7% (n = 8) over two steps with a radiochemical purity of >99%. The molar activity amounted to 20−137 GBq/μmol. [^{18}F]ALX5406, in turn, was produced in a RCY of 62 ± 5% (n = 4), with a radiochemical purity of >95% and a molar activity of 14−74 GBq/μmol. Cu and Pd content in the final products, as determined by ICP-MS, was well below any level of concern (<10 μg of each metal/batch).[40]

Stability of [^{18}F]ALX5406 and [^{18}F]ALX5407 in Human and Rat Blood Plasma. Whereas no significant degradation of [^{18}F]ALX5407 in human and rat blood plasma at 37 °C for 5−60 min occurred (data not shown), a rapid hydrolysis of [^{18}F]ALX5406 to [^{18}F]ALX5407 with $t_{1/2}$ = 12 min was observed in rat blood plasma (Supporting Information, Figures S4 and S5). In contrast, under the same conditions only insignificant demethylation of [^{18}F]ALX5406 took place in human blood plasma within 5−60 min (Supporting Information, Figures S6 and S7).

Lipophilicity. Tracer lipophilicity strongly affects important characteristics like passive blood−brain barrier (BBB) penetration, route of elimination, and nonspecific binding. This parameter is usually described by partition or distribution coefficients between water or aqueous buffer and a water-insoluble solvent like 1-octanol. We determined the distribution coefficients for ALX5406 and ALX5407 (log$D_{7.4}$) using the shake-flask method described by Wilson et al.[41] The experimental log$D_{7.4}$ values were compared with those calculated using the ADMETlab platform[42] (Table 1). The

Table 1. Measured and Calculated log$D_{7.4}$ Values

	calculated log$D_{7.4}$ (ADMETlab)	measured log$D_{7.4}$ (shake-flask method)
ALX5406	1.77	2.53 ± 0.09 (n = 9)
ALX5407	1.19	2.19 ± 0.08 (n = 9)

measured log$D_{7.4}$ values for both compounds were in the range of 2.0−3.5, which is considered to be optimal for high BBB penetration and target to nontarget ratios.[43,44] The predicted values were about one log unit lower but otherwise consistent with the experimental values (Table 1).

Autoradiographic Studies. [^{18}F]ALX5406 and [^{18}F]ALX5407 binding in the rat brain was investigated by *in vitro* autoradiography. As illustrated in Figure 1, autoradiograms obtained with [^{18}F]ALX5406 showed a homogeneous

https://doi.org/10.1021/acschemneuro.1c00284
ACS Chem. Neurosci. 2021, 12, 3335−3346

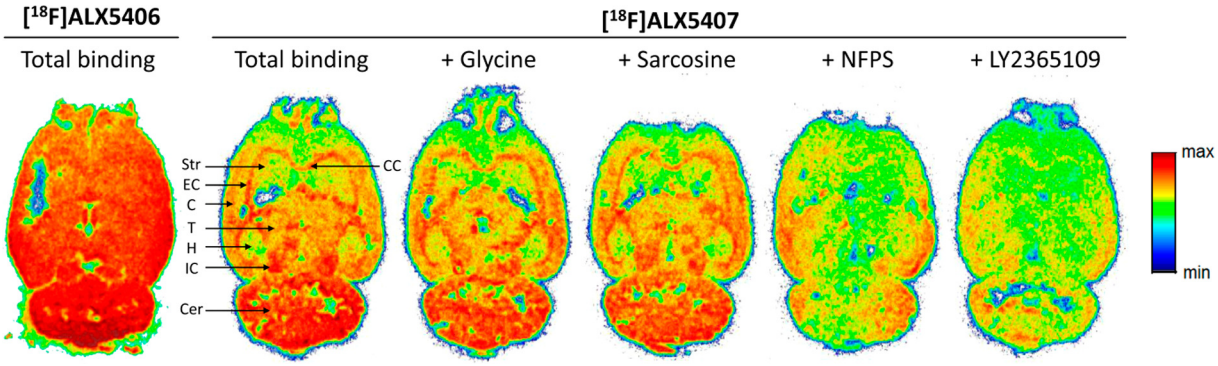

Figure 1. *In vitro* autoradiographs with [^{18}F]ALX5406 and [^{18}F]ALX5407 in rat brain slices. Competitive displacement studies were performed with 5 μM glycine, sarcosine, NFPS, or LY2365109 as indicated above. Regions with high or intermediate tracer binding are shown in red or yellow, while regions with low or no tracer binding are depicted in green or blue, respectively. Abbreviations: C, cortex; CC, corpus callosum; Cer, cerebellum; EC, external capsule; H, hippocampus; IC, inferior colliculus; Str, striatum; T, thalamus.

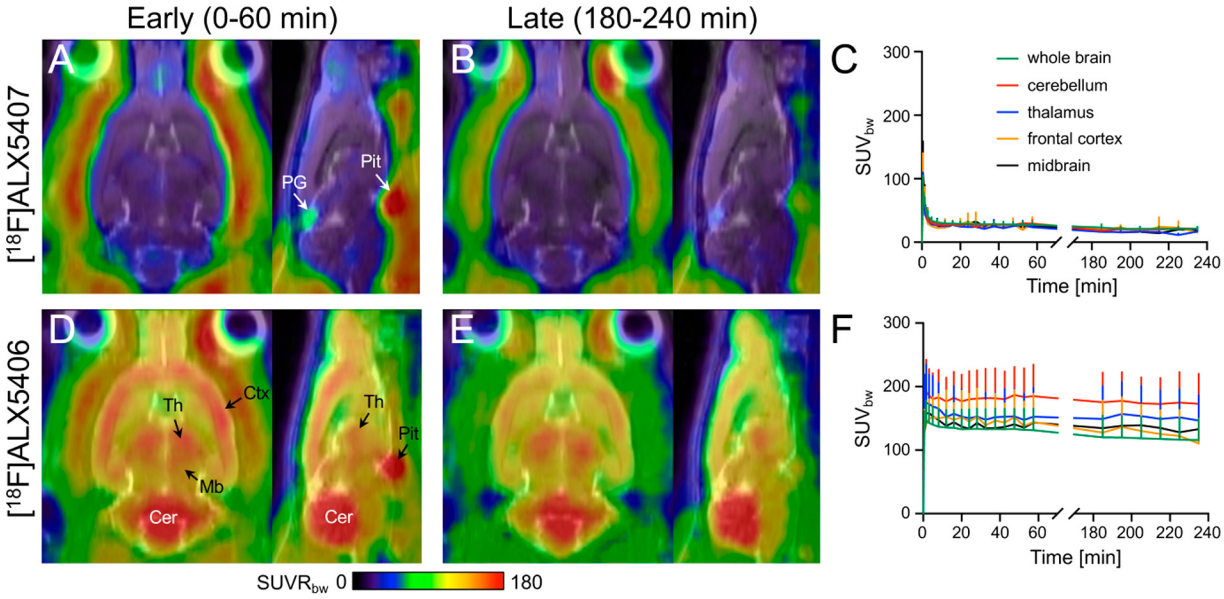

Figure 2. *In vivo* μPET imaging with [^{18}F]ALX5406 and [^{18}F]ALX5407 in healthy rats. Average μPET images (n = 3 per tracer; summed images over 60 min each) were projected onto an MRI template in the horizontal plane. Rats were injected with [^{18}F]ALX5407 (A–C) or [^{18}F]ALX5406 (D–F), and measurements were performed 0–60 min (early (A, D)) and 180–240 min (late (B, E)) after tracer administration in the same animals. Also shown are mean time–activity curves (TACs ± standard deviation) with [^{18}F]ALX5407 (C) or [^{18}F]ALX5406 (F). Abbreviations: Cer, cerebellum; Ctx, cortex; Mb, midbrain; PG, pineal gland; Pit, pituitary gland; Th, thalamus.

distribution of tracer throughout the whole brain slice, suggesting that esterification of the carboxylic acid function interferes with specific binding to GlyT1. In contrast, the results obtained with [^{18}F]ALX5407 (total binding) revealed heterogeneous binding of the tracer in distinct brain regions. In particular, binding of [^{18}F]ALX5407 was most pronounced in cerebellum, inferior colliculus, corpus callosum, external capsule, and thalamus, while intermediate levels were observed in the cortical gray matter, hippocampus, and striatum. A similar distribution was previously observed in autoradiographic studies with the non-sarcosine-based ligand [^{35}S]ACPPB, which showed high levels of binding in spinal cord gray matter, brainstem, cerebellar white matter, thalamus, and cortical white matter.[45] Moreover, even though early studies failed to detect significant cortical GlyT1 immunoreactivity in rodents,[46,19] more recent work with novel sequence specific antibodies[47] and functional studies[48] have provided evidence for a more pronounced GlyT1 expression in the neocortex and other forebrain regions. Likewise, a number of *in vivo* PET studies in different species have since demonstrated binding of GlyT1-specific tracers throughout the whole brain, with high levels in cerebellum, pons, thalamus, and white matter of the frontal cortex and lower but evident binding in the cortical gray matter, caudate, and putamen (reviewed in ref 49), which is in excellent agreement with the distribution of [^{18}F]ALX5407 observed in the present study.

Next, total binding of [^{18}F]ALX5407 in rat brain slices was compared with the results of competitive displacement and blocking experiments performed using the GlyT1 substrate glycine, the low affinity GlyT1 inhibitor and substrate sarcosine, as well as the selective and potent nonsubstrate sarcosine-based GlyT1 inhibitors NFPS (racemic ALX5407) and LY2365109. Glycine and sarcosine had little effect and displaced [^{18}F]ALX5407 binding by 15 ± 3% and 16 ± 3%, respectively, while the pattern of tracer distribution was essentially unaffected (Figure 1). This is consistent with previous reports that nonsubstrate sarcosine-based inhibitors like ALX5407 act by binding to an allosteric site that is distant

https://doi.org/10.1021/acschemneuro.1c00284
ACS Chem. Neurosci. 2021, 12, 3335–3346

Table 2. CNS PET MPO Evaluation of ALX5406 and ALX5407[a]

	clogP		$clogD_{7.4}$		TPSA		MW		HBD		pK_a		
	value	T_0	value	T_0	value	T_0	value	T_0	value	T_0	value	T_0	CNS PET MPO score
ALX5407	3.99	0.01	1.19	1.00	49.8	1.00	393.5	0.00	1	1.00	9.42	0.03	3.0
ALX5406	6.23	0.00	1.77	0.94	38.8	0.52	407.5	0.00	0	1.00	6.52	1.00	3.5

[a]Parameters were calculated using ChemOffice 2019 (clogP, TPSA, MW, HBD, pK_a) or the ADMETlab platform[42] ($clogD_{7.4}$) respectively. Abbreviations: clogP, calculated partition coefficient; $clogD_{7.4}$, calculated distribution coefficient at pH 7.4; TPSA, topological polar surface area; MW, molecular weight; pK_a, ionization constant of the most basic center.

from the substrate (glycine) binding site but may have a small degree of overlap.[32,50,51] Competition studies with the nonsubstrate sarcosine-based inhibitors NFPS or LY2365109 revealed a more pronounced displacement of [^{18}F]ALX5407 binding by 31 ± 6% or 33 ± 5%, respectively, and resulted in an almost homogeneous residual tracer distribution in most brain regions (Figure 1). Comparable results were obtained in blocking studies with the same inhibitors (data not shown). However, as exemplified in Figure 1, some degree of region-specific residual binding in the presence of NFPS and, to a lesser extent, LY2365109 was still observed in the hippocampus, parietal-temporal cortex, occipital cortex and in parts of the cerebellum. Since relatively low concentrations of racemic ALX5407 (100 nM) have previously been shown to inhibit [^{3}H]mesulergine binding to pig choroid plexus membranes by about 25%,[52] at least some of the residual signals observed after displacement with LY2365109 could reflect tracer binding to serotonergic 5-HT_{2C} receptors, which are prominently expressed in all of the aforementioned brain regions.[53,54] It should also be noted that our results may somewhat underestimate the true degree of specific binding, as both reversal of ALX5407-induced suppression of human GlyT1 ($t_{1/2}$ = 13 h [55]) and displacement of [^{3}H]NFPS from rat forebrain membranes by unlabeled NFPS ($t_{1/2}$ ∼ 30 min [50]) have been shown to be extremely slow so that our incubations with the radioligand for 90 min may still have been too short to reach an equilibrium. In this context, the results of a previous *in vivo* microdialysis study furthermore indicate that the residence time of ALX5407 in the brain may be region-specific, as reflected in a much more sustained elevation of glycine levels in caudal brain areas,[22] which is in line with some of our own *in vivo* findings (see next section) and might have contributed to incomplete *in vitro* displacement of [^{18}F]ALX5407 from the cerebellum as well.

***In Vivo* and *Ex Vivo* Evaluation.** [^{18}F]ALX5407 biodistribution in naïve rats was studied using μPET measurements performed 0−60 min and 180−240 min after tracer administration. As illustrated in Figure 2A−C, the results showed almost exclusive accumulation of the tracer in peripheral tissues, suggesting that it does not readily cross the BBB. In rodents, lipophilic compounds are often substrates of the active efflux transporter P-gp, which rapidly exports them back into the peripheral blood. In order to clarify whether active efflux is responsible for low brain uptake of the tracer, [^{18}F]ALX5407 was studied in a rat pretreated with the P-gp inhibitor elacridar. However, in this experiment, brain uptake of [^{18}F]ALX5407 was low as well (Supporting Information, Figure S14), suggesting that BBB penetration was not limited by active efflux via P-gp. This is in line with previous findings demonstrating that the brain-to-plasma ratio of NFPS (racemic ALX5407) is similar in wild-type and P-gp/MDR1 knockout mice.[56] Alternatively, the observed results could be explained by slow kinetics of brain penetration. In the case of NFPS, it takes approximately 6 h to reach brain C_{max} after s.c. injection in rats.[57] On the other hand, oral dosing of ALX5407 was reported to increase glycine levels in CSF within 1 h and in cerebellum within 3−4 h after administration.[22] These data are in apparent contradiction with the complete absence of [^{18}F]ALX5407 brain uptake observed by us, even if μPET measurements were performed 3−4 h after tracer administration (Figure 2B). However, the time required for half-maximal *in vitro* suppression of cloned GlyT1 by NFPS has been shown to increase markedly if the concentration of NFPS is reduced from 1 μM ($t_{1/2}$ ∼ 1 min) to <10 nM ($t_{1/2}$∼ 15 min).[32] Even more importantly, a previous *in vivo* study found that ALX5407-induced locomotor side-effects in mice exhibit a dose-dependent shift in time of onset, with first effects after i.p. injection observed after 2.75 h at 30 mg/kg, 4.25 h at 10 mg/kg, and 7 h at 6 mg/kg and with no effects at 3 mg/kg.[58] The latter could point to a saturable process that limits entry of the inhibitor into the brain. In this case, BBB penetration of [^{18}F]ALX5407 might be concentration-dependent and simply too slow if no-carrier-added (n.c.a.) tracer is used. Consequently, we performed additional PET measurements where [^{18}F]ALX5407 was injected together with 1.5 mg/kg or 3 mg/kg of non-radioactive ALX5407. However, no increased brain uptake in comparison to the n.c.a. tracer alone was observed (Supporting Information, Figure S14). To obtain insight into the physicochemical properties that could be responsible for poor brain uptake of the tracer, we performed a multiparameter optimization (MPO) evaluation, using the previously described CNS PET MPO algorithm.[59] As illustrated in Table 2, ALX5407 failed to reach a CNS PET MPO score in the desirable range of >3, and this could be attributed to unfavorable lipophilicity (i.e., clogP > 2.8), molecular weight (i.e., MW > 305.3), and ionization constant of the most basic center (i.e., pK_a > 7.2). A relatively high lipophilicity is undesirable in terms of nonspecific brain tissue binding. However, it should not interfere with passive transfer across the BBB per se and could even partly compensate for the unfavorably high molecular weight.[60,61] However, owing to the presence of a free carboxylic acid function adjacent to the basic amino group in the sarcosine motif, the predominant form of ALX5407 at physiological pH values is a zwitterion. Previous findings indicate that such compounds are characterized by poor BBB penetration unless they are subject to active transport into the brain.[62−66] The corresponding methyl ester ALX5406 lacks a free carboxylic acid function and reached a CNS MPO PET score of 3.5 (Table 2), indicating that it may be more effective in crossing the BBB. With this in mind, we next followed a prodrug strategy and examined if the methyl ester could be used as a BBB-penetrating prodrug for delivery of [^{18}F]ALX5407 into the brain. As illustrated in Figure 2D,E, [^{18}F]ALX5406 showed high brain uptake, with radioactivity accumulation in the cerebellum (very high), the dorsal midbrain/superior and inferior colliculus (high), the

https://doi.org/10.1021/acschemneuro.1c00284
ACS Chem. Neurosci. 2021, 12, 3335−3346

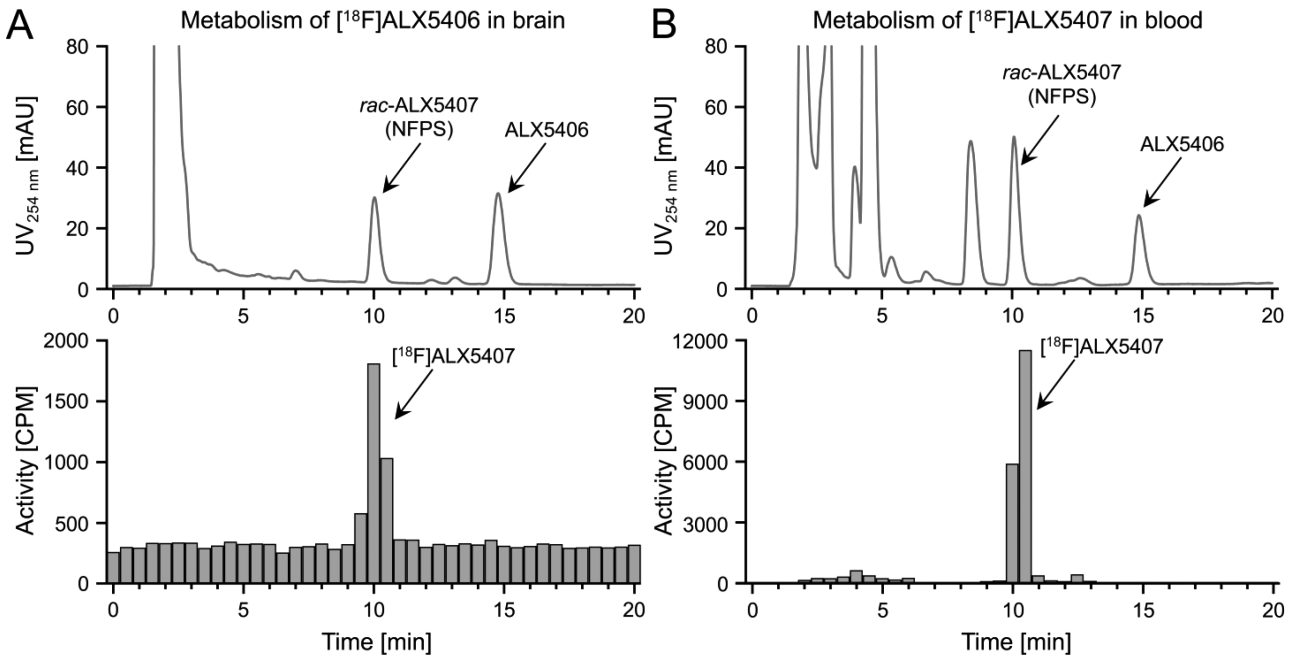

Figure 3. Results of *ex vivo* HPLC analysis of radiometabolites in rat brain tissue and blood after administration of [^{18}F]ALX5406 or [^{18}F]ALX5407. Representative UV traces (top) and radiotraces (bottom) of brain tissue extract obtained from a rat sacrificed 30 min after administration of [^{18}F]ALX5406 (A) or blood obtained from a rat sacrificed 30 min after administration of [^{18}F]ALX5407 (B) are shown. To facilitate compound identification, both samples were spiked with non-radioactive ALX5406 (t_R = 15 min) and *rac*-ALX5407 (NFPS) (t_R = 10 min). For reconstruction of radio-HPLC traces, the radioactivity in 30 s fractions was measured using a γ-counter.

thalamus (high), and the cortex (high from 0−60 min, moderate from 180−240 min). Taken together, especially the distribution of radioactivity observed during the late time-point (180−240 min) was in good agreement with the distribution observed in our autoradiographic experiments with [^{18}F]ALX5407 or previous studies with various GlyT1-specific ligands,[49] suggesting that [^{18}F]ALX5406 behaves as a prodrug and is effectively hydrolyzed to [^{18}F]ALX5407 in the brain. This was confirmed by *ex vivo* radiometabolite analysis of blood and brain extracts after administration of [^{18}F]ALX5406 in rats (Figure 3A, Supporting Information Figures S8−S11, Supporting Information Tables S4 and S5), which demonstrated conversion of [^{18}F]ALX5406, mainly into [^{18}F]ALX5407, 30 min p.i., with only a minor residual signal possibly corresponding to [^{18}F]ALX5406 in blood and brain and with additional minor signals presumably corresponding to unidentified radiometabolites or matrix effects. The latter minor signals were also observed in the analysis of radiometabolites in blood after administration of [^{18}F]ALX5407 (Figure 3B, Supporting Information Figures S12 and S13, Supporting Information Table S6), suggesting that they cannot be attributed to metabolism of the methyl ester prodrug.

As can be seen by close inspection of the early and late measurements with [^{18}F]ALX5406 (Figure 2F), radioactivity in all brain regions except for the thalamus decreased somewhat between the two successive μPET measurements, which could reflect clearance of small amounts of unconverted methyl ester or unbound [^{18}F]ALX5407 from brain. With regard to the lack of changes in thalamus, it is interesting to note that a previous PET study in non-human primates with the GlyT1 ligand *N*-[^{11}C]methyl-SSR504734 also found that this region behaves differently from other brain regions, which was proposed to be due to a different GlyT1 occupancy or a different non-displaceable component.[67] In addition to the minor decrease of radioactivity between early and late measurements, the TACs for cerebral cortex showed a more pronounced decline during the late measurement that started roughly 200 min after tracer administration and that was not observed in cerebellum and midbrain (Figure 2F), supporting previous evidence for a reduced residence time of ALX5407 in forebrain compared to caudal brain regions.[22] Finally, it should be noted that in contrast to the prominent binding of [^{18}F]ALX5407 to the corpus callosum observed in our *in vitro* experiments (Figure 1), there was little accumulation of radioactivity in this tract during the μPET measurements with [^{18}F]ALX5406 (Figure 2D,E). Similar inconsistencies between *in vitro* and *in vivo* binding of GlyT1-specific ligands to the corpus callosum have been observed before[68] and can most likely be attributed to lower regional blood flow in and thus less effective tracer supply to white matter tracts like the corpus callosum as compared to other brain regions.[69,70]

Taken together, esterification of the carboxylic acid function in [^{18}F]ALX5407 appears to be a viable approach for the development of GlyT1-selective PET tracers for preclinical imaging in rodents. However, consistent with the well-known fact that there can be considerable inter- and intraspecies differences in the activity or expression of enzymes involved in the activation of ester-based prodrugs,[71,72] our *in vitro* experiments also indicate that hydrolysis of [^{18}F]ALX5406 in humans could be less effective, with at least 88% remaining intact after incubation in human plasma for up to 60 min (Supporting Information, Figures S6 and S7). For comparison, when the same experiment was performed with rat plasma, hydrolysis of [^{18}F]ALX5406 was rapid and <2% of the prodrug remained intact after 60 min (Supporting Information, Figures S4 and S5). Although reduced peripheral cleavage of the ester in blood should in principle facilitate brain penetration of the intact prodrug, the rate of hydrolysis in brain tissue is generally

https://doi.org/10.1021/acschemneuro.1c00284
ACS Chem. Neurosci. 2021, 12, 3335−3346

well below that in blood or metabolizing organs particularly in liver,[73,74] suggesting that demethylation of [^{18}F]ALX5406 in the human brain could be too slow as well. Nevertheless, the enzymatic cleavage rate can be tuned up by the application of faster hydrolyzable propyl, butyl, or acetoxymethyl esters.[75,76]

CONCLUSION

^{18}F-Labeled glycine transporter 1 inhibitor [^{18}F]ALX5407 is easily accessible by alcohol-enhanced Cu-mediated radiofluorination and shows accumulation consistent with the distribution of GlyT1 in *in vitro* autoradiographic studies with rat brain slices. While low brain uptake of the tracer, presumably due to slow BBB penetration, precludes an application of [^{18}F]ALX5407 for *in vivo* studies, the corresponding methyl ester, [^{18}F]ALX5406, could serve as a prodrug. Thus, [^{18}F]ALX5406 showed rapid brain uptake in rats and was converted to [^{18}F]ALX5407 by brain esterases on a time scale typical for PET measurements, enabling GlyT1 specific preclinical imaging. However, further studies could be required to adjust this approach for human applications.

MATERIALS AND METHODS

Chemistry. *General Conditions.* All reagents and solvents were purchased from commercial sources (Sigma-Aldrich, VWR, ABCR Germany, etc.) and used without further purification. Bis(pinacolato)-diboran, [1,1′-bis(diphenylphosphino)ferrocene]palladium(II) dichloride, and KOAc were dried under reduced pressure (at ambient temperature and 100 °C, respectively) overnight and stored under argon. Proton and carbon nuclear magnetic resonance (^{1}H and ^{13}C NMR) spectra were recorded on a Bruker Avance Neo (400 MHz) spectrometer. Chemical shifts are reported in parts per million (ppm) relative to residual peaks of deuterated solvents or to tetramethylsilane (TMS). The observed signal multiplicities are characterized as follows: s = singlet, d = doublet, t = triplet, m = multiplet, and br = broad. Coupling constants (J) are reported in hertz (Hz). Unless noted otherwise, all reactions were carried out with magnetic stirring and, if air or moisture sensitive substrates and/or reagents were handled, in flame-dried glassware under argon or nitrogen. Organic extracts were dried with anhydrous Na_2SO_4 or $MgSO_4$. ALX5406 was prepared in a three-step synthesis starting from 4′-fluoro-3-chloropropiophenone according to the literature.[55] ALX5407 hydrochloride was purchased from Sigma-Aldrich.

Column Chromatography. Merck silica gel, grade 60, 230−400 mesh, was used. Solvent proportions are indicated in a volume/volume ratio. Thin layer chromatography (TLC) was performed using precoated sheets, 0.25 mm Sil G/UV254 from Merck KGaA (Darmstadt, Germany). The chromatograms were viewed under UV light (λ = 254 nm) and/or using $KMnO_4$ stain solution. For flash chromatography, a Grace Reveleris iES flash chromatography system equipped with RevealX detector, allowing for multisignal (UV/ELSD) collection, and Reveleris flash silica cartridges (40 μm SiO_2) were employed. Solvent proportions are indicated in a volume/volume ratio. High resolution mass spectra (HRMS) were measured with a LTQ Orbitrap XL (Thermo Fisher Scientific Inc., Bremen, Germany) and are reported as the m/z values of the pseudoion $[M + H]^+$. Elementary analysis of **2** was performed by HEKAtech GmbH (Wegberg, Germany).

Synthesis of (*S*)-1-(4-Bromophenyl)-3-chloropropan-1-ol (1).[35] A suspension of copper acetate hydrate (109 mg, 0.60 mmol, 0.03 equiv) and (*S*)-P-Phos (100 mg, 0.16 mmol, 0.8 mol %) in toluene (10 mL) was stirred for 20 min under air. Afterward, phenylsilane (2.96 mL, 24 mmol, 1.2 equiv) was added dropwise and the blue solution was cooled to −10 °C. A solution of 4′-bromo-3-chloropropiophenone (5.00 g, 20 mmol, 1 equiv) in toluene (7 mL) was added slowly, and the reaction mixture was gradually warmed to ambient temperature and stirred for another 15 h. The black reaction mixture was treated with 10% HCl (20 mL), and the precipitated solid was filtered over a plug of Celite. The organic phase was separated, and the aqueous phase was extracted with Et_2O (3 × 20 mL). The combined organic fractions were dried and concentrated under reduced pressure. The crude product was purified by column chromatography (petroleum ether/EtOAc 9:1) to afford the title compound as a yellow oil (4.01 g, 16.1 mmol, 80% yield). The enantiomeric excess (*ee*) of the product, determined by chiral HPLC, amounted to 96.5%. R_f = 0.15 (petroleum ether/EtOAc 9:1). ^{1}H NMR (400 MH, $CDCl_3$): δ = 1.86 (br, 1H), 2.03−2.12 (m, 1H), 2.18−2.26 (m, 1H), 3.56 (dt, J = 11.1, 5.8 Hz, 1H), 3.77 (ddd, J = 11.1, 8.4, 4.9 Hz, 1H), 4.96 (dd, J = 8.4, 4.9 Hz, 1H), 7.26−7.29 (m, 2H), 7.49−7.53 (m, 2H). ^{13}C NMR (100 MHz, $CDCl_3$): δ = 41.50, 41.64, 70.81, 121.81, 127.63, 131.89, 142.85. Chiral HPLC: Lux 5 μm cellulose-1, 4.6 mm × 250 mm (Phenomenex, Aschaffenburg, Germany); eluent, *i*PrOH/hexane 10:90; flow rate, 0.5 mL/min; detection, UV, λ = 254 nm; t_R [(*S*)-**1**] = 14.1 min, t_R [(*R*)-**1**] = 15.0 min.

Synthesis of (*R*)-4-[1-(4-Bromophenyl)-3-chloropropoxyl]-1,1′-biphenyl (2). Diethyl azodicarboxylate (DEAD) (0.87 mL, 0.97 g, 5.52 mmol, 1 equiv) was slowly added to an ice-cold solution of **1** (1.38 g, 5.52 mmol, 1 equiv), Ph_3P (1.45 g, 5.52 mmol, 1 equiv), and 4-phenylphenol (0.94 g, 5.52 mmol, 1 equiv) in anhydrous THF (17 mL) under argon. The reaction mixture was warmed to ambient temperature and stirred for another 15 h. After completion of the reaction (TLC control), all volatiles were removed under reduced pressure and the residue was purified by flash chromatography (petroleum ether/EtOAc 49:1) to afford the title compound as a yellowish solid (1.41 g, 3.52 mmol, 64% yield). This material (1.6 g) could be recrystallized from *n*-hexane (15 mL) furnishing **2** (1.2 g) as colorless needles. The *ee* of the product determined by chiral HPLC amounted to 98%. R_f = 0.27 (petroleum ether/EtOAc 49:1). ^{1}H NMR (400 MHz, $CDCl_3$): δ = 2.23 (dddd, J = 14.3, 8.7, 5.7, 4.3 Hz, 1H), 2.49 (ddt, J = 14.3, 8.7, 5.3 Hz, 1H), 3.65 (dt, J = 11.1, 5.7 Hz, 1H), 3.85 (ddd, J = 11.1, 8.7, 5.3 Hz, 1H), 5.42 (dd, J = 8.7, 4.3 Hz, 1H), 6.91−6.94 (m, 2H), 7.28−7.33 (m, 3H), 7.39−7.46 (m, 4H), 7.50−7.53 (m, 4H). ^{13}C NMR (100 MHz, $CDCl_3$): δ = 41.24, 41.38, 76.39, 116.33, 121.93, 126.86, 127.82, 128.28, 128.83, 132.14, 134.55, 140.05, 140.74, 149.06, 157.30. Chiral HPLC. Lux 5 μm cellulose-1, 4.6 mm × 250 mm (Phenomenex, Aschaffenburg, Germany); eluent, *i*PrOH/hexane 5:95; flow rate, 0.5 mL/min; detection, UV, λ = 254 nm; t_R [(*R*)-**2**] = 10.2 min, t_R [(*S*)-**2**] = 11.0 min. Elementary analysis, calculated for $C_{21}H_{18}BrClO$ (%): C (62.79), H (4.52), O(3.98). Found: C (62.92 ± 0.03), H (4.57 ± 0.02), O (4.02 ± 0.02).

Synthesis of (*R*)-*N*-{3-[(1,1′-Biphenyl)-4-yloxy]-3-(4-bromophenylpropyl}sarcosine Methyl Ester (3). A suspension of **2** (400 mg, 1.0 mmol, 1 equiv), sarcosine methyl ester hydrochloride (251 mg, 1.80 mmol, 1.8 equiv), K_2CO_3 (401 mg, 2.9 mmol, 2.9 equiv), and KI (66 mg, 0.40 mmol, 0.4 equiv) in MeCN (6 mL) was heated under reflux for 24 h. Thereafter, the reaction mixture was cooled down to ambient temperature, the precipitate was filtered off, washed with MeCN, and the filtrate was evaporated under reduced pressure. The residue was purified by flash chromatography (CH_2Cl_2/Et_2O 14:1) to afford **3** as a colorless solid (222 mg, 0.47 mmol, 47% yield). R_f = 0.31 (CH_2Cl_2/Et_2O 14:1). ^{1}H NMR (400 MHz, $CDCl_3$): δ = 1.99 (dddd, J = 14.0, 8.0, 6.6, 4.8 Hz, 1H), 2.20 (dtd, J = 14.0, 8.0, 5.6 Hz, 1H), 2.43 (s, 3H), 2.67−2.77 (m, 2H), 3.31 (s, 2H), 3.70 (s, 3H), 5.29 (dd, J = 8.2, 4.8 Hz, 1H), 6.90−6.92 (m, 2H), 7.28−7.32 (m, 3H), 7.38−7.45 (m, 4H), 7.48−7.52 (m, 4H). ^{13}C NMR (100 MHz, $CDCl_3$): δ = 36.78, 42.46, 51.67, 53.26, 58.75, 77.59, 116.29, 121.53, 126.80, 126.83, 127.91, 128.19, 128.81, 131.94, 134.16, 140.84, 141.07, 157.62, 171.51. HRMS calculated for $C_{25}H_{26}BrNO_3$ ($[M + H^+]$) 468.1168; found 468.1174.

Synthesis of (*R*)-*N*-(3-{[(1,1′-Biphenyl)-4-yloxy]-3-[4-(4,4,5,5-tetramethyl-1,3,2-dioxaborolane-2-yl)]phenyl}propyl)-sarcosine Methyl Ester (4). A solution of **3** (222 mg, 0.47 mmol, 1 equiv) in anhydrous 1,4-dioxane (2 mL) was added to a suspension of bis(pinacolato)diborane (142 mg, 0.56 mmol, 1.2 equiv), [1,1′-bis(diphenylphosphino)ferrocene]palladium(II) dichloride (10.3 mg, 14.1 μmol, 3 mol %), and KOAc (138 mg, 1.41 mmol, 3 equiv) in 1,4-dioxane (2 mL) under argon, and the resulting suspension was stirred

https://doi.org/10.1021/acschemneuro.1c00284
ACS Chem. Neurosci. 2021, 12, 3335−3346

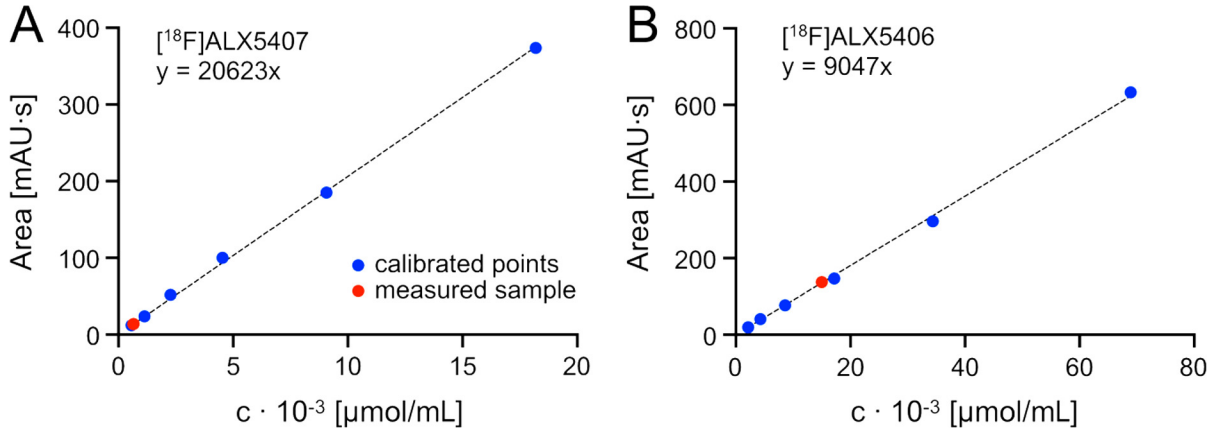

Figure 4. Calibration curves used to determine the molar activities of [^{18}F]ALX5407 (A) and [^{18}F]ALX5406 (B). The raw data used for construction of the curves are provided in Tables 3 and 4.

under reflux for 6 h (TLC control). The mixture was diluted with H_2O (3 mL), and the precipitated solid was filtered over a plug of Celite. The filter cake was washed with Et_2O (10 mL). The filtrate was extracted with Et_2O (3 × 10 mL). The combined organic extracts were dried and concentrated under reduced pressure. The crude product was purified by flash chromatography (CH_2Cl_2/Et_2O 14:1) to afford **4** as a faint yellow solid (156 mg, 0.30 mmol, 64% yield). R_f = 0.19 CH_2Cl_2/Et_2O 14:1). ^{1}H NMR (400 MHz, CD_3OD): δ = 1.34 (s, 12H), 1.98−2.08 (m, 1H), 2.12−2.23 (m, 1H), 2.34 (s, 3H), 2.70 (dd, J = 8.1, 6.6 Hz, 2H), 3.31 (s, 2H), 3.67 (s, 3H), 5.38 (dd, J = 8.1, 4.0 Hz, 1H), 6.88−6.97 (m, 2H), 7.21−7.28 (m, 2H), 7.32−7.39 (m, 2H), 7.48 (dd, J = 8.1, 4.0 Hz, 4H), 7.47−7.54 (m, 2H), 7.70−7.76 (m, 2H). ^{13}C NMR (100 MHz, CD_3OD): δ = 25.18, 37.12, 42.69, 52.02, 54.45, 58.93, 79.17, 85.07, 117.35, 126.57, 127.54, 127.60, 128.84, 129.68, 135.13, 136.05, 142.01, 146.49, 158.97, 172.55. *C*-Bpin was not observed. HRMS: calculated for $C_{31}H_{39}BNO_5$ ([M + H$^+$]) 516.2916; found 516.2917.

Radiochemistry. *General Conditions.* [^{18}F]Fluoride was produced by bombardment of enriched [^{18}O] water with 17 MeV protons at the BC1710 cyclotron (The Japan Steel Works, Tokyo, Japan) of the INM-5 (Forschungszentrum Jülich) using the ^{18}O(p,n)^{18}F nuclear reaction. Radioactivity was measured using a CRC-55tR dose calibrator from Capintec, Inc. (Florham Park, The Netherlands). The following cartridges were used for radiosyntheses and solid phase extractions: Sep-Pak Accell Plus QMA carbonate cartridges (130 mg sorbent, part no. 186004051; preconditioned with 1 mL of H_2O) and Strata-X RP cartridges (30 mg sorbent, part no. 8B-S100-TAK; preconditioned with 1 mL of EtOH and 20 mL of H_2O) from Phenomenex (Aschaffenburg, Germany).

The identity of radiolabeled products was confirmed by co-injection of the non-radioactive reference compounds. Radiochemical yields corrected for decay to the start of synthesis are provided for analytically pure radiolabeled compounds purified by HPLC. $Cu(OTf)_2(py)_4$ was prepared according to the literature.[77] All radiosyntheses were carried out with magnetic stirring under ambient or synthetic air.

Preprocessing of [^{18}F]Fluoride. Aqueous [^{18}F]fluoride was loaded onto an anion-exchange resin (e.g., QMA cartridge). It should be noted that aqueous [^{18}F]fluoride was loaded, flushed and washed from the male side, whereas ^{18}F$^-$ elution was carried out from the female side. If the QMA cartridge was loaded, flushed, and eluted from the female side only, sometimes a significant amount of [^{18}F]fluoride remained on the resin. This can probably be ascribed to the fact that the QMA-light (46 mg) cartridge contains only a single frit on the male side but four frits on the female side.

High-Performance Liquid Chromatography (HPLC). Analytical HPLC was performed on a HPLC system (Knauer, Berlin, Germany) with Azura P 6.1L pump and Azura UVD 2.1S UV/Vis detector coupled in series with a HERM LB 500 radioflow monitor (Berthold Technologies, Bad Wildbad, Germany). The UV and radioactivity detectors were connected in series, giving a time delay of 0.1−0.3 min between the corresponding responses, depending on the flow rate. The identity of [^{18}F]ALX5406 and [^{18}F]ALX5407 was confirmed by co-injection of the non-radioactive reference compounds. Semipreparative HPLC was performed on a dedicated semipreparative system consisting of a Knauer K-100 pump, a Knauer K-2501 UV detector, a Rheodyne 6 port injection valve equipped with a 2 mL injection loop and a custom-made Geiger counter.

Analytical HPLC. Column: Synergi Hydro-RP, 4 μm, 250 mm × 4.6 mm (Phenomenex, Aschaffenburg, Germany). [^{18}F]ALX5406 eluent: 45% MeCN (0.1% TFA); flow rate, 1.5 mL/min, t_R = 12.1 min. [^{18}F]ALX5407 eluent: 45% MeCN (0.1% TFA); flow rate, 1.5 mL/min, t_R = 8.3 min. Column: Kinetex EVO C18, 5 μm, 250 mm × 4.6 mm (Phenomenex, Aschaffenburg, Germany). [^{18}F]ALX5406 eluent: 40% MeCN (0.1% TFA); flow rate, 1.0 mL/min, t_R = 10.5. [^{18}F]ALX5407 eluent: 40% MeCN (0.1% TFA); flow rate, 1.0 mL/min, t_R = 7.70 min.

Preparative HPLC. [^{18}F]ALX5406: column, Eurospher, 4 μm, 250 mm × 20 mm (Knauer, Berlin, Germany); eluent, 40% MeCN (0.1% TFA); flow rate, 27.0 mL/min, t_R ~ 51 min. [^{18}F]ALX5407: column, Gemini C18 110A, 5 μm, 250 mm × 10 mm (Phenomenex, Aschaffenburg, Germany); eluent, 35% MeCN (0.1% AcOH); flow rate, 7.4 mL/min, t_R ~ 25 min.

[^{18}F]ALX5406. [^{18}F]Fluoride was eluted from the QMA cartridge with a solution of Et_4NHCO_3 (1 mg) in anhydrous *n*-BuOH (400 μL) directly into a solution of **4** (15 mg, 30 μmol) and $Cu(OTf)_2(py)_4$ (20 mg, 30 μmol) in anhydrous DMA (800 μL), and the reaction mixture was stirred for 10 min at 110 °C to afford [^{18}F]ALX5406. If the radiolabeled ester should not be further transformed into [^{18}F]ALX5407, the mixture was cooled to ambient temperature, 6 M HCl (50 μL) followed by H_2O (20 mL) was added, and the resulting solution was loaded onto a Strata-X cartridge. The cartridge was washed with H_2O (5 mL), and the crude [^{18}F]ALX5406 was eluted with MeCN (500 μL). The resulting solution was diluted with 0.1% TFA (1 mL) and loaded onto a preparative HPLC column. The product fraction was diluted with H_2O (100 mL) and loaded onto a Strata-X cartridge. The latter was washed with H_2O (5 mL) and dried for 2 min with a stream of argon. [^{18}F]ALX5406 was eluted with MeOH (800 μL). The resulting solution was evaporated to dryness under reduced pressure at 60 °C, and the residue was taken up into a sterile filtered 1% Tween 80 solution (500 μL), affording [^{18}F]ALX5406 in a ready-to-use form.

[^{18}F]ALX5407. The radiosynthesis of [^{18}F]ALX5406 was performed as described above. Afterward, 6 M NaOH (250 μL) was added and the mixture was stirred at 110 °C for 10 min. After cooling to ambient temperature, 6 M HCl (400 μL) was added, and the reaction mixture was diluted with H_2O (20 mL) and loaded onto a Strata-X cartridge. The cartridge was washed with H_2O (5 mL), and crude [^{18}F]ALX5407 was eluted with MeCN (500 μL). The resulting solution was diluted with 0.1% AcOH (1 mL) and loaded onto a

https://doi.org/10.1021/acschemneuro.1c00284
ACS Chem. Neurosci. 2021, 12, 3335−3346

preparative HPLC column. The product fraction, which eluted at about 25 min, was taken up in H_2O (100 mL) and loaded onto a Strata-X cartridge. The cartridge was washed with H_2O (5 mL) and dried for 2 min with a flow of argon. [^{18}F]ALX5407 was eluted with EtOH (800 μL), and the solvent was removed under reduced pressure at 70 °C. The residue was taken up into a sterile filtered 1% Tween 80 solution (500 μL), affording [^{18}F]ALX5407 in a ready-to-use form.

Determination of Carrier Amount and Molar Activity. An aliquot of the tracer solution (20 μL) was analyzed by HPLC as described above. Simultaneously, the carrier concentration was determined from the peak area and the molar activity was calculated according to a calibration curve (Figure 4), which was obtained using different concentrations of the reference compounds (Tables 3 and 4).

$$A_M = \frac{A\left[\frac{\text{GBq}}{\text{mL}}\right]}{c\left[\frac{\mu\text{mol}}{\text{mL}}\right]}$$

Table 3. Calibration Data (Measured at 254 nm) for Determination of Molar Activity of [^{18}F]ALX5407

concentration [μmol/mL]	amount [μg]	peak area [mAU·s]
0.0182	7.82	374
0.00907	3.90	185
0.00454	1.95	100
0.00227	0.976	51.9
0.00114	0.490	23.7
0.000568	0.244	12.2
measured sample		
0.0128	2.52	264
volume (mL)		0.5
activity (MBq)		129.0
carrier concentration (μmol/mL)		0.0128
molar activity (GBq/μmol)		20.2

Table 4. Calibration Data (Measured at 254 nm) for Determination of Molar Activity of [^{18}F]ALX5406

concentration [μmol/mL]	amount [μg]	peak area [mAU·s]
0.0689	30.6	633
0.0344	15.3	296
0.0172	7.64	147
0.00861	3.82	77
0.00430	1.91	41
0.00215	0.954	20
measured sample		
0.015	6.10	137.8
volume (mL)		0.5
activity (MBq)		455
carrier concentration (μmol/mL)		0.015
molar activity (GBq/μmol)		60.7

Determination of log$D_{7.4}$ Values. A solution of ALX5406 or ALX5407 in EtOH (0.01 M, 5 μL) was added to a mixture of 1-octanol (1 mL) and 0.1 M sodium phosphate buffer (pH = 7.4; 1 mL). The mixtures were vortexed for 2 min and centrifuged for 2 min at 7000 rpm. Aliquots of both fractions (20 μL each) were analyzed by HPLC.

***In Vitro* Autoradiography.** Adult male rats were sacrificed, the brain was quickly removed, immediately frozen in 2-methylbutane, and stored at −80 °C until cryosectioning (INM-2, Institute for Neuroscience and Medicine, Molecular Organization of the Brain, Forschungszentrum Jülich, Germany). Coronal and transversal brain sections (20 μm thickness) were prepared in a CM 3050 cryostat microtome (Leica Mikrosysteme Vertrieb GmbH, Germany), thaw-mounted onto silanized slides (Laboroptik GmbH, Germany), dried, and stored at −80 °C.

Competition studies were performed as follows: brain sections were thawed at 37 °C in a drying cabinet and preincubated for 15 min at ambient temperature in an incubation buffer composed of 120 mM NaCl, 2 mM KCl, 1 mM $MgCl_2$, 1 mM $CaCl_2$, and 50 mM Tris buffer, pH 7.4.[45] Thereafter, the brain sections were transferred into fresh incubation buffer containing either the radioligand [5 kBq/mL] only (for determination of total binding) or the radioligand [5 kBq/mL] and 5 μM of the respective competitor (for determination of nonspecific binding). After incubation for 90 min at ambient temperature, the sections were dried at 37 °C for 15 min and placed on a phosphor imaging plate (Fuji Pharma, Japan). After 45 min exposure, the plates were scanned by laser using a BAS 5000 phosphor imager (Fuji Pharma, Japan) controlled with software provided by the vendor (version 2.11a). Data from regions of interest (ROIs) were analyzed using the advanced image analyzer program AIDA 3.10 (Raytest Isotopenmessgeräte, Germany). The anatomical assignment was carried out visually using a rat brain atlas.[78]

***In Vitro* Analysis of [^{18}F]ALX5406 and [^{18}F]ALX5407 Radiometabolites in Rat and Human Blood Plasma.** The *in vitro* stability of [^{18}F]ALX5406 and [^{18}F]ALX5407 in human or rat plasma obtained by centrifugation (300 rcf) of fresh, heparinized blood at 4 °C for 10 min was analyzed by radio-TLC using the same equipment as that used for the *ex vivo* radiometabolite studies (*vide infra*). To this end, a 2 mL Eppendorf vial with 500 μL of plasma was prewarmed in a thermoshaker at 37 °C for 5 min. A solution of the radiotracer in DMSO (0.5 μL, approximately 0.5−1 MBq) was then added, and the mixture was further shaken at 37 °C. 80 μL aliquots of the mixture were removed at 5, 15, 30, and 60 min. To determine the recovery rate, 2.5 μL of the aliquots was immediately spotted on a paper strip (back-side coated with a polymer layer), while 60 μL was transferred into an Eppendorf vial containing 120 μL of MeCN for precipitation of plasma proteins. The vials were vigorously vortexed for 2 min and centrifuged at 20000 rcf for 2 min, after which the supernatant was spotted on the combination layer of a TLC plate (three lanes, 2.5 μL per time-point). When samples for all time-points had been spotted on the TLC plate, the non-radioactive reference compounds were spotted on separate lanes at the edges of the plate, and the plate was air-dried and then developed using MeOH as mobile phase. After the plate had been developed, the UV-active spots of the reference compounds as well as the starting spot, the end of the combination layer, and the solvent front at both edges of the TLC plate were spiked with a diluted radioactive solution, and the TLC was scanned by the phosphor imager. The TLC plate was scanned simultaneously with the paper strips containing the untreated plasma samples so that radioactivity recovery for the precipitation step could be determined by comparison of the activity concentration of the untreated plasma samples and the supernatant after protein precipitation, taking into account the dilution factor. For analysis, all peaks were integrated and the background was subtracted to give the net counts, which were averaged across the three lanes for each time-point and normalized by the sum of the net counts in all detected peaks. [^{18}F]ALX5406 and [^{18}F]ALX5407 were identified by comparison of the migration distance of the radioactive spots with those of the non-radioactive reference compounds.

***Ex Vivo* Analysis of [^{18}F]ALX5406 Radiometabolites in Rat Blood Plasma and Brain Homogenate and [^{18}F]ALX5407 Radiometabolites in Rat Blood Plasma.** [^{18}F]ALX5406 or [^{18}F]ALX5407 (110 MBq or 205 MBq, respectively) was injected into the lateral tail vein of an anesthetized rat (667 or 438 g, respectively). At 30 min p.i., the rat was decapitated to remove the brain (for experiments with [^{18}F]ALX5406 only) and obtain blood (2 and 5 mL for experiments with [^{18}F]ALX5406 and [^{18}F]ALX5407, respectively). The rat brain was frozen on dry ice while the recovered blood was immediately heparinized and cooled to 0−4 °C. An aliquot of the blood (1.0 mL) was then centrifuged at 2000 rcf and 4 °C for 5 min, and the supernatant plasma (500 μL) was separated, diluted with an equal volume of MeCN, gently shaken for 2 min at 0−4 °C, and

https://doi.org/10.1021/acschemneuro.1c00284
ACS Chem. Neurosci. 2021, 12, 3335−3346

again centrifuged at 20000 *rcf* and 4 °C for 5 min. The supernatant was separated and analyzed by TLC and HPLC as described below. Before HPLC analysis, a reference solution prepared by dilution of premixed solutions of ALX5406 (1 mg/mL; 10 μL) and NFPS (racemic ALX5407, 1 mg/mL; 20 μL) with 50% MeCN (0.2% TFA) (1 vol %) and an equal volume of 0.2% TFA were added to the supernatant. For analysis of radiometabolites in brain tissue, the frozen brain (2.07 g) was warmed to 0 °C and homogenized using a Potter S (Sartorius Lab Instruments, Göttingen, Germany) at 1500 rpm for 2 min. The ice-cold homogenate was sequentially treated with ice-cold 0.05 M Tris buffer (pH 7.4, 4 mL) and ice-cold MeCN (6 mL), gently shaken for 5 min at 0−4 °C, and centrifuged at 20000 rcf and 4 °C for 5 min. The supernatant was separated, the reference solution described above (1 vol %) was added, and radiometabolites were analyzed by HPLC and TLC as described below.

HPLC analysis. System: Knauer (Berlin, Germany) HPLC system (*vide supra*) equipped with a 3 in. NaI(Tl) borehole detector and a EG&G Ortec ACEMate 925 spectroscopy system (ORTEC, Oak Ridge, USA). Conditions: column, Kromasil C18 5 μm, 100 Å, 250 mm × 4.6 mm (Nouryon, Bohus, Sweden); eluent, 50% MeCN (0.2% TFA); flow rate, 1 mL/min; detection, UV, 254 nm and radioactivity, injection, 250 μL. Retention times: NFPS (10.0 min), ALX5406 (14.5 min).

As the concentration of radioactive products in the samples was close to or below the limit of detection of the online γ-detector, 30 s fractions (0−20 min; total 40 fractions) were collected and each was measured offline for 60 s using an automatic γ-counter (Hidex, Turku, Finland).

TLC analysis. TLC reader, Bas-5000 imager (Fujifilm Europe GmbH, Düsseldorf, Germany); storage screen, BAS-IP MS (multi-purpose standard). Images were analyzed with Aida image analyzer 5.0 (Raytest, Straubenhardt, Germany). TLC plates: Alugram Xtra Silgur TLC plates silica with concentrating zone (kieselguhr) (Macherey-Nagel GmbH, Düren, Germany); eluent, MeOH. Quantification: In each chromatogram only the best resolved trace was quantified; each integrated peak was quantified and expressed as percentage of the sum of all integrated peaks.

Animals. Experiments were carried out in accordance with the EU directive 2010/63/EU for animal experiments and the German Animal Welfare Act (TierSchG, 2006) and were approved by regional authorities (LANUV NRW; application number 84-02.04.2017.A288). Nine adult male rats (body weight 246−699 g) were used for this study. They were housed in groups in individually ventilated cages (NextGen, Ecoflow, Phantom, Allentown) under controlled ambient conditions (22 ± 1 °C and 55 ± 5% relative humidity) on a 12 h light/dark schedule. They had free access to food and water.

PET Experiments. Animals were anesthetized (initial dosage: 5% isoflurane in O_2/air 3:7, then reduction to 2%), and a catheter for tracer injection was inserted into the lateral tail vein. Rats were placed on an animal holder (Equipment Vétérinaire Minerve, Esternay, France) and fixed with a tooth bar in a respiratory mask. Body temperature was maintained at 37 °C by continuous warm air flow through the wall of the animal bed. Eyes were protected from drying with Bepanthen eye and nose ointment (Bayer). A dynamic PET scan in list mode was conducted using a Focus 220 micro-PET scanner (CTI-Siemens, Erlangen, Germany) with a resolution at the center of field of view of 1.4 mm. Data acquisition started with intravenous tracer injection (activity, 33−77 MBq; volume, 500 μL); scan time was 60 min. This was followed by a 10 min transmission scan using a ^{57}Co point source for attenuation correction. After the scan was finished, the catheter was removed and the rats woke up in their home cage.

PET scans with [^{18}F]ALX5407 or [^{18}F]ALX5406 were performed in untreated rats, after pretreatment with Elacridar (4 mg/kg, injected i.v. 30 min before the tracer) or non-radioactive ALX5407 (3 mg/kg, injected i.v. 30 min before the tracer) or together with non-radioactive ALX5407 (1.5 and 3 mg/kg, injected i.v. together with the tracer) (n = 1 for each condition; see also Supporting Information Table S7). Five animals were measured once, and one rat was measured twice ([^{18}F]ALX5406 alone and with ALX5407). In a second set of experiments, three untreated rats were measured with both [^{18}F]ALX5407 and [^{18}F]ALX5406 (on separate days) at early and late time points, respectively. The early PET-scan was performed as described above (0−60 min postinjection). Subsequently, the rats spent 2 h in their home cage and were then measured again for 1 h (180−240 min p.i.).

After Fourier rebinning, summed images were reconstructed using the iterative OSEM3D/MAP procedure resulting in voxel sizes of 0.38 mm × 0.38 mm × 0.80 mm. From each PET scan, a summed image over the whole period of 60 min was generated. For the experiments with both early and late measurements, the 60 min scans were subdivided into shorter time frames (2 × 1 min, 2 × 2 min, 6 × 4 min, 6 × 5 min for the early measurement and 6 × 10 min for the late measurement) and used to compile time−activity curves. For all further processing the software VINCI 4.72 for MacOS X (Max Planck Institute for Metabolism Research, Cologne, Germany) was used. Images were manually co-registered to an MRI template and intensity-normalized to injected dose. To this end, images were divided by injected dose and multiplied by body weight × 100, resulting in dimensionless SUVbw. With the help of a whole brain volume of interest (VOI), whole brain uptake was extracted as the mean value across all 17 233 voxels of the VOI. Additional VOIs were generated from cerebellum (684 voxels), frontal cortex (68 voxels), midbrain (182 voxels), and thalamus (127 voxels).

■ ASSOCIATED CONTENT

Supporting Information

The Supporting Information is available free of charge at https://pubs.acs.org/doi/10.1021/acschemneuro.1c00284.

^{1}H and ^{13}C NMR spectra, HPLC chromatograms, and additional experimental details and results from the *in vitro* and *ex vivo* radiometabolite analyses and *in vivo* μPET experiments (PDF)

■ AUTHOR INFORMATION

Corresponding Author

Bernd Neumaier − *Nuclear Chemistry (INM-5), Institute of Neuroscience and Medicine, Forschungszentrum Jülich GmbH, 52425 Jülich, Germany; Institute of Radiochemistry and Experimental Molecular Imaging, University of Cologne, Faculty of Medicine, and University Hospital Cologne, 50937 Cologne, Germany; Max Planck Institute of Metabolism Research, 50931 Cologne, Germany;* orcid.org/0000-0001-5425-3116; Email: b.neumaier@fz-juelich.de

Authors

Chris Hoffmann − *Nuclear Chemistry (INM-5), Institute of Neuroscience and Medicine, Forschungszentrum Jülich GmbH, 52425 Jülich, Germany; Institute of Radiochemistry and Experimental Molecular Imaging, University of Cologne, Faculty of Medicine, and University Hospital Cologne, 50937 Cologne, Germany*

Sibel Evcüman − *Nuclear Chemistry (INM-5), Institute of Neuroscience and Medicine, Forschungszentrum Jülich GmbH, 52425 Jülich, Germany*

Felix Neumaier − *Nuclear Chemistry (INM-5), Institute of Neuroscience and Medicine, Forschungszentrum Jülich GmbH, 52425 Jülich, Germany; Institute of Radiochemistry and Experimental Molecular Imaging, University of Cologne, Faculty of Medicine, and University Hospital Cologne, 50937 Cologne, Germany*

Boris D. Zlatopolskiy − *Nuclear Chemistry (INM-5), Institute of Neuroscience and Medicine, Forschungszentrum Jülich GmbH, 52425 Jülich, Germany; Institute of*

Radiochemistry and Experimental Molecular Imaging, University of Cologne, Faculty of Medicine, and University Hospital Cologne, 50937 Cologne, Germany; orcid.org/0000-0001-5818-1260

Swen Humpert − *Nuclear Chemistry (INM-5), Institute of Neuroscience and Medicine, Forschungszentrum Jülich GmbH, 52425 Jülich, Germany*

Dirk Bier − *Nuclear Chemistry (INM-5), Institute of Neuroscience and Medicine, Forschungszentrum Jülich GmbH, 52425 Jülich, Germany;* orcid.org/0000-0001-9231-4303

Marcus Holschbach − *Nuclear Chemistry (INM-5), Institute of Neuroscience and Medicine, Forschungszentrum Jülich GmbH, 52425 Jülich, Germany*

Annette Schulze − *Nuclear Chemistry (INM-5), Institute of Neuroscience and Medicine, Forschungszentrum Jülich GmbH, 52425 Jülich, Germany*

Heike Endepols − *Nuclear Chemistry (INM-5), Institute of Neuroscience and Medicine, Forschungszentrum Jülich GmbH, 52425 Jülich, Germany; Institute of Radiochemistry and Experimental Molecular Imaging and Nuclear Medicine Department, University of Cologne, Faculty of Medicine, and University Hospital Cologne, 50937 Cologne, Germany*

Complete contact information is available at: https://pubs.acs.org/10.1021/acschemneuro.1c00284

Author Contributions

[⊥]C.H. and S.E. contributed equally. C.H., S.E., and B.D.Z. performed the (radio)chemical syntheses. S.H., H.E., D.B., and M.H. performed the radiometabolite analyses. B.N. and B.D.Z. conceived and designed the (radio)chemical procedures. F.N., C.H., S.E., B.D.Z., and B.N. wrote the paper. A.S. and D.B. designed and performed the autoradiographic experiments. H.E. performed and analyzed results of the PET experiments. All authors have read and agreed to the published version of the manuscript.

Notes

The authors declare no competing financial interest.

■ ACKNOWLEDGMENTS

This work was financially supported by DFG (Grant ZL 65/1-1). The authors thank Prof. S. M. Ametamey (ETH Zürich, Switzerland) for his suggestion to apply the methyl ester of [^{18}F]ALX5407 as a prodrug.

■ REFERENCES

(1) Betz, H. Ligand-gated Ion Channels in the Brain: The Amino Acid Receptor Superfamily. *Neuron* **1990**, *5* (4), 383−392.

(2) Béchade, C.; Sur, C.; Triller, A. The Inhibitory Neuronal Glycine Receptor. *BioEssays* **1994**, *16* (10), 735−744.

(3) Johnson, J. W.; Ascher, P. Glycine Potentiates the NMDA Response in Cultured Mouse Brain Neurons. *Nature* **1987**, *325* (6104), 529−531.

(4) Danysz, W.; Parsons, C. G. Glycine and N-Methyl-D-Aspartate Receptors: Physiological Significance and Possible Therapeutic Applications. *Pharmacol. Rev.* **1998**, *50*, 597−664.

(5) Newcomer, J. W.; Krystal, J. H. NMDA Receptor Regulation of Memory and Behavior in Humans. *Hippocampus* **2001**, *11* (5), 529−542.

(6) Lahti, A. Effects of Ketamine in Normal and Schizophrenic Volunteers. *Neuropsychopharmacology* **2001**, *25* (4), 455−467.

(7) Javitt, D. C. Negative Schizophrenic Symptomatology and the PCP (Phencyclidine) Model of Schizophrenia. *Hillside J. Clin Psychiatry* **1987**, *9* (1), 12−35.

(8) Carlsson, M.; Carlsson, A. Interactions between Glutamatergic and Monoaminergic Systems within the Basal Ganglia-Implications for Schizophrenia and Parkinson's Disease. *Trends Neurosci.* **1990**, *13*, 272.

(9) Gomeza, J.; Ohno, K.; Betz, H. Glycine Transporter Isoforms in the Mammalian Central Nervous System: Structures, Functions and Therapeutic Promises. *Curr. Opin. Drug Discovery Dev.* **2003**, *6* (5), 675−682.

(10) Javitt, D. C.; Zukin, S. R. Recent Advances in the Phencyclidine Model of Schizophrenia. *Am. J. Psychiatry* **1991**, *148*, 1301−1308.

(11) Olney, J. W.; Newcomer, J. W.; Farber, N. B. NMDA Receptor Hypofunction Model of Schizophrenia. *J. Psychiatr. Res.* **1999**, *33*, 523.

(12) Choi, D. W. Glutamate Receptors and the Induction of Excitotoxic Neuronal Death. *Prog. Brain Res.* **1994**, *100*, 47−51.

(13) Javitt, D. C.; Zylberman, I.; Zukin, S. R.; Heresco-Levy, U.; Lindenmayer, J.-P. Amelioration of Negative Symptoms in Schizophrenia by Glycine. *Am. J. Psychiatry* **1994**, *151* (8), 1234−1236.

(14) Heresco-Levy, U.; Javitt, D. C.; Ermilov, M.; Mordel, C.; Horowitz, A.; Kelly, D. Double-Blind, Placebo-Controlled, Crossover Trial of Glycine Adjuvant Therapy for Treatment-Resistant Schizophrenia. *Br. J. Psychiatry* **1996**, *169* (5), 610−617.

(15) Heresco-Levy, U.; Javitt, D. C.; Ermilov, M.; Mordel, C.; Silipo, G.; Lichtenstein, M. Efficacy of High-Dose Glycine in the Treatment of Enduring Negative Symptoms of Schizophrenia. *Arch. Gen. Psychiatry* **1999**, *56* (1), 29.

(16) Heresco-Levy, U.; Ermilov, M.; Lichtenberg, P.; Bar, G.; Javitt, D. C. High-Dose Glycine Added to Olanzapine and Risperidone for the Treatment of Schizophrenia. *Biol. Psychiatry* **2004**, *55* (2), 165−171.

(17) Tsai, G.; Yang, P.; Chung, L.-C.; Lange, N.; Coyle, J. T. D-Serine Added to Antipsychotics for the Treatment of Schizophrenia. *Biol. Psychiatry* **1998**, *44* (11), 1081−1089.

(18) Borowsky, B.; Mezey, É.; Hoffman, B. J. Two Glycine Transporter Variants with Distinct Localization in the CNS and Peripheral Tissues Are Encoded by a Common Gene. *Neuron* **1993**, *10*, 851.

(19) Zafra, F.; Gomeza, J.; Olivares, L.; Aragón, C.; Giménez, C. Regional Distribution and Developmental Variation of the Glycine Transporters GlyT1 and GlyT2 in the Rat CNS. *Eur. J. Neurosci.* **1995**, *7*, 1342.

(20) Eulenburg, V.; Armsen, W.; Betz, H.; Gomeza, J. Glycine Transporters: Essential Regulators of Neurotransmission. *Trends Biochem. Sci.* **2005**, *30*, 325.

(21) Harsing, L. The Glycine Transporter-1 Inhibitors NFPS and Org 24461: A Pharmacological Study. *Pharmacol., Biochem. Behav.* **2003**, *74* (4), 811−825.

(22) Perry, K. W.; Falcone, J. F.; Fell, M. J.; Ryder, J. W.; Yu, H.; Love, P. L.; Katner, J.; Gordon, K. D.; Wade, M. R.; Man, T.; Nomikos, G. G.; Phebus, L. A.; Cauvin, A. J.; Johnson, K. W.; Jones, C. K.; Hoffmann, B. J.; Sandusky, G. E.; Walter, M. W.; Porter, W. J.; Yang, L.; Merchant, K. M.; Shannon, H. E.; Svensson, K. A. Neurochemical and Behavioral Profiling of the Selective GlyT1 Inhibitors ALX5407 and LY2365109 Indicate a Preferential Action in Caudal vs. Cortical Brain Areas. *Neuropharmacology* **2008**, *55* (5), 743−754.

(23) Chaki, S.; Shimazaki, T.; Karasawa, J.; Aoki, T.; Kaku, A.; Iijima, M.; Kambe, D.; Yamamoto, S.; Kawakita, Y.; Shibata, T.; Abe, K.; Okubo, T.; Sekiguchi, Y.; Okuyama, S. Efficacy of a Glycine Transporter 1 Inhibitor TASP0315003 in Animal Models of Cognitive Dysfunction and Negative Symptoms of Schizophrenia. *Psychopharmacology (Berl).* **2015**, *232* (15), 2849−2861.

(24) Boulay, D.; Bergis, O.; Avenet, P.; Griebel, G. The Glycine Transporter-1 Inhibitor SSR103800 Displays a Selective and Specific Antipsychotic-like Profile in Normal and Transgenic Mice. *Neuropsychopharmacology* **2010**, *35* (2), 416−427.

(25) Kinney, G. G.; Sur, C.; Burno, M.; Mallorga, P. J.; Williams, J. B.; Figueroa, D. J.; Wittmann, M.; Lemaire, W.; Conn, P. J. The Glycine Transporter Type 1 Inhibitor N-[3-(4′-Fluorophenyl)-3-(4′-Phenylphenoxy)Propyl]Sarcosine Potentiates NMDA Receptor-Medi-

ated Responses in Vivo and Produces an Antipsychotic Profile in Rodent Behavior. *J. Neurosci.* **2003**, *23* (20), 7586−7591.
(26) Chen, L.; Muhlhauser, M.; Yang, C. R. Glycine Tranporter-1 Blockade Potentiates NMDA-Mediated Responses in Rat Prefrontal Cortical Neurons in Vitro and in Vivo. *J. Neurophysiol.* **2003**, *89* (2), 691−703.
(27) Le Pen, G.; Kew, J.; Alberati, D.; Borroni, E.; Heitz, M.-P.; Moreau, J.-L. Prepulse Inhibition Deficits of the Startle Reflex in Neonatal Ventral Hippocampal−Lesioned Rats: Reversal by Glycine and a Glycine Transporter Inhibitor. *Biol. Psychiatry* **2003**, *54* (11), 1162−1170.
(28) Lane, H. Y.; Lin, C. H.; Huang, Y. J.; Liao, C. H.; Chang, Y. C.; Tsai, G. E. A Randomized, Double-Blind, Placebo-Controlled Comparison Study of Sarcosine (N-Methylglycine) and d-Serine Add-on Treatment for Schizophrenia. *Int. J. Neuropsychopharmacol.* **2010**, *13*, 451.
(29) Tsai, G.; Lane, H. Y.; Yang, P.; Chong, M. Y.; Lange, N. Glycine Transporter I Inhibitor, N-Methylglycine (Sarcosine), Added to Antipsychotics for the Treatment of Schizophrenia. *Biol. Psychiatry* **2004**, *55*, 452.
(30) Dunayevich, E.; Buchanan, R. W.; Chen, C.-Y.; Yang, J.; Nilsen, J.; Dietrich, J. M.; Sun, H.; Marder, S. Efficacy and Safety of the Glycine Transporter Type-1 Inhibitor AMG 747 for the Treatment of Negative Symptoms Associated with Schizophrenia. *Schizophr. Res.* **2017**, *182*, 90−97.
(31) Schoemaker, J. H.; Jansen, W. T.; Schipper, J.; Szegedi, A. The Selective Glycine Uptake Inhibitor Org 25935 as an Adjunctive Treatment to Atypical Antipsychotics in Predominant Persistent Negative Symptoms of Schizophrenia. *J. Clin. Psychopharmacol.* **2014**, *34* (2), 190−198.
(32) Aubrey, K. R.; Vandenberg, R. J. N-[3-(4′-Fluorophenyl)-3-(4′-Phenylphenoxy)Propyl]Sarcosine (NFPS) Is a Selective Persistent Inhibitor of Glycine Transport. *Br. J. Pharmacol.* **2001**, *134* (7), 1429−1436.
(33) Porter, R. A.; Dawson, L. A. GlyT-1 Inhibitors. *Top. Med. Chem.* **2014**, *13*, 51−99.
(34) Ravert, H. T.; Mathews, W. B.; Klitenick, M. A.; Wong, D. F.; Dannals, R. F. Radiosynthesis of a Ligand for Studying the Glycine Transporter: [^{11}C]ALX-5407. *J. Labelled Compd. Radiopharm.* **2001**, *44*, 241.
(35) Zhou, J. N.; Fang, Q.; Hu, Y. H.; Yang, L. Y.; Wu, F. F.; Xie, L. J.; Wu, J.; Li, S. Copper(II)-Catalyzed Enantioselective Hydrosilylation of Halo-Substituted Alkyl Aryl and Heteroaryl Ketones: Asymmetric Synthesis of (R)-Fluoxetine and (S)-Duloxetine. *Org. Biomol. Chem.* **2014**, *12* (6), 1009−1017.
(36) De Angelis, S.; De Renzo, M.; Carlucci, C.; Degennaro, L.; Luisi, R. A Convenient Enantioselective CBS-Reduction of Arylketones in Flow-Microreactor Systems. *Org. Biomol. Chem.* **2016**, *14* (18), 4304−4311.
(37) Zischler, J.; Kolks, N.; Modemann, D.; Neumaier, B.; Zlatopolskiy, B. D. Alcohol-Enhanced Cu-Mediated Radiofluorination. *Chem. - Eur. J.* **2017**, *23* (14), 3251−3256.
(38) Zlatopolskiy, B. D.; Neumaier, F.; Rüngeler, T.; Drewes, B.; Kolks, N.; Neumaier, B. Preparation of a First ^{18}F-Labeled Agonist for M1 Muscarinic Acetylcholine Receptors. *Molecules* **2020**, *25* (12), 2880.
(39) Zarrad, F.; Zlatopolskiy, B. D.; Krapf, P.; Zischler, J.; Neumaier, B. A Practical Method for the Preparation of ^{18}F-Labeled Aromatic Amino Acids from Nucleophilic [^{18}F]Fluoride and Stannyl Precursors for Electrophilic Radiohalogenation. *Molecules* **2017**, *22*, 2231.
(40) Committee for Human Medicinal Products. ICH Harmonised Guideline for Elemental Inpurities. European Medicines Agency, 2019.
(41) Wilson, A. A.; Jin, L.; Garcia, A.; DaSilva, J. N.; Houle, S. An Admonition When Measuring the Lipophilicity of Radiotracers Using Counting Techniques. *Appl. Radiat. Isot.* **2001**, *54*, 203.
(42) Dong, J.; Wang, N.-N.; Yao, Z.-J.; Zhang, L.; Cheng, Y.; Ouyang, D.; Lu, A.-P.; Cao, D.-S. ADMETlab: A Platform for Systematic ADMET Evaluation Based on a Comprehensively Collected ADMET Database. *J. Cheminf.* **2018**, *10* (1), 29.
(43) Pike, V. W. PET Radiotracers: Crossing the Blood−Brain Barrier and Surviving Metabolism. *Trends Pharmacol. Sci.* **2009**, *30* (8), 431−440.
(44) Waterhouse, R. Determination of Lipophilicity and Its Use as a Predictor of Blood−Brain Barrier Penetration of Molecular Imaging Agents. *Mol. Imaging Biol.* **2003**, *5* (6), 376−389.
(45) Zeng, Z.; O'Brien, J. A.; Lemaire, W.; O'Malley, S. S.; Miller, P. J.; Zhao, Z.; Wallace, M. A.; Raab, C.; Lindsley, C. W.; Sur, C.; Williams, D. L. A Novel Radioligand for Glycine Transporter 1: Characterization and Use in Autoradiographic and in Vivo Brain Occupancy Studies. *Nucl. Med. Biol.* **2008**, *35* (3), 315−325.
(46) Zafra, F.; Aragon, C.; Olivares, L.; Danbolt, N. C.; Giménez, C.; Storm-Mathisen, J. Glycine Transporters Are Differentially Expressed among CNS Cells. *J. Neurosci.* **1995**, *15* (5), 3952−3969.
(47) Cubelos, B.; Giménez, C.; Zafra, F. Localization of the GLYT1 Glycine Transporter at Glutamatergic Synapses in the Rat Brain. *Cereb. Cortex* **2005**, *15* (4), 448−459.
(48) Herdon, H.; Godfrey, F.; Brown, A.; Coulton, S.; Evans, J.; Cairns, W. Pharmacological Assessment of the Role of the Glycine Transporter GlyT-1 in Mediating High-Affinity Glycine Uptake by Rat Cerebral Cortex and Cerebellum Synaptosomes. *Neuropharmacology* **2001**, *41* (1), 88−96.
(49) Passchier, J.; Gunn, R. N.; van Waarde, A. Imaging Type 1 Glycine Transporters in the CNS Using Positron Emission Tomography. In *PET and SPECT of Neurobiological Systems*; Springer: Berlin, 2014; pp 321−330; DOI: 10.1007/978-3-642-42014-6_12.
(50) Mallorga, P. J.; Williams, J. B.; Jacobson, M.; Marques, R.; Chaudhary, A.; Conn, P. J.; Pettibone, D. J.; Sur, C. Pharmacology and Expression Analysis of Glycine Transporter GlyT1 with [^{3}H]-(N-[3-(4′-Fluorophenyl)-3-(4′-phenylphenoxy)propyl])sarcosine. *Neuropharmacology* **2003**, *45* (5), 585−593.
(51) Mezler, M.; Hornberger, W.; Mueller, R.; Schmidt, M.; Amberg, W.; Braje, W.; Ochse, M.; Schoemaker, H.; Behl, B. Inhibitors of GlyT1 Affect Glycine Transport via Discrete Binding Sites. *Mol. Pharmacol.* **2008**, *74* (6), 1705−1715.
(52) Harsing, L. G., Jr.; Gacsalyi, I.; Szabo, G.; Schmidt, E.; Sziray, N.; Sebban, C.; Tesolin-Decros, B.; Matyus, P.; Egyed, A.; Spedding, M.; Levay, G.; Harsing, L. The Glycine Transporter-1 Inhibitors NFPS and Org 24461: A Pharmacological Study. *Pharmacol., Biochem. Behav.* **2003**, *74* (4), 811−825.
(53) Clemett, D. A.; Punhani, T.; Duxon, M. S.; Blackburn, T. P.; Fone, K. C. Immunohistochemical Localisation of the 5-HT_{2C} Receptor Protein in the Rat CNS. *Neuropharmacology* **2000**, *39* (1), 123−132.
(54) Orban, G.; Bombardi, C.; Marino Gammazza, A.; Colangeli, R.; Pierucci, M.; Pomara, C.; Pessia, M.; Bucchieri, F.; Arcangelo, B.; Smolders, I.; De Deurwaerdère, P.; Di Giovanni, G. Role(s) of the 5-HT_{2C} Receptor in the Development of Maximal Dentate Activation in the Hippocampus of Anesthetized Rats. *CNS Neurosci. Ther.* **2014**, *20* (7), 651−661.
(55) Atkinson, B. N.; Bell, S. C.; De Vivo, M.; Kowalski, L. R.; Lechner, S. M.; Ognyanov, V. I.; Tham, C.-S.; Tsai, C.; Jia, J.; Ashton, D.; Klitenick, M. A. ALX5407: A Potent, Selective Inhibitor of the HGlyT1 Glycine Transporter. *Mol. Pharmacol.* **2001**, *60* (6), 1414−1420.
(56) Becker, S.; Liu, X. Evaluation of the Utility of Brain Slice Methods to Study Brain Penetration. *Drug Metab. Dispos.* **2006**, *34* (5), 855−861.
(57) Liu, X.; Smith, B. J.; Chen, C.; Callegari, E.; Becker, S. L.; Chen, X.; Cianfrogna, J.; Doran, A. C.; Doran, S. D.; Gibbs, J. P.; Hosea, N.; Liu, J.; Nelson, F. R.; Szewc, M. A.; Van Deusen, J. Use of a Physiologically Based Pharmacokinetic Model to Study the Time to Reach Brain Equilibrium: An Experimental Analysis of the Role of Blood-Brain Barrier Permeability, Plasma Protein Binding, and Brain Tissue Binding. *J. Pharmacol. Exp. Ther.* **2005**, *313* (3), 1254−1262.
(58) Kopec, K.; Flood, D. G.; Gasior, M.; McKenna, B. A. W.; Zuvich, E.; Schreiber, J.; Salvino, J. M.; Durkin, J. T.; Ator, M. A.;

Marino, M. J. Glycine Transporter (GlyT1) Inhibitors with Reduced Residence Time Increase Prepulse Inhibition without Inducing Hyperlocomotion in DBA/2 Mice. *Biochem. Pharmacol.* **2010**, *80* (9), 1407−1417.
(59) Zhang, L.; Villalobos, A.; Beck, E. M.; Bocan, T.; Chappie, T. A.; Chen, L.; Grimwood, S.; Heck, S. D.; Helal, C. J.; Hou, X.; Humphrey, J. M.; Lu, J.; Skaddan, M. B.; McCarthy, T. J.; Verhoest, P. R.; Wager, T. T.; Zasadny, K. Design and Selection Parameters to Accelerate the Discovery of Novel Central Nervous System Positron Emission Tomography (PET) Ligands and Their Application in the Development of a Novel Phosphodiesterase 2A PET Ligand. *J. Med. Chem.* **2013**, *56* (11), 4568−4579.
(60) Waring, M. J. Defining Optimum Lipophilicity and Molecular Weight Ranges for Drug Candidates—Molecular Weight Dependent Lower LogD Limits Based on Permeability. *Bioorg. Med. Chem. Lett.* **2009**, *19* (10), 2844−2851.
(61) Waring, M. J. Lipophilicity in Drug Discovery. *Expert Opin. Drug Discovery* **2010**, *5* (3), 235−248.
(62) Sowa, A. R.; Brooks, A. F.; Shao, X.; Henderson, B. D.; Sherman, P.; Arteaga, J.; Stauff, J.; Lee, A. C.; Koeppe, R. A.; Scott, P. J. H.; Kilbourn, M. R. Development of Positron Emission Tomography Radiotracers for the GABA Transporter 1. *ACS Chem. Neurosci.* **2018**, *9* (11), 2767−2773.
(63) Hitchcock, S. A.; Pennington, L. D. Structure-Brain Exposure Relationships. *J. Med. Chem.* **2006**, *49* (26), 7559−7583.
(64) Ghose, A. K.; Herbertz, T.; Hudkins, R. L.; Dorsey, B. D.; Mallamo, J. P. Knowledge-Based, Central Nervous System (CNS) Lead Selection and Lead Optimization for CNS Drug Discovery. *ACS Chem. Neurosci.* **2012**, *3* (1), 50−68.
(65) Pike, V. W. Considerations in the Development of Reversibly Binding PET Radioligands for Brain Imaging. *Curr. Med. Chem.* **2016**, *23* (18), 1818−1869.
(66) Sowa, A. R.; Shao, X.; Brooks, A. F.; Scott, P. J.; Kilbourn, M. R. Towards the Development of Brain Penetrant, GAT-1 Selective Radioligands. *J. Nucl. Med.* **2018**, *59* (Suppl. 1), 1027.
(67) Fuchigami, T.; Takano, A.; Gulyás, B.; Jia, Z.; Finnema, S. J.; Andersson, J. D.; Nakao, R.; Magata, Y.; Haratake, M.; Nakayama, M.; Halldin, C. Synthesis and Evaluation of 2-Chloro N-[(S)-{(S)-1-[^{11}C]Methylpiperidin-2-Yl}(Phenyl)Methyl]3-Trifluoromethyl-Benzamide ([^{11}C]N-Methyl-SSR504734) as a PET Radioligand for Glycine Transporter 1. *EJNMMI Res.* **2012**, *2* (1), 37.
(68) Fuchigami, T.; Haratake, M.; Magata, Y.; Haradahira, T.; Nakayama, M. Synthesis and Characterization of [^{125}I]2-Iodo-N-[(S)-{(S)-1-Methylpiperidin-2-Yl}(Phenyl)Methyl]3-Trifluoromethyl-Benzamide as Novel Imaging Probe for Glycine Transporter 1. *Bioorg. Med. Chem.* **2011**, *19* (21), 6245−6253.
(69) Lear, J. L.; Ackermann, R. F.; Kameyama, M.; Kuhl, D. E. Evaluation of [^{123}I]Isopropyliodoamphetamine as a Tracer for Local Cerebral Blood Flow Using Direct Autoradiographic Comparison. *J. Cereb. Blood Flow Metab.* **1982**, *2* (2), 179−185.
(70) Lear, J. L.; Navarro, D. Autoradiographic Comparison of Thallium-201 Diethyldithiocarbamate, Isopropyliodoamphetamine and Iodoantipyrine as Cerebral Blood Flow Tracers. *J. Nucl. Med.* **1987**, *28* (4), 481−486.
(71) Hosokawa, M.; Maki, T.; Satoh, T. Characterization of Molecular Species of Liver Microsomal Carboxylesterases of Several Animal Species and Humans. *Arch. Biochem. Biophys.* **1990**, *277* (1), 219−227.
(72) Imai, T. Human Carboxylesterase Isozymes: Catalytic Properties and Rational Drug Design. *Drug Metab. Pharmacokinet.* **2006**, *21* (3), 173−185.
(73) Anderson, B. D.; Galinsky, R. E.; Baker, D. C.; Chi, S.-C.; Hoesterey, B. L.; Morgan, M. E.; Murakami, K.; Mitsuya, H. Approaches toward the Optimization of CNS Uptake of Anti-AIDS Agents. *J. Controlled Release* **1992**, *19* (1−3), 219−229.
(74) Durrer, A.; Walther, B.; Racciatti, A.; Boss, G.; Testa, B. Structure-Metabolism Relationships in the Hydrolysis of Nicotinate Esters by Rat Liver and Brain Subcellular Fractions. *Pharm. Res.* **1991**, *8* (7), 832−839.
(75) Karaman, R. Prodrugs Design Based on Inter- and Intramolecular Chemical Processes. *Chem. Biol. Drug Des.* **2013**, *82* (6), 643−668.
(76) Lavis, L. D. Ester Bonds in Prodrugs. *ACS Chem. Biol.* **2008**, *3* (4), 203−206.
(77) Haynes, J. S.; Rettig, S. J.; Sams, J. R.; Trotter, J.; Thompson, R. C. Pyrazine and Pyridine Complexes of Copper(II) Trifluoromethanesulfonate. Crystal Structure of Tetrakis(Pyridine)Bis-(Trifluoromethanesulfonato-O)Copper(II) and Magnetic Exchange in (Pyrazine)Bis(Trifluoromethanesulfonato-O)Copper(II). *Inorg. Chem.* **1988**, *27* (7), 1237−1241.
(78) Paxinos, G.; Watson, C. *The Rat Brain in Stereotaxic Coordinates* 7th ed.; Elsevier Academic Press, 2014.

https://doi.org/10.1021/acschemneuro.1c00284
ACS Chem. Neurosci. 2021, 12, 3335−3346

3.1.2 Next Generation Copper Mediators for the Efficient Production of ^{18}F-Labeled Aromatics

Wie in Kapitel 1.4 erwähnt, stellt die Cu-vermittelte Radiofluorierung eine einfach anzuwendende Methode für die ^{18}F-Markierung von aromatischen $B(OH)_2$-[108], BPin-[107] oder $SnMe_3$[137]-Vorläufermolekülen dar. Aufgrund der guten und einfachen Zugänglichkeit der Vorläufer ermöglicht diese Methode die Herstellung von Radiotracern, die über nukleophile Substitutionsreaktionen mit $[^{18}F]F^-$ schwer oder gar nicht zugänglich wären.

Seit Einführung des Standardprotokolls der „Alkohol-verstärkten“ CVRF mit $Cu(Py)_4(OTf)_2$ in DMA/*n*BuOH bei 110 °C hat sich diese Methode als robustes Radiomarkierungverfahen mit guten und reproduzierbaren RCAs etabliert. Dennoch ist zu beachten, dass nicht alle Radiotracer mit guten RCAs erhalten werden können, obwohl entsprechende Optimierungsvorschläge in der Literatur zu finden sind.[126,138] Ein wesentlicher Nachteil der Methode ist, dass große Substratmengen (>20 µmol) erforderlich sind, um hohe und reproduzierbare RCAs zu erzielen. Dies führt zu erhöhten Produktionskosten und erschwert aufgrund der vermehrten Bildung chemischer Nebenprodukte bei der Radiosynthese häufig die Isolierung der Produkte über präparative HPLC.

Um diese Nachteile zu überwinden, wurden neue Cu(II)-Komplexe aus verschiedenen substituieren *N*-heterozyklischen Liganden und Gegenionen synthetisiert. Anschließend wurde ihre Effizienz durch Radiosynthesen mit elektronenarmen und -reichen $B(OH)_2$ und BPin-Vorläufern evaluiert. Nach dieser ersten Vorauswahl wurden die aussichtsreichsten Cu(II)-Komplexe für eine weitere Optimierung der Reaktionsbedingungen in Hinblick auf Lösungsmittel, Temperatur und Reaktionsdauer verwendet. Schließlich wurde das optimierte Protokoll auf Radiosynthesen mit $SnMe_3$-Vorläufern angewendet, wobei auch die Anwendbarkeit der neuen Cu(II)-Komplexe bei reduzierter Substratmenge überprüft wurde. Zusätzlich wurde das optimierte Protokoll auf die manuelle und automatisierte Herstellung von literaturbekannten Radiotracern übertragen.

Das Konzept der Publikation wurde gemeinschaftlich von C. Hoffmann und Prof. Dr. B. D. Zlatopolskiy mit Unterstützung von Prof. Dr. B. Neumaier entwickelt. Die Synthesen der Cu(II)-Komplexe wurden von N. Kolks, C. Hoffmann und Prof. Dr. B. D. Zlatopolskiy durchgeführt. Kristallstrukturaufklärung wurden von D. Smets und A.

Haseloer mit Unterstützung von Prof. Dr. U. Ruschewitz und Prof. Dr. A. Klein durchgeführt. Organische Synthesen wurden von C. Hoffmann, E. A. Urusova und Prof. Dr. B. D. Zlatopolskiy durchgeführt. Radiosynthesen und deren Optimierungen wurden von C. Hoffmann durchgeführt. Die Radiosynthesen der Aminosäure-PET-Tracer wurde von B. Gröner durchgeführt. Statistische Auswertungen über ANOVA wurden von Prof. Dr. H. Endepols durchgeführt. Der Artikel wurde gemeinschaftlich von C. Hoffmann, B. Gröner, Prof. Dr. H. Endepols, Dr. F. Neumaier, Prof. Dr. B. D. Zlatopolskiy und Prof. Dr. B. Neumaier verfasst.

Im Rahmen dieser Dissertation wurde der Artikel mit allen erhobenen experimentellen und analytischen Daten als Kapitel eingefügt und die dazugehörige „Supporting Information“ im Anhang B hinterlegt.[139]

Copyright

Chemistry–A European Journal
Research Article
doi.org/10.1002/chem.202202965
Chemistry Europe
European Chemical Societies Publishing
www.chemeurj.org

Next Generation Copper Mediators for the Efficient Production of ^{18}F-Labeled Aromatics

Chris Hoffmann,[a, b] Niklas Kolks,[a, b] Daniel Smets,[c] Alexander Haseloer,[c] Benedikt Gröner,[a, b] Elizaveta A. Urusova,[a, b] Heike Endepols,[a, b, d] Felix Neumaier,[a, b] Uwe Ruschewitz,[c] Axel Klein,[c] Bernd Neumaier,*[a, b] and Boris D. Zlatopolskiy[a, b]

Abstract: Cu-mediated radiofluorination is a versatile tool for the preparation of ^{18}F-labeled (hetero)aromatics. In this work, we systematically evaluated a series of complexes and identified several generally applicable mediators for highly efficient radiofluorination of aryl boronic and stannyl substrates. Utilization of these mediators in *n*BuOH/DMI or DMI significantly improved ^{18}F-labeling yields despite use of lower precursor amounts. Impressively, application of 2.5 μmol aryl boronic acids was sufficient to achieve ^{18}F-labeling yields of up to 75%. The practicality of the novel mediators was demonstrated by efficient production of five PET-tracers and transfer of the method to an automated radiosynthesis module. In addition, (*S*)-3-[^{18}F]FPhe and 6-[^{18}F]FDOPA were prepared in activity yields of 23 ± 1% and 30 ± 3% using only 2.5 μmol of the corresponding boronic acid or trimethylstannyl precursor.

Introduction

Positron emission tomography (PET) is a non-invasive imaging technique that employs probes labeled with β^+-emitting radionuclides to visualize biochemical processes for research or diagnostic purposes. The most widely used PET radionuclide is fluorine-18, which is readily accessible in the form of [^{18}F]fluoride ([^{18}F]F$^-$) from [^{18}O]H_2O via the ^{18}O(p,n)^{18}F nuclear reaction. Fluorine-18 has advantageous decay properties (high β^+-emission probability, relatively low β^+ energy, suitably long half-life of 110 min) compared to other common short-lived PET isotopes like ^{11}C, ^{13}N, ^{15}O or ^{68}Ga.[1] However, direct application of [^{18}F]F$^-$ in [^{18}O]H_2O for radiofluorination is usually not feasible due to its high degree and strength of hydration.[2] As such, time consuming azeotropic drying steps and addition of bases and phase transfer catalysts are usually required to obtain highly nucleophilic [^{18}F]F$^-$ that can be further used for S_N2, S_NAr or transition metal-catalyzed reactions.[3] Owing to radioactive decay and inevitable heating-induced adsorption of [^{18}F]F$^-$ to the reactor walls, azeotropic drying and other pre-processing steps are invariably associated with radioactivity losses. However, these steps and the use of additives can be omitted, for example, by applying the "minimalist"[4] or related[5] protocols for S_N2, S_NAr or Cu-mediated radiofluorination.

Recently introduced approaches for Cu-mediated production of ^{18}F-labeled (hetero)arenes from different substrates,[6] including readily available aryl boronic acids,[7] pinacol boronates[8] and trialkylstannanes,[9] have granted access to emerging or established but otherwise hardly accessible radiotracers. Whereas the original procedures were rather inefficient and not well suited for radiotracer production on a preparative scale, several approaches to circumvent these limitations have since been proposed,[5b,10] which significantly contributed to the dramatic growth of PET imaging in the last 5–7 years. Main drawback of these procedures in their current form is that relatively large amounts of labeling precursor and Cu(Py)$_4$(OTf)$_2$ (≥ 20 μmol of each) are often required to achieve high and reproducible radiochemical yields (RCYs),[11] especially when radiosyntheses are performed in remotely controlled synthesis units. This not only increases production costs, but in many cases also complicates purification of the resulting PET-tracers. Surprisingly, to date, no significant efforts have been made to

[a] C. Hoffmann, N. Kolks, B. Gröner, E. A. Urusova, Prof. Dr. H. Endepols, Dr. F. Neumaier, Prof. Dr. B. Neumaier, Dr. B. D. Zlatopolskiy
Faculty of Medicine and University Hospital Cologne
Institute of Radiochemistry and Experimental Molecular Imaging
University of Cologne
Kerpener Straße 62, 50937 Cologne (Germany)

[b] C. Hoffmann, N. Kolks, B. Gröner, E. A. Urusova, Prof. Dr. H. Endepols, Dr. F. Neumaier, Prof. Dr. B. Neumaier, Dr. B. D. Zlatopolskiy
Institute of Neuroscience and Medicine
Nuclear Chemistry (INM-5)
Forschungszentrum Jülich GmbH
Wilhelm-Johnen-Straße, 52428 Jülich (Germany)
E-mail: b.neumaier@fz-juelich.de
Homepage: https://www.fz-juelich.de/de/inm/inm-5

[c] Dr. D. Smets, Dr. A. Haseloer, Prof. Dr. U. Ruschewitz, Prof. Dr. A. Klein
Faculty of Mathematics and Natural Sciences
Department of Chemistry, Institute of Inorganic Chemistry
University of Cologne
Greinstr. 6, 50939 Cologne (Germany)

[d] Prof. Dr. H. Endepols
Faculty of Medicine and University Hospital Cologne
Department of Nuclear Medicine
University of Cologne
Kerpener Straße 62, 50937 Cologne (Germany)

Supporting information for this article is available on the WWW under https://doi.org/10.1002/chem.202202965

find more efficient radiolabeling mediators, which could help to eliminate this bottleneck.

In this study, we first prepared a series of Cu(II) complexes and evaluated their efficiencies as mediators for radiofluorination of various model substrates bearing -$B(OH)_2$ or -Bpin groups (Scheme 1A). The most promising candidates were selected and used in subsequent experiments to optimize further reaction parameters like solvent, time and temperature (Scheme 1B). In addition, the developed radiofluorination protocol was adapted to radiolabeling of aryl trialkylstannanes (Scheme 1B) and to the use of low precursor amounts (Scheme 1C). Finally, we exemplified the suitability of the optimized protocol for the manual and automated preparation of several PET-tracers (Scheme 1D).

Results and Discussion

In order to assess the influence of different ligands on radiofluorination, we prepared a series of Cu(II) complexes with fifteen N-heterocycles and nine counter ions. For comparison, Co(II) perchlorate and Ni(II) triflate pyridine complexes were also synthesized. For three copper complexes, including the literature known $Cu(Py)_4(OTf)_2$ (with known crystal structure)[12] as well as $Cu(3,4\text{-}Me_2Py)_4(OTf)_2$ and $Cu(4\text{-}MeOPy)_4(ClO_4)_2$, the crystal structures were determined (see Supporting Information for more details).

For our initial optimization studies, we used sterically unhindered, moderately electron-rich 4-biphenyl- and CH acidic electron-poor 4-acetylphenyl-boronic acids and pinacol boronates as "simple" and "difficult" model radiolabeling precursors, respectively (Scheme 2).

Since copper complexes are prone to decomposition under basic conditions,[4e] non-basic tetraethylammonium triflate (Et_4NOTf) was selected for $[^{18}F]F^-$ elution. Radiolabeling was carried out according to the alcohol-enhanced protocol[5b] as follows. $[^{18}F]F^-$ trapped on an anion exchange resin was eluted with Et_4NOTf (1 mg, 4 μmol) in *n*BuOH (400 μL) directly into a solution of the copper complex and precursor (10 μmol of each) in DMA (800 μmol). The reaction mixture was heated at 110 °C for 10 min under air, diluted with H_2O (2 mL), and radiochemical conversions (RCCs)[11] were determined by HPLC. The results of the screening experiments were statistically evaluated using GraphPad Prism software. While highly reproducible $[^{18}F]F^-$ elution efficiencies of 90–95 % were observed, the RCCs varied markedly depending on the applied Cu mediator (Figure 1). The use of Ni or Co complexes as well as Cu(II) complexes with Br^-, Cl^-, OAc^-, OMs^- or SO_4^{2-} counter ions did not result in the formation of radiolabeled products (data not shown). Copper(II) complexes formed by pyridines containing electron donating methyl, phenyl and methoxy substituents in the *p*- or *p*- and *m*-positions, isoquinoline (Isoq) or imidazo[1,2-b]pyridazine (Impdz)[13] as monodentate ligands with triflate or perchlorate counter ions were the most suitable mediators for radiofluorination (Scheme 2, Figures 1 and S13, Tables S18–S22).

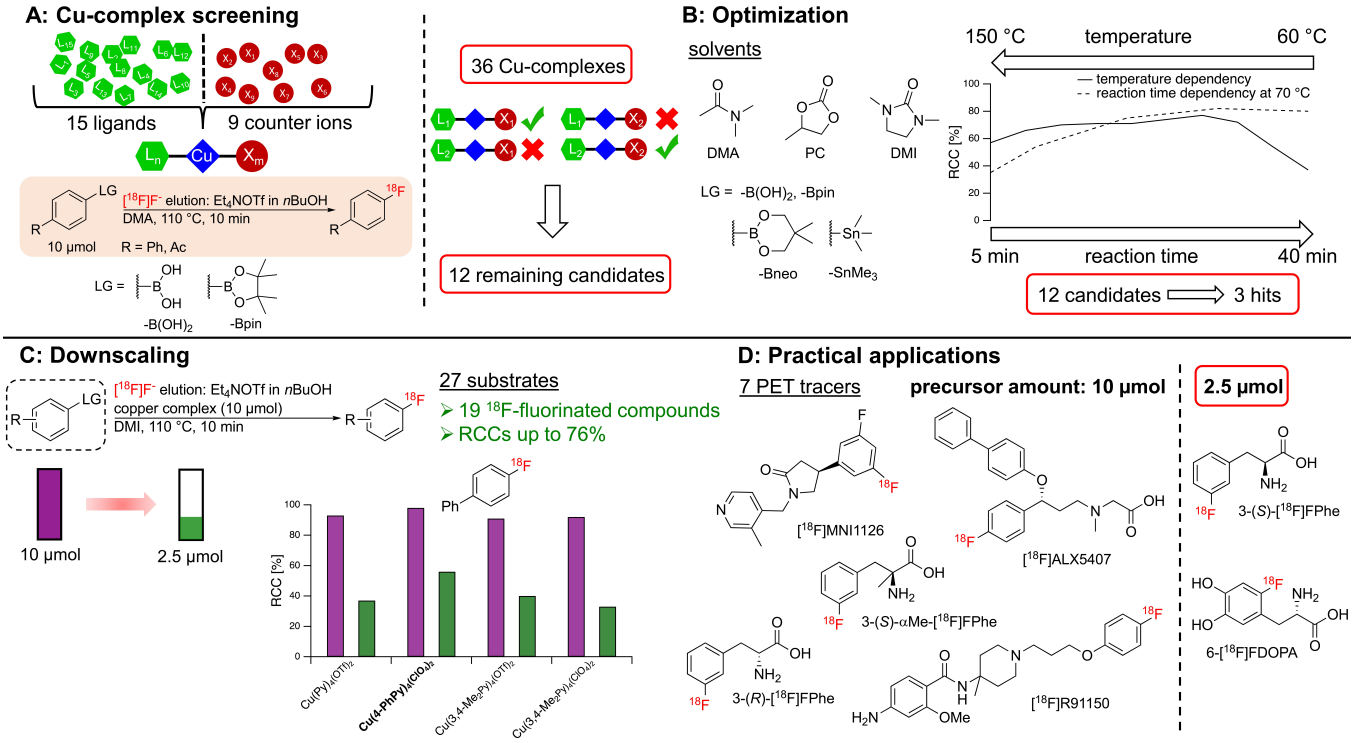

Scheme 1. Workflow of the present study on different Cu(II) complexes for efficient radiofluorination of aryl boronic and stannyl substrates. A) During an initial screening of a total of 36 Cu(II) complexes with different ligands and counter ions, B) the 12 most promising candidates were identified and used for subsequent optimization studies. C) Following downscaling experiments with various model compounds, D) three of the candidate complexes were used to prepare different PET-tracers.

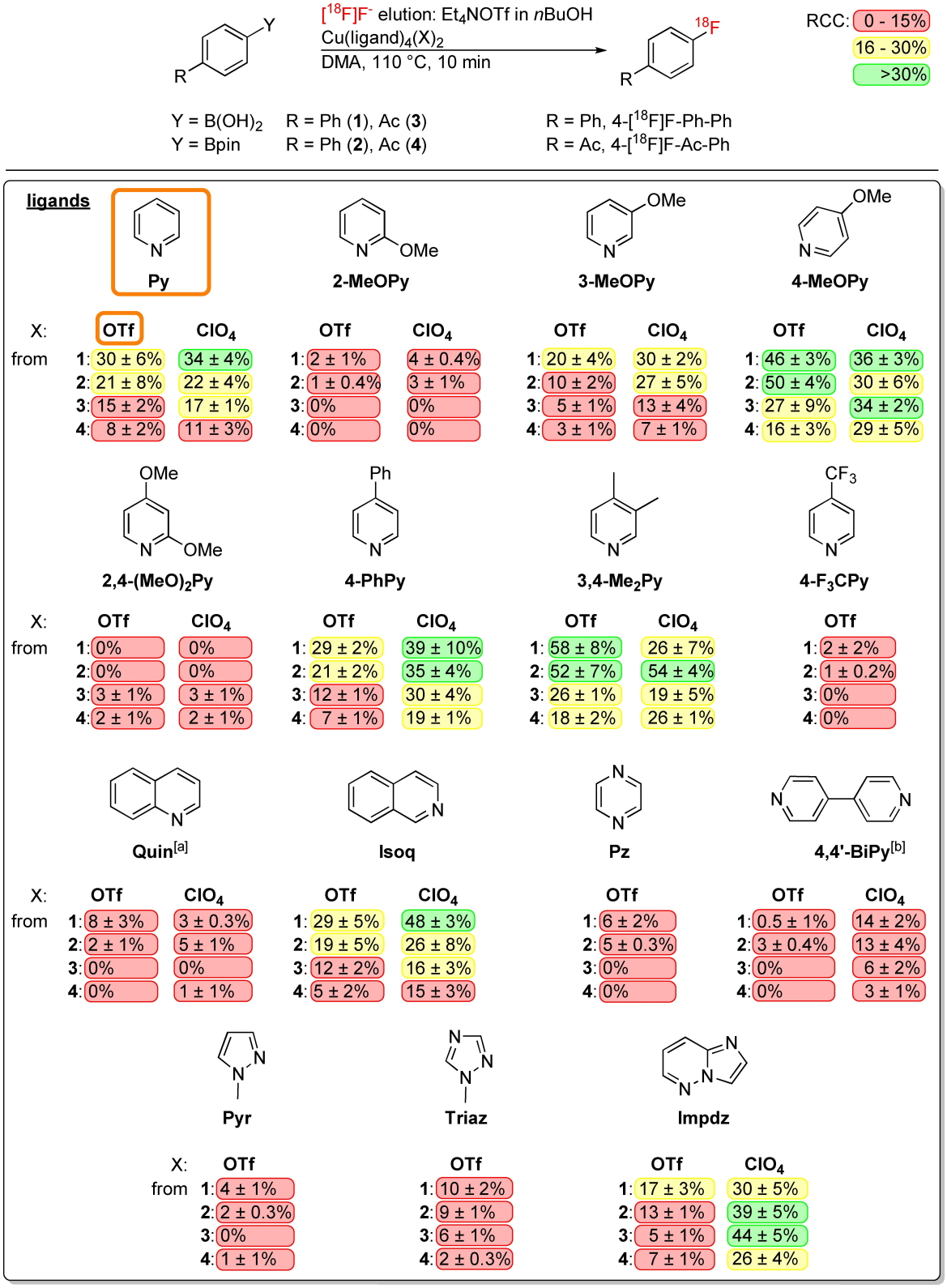

Scheme 2. Radiofluorination of aryl boronic acids and pinacol boronates using different mediators in *n*BuOH/DMA. Conditions: i) elution of $[^{18}F]F^-$ (10–50 MBq) with Et_4NOTf (1 mg, 4 μmol) in nBuOH (400 μL) into a solution of substrates **1**–**4** (10 μmol, 1 eq.) and $Cu(ligand)_4(X)_2$ (10 μmol, 1 eq.) in DMA (800 μL); ii) 110 °C for 10 min under air; iii) addition of H_2O (1 mL). Radiochemical conversions (RCCs) are provided in the following format: mean RCC ± standard deviation (%). All experiments were carried out at least in triplicate. Conventional $Cu(Py)_4(OTf)_2$ is highlighted with an orange frame, while RCCs are color-coded in red (0–15 %), yellow (16–30 %) or green (> 30 %) as indicated in the upper right corner. Py (pyridine), 2-MeOPy (2-methoxypyridine), 3-MeOPy (3-methoxypyridine), 4-MeOPy (4-methoxypyridine), 2,4-$(MeO)_2$Py (2,4-dimethoxypyridine), 4,4′-BiPy (4,4′-bipyridine), 4-PhPy (4-phenylpyridine), 3,4-Me_2Py (3,4-lutidine), 4-F_3CPy (4-trifluoromethylpyridine), Pz (pyrazine), Triaz (N-methyl-1,2,4-triazole), Pyr (N-methylpyrazole), Quin (quinoline), Isoq (isoquinoline), Impdz (imidazo(1,2-b)pyridazine).[a] $Cu(Quin)_3(MeOH)X_2$;[b] $Cu(4,4'\text{-BiPy})_2X_2$.

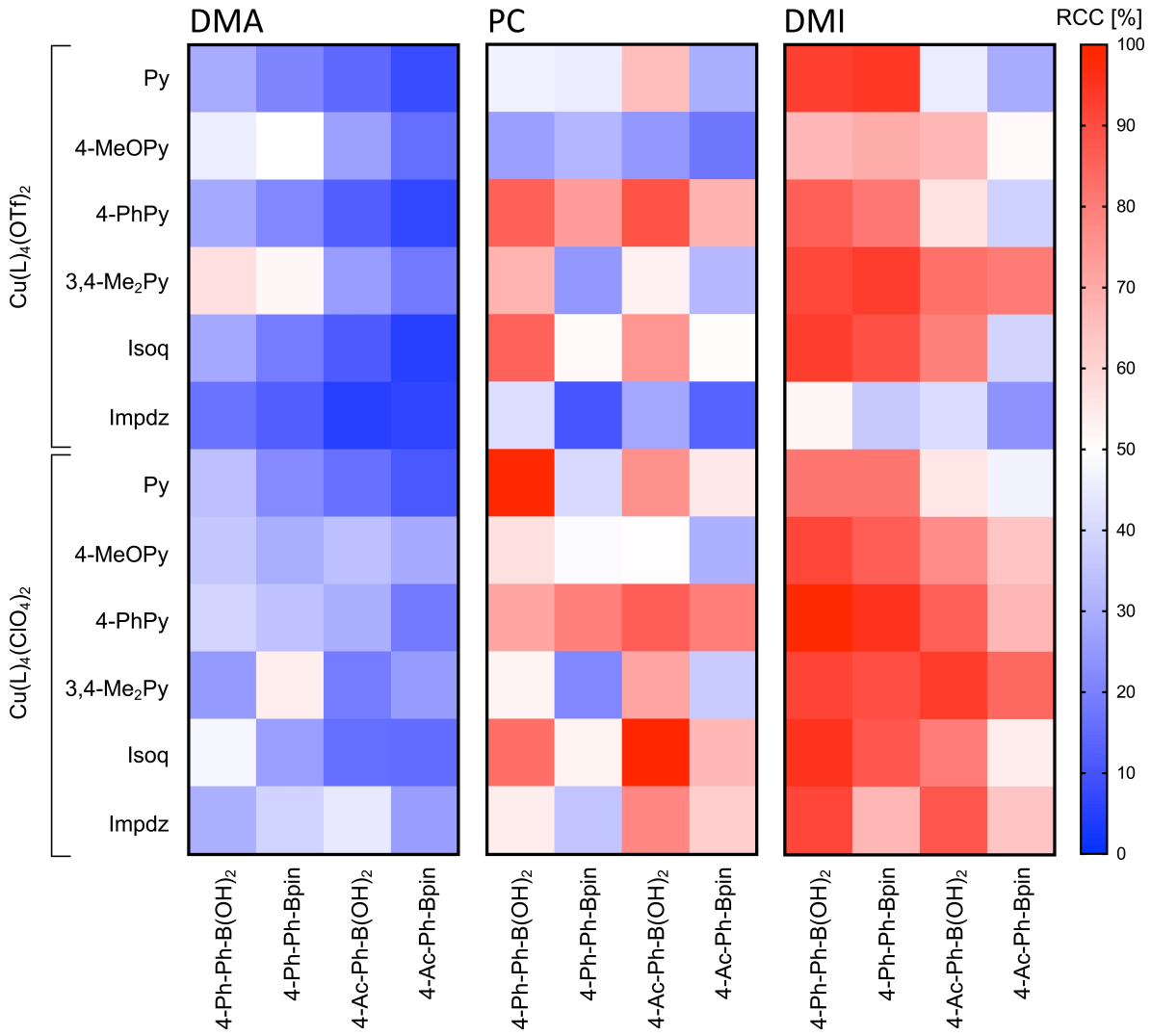

Figure 1. Dependency of radiochemical conversions (RCCs) on radiolabeling substrate and Cu mediator in different reaction solvents. Reaction conditions: [^{18}F]F$^-$ (10–50 MBq), radiolabeling substrate (10 μmol), Cu(L)$_4$X$_2$ (10 μmol) and Et$_4$NOTf (1 mg, 4 μmol) in *n*BuOH/reaction solvent 1 : 2 (1.2 mL) at 110 °C for 10 min, followed by addition of H_2O (2 mL). RCCs were determined by HPLC as described in the Supporting Information. All experiments were performed at least in triplicate. The color bar represents RCC (%). For full statistics including main effects and factor interactions, see Tables S18–S21 and S27–S34.

Thus, ^{18}F-labeling of biphenyl substrates and 4-Ac-Ph-B(OH)$_2$ was significantly more efficient if Cu(4-MeOPy)$_4$(OTf)$_2$ or Cu(3,4-Me$_2$Py)$_4$(OTf)$_2$ were used instead of Cu(Py)$_4$(OTf)$_2$. In the case of 4-Ac-Ph-Bpin on the other hand, differences in the RCCs obtained with different mediators did not reach statistical significance. For all tested Cu complexes, 4-phenyl-substituted substrates afforded higher RCCs than 4-acetyl-substituted substrates. In the majority of cases, B(OH)$_2$ was a slightly better leaving group than Bpin. If Cu(4-MeOPy)$_4$(OTf)$_2$ was used as the mediator, RCCs for 4-Ac-Ph-B(OH)$_2$ were significantly higher than for 4-Ac-Ph-Bpin. Among the perchlorate complexes, Cu(Impdz)$_4$(ClO$_4$)$_2$ furnished significantly higher RCCs with 4-Ph-Ph-Bpin, 4-Ac-Ph-B(OH)$_2$ and 4-Ac-Ph-Bpin precursors as compared to Cu(Py)$_4$(OTf)$_2$. Copper perchlorate complexes with 4-methoxypyridine and 3,4-lutidine ligands were significantly more efficient for radiofluorination of 4-acetyl-substituted substrates and aryl boronic acids, respectively. Cu(Isoq)$_4$(ClO$_4$)$_2$ was a significantly better mediator for radiolabeling of 4-Ph-Ph-B(OH)$_2$ than Cu(Py)$_4$(OTf)$_2$, and Cu(Impdz)$_4$(OTs)$_2$ was at least as effective as the corresponding triflate and perchlorate complexes (Figure 2, Table S23). Noteworthy, among all tested Cu complexes, only Cu(Impdz)$_4$(ClO$_4$)$_2$ enabled the preparation of 4-[^{18}F]F-Ph-Ph and 4-[^{18}F]F-Ac-Ph from the respective trimethylstannyl precursors in reasonable RCCs (20 ± 4% and 23 ± 2%, respectively, Table S24).

Although application of the alternative mediators significantly improved the radiolabeling yields in *n*BuOH/DMA, they remained moderate and did not exceed 58%. Consequently, the influence of aprotic reaction solvents other than DMA was studied.

Based on an initial solvent screening, propylene carbonate (PC) and 1,3-dimethyl-2-imidazolidinone (DMI) were selected for further evaluation in the following experiments (Figures 1 and S22). For a total of seven precursor/Cu mediator combinations,

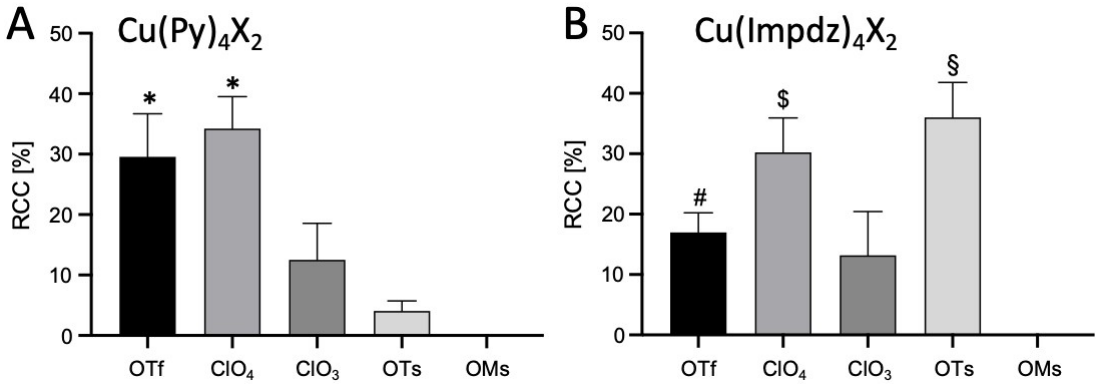

Figure 2. Radiochemical conversions (RCCs) for labeling of 4-Ph-Ph-B(OH)$_2$ using A) Cu(Py)$_4$X$_2$ and B) Cu(Impdz)$_4$X$_2$ in *n*BuOH/DMA. Reaction conditions: [^{18}F]F$^-$ (10–50 MBq), 4-biphenyl boronic acid (10 μmol), Cu(L)$_4$X$_2$ (10 μmol) and Et$_4$NOTf (1 mg, 4 μmol) in *n*BuOH/DMA 1:2 (1.2 mL) at 110 °C for 10 min, followed by addition of H$_2$O (2 mL). RCCs were determined by HPLC as described in the Supporting Information. All experiments were performed in triplicate. Statistics: *: $p < 0.05$ for comparison with ClO$_3$, OTs and OMs; #: $p < 0.05$ for comparison with OMs; $: $p < 0.05$ for comparison with ClO$_3$ and OMs; §: $p < 0.05$ for comparison with OTf, ClO$_3$ and OMs. For full statistics including main effects and factor interactions, see Tables S22 and S23.

application of *n*BuOH/PC gave significantly higher labeling yields when compared to those obtained using DMA (Figures S21 and S22, symbol #), whereas in *n*BuOH/DMA no significantly higher ^{18}F-incorporation was observed for any precursor/Cu mediator combination. In particular, application of Cu complexes with 4-PhPy ligands in *n*BuOH/PC afforded RCCs of 70–86% for all four model substrates. For the boronic acid substrates, 4-Ph-Ph- and 4-Ac-Ph-B(OH)$_2$, almost quantitative (>98%) RCCs in *n*BuOH/PC were obtained with Cu(Py)$_4$(ClO$_4$)$_2$ and Cu(Isoq)$_4$(ClO$_4$)$_2$, respectively.

For reactions performed with DMI as reaction solvent, significantly higher RCCs compared to the corresponding reactions with DMA were observed for eight combinations of Cu complex and radiofluorination substrate (Figures S21 and S22, symbol §), while DMA showed no significant advantage over DMI for any of the remaining combinations examined. In particular, in *n*BuOH/DMI, both 3,4-lutidine complexes allowed radiolabeling of all four model substrates in RCCs ≥80%. Perchlorate complexes with 4-MeOPy, 4-PhPy and Isoq ligands were also efficient mediators for radiofluorination of all model substrates (except for 4-Ac-Ph-Bpin) in DMI, affording labeling efficacies of >75%. Conventional Cu(Py)$_4$(OTf)$_2$ in DMI enabled highly efficient preparation of electron-rich 4-[^{18}F]fluorobiphenyl but not electron-poor 4-[^{18}F]fluoroacetophenone (RCCs >90% vs. ≤45%, respectively), while Cu(Impdz)$_4$(ClO$_4$)$_2$ was an efficient mediator for radiofluorination of both model aryl boronic acids (RCCs >85%).

Generally, under the conditions examined (aprotic reaction solvent, radiolabeling mediator), 4-biphenyl precursors often provided significantly higher RCCs than 4-acetylphenyl substrates (Figure S22, symbols # and § over black and dark grey bars). In the majority of cases, boronic acid substrates and, particularly, 4-Ac-Ph-B(OH)$_2$ were more efficient radiolabeling precursors than the corresponding pinacol boronates. Among all tested solvent/precursor combinations, comparison with Cu(Py)$_4$(OTf)$_2$ showed that triflate complexes were significantly better mediators in 16 cases and significantly worse mediators in 11 cases, while perchlorate complexes were significantly better in 31 cases and significantly worse in two cases (Figure S22 and Tables S29, S31 and S33). Nearly quantitative (>95%) RCCs were observed in five cases: for radiolabeling of 4-Ph-Ph-B(OH)$_2$ with Cu(4-PhPy)$_4$(ClO$_4$)$_2$ or Cu(Isoq)$_4$(ClO$_4$)$_2$ in DMI, for radiolabeling of 4-Ph-Ph-Bpin with Cu(4-PhPy)$_4$(ClO$_4$)$_2$ in DMI, as well as for radiolabeling of 4-Ph-Ph-B(OH)$_2$ with Cu(Py)$_4$(ClO$_4$)$_2$ or Cu(Isoq)$_4$(ClO$_4$)$_2$ in PC. Notably, in all cases except for 4-Ph-Ph-B(OH)$_2$ in *n*BuOH/PC, Cu(Impdz)$_4$(ClO$_4$)$_2$ afforded significantly higher RCCs than the known mediator Cu(Impdz)$_4$(OTf)$_2$[13] (Figure S23, Table S35). Compared to Cu(Py)$_4$(OTf)$_2$, Cu(4-PhPy)$_4$(ClO$_4$)$_2$ and Cu(Isoq)$_4$(ClO$_4$)$_2$ delivered significantly higher RCCs in eight and six cases, respectively, whereas Cu(Impdz)$_4$(ClO$_4$)$_2$ afforded significantly higher RCCs in six cases and significantly lower RCCs in one case (Figure S22, Tables S29, S31 and S33).

Direct comparison of PC and DMI as reaction co-solvents demonstrated that four substrate/Cu complex combinations provided significantly higher RCCs in *n*BuOH/DMI (Figures S21 and S22, symbol $), while only one combination gave significantly higher RCCs in *n*BuOH/PC. Since these observations pointed to DMI as an advantageous reaction solvent in comparison to PC, the former was chosen for further studies. In *n*BuOH/DMI, the highest mean RCCs for four tested substrates were observed with Cu(3,4-Me$_2$Py)$_4$(OTf)$_2$, Cu(3,4-Me$_2$Py)$_4$(ClO$_4$)$_2$ and Cu(4-PhPy)$_4$(ClO$_4$)$_2$ (87±7%, 90±5% and 87±14%, respectively). Consequently, these complexes were selected for all further optimization studies.

In the next step, the influence of reaction time and temperature on labeling efficacy was evaluated. Using Cu(4-PhPy)$_4$(ClO$_4$)$_2$ as the Cu mediator, 4-Ph-Ph-B(OH)$_2$ was radiofluorinated in RCCs of 65–80% over a broad range of reaction temperatures and times (5–20 min at 80–140 °C; Figure S24A). At reaction temperatures of ≥140 °C, an increase in the variability of ^{18}F-incorporation was observed. Reaction times of less than 5 min at 110 °C led to a drop of labeling efficacy (down to 57±4% and 20±13% for reaction times of three and

one min, respectively; Figure S24B), while RCCs of 54±2% and 37±7% were still observed after 10 min at lower temperatures of 70 and 60 °C, respectively. A further increase of the incubation time at these reaction temperatures to 30 min led to RCCs of 82±1% and 66±8%, respectively (Figure S24C).

Having established optimized radiofluorination conditions for boronic acids and pinacol boronates, we next extended the procedure to labeling of neopentyl glycol boronates (Bneo) and trimethylstannanes, using 4-Ph-Ph-Bneo, 4-Ac-Ph-Bneo, 4-Ph-Ph-$SnMe_3$ and 4-Ac-Ph-$SnMe_3$ as model substrates (Table 1). Radiolabeling of both Bneo precursors with Cu(4-PhPy)$_4$(ClO$_4$)$_2$ as mediator furnished the corresponding ^{18}F-fluorinated compounds in RCCs of 84±1% and 59±18% for the 4-Ph- and 4-Ac-substituted substrates, respectively. 4-Phenyl- and 4-acetylphenyltrimethylstannane were radiolabeled in moderate RCCs of up to 29% and 44%, respectively. Notably, conventional radiolabeling conditions [10 μmol stannane and Cu(Py)$_4$(OTf)$_2$ in *n*BuOH/DMA, 10 min at 110 °C] afforded RCCs of only 2–14%. In our previous work,[14] we already observed that, even though Cu-mediated radiofluorination of aryl stannanes tolerated alcohols as co-solvents, no increase of the RCCs was typically observed when using alcohol-containing media. Applying Cu(4-PhPy)$_4$(ClO$_4$)$_2$ as the mediator in pure DMI, electron-rich 4-Ph-Ph-$SnMe_3$ was radiolabeled in significantly improved RCCs of 38±2% (vs. 26±4% in DMI/*n*BuOH; p=0.0552). Exclusion of *n*BuOH, however, did not improve the RCCs of electron-deficient 4-[^{18}F]fluoroacetophenone (44±4% vs. 45±4%). In the next step, we evaluated the influence of reaction atmosphere (air vs. argon) on the radiolabeling efficiency (see Ref. [15] for a relevant discussion). Use of an argon atmosphere significantly increased RCCs for ^{18}F-fluorination of 4-Ph-Ph-$SnMe_3$ to 57±4% (p=0.0091), while the labeling efficacy of 4-Ac-Ph-$SnMe_3$ (47±6%) remained essentially unaffected. Finally, reduction of the reaction temperature to 90 °C enabled ^{18}F-fluorination of 4-Ph- and 4-Ac-Ph-$SnMe_3$ in RCCs of 60±3 and 63±10%, respectively.

Table 1. Radiofluorination of stannyl precursors.

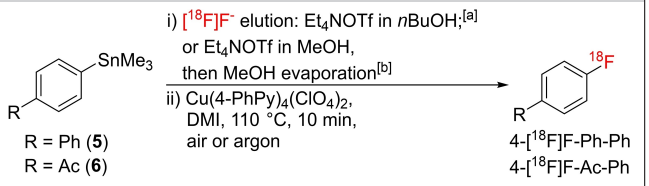

Entry	Precursor	Elution	Conditions	RCC [%]
1	**5**	*n*BuOH[a]	air	20±8
2			argon	22±6
3		MeOH[b]	air	38±2
4			argon	57±3
5			argon[c]	60±3
6	**6**	*n*BuOH[a]	air	44±3
7			argon	33±11
8		MeOH[b]	air	45±3
9			argon	47±6
10			argon[c]	63±10

Conditions: i) [a] [^{18}F]F$^-$ (10-50 MBq) was eluted with a solution of Et$_4$NOTf (1 mg, 4 μmol) in *n*BuOH (400 μL) into a solution of **5** or **6** (10 μmol, 1 eq.) and Cu(4-PhPy)$_4$(ClO$_4$)$_2$ (10 μmol, 1 eq.) in DMI (800 μL) or [b] [^{18}F]F$^-$ (10–50 MBq) was eluted with a solution of Et$_4$NOTf (1 mg, 4 μmol) in MeOH (400 μL), MeOH was evaporated at 60 °C under reduced pressure and in a stream of air or argon within 3 min, and the residue was taken up into a solution of **5** or **6** (10 μmol, 1 eq.) and Cu(4-PhPy)$_4$(ClO$_4$)$_2$ (10 μmol, 1 eq.) in DMI (800 μL); ii) 110 °C for 10 min and then cooling and addition of H$_2$O (1 mL). [c] same as [b] but ii) 90 °C for 10 min. Radiochemical conversions (RCCs) were determined by HPLC. All experiments were carried out at least in triplicate.

To demonstrate the practical suitability of the novel Cu mediators, we next applied them for the preparation of several PET-tracers: [^{18}F]R91150,[16] [^{18}F]ALX5407,[17] [^{18}F]MNI1126,[18] 3-(*S*)- and (*R*)-[^{18}F]FPhes,[19] and (*S*)-αMe-3-[^{18}F]FPhe.[20]

Radiosynthesis of [^{18}F]R91150, a promising 5-HT$_{2A}$-selective PET-tracer,[16b] from the corresponding Bpin precursor **7** was performed according to the developed protocol using Cu(4-PhPy)$_4$(ClO$_4$)$_2$ as the mediator. After subsequent deprotection and HPLC purification, the tracer was obtained in activity yields (AYs)[11] of 23±5% (Scheme 3), as compared to AYs of 10–15% obtained under standard conditions [Cu(Py)$_4$(OTf)$_2$ in DMA/*n*BuOH]. Application of the method for preparation of [^{18}F]ALX5407, a glycine transporter type 1 (GlyT$_1$) radioligand,[17] from the appropriate Bpin precursor **8** using Cu(4-PhPy)$_4$(ClO$_4$)$_2$ improved AYs (30±5% vs. 14±6%), allowed for a reduction of precursor and mediator amounts from 30 to 10 μmol, and thus simplified preparative HPLC purification of the radiolabeled product (Scheme 3).

[^{18}F]MNI1126, a specific PET-probe for the ubiquitous synaptic vesicle glycoprotein 2A (SV2A),[18] was most efficiently prepared from the corresponding stannyl precursor **9**. In this case, application of Cu(3,4-Me$_2$Py)$_4$(OTf)$_2$ as radiolabeling mediator and DMI as reaction solvent furnished the tracer in RCCs of 47±5% (Scheme 3), as compared to RCCs of 6±2% under standard conditions [Cu(Py)$_4$(OTf)$_2$ in DMA].

^{18}F-Labeled fluorophenylalanines ([^{18}F]FPhes) and α-methyl-fluorophenylalanines (αMe-FPhes) are promising PET probes for the visualization of increased amino acid uptake associated with increased protein synthesis rates in cerebral and peripheral tumors.[19,21] We recently published a procedure for preparation of these and other radiolabeled aromatic amino acids via alcohol-enhanced Cu-mediated radiofluorination of Bpin-substituted chiral complexes using Ni/Cu-BPB/BPA templates as double protecting groups.[20] Application of 30 μmol Bpin precursor and 60 μmol Cu(Py)$_4$(OTf)$_2$ in *n*BuOH/DMA delivered the corresponding ^{18}F-labeled complexes in good to excellent RCCs, but downscaling of the precursor/Cu mediator amounts led to a sharp decrease of the conversions. This problem could be circumvented by elution of [^{18}F]F$^-$ from an anion exchange resin with Et$_4$NHCO$_3$ in MeOH, followed by evaporation of MeOH and addition of the radiolabeling precursor and Cu(Py)$_4$(OTf)$_2$ in *n*BuOH/DMA. However, complete omission of all evaporation steps would further reduce the synthesis time and simplify transfer of the method to an automated synthesis module. With this in mind, we applied the procedure for radiolabeling of the corresponding Bpin- and B(OH)$_2$-substituted Ni(II)-BPX complexes (Scheme 4). The latter were prepared by transesterification of the appropriate Bpin boronates with MeB(OH)$_2$.[22] Using 10 μmol precursor and Cu(3,4-Me$_2$Py)$_4$(OTf)$_2$ as the Cu mediator, (*S*,*S*)- and (*R*,*R*)-Ni-BPB-3-[^{18}F]FPhes as well as (*S*,*S*)-Ni-BPA-αMe-3-[^{18}F]FPhe were prepared in RCCs of 69–

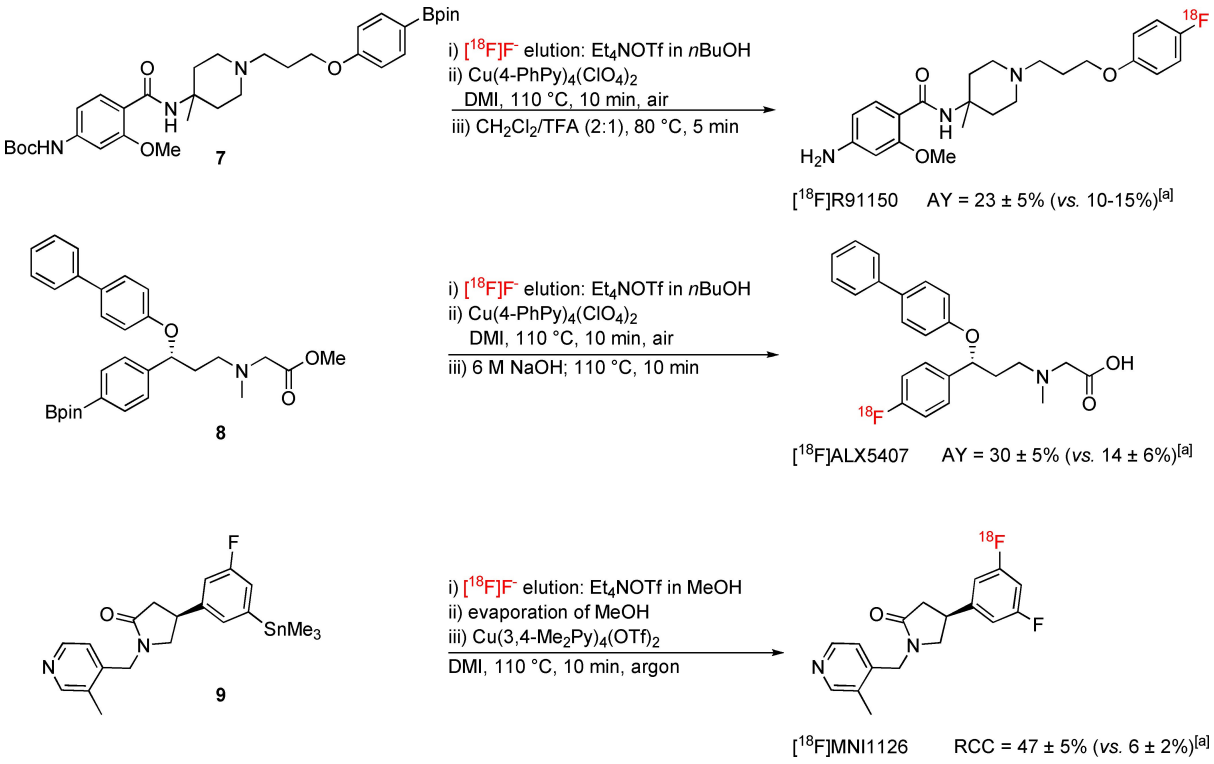

Scheme 3. Production of the PET-tracers [^{18}F]R91150, [^{18}F]ALX5407 and [^{18}F]MNI1126. [a] AY or RCC of radiosynthesis if the ^{18}F-labeling step was performed under standard conditions [$Cu(Py)_4(OTf)_2$ in nBuOH/DMA]. All radiosyntheses were carried out in triplicate. AY – activity yield; RCC – radiochemical conversion.

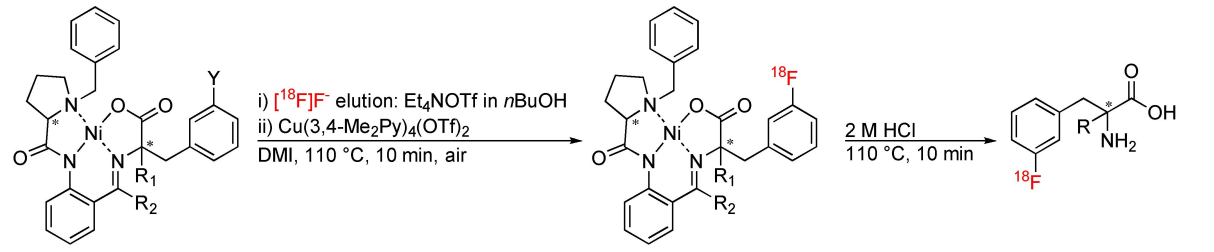

	RCC [%]	AY [%]
R_1 = H, R_2 = Ph, Y = $B(OH)_2$ [(*S*,*S*)-**10**]	91 ± 4 (*vs.* 17 ± 6)[a]	(*S*)-3-[^{18}F]FPhe 41 ± 2 (*vs.* 17 ± 6)[a]
R_1 = H, R_2 = Ph, Y = Bpin [(*S*,*S*)-**11**]	74 ± 1 (*vs.* 8 ± 1)[a]	n. d.
R_1 = H, R_2 = Ph, Y = $B(OH)_2$ [(*R*,*R*)-**10**]	78 ± 3 (*vs.* 14 ± 4)[a]	(*R*)-3-[^{18}F]FPhe 33 ± 0.5 (*vs.* 14 ± 4)[a]
R_1 = H, R_2 = Ph, Y = Bpin [(*R*,*R*)-**11**]	70 ± 7 (*vs.* 11 ± 2)[a]	n. d.
R_1 = Me, R_2 = H, Y = $B(OH)_2$ [(*S*,*S*)-**12**]	69 ± 11 (*vs.* 14 ± 2)[a]	
R_1 = Me, R_2 = H, Y = Bpin [(*R*,*R*)-**13**]	76 ± 2 (*vs.* 9 ± 2)[a]	

Scheme 4. Preparation of 3-[^{18}F]FPhes and protected αMe-3-[^{18}F]FPhes using the novel radiolabeling protocol. [a] AY or RCC of radiosynthesis if the ^{18}F-labeling step was performed under standard conditions [$Cu(Py)_4(OTf)_2$ in *n*BuOH/DMA]. AY – activity yield; RCC – radiochemical conversion.

91 %. Subsequent hydrolysis, HPLC isolation and formulation furnished (*S*)- and (*R*)-3-[^{18}F]FPhe from the respective boronic acid precursors as solutions ready for application in AYs of 43 ± 3 (n = 3) and 33 ± 1 % (n = 3), respectively. Molar activity amounted to 538 GBq/μmol for 1.8 GBq (*S*)-3-[^{18}F]FPhe (from 4 GBq [^{18}F]F^-).

The developed protocol was also successfully implemented into a remotely controlled synthesis unit (AllInOne, Trasis), enabling the automated preparation of (*S*)-3-[^{18}F]FPhe in AYs of 18 ± 2 % (n = 3) within 70 min.

The improved performance of the procedure raised the question whether even lower precursor loadings could be efficiently applied. To address this, we first evaluated radiolabeling of 2.5 μmol 4-Ph-Ph-$B(OH)_2$ in 1.2 mL *n*BuOH/DMI (1 : 2) using Et_4NOTf (1 mg, 4 μmol) for [^{18}F]F^- elution and 10 μmol $Cu(Py)_4(OTf)_2$, $Cu(3,4\text{-}Me_2Py)_4(OTf)_2$, $Cu(3,4\text{-}Me_2Py)_4(ClO_4)_2$ or $Cu(4\text{-}PhPy)_4(ClO_4)_2$ as labeling mediator at 110 °C for 10 min

(Scheme 5, Figure S60, Tables S50 and S51). Under these conditions, $Cu(4\text{-}PhPy)_4(ClO_4)_2$ was significantly more efficient than the other Cu complexes examined and afforded 4-[^{18}F]F-Ph-Ph in satisfactory RCCs of 56±2%, so that it was selected for further experiments. Next, 2.5 µmol scale radiolabeling reactions with different 4-Ph- and 4-Ac-substituted boronic compounds and stannanes were evaluated (Scheme 5, Tables S52 and S53). Radiolabeling of boronic substrates was carried out in *n*BuOH/DMI (1:2; 1.2 mL) and of stannyl precursors in DMI (0.8 mL). Whereas RCCs for both $B(OH)_2$ substrates and 4-Ph-Ph-Bneo were comparable (53–63%), they were lower for the other precursors examined (25–48%).

Next, the procedure was applied for 2.5 µmol scale radiolabeling of fifteen additional aryl boronic acids. Thus, electron-rich and electron-poor ^{18}F-fluorinated aromatics including unprotected 4-[^{18}F]fluoro-aniline and -phenol were synthesized in RCCs of 18–76% (Scheme 5). Noteworthy, 1.0 and 0.5 µmol of 1-naphthyl boronic acid were sufficient to obtain 1-[^{18}F]fluoronaphthalene in RCCs of 62±17% and 29±8%, respectively. The sensitive radiofluorinated active ester [^{18}F]**26**[4b] was also successfully prepared in RCCs of 28±3% (in pure DMI; 63±2% RCCs from 10 µmol precursor; 6±1% RCCs in DMI/*n*BuOH). Strikingly, 2.5 µmol of Ni-BPB-3-$B(OH)_2$Phes as well as (*S*,*S*)-Ni-BPA-αMe-3-$B(OH)_2$Phe were sufficient to achieve RCCs of 46–62%. Exemplarily, hydrolysis of (*S*,*S*)-Ni-BPB-3-[^{18}F]FPhe

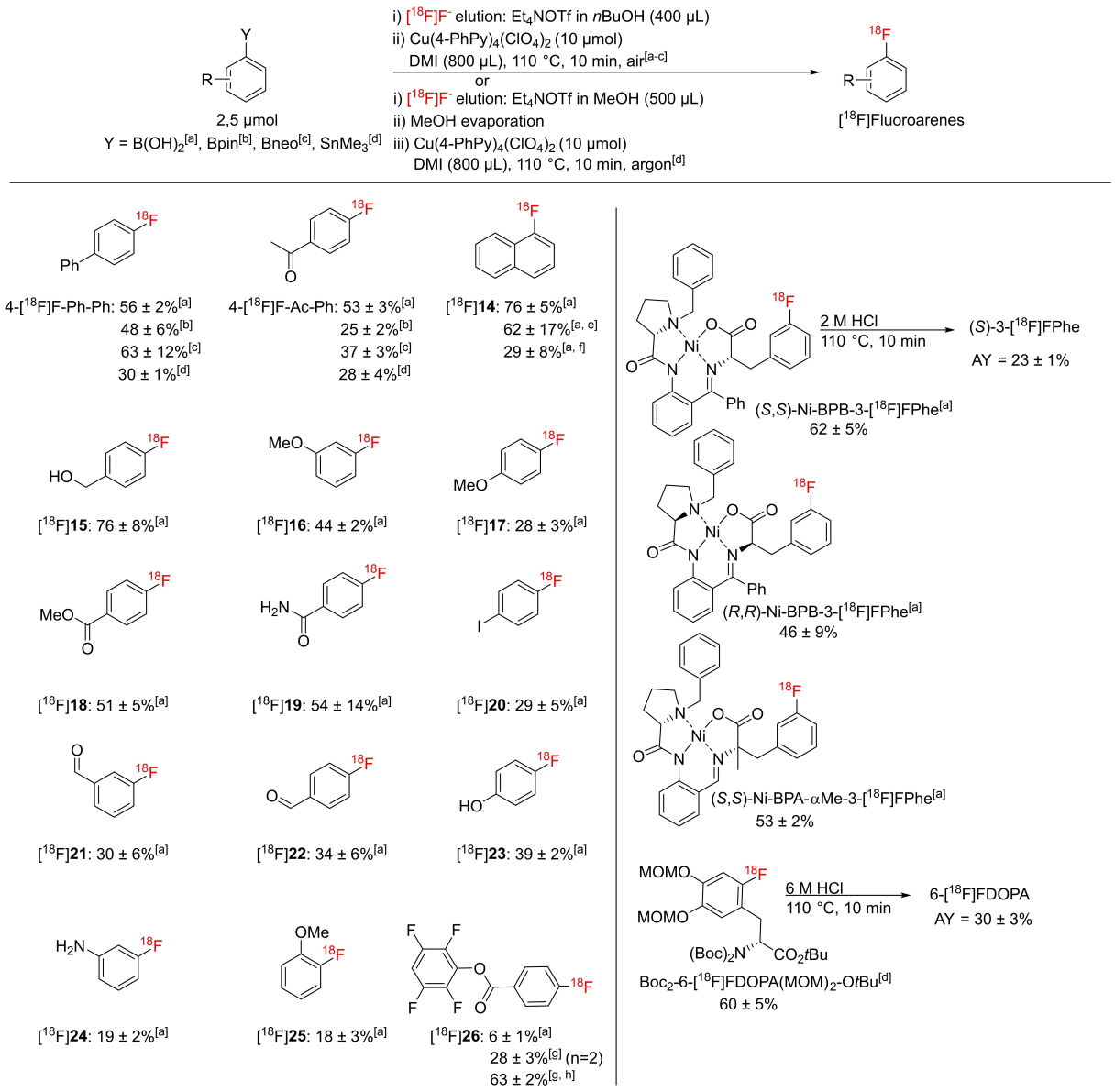

Scheme 5. Substrate scope of the developed protocol using 2.5 µmol substrate loading. Radiolabeled products were prepared from the respective [a] aryl boronic acid, [b] pinacol boronate, [c] neopentyl glycol boronate or [d] trimethyl stannyl precursors. [e] Prepared from 1 µmol precursor. [f] Prepared from 0.5 µmol precursor. [g] Radiosyntheses were performed in pure DMI and elution of [^{18}F]F^- with Et_4NOTf in MeOH followed by evaporation of MeOH at 60 °C in a stream of argon. [h] Prepared from 10 µmol precursor. If not otherwise stated, mean RCCs ± standard deviations are provided and all experiments were carried out at least in triplicate. AY – activity yield; RCC – radiochemical conversion.

followed by HPLC purification furnished (*S*)-3-[^{18}F]FPhe in 23 ± 1 % AYs.

Finally, we utilized the procedure for a 2.5 μmol scale preparation of 6-[^{18}F]fluoro-3,4-dihydroxyphenylalanine (6-[^{18}F]FDOPA; Scheme 5). 6-[^{18}F]FDOPA is widely used for measuring the integrity and function of the nigrostriatal dopaminergic system, for example, in Parkinson's disease[23] as well as for the detection and staging of neuroendocrine tumors.[24] Using conventional $Cu(Py)_4(OTf)_2$, 6-[^{18}F]FDOPA was previously prepared from 5 μmol of Boc_2-6-Bpin-DOPA(MOM)$_2$-O*t*Bu in AYs of 6 ± 1 %.[25] Radiofluorination of 2.5 μmol of Boc_2-6-Bpin-DOPA(MOM)$_2$-OMe precursor with $Cu(4\text{-}PhPy)_4(ClO_4)_2$ as mediator furnished protected 6-[^{18}F]FDOPA in < 20 % RCC. In contrast, for the corresponding stannyl precursor, Boc_2-6-Me_3Sn-DOPA(MOM)$_2$-OMe, higher RCCs of 60 ± 5 % were observed. Interestingly, in this case, the reduction of the precursor amount from 10 to 2.5 μmol did not lead to a decrease of the RCCs (58 ± 4 vs. 60 ± 5 %). Subsequent deprotection and HPLC isolation delivered the desired tracer in good AYs of 30 ± 3 %.

In summary, based on the results of the present study, the following general recommendations can be made for Cu-mediated radiofluorination of aromatic boronyl and stannyl substrates:

- *n*BuOH/DMI is the solvent of choice for radiolabeling of boronyl substrates while pure DMI is well suited for radiolabeling of stannyl substrates;
- Boronic acids are frequently better radiofluorination substrates then the corresponding BPin esters;
- For ^{18}F-fluorinations performed with 10 μmol of the radiolabeling precursor, $Cu(4\text{-}PhPy)_4(ClO_4)_2$, $Cu(3,4\text{-}Me_2Py)_4(OTf)_2$ and $Cu(3,4\text{-}Me_2Py)_4(ClO_4)_2$ are the most efficient mediators;
- At 2.5 μmol substrate loading, $Cu(4\text{-}PhPy)_4(ClO_4)_2$ is the preferred mediator;
- Radiofluorination of boronyl substrates should be carried out under air; while stannyl precursor are preferably radiofluorinated under argon;
- Thermolabile substrates can be efficiently radiolabeled at 70–90 °C.

Conclusion

In conclusion, our screening study led to the discovery of several highly efficient mediators for Cu-mediated radiofluorination like $Cu(4\text{-}PhPy)_4(ClO_4)_2$, $Cu(3,4\text{-}Me_2Py)_4(OTf)_2$ and $Cu(3,4\text{-}Me_2Py)_4(ClO_4)_2$. Especially in DMI or *n*BuOH/DMI as reaction media, these copper complexes enabled highly efficient ^{18}F-labeling of different boronic and stannyl substrates. The optimized protocol worked well at reaction temperatures in the range of 60–90 °C, indicating its suitability for radiofluorination of thermolabile substrates. The practicality of the method was demonstrated by preparation of several PET-tracers, including 6-[^{18}F]FDOPA, in improved radiochemical yields and/or using significantly lower precursor loadings. Furthermore, the procedure was successfully implemented into a remote-controlled synthesis unit, highlighting its applicability for GMP-compliant production of clinically relevant PET-tracers.

Experimental Section

Chemistry: Detailed information on the synthesis of metal complexes and radiolabeling precursors as well as the corresponding analytical data (^{1}H, ^{13}C, LR-MS-ESI, HR-MS-ESI, elemental analysis, IR and crystallographic data) are provided in the Supporting Information.

Radiochemistry: Detailed descriptions of radiolabeling procedures, optimization studies, statistical evaluation and PET-tracer syntheses with representative HPLC analytic and quality controls are provided in the Supporting Information.

Processing of fluoride-18: Aqueous [^{18}F]F$^-$ was loaded onto a QMA cartridge (preconditioned with 1 mL H_2O) from the female side to the male side. The cartridge was washed (from the male side) with anhydrous MeOH (1 mL) to remove residual H_2O and dried (from the female side) with air (2 × 10 mL). [^{18}F]F$^-$ was eluted (from the female to the male side) with a solution of Et_4NOTf in *n*BuOH or MeOH.

Optimized procedure for radiofluorination of boranyl precursors: [^{18}F]F$^-$ (500 μL, 20–5000 MBq) was loaded onto a QMA cartridge and eluted with a solution of Et_4NOTf (1 mg, 3.6 μmol) in *n*BuOH (400 μL) into a solution of the respective Cu complex and precursor (10 μmol of each or 10 μmol of mediator and 2.5 μmol of boranyl substrate) in DMI (800 μL). The reaction mixture was heated at 110 °C for 10 min in atmospheric or synthetic air, cooled to ambient temperature and diluted with H_2O (2 mL). RCCs were determined by radio-HPLC. PET-tracers were isolated by preparative HPLC and formulated as ready-to-use solutions. At high atmospheric humidity (e.g., during the midsummer), a significant drop of the RCCs was sometimes observed, presumably owing to the hygroscopicity of Et_4NOTf. In such cases, [^{18}F]F$^-$ should preferably be eluted with a solution of Et_4NOTf in MeOH. MeOH was removed at 60 °C for 2–3 min under reduced pressure in a stream of argon and the residue was taken up into a solution of the respective Cu mediator and precursor (10 μmol of each if not otherwise noted) in a mixture of the corresponding solvent and *n*BuOH (1200 μL; 2 : 1).

Optimized procedure for radiofluorination of stannyl precursors: [^{18}F]F$^-$ was loaded onto a QMA carbonate cartridge and eluted with Et_4NOTf (1 mg, 3.6 μmol) in MeOH (500 μL) into a V–Vial as described above, followed by evaporation of MeOH at 60 °C under reduced pressure in a stream of argon. The V-Vial was filled with argon, sealed with a silicon septum and a solution of the appropriate precursor and copper complex (10 μmol of each if not otherwise noted) in DMI (800 μL) was added via a cannula through the septum. The reaction mixture was heated at 90 or 110 °C for 10 min, cooled to ambient temperature and diluted with H_2O (2 mL). RCCs were determined by radio-HPLC. PET-tracers were isolated by preparative HPLC and formulated as ready-to-use solutions.

Crystal data: Deposition Numbers 2202867 [for $Cu(Py)_4(OTf)_2$], 2202868 [for $Cu(4\text{-}MeOPy)_4(ClO_4)_2$] and 2202858 [for $Cu(3,4\text{-}Me_2Py)_4(OTf)_2$] contain the supplementary crystallographic data for this paper. These data are provided free of charge by the joint Cambridge Crystallographic Data Centre and Fachinformationszentrum Karlsruhe Access Structures service.

Acknowledgements

We thank Max Fischer, INM-5, Forschungszentrum Jülich, Jülich, Germany, for his excellent technical assistance and Dmitrii Antuganov, Russian Scientific Center of Radiology and Surgical

Technologies, Saint-Petersburg, Russian Federation, for the helpful discussions. This work was supported by the DFG grants ZL 65/1-1, ZL 65/3-1 and ZL 65/4-1. Open Access funding enabled and organized by Projekt DEAL.

Conflict of Interest

The authors declare no conflict of interest.

Data Availability Statement

The data that support the findings of this study are available from the corresponding author upon reasonable request.

Keywords: copper · fluorine-18 · positron emission tomography · radiochemistry · radiopharmaceuticals

[1] G. Audi, O. Bersillon, J. Blachot, A. H. Wapstra, *Nucl. Phys. A* **2003**, *729*, 3–128.
[2] V. M. Vlasov, *J. Fluorine Chem.* **1993**, *61*, 193–216.
[3] a) J. Ajenjo, G. Destro, B. Cornelissen, V. Gouverneur, *EJNMMI Radiopharm. Chem.* **2021**, *6*, 33; b) K. Bratteby, V. Shalgunov, M. M. Herth, *ChemMedChem* **2021**, *16*, 2612–2622; c) S. Preshlock, M. Tredwell, V. Gouverneur, *Chem. Rev.* **2016**, *116*, 719–766; d) L. Cai, S. Lu, V. W. Pike, *Eur. J. Org. Chem.* **2008**, *2008*, 2853–2873.
[4] a) V. V. Orlovskaya, D. J. Modemann, O. F. Kuznetsova, O. S. Fedorova, E. A. Urusova, N. Kolks, B. Neumaier, R. N. Krasikova, B. D. Zlatopolskiy, *Molecules* **2019**, *24*, 3197; b) R. Richarz, P. Krapf, F. Zarrad, E. A. Urusova, B. Neumaier, B. D. Zlatopolskiy, *Org. Biomol. Chem.* **2014**, *12*, 8094–8099; c) B. D. Zlatopolskiy, J. Zischler, P. Krapf, R. Richarz, K. Lauchner, B. Neumaier, *J. Labelled Compd. Radiopharm.* **2019**, *62*, 404–410; d) J. Zischler, P. Krapf, R. Richarz, B. D. Zlatopolskiy, B. Neumaier, *Appl. Radiat. Isot.* **2016**, *115*, 133–137; e) B. D. Zlatopolskiy, J. Zischler, P. Krapf, F. Zarrad, E. A. Urusova, E. Kordys, H. Endepols, B. Neumaier, *Chem. Eur. J.* **2015**, *21*, 5972–5979.
[5] a) F. Basuli, X. Zhang, E. M. Jagoda, P. L. Choyke, R. E. Swenson, *Nucl. Med. Biol.* **2016**, *43*, 770–772; b) J. Zischler, N. Kolks, D. Modemann, B. Neumaier, B. D. Zlatopolskiy, *Chem. Eur. J.* **2017**, *23*, 3251–3256; c) G. D. Bowden, N. Chailanggar, B. J. Pichler, A. Maurer, *Org. Biomol. Chem.* **2021**, *19*, 6995–7000; d) S. O. Lahdenpohja, N. A. Rajala, J. Rajander, A. K. Kirjavainen, *EJNMMI Radiopharm. Chem.* **2019**, *4*, 28.
[6] a) S. J. Lee, K. J. Makaravage, A. F. Brooks, P. J. H. Scott, M. S. Sanford, *Angew. Chem. Int. Ed.* **2019**, *58*, 3119–3122; *Angew. Chem.* **2019**, *131*, 3151–3154; b) N. Ichiishi, A. F. Brooks, J. J. Topczewski, M. E. Rodnick, M. S. Sanford, P. J. H. Scott, *Org. Lett.* **2014**, *16*, 3224–3227; c) L. S. Sharninghausen, A. F. Brooks, W. P. Winton, K. J. Makaravage, P. J. H. Scott, M. S. Sanford, *J. Am. Chem. Soc.* **2020**, *142*, 7362–7367.
[7] A. V. Mossine, A. F. Brooks, K. J. Makaravage, J. M. Miller, N. Ichiishi, M. S. Sanford, P. J. H. Scott, *Org. Lett.* **2015**, *17*, 5780–5783.
[8] M. Tredwell, S. M. Preshlock, N. J. Taylor, S. Gruber, M. Huiban, J. Passchier, J. Mercier, C. Génicot, V. Gouverneur, *Angew. Chem. Int. Ed.* **2014**, *53*, 7751–7755; *Angew. Chem.* **2014**, *126*, 7885–7889.
[9] K. J. Makaravage, A. F. Brooks, A. V. Mossine, M. S. Sanford, P. J. H. Scott, *Org. Lett.* **2016**, *18*, 5440–5443.
[10] a) D. Antuganov, M. Zykov, V. Timofeev, K. Timofeeva, Y. Antuganova, V. Orlovskaya, O. Fedorova, R. Krasikova, *Eur. J. Org. Chem.* **2019**, *2019*, 918–922; b) V. Orlovskaya, O. Fedorova, O. Kuznetsova, R. Krasikova, *Eur. J. Org. Chem.* **2020**, *2020*, 7079–7086.
[11] Throughout this article, radiochemical yields (RCYs) refer to the *decay-corrected* isolated yield of radiochemically and chemically pure radio-labeled compounds, while activity yields (AYs) refer to the *non-decay-corrected* isolated yield of radiochemically and chemically pure radio-labeled compounds. Radiochemical conversions (RCCs) refer to the amount of [^{18}F]fluoride which is transformed to the desired ^{18}F-labeled compounds (e.g., ^{18}F-incorporation) and are determined by radio-HPLC through comparison of the peaks areas for the radiolabeled product and a post-column injection of the reaction mixture.
[12] J. S. Haynes, S. J. Rettig, J. R. Sams, J. Trotter, R. C. Thompson, *Inorg. Chem.* **1988**, *27*, 1237–1241.
[13] N. J. Taylor, E. Emer, S. Preshlock, M. Schedler, M. Tredwell, S. Verhoog, J. Mercier, C. Genicot, V. Gouverneur, *J. Am. Chem. Soc.* **2017**, *139*, 8267–8276.
[14] a) F. Zarrad, B. D. Zlatopolskiy, P. Krapf, J. Zischler, B. Neumaier, *Molecules* **2017**, *22*, 2231; b) B. D. Zlatopolskiy, J. Zischler, D. Schäfer, E. A. Urusova, M. Guliyev, O. Bannykh, H. Endepols, B. Neumaier, *J. Med. Chem.* **2018**, *61*, 189–206.
[15] G. D. Bowden, B. J. Pichler, A. Maurer, *Sci. Rep.* **2019**, *9*, 11370.
[16] a) U. Mühlhausen, J. Ermert, H. H. Coenen, *J. Labelled Compd. Radiopharm.* **2009**, *52*, 13–22; b) M. Willmann, J. Hegger, B. Neumaier, J. Ermert, *ACS Med. Chem. Lett.* **2021**, *12*, 738–744.
[17] C. Hoffmann, S. Evcüman, F. Neumaier, B. D. Zlatopolskiy, S. Humpert, D. Bier, M. Holschbach, A. Schulze, H. Endepols, B. Neumaier, *ACS Chem. Neurosci.* **2021**, *12*, 3335–3346.
[18] C. C. Constantinescu, C. Tresse, M. Zheng, A. Gouasmat, V. M. Carroll, L. Mistico, D. Alagille, C. M. Sandiego, C. Papin, K. Marek, J. P. Seibyl, G. D. Tamagnan, O. Barret, *Mol. Imaging Biol.* **2019**, *21*, 509–518.
[19] F. Krämer, B. Gröner, C. Hoffmann, A. Craig, M. Brugger, A. Drzezga, M. Timmer, F. Neumaier, B. D. Zlatopolskiy, H. Endepols, B. Neumaier, *Cancers (Basel).* **2021**, *13*, 6030.
[20] A. Craig, N. Kolks, E. A. Urusova, J. Zischler, M. Brugger, H. Endepols, B. Neumaier, B. D. Zlatopolskiy, *Chem. Commun.* **2020**, *56*, 9505–9508.
[21] I. Mahendra, H. Hanaoka, A. Yamaguchi, T. Amartuvshin, Y. Tsushima, *Ann. Nucl. Med.* **2020**, *34*, 329–336.
[22] S. P. A. Hinkes, C. D. P. Klein, *Org. Lett.* **2019**, *21*, 3048–3052.
[23] a) J. Darcourt, A. Schiazza, N. Sapin, M. Dufour, M. J. Ouvrier, D. Benisvy, X. Fontana, P. M. Koulibaly, *Q. J. Nucl. Med. Mol. Imaging* **2014**, *58*, 355–65; b) J. Puñal-Riobóo, A. Serena-Puig, L. Varela-Lema, A. M. Alvarez-Páez, A. Ruano-Ravina, *Rev. Esp. Med. Nucl.* **2009**, *28*, 106–13.
[24] C. Nanni, D. Rubello, S. Fanti, *Eur. J. Nucl. Med. Mol. Imaging* **2006**, *33*, 509–513.
[25] A. V. Mossine, S. S. Tanzey, A. F. Brooks, K. J. Makaravage, N. Ichiishi, J. M. Miller, B. D. Henderson, T. Erhard, C. Bruetting, M. B. Skaddan, M. S. Sanford, P. J. H. Scott, *Nat. Protoc.* **2020**, *15*, 1742–1759.

Manuscript received: September 22, 2022
Accepted manuscript online: October 10, 2022
Version of record online: November 17, 2022

3.1.3 [^{18}F]R91150: Improved radiosynthesis and in vivo evaluation as imaging probe for 5-HT$_{2A}$ receptors

Die 5-HT$_{2A}$-Rezeptoren sind vorwiegend im Kortex und Vorderhirnstrukturen exprimiert und spielen eine Schlüsselrolle für kognitive, Emotions- und erinnerungsbezogene Prozesse.[140–142] Eine Störung der Neurotransmission über diese Rezeptoren ist mit neurodegenerativen Erkrankungen wie Schizophrenie, Depression oder Alzheimer assoziiert.[143–149] Die 5-HT$_{2A}$-Rezeptoren stellen daher ein vielversprechendes biologisches Target für die PET-Bildgebung dar, so dass verschiedene Radioliganden wie [^{18}F]Altanserin, [^{18}F]Setoperon und [^{11}C]MDL100907 entwickelt wurden. Diese Radioliganden zeigen zwar eine gute Affinität für die Rezeptoren, weisen aber unterschiedliche Selektivität auf oder werden zu hirngängigen Radiometaboliten verstoffwechselt.[150–154] Im Vergleich dazu weist der Ligand R91150 nicht nur eine gute Affinität, sondern auch eine entsprechende Selektivität und eine geringe Lipophilie auf, weshalb [^{18}F]R91150 einen potenziellen Radiotracer-Kandidaten darstellt. Bislang wurde [^{18}F]R91150 über eine mehrstufige Synthese oder über die CVRF mit moderaten RCAs hergestellt und präklinisch evaluiert. Die Ergebnisse zeigten eine gute Stabilität gegenüber Metabolisierung im Gehirn von Nagetieren und ein Verteilungsmuster in Rattenhirnschnitten, dass der 5-HT$_{2A}$-Rezeptorverteilung entspricht.[155,156] Bisher wurde jedoch keine In-vivo-Evaluation über µPET-Messungen durchgeführt.

Das Ziel dieses Projektes war die Optimierung der Radiosynthese über das modifizierte CVRF-Protokoll mit „*NextGen*“-Cu-Komplexen aus dem Boc-geschützten Vorläufer. Zusätzlich wurde die Herstellung von [^{18}F]R91150 auch aus dem nicht-geschützen Vorläufer durchgeführt, um die Gesamtsynthesezeit durch Vermeidung des Hydrolyseschritts zu verkürzen. Abschließend wurde der Radiotracer durch µPET-Messungen in gesunden Mäusen und Ratten präklinisch evaluiert.

Das Konzept des Manuskripts wurde gemeinschaftlich von C. Hoffmann und Prof. Dr. B. D. Zlatopolskiy mit Unterstützung von Prof. Dr. B. Neumaier entwickelt. Die organischen Synthesen wurden von C. Hoffmann, E. A. Urusova und Prof. Dr. B. D. Zlatopolskiy durchgeführt. Radiosynthesen und deren Optimierungen wurden von C. Hoffmann und D. Elchine durchgeführt. In-vivo µPET-Messungen wurden von Prof. Dr. H. Endepols durchgeführt. Das Manuskript wurde gemeinschaftlich von C. Hoffmann,

Prof. Dr. H. Endepols, Dr. F. Neumaier, Prof. Dr. B. D. Zlatopolskiy und Prof. Dr. B. Neumaier verfasst.

Im Rahmen dieser Dissertation wurde das Manuskript mit allen erhobenen experimentellen und analytischen Daten als Kapitel eingefügt und die dazugehörige „Supporting Information“ im Anhang B hinterlegt.

[^{18}F]R91150: Improved radiosynthesis and in vivo evaluation as imaging probe for 5-HT$_{2A}$ receptors

Chris Hoffmann[1,2], Heike Endepols[1,2,3], Elizaveta A. Urusova[1,2], Dominik Elchine[1], Felix Neumaier[1,2], Bernd Neumaier[1,2]*, Boris D. Zlatopolskiy[1,2]

[1] *Forschungszentrum Jülich GmbH, Institute of Neuroscience and Medicine, Nuclear Chemistry (INM-5), Wilhelm-Johnen-Straße, 52428 Jülich, Germany.*

[2] *University of Cologne, Faculty of Medicine and University Hospital Cologne, Institute of Radiochemistry and Experimental Molecular Imaging, Kerpener Straße 62, 50937 Cologne, Germany.*

[3] *University of Cologne, Faculty of Medicine and University Hospital Cologne, Department of Nuclear Medicine, Kerpener Straße 62, 50937 Cologne, Germany.*

* *Corresponding author; e-mail: b.neumaier@fz-juelich.de*

Abstract

Serotonergic 5-HT$_{2A}$ receptors in the cortex and other forebrain structures have been linked to cognitive, emotional and memory processes. In addition, dysfunction or altered expression of these receptors is associated with neuropsychiatric and neurodegenerative disorders. [^{18}F]R91150 is a candidate radiotracer for positron emission tomography (PET) imaging of 5-HT$_{2A}$ receptors, which showed promising properties in *in vitro* studies. However, existing methods for the production of [^{18}F]R91150 are rather inefficient and its imaging properties have not been studied *in vivo*. In the present work, we describe improved protocols for preparation of [^{18}F]R91150, the corresponding reference compound and two alternative boronate radiolabeling precursors. Furthermore, we present the results of an *in vivo* evaluation of the radioligand in rodents. [^{18}F]R91150 was prepared in activity yields of 20±5% (two-step radiosynthesis) or 12±2% (one-step radiosynthesis) and with molar activities of >200 GBq/µmol. µPET measurements in mice revealed sufficient stability against *in vivo* defluorination and predominantly hepatobiliary excretion of the tracer, with high radioactivity uptake in gall bladder and intestines. µPET imaging in rats demonstrated preferential tracer accumulation in the cortex and subcortical forebrain structures, which could be reduced by pretreatment or displacement with the 5-HT$_{2A}$ receptor ligands altanserin or ketanserin. In addition, [^{18}F]R91150 showed high uptake in the 5-HT$_{2C}$-rich choroid plexus that was unaffected by altanserin pretreatment and much less sensitive to displacement with ketanserin. Taken together, our results confirm that [^{18}F]R91150 is a promising candidate for *in vivo* PET imaging of cortical 5-HT$_{2A}$ receptors, although further studies will be required to firmly establish the role of 5-HT$_{2C}$ receptors for tracer binding in the choroid plexus and subcortical forebrain structures.

Keywords: 5-HT$_{2A}$ receptors, Copper-mediated radiofluorination, Fluorine-18, Positron emission tomography, Radiopharmaceuticals, Imaging agents.

1 Introduction

The serotonergic 5-HT_{2A} receptor system in the cortex and other forebrain structures has been linked to various cognitive, emotional, and memory processes[1–3]. It has also been implicated in the pathogenesis of neuropsychiatric and neurodegenerative diseases[4–7]. In addition, 5-HT_{2A} receptor antagonists have been identified as promising therapeutic agents for certain diseases, like depression, anxiety disorders, or schizophrenia[8–10]. Methods to visualize 5-HT_{2A} receptors and their interaction with drug candidates are an important prerequisite for studies on their pathophysiological significance as well as for the development of appropriate therapeutic approaches. Nuclear medicine techniques such as positron emission tomography (PET) or single photon emission computed tomography (SPECT) are particularly well suited for this purpose, as they enable non-invasive molecular imaging in living subjects. Accordingly, several 5-HT_{2A} receptor antagonists labeled with positron-emitting radionuclides, such as [^{18}F]altanserin[11–14], [^{18}F]setoperone[15–18] or [^{11}C]MDL100907[19–21] (**Fig. 1A**), have been developed and used for preclinical and clinical PET studies. However, their practical utility is limited by the formation of brain-penetrating radiometabolites (e.g., [^{18}F]altanserin[22]), off-target binding (e.g., [^{18}F]altanserin and [^{18}F]setoperone[15,23,24]) or the short half-life of carbon-11 (e.g., [^{11}C]MDL100907[19]). Alternatively, SPECT imaging with 5-[^{123}I]iodo-R91150 ([^{123}I]R93274), a radioiodinated analog of the potent and selective 5-HT_{2A} receptor antagonist R91150 (**Fig. 1B**), has been extensively used in preclinical and clinical studies[25–32]. While the widespread availability of SPECT facilities makes [^{123}I]R93274 an attractive tool for investigation of 5-HT_{2A} receptors in the brain, its applicability for quantitative studies is restricted by the lower spatial resolution and limited quantifiability of SPECT compared to PET. In addition, radioiodination increases the lipophilicity of [^{123}I]R93274 compared to the parent compound R91150 more than 10-fold[33], which leads to higher non-specific binding and thereby reduces the attainable signal-to-noise ratios. With this in mind, the PET tracer candidate [^{18}F]R91150 (**Fig. 1B**) with the more desirable physicochemical properties of the parent compound R91150 was prepared[33,34]. Initial *ex vivo* biodistribution studies in mice revealed good brain uptake of [^{18}F]R91150 and no formation of brain-derived radiometabolites for at least 30 min[33]. In addition, *in vitro* autoradiography in rat brain slices demonstrated a distribution pattern consistent with selective binding to 5-HT_{2A} receptors and a low degree of non-specific binding[34]. However, a more detailed evaluation of [^{18}F]R91150 by *in vivo* PET imaging is still lacking. Moreover, while the original multi-step radiosynthesis of [^{18}F]R91150[33] could be simplified by application of late-stage alcohol-enhanced Cu-mediated radiofluorination of the corresponding *N*-Boc-protected pinacol boronate precursor[34], there is

still a need for more efficient preparation procedures for practical applications. In the present article, we describe improved protocols for the production of [^{18}F]R91150, the corresponding reference compound and radiofluorination precursors. In addition, we performed a preclinical evaluation of [^{18}F]R91150 by µPET imaging in mice and rats to assess its *in vivo* biodistribution, stability and binding behavior.

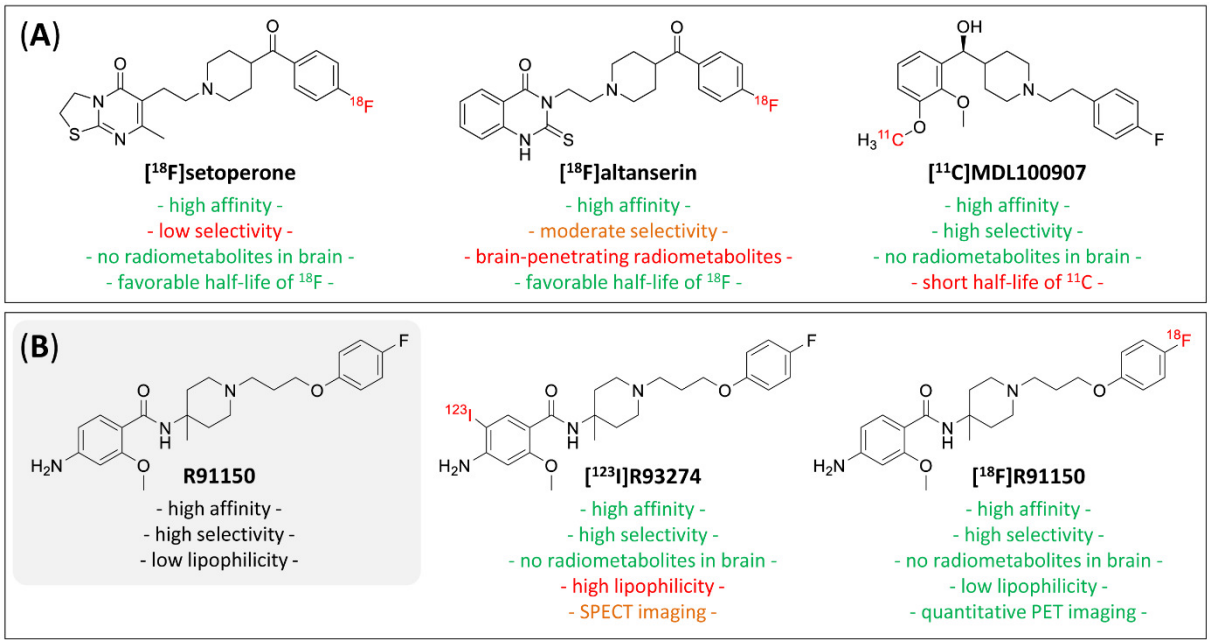

Figure 1. Brief summary of radiolabeled 5-HT$_{2A}$ receptor antagonists used as imaging agents. (**A**) Established PET radioligands. (**B**) R91150 and derived radioligands for SPECT ([^{123}I]R93274) or PET ([^{18}F]R91150) imaging.

2 Results and discussion

2.1. Preparation of radiolabeling precursors and reference compound

According to our previous observations[35], aromatic amino groups are compatible with the protocol for alcohol-enhanced Cu-mediated radiofluorination, making it suitable for one-step preparation of ^{18}F-labeled anilines like [^{18}F]R91150 from appropriate non-protected precursors. In order to evaluate the efficacy of such a one-step procedure, we prepared the non-protected radiolabeling precursor **1** and the reference compound R91150 as follows (Scheme 1). First, the substituted phenoxypropyl bromides **3a**[36] and **3b**[37] were conveniently prepared by alkylation of the respective phenols (**2a** and **2b**) with an eight-fold excess of 1,3-dibromopropane, which afforded the desired intermediates in yields of 75% and 55%, respectively.

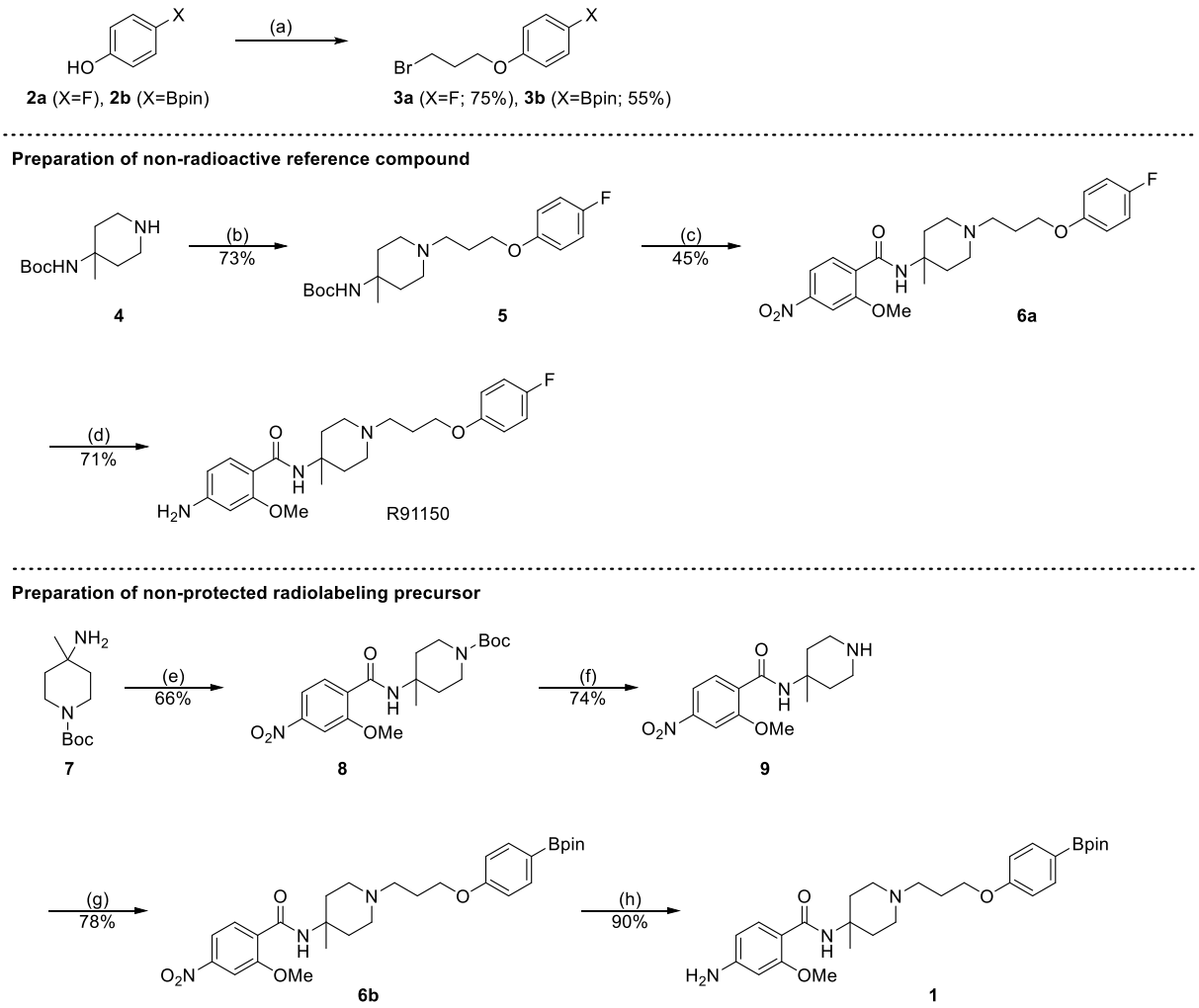

Scheme 1: Preparation of R91150 and non-protected radiolabeling precursor **1**. Conditions: (a) 1,3-dibromopropane, K_2CO_3, MeCN, 70 °C, 7 h; (b) **3a**, K_2CO_3, KI, DMF, rt, 16 h; (c) i. TFA/TIS/H_2O (95:2.5:2.5 v/v), ii. sat. $NaHCO_3$, iii. 2-methoxy-4-nitrobenzoyl chloride, DIEA, CH_2Cl_2, rt, 1 h; (d) Zn/NH_4Cl, EtOH/EtOAc, rt, 3 h; e) 2-methoxy-4-nitrobenzoyl chloride, DIEA, CH_2Cl_2, rt, 1 h; (f) i. TFA/TIS/H_2O (95:2.5:2.5 v/v), ii. sat. $NaHCO_3$; (g) **3b**, K_2CO_3, KI, DMF, rt, 16 h; (h) Zn/NH_4Cl, EtOH/EtOAc, rt, 12 h.

For preparation of the reference compound R91150, commercially available *tert*-butyl 4-amino-4-methylpiperidine-1-carbamate (**4**) was then alkylated with **3a** to afford intermediate **5**, which was Boc deprotected and acylated with 2-methoxy-4-nitrobenzoyl chloride (prepared *in situ* from the respective acid). Finally, the NO_2-substituted intermediate **6a** thus obtained was reduced with Zn/NH_4Cl in EtOAc/EtOH according to Renk et al.[38] to obtain R91150 in 17% total yield over four steps. For preparation of the non-protected radiolabeling precursor, the amino amide **9** was synthesized from *tert*-butyl 4-amino-4-methylpiperidine-1-carboxylate (**7**) and 2-methoxy-4-nitrobenzoic acid in 49% yield over two steps. Subsequent alkylation of **9** with **3b** furnished the NO_2-substituted intermediate **6b**, which was reduced with Zn/NH_4Cl in EtOAc/EtOH to obtain the radiolabeling precursor **1** in 70% yield over two steps.

Due to the limited shelf life of precursor **1** under ambient conditions (see below), we also prepared the corresponding *N*-Boc protected radiolabeling precursor **10.** Since direct *N*-Boc protection of **1** proved to be inefficient under all reaction conditions examined, the synthesis of **10** was instead performed by an alternative protocol that started with Z-protection of **4** followed by removal of the Boc-group to obtain the mono-protected diamine **11** in 75% yield over two steps (Scheme 2).

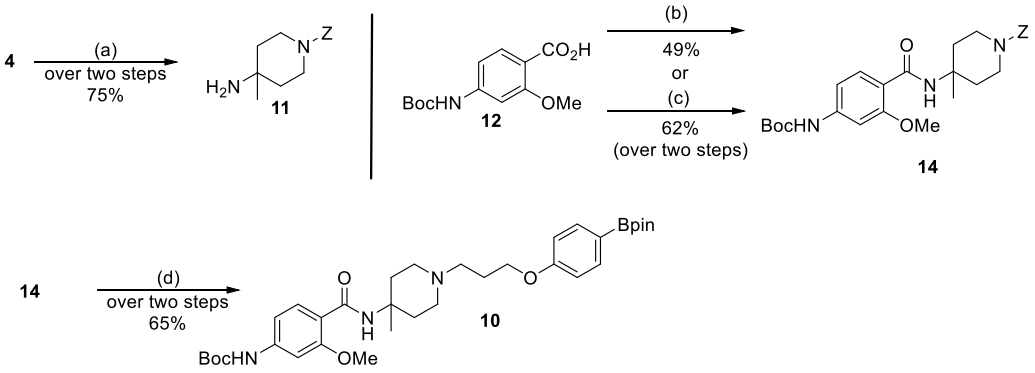

Scheme 2: Synthesis of *N*-Boc protected radiolabeling precursor **10**. Conditions: (a) i. Z-Cl, K_2CO_3, THF, 1.5 h, ii. 20% TFA in CH_2Cl_2, rt, 16 h, iii. sat. $NaHCO_3$; (b) **11**, HATU, DIPEA, DMF, rt, 4 h; (c) i. 2,3,5,6-tetrafluorophenol, EDC, CH_2Cl_2, rt, 26 h, ii. **11**, DIPEA, DMF, 60 °C, 16 h; (d) i. Pd/C, H_2, MeOH, rt, 16 h, ii. **3b**, K_2CO_3, KI, DMF, rt, 4 h.

11 was then acylated with *N*-Boc protected 4-amino-2-methoxybenzoic acid **12**[33] using HATU as coupling agent to furnish intermediate **14** in 49% yield. Alternatively, conversion of **12** into the bench stable 2,3,5,6-tetrafluorophenyl active ester **13** followed by acylation of **11** with **13** gave **14** in 62% yield over two steps. Subsequent Z-deprotection by catalytic hydrogenation over Pd/C followed by alkylation of the resulting intermediate with **3b** afforded the desired radiolabeling precursor **10** in 24% or 30% total yield over five or six steps, respectively. Thus, compared to existing methods for preparation of R91150 and radiolabeling precursor **10,** which are rather laborious and low-yielding (3−7% over 6−7 steps[34]), the developed protocols afforded the desired compounds in > 2-fold (R91150) and > 8-fold (**10**) higher yields, respectively.

2.2. Radiosynthesis of [^{18}F]R91150

To prepare [^{18}F]R91150, we first optimized the conditions for Cu-mediated radiofluorination of the unprotected radiolabeling precursor **1** (for details see section 2.1 in the supporting information). The best results were obtained when the radiosynthesis was performed as follows. [^{18}F]Fluoride ([^{18}F]F^-) was loaded onto an anion exchange resin and eluted with a solution

Et_4NOTf (4 µmol) in MeOH. The solvent was removed under reduced pressure in a stream of argon and a solution of precursor **1** (5 µmol) and $Cu(4\text{-}PhPy)_4(ClO_4)_2$ (10 µmol) in 1,3-dimethyl-2-imidazolidinone (DMI)/*n*BuOH (2:1) was added. The reaction mixture was then heated at 110 °C for 10 min under air to afford the crude radiotracer in radiochemical conversions (RCCs) of 35–46% (n=5). The bulk of the high-boiling DMI/*n*BuOH was removed by solid phase extraction (SPE) to obtain a crude product solution suitable for HPLC purification. After HPLC purification and formulation, [^{18}F]R91150 was obtained as a ready-to-use solution in activity yields (AYs) of 12±2% (n=7) and a radiochemical purity (RCP) of 90% within 65–75 min. The molar activity (A_m) of the radiotracer amounted to 240 GBq/µmol for 1.03 GBq tracer. While this protocol enabled one-step preparation of [^{18}F]R91150 in acceptable AYs, handling and storage of the unprotected radiolabeling precursor **1** was complicated by its hygroscopicity and limited shelf life under ambient conditions. To avoid these obstacles, we employed the same conditions for radiofluorination of the *N*-Boc-protected Bpin ester **10** (10 µmol) as a more stable radiolabeling precursor, which afforded the ^{18}F-labeled intermediate Boc-[^{18}F]R91150 in RCCs of 70–86% (n=6). Following removal of the reaction solvents by SPE as described above, the intermediate was deprotected with 6 M HCl at 80 °C for 10 min. Finally, HPLC purification and formulation furnished [^{18}F]R91150 as a ready-to-use solution in AYs of 24±2% (n=5) within 90–100 min and with an A_m of up to 217 GBq/µmol (1.46 GBq tracer).

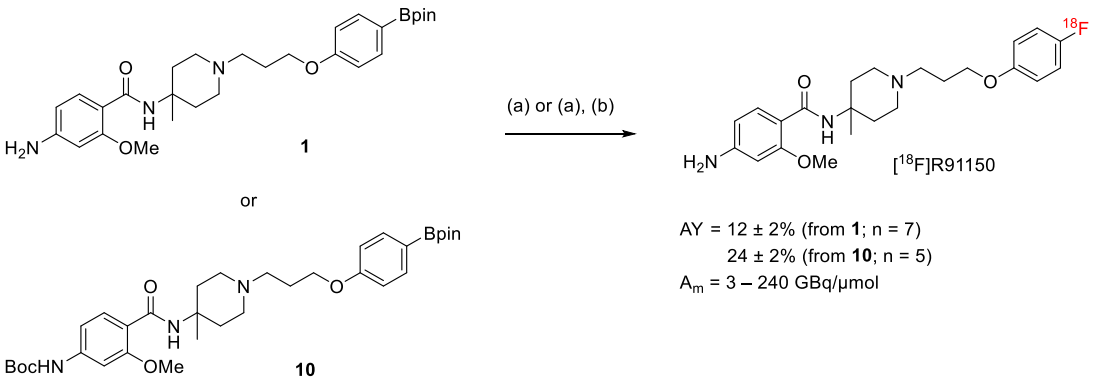

Scheme 3: Preparation of [^{18}F]R91150 from non-protected precursor **1** or *N*-Boc-protected precursor **10**. Conditions: (a) [^{18}F]F^- elution with Et_4NOTf (1 mg, 4 µmol) in MeOH (500 µL) followed by removal of MeOH and addition of **1** (5 µmol) or **10** (10 µmol) and $Cu(4\text{-}PhPy)_4(ClO_4)_2$ (10 µmol) in DMI/*n*BuOH (2:1), air, 110 °C, 10 min. (b) for preparation from **10**: 6 M HCl, 80 °C, 10 min. Abbreviations: AY – activity yield, A_m – molar activity.

2.3. Preclinical *in vivo* evaluation of [^{18}F]R91150

Having established an efficient protocol for the preparation of [^{18}F]R91150, we next evaluated the *in vivo* properties of the tracer by biodistribution studies in rodents. The whole body distribution and excretion of [^{18}F]R91150 were studied by µPET measurements in healthy mice (n=4), which revealed a low background uptake into muscles and other 5-HT$_{2A}$-negative tissues (Fig. 2A). In addition, low accumulation of radioactivity in bones indicated sufficient stability of the probe against *in vivo* defluorination (Fig. 2). Excretion of [^{18}F]R91150 in mice was mainly hepatobiliary, with high tracer accumulation in gall bladder and intestines (Fig. 2). Apart from the presence of radiometabolites in feces, high radioactivity uptake in the intestines could in part reflect tracer binding to 5-HT$_{2A}$ receptors present in the enteric nervous system of both small intestine and colon[39]. However, the travel of radioactive bowel contents during the 2 h measurements was clearly visible (Suppl. Fig. S13). In contrast, liver uptake due to hepatic metabolism and possibly binding to 5-HT$_{2A}$ receptors present in the liver[40] was relatively low (peak SUV$_{bw}$ 210 ± 13).

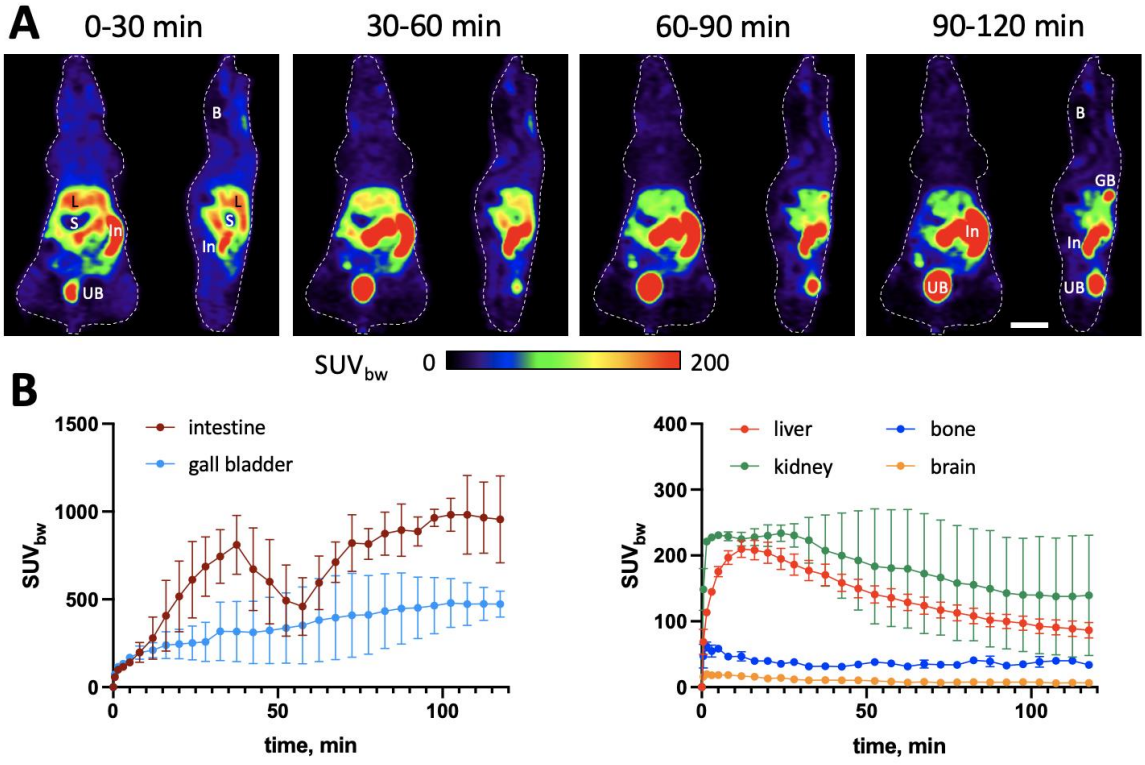

Figure 2. *In vivo* biodistribution of [^{18}F]R91150 in healthy mice. (A) Representative horizontal (left) and sagittal (right) summed µPET images for the indicated time periods (p.i.). White outlines indicate body contours. (B) Time-activity curves (mean ± standard deviation, n=4) for volumes of interest placed in the indicated organs or tissues. Scale bar: 10 mm. Abbreviations: B - brain, GB - gall bladder, In - intestines, L - liver, S - stomach, UB - urinary bladder.

Next, brain uptake and the cerebral distribution of [^{18}F]R91150 were evaluated by µPET measurements in healthy rats (n=3) (Fig. 3). The distribution pattern in the brain of naïve rats (Fig. 3A, top row) was similar to that previously observed in *in vitro* and *ex vivo* autoradiography experiments with [^{18}F]R91150[34]. In particular, radioactivity uptake was pronounced in the cortex and subcortical forebrain structures but low in the cerebellum and midbrain, which is consistent with the expression pattern of 5-HT$_{2A}$ receptors demonstrated by immunohistochemistry[41] and *in situ* hybridization[42,43]. In addition, pretreatment with 1.5 mg/kg altanserin (Fig. 3A, middle row) or displacement with 1.5 mg/kg ketanserin at 60 min p.i. (Fig. 3A, bottom row) reduced tracer uptake in the cerebral cortex by approximately 30–50% (Fig. 3B), indicating specific binding of [^{18}F]R91150 to cortical 5-HT$_{2A}$ receptors. Interestingly, very high tracer uptake that was unaffected by pretreatment with altanserin and much less sensitive to displacement with ketanserin was also observed in the choroid plexus (Fig. 3), a region characterized by very high levels of 5-HT$_{2C}$ receptors[44]. Although R91150 appears to be relatively selective (~75-fold) for 5-HT$_{2A}$ over 5-HT$_{2C}$ receptors, it has been shown to inhibit binding of the 5-HT$_{2C}$ ligand [^{3}H]mesulergine with an IC$_{50}$ of 12.5 nM[45]. Accordingly, accumulation of [^{18}F]R91150 in the choroid plexus could at least in part represent binding to 5-HT$_{2C}$ receptors, as has been reported for several other 5-HT$_{2A}$ radioligands[43,46]. Partial displacement of [^{18}F]R91150 binding in this region by ketanserin could indicate the presence of both, 5-HT$_{2A}$ and 5-HT$_{2C}$ receptors, in the choroid plexus, or simply reflect the limited selectivity of ketanserin for 5-HT$_{2A}$ over 5-HT$_{2C}$ receptors (8–33-fold[47–49]). In favor of the latter explanation, knockout of the 5-HT$_{2C}$ receptor in mice has been shown to completely abolish binding of [^{3}H]5-HT and several other 5-HT$_{2}$-targeting radioligands in the choroid plexus, suggesting very low or no expression of 5-HT$_{2A}$ receptors in this region[50]. In addition, binding of [^{18}F]R91150 in the choroid plexus was unaffected by pretreatment with the more selective 5-HT$_{2A}$ receptor antagonist altanserin, which is in line with previous studies showing no binding of [^{18}F]altanserin in this region[51,52]. As such, while [^{18}F]R91150 represent a promising candidate for PET imaging of cortical 5-HT$_{2A}$ receptors (and possibly 5-HT$_{2C}$ receptors in the choroid plexus), visualization of 5-HT$_{2A}$ receptors in certain subcortical structures (e.g., hippocampus) with this radioligand could be complicated by spillover effects from the choroid plexus in nearby ventricles. In addition, a contribution of 5-HT$_{2C}$ receptors to [^{18}F]R91150 binding in 5-HT$_{2C}$-expressing subcortical forebrain structures like the basal ganglia or hippocampus cannot be excluded. However, previous studies indicate that the density of 5-HT$_{2C}$ receptors in these brain regions is more than 40-fold lower than in the choroid plexus and about 10-fold lower than the density of 5-HT$_{2A}$ receptors[53,54].

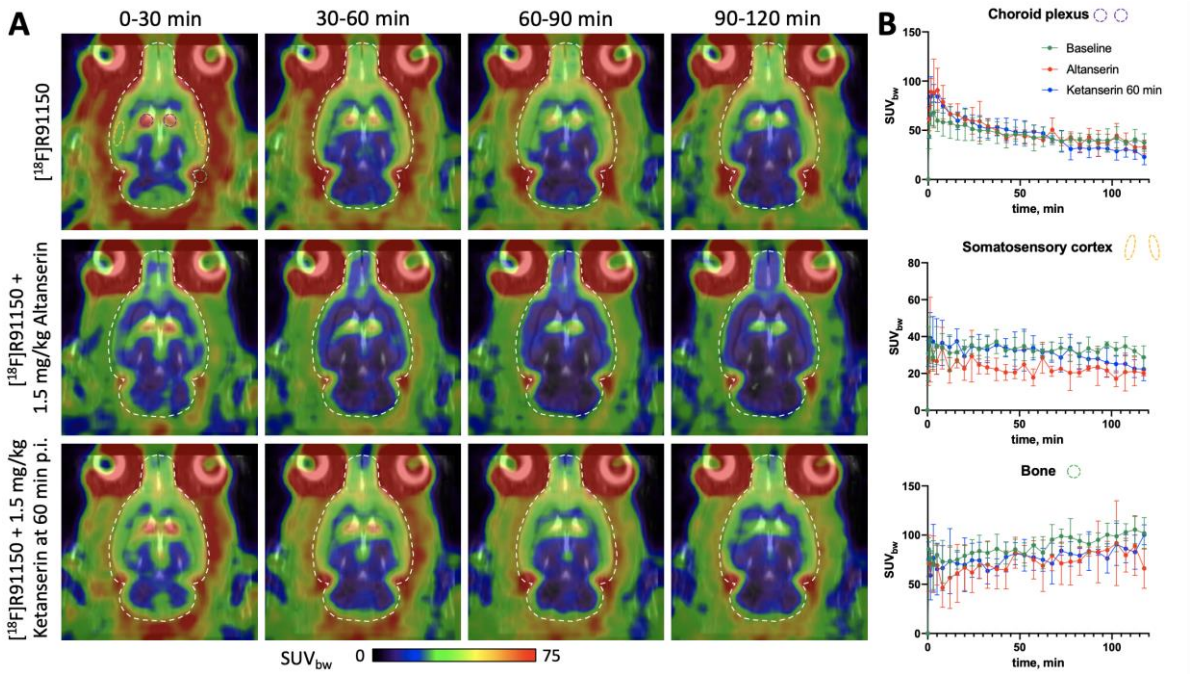

Figure 3. *In vivo* brain distribution of [^{18}F]R91150 in healthy rats. (A) Representative summed PET images for the indicated time periods obtained in experiments with [^{18}F]R91150 alone (top row), after pretreatment with 1.5 mg/kg altanserin (i.v.) administered 50 min before tracer injection (middle row) and in displacement studies with 1.5 mg/kg ketanserin (i.v.) administered 60 min after tracer injection (bottom row). PET images are projected onto an MRI template and the brain contours are indicated by white outlines. (B) Time-activity curves (mean ± standard deviation, n=3) for volumes of interest (VOIs) placed in the choroid plexus, somatosensory cortex and bone. VOIs are shown as dashed outlines in the [^{18}F]R91150/0–30 min image in A.

2.4. Conclusion

In conclusion, we have developed efficient protocols for the preparation of R91150 and two Bpin-substituted radiolabeling precursors for [^{18}F]R91150. Cu-mediated radiofluorination of the precursors afforded [^{18}F]R91150 in improved activity yields of 12–24% over one or two steps. Preclinical evaluation of the probe by μPET imaging in rodents confirmed that [^{18}F]R91150 is a promising candidate for PET imaging of cortical 5-HT$_{2A}$ receptors, although further studies will be required to firmly establish the role of 5-HT$_{2C}$ receptors for tracer binding in the choroid plexus and subcortical forebrain structures.

3 Materials and methods

3.1 Chemistry

General conditions

Unless otherwise stated, all reagents and solvents were purchased from Sigma-Aldrich (Steinheim, Germany), Acros (Fisher Scientific GmbH, Nidderrau, Germany), Alfa Aesar [Thermo Fisher (Kandel) GmbH, Kandel, Germany], BLDPharm (Kaiserslautern, Germany) or

Key Organics (Camelford, UK), and used without further purification. Unless otherwise stated, all reactions were carried out with magnetic stirring and, if air or moisture sensitive substrates and/or reagents were used, in flame-dried glassware under argon. Organic extracts were dried over anhydrous Na_2SO_4 or $MgSO_4$. Solutions were concentrated under reduced pressure (1–900 mbar) at 40–50 °C using a rotary evaporator. Column chromatography was performed with silica gel, 60 Å, 230–400 mesh particle size from VWR International GmbH (Darmstadt, Germany) or silica gel (w/Ca, 0.1%), 60 Å, 230–400 mesh particle size from Sigma-Aldrich GmbH (Steinheim, Germany). Thin layer chromatography (TLC) was performed using aluminum sheets coated with silica gel 0.25 mm SIL G/UV 254 (Merck KGaA, Darmstadt, Germany). Chromatograms were inspected under UV light (λ = 254 nm) and/or stained with phosphomolybdic acid (4 wt% in EtOH), ninhydrin (0.5% in 1-butanol) or potassium permanganate solution (0.75 wt% $KMnO_4$, 5 wt% K_2CO_3 and 0.63 v% 10% NaOH in water) Proton, carbon and fluorine nuclear magnetic resonance (^{1}H-, ^{13}C- and ^{19}F-NMR) spectra were recorded on a Bruker Avance Neo (400 MHz) spectrometer. Chemical shifts are reported in parts per million (ppm) relative to residual peaks of deuterated solvents. The observed signal multiplicities are characterized as follows: s = singlet, d = doublet, t = triplet, p = pentet, m = multiplet, dd = doublet of doublets, dt = doublet of triplets, ddd = doublet of doublets of doublets and br = broad. Coupling constants (*J*) are reported in hertz (Hz). Low resolution mass spectra (LRMS) were measured with an MSQ PlusTM mass spectrometer (Thermo Electron Corperation, San Jose, USA). High resolution mass spectra (HRMS) were measured with an LTQ Orbitrap XL (Thermo Fischer Scintific Inc., Bremen, Germany).

Organic syntheses

1-(3-Bromopropoxy)-4-fluorobenzene (3a)[55]**:** Anhydrous K_2CO_3 (19.6 g, 142 mmol, 1.6 eq.) was added to a solution of 1,3-dibromopropane (72.7 mL, 144 g, 713 mmol, 8 eq) and 4-fluorophenol (**2a**) (10 g, 89.2 mmol, 1 eq.) in anhydrous MeCN (125 mL) and the resulting suspension was vigorously stirred at 70 °C for 16 h. The reaction mixture was allowed to cool to ambient temperature, filtered through Celite® and concentrated under reduced pressure. The crude product was purified by kugelrohr distillation at 10 mbar to afford the title compound (15.5 g, 66.5 mmol, 75%) as a colorless liquid. ^{1}H-NMR (400 MHz, $CDCl_3$): δ = 7.01 – 6.94 (m, 2H), 6.87 – 6.82 (m, 2H), 4.07 (t, *J* = 5.8 Hz, 2H), 3.60 (t, *J* = 6.4 Hz, 2H), 2.31 (dt, *J* = 5.8, 6.4 Hz, 2H). ^{13}C-NMR (101 MHz, $CDCl_3$): δ = 157.51 (d, *J* = 239.4 Hz), 154.97 (d, *J* = 3.0 Hz), 115.91 (d, *J* = 23.2 Hz), 115.70 (d, *J* = 9.1 Hz), 66.11, 32.49, 30.07. ^{19}F-NMR (376 MHz, $CDCl_3$): δ = -123.86. GC-HRMS (EI, 70 eV) m/z: $[M]^{\cdot+}$ calculated for $C_9H_{10}BrFO^+$: 233.98731, 231.98936; found: 233.9871, 231.9892.

2-[4-(3-Bromopropoxy)phenyl]-4,4,5,5-tetramethyl-1,3,2-dioxaborolane (3b)[37]: 3b (4.1 g, 12 mmol, 55%, colorless oil which solidified on standing) was prepared from 4-(4,4,5,5-tetramethyl-1,3,2-dioxaborolan-2-yl)phenol (4.8 g, 22 mmol, 1 eq.), 1,3-dibromopropane (18.0 mL, 35.7 g, 177 mmol, 8 eq.) and anhydrous K_2CO_3 (4.8 g, 35 mmol, 1.6 eq.) in anhydrous MeCN (125 mL) using the same procedure as described for **3a** and isolated by column chromatography (silica gel with 0.1% Ca, hexane/EOAc, 1.4:1). ^{1}H-NMR (400 MHz, $CDCl_3$): δ = 7.75 (d, *J* = 8.7 Hz, 2H), 6.90 (d, *J* = 8.7 Hz, 2H), 4.13 (t, *J* = 5.8 Hz, 2H), 3.60 (t, *J* = 6.5 Hz, 2H), 2.32 (p, *J* = 6.2 Hz, 2H), 1.34 (s, 6H). ^{13}C-NMR (101 MHz, $CDCl_3$) δ 161.37, 136.68, 113.98, 83.70, 65.22, 32.46, 30.06, 24.99. The signal of *C*-Bpin was not observed.

***tert*-Butyl {1-[3-(4-fluorophenoxy)propyl]-4-methylpiperidin-4-yl}carbamate (5):** Anhydrous K_2CO_3 (4.7 g, 34 mmol, 3.7 eq.) was added to a solution of **3a** (2.2 g, 9.5 mmol, 1.02 eq.), **4** (2.0 g, 9.3 mmol, 1 eq.), and KI (15 g, 93 mmol, 10 eq.) in anhydrous DMF (10 mL) and the resulting suspension was vigorously stirred for 16 h. After filtration and concentration of the reaction mixture under reduced pressure, the residue was purified by column chromatography (hexane/EtOAc, 1.5:1) to afford the title compound (2.5 g, 6.8 mmol, 73%) as a colorless solid. ^{1}H-NMR (400 MHz, $CDCl_3$): δ = 6.98 – 6.92 (m, 2H), 6.84 – 6.80 (m, 2H), 4.31 (s, 1H), 3.96 (t, *J* = 6.3 Hz, 2H), 2.66 (d, *J* = 11.5 Hz, 2H), 2.659 – 2.55 (m, 2H), 2.33 (t, *J* = 10.5 Hz, 2H), 2.03 – 1.96 (m, 4H), 1.67 (dt, *J* = 33.4, 11.5 Hz, 2H), 1.43 (s, 9H), 1.34 (s, 3H). ^{13}C-NMR (101 MHz, $CDCl_3$): δ = 157.33 (d, *J* = 239.4 Hz), 155.18 (d, *J* = 1.0 Hz), 154.65, 115.88 (d, *J* = 22.2 Hz), 115.56 (d, *J* = 8.1 Hz), 79.11, 66.94, 55.30, 50.24, 49.57, 36.29, 28.59, 26.85, 26.49. The signal of *C*O-O*t*Bu was overlaid by one of the components of the *C*-F doublet (at 158.51 ppm). ^{19}F-NMR (376 MHz, $CDCl_3$): δ = -124.17. LRMS (ESI) m/z: $[M+H]^+$ calculated for $C_{20}H_{32}FN_2N_2O_3^+$: 367.24; found: 367.29. HRMS (ESI) m/z: $[M+H]^+$ calculated for $C_{20}H_{32}FN_2N_2O_3^+$: 367.23915; found: 367.23895.

***N*-{1-[3-(4-Fluorophenoxy)propyl]-4-methylpiperidin-4-yl}-2-methoxy-4-nitrobenzamide (6a):**

a) 1-[3-(4-Fluorophenoxy)propyl]-4-methylpiperidine-4-amine[33]

A solution of **5** (2.45 g, 6.69 mmol, 1 eq.) in TFA/TIS/H_2O (20 mL, 95/2.5/2.5 v/v) was allowed to stand for 5 min at ambient temperature and concentrated under reduced pressure. The residue was taken up into toluene (50 mL) and the resulting emulsion was concentrated under reduced pressure (×3). The residue was dissolved in EtOAc (100 mL) and the solution was washed with sat. $NaHCO_3$ (100 mL), dried and concentrated under reduced pressure to afford 1-[3-(4-fluorophenoxy)propyl]-4-methylpiperidine-4-amine (1.56 g, 5.86 mmol, 88%) as a colorless oil, which was used for the next step without further purification or characterization.

b) 2-Methoxy-4-nitrobenzoyl chloride[56]

DMF (one drop) was added to a suspension of 2-methoxy-4-nitrobenzoic acid (1.30 g, 6.59 mmol, 1.12 eq.) in oxalyl chloride (4.0 mL, 5.9 g, 46 mmol) and the resulting suspension was stirred until complete dissolution of the solids and cessation of gas evolution (approximately 15 min). The mixture was concentrated under reduced pressure, the residue was taken up into toluene (50 mL) and the resulting solution was concentrated under reduced pressure (×3) to afford crude 2-methoxy-4-nitrobenzoyl chloride as a yellow oil, which was immediately used for the next step without further purification or characterization.

c) *N*-{1-[3-(4-Fluorophenoxy)propyl]-4-methylpiperidin-4-yl}-2-methoxy-4-nitrobenzamide (**6a**)

A solution of 2-methoxy-4-nitrobenzoyl chloride in anhydrous CH_2Cl_2 (10 mL) was added to a solution 1-[3-(4-fluorophenoxy)propyl]-4-methylpiperidine-4-amine (1.56 g, 5.86 mmol, 1 eq.) and DIPEA (2.0 mL, 1.5 g, 12 mmol, 2 eq.) in anhydrous CH_2Cl_2 (20 mL) and the resulting mixture was stirred for 1 h. The reaction mixture was then concentrated under reduced pressure and the residue was taken up into EtOAc and H_2O (80 mL of each). The organic layer was washed with 5% $NaHCO_3$ (3×40 mL), 1 M $NaHSO_4$ (3×40 mL), H_2O (3×40 mL) and brine (2×40 mL), and concentrated under reduced pressure. The residue was purified by column chromatography ($CHCl_3$/MeOH, 9:1) to afford **6a** (1.34 g, 3.01 mmol, 45% over three steps) as a faint yellow solid. ^{1}H-NMR [400 MHz, $(CD_3)_2SO$]: δ = 7.88 – 7.85 (m, 2H), 7.78 (s, 1H), 7.74 – 7.71 (m, 1H), 7.13 – 7.06 (m, 2H), 6.95 – 6.90 (m, 2H), 3.99 (s, 3H), 3.96 (t, *J* = 6.8 Hz, 2H), 2.57 (d, *J* = 11.2 Hz, 2H), 2.42 (t, *J* = 6.8 Hz, 2H), 2.23 (t, *J* = 11.2 Hz, 2H), 2.17 (t, *J* = 16.4 Hz, 2H), 1.86 (p, *J* = 6.6 Hz, 2H), 1.50 (dd, *J* = 16.4, 6.6 Hz, 2H), 1.37 (s, 3H). ^{13}C-NMR [101 MHz, $(CD_3)_2SO$]: δ = 163.47, 157.55, 156.83 (d, *J* = 236.3 Hz), 155.20, 154.98 (d, *J* = 2.0 Hz), 148.99, 131.96, 130.39, 115.78 (d, *J* = 20.2 Hz), 115.63 (d, *J* = 5.1 Hz), 115.45, 106.83, 66.43, 56.59, 54.62, 51.55, 49.03, 35.43, 26.40, 26.17. ^{19}F-NMR [376 MHz, $(CD_3)_2SO$]: δ = -124.26. LRMS (ESI) m/z: $[M+H]^+$ calculated for $C_{23}H_{29}FN_3O_5^+$: 446.21; found: 446.26. HRMS (ESI) m/z: $[M+H]^+$ calculated for $C_{23}H_{29}FN_3O_5^+$: 446.20858; found: 446.20877.

4-Amino-*N*-{1-[3-(4-fluorophenoxy)propyl]-4-methylpiperidin-4-yl}-2-methoxybenzamide (R91150)[33]: NH_4Cl (0.4 g, 7 mmol) followed by Zn dust (0.5 g, 7 mmol, 10 eq.) were added to a solution of **6a** (0.3 g, 0.7 mmol, 1 eq.) in 50% EtOH in EtOAc (50 mL) and the resulting suspension was vigorously stirred for 3 h. The reaction mixture was then filtered through Celite® and concentrated under reduced pressure. The residue was purified by column chromatography ($CHCl_3$/MeOH, 9:1) to afford the title compound (0.2 g, 0.5 mmol, 71%) as a colorless foam. ^{1}H-NMR (400 MHz, $CDCl_3$): δ = 7.96 (d, *J* = 8.5 Hz, 1H), 7.62 (s, 1H), 6.97 –

6.891 (m, 2H), 6.84 – 6.79 (m, 2H), 6.33 (dd, *J* = 8.5, 2.1 Hz, 1H), 6.20 (d, *J* = 2.1 Hz, 1H), 4.00 (s, 2H), 3.96 (t, *J* = 6.3 Hz, 2H), 3.89 (s, 3H), 2.73 (d, *J* = 11.8 Hz, 2H), 2.54 (dd, *J* = 16.4, 9.2 Hz, 2H), 2.30 (t, *J* = 11.8 Hz, 2H), 2.22 (t, *J* = 16.4 Hz, 2H), 2.01 – 1.95 (m, 2H), 1.74 (dt, *J* = 19.9, 4.5 Hz, 2H), 1.50 (s, 3H). ^{13}C-NMR (101 MHz, $CDCl_3$): δ = 164.79, 158.96, 157.27 (d, *J* = 238.4 Hz), 155.24 (d, *J* = 2.0 Hz), 150.87, 133.71, 115.97, 115.74 (d, *J* = 23.2 Hz), 115.51 (d, *J* = 8.1 Hz), 112.98, 107.84, 97.43, 67.01, 55.88, 55.45, 51.22, 49.74, 36.51, 26.94, 26.66. ^{19}F-NMR (376 MHz, $CDCl_3$): δ = -124.23. LRMS (ESI) m/z: $[M+H]^+$ calculated for $C_{23}H_{31}FN_3O_3^+$: 416.23; found: 416.29. HRMS (ESI) m/z: $[M+H]^+$ calculated for $C_{23}H_{31}FN_3O_3^+$: 416.23440; found: 416.23454.

***tert*-Butyl 4-(2-methoxy-4-nitrobenzamido)-4-methylpiperidine-1-carboxylate (8):** A solution of 2-methoxy-4-nitrobenzoyl chloride [prepared from 2-methoxy-4-nitrobenzoic acid (2.0 g, 9.9 mmol, 1.06 eq.) and oxalyl chloride (5.0 mL, 7.4 g, 58 mmol) as described above for the synthesis of **6a**] in anhydrous CH_2Cl_2 (10 mL) was added to a solution of *tert*-butyl 4-amino-4-methylpiperidine-1-carboxylate (**7**) (2.0 g, 9.3 mmol, 1 eq.) and DIPEA (3.4 mL, 2.5 g, 19 mmol, 2 eq.) in anhydrous CH_2Cl_2 (50 mL) and the resulting mixture was stirred for 1 h. The reaction mixture was then concentrated under reduced pressure and the residue was taken up into EtOAc and H_2O (80 mL of each). The organic layer was washed with 5% $NaHCO_3$ (3×40 mL), 1 M $NaHSO_4$ (3×40 mL), H_2O (3×40 mL) and brine (2×40 mL), and concentrated under reduced pressure. The residue was purified by column chromatography (hexane/$CHCl_3$/EtOAc/MeOH, 20:9:8:1) to afford the title compound (2.4 g, 6.1 mmol, 66%) as a faint yellow solid. ^{1}H-NMR [400 MHz, $(CD_3)_2CO$]: δ = 8.06 (dd, *J* = 8.4, 0.3 Hz, 1H), 7.92 (d, *J* = 2.0 Hz, 1H), 7.90 – 7.85 (m, 1H), 7.70 (s, 1H), 4.15 (s, 3H), 3.79 (d, *J* = 13.7 Hz, 2H), 3.24 – 3.06 (m, 2H), 2.34 – 2.18 (m, 2H), 1.58 – 1.50 (m, 2H), 1.49 (s, 3H), 1.44 (s, 9H). ^{13}C-NMR [101 MHz, $(CD_3)_2CO$]: δ = 163.79, 158.46, 155.12, 150.89, 132.65, 130.90, 116.28, 107.77, 79.42, 57.40, 52.98, 36.44, 28.58, 26.45. LRMS (ESI) m/z: $[M+H]^+$ calculated for $C_{19}H_{28}N_3O_6^+$: 394.20; found: 394.22. HRMS (ESI) m/z: $[M+Na]^+$ calculated for $C_{19}H_{27}N_3O_6Na^+$: 416.17921; found: 416.17991.

2-Methoxy-*N*-(4-methylpiperidin-4-yl)-4-nitrobenzamide (9): A solution of **8** (2.35 g, 5.97 mmol, 1 eq.) in TFA/TIS/H_2O 95/2.5/2.5 (10 mL) was allowed to stand for 5 min at ambient temperature and then concentrated under reduced pressure. The residue was taken up into toluene (50 mL) and the resulting emulsion was concentrated under reduced pressure (×3). The residue was dissolved in EtOAc (100 mL) and the solution was washed with sat. $NaHCO_3$ (100 mL), dried and concentrated under reduced pressure to afford the title compound (1.3 g, 4.4 mmol, 74%) as a yellow solid. ^{1}H-NMR [400 MHz, $(CD_3)_2CO$]: δ = 7.95 – 7.87 (m, 3H),

7.76 (s, 1H), 4.14 (s, 3H), 3.45 – 3.33 (m, 4H), 2.60 (d, *J* = 13.1 Hz, 2H), 1.99 (ddd, *J* = 12.2, 7.4, 5.2 Hz, 2H), 1.54 (s, 3H). ^{13}C-NMR [101 MHz, $(CD_3)_2CO$]: δ = 164.80, 158.34, 150.85, 132.11, 131.69, 116.30, 107.61, 57.29, 51.75, 40.85, 33.20, 26.62. LRMS (ESI) m/z: $[M+H]^+$ calculated for $C_{14}H_{20}N_3O_4^+$: 294.15; found: 294.11. HRMS (ESI) m/z: $[M+H]^+$ calculated for $C_{14}H_{20}N_3O_4^+$: 294.14483; found: 294.14510.

2-Methoxy-*N*-(4-methyl-1-{3-[4-(4,4,5,5-tetramethyl-1,3,2-dioxaborolan-2-yl)phenoxy]-propyl}piperidin-4-yl)-4-nitrobenzamide (6b): 6b (3.1 g, 5.6 mmol, 78%, faint yellow solid) was prepared from **9** (2.1 g, 7.2 mmol, 1 eq.), **3b** (2.5 g, 7.3 mmol, 1.01 eq.), anhydrous K_2CO_3 (1.0 g, 7.2 mmol, 1 eq.) and KI (1.2 g, 7.23 mmol) in anhydrous DMF (25 mL) using the same procedure as described for **6a**. The crude product was purified by column chromatography (silica gel with 0.1% Ca, $CHCl_3$: MeOH = 11:1). ^{1}H-NMR (400 MHz, $CDCl_3$): δ = 8.28 (d, *J* = 8.6 Hz, 1H), 7.92 (dd, *J* = 8.6, 2.1 Hz, 1H), 7.84 (d, *J* = 2.0 Hz, 1H), 7.72 (t, *J* = 5.4 Hz, 2H), 7.55 (s, 1H), 6.86 (d, *J* = 8.6 Hz, 2H), 4.08 (s, 3H), 4.04 (t, *J* = 6.1 Hz, 2H), 2.92 – 2.80 (m, 2H), 2.68 (t, *J* = 7.1 Hz, 2H), 2.49 – 2.38 (m, 2H), 2.27 (d, *J* = 13.9 Hz, 2H), 2.08 – 2.03 (m, 2H), 1.89 – 1.84 (m, 2H), 1.53 (s, 3H), 1.32 (s, 12H). ^{13}C-NMR (101 MHz, $CDCl_3$): δ = 162.53, 161.46, 157.36, 150.29, 136.64, 133.25, 128.36, 116.32, 113.91, 106.87, 83.71, 65.79, 56.98, 55.43, 51.96, 49.66, 35.81, 26.43, 24.97. The signal of *C*-Bpin was not observed. LRMS (ESI) m/z: $[M+H]^+$ calculated for $C_{29}H_{41}BN_3O_7^+$: 554.30; found: 554.34. HRMS (ESI) m/z: $[M+H]^+$ calculated for $C_{29}H_{41}BN_3O_7^+$: 554.30321; found: 554.30247. Correct isotopic pattern.

4-Amino-2-methoxy-*N*-(4-methyl-1-{3-[4-(4,4,5,5-tetramethyl-1,3,2-dioxaborolan-2-yl)phenoxy]propyl}piperidin-4-yl)benzamide (1)[34]: 1 (0.9 g, 1.7 mmol, 90%, colorless oil or foam) was prepared from **6b** (1.04 g, 1.88 mmol, 1 eq.), pulverized Zn (1.23 g, 18.8 mmol, 10 eq.) and NH_4Cl (1.00 g, 18.8 mmol, 10 eq.) in 50% EtOH in EtOAc (50 mL) using the same procedure as described for R91150 except that the reaction time was increased to 24 h. The crude product was purified by column chromatography (SiO_2 with 0.1% Ca, $CHCl_3$/MeOH, 11:1). ^{1}H-NMR (400 MHz, $CDCl_3$): δ = 7.94 (d, *J* = 8.5 Hz, 1H), 7.72 (d, *J* = 8.6 Hz, 2H), 7.59 (s, 1H), 6.85 (d, *J* = 8.6 Hz, 2H), 6.34 (dd, *J* = 8.5, 2.1 Hz, 1H), 6.20 (d, *J* = 2.0 Hz, 1H), 4.03 (t, *J* = 6.0 Hz, 4H), 3.90 (s, 3H), 3.01 – 2.89 (m, 2H), 2.79 – 2.69 (m, 2H), 2.51 (t, *J* = 10.6 Hz, 2H), 2.31 (d, *J* = 13.8 Hz, 2H), 2.13 – 2.02 (m, 2H), 1.84 (t, *J* = 11.1 Hz, 2H), 1.50 (s, 3H), 1.32 (s, 12H). ^{13}C-NMR (101 MHz, $CDCl_3$): δ = 165.05, 161.40, 158.96, 151.07, 136.64, 133.72, 113.90, 112.61, 107.88, 97.37, 83.69, 65.72, 55.95, 55.44, 50.86, 49.66, 35.68, 26.58, 26.13, 24.97. The signal of *C*-Bpin was not observed. LRMS (ESI) m/z: $[M+H]^+$ calculated for $C_{29}H_{43}BN_3O_5^+$: 524.33; found: 524.25. HRMS (ESI) m/z: $[M+H]^+$ calculated for $C_{29}H_{43}BN_3O_5^+$: 524.32903; found: 524.32865. Correct isotopic pattern.

Benzyl 4-amino-4-methylpiperidine-1-carboxylate (11)[57]:

a) Benzyl 4-[(*tert*-butoxycarbonyl)amino]-4-methylpiperidine-1-carboxylate

Z-Cl (3.9 mL, 4.8 g, 28 mmol, 1.2 eq.) was added dropwise to K_2CO_3 (9.7 g, 70 mmol, 3 eq.) suspended in a solution of **4** (5.0 g, 23 mmol, 1 eq.) in anhydrous THF (117 mL). The reaction mixture was stirred at ambient temperature for 1.5 h, after which H_2O (117 mL) was added and the reaction mixture stirred for another 20 min. The aqueous phase was separated and extracted with EtOAc (3×150 mL). The combined organic phases were washed with sat. $NaHCO_3$ (2×100 mL), dried and concentrated under reduced pressure. The residue was purified by column chromatography (cyclohexane/EtOAc, 9:1) to afford benzyl 4-[(*tert*-butoxycarbonyl)amino]-4-methylpiperidine-1-carboxylate (8.1 g, 23 mmol, >99%) as a colorless oil, which gradually solidified to a colorless solid. $R_f = 0.22$ (cyclohexane/EtOAc, 9:1). ^{1}H-NMR (400 MHz, $CDCl_3$): δ = 7.38 – 7.30 (m, 5H), 5.12 (s, 2H), 4.35 (s, 1H), 3.83 – 3.68 (m, 2H), 3.26 – 3.19 (m, 2H), 2.06 – 1.91 (m, 2H), 1.54 – 1.48 (m, 2H), 1.43 (s, 9H), 1.34 (s, 3H). ^{13}C-NMR (101 MHz, $CDCl_3$): δ = 155.40, 136.94, 128.60, 128.09, 127.98, 127.09, 67.18, 50.59, 40.05, 36.20, 28.54, 27.03, 26.26. LRMS (ESI) m/z: $[M+H]^+$ calculated for $C_{19}H_{29}N_2O_4^+$: 349.21; found: 349.14. HRMS (ESI) m/z: $[M+Na]^+$ calculated for $C_{19}H_{29}N_2O_4Na^+$: 371.19413; found: 371.19387.

b) Benzyl 4-amino-4-methylpiperidine-1-carboxylate (**11**)

Benzyl 4-[(*tert*-butoxycarbonyl)amino]-4-methylpiperidine-1-carboxylate (8.1 g, 23 mmol, 1 eq.) was taken up into 20% TFA in CH_2Cl_2 (47 mL) and stirred for 16 h at ambient temperature. The reaction mixture was cooled to 0 °C, and saturated $NaHCO_3$ (100 mL) was slowly added. The mixture was allowed to warm up to ambient temperature and stirred for 10 min, after which the aqueous phase was separated and extracted with Et_2O (3×150 mL). The combined organic phases were dried over Na_2SO_4 and concentrated under reduced pressure to afford **11** (4.3 g, 17 mmol, 75%) as a colorless solid. ^{1}H-NMR (400 MHz, $CDCl_3$): δ = 7.37 – 7.28 (m, 5H), 6.92–6.10 (br, 2H), 5.10 (s, 2H), 3.83 – 3.80 (m, 2H), 3.27 – 3.22 (m, 2H), 1.78 – 1.69 (m, 4H), 1.37 (s, 3H). ^{13}C-NMR (101 MHz, $CDCl_3$): δ = 155.23, 136.53, 128.67, 128.26, 128.00, 67.58, 52.58, 39.84, 35.33, 23.13. LRMS (ESI) m/z: $[M+H]^+$ calculated for $C_{14}H_{21}N_2O_2^+$: 249.16; found: 249.10. HRMS (ESI) m/z: $[M+H]^+$ calculated for $C_{14}H_{21}N_2O_2^+$: 249.15975; found: 249.15980.

4-[(*tert*-Butoxycarbonyl)amino]-2-methoxybenzoic acid (12)[33]:

Boc_2O (9.6 mL, 9.8 g, 45 mmol, 1.5 eq.) was added (in one portion) to a solution of 4-aminobenzoic acid (5.0 g, 30 mmol, 1 eq.) and Et_3N (5.0 mL, 3.6 g, 36 mmol, 1.2 eq.) in MeOH (40 mL) and the reaction mixture was stirred at room temperature for 16 h. The solvent was

removed under reduced pressure and the residue was dissolved in EtOAc. The resulting solution was washed with 10% citric acid, the EtOAc was removed under reduced pressure and the product crystalized in cyclohexane/EtOAc (2:1, 78 mL/g) to afford the title compound (3.9 g, 15 mmol, 49%, purity: > 99%) as a colorless solid. The volume of the mother liquor was then reduced by half to afford, after crystallization, a second crop of **12** (1.05 g, 3.34 mmol, 11%, purity: 85%). R_f = 0.29 ($CHCl_3$/MeOH, 49:1). ^{1}H-NMR [400 MHz, $(CD_3)_2SO$]: δ = 12.16 (br, 1H), 9.65 (s, 1H), 7.63 (d, *J* = 8.5 Hz, 1H), 7.35 (d, *J* = 1.8 Hz, 1H), 7.04 (dd, *J* = 8.6, 1.9, 1H), 3.76 (s, 3H), 1.48 (s, 9H). ^{13}C-NMR [101 MHz, $(CD_3)_2SO$]: δ = 166.44, 159.67, 152.53, 144.63, 132.40, 113.48, 109.22, 101.40, 79.70, 55.48, 28.06. LRMS (ESI) m/z: $[M+H]^+$ calculated for $C_{13}H_{18}NO_5^+$: 268.12; found: 268.11. HRMS (ESI) m/z: $[M+H]^+$ calculated for $C_{13}H_{18}NO_5^+$: 268.11795; found: 268.11829.

2,3,5,6-Tetrafluorophenyl 4-[(*tert*-butoxycarbonyl)amino]-2-methoxybenzoate (13):

1-Ethyl-3-(3-dimethylaminopropyl)carbodiimide hydrochloride (186 mg, 0.97 mmol, 1.3 eq.) was added to an ice-cold solution of **12** (200 mg, 0.75 mmol, 1 eq.) and 2,3,5,6-tetrafluorophenol (260 mg, 1.57 mmol, 2.1 eq.) in anhydrous CH_2Cl_2 (7.5 mL), and the mixture was stirred at ambient temperature for 16 h. The resulting dark red solution was diluted with CH_2Cl_2 and washed with H_2O (3×15 mL) and brine (3×15 mL). The organic phase was dried and concentrated under reduced pressure. The crude was product was purified by column chromatography (cyclohexane/EtOAc, 9:1) to afford the title compound (187 mg, 0.45 mmol, 60%) as a colorless solid. ^{1}H-NMR (400 MHz, $CDCl_3$): δ = 8.06 (d, *J* = 8.6 Hz, 1H), 7.51 (d, *J* = 7.51 Hz, 1H), 6.99 (m, 1H), 6.75 (dd, *J* = 8.6, 2.0 Hz, 2H), 3.96 (s, 3H), 1.54 (s, 9H). ^{13}C-NMR (101 MHz, $CDCl_3$): δ = 162.58, 160.38, 151.95, 147.30, 145.59, 134.15, 109.67, 109.31, 103.02, 102.80, 102.57, 101.26, 81.65, 56.13, 28.26. ^{19}F-NMR (376 MHz, $CDCl_3$): δ = -139.59 (dd, J = 22.2, 9.7 Hz, 2F), -152.70 (dd, J = 22.2, 9.7, 2F). LRMS (ESI) m/z: $[M+H]^+$ calculated for $C_{19}H_{18}F_4NO_5^+$: 416.10; found: 416.03.

Benzyl 4-{4-[(*tert*-butoxycarbonyl)amino]-2-methoxybenzamido}-4-methylpiperidine-1-carboxylate (14):

Method A: HATU (4.98 g, 6.57 mmol, 1.5 eq.) was added in small portions to an ice-cold solution of **12** (1.76 g, 6.57 mmol, 1.5 eq.) and DIPEA (2.20 mL, 1.69 g, 13.1 mmol, 3 eq.) in anhydrous DMF (59 mL) and the mixture was stirred for 20 min. A solution of **11** (1.09 g, 4.37 mmol, 1 eq.) in anhydrous DMF (6.6 mL) was added dropwise to the resulting dark yellow solution and the reaction mixture was stirred at ambient temperature for 4 h. Ethylenediamine (1.5 mL) was then added and stirring was continued for 16 h, after which 1 M NaOH (50 mL) was added and the mixture stirred for another 15 min. The reaction mixture was diluted with

H_2O (250 mL) and extracted with EtOAc (3×200 mL). The combined organic phases were washed with 1 M NaOH (200 mL), 0.5 M HCl (3×200 mL) and brine (3×200 mL), dried and concentrated under reduced pressure. The residue was purified by column chromatography (cyclohexane/EtOAc, 2:1, R_f = 0.20) to afford the title compound (1.07 g, 2.14 mmol, 49%) as a colorless solid.

Method B: A solution of **13** (199 mg, 0.48 mmol, 1 eq.), **11** (172 mg, 0.69 mmol, 1.4 eq.) and DIPEA (127 µL, 171 mg, 1.32 mmol, 3 eq.) in anhydrous DMA (4.4 mL) was stirred at 60 °C for 16 h. The reaction mixture was diluted with H_2O (50 mL) and extracted with EtOAc (3×50 mL). The combined organic phases were washed with 0.5 M NaOH (3×50 mL), 0.5 M HCl (3×50 mL) and brine (3×50 mL), and dried over Na_2SO_4. The solvent was removed under reduced pressure to afford the title compound (233 mg, 0.47 mmol, 98%) as a colorless solid.

^{1}H-NMR [400 MHz, $(CD_3)_2SO$]: δ = 8.04 (d, *J* = 8.5 Hz, 1H), 7.76 (s, 1H), 7.54 (s, 1H), 7.36 – 7.29 (m, 5H), 6.73 (s, 1H), 6.68 (dd, *J* = 8.6, 2.0 Hz, 1H), 5.13 (s, 2H), 3.06 (s, 3H), 3.17 (t, *J* = 13.9 Hz, 2H), 2.26 – 2.16 (m, 2H), 1.68 – 1.57 (m, 4H), 1.52 (s, 9H), 1.51 (s, 3H). ^{13}C-NMR [101 MHz, $(CD_3)_2SO$]: δ = 164.45, 158.34, 155.47, 152.41, 142.81, 136.95, 132.71, 128.62, 128.12, 128.01, 116.74, 110.59, 101.06, 81.29, 67.22, 56.26, 51.65, 40.16, 29.83, 28.43, 26.44. LRMS (ESI) m/z: $[M+H]^+$ calculated for $C_{27}H_{36}N_3O_6^+$: 498.26; found: 498.14.

4-[(*tert*-Butoxycarbonyl)amino]-2-methoxy-*N*-(4-methyl-1-{3-[4-(4,4,5,5-tetramethyl-1,3,2-dioxaborolan-2-yl)phenoxy]propyl}piperidin-4-yl)benzamide (10)[34]:

a) 4-[(*tert*-Butoxycarbonyl)amino]-2-methoxy-*N*-(4-methyl-piperidine-4-yl)benzamide

10% Pd/C (107 mg, w/w) was added to a solution **14** (1.07 g, 2.14 mmol, 1 eq.) in anhydrous MeOH (10 mL) and the reaction mixture was stirred in a hydrogen atmosphere for 16 h. The mixture was filtered through Celite® and concentrated under reduced pressure to afford 4-[(*tert*-butoxycarbonyl)amino]-2-methoxy-*N*-(4-methyl-piperidine-4-yl)benzamide (726 mg, 2.00 mmol, 93%) as a colorless solid, which was used for the next step without further purification. ^{1}H-NMR [400 MHz, $(CD_3)_2SO$]: δ = 9.62 (s, 1H), 7.69 (s, 1H), 7.65 (d, *J* = 8.6 Hz, 1H), 7.38 (d, *J* = 1.4 Hz, 1H), 7.06 (dd, *J* = 8.5, 1.7 Hz, 1H), 3.87 (s, 3H), 2.87 – 2.83 (m, 2H), 2.77 – 2.71 (m, 2H), 2.14 (d, *J* = 13.4 Hz, 2H), 1.54 – 1.48 (m, 11H), 1.37 (s, 3H).

b) 4-[(*tert*-Butoxycarbonyl)amino]-2-methoxy-*N*-(4-methyl-1-{3-[4-(4,4,5,5-tetramethyl-1,3,2-dioxaborolan-2-yl)phenoxy]propyl}piperidin-4-yl)benzamide (**10**)

K_2CO_3 (1.00 g, 7.25 mmol, 3.7 eq.) and KI (3.26 g, 19.6 mmol, 10 eq.) were added to a solution of 4-[(*tert*-butoxycarbonyl)amino]-2-methoxy-*N*-(4-methyl-piperidine-4-yl)benzamide in anhydrous DMF (5 mL). **3b** (675 mg, 1.98 mmol, 1.01 eq.) was added in one portion to the resulting suspension and the reaction mixture was stirred for 4 h, after which H_2O (30 mL)

followed by EtOAc (30 mL) were added. The organic phase was removed and the aqueous phase extracted with EtOAc (3×45 mL). The combined organic phases were washed with 0.1 M HCl (3×70 mL) and brine (3×70 mL), dried and concentrated under reduced pressure. The residue was purified by column chromatography ($CHCl_3$/MeOH, 19:1, R_f = 0.32) to afford **10** (864 mg, 1.39 mmol, 70%) as a colorless solid. ^{1}H-NMR (400 MHz, $CDCl_3$): δ = 8.01 (d, *J* = 8.5 Hz, 1H), 7.71 (d, *J* = 8.7 Hz, 2H), 7.60 (d, *J* = 30.1 Hz, 2H), 6.83 (d, *J* = 8.5 Hz, 3H), 6.71 (dd, *J* = 8.7, 2.0 Hz, 1H), 4.05 (t, *J* = 5.8 Hz, 2H), 3.98 (s, 3H), 3.27 – 3.06 (m, 2H), 3.01 – 2.85 (m, 2H), 2.81 – 2.57 (m, 2H), 2.43 (d, *J* = 14.5 Hz, 2H), 2.34 – 2.23 (m, 2H), 2.21 – 2.09 (m, *J* = 10.1 Hz, 2H), 1.53 (s, 3H), 1.52 (s, 9H), 1.32 (s, 12H). ^{13}C-NMR (101 MHz, $CDCl_3$): δ = 164.78, 161.12, 158.29, 152.40, 143.08, 136.68, 132.70, 116.40, 113.83, 110.71, 101.13, 83.72, 81.35, 65.26, 56.36, 55.27, 50.76, 49.36, 34.54, 28.41, 25.15, 24.96. The signal of *C*-Bpin was not observed. LRMS (ESI) m/z: $[M+H]^+$ calculated for $C_{34}H_{51}BN_3O_7^+$: 624.37; found: 624.32. Correct isotopic pattern.

3.2 Radiochemistry

General conditions

[^{18}F]Fluoride ([^{18}F]F^-) was produced via the $^{18}O(p,n)^{18}F$ nuclear reaction by bombardment of enriched [^{18}O]H_2O with 16.5 MeV protons using a BC1710 cyclotron (The Japan Steel Works Ltd., Shinagawa, Japan) at the INM-5 (Forschungszentrum Jülich). All radiosyntheses were carried out in 5 mL Wheaton V-Vials equipped with PTFE-coated wing stir bars. Anhydrous solvents (DMI, *n*BuOH and MeOH, dried over molecular sieves) were purchased from Sigma-Aldrich (Steinheim, Germany). Anion exchange resins (Sep-Pak Accell Plus QMA carbonate plus light cartridges with 40 mg sorbent per cartridge) were obtained from Waters (Eschborn, Germany) and polymeric-based StrataX cartridges (60 mg) were obtained from Phenomenex (Aschaffenburg, Germany).

Processing of [^{18}F]F^-

Aqueous [^{18}F]F^- was loaded (from the female side) onto a QMA cartridge (preconditioned with 1 mL H_2O) and the cartridge was washed (from the male side) with anhydrous MeOH (1 mL) to remove residual H_2O and dried (from the female side) with air (2×10 mL). [^{18}F]F^- was eluted (from the female to the male side) with a solution of Et_4NOTf in MeOH (500 µL), and the MeOH was evaporated at 80 °C under reduced pressure in a stream of argon to give Et_4N[^{18}F]F/Et_4NOTf, which was used for the radiosyntheses as described below.

High-performance liquid chromatography (HPLC)

Analytical radio-HPLC was performed on a HPLC system (Knauer Wissenschaftliche Geräte GmbH, Berlin, Germany) with Azura P 6.1L pump and Azura UVD 2.1S UV/Vis detector. For monitoring UV absorbance and radioactivity, the UV/Vis detector was coupled in series with a Berthold NaI detector, giving a time of delay of 0.1–0.3 min (depending on the flow rate) between the corresponding responses. Radiochemical conversions (RCCs) were determined by radio-HPLC with post-column injection (for details see[58]) after dilution of the reaction mixtures with H_2O (1 mL) or 20% MeCN (1 mL). The identity of radiolabeled products was confirmed by co-injection of the corresponding non-radiolabeled reference compound. Activity yields (AY) were determined as the ratio between the activity of the purified radiolabeled product and the initial activity of $[^{18}F]F^-$ on the QMA cartridge.

Purification of crude [^{18}F]R91150 by semipreparative HPLC was performed with a dedicated HPLC system consisting of a Knauer pump 40P, a Knauer K-2500 detector, a Rheodyne 6-way valve and a Geiger-Müller counter.

Analytical HPLC conditions

[^{18}F]R91150 prepared from **1**: Column: MultoKrom® 100-5, 5 µm, 250×4.6 mm (CS-Chromatography Service GmbH, Langerwehe, Germany); eluent: 30% MeCN (0.1% TFA); flow rate: 1.3 mL/min; t_R = 7.85 min.

Boc-[^{18}F]R91150 prepared from **10**: Column: MultoKrom® 100-5, 5 µm, 250×4.6 mm (CS-Chromatography Service GmbH, Langerwehe, Germany); eluent: 50% MeCN (0.1% TFA); flow rate: 1.5 mL/min; t_R = 4.62 min.

Preparative HPLC conditions

Column: Gemini C18 110A, 5 µm, 250×10 mm (Phenomenex Ltd, Aschaffenburg, Germany); eluent: 25% MeCN in 25 mM sodium acetate buffer (pH=5.18); flow rate: 7.1 mL/min; t_R = 18–21 min.

Quality control

For [^{18}F]R91150 prepared from **1**: Column: Kinetex EVO C18, 5 µm, 250×4.6 mm (Phenomenex Ltd, Aschaffenburg, Germany); eluent: 20% MeCN (0.1% TFA), flow rate: 1.0 mL, t_R = 9.55 min.

For [^{18}F]R91150 prepared from **10**: Column: MultoKrom® 100-5, 5 µm, 250×4.6 mm (CS-Chromatography Service GmbH, Langerwehe, Germany); eluent: 30% MeCN (0.1% TFA); flow rate: 1.5 mL/min; t_R = 8.98 min.

Preparation of [^{18}F]R91150:

*Preparation from **1** (non-protected precursor)*. $Et_4N[^{18}F]F/Et_4NOTf$ (0.02–6.8 GBq) was taken up into a solution of **1** (2.6 mg, 5 µmol) and $Cu(4\text{-}PhPy)_4(ClO_4)_2$ (8.8 mg, 10 µmol) in DMI/*n*BuOH (1.2 mL, 2:1 ratio) and the reaction mixture was stirred under air at 110 °C for 10 min. The mixture was diluted with H_2O (19 mL) and loaded onto a StrataX cartridge. The cartridge was washed with H_2O (5 mL) and the crude radiolabeled product was eluted with MeCN (500 µL). The resulting solution was diluted with 25 mM sodium acetate buffer (pH=5.18; 1 mL) and loaded onto a preparative HPLC column. The product fraction was collected at 18–21 min, diluted with H_2O (19 mL) and loaded onto a StrataX cartridge. The cartridge was washed with H_2O (5 mL) and the radiolabeled product was eluted with EtOH (600 µL). The resulting solution was concentrated to approximately 50 µL at 40 °C in a stream of argon under reduced pressure, and the residue was taken up into 2% Tween-80 (0.6 mL) to afford [^{18}F]F91150 as ready-to-inject solution.

*Preparation from **10** (N-Boc-protected precursor)*. $Et_4N[^{18}F]F/Et_4NOTf$ (0.1–5.7 GBq) was taken up into a solution of **10** (6.2 mg, 10 µmol) and $Cu(4\text{-}PhPy)_4(ClO_4)_2$ (8.7 mg, 10 µmol) in DMI/*n*BuOH 2:1 (1.2 mL) and the reaction mixture was stirred under air at 110 °C for 10 min. The reaction mixture was diluted with H_2O (19 mL) and loaded onto a StrataX cartridge. The cartridge was washed with H_2O (5 mL) and the crude radiolabeled intermediate was eluted with MeOH (600 µL). The solvent was removed at 60 °C in a stream of argon under reduced pressure and 6 M HCl (500 µL) was added. The mixture was stirred at 80 °C for 10 min to de-protect the radiolabeled intermediate and then diluted with 6 M NaOH (350 µL) and H_2O (1 mL). [^{18}F]F91150 was isolated and formulated as described above.

3.3 *In vivo* experiments

Experimental animals

Animal experiments were carried out in accordance with the EU directive 2010/63/EU and the German Animal Welfare Act (TierSchG, 2006), and were approved by regional authorities (Ministry for Environment, Agriculture, Conservation and Consumer Protection of the State of North Rhine-Westphalia, license number 84-02.04.2017.A288). Three healthy Long Evans rats (females; 320–460 g) and four healthy C57BL/6 mice (females, 18–20 g) were used for this study. Animals were housed in groups of 2–4 in individually ventilated cages (NexGen Ecoflo,

Allentown Inc., Allentown, NJ, USA) under controlled ambient conditions (22 ± 1 °C and 55 ± 5% relative humidity). Food and water were available *ad libitum*.

***In vivo* PET experiments**

Prior to PET measurements, animals were anesthetized with isoflurane in O_2/air (3:7) [5% for induction, 1.5–2.5% for maintenance], and a catheter for tracer injection was inserted into the lateral tail vein. Animals were placed on an animal holder (Equipment Vétérinaire Minerve, Esternay, France for rats, and Medres, Cologne for mice), and fixed with a tooth bar in a respiratory mask. PET scans in list mode were performed using a Focus 220 micro PET scanner (CTI-Siemens, Germany) with a resolution at the center of field of view of 1.4 mm. Data acquisition started with injection of the tracer (59.7 ± 5.9 MBq in 500 µL for rats and 9.5 ± 0.9 MBq in 125 µL for mice), continued for 120 min and was followed by a 10 min transmission scan using a ^{57}Co point source. Breathing rate was monitored and maintained at around 60/min by adjusting the isoflurane concentration (1.5–2.5%). Body temperature was maintained at 37 °C by a feedback-controlled system. After the scan, the animals were returned to their home cage.

The emission scans were histogrammed into time frames (2×1 min, 2×2 min, 6×4 min, 18×5 min for time-activity curves, and 4×30 min for display) and fully 3D rebinned (span 3, ring difference 47), followed by OSEM3D/MAP reconstruction. The resulting voxel sizes were 0.38 × 0.38 × 0.80 mm^3 for rats, and 0.47 × 0.47 × 0.80 mm^3 for mice. Postprocessing and image analysis was performed with VINCI 5.21 (Max-Planck-Institute for Metabolism Research, Cologne, Germany). Images were intensity-normalized to injected dose and corrected for body weight (SUV_{bw}). To this end, every frame was divided by injected dose and multiplied by body weight times 100.

4 Abbreviations

[^{18}F]F^-, [^{18}F]fluoride; A_m, molar activity; AY, activity yield; DMI, 1,3-dimethyl-2-imidazolidinone; HPLC, high-performance liquid chromatography; PET, positron emission tomography; RCC, radiochemical conversion; SPE, solid phase extraction; SPECT, single photon emission computed tomography; TLC, thin layer chromatography.

5 Author information

Corresponding author

* correspondence: b.neumaier@fz-juelich.de

Author contributions

The manuscript was written through contributions of all authors. All authors have given approval to the final version of the manuscript.

Funding sources

This work was supported by Deutsche Forschungsgemeinschaft (DFG) grants ZL 65/1-1, ZL 65/3-1 and ZL 65/4-1.

6 Supporting information

^{1}H-, ^{13}C- and ^{19}F-NMR spectra for all prepared compound; results of optimization studies for the radiosynthesis of [^{18}F]R91150 from precursor **1**; HPLC chromatograms for [^{18}F]R91150 and details on the determination of carrier amount and molar activity; additional results of the *in vivo* evaluation of [^{18}F]R91150 in mice (PDF).

7 References

(1) Barnes, N. M.; Ahern, G. P.; Becamel, C.; Bockaert, J.; Camilleri, M.; Chaumont-Dubel, S.; Claeysen, S.; Cunningham, K. A.; Fone, K. C.; Gershon, M.; Di Giovanni, G.; Goodfellow, N. M.; Halberstadt, A. L.; Hartley, R. M.; Hassaine, G.; Herrick-Davis, K.; Hovius, R.; Lacivita, E.; Lambe, E. K.; Leopoldo, M.; Levy, F. O.; Lummis, S. C. R.; Marin, P.; Maroteaux, L.; McCreary, A. C.; Nelson, D. L.; Neumaier, J. F.; Newman-Tancredi, A.; Nury, H.; Roberts, A.; Roth, B. L.; Roumier, A.; Sanger, G. J.; Teitler, M.; Sharp, T.; Villalón, C. M.; Vogel, H.; Watts, S. W.; Hoyer, D. International Union of Basic and Clinical Pharmacology. CX. Classification of Receptors for 5-Hydroxytryptamine; Pharmacology and Function. *Pharmacol. Rev.* **2021**, *73* (1), 310–520. https://doi.org/10.1124/pr.118.015552.

(2) Schmitt, J.; Wingen, M.; Ramaekers, J.; Evers, E.; Riedel, W. Serotonin and Human Cognitive Performance. *Curr. Pharm. Des.* **2006**, *12* (20), 2473–2486. https://doi.org/10.2174/138161206777698909.

(3) Zhang, G.; Stackman, R. W. The Role of Serotonin 5-HT2A Receptors in Memory and Cognition. *Front. Pharmacol.* **2015**, *6* (225). https://doi.org/10.3389/fphar.2015.00225.

(4) Naughton, M.; Mulrooney, J. B.; Leonard, B. E. A Review of the Role of Serotonin Receptors in Psychiatric Disorders. *Hum. Psychopharmacol. Clin. Exp.* **2000**, *15* (6), 397–415. https://doi.org/10.1002/1099-1077(200008)15:6<397::AID-HUP212>3.0.CO;2-L.

(5) Dean, B.; Hayes, W. Decreased Frontal Cortical Serotonin2A Receptors in Schizophrenia. *Schizophr. Res.* **1996**, *21* (3), 133–139. https://doi.org/10.1016/0920-9964(96)00034-5.

(6) Rodríguez, J. J.; Noristani, H. N.; Verkhratsky, A. The Serotonergic System in Ageing and Alzheimer's Disease. *Prog. Neurobiol.* **2012**, *99* (1), 15–41. https://doi.org/10.1016/j.pneurobio.2012.06.010.

(7) Perry, E. K.; Perry, R. H.; Candy, J. M.; Fairbairn, A. F.; Blessed, G.; Dick, D. J.; Tomlinson, B. E. Cortical Serotonin-S2 Receptor Binding Abnormalities in Patients with Alzheimer's Disease: Comparisons with Parkinson's Disease. *Neurosci. Lett.* **1984**, *51* (3), 353–357. https://doi.org/10.1016/0304-3940(84)90402-6.

(8) Kroeze, W.; Roth, B. The Molecular Biology of Serotonin Receptors: Therapeutic Implications for the Interface of Mood and Psychosis. *Biol. Psychiatry* **1998**, *44* (11), 1128–1142. https://doi.org/10.1016/S0006-3223(98)00132-2.

(9) Meltzer, H. The Role of Serotonin in Antipsychotic Drug Action. *Neuropsychopharmacology* **1999**, *21* (2), 106S-115S. https://doi.org/10.1016/S0893-133X(99)00046-9.

(10) Cohen, H. Anxiolytic Effect and Memory Improvement in Rats by Antisense Oligodeoxynucleotide to 5-Hydroxytryptamine-2A Precursor Protein. *Depress. Anxiety* **2005**, *22* (2), 84–93. https://doi.org/10.1002/da.20087.

(11) Lemaire, C.; Cantineau, R.; Guillaume, M.; Plenevaux, A.; Christiaens, L. Fluorine-18-Altanserin: A Radioligand for the Study of Serotonin Receptors with PET: Radiolabeling and in Vivo Biologic Behavior in Rats. *J. Nucl. Med.* **1991**, *32* (12), 2266–2272.

(12) Meltzer, C. C.; Smith, G.; Price, J. C.; Reynolds, C. F.; Mathis, C. A.; Greer, P.; Lopresti, B.; Mintun, M. A.; Pollock, B. G.; Ben-Eliezer, D.; Cantwell, M. N.; Kaye, W.; DeKosky, S. T. Reduced Binding of [18F]Altanserin to Serotonin Type 2A Receptors in Aging: Persistence of Effect after Partial Volume Correction. *Brain Res.* **1998**, *813* (1), 167–171. https://doi.org/10.1016/S0006-8993(98)00909-3.

(13) Pinborg, L. H.; Adams, K. H.; Yndgaard, S.; Hasselbalch, S. G.; Holm, S.; Kristiansen,

H.; Paulson, O. B.; Knudsen, G. M. [18F]Altanserin Binding to Human 5HT2A Receptors Is Unaltered after Citalopram and Pindolol Challenge. *J. Cereb. Blood Flow Metab.* **2004**, *24* (9), 1037–1045. https://doi.org/10.1097/01.WCB.0000126233.08565.E7.

(14) Pauwelyn, G.; Vlerick, L.; Dockx, R.; Verhoeven, J.; Dobbeleir, A.; Bosmans, T.; Peremans, K.; Vanhove, C.; Polis, I.; De Vos, F. Kinetic Analysis of [18F]Altanserin Bolus Injection in the Canine Brain Using PET Imaging. *BMC Vet. Res.* **2019**, *15* (1), 415. https://doi.org/10.1186/s12917-019-2165-5.

(15) Blin, J.; Sette, G.; Fiorelli, M.; Bletry, O.; Elghozi, J. L.; Crouzel, C.; Baron, J. C. A Method for the In Vivo Investigation of the Serotonergic 5-HT 2 Receptors in the Human Cerebral Cortex Using Positron Emission Tomography and 18 F-Labeled Setoperone. *J. Neurochem.* **1990**, *54* (5), 1744–1754. https://doi.org/10.1111/j.1471-4159.1990.tb01229.x.

(16) Beversdorf, D. Q.; Nordgren, R. E.; Bonab, A. A.; Fischman, A. J.; Weise, S. B.; Dougherty, D. D.; Felopulos, G. J.; Zhou, F. C.; Bauman, M. L. 5-HT2 Receptor Distribution Shown by [18F]Setoperone PET in High-Functioning Autistic Adults. *J. Neuropsychiatry Clin. Neurosci.* **2012**, *24* (2), 191–197. https://doi.org/10.1176/appi.neuropsych.11080202.

(17) Meyer, J. H.; Kapur, S.; Houle, S.; DaSilva, J.; Owczarek, B.; Brown, G. M.; Wilson, A. A.; Kennedy, S. H. Prefrontal Cortex 5-HT2 Receptors in Depression: An [18F]Setoperone PET Imaging Study. *Am. J. Psychiatry* **1999**, *156* (7), 1029–1034. https://doi.org/10.1176/ajp.156.7.1029.

(18) Attar-Lévy, D.; Martinot, J.-L.; Blin, J.; Dao-Castellana, M.-H.; Crouzel, C.; Mazoyer, B.; Poirier, M.-F.; Bourdel, M.-C.; Aymard, N.; Syrota, A.; Féline, A. The Cortical Serotonin2 Receptors Studied with Positron-Emission Tomography and [18F]-Setoperone during Depressive Illness and Antidepressant Treatment with Clomipramine. *Biol. Psychiatry* **1999**, *45* (2), 180–186. https://doi.org/10.1016/S0006-3223(98)00007-9.

(19) Ito, H.; Nyberg, S.; Halldin, C.; Lundkvist, C.; Farde, L. PET Imaging of Central 5-HT2A Receptors with Carbon-11-MDL 100,907. *J. Nucl. Med.* **1998**, *39* (1), 208–214.

(20) Bhagwagar, Z.; Hinz, R.; Taylor, M.; Fancy, S.; Cowen, P.; Grasby, P. Increased 5-HT 2A Receptor Binding in Euthymic, Medication-Free Patients Recovered From Depression: A Positron Emission Study With [11 C]MDL 100,907. *Am. J. Psychiatry* **2006**, *163* (9), 1580–1587. https://doi.org/10.1176/ajp.2006.163.9.1580.

(21) Simpson, H. B.; Slifstein, M.; Bender, J.; Xu, X.; Hackett, E.; Maher, M. J.; Abi-Dargham, A. Serotonin 2A Receptors in Obsessive-Compulsive Disorder: A Positron Emission Tomography Study with [11C]MDL 100907. *Biol. Psychiatry* **2011**, *70* (9), 897–904. https://doi.org/10.1016/j.biopsych.2011.06.023.

(22) Tan, P.-Z.; Baldwin, R. .; Van Dyck, C. .; Al-Tikriti, M.; Roth, B.; Khan, N.; Charney, D. .; Innis, R. . Characterization of Radioactive Metabolites of 5-HT2A Receptor PET Ligand [18F]Altanserin in Human and Rodent. *Nucl. Med. Biol.* **1999**, *26* (6), 601–608. https://doi.org/10.1016/S0969-8051(99)00022-0.

(23) Leysen, J. E. Use of 5HT Receptor Agonists and Antagonists for the Characterization of Their Respective Receptor Sites. In *Drugs as Tools in Neurotransmitter Research*; Humana Press: New Jersey, 1989; pp 299–350. https://doi.org/10.1385/0-89603-122-5:299.

(24) Blin, J.; Pappata, S.; Kiyosawa, M.; Crouzel, C.; Baron, J. C. [18F]Setoperone: A New High-Affinity Ligand for Positron Emission Tomography Study of the Serotonin-2 Receptors in Baboon Brain in Vivo. *Eur. J. Pharmacol.* **1988**, *147* (1), 73–82. https://doi.org/10.1016/0014-2999(88)90635-8.

(25) Mertens, J.; Terriere, D.; Sipido, V.; Gommeren, W.; Janssen, P. M. F.; Leysen, J. E. Radiosynthesis of a New Radioiodinated Ligand for Serotonin-5HT2-Receptors, a Promising Tracer for γ-Emission Tomography. *J. Label. Compd. Radiopharm.* **1994**, *34* (9), 795–806. https://doi.org/10.1002/jlcr.2580340902.

(26) Terriere, D.; Janssen, P. M. F.; Gommeren, W.; Gysemans, M.; Mertens, J. J. R.; Leysen, J. E. Evaluation of Radioiodo-4-Amino-N-[1-[3-(4-Fluorophenoxy)-Propyl]-4-Methyl-4-Piperidinyl]-5-IODO-2-Methoxybenzamide as a Potential 5HT2 Receptor Tracer for SPE(C)T. *Nucl. Med. Biol.* **1995**, *22* (8), 1005–1010. https://doi.org/10.1016/0969-8051(95)02023-3.

(27) Baeken, C.; De Raedt, R.; Bossuyt, A.; Van Hove, C.; Mertens, J.; Dobbeleir, A.; Blanckaert, P.; Goethals, I. The Impact of HF-RTMS Treatment on Serotonin2A Receptors in Unipolar Melancholic Depression. *Brain Stimul.* **2011**, *4* (2), 104–111. https://doi.org/10.1016/j.brs.2010.09.002.

(28) Vermeire, S. T.; Audenaert, K. R.; Dobbeleir, A. A.; De Meester, R. H.; De Vos, F. J.; Peremans, K. Y. Evaluation of the Brain 5-HT2A Receptor Binding Index in Dogs with Anxiety Disorders, Measured with 123 I-5I-R91150 and SPECT. *J. Nucl. Med.* **2009**, *50* (2), 284–289. https://doi.org/10.2967/jnumed.108.055731.

(29) Peremans, K.; De Spiegeleer, B.; Buntinx, E.; Dobbeleir, A.; Vermeire, S.;

Vandermeulen, E.; De Vos, F.; Megens, A.; Eersels, J.; Audenaert, K. Evaluation of Serotonin-2A Receptor Occupancy with 123I-5-I-R91150 and Single-Photon Emission Tomography before and after Low-Dose Pipamperone Administration in the Canine Brain. *Nucl. Med. Commun.* **2008**, *29* (8), 724–729. https://doi.org/10.1097/MNM.0b013e3282fdc989.

(30) Audenaert, K.; Van Laere, K.; Dumont, F.; Vervaet, M.; Goethals, I.; Slegers, G.; Mertens, J.; van Heeringen, C.; Dierckx, R. A. Decreased 5-HT2a Receptor Binding in Patients with Anorexia Nervosa. *J. Nucl. Med.* **2003**, *44* (2), 163–169.

(31) Travis, M. J.; Busatto, G. F.; Pilowsky, L. S.; Mulligan, R.; Acton, P. D.; Gacinovic, S.; Mertens, J.; Terrière, D.; Costa, D. C.; Ell, P. J.; Kerwin, R. W. 5-HT2A Receptor Blockade in Patients with Schizophrenia Treated with Risperidone or Clozapine. *Br. J. Psychiatry* **1998**, *173* (3), 236–241. https://doi.org/10.1192/bjp.173.3.236.

(32) Melse, M.; Tan, S. K. H.; Temel, Y.; van Kroonenburgh, M. J. P. G.; Leentjens, A. F. G. Changes in 5-HT2A Receptor Expression in Untreated, de Novo Patients with Parkinson's Disease. *J. Parkinsons. Dis.* **2014**, *4* (2), 283–287. https://doi.org/10.3233/JPD-130300.

(33) Mühlhausen, U.; Ermert, J.; Coenen, H. H. Synthesis, Labelling and First Evaluation of [18F]R91150 as a Serotonin 5-HT2A Receptor Antagonist for PET. *J. Label. Compd. Radiopharm.* **2009**, *52* (1), 13–22. https://doi.org/10.1002/jlcr.1565.

(34) Willmann, M.; Hegger, J.; Neumaier, B.; Ermert, J. Radiosynthesis and Biological Evaluation of [18F]R91150, a Selective 5-HT2A Receptor Antagonist for PET-Imaging. *ACS Med. Chem. Lett.* **2021**, *12* (5), 738–744. https://doi.org/10.1021/acsmedchemlett.0c00658.

(35) Zischler, J.; Kolks, N.; Modemann, D.; Neumaier, B.; Zlatopolskiy, B. D. Alcohol-Enhanced Cu-Mediated Radiofluorination. *Chem. - A Eur. J.* **2017**, *23* (14), 3251–3256. https://doi.org/10.1002/chem.201604633.

(36) Bernard, A. M.; Cabiddu, M. G.; De Montis, S.; Mura, R.; Pompei, R. Synthesis of New Compounds with Promising Antiviral Properties against Group A and B Human Rhinoviruses. *Bioorg. Med. Chem.* **2014**, *22* (15), 4061–4066. https://doi.org/10.1016/j.bmc.2014.05.066.

(37) Hudkins, R. L.; Knutsen, L. J. S.; P., P. C.; SUndar, B. G.; Wells-Knecht, K. J. Substituted Pyridazine Derivatives Which Have Histamine H3 Antagonist Activity. WO 2009/097306 A1, 2009. https://lens.org/106-000-855-446-766.

(38) Renk, D. R.; Skraban, M.; Bier, D.; Schulze, A.; Wabbals, E.; Wedekind, F.; Neumaier,

F.; Neumaier, B.; Holschbach, M. Design, Synthesis and Biological Evaluation of Tozadenant Analogues as Adenosine A2A Receptor Ligands. *Eur. J. Med. Chem.* **2021**, 113214. https://doi.org/10.1016/j.ejmech.2021.113214.

(39) Fiorica-Howells, E.; Hen, R.; Gingrich, J.; Li, Z.; Gershon, M. D. 5-HT2A Receptors: Location and Functional Analysis in Intestines of Wild-Type and 5-HT2A Knockout Mice. *Am. J. Physiol. Liver Physiol.* **2002**, *282* (5), G877–G893. https://doi.org/10.1152/ajpgi.00435.2001.

(40) Li, X.; Guo, K.; Li, T.; Ma, S.; An, S.; Wang, S.; Di, J.; He, S.; Fu, J. 5-HT2 Receptor Mediates High-Fat Diet-Induced Hepatic Steatosis and Very Low Density Lipoprotein Overproduction in Rats. *Obes. Res. Clin. Pract.* **2018**, *12* (1), 16–28. https://doi.org/10.1016/j.orcp.2016.03.015.

(41) Weber, E. T.; Andrade, R. Htr2a Gene and 5-HT2A Receptor Expression in the Cerebral Cortex Studied Using Genetically Modified Mice. *Front. Neurosci.* **2010**. https://doi.org/10.3389/fnins.2010.00036.

(42) Pompeiano, M.; Palacios, J. M.; Mengod, G. Distribution of the Serotonin 5-HT2 Receptor Family MRNAs: Comparison between 5-HT2A and 5-HT2C Receptors. *Mol. Brain Res.* **1994**, *23* (1–2), 163–178. https://doi.org/10.1016/0169-328X(94)90223-2.

(43) López-Giménez, J. F.; Mengod, G.; Palacios, J. M.; Vilaró, M. T. Selective Visualization of Rat Brain 5-HT2A Receptors by Autoradiography with [3H]MDL 100,907. *Naunyn. Schmiedebergs. Arch. Pharmacol.* **1997**, *356* (4), 446–454. https://doi.org/10.1007/PL00005075.

(44) Abramowski, D.; Rigo, M.; Duc, D.; Hoyer, D.; Staufenbiel, M. Localization of the 5-Hydroxytryptamine2C Receptor Protein in Human and Rat Brain Using Specific Antisera. *Neuropharmacology* **1995**, *34* (12), 1635–1645. https://doi.org/10.1016/0028-3908(95)00138-7.

(45) Leysen, J. M. F.; Van Daele, G. H. P. 4-Amino-N-(4-Methyl-4-Piperidinyl)-2-Methoxybenzamides. WO 9402462, 1994.

(46) Finnema, S. J.; Stepanov, V.; Ettrup, A.; Nakao, R.; Amini, N.; Svedberg, M.; Lehmann, C.; Hansen, M.; Knudsen, G. M.; Halldin, C. Characterization of [11C]Cimbi-36 as an Agonist PET Radioligand for the 5-HT2A and 5-HT2C Receptors in the Nonhuman Primate Brain. *Neuroimage* **2014**, *84*, 342–353. https://doi.org/10.1016/j.neuroimage.2013.08.035.

(47) Herndon, J. L.; Ismaiel, A.; Ingher, S. P.; Teitler, M.; Glennon, R. A. Ketanserin Analogs: Structure-Affinity Relationships for 5-HT2 and 5-HT1C Serotonin Receptor

Binding. *J. Med. Chem.* **1992**, *35* (26), 4903–4910. https://doi.org/10.1021/jm00104a017.

(48) Titeler, M.; Lyon, R. A.; Davis, K. H.; Glennon, R. A. Selectivity of Serotonergic Drugs for Multiple Brain Serotonin Receptors. *Biochem. Pharmacol.* **1987**, *36* (19), 3265–3271. https://doi.org/10.1016/0006-2952(87)90643-5.

(49) Knight, A.; Misra, A.; Quirk, K.; Benwell, K.; Revell, D.; Kennett, G.; Bickerdike, M. Pharmacological Characterisation of the Agonist Radioligand Binding Site of 5-HT2A, 5-HT2B and 5-HT2C Receptors. *Naunyn. Schmiedebergs. Arch. Pharmacol.* **2004**, *370* (2). https://doi.org/10.1007/s00210-004-0951-4.

(50) López-Giménez, J. F.; Tecott, L. H.; Palacios, J. M.; Mengod, G.; Vilaró, M. T. Serotonin 2C Receptor Knockout Mice: Autoradiographic Analysis of Multiple Serotonin Receptors. *J. Neurosci. Res.* **2002**, *67* (1), 69–85. https://doi.org/10.1002/jnr.10072.

(51) Kroll, T.; Elmenhorst, D.; Matusch, A.; Wedekind, F.; Weisshaupt, A.; Beer, S.; Bauer, A. Suitability of [18F]Altanserin and PET to Determine 5-HT2A Receptor Availability in the Rat Brain: In Vivo and In Vitro Validation of Invasive and Non-Invasive Kinetic Models. *Mol. Imaging Biol.* **2013**, *15* (4), 456–467. https://doi.org/10.1007/s11307-013-0621-3.

(52) Riss, P. J.; Hong, Y. T.; Williamson, D.; Caprioli, D.; Sitnikov, S.; Ferrari, V.; Sawiak, S. J.; Baron, J.-C.; Dalley, J. W.; Fryer, T. D.; Aigbirhio, F. I. Validation and Quantification of [18F]Altanserin Binding in the Rat Brain Using Blood Input and Reference Tissue Modeling. *J. Cereb. Blood Flow Metab.* **2011**, *31* (12), 2334–2342. https://doi.org/10.1038/jcbfm.2011.94.

(53) Marazziti, D.; Rossi, A.; Palego, L.; Giannaccini, G.; Naccarato, A.; Lucacchini, A.; Cassano, G. B. [3H]Ketanserin Binding in Human Brain Postmortem. *Neurochem. Res.* **1997**, *22* (6), 753–757. https://doi.org/10.1023/a:1027366413289.

(54) Marazziti, D.; Rossi, A.; Giannaccini, G.; Zavaglia, K. M.; Dell'Osso, L.; Lucacchini, A.; Cassano, G. B. Distribution and Characterization of [3H]Mesulergine Binding in Human Brain Postmortem. *Eur. Neuropsychopharmacol.* **1999**, *10* (1), 21–26. https://doi.org/10.1016/S0924-977X(99)00045-0.

(55) Kubota, H.; Kakefuda, A.; Watanabe, T.; Ishii, N.; Wada, K.; Masuda, N.; Sakamoto, S.; Tsukamoto, S. Synthesis and Pharmacological Evaluation of 1-Oxo-2-(3-Piperidyl)-1,2,3,4- Tetrahydroisoquinolines and Related Analogues as a New Class of Specific Bradycardic Agents Possessing I f Channel Inhibitory Activity. *J. Med. Chem.* **2003**, *46* (22), 4728–4740. https://doi.org/10.1021/jm0301742.

(56) Adler, M. J.; Hamilton, A. D. Oligophenylenaminones as Scaffolds for α-Helix Mimicry. *J. Org. Chem.* **2011**, *76* (17), 7040–7047. https://doi.org/10.1021/jo200917d.

(57) Su, Y.; Wang, J.; Bao, R. Inhibitor Containing Bicyclic Derivative, Preparation Method Therefor and Use Thereof. EP 3971187 A1, 2020. https://lens.org/109-145-360-365-653.

(58) Humpert, S.; Hoffmann, C.; Neumaier, F.; Zlatopolskiy, B. D.; Neumaier, B. Validation of Analytical HPLC with Post-Column Injection as a Method for Rapid and Precise Quantification of Radiochemical Yields. *J. Chromatogr. B* **2023**, 123847. https://doi.org/10.1016/j.jchromb.2023.123847.

Graphical Abstract

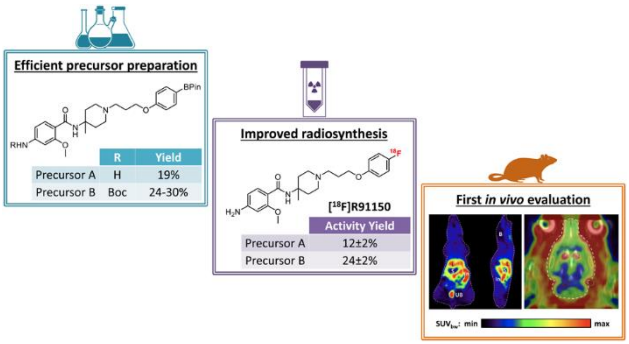

3.2 Nicht publizierte wissenschaftliche Ergebnisse

3.2.1 Herstellung von 6-[^{18}F]Fluor-4-((*S*)-[2-(2-cyano-4,4-difluoropyrrolidin-1-yl)-2-oxoethyl])carbonsäureamid (6-[^{18}F]F-FAPI)

Das Fibroblasten-Aktivierungs-Protein (FAP) gehört zur Familie der membrangebunden Typ II Glykoproteine und wirkt als Prolin-selektive Serinprotease.[157] FAP ist in gesunden Geweben kaum exprimiert oder nicht nachweisbar, wird jedoch stark durch die krebsassoziierten Fibroblasten (engl. „*cancer-assoziated fibroblast*“ – CAF) in soliden Tumoren exprimiert.[157,158] Entsprechend stellt es ein vielversprechendes biologisches Target für die PET-Bildgebung mit radiomarkierten FAP Inhibitoren (FAPI) dar. Die ersten entwickelten FAPI-Radiotracer, auf Basis einer Chinolin-Leitsturktur, wie [^{68}Ga]FAPI-02[159], [^{68}Ga]FAPI-04[160] und [^{68}Ga]FAPI-46[161] zeigten zwar eine geringe Aufnahme in gesunden Geweben und eine schnelle Internalisierung, lieferten jedoch aufgrund der hohen β^+-Energie von ^{68}Ga keine optimalen PET-Bilder. Mit [^{18}F]AlF-markierte Radiotracer wie [^{18}F]AlF-FAPI-42[162] wiesen ähnliche oder sogar bessere Eigenschaften als die entsprechenden ^{68}Ga-markierten Tracer auf.

Die ersten ^{18}F-Direktmarkierungen des Chinolingerüstes zur Herstellung von 6-[^{18}F]F-FAPI wurden von Zhang und Yu et al. über $B(OH)_2$ und $SnMe_3$-Vorläufer mittels des von Tredwell und Makaravage beschriebenen CVRF-Protokolls durchgeführt. Dabei betrugen die erhaltenen Ausbeuten 43%[163] und 16%[164].

Zur weiteren Steigerung der RCA über $SnMe_3$-Vorläufer wurde der „*NextGen*“ Cu-Komplex $Cu(4\text{-}PhPy)_4(ClO_4)_2$ für die CVRF unter optimierten Bedingungen verwendet.

Die Verbindungen (*S*)-*tert*-Butyl-2-(2-carbamoyl-4,4-difluorpyrrolidin-1-yl)-2-oxo-ethylcarbamate (**1**), 6-Bromchinolin-4-carbonsäure-2,3,5,6-tetrafluorophenolester (**2**) und 6-Fluor-chinolin-4-carbonsäure-(*S*)-[2-(2-cyano-4,4-difluor-pyrrolidin-1-yl-2-oxo-ethyl]-amid (6-F-FAPI) wurden freundlicherweise von Herr Dr. Victor Bahutski zur Verfügung gestellt.

Vorläufersynthese

Der Molekülbaustein (*S*)-*tert*-Butyl-2-(2-cyano-4,4-difluorpyrrolidin-1-yl)-2-oxoethyl-carbamat (**3**) wurde durch Verwendung von **1** in Anlehnung an die Vorschrift in Jansen et al.[165] mit einer Ausbeute von 76% hergestellt.

Der Stannylvorläufer 6-(Trimethylstannyl)-chinolin-4-carbonsäure-(*S*)-[2-(2-cyano-4,4-difluor-pyrrolidin-1-yl-2-oxoethyl]-amid (**4**) für die Herstellung von 6-[^{18}F]F-FAPI mittels CVRF wurde wie folgt synthetisiert (**Schema 25**).

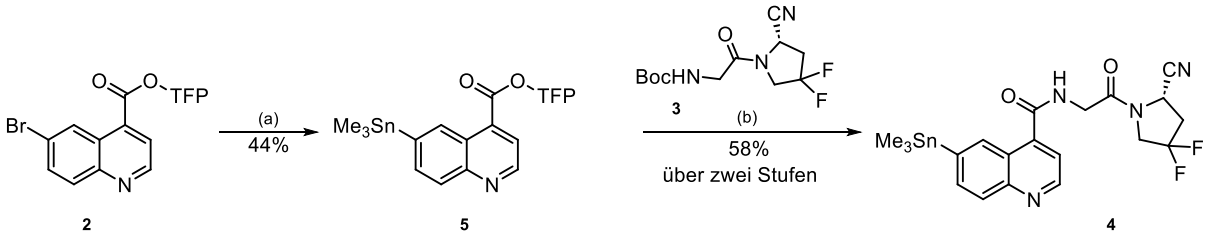

Schema 25: Synthese von Trimethylstannyl-Vorläufer **4** für die Herstellung von 6-[^{18}F]F-FAPI mittels Cu-vermittelter Radiofluorierung . Reaktionsbedingungen: (a) $Pd(Ph_3P)_4$, LiCl, Toluol, 120 °C, 2,5 h. (b) i. TFA, CH_2Cl_2, RT, 1 h ii. NEt_3, CH_2Cl_2, RT, 3,5 h. Abkürzungen: TFP – 2,3,5,6-Tetrafluorophenol; TFA – Trifluoracetat.

Der Aktivester **2** wurde über eine Miyaura-Stannylierung mit Hexamethylditin zu 6-(Trimethylstannyl)-chinolin-4-carbonsäure-2,3,5,6-tetrafluorphenylester (**5**) überführt. Daraufhin wurde die Boc-Schutzgruppe von **3** mit 20% TFA in CH_2Cl_2 entfernt und das resultierende Trifluoracetat-Salz mit **5** in Anwesenheit der Base Et_3N in ein Amid überführt. Der erhaltene $SnMe_3$-Vorläufer **4** wurde in einer Gesamtausbeute von 32% über drei Stufen erhalten.

Nach der Synthese vom Aktivester **5** zeigte das ^{19}F-NMR-Spektrum zwei zusätzliche Signale nach der Isolierung über Säulechromatographie. Diese Verunreinigungen können auf 2,3,5,6-Tetrafluorphenol aus einer vorherigen Reaktion zu Verbindung **2** zurückzuführen sein, die nicht vom Produkt getrennt werden konnte. Für die darauffolgende Reaktion zum Amid **4** störte diese Verunreinigung nicht und konnte bei der letzten Isolierung getrennt werden.

Radiosynthese zu 6-[^{18}]F-FAPI

Der Radiotracer 6-[^{18}F]F-FAPI wurde aus dem Me_3Sn-Vorläufer **4** unter Verwendung von $Cu(4\text{-}PhPy)_4(ClO_4)_2$ unter den für Stannan-Vorläufer optimierten Bedingungen hergestellt (**Schema 26**).

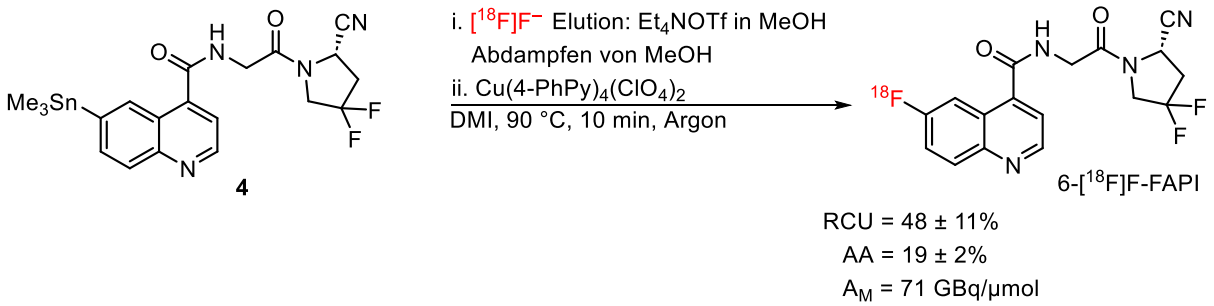

Schema 26: Radiosynthese zu 6-[^{18}F]F-FAPI ausgehend von $SnMe_3$-Vorläufer **4** mit $Cu(4\text{-}PhPy)_4(ClO_4)_2$ unter optimierten Bedingungen für die Cu-vermittelte Radiofluorierung von $SnMe_3$-Vorläufern.

Wässriges [^{18}F]F$^-$ wurde auf einer Anionenaustauscherharz-Kartusche fixiert und anschließend das Restwasser durch Spülen mit trockenem MeOH entfernt. Die Kartusche wurde mit Luft getrocknet und das [^{18}F]F$^-$ mit einer Lösung von Tetraethylammoniumtriflat (Et_4NOTf) in trockenem MeOH eluiert. Nach Entfernen des MeOH wurde der Reaktor mit Argon geflutet und eine Lösung von Vorläufer **4** und $Cu(4\text{-}PhPy)_4(ClO_4)_2$ (jeweils 10 µmol) in trockenem DMI (800 µL) unter Argon hinzugefügt. Die Reaktionslösung wurde bei 90 °C für 10 min erhitzt, wodurch 6-[^{18}F]F-FAPI mit guten RCUs von 48 ± 11% (n = 6) erhalten wurde.

Vor der Isolierung mittels semipräparativer HPLC musste das Reaktionslösungsmittel über eine Festphasenextraktion (engl. "*solid phase extraction*", SPE) vom 6-[^{18}F]F-F-FAPI abgetrennt werden. Nach Verdünnen der Reaktionslösung mit Wasser auf insgesamt 5-10% organischen Anteil konnte das rohe Radioprodukt vollständig auf einer StrataX-Kartusche mit C18-Sorbensmaterial (60 mg) fixiert werden. Bei Verwendung einer StrataX-Kartusche mit 30 mg Sorbensmaterial konnte über analytische HPLC noch 6-[^{18}F]F-FAPI im Durchlauf gefunden werden. Die darauffolgende Elution von der Kartusche erfolgte mit nur 500 µL MeCN und mit einer sehr guten Elutionseffizienz von 95%. Nach Verdünnen mit Wasser (1 mL) war die Lösung injektionsfertig für die Isolierung über semipräparative HPLC (**Abbildung 18**).

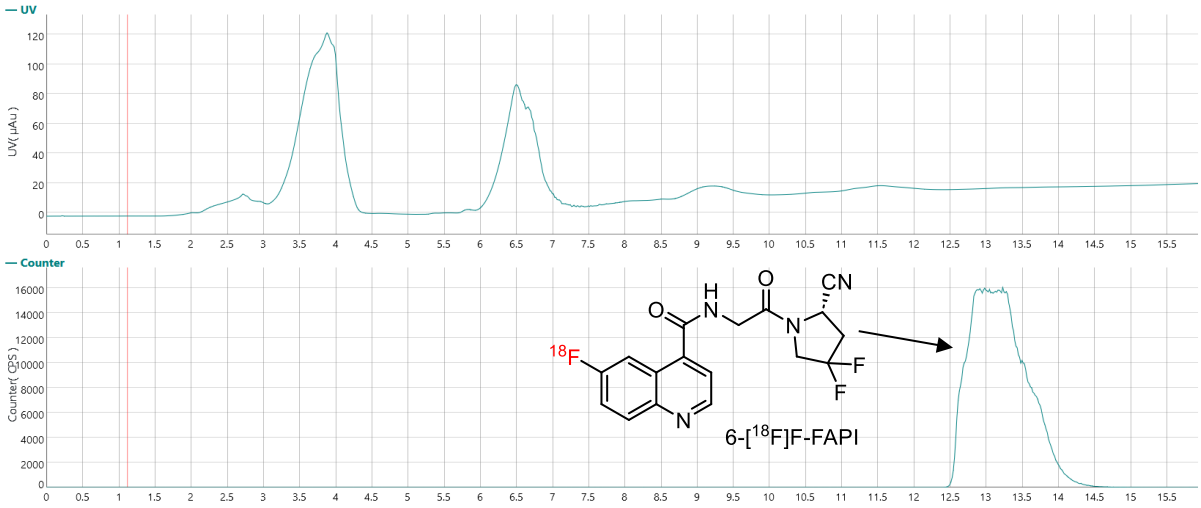

Abbildung 18: Isolierung von 6-[^{18}F]F-FAPI über semipräparative HPLC (oben: UV-Kanal, λ=254 nm; unten: Radiokanal).

Die Formulierung wurde ebenfalls unter Verwendung einer StrataX-Kartusche (60 mg Sorbensmaterial) durchgeführt, um ein vollständiges Beladen des Radiotracers zu gewährleisten. Die aufgefangene HPLC-Fraktion wurde mit Wasser (20 mL) verdünnt und die Kartusche mit dem aufgereinigten 6-[^{18}F]F-FAPI beladen. Nach zusätzlichem Waschen mit Wasser (5 mL) erfolgte die Elution mit EtOH mit einer guten Elutionseffizienz von 90%. Das EtOH wurde bei 40–50 °C entfernt und 6-[^{18}F]F-FAPI in 1% Tween80 aufgenommen. 6-[^{18}F]F-FAPI wurde nach dem Formulierungsschritt in einer Aktivitätsausbeute (AA) von 19 ± 2% (n = 6) als injektionsfertige Lösung erhalten. Die Ergebnisse der Qualitätskontrolle von 6-[^{18}F]F-FAPI zeigten, dass im Radioprodukt keine signifikanten Mengen an chemischen Verunreinigungen enthalten waren (**Abbildung 19**).

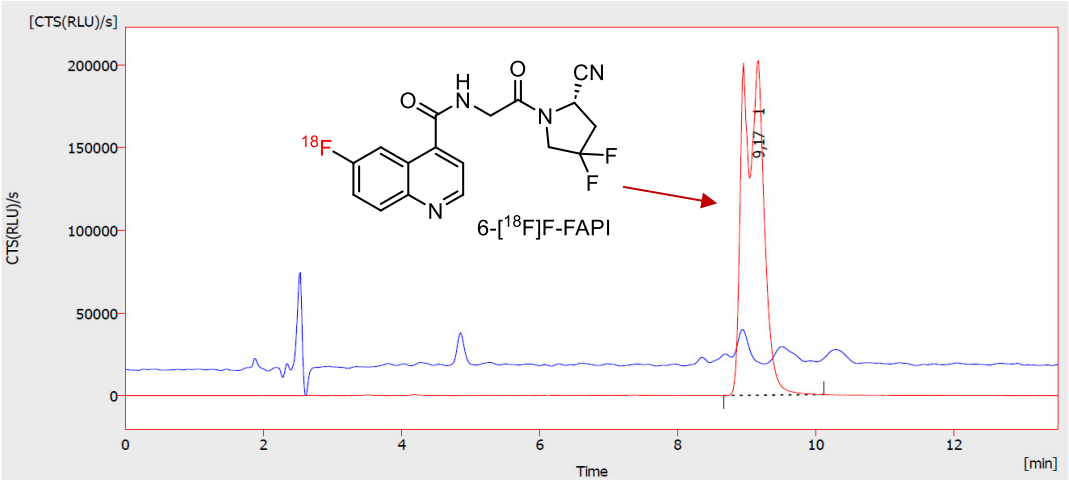

Result Table (Uncal - Data|alc-enhanced_323_28_10_2021_[4 DMI]_[18F]FAPI_liefersynthese_molar_activity - HERM)

	Reten. Time [min]	Area [CTS(RLU)/s.s]	Height [CTS(RLU)/s]	Area [%]
1	9,167	4229131,500	202295,069	100,0
	Total	4229131,500	202295,069	100,0

Abbildung 19: HPLC-Chromatogramm von isoliertem 6-[^{18}F]F-FAPI zur Qualitätskontrolle der chemischen Reinheit und Bestimmung der A_M (blau: UV-Kanal, λ=254 nm; rot: Radiokanal).

Zusätzlich konnte eine radiochemische Reinheit von >99% erhalten werden und mittels Koinjektion der nicht-radioaktiven Referenzverbindung 6-F-FAPI der Radiotracer identifiziert werden (**Abbildung 20** & **Abbildung *21***). Die A_M in einem Radiotracer-Batch (1,1 GBq) betrug 71 GBq/µmol (Startaktiviät: 5,8 GBq).

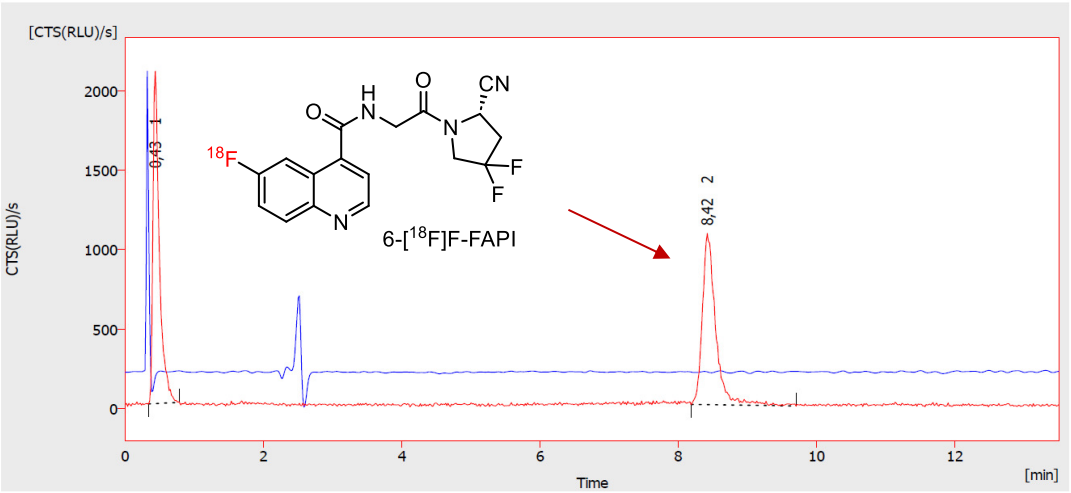

Result Table (Uncal - Data|alc-enhanced_324_28_10_2021_[4 DMI]_[18F]FAPI_liefersynthese_radio_purity - HERM)

	Reten. Time [min]	Area [CTS(RLU)/s.s]	Height [CTS(RLU)/s]	Area [%]
1	0,433	13557,000	2093,778	48,3
2	8,417	14515,500	1078,385	51,7
	Total	28072,500	3172,162	100,0

Abbildung 20: HPLC-Chromatogramm von isoliertem 6-[^{18}F]F-FAPI zur Qualitätskontrolle der radiochemischen Reinheit (blau: UV-Kanal, λ=254 nm; rot: Radiokanal).

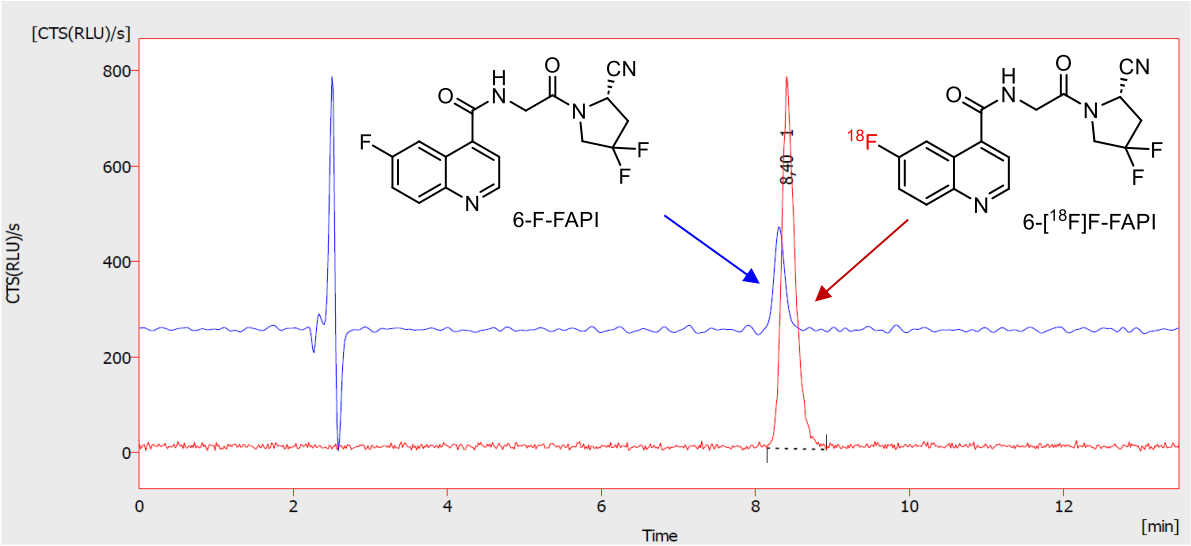

Result Table (Uncal - Data\alc-enhanced_325_28_10_2021_[4 DMI]_[18F]FAPI_liefersynthese_spiked - HERM)

	Reten. Time [min]	Area [CTS(RLU)/s.s]	Height [CTS(RLU)/s]	Area [%]
1	8,400	9540,000	779,978	100,0
	Total	9540,000	779,978	100,0

Abbildung 21: HPLC-Chromatogramm von isoliertem 6-[^{18}F]F-FAPI mit Koinjektion der nicht-radioaktiven Referenzverbindung 6-F-FAPI (blau: UV-Kanal, λ=254 nm; rot: Radiokanal).

Mit einer Gesamtsynthesezeit von ca. 70 min konnte der Radiotracer 6-[^{18}F]F-FAPI erfolgreich unter Verwendung des „*NextGen*“ Cu-Komplexes $Cu(4\text{-}PhPy)_4(ClO_4)_2$ hergestellt werden. Obwohl die AA von 19% nur geringfügig höher lag als die angegebene Ausbeute von Yu et al., wurden für die Radiotracer-Herstellung keine weiteren Optimierungen durchgeführt. Eine 1:1 Übertragung der Reaktionsbedingungen für das modifizierte Protokoll zur CVRF von Me_3Sn-Vorläufern reichte aus, um gute RCUs bzw. ausreichende AAs zu erhalten und den FAP-Radioligand präklinisch zu evaluieren.

Präklinische Evaluation

Der Radiotracer-Kandidat 6-[^{18}F]F-FAPI wurde nach erfolgreicher Radiosynthese von Prof. Dr. Heike Endepols, Lukas Vieth und Otari Gokhadze in verschiedenen Modellen über µPET-Messungen präklinisch evaluiert. Außerdem wurden in dieser Studie die Radiotracer [^{18}F]AlF-FAPI-42 und der in der Klinik etablierte PET-Tacer [^{18}F]FET als Referenz mit aufgenommen, um die Qualität von 6-[^{18}F]F-FAPI beurteilen zu können.

Das subkutane Xenograft-Modell wurde mit HT1080-Zellen in CB17-SCID Mäusen durchgeführt. Die transfizierten Zellen HT1080-FAP besaßen eine Überexpression von FAP an der Zelloberfläche und galten als Positivkontrolle (FAP^+) wohingegen der Wildtyp HT1080-WT die Negativkontrolle (FAP^-) darstellte. Bei den µPET-Messungen zeigte sich für 6-[^{18}F]F-FAPI im Vergleich zum Referenztracer [^{18}F]AlF-FAPI-42 eine höhere Anreicherung in FAP^+-Tumoren und eine geringe Auswaschung nach 120 min (**Abbildung 22**).

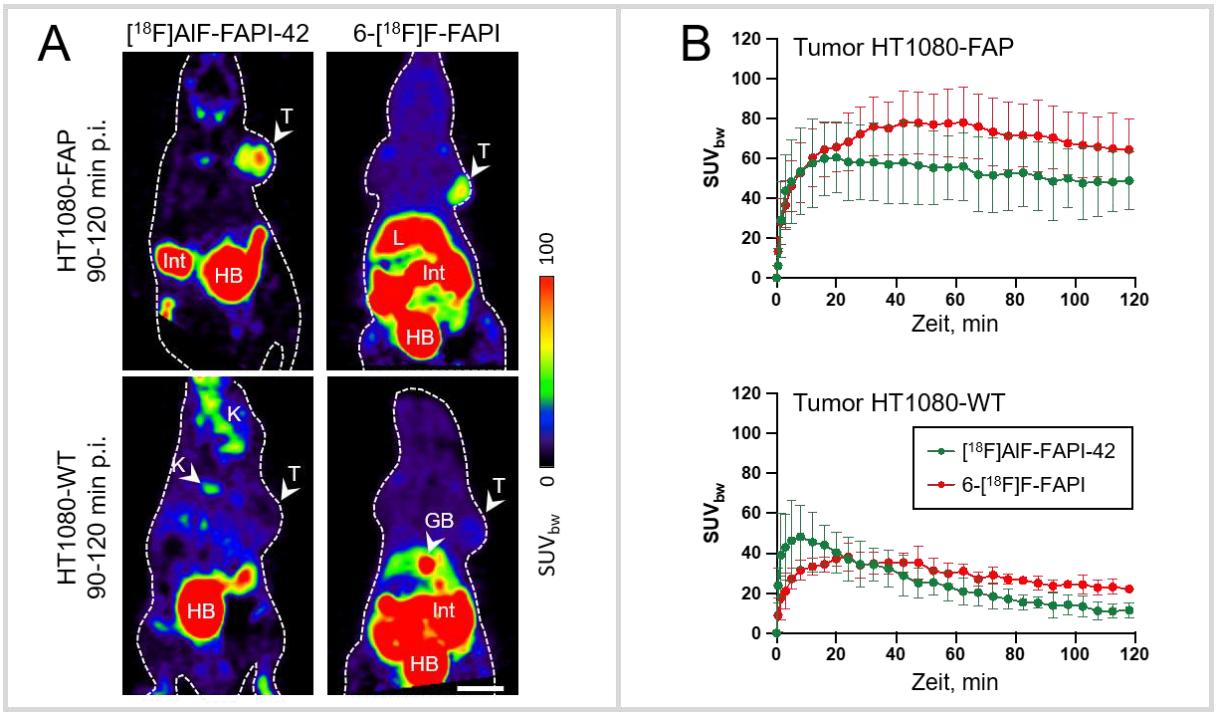

Abbildung 22: Vergleich der FAP-Radioliganden [^{18}F]AlF-FAPI-42 und 6-[^{18}F]F-FAPI im subkutanen Xengraft Mausmodel mit FAP-positiven (HT1080-FAP) und FAP-negativen (HT1080-WT) HT1080-Tumorzellen. (A) Repräsentative summierte PET-Bilder (horizontal) von Mäusen mit HT1080-FAP (obere Reihe) oder HT1080-WT (untere Reihe) Tumoren 90–120 min nach Tracerinjektion. (B) Zeit-Aktivitäts-Kurven (Mittelwert ± Standardabweichung) von beiden Radiotracern in HT1080-FAP (obere Reihe) und HT1080-WT (untere Reihe) Tumoren. Abkürzungen: GB – Gallenblase, HB – Harnblase, Int – Intestinaltrakt, K – Knochen, L – Leber, T – Tumor.

In FAP^--Tumoren wurde im Vergleich zu den FAP-exprimierenden Tumoren eine deutlich geringere Anreicherung beobachtet. Die PET-Bilder zeigten außerdem eine hohe Anreichung von 6-[^{18}F]F-FAPI in Leber bzw. Blase, was für eine hepatobiläre und renale Ausscheidung spricht, aber auch in der Gallenblase und Intestinaltrakt. Die schnelle und hohe Tumoranreicherung von 6-[^{18}F]F-FAPI konnte auch in einem subkutanen Allograft-Modell mit FAP-positiven CAFs der Pankreastumor-Zellline DSL-6A/C1 in Ratten beobachtet werden (**Abbildung 23**).

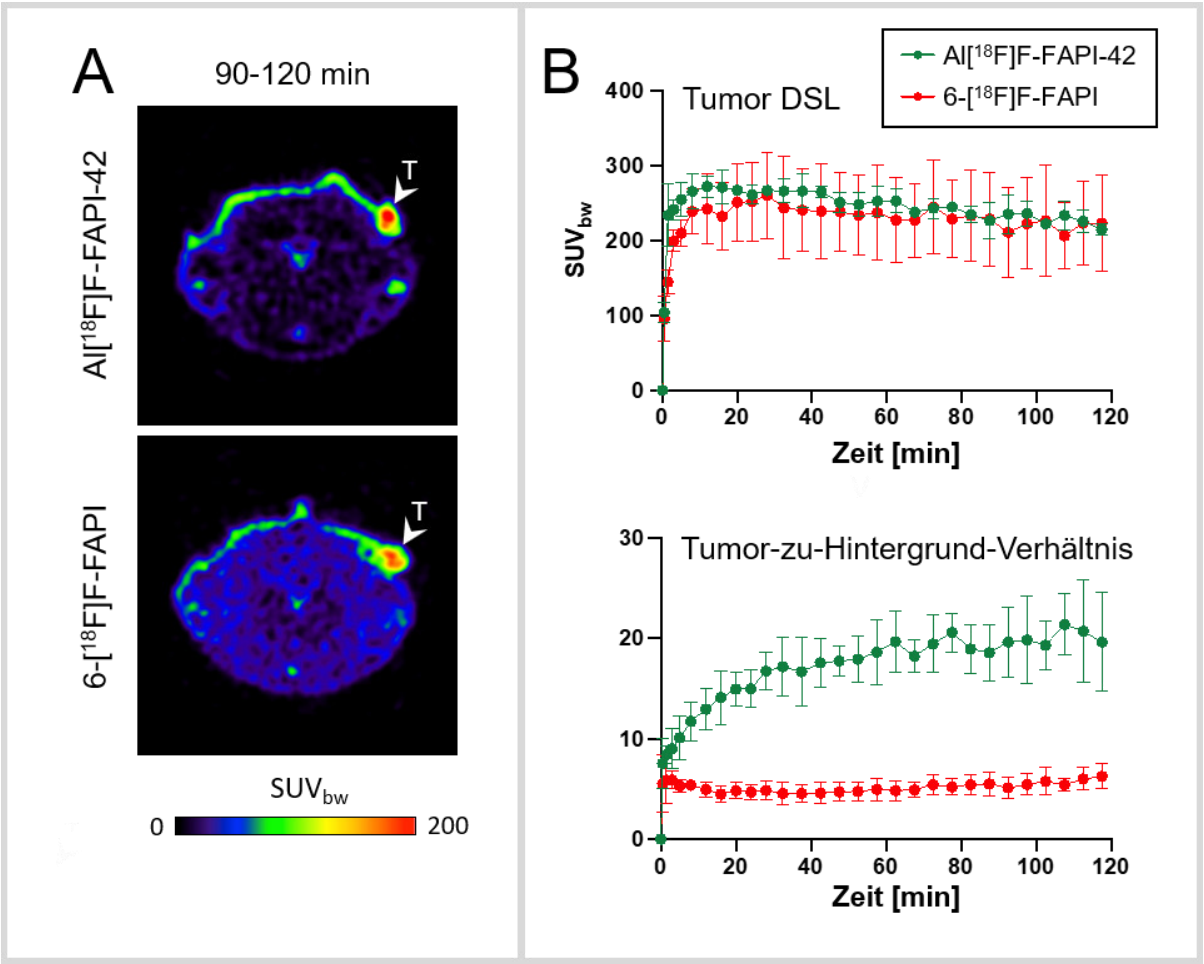

Abbildung 23: Vergleich der FAP-Radioliganden [^{18}F]AlF-FAPI-42 und 6-[^{18}F]F-FAPI im subkutanen Allograft DSL-6A/C1 Pankreastumormodell in Ratten. (A) Repräsentative summierte PET-Bilder (transversal) von implantierten Pankreastumorzellen in derselben Ratte 90–120 min nach Tracerinjektion. (B) Zeit-Aktivitäts-Kurven (Mittelwert ± Standardabweichung) der beiden Radiotracern für die Tumoranreicherung (obere Reihe) und Tumor-zu-Hintergrund-Verhältnis (untere Reihe). Abkürzungen: T – Tumor.

Der Vergleich von 6-[^{18}F]F-FAPI und [^{18}F]AlF-FAPI-42 in diesem Modell ergab keinen Unterschied in der Turmoranreicherung und Auswaschung nach 120 min. Allerdings wies 6-[^{18}F]F-FAPI aufgrund einer langsameren Auswaschung aus gesunden Geweben eine geringeres Tumor-zu-Hintergrund-Verhältnis (THV) als [^{18}F]AlF-FAPI-42 auf.

Zuletzt wurde 6-[^{18}F]F-FAPI in einem orthotopen U87 Gliom Xenograft-Modell in Ratten mit [^{18}F]AlF-FAPI-42 und [^{18}F]FET als Referenztracer evaluiert sowie Blockierungs- und Verdrängungsstudien mit dem FAP-selektiven Liganden UAMC1110 durchgeführt (**Abbildung *24***). Die resultierenden µPET-Bilder zeigten eine Tumoranreichungen von allen drei Radiotracern. Die Anreicherung von 6-[^{18}F]F-

FAPI im Gliom war zwar deutlich niedriger als die des klinisch etablierten Referenztracers [^{18}F]FET, dafür wurde aufgrund einer geringeren Aufnahme durch gesundes Hirngewebe mit 6-[^{18}F]F-FAPI ein deutlich besseres THV erreicht. Zudem ließ sich mit 6-[^{18}F]F-FAPI der Tumor besser von gesundem Hirngewebe abgrenzen als mit [^{18}F]FET, da der Referenztracer ein sehr viel diffuseres Verteilungsmuster aufwies. Außerdem zeigte die Anreicherung im Tumor und die THV in diesem Modell, dass es keinen signifikanten Unterschied zwischen 6-[^{18}F]F-FAPI und [^{18}F]AlF-FAPI-42 gab, obwohl in der Zeit-Akvititäts-Kurve eine höhere Tumoranreicherung von 6-[^{18}F]F-FAPI darstellte.

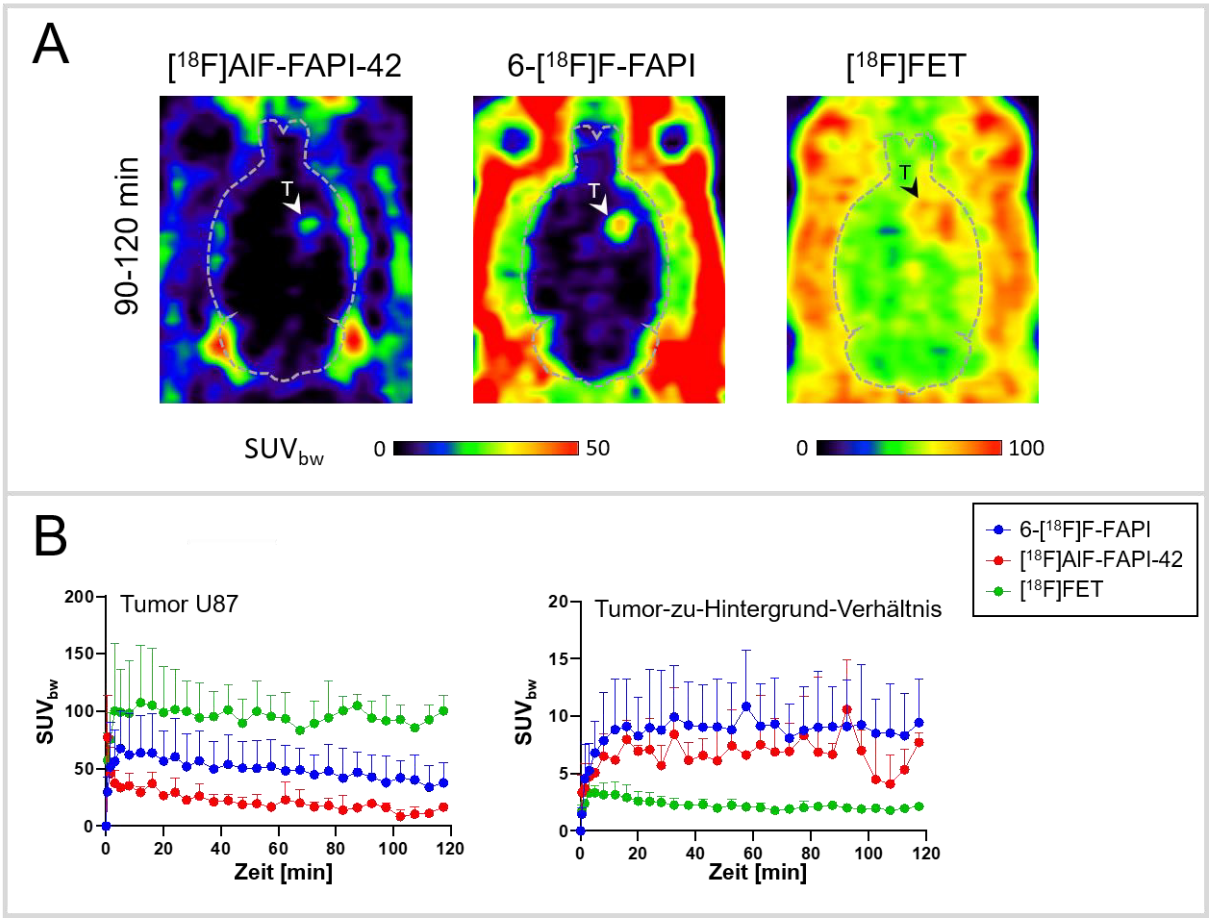

Abbildung 24: Vergleich der FAP-Radioliganden [^{18}F]AlF-FAPI-42, 6-[^{18}F]F-FAPI und [^{18}F]FET im orthotopen U87 Gliommodell in Ratte. (A) Repräsentative summierte PET-Bilder (horizontal) von implantierten Gliomtumorzellen in derselben Ratte bei 90–120 min nach Tracerinjektion. (B) Zeit-Aktivitäts-Kurven (Mittelwert ± Standardabweichung) der Radiotracer für die Tumoranreicherung (obere Reihe) und Tumor-zu-Hintergrund-Verhältnis (untere Reihe). Abkürzungen: T – Tumor.

Schließlich konnte im Rahmen von Blockierungs- und Verdrängungsversuchen gezeigt werden, das die Tumoraufnahme von 6-[^{18}F]F-FAPI durch den FAP-selektiven Liganden UAMC1110 um 70% (bei Koinjektion mit UAMC1110) bzw. bis zu 68% (bei UAMC1110-Injektion 60 min nach Radiotracerinjektion) reduziert werden konnte (**Abbildung 25**).

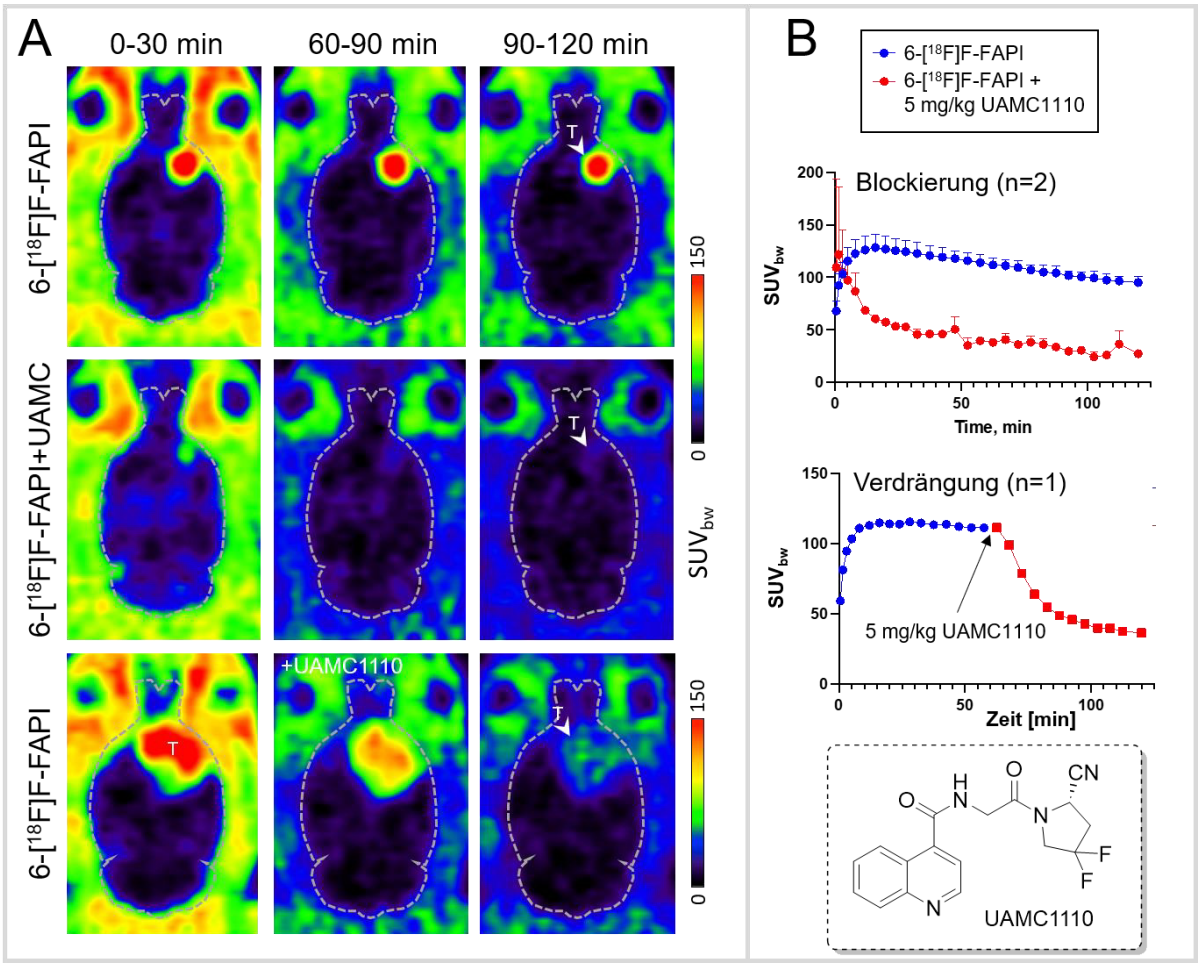

Abbildung 25: Blockierungs- und Verdrängungsstudien von 6-[^{18}F]F-FAPI im orthotopen U87 Gliommodel in der Ratte. (A) Repräsentatives summierte PET-Bilder (horizontal) von implantierten Gliomtumorzellen in derselben Ratte von Blockierungs- und Verdrängungsstudien mit UAMC1110 (5 mg/Kg): ohne (obere Reihe), mit Koinjektion (mittlere Reihe) und Injektion nach 60 min Tracerinjektion (untere Reihe). (B) Zeit-Aktivitäts-Kurven (Mittelwert ± Standardabweichung) der Radiotracer für die Blockierung (obere Reihe) und Verdrängung mit UAMC1110 (untere Reihe). Abkürzungen: T – Tumor.

3.2.2 Herstellung von (*S*)-5-[^{18}F]Fluor-*m*-Tyrosin [(*S*)-5-[^{18}F]FMT]

Parkinson ist eine neurodegenerative Erkrankung, die durch eine Dysfunktion in der dopaminergen Neurotransmission der Basalganglien entsteht.[166] Bei einem stetigen Verlust von Nervenzellen im Gehirn führt dies zu einem Dopaminmangel, was wiederum Bewegungsstörungen, Tremor und weitere Symptome verursacht. Obwohl der Dopaminmangel durch die Verabreichung des Dopamin-Vorläufers L-DOPA teilweise kompensiert werden kann, lindert dieser lediglich die Symptomatik und verhindert nicht das Fortschreiten der Erkrankung. Daher ist die Früherkennung über Diagnoseverfahren wie die PET-Bildgebung mit dem PET-Tracer 6-[^{18}F]FDOPA zur Darstellung der präsynaptischen dopaminergen Funktion von großer Bedeutung.

Jedoch unterliegt 6-[^{18}F]FDOPA, genau wie die L-DOPA, einer starken peripheren Metabolisierung durch die Enzyme aromatische Aminosäuren Decarboxylase (AADC) und Catchol-*O*-methyltransferase (COMT).[167,168] Die bei der Verstoffwechslung durch COMT entstehenden Radiometaboliten überwinden zudem die Blut-Hirn-Schranke und tragen zum Hintergrundsignal im Gehirn bei, was zu schlechteren PET-Bildern führt. Daher besteht ein Bedarf nach alternativen *m*-Tyrosin-Analoga wie 6-[^{18}F]FMT und 5-[^{18}F]FMT, um die periphere Metabolisierung zu reduzieren. Da diese Radiotracer-Kandidaten keine Catechol-Struktur besitzen, werden sie anders als L-DOPA nicht durch COMT verstoffwechselt.

Bisher wurde die Herstellung und präklinische Evaluation von 6-[^{18}F]FMT in der Literatur beschrieben,[167,169] jedoch fehlt bis heute eine beschriebene Radiosynthese und biologische Evaluation von 5-[^{18}F]FMT. Um diese Lücke zu schließen, wurde das modifizierte Protokoll für die CVRF zur Herstellung von (*S*)-5-[^{18}F]FMT verwendet.

Der geschützte BPin-Vorläufer **6** wurde freundlicherweise von Herr Prof. Dr. Boris Zlatopolskiy zur Verfügung gestellt und unter Verwendung des „*NextGen*“ Cu-Komplex Cu(4-PhPy)$_4$(ClO$_4$)$_2$ mittels „Alkohol-verstärkter“ CVRF ^{18}F-markiert (**Schema 27**).

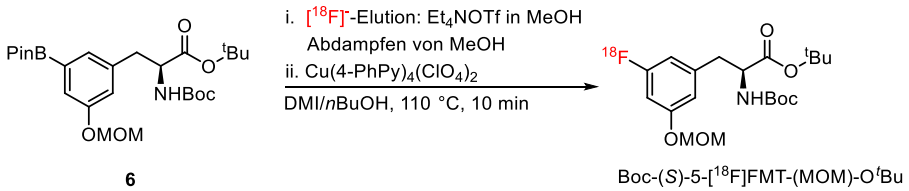

Schema 27: Radiosynthese von Boc-(*S*)-5-[^{18}F]FMT-(MOM)-O^{t}Bu über die „Alkohol-verstärkte“ CVRF des geschützten BPin-Vorläufers **6** mit Cu(4-PhPy)$_4$(ClO$_4$)$_2$ in DMI/*n*BuOH.

Als Initialkonditionen wurden jeweils 10 µmol des geschützten BPin-Vorläufers **6** und $Cu(4\text{-}PhPy)_4(ClO_4)_2$ bei einer Temperatur von 110 °C ausgewählt. Die Elution des $[^{18}F]F^-$ von der Anionenaustauscher-Kartusche erfolgte mit Et_4OTf in *n*BuOH (400 µL) direkt in die Reaktionslösung. Nach 10 min Reaktionszeit wurde dabei das ^{18}F-markierte Intermediat Boc-(*S*)-5-[^{18}F]FMT-(MOM)-O*t*Bu mit sehr guten RCUs von 74 ± 1% erhalten (**Tabelle 3**, **Eintrag 1**).

Tabelle 3: RCUs der Radiosynthesen von (*S*)-5-[^{18}F]FMT über *n*BuOH oder MeOH-Elution und reduzierter Substratmenge.

Nr.	Elution	V [mL]	n [µmol]	t [min]	RCU [%]
1	*n*BuOH	1,2	10	10	74 ± 1
2			2,5		35 ± 2
3				20	38 (n=1)
4	MeOH	1,2	10	10	82 ± 6
5			2,5		79 ± 6

Leider konnte die Vorläufermenge bei den oben genannten Reaktionsbedingungen nicht reduziert werden, so dass es zu einem Einbruch der RCUs auf 35 ± 2% kam. Trotz Verlängerung der Reaktionszeit auf 20 min wurde keine Verbesserung des RCU erhalten (**Tabelle 3**, **Eintrag 2** & **3**). Die Vermutung lag nahe, dass bei der Elutionsmethode mit *n*BuOH noch genug Restwasser in der Reaktionslösung vorhanden war, um die Radiofluorierung bei einer Vorläufermenge von 2,5 µmol zu stören. Nach einem Wechsel der Elutionsmethode zu Et_4NOTf in MeOH und darauffolgendem Abdampfen von MeOH bei 60 °C unter reduziertem Druck und im Argonstrom konnten sowohl mit 10 µmol Vorläufer als auch mit 2,5 µmol Vorläufer sehr gute RCUs von 82 ± 6% bzw. 79 ± 6% erhalten werden (**Tabelle 3**, **Eintrag 4** & **5**).

Zum Entfernen des Lösungsmittels wurde das ^{18}F-markierte Intermediat auf einer C18-Kartusche fixiert und anschließend mit MeOH eluiert, nachdem die Kartusche mit Wasser gewaschen wurde. Nach Entfernen des MeOH erfolgte die Hydrolyse bei 80 °C mit 6 M HCl in 20% MeOH und (*S*)-5-[^{18}F]FMT wurde nach semipräparativer HPLC und Formulierung in einer AA von 30 ± 2% erhalten (**Schema 28**).

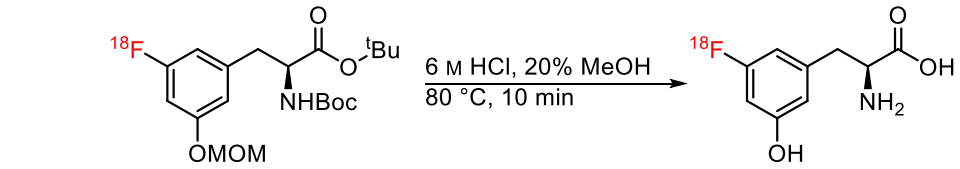

Boc-(*S*)-5-[^{18}F]FMT-(MOM)-O^{t}Bu (*S*)-5-[^{18}F]FMT AA = 30 ± 2%

A_M = 4-19 GBq/µmol

Schema 28: Hydrolyse von Boc-(*S*)-5-[^{18}F]FMT zu (*S*)-5-[^{18}F]FMT mit 6 M HCl in 20% MeOH bei 80 °C für 10 min.

Die Isolierung über semipräparative HPLC konnte erfolgreich und ohne wesentliche Optimierungen durchgeführt werden. Die Menge an chemischen Nebenprodukten bei der Radiosynthese war auch verhältnismäßig gering, da nur 2,5 µmol an Vorläufer für die Radiosynthese verwendet wurde (**Abbildung 26**).

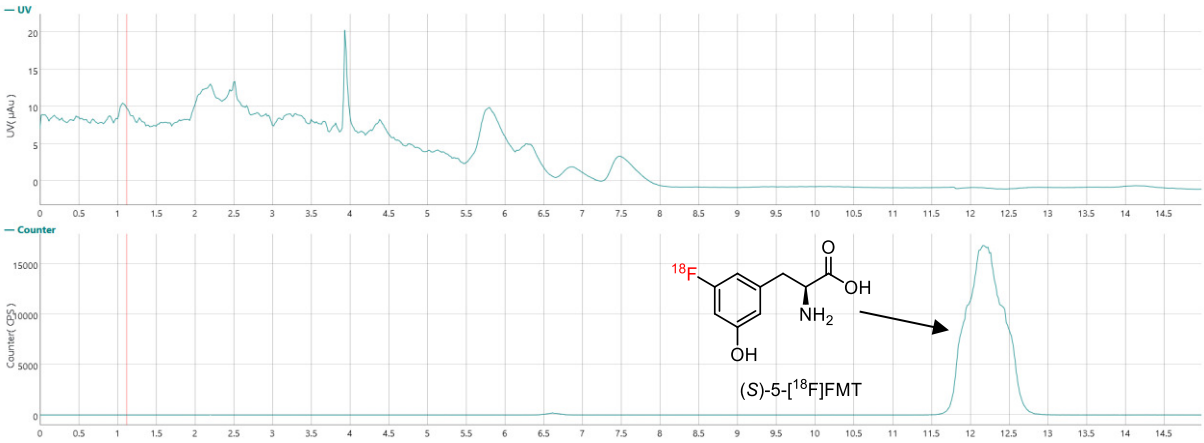

Abbildung 26: Isolierung von (*S*)-5-[^{18}F]FMT über semipräparative HPLC (oben: UV-Kanal, λ=254 nm; unten: Radiokanal).

Die Formulierung zu einer injektionfähigen Lösung erfolgte über eine starke Kationenaustauscher-Kartusche, auf welcher das isolierte (*S*)-5-[^{18}F]FMT fixiert und mit Wasser gewaschen wurde. Danach konnte das Radioprodukt mit 2 M NH_3 in ethanolischer Lösung eluiert und das Lösungsmittel bei 40 °C unter reduzierten Druck und im Argonstrom entfernt werden. Der Rückstand wurde dann in PBS-Puffer aufgenommen, wodurch eine injektionsfähige Lösung erhalten wurde. Die Ergebnisse der Qualitätskontrolle von (S)-5-[^{18}F]FMT zeigten, dass im Radioprodukt keine signifikanten Mengen an chemischen Verunreinigungen enthalten waren (**Abbildung 27**).

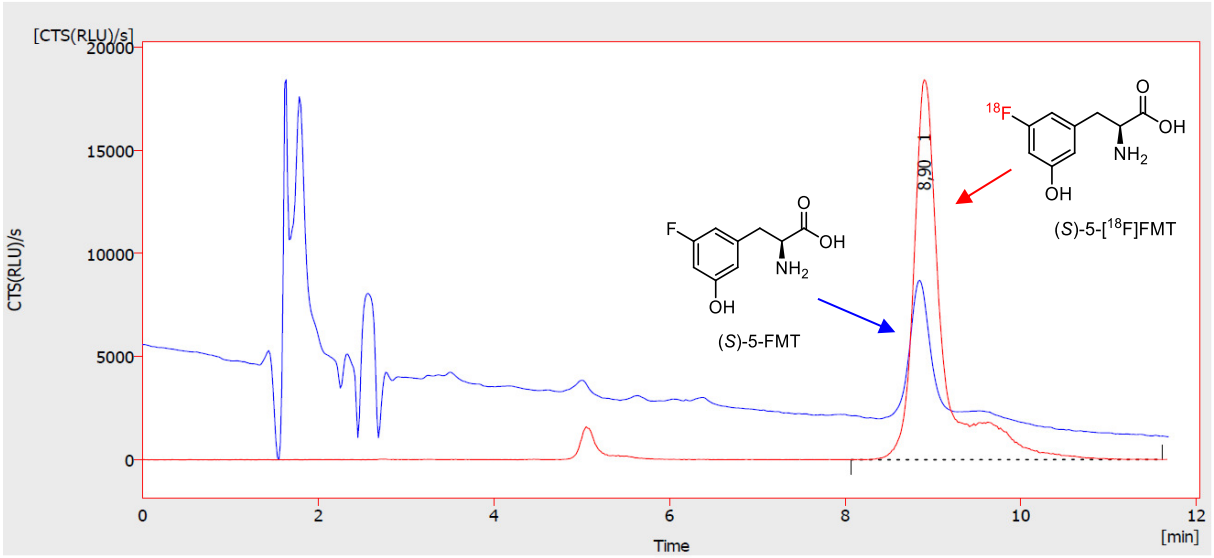

Result Table (Uncal - Data\alc-enhanced_1105_06_03_2023_[4 DMI]5-[18F]FMT_Bpin_2,5µmol_carrier - HERM)

	Reten. Time [min]	Area [CTS(RLU)/s.s]	Height [CTS(RLU)/s]	Area [%]
1	8,900	417539,500	18404,418	100,0
	Total	417539,500	18404,418	100,0

Abbildung 27: HPLC-Chromatogramm von isoliertem (*S*)-5-[^{18}F]FMT zur Qualitätskontrolle der chemischen Reinheit und Bestimmung der A_M (blau: UV-Kanal, λ=254 nm; rot: Radiokanal).

Zusätzlich konnte eine radiochemische Reinheit von >99% erhalten werden und mittels Koinjektion der nicht-radioaktiven Referenzverbindung (*S*)-5-FMT der Radiotracer identifiziert werden (**Abbildung 28** & ***Abbildung 29***). Die A_M in einem Radiotracer-Batch (95 MBq) betrug 19 GBq/µmol (Startaktiviät: 342 MBq).

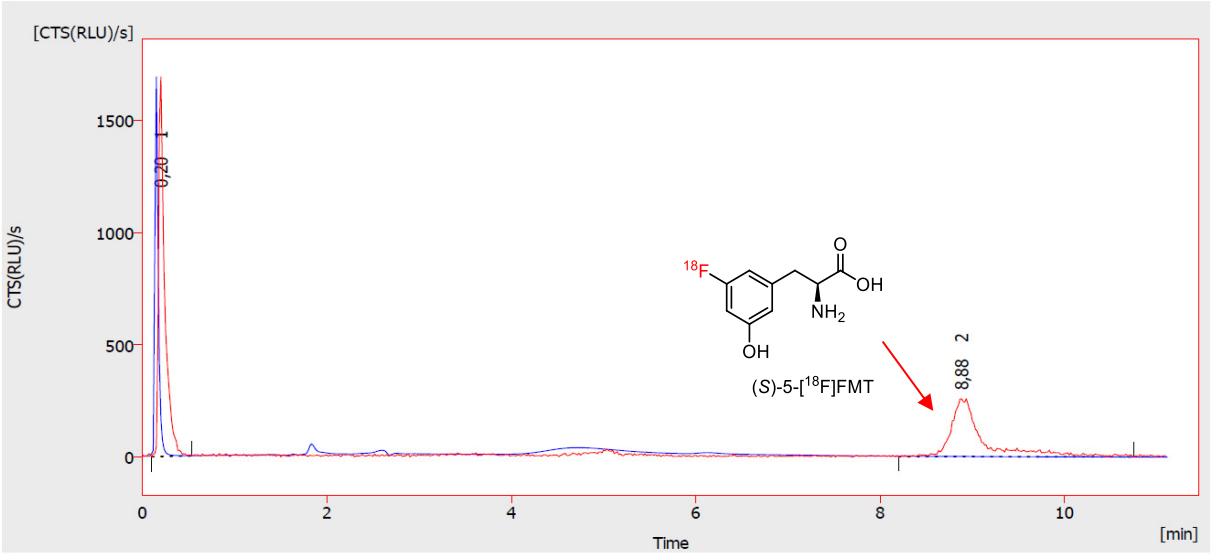

Result Table (Uncal - Data\alc-enhanced_1106_06_03_2023_[4 DMI]5-[18F]FMT_Bpin_2,5µmol_radio_purity - HERM)

	Reten. Time [min]	Area [CTS(RLU)/s.s]	Height [CTS(RLU)/s]	Area [%]
1	0,200	7929,000	1691,308	56,5
2	8,883	6097,000	257,536	43,5
	Total	14026,000	1948,844	100,0

Abbildung 28: HPLC-Chromatogramm von isoliertem (*S*)-5-[^{18}F]FMT zur Qualitätskontrolle der radiochemischen Reinheit (blau: UV-Kanal, λ=254 nm; rot: Radiokanal).

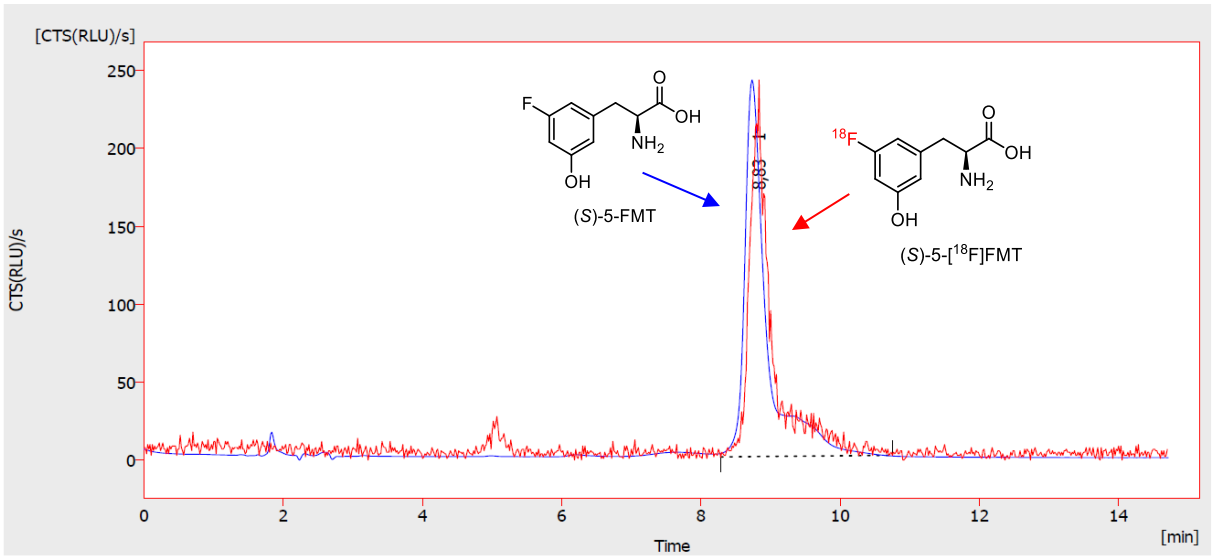

Result Table (Uncal - Data\alc-enhanced_1107_06_03_2023_[4 DMI]5-[18F]FMT_Bpin_2,5µmol_spiked - HERM)

	Reten. Time [min]	Area [CTS(RLU)/s.s]	Height [CTS(RLU)/s]	Area [%]
1	8,833	5175,000	241,777	100,0
	Total	5175,000	241,777	100,0

Abbildung 29: HPLC-Chromatogramm von isoliertem (*S*)-5-[^{18}F]FMT mit Koinjektion der nicht-radioaktiven Referenzverbindung (*S*)-5-FMT (blau: UV-Kanal, λ=254 nm; rot: Radiokanal).

4 Zusammenfassung

Die Einführung der CVRF hat die Synthese ^{18}F-Markierter Aromaten mit guten und reproduzierbaren RCUs sowie die Herstellung von Radiotracern, welche über konventionelle nukleophile Substitutionen nicht zugänglich waren, ermöglicht. Trotz dieser Erfolge bestand die Notwendigkeit einer Optimierung durch die Identifikation effektiverer Cu-Vermittler zur Steigerung der RCUs bei geringerer Substratmenge. Zur Optimierung des CVRF-Protokolls wurden verschiedene Cu(II)-Komplexe mit insgesamt 15 verschiedenen *N*-heterozyklischen Liganden und neun Gegenionen hergestellt. Diese wurden mit elektronenreichen und -armen Aryl-B(OH)$_2$ und –Bpin Substraten zunächst unter Standardbedingungen (10 µmol, DMA, 110 °C, 10 min) evaluiert. Als Liganden wurden mit Elektronendonoren und –akzeptoren substituierte Pyridine, Chinoline, Pyrazin, *N*-Methylpyrazol, *N*-Methyltriazol und Imidazo(1,2b)pyridazin verwendet. Die Gegenionen umfassten Cl^-, Br^-, AcO^-, MsO^-, TsO^-, TfO^-, SO_4^-, ClO_4^-, ClO_3^-.

Bei der ersten Evaluation zeigte sich, dass elektronenreichere Pyridine in Kombination mit nicht koordinierenden Gegenionen wie TfO^- oder ClO_4^- für die „Alkohol-verstärkte“-CVRF beider Substratklassen geeignet waren und teilweise höhere RCUs (16–58%) ermöglichten als der Standardkomplex Cu(Py)$_4$(OTf)$_2$ (RCU: 30%). Nach weiteren Optimierungen mit verschiedenen Lösungsmitteln wie Propylencarobonat (PC) oder DMI bei gleicher Temperatur und Reaktionszeit wurden die drei Cu(II)-Komplexe Cu(4-PhPy)$_4$(ClO$_4$)$_2$, Cu(3,4-Me$_2$Py)(OTf)$_2$ und Cu(3,4-Me$_2$Py)(ClO$_4$)$_2$ als die effizientesten Vermittler identifiziert, welche z.T. nahezu quantitative RCUs lieferten.

Die Temperatur- und Reaktionszeitoptimierungen zeigten die Robustheit der Methode, wobei sogar Radiofluorierungen bei niedrigen Temperaturen durchgeführt werden konnten. Am Beispiel der Radiofluorierung von 4-Biphenyl-B(OH)$_2$ mit Cu(4-PhPy)$_4$(ClO$_4$)$_2$ als Vermittler erwies sich die zunächst gewählte Reaktionszeit von 10 min bereits als optimal für hohe und reproduzierbare RCUs. Die Radiosynthesen waren auch bei Temperaturen von bis zu 130 °C möglich, ohne dass es zu einer wesentlichen Abnahme der RCUs kam. Bemerkenswert war jedoch, dass auch Radiofluorierungen bei 60 °C und längerer Reaktionszeit sehr gute RCUs von 69 ± 8% lieferte (im Vergleich: 37 ± 7% bei 10 min). Dies eröffnet die Möglichkeit, auch

temperatursensitive Vorläufermoleküle über diese Methode zu markieren. Zudem ist die gewählte Reaktionszeit von 40 min immer noch gut mit der Halbwertszeit von ^{18}F ($T_{1/2}$ = 109,77 min) vereinbar.

Auch bei der Verwendung der neuartigen Cu(II)-Komplexe für die CVRF von Arylstannanen konnte eine Steigerung und verbesserte Reproduzierbarkeit der RCUs festgestellt werden. Während unter Standardbedingungen RCUs von 2–14% erzielt wurden, konnten bei Verwendung von $Cu(4\text{-}PhPy)_4(ClO_4)_2$ die RCUs auf 20–44% gesteigert werden. Bei der Umsetzung von Arylstannen zeigte sich, dass nicht nur der jeweilige Cu-Komplex Einfluss auf die RCUs hatte, sondern auch die Elutionsmethode und die Atmosphäre, in der die Radiosynthese durchgeführt wurde. So konnte eine signifikante Steigerung der RCUs auf bis zu 47–57% durch Änderung der Elutionsmethode zu Et_4NOTf in MeOH mit anschließendem Abdampfschritt und ^{18}F-Markierung unter Argonatmosphäre erreicht werden. Die optimale Temperatur für die Radiofluorierung von Aryl-$SnMe_3$ lag bei 90 °C im Vergleich zu 110 °C für Aryl-$B(OH)_2$/BPin-Vorläufer. Der Einsatz von *n*BuOH als protisches Kolösungsmittel erwies sich in diesem Fall als kontraproduktiv.

Des Weiteren erwies sich die Verwendung von $Cu(4\text{-}PhPy)_4(ClO_4)_2$ als Mediator bei weiterer Reduzierung der Substratmenge auf 2,5 µmol als effizient. Nach Anwendung des modifizierten Protokolls konnten 4-Biphenyl- und 4-Acetylphenyl-$B(OH)_2$, -BPin, -Bneo und -$SnMe_3$ mit RCUs von 25–63% radiomarkiert werden. Auch die Radiofluorierung von funktionalisierte Verbindungen wie Benzylalkohol, Anisol, Benzoesäuremethylester, Benzamid, Phenyliodid, Benzaldehyd, Phenol, *m*-Anilin und Benzoesäure-2,3,5,6-Tetrafluorphenolester konnten mit akzeptablen bis sehr guten RCUs von 18–76% produziert werden.

Zusammengefasst konnten in dieser Studie aus insgesamt 36 hergestellten Cu(II)-Komplexen die drei besten als die „Nächste Generation“ von Cu(II)-Vermittlern für die („Alkohol-verstärkte“) CVRF identifiziert werden. Die darauffolgende akribische Optimierung der Reaktionsparameter ermöglichte es die RCAs zu verbessern und/oder die Substratmenge zu reduzieren. Zusätzlich konnten noch weitere Schlussfolgerungen aus den Studien gezogen werden:

- Das Lösungsmittel DMI/*n*BuOH ist für die ^{18}F-Markierung von Boronsubstraten am besten geeignet wohingegen reines DMI für Stannylsubstrate besser geeignet ist.
- $B(OH)_2$ Vorläufer lassen sich häufig besser ^{18}F-markieren als BPin oder Bneo Vorläufer.
- $Cu(4\text{-}PhPy)_4(ClO_4)_2$ ist für ^{18}F-Markierungen bei 2,5 µmol Vorläufermenge am besten geeignet.
- Stannylvorläufer lassen sich besser unter Argonatmosphäre radiofluorieren, während bei Boronsubstrate bessere RCUs unter Luftsauerstoff erzielt werden können.

Die neuen Cu(II)-Komplexe $Cu(4\text{-}PhPy)_4(ClO_4)_2$ und $Cu(3,4\text{-}Me_2Py)_4(OTf)_2$ wurden anschließend für die Herstellung von insgesamt neun verschiedenen Radiotracern aus $B(OH)_2$, BPin oder $SnMe_3$-Vorläufern verwendet, um ihre Praktikabilität und Effizienz sowie die Reproduzierbarkeit der AAs zu demonstrieren (**Abbildung 30**).

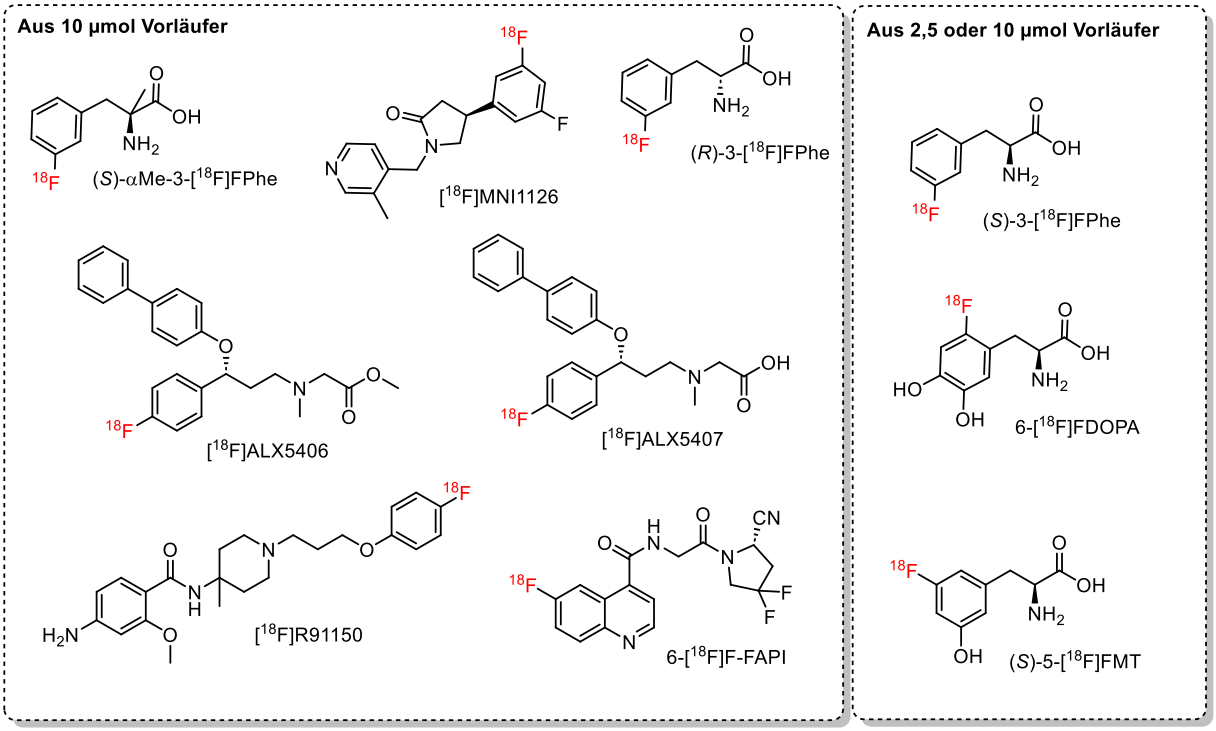

Abbildung 30: Übersicht aller hergestellten PET-Tracer und Radiotracer-Kandidaten über das optimierte Protokoll der CVRF mit neuen und effizienten Cu(II)-Komplexen.

Im Rahmen der Radiosynthese der Aminosäure-PET-Tracer 3-[^{18}F]FPhes konnten ausgehend von Ni-BPB- und Ni-BPA-Komplexen die entsprechenden ^{18}F-markierten Intermediate (*S*,*S*)-Ni-BPB-3-[^{18}F]FPhe, (*R*,*R*)-Ni-BPB-3-[^{18}F]FPhe und (*S*,*S*)-Ni-BPA-αMe-3-[^{18}F]FPhe mit RCUs von 69–91% (*vs*. 8–17%) erhalten werden. Die Hydrolyse von (*S*,*S*)-Ni-BPB-3-[^{18}F]FPhe und (*R*,*R*)-Ni-BPB-3-[^{18}F]FPhe ergab AAs von 41 ± 2% (*vs*. 17 ± 6%) und 33 ± 0,5% (*vs*. 14 ± 4%) für (*S*)-3-[^{18}F]FPhe und (*R*)-3-[^{18}F]FPhe. Auch bei Reduzierung der Vorläufermenge für die Herstellung von (*S*)-3-[^{18}F]FPhe auf 2,5 µmol konnten gute AAs von 23 ± 1% erhalten werden. Außerdem wurde der Radiotracer 6-[^{18}F]FDOPA zur Bildgebung des dopaminergen Systems mit AAs von 30 ± 3% bei einer reduzierten Vorläufermenge von nur 2,5 µmol erhalten. Im Vergleich dazu erzielten Mossine et al. mit einer Vorläufermenge von 5 µmol AAs von nur 6 ± 1%.[170] Der Radiotracer [^{18}F]MNI1126, ein Radioligand für die Bildgebung des synaptischen Vesikel-Glykoprotein 2A (SV_{2A}), wurde ebenfalls mit höheren RCUs (47 ± 5%) als bei der Verwendung von $Cu(Py)_4(OTf)_2$ in DMA (6 ± 2%) produziert.

Die Herstellung von [^{18}F]ALX5407, ein Radiotracer-Kandidat für die PET-Bildgebung von GlyT1 im Gehirn, lieferte bei Verwendung des Standard-Protokolls [$Cu(Py)_4(OTf)_2$ in DMA/*n*BuOH] AAs von 14 ± 6%, wobei hohe Vorläufermengen (30 µmol) erforderlich waren. Bei Anwendung des optimierten Protokolls mit $Cu(4\text{-}PhPy)_4(ClO_4)_2$ als Vermittler konnte die Vorläufermenge deutlich reduziert (10 µmol) und zudem höhere AAs von 30 ± 5% erreicht werden. In der Präklinik wurde der Radiotracer-Kandidat mittels In-vitro-Autoradiographie in Rattenhirnschnitten evaluiert, wobei ein mit der GlyT1-Verteilung im Gehirn übereinstimmendes Verteilungsmuster beobachtet wurde. Jedoch war [^{18}F]ALX5407 bei der In-vivo-Evaluation in gesunden Nagetieren nicht in der Lage, die Blut-Hirn-Schranke (BHS) zu überwinden. In weiteren Versuchen konnte jedoch gezeigt werden, dass der Methylester [^{18}F]ALX5406 die BHS überwindet und im Gehirn durch Esterasen zu [^{18}F]ALX5407 hydrolisiert wird. Durch diesen vielversprechenden Prodrug-Ansatz war es möglich, das biologische Target zu adressieren und PET-Bilder mit einem Verteilungsmuster zu erhalten, die der von [^{18}F]ALX5407 in Rattenhirnschnitten entsprachen.

Ein weiteres Beispiel für einen erfolgsversprechenden Radiotracer-Kandidaten ist [^{18}F]R91150 für die Bildgebung von 5-HT$_{2A}$-Rezeptoren. Obwohl die Ergebnisse der In-vitro-Autoradiographie die entsprechende 5-HT$_{2A}$-Rezeptorverteilungen sehr gut zeigten, bestand die Notwendigkeit einer Optimierung der Herstellungsprozedur für eine In-vivo-Applikation. Daher wurde [^{18}F]R91150 sowohl aus einem nicht geschützten als auch aus einem Boc-geschützten BPin-Vorläufer unter Verwendung von Cu(4-PhPy)$_4$(ClO$_4$)$_2$ mit AAs von 12 ± 2% und 24 ± 2% hergestellt. Der Boc-geschützten Vorläufer wies jedoch eine deutlich bessere Lagerungsbeständigkeit auf, wodurch durchgehend hohe und reproduzierbare RCUs erzielt werden konnten. Bei Radiosynthesen mit dem nicht geschützten Vorläufer kam es dagegen selbst bei Lagerung unter Argon und bei tiefen Temperaturen nach längerer Lagerungszeit aufgrund seiner Hygroskopie zu schlechteren RCUs. Die µPET-Messungen in Mäusen zeigten eine gute In-vivo-Stabilität und hepatobiliäre Ausscheidung, mit hoher Traceraufnahme in Galle und Darm. Das zerebrale Verteilungsmuster von [^{18}F]R91150 in Ratten entsprach der bekannten Verteilung von 5-HT$_{2A}$-Rezeptoren im Gehirn. Zudem konnte die Bindung von [^{18}F]R91150 im 5-HT$_{2A}$-reichen Kortex durch Ko-Injektion von Altanserin sowie in Verdrängungsversuchen mit Ketanserin um bis zu 30% reduziert werden. Im Plexus Choroideus hingegen wurde eine nur leichte Verdrängung mit Ketanserin beobachtet. Hier gilt es durch weitere Blockierungs- bzw. Verdrängungsstudien mit selektiveren 5-HT$_{2A}$-Rezeptorliganden die Selektivität weiter zu untersuchen.

Der Radiotracer 6-[^{18}F]F-FAPI zur Bildgebung von CAFs in soliden Tumoren konnte nach Anwendung des optimierten CVRF-Protokolls für SnMe$_3$-Vorläufer in AAs von 19 ± 2% erhalten werden. Zu erwähnen ist, dass die erhaltenen Aktivitätsausbeuten ohne jegliche Optimierung der Radiosynthese erreicht wurden. Somit besteht die Möglichkeit, die Ausbeute durch weitere Optimierung der Reaktionsparameter zu erhöhen und auch die verwendete Vorläufermenge zu reduzieren. In der präklinischen Evaluation zeigten die µPET-Messungen von 6-[^{18}F]F-FAPI eine schnelle und hohe Tumoranreicherung in verschiedenen Tiermodellen und eine geringe Auswaschung bis zu 120 min nach Tracerinjektion. Im Vergleich zu [^{18}F]AlF-FAPI-42 gab es in zwei subkutanen Tumormodellen keine signifikanten Unterschiede in der Tumoranreicherung, allerdings war das Tumor-Hintergrund-Verhältnis von 6-[^{18}F]F-FAPI deutlich schlechter. Zudem ergab der Vergleich mit dem klinisch etablierten PET-

Tracer [^{18}F]FET eine deutlich bessere Tumordarstellung und -abgrenzung gegenüber gesundem Hirngewebe. Zuletzt konnte in Blockierungs- und Verdrängungsstudien mit dem FAP-selektiven Liganden UAMC1110 die Tumoraufnahme von 6-[^{18}F]F-FAPI sowohl blockiert als auch verdrängt werden.

Schließlich konnte (*S*)-5-[^{18}F]FMT ein vielversprechender Radiotracer zur Darstellung des dopaminergen Systems aus dem geschützten BPin-Vorläufer unter Verwendung von $Cu(4\text{-}PhPy)_4(ClO_4)_2$ als Vermittler in AAs von 30 ± 2% hergestellt werden. Dabei konnte die Vorläufermenge bis auf 2,5 µmol reduziert werden, ohne dass es zu einem Einbruch der RCUs bzw. AAs kam. Die Isolierung des Radiotracers gestaltete sich ebenfalls einfach, da aufgrund der geringen Vorläufermenge nur wenige chemische Nebenprodukte abzutrennen waren.

5 Experimenteller Teil

5.1 Organische Chemie

5.1.1 Materialien und Methoden

Sofern nicht anders erwähnt, wurden alle Chemikalien von Sigma-Aldrich (Steinheim, Deutschland), Acros (Fischer Scientific GmbH, Nidderrau, Deutschland), Alfa Aesar [Thermo Fischer (Kandel) GmbH, Kandel, Deutschland], BLDPham (Kaiserslautern, Deutschland) oder Key Organics (Camelforf, Vereinigtes Königreich) kommerziell erworben und ohne weitere Aufreinigung verwendet. Alle Reaktionen wurden mit teflonbeschichteten Magnetrührfischen durchgeführt. Luftsensitive Reaktionen oder Substrate wurden in ausgeheizten Glasgeräten und unter Argonatmosphäre durchgeführt. Protonen-, Kohlenstoff- und Fluorkernspinresonanzspektren (^{1}H, ^{13}C und ^{19}F-NMR-Spektren) wurden mit dem Bruker Avance Neo (400 MHz) Spektrometer aufgenommen. Chemische Verschiebungen sind in parts per million (ppm) in Relation zum deuterierten Lösungsmittel angegeben. Die Muliplizität der beobachteten Signale sind wie folgt charakterisiert: s = Singulett, d = Dublett, t = Triplett, q = Quartett, m = Multiplett und dd = Dublett von Dubletts. Kupplungskonstante *J* wurden in der Einheit Hertz (Hz) angegeben. Hochaufgelöste Massenspektren (HRMS) wurden am LTQ Orbitrab XL (Thermo Fischer Scintific Inc., Bremen, Deutschland) aufgenommen.

5.1.2 Synthese von (*S*)-*tert*-Butyl-2-(2-cyano-4,4-difluorpyrrolidin-1-yl)-2-oxoethylcarbamat (3)

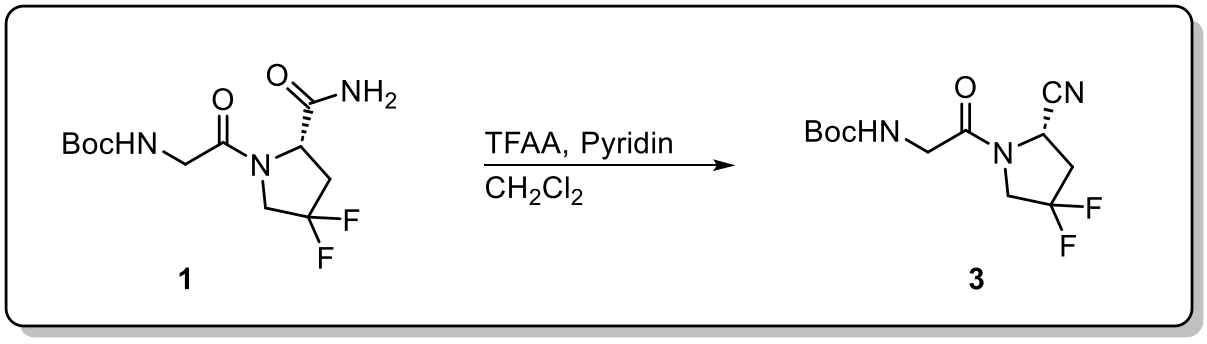

(*S*)-*tert*-Butyl-2-(2-carbamoyl-4,4-difluoropyrrolidin-1-yl)-2-oxoethylcarbamat **1** (3,0 g, 9,8 mmol, 1 Äq.) und Pyridin (1,6 mL, 1,6 g, 20 mmol, 2 Äq.) wurden in trockenem CH_2Cl_2 (24 mL) gelöst und die Lösung auf -10 °C gekühlt. Anschließend wurde Trifluoressigsäureanhydrid (1,5 mL, 2,3 g, 11 mmol, 1,12 Äq.) langsam hinzu getropft

und für 15 min bei gleicher Temperatur gerührt. Das Eisbad wurde entfernt und die Reaktionslösung bei Raumtemperatur für 1,5 h gerührt. Danach wurde das Lösungsmittel unter verminderten Druck entfernt und der Rückstand in EtOAc/H_2O (80 mL, 5:3) aufgenommen. Die organische Phase wurde abgetrennt und die wässrige Phase mit EtOAc (3 × 30mL) extrahiert. Die vereinigten organischen Phasen wurden mit gesättigter $NaCl_{aq.}$ (30 mL) und $NaHCO_3$ (30 mL) gewaschen, und über Na_2SO_4 getrocknet. Das Lösungsmittel wurde unter verminderten Druck entfernt und der Rückstand über Säulenchromatographie (SiO_2, CyHex/EtOAc, 2:1, R_f = 0,34) aufgereinigt. Die Titelverbindung **3** wurde als farbloser Feststoff erhalten (1,4 g, 4,9 mmol, 76%).

^{1}H-NMR (400 MHz, $CDCl_3$): δ = 5.41 (s, 1H), 4.96 (t, *J* = 13, 6.5 Hz, 1H), 3.91 (m, 4H), 2.74 (m, 2H), 1.44 (s, 9H).

^{13}C-NMR (101 MHz, $CDCl_3$): δ = 168.47, 155.99, 127.96, 125.47, 116.36, 80.42, 52.06 (t, *J* = 65, 32.5 Hz), 44.30, 43.14, 37.44 (t, *J* = 51, 25.5 Hz), 28.41.

^{19}F-NMR (376 MHz, $CDCl_3$): δ = -95.38, -95.99, -103.67, -104.28.

5.1.3 Synthese von 6-Trimethylstannyl-chinolin-4-carbonsäure-2,3,5,6-tetrafluorophenylester (5)

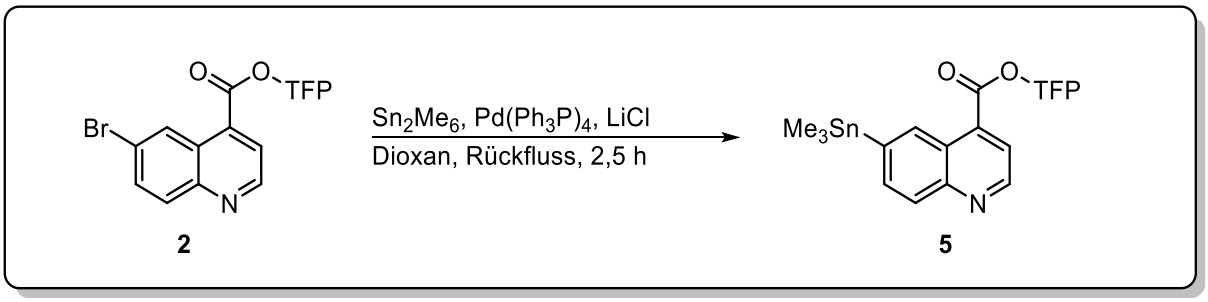

Zu einer Suspension von **2** (1,4 g, 3,5 mmol, 1 Äq.), $Pd(Ph_3P)_4$ (0,90 mg, 0,78 mmol, 0,2 Äq.) und LiCl (0,84 mg, 20 mmol, 4,8 Äq.) in trockenem 1,4-Dioxan (49 mL) wurde bei Raumtemperatur und unter Argonatmosphäre Sn_2Me_6 (0,80 mL, 2,0 g, 6,1 mmol, 1,5 Äq.) langsam hinzu getropft und anschließend für 2,5 h unter Rückfluss erhitzt. Nachdem die Reaktionsmischung auf Raumtemperatur abgekühlt war, wurde der Feststoff über Celite® abfiltriert und der Filterkuchen mit Et_2O gewaschen. Die organische Phase wurde mit gesättigter $NaCl_{aq.}$ (2 × 30mL) gewaschen und über MgSO4 getrocknet. Anschließend wurde das Lösungsmittel am Rotationsverdampfer entfernt und der Rückstand über Säulenchromatographie (SiO_2,

CyHex/EtOAc, 19:1) aufgereinigt. Die Titelverbindung **5** wurde als farbloser Feststoff (0,75 mg, 1,9 mmol, 44%) erhalten.

^{1}H-NMR (400 MHz, $CDCl_3$): δ = 9.13 (d, *J* = 4.44 Hz, 1H), 8.95 (s, 1H), 8.22 (m, *J* = 4.10 Hz, 3H), 7.99 (dd, *J* = 0.96, 8.24 Hz, 1H), 7.14 (m, *J* = 4.24 Hz, 1H), 0.42 (s, 9H).

^{13}C-NMR (101 MHz, $CDCl_3$): δ = 161.94, 149.19, 148.55, 147.56, 146.20, 145.13, 137.53, 132.76, 131.93, 128.24, 124.64, 123.31, 104.07 (t, *J* = 22.7 Hz), 95.91 (t, *J* = 23.2 Hz), 77.16, -9.23.

^{19}F-NMR (376 MHz, $CDCl_3$): δ = -162.50 (q, *J* = 9.16 Hz, 1F), -152.37 (q, *J* = 10.19 Hz, 1F), -140.83 (q, *J* = 9.71 Hz, 1F), -138.17 (q, *J* = 10.22 Hz, 1F).

HR-MS-ESI: m/z $[M+H]^+$ berechnet für $[C_{19}H_{16}F_4NO_2Sn]^+$ = 486,0133; gefunden: 486,01336.

5.1.4 Synthese von 6-Trimethylstannyl-chinolin-4-carbonsäure-[2-(2-cyano-4,4-difluoropyrrolidin-1-yl-2-oxoethyl]amid (4)

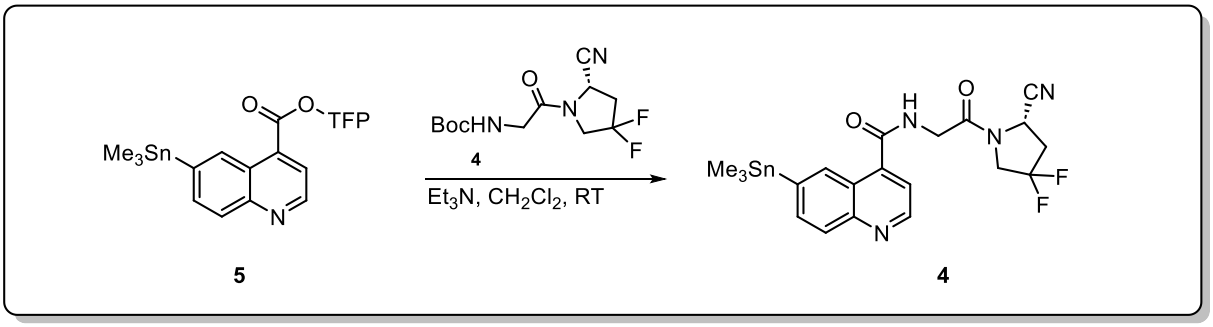

Zu einer Lösung von **3** (0,20 mg, 0,70 mmol, 1,04 Äq.) in CH_2Cl_2 (7 mL) wurde TFA (1,4 mL) langsam bei Raumtemperatur hinzu getropft und für 1 h gerührt. Danach wurden alle flüchtigen Stoffe unter verminderten Druck entfernt und der Rückstand unter Argonatmosphäre in trockenes CH_2Cl_2 (5 mL) und Et_3N (0,2 mL) aufgenommen. Anschließend wurde eine Lösung von **5** (0,26 mg, 0,67 mmol, 1 Äq.) in CH_2Cl_2 bei 0 °C hinzu getropft und für eine weitere Stunde bei Raumtemperatur gerührt. Alle flüchtigen Stoffe wurden am Rotationsverdampfer entfernt und der Rückstand über Säulenchromatographie (SiO_2, CyHex/Aceton, 2:1, R_f = 0,09) aufgereinigt. Die Titelverbindung **4** wurde als farbloser Feststoff (0,20 g, 0,39 mmol, 58%) erhalten.

^{1}H-NMR (400 MHz, $CDCl_3$): δ = 8.85 (d, *J* = 4.3 Hz, 1H), 8.48 – 8.27 (m, 1H), 8.15 – 8.00 (m, 1H), 7.97 – 7.77 (m, 1H), 7.45 (d, *J* = 4.3 Hz, 1H), 7.16 (t, *J* = 4.6 Hz, 1H),

4.95 (t, *J* = 6.5 Hz, 1H), 4.41 (dd, *J* = 17.5, 5.5 Hz, 1H), 4.17 (dd, *J* = 17.5, 4.3 Hz, 1H), 4.09 – 3.86 (m, 2H), 2.98 – 2.68 (m, 2H), 0.36 (s, 9H).

^{13}C-NMR (101 MHz, $CDCl_3$): δ = 167.64 (d, J = 41.3 Hz), 149.80, 148.78, 143.75, 140.23, 136.91, 132.87, 128.83, 125.30, 123.96, 118.88, 116.14, 77.16, 52.18 (t, J = 32.1 Hz), 44.42, 44.38, 42.38, 37.50 (t, J = 25.5 Hz), 28.71, -9.18.

^{19}F-NMR (376 MHz, $CDCl_3$): δ = -96.46 (t, *J* = 235.8 Hz), -99.30 (dd, *J* = 1366.4, 238.1 Hz), -102.66 (d, *J* = 232.9 Hz), -104.33 (d, *J* = 240.2 Hz).

HR-MS-ESI: m/z $[M+H]^+$ berechnet für $[C_{20}H_{23}F_2N_4O_2Sn]^+$ = 509,08056; gefunden: 509,08026.

5.2 Radiochemie

5.2.1 Materialien und Methoden

Die Produktion von Fluorid-18 ($[^{18}F]F^-$) erfolgte über die $^{18}O(p,n)^{18}F^-$ Kernreaktion durch Bombardement von angereichertem $^{18}O[H_2O]$ mit 16,5 MeV Protonen am BC1710 Zyklotron (The Japan Steel Works Ltd., Shinagawa, Japan) des INM-5 (Forschungszentrum Jülich, Deutschland). Alle Radiosynthesen wurden in 5 mL Wheaton V-Vials mit PTFE beschichteten Flügelmagnetrührfischen durchgeführt. Trockenes DMI, *n*BuOH und MeOH wurden bei Sigma-Aldrich (Steinheim, Deutschland) kommerziell erworben. Die Anionenaustauscher-Kartuschen [Sep-Pak Accell Plus QMA carbonate plus light (46 mg) Cartridges], Kationenaustauschern [Oasis MCX Plus Short Cartridges (225 mg)] und Festphasenextraktions-Kartuschen [Sep-Pak C18 (130 mg) und HLB short (360 mg) Cartridges] wurden von Waters GmbH (Eschborn, Deutschland) erworben. Polymerbasierte StrataX-Kartuschen (60 mg) wurden von Phenomenex (Aschaffenburg, Deutschland) erworben.
Die analytische High performance liquid chromatography (HPLC) wurde auf einem Knauer HPLC-System (Knauer Wissenschaftliche Geräte GmbH, Berlin, Deutschland) mit einer Azura P 6.1L – Pumpe und einem Azura UVD 2.1 UV/Vis – Detektor durchgeführt. Für die Detektion der Absorption und Radioaktivität wurde der UV-Detektor mit einem Berthold NaI – Detektor in Serie geschaltet. Die Verzögerung der korrespondierenden Signale betrug 0,1 – 0,3 min und war abhängig von der Flussgeschwindigkeit. Für die Bestimmung der Radiochemischen Umsätze (RCUs) wurden die Reaktionsansätze mit H_2O (1 mL), 20% MeCN (1 mL) oder 20% MeCN + 0,1% TFA (1 mL) verdünnt und gemäß der post-column injection – Methode[171] jeweils

Proben vor und hinter (=post-column) der Säule in die HPLC injiziert. Die RCUs wurden dann über die Bildung des Quotienten der Peakflächen des Radioproduktes und der post-column injection berechnet (Gleichung 1).

$$RCU = \frac{Fläche_{Radioprodukt}}{Fläche_{post-column\ injection}} \quad (1)$$

Für die Reinigung der hergestellten Radiotracer wurde ein selbst gebautes semipräparatives HPLC-System bestehend aus einer KNAUER Pumpe 40P, einem Knauer K-2500 UV-Detektor, einem Rheodyne 6-Wege Injektionsventil und einem Geiger-Müller-Zähler verwendet.

5.2.2 HPLC Bedingungen

Analytische HPLC

6-[^{18}F]F-FAPI: MultoKrom® 100-5, 5 µm, 250×4,6 mm (CS-Chromtography, Langerwehe, Deutschland); 30% MeCN; 1,0 mL/min; t_R = 12,2 min.

Boc-(*S*)-5-[^{18}F]FMT-(MOM)-^{t}OBu: Synergi Hydro-RP, 80 Å, 4 µm, 250×4,6 mm (Phenomenex, Aschaffenburg, Deutschland); 70% MeCN, 1,5 mL, t_R = 6,08 min.

Semipräparative HPLC

6-[^{18}F]F-FAPI: Gemini C18 110A, 5 µm, 250×10 mm (Phenomenex, Aschaffenburg, Deutschland); 30% MeCN; 7,1 mL/min; t_R = 12,5 – 14 min.

5-[^{18}F]FMT: Synergi Hydro-RP, 10 µm, 250×10 mm (Phenomenex, Aschaffenburg, Deutschland); 3% EtOH + 0,1% H_3PO_4; 7,1 mL/min; t_R = 11,5 – 13 min.

Qualitätskontrolle

6-[^{18}F]F-FAPI: Kinetex EVO C18, 5 µm, 250×4,6 mm (Phenomenex, Aschaffenburg, Deutschland); 20% MeCN; 1,0 mL/min; t_R = 8,42 min.

5-[^{18}F]FMT: Kinetex EVO C18, 5 µm, 250×4,6 mm (Phenomenex, Aschaffenburg, Deutschland); 3% EtOH + 0,1% H_3PO_4; 1,5 mL/min; t_R = 8,42 min.

5.2.3 Bestimmung der molaren Aktivität

Eine Probe der Radiotracer-Lösung (20 µL) wurde mittels analytischer HPLC analysiert. Der Trägergehalt wurde aus der Signalfläche der Probe im UV-Kanal bestimmt und die molare Aktivität wurde anhand von Kalibrierungskurven (**Abbildung**

31 & **Abbildung *32***) berechnet. Die Kalibrierungskurven wurde durch Messungen mit verschiedenen Konzentrationen der nicht radioaktiven Referenzverbindungen 6-F-FAPI und (*S*)-5-FMT erstellt (**Tabelle 4** & **Tabelle *5***).

6-[^{18}F]F-FAPI

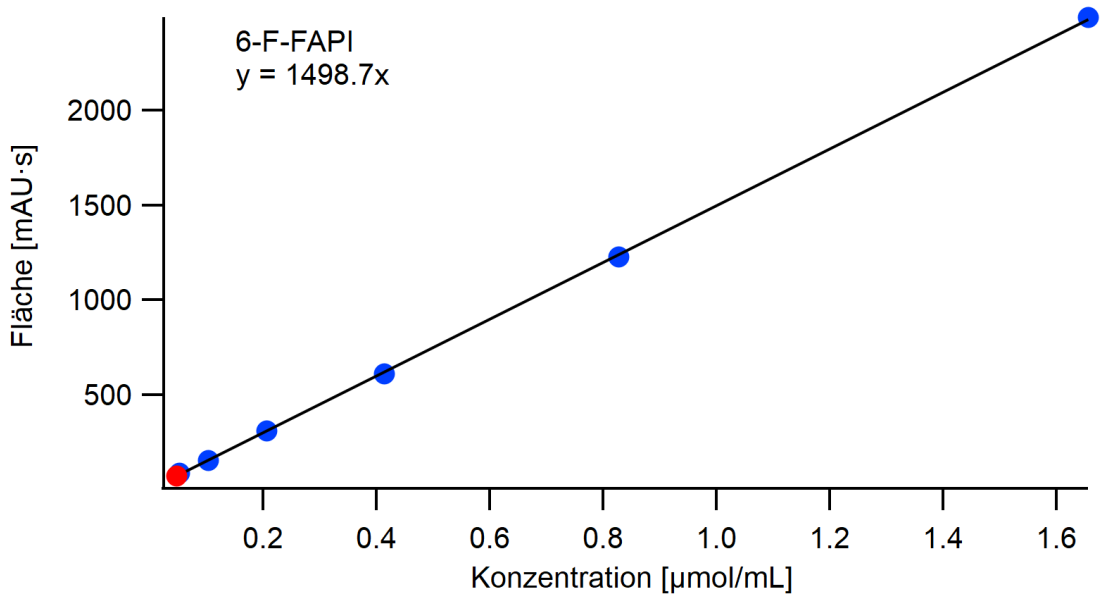

Abbildung 31: Kalibrierungskurve für die Berechnung der molaren Aktivität von 6-[^{18}F]F-FAPI.

Tabelle 4: Daten für die Kalibrierungskurve (gemessen bei λ=254 nm) für die Bestimmung der molaren Aktivität von 6-[^{18}F]F-FAPI.

Konzentration [µmol/mL]	**Menge [µg]**	**Peakfläche [mAU·min]**
1,66	600	2491,8
0,828	300	1225,8
0,414	150	610,9
0,207	75,0	309,5
0,104	37,5	153,7
0,0518	18,8	85,4
Gemessene Probe:		34,745
Volumen [mL]		0,67
Aktivität [MBq]		1096
Trägergehalt (µg)		5,61
Trägerkonzentration [µmol/mL]		$23{,}1\cdot10^{-3}$
Molare Aktivität [GBq/µmol]		71

(*S*)-5-[^{18}F]FMT

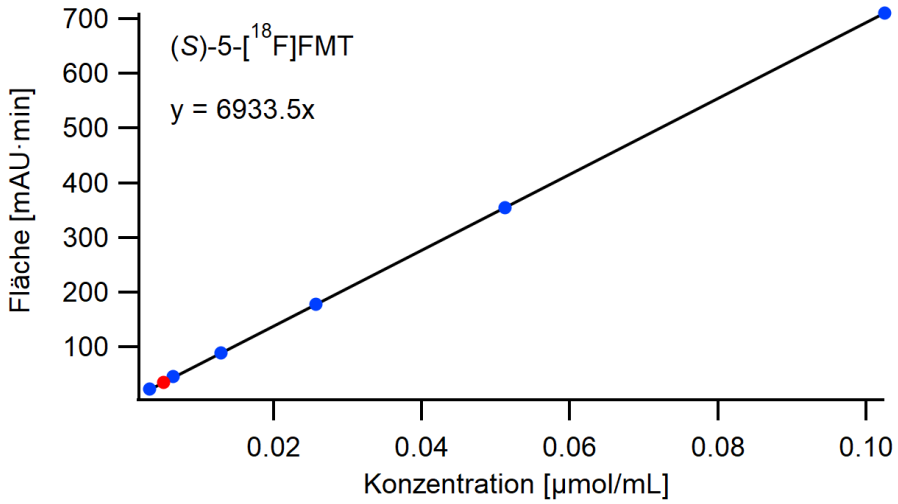

Abbildung 32: Kalibrierungskurve für die Berechnung der molaren Aktivität von (*S*)-5-[^{18}F]FMT.

Tabelle 5: Daten für die Kalibriergeraden (gemessen bei λ=220 nm) für die Bestimmung der molaren Aktivität von (*S*)-5-[^{18}F]FMT.

Konzentration [µmol/mL]	**Menge [µg]**	**Peakfläche [mAU·min]**
0,102	20,3	710
0,0510	10,2	355
0,0255	5,08	179
0,0127	2,54	90,1
0,00637	1,27	46,6
0,00319	0,635	23,0
Gemessene Probe:		35,04
Volumen [mL]		1,0
Aktivität [MBq]		95
Trägergehalt (µg)		1,01
Trägerkonzentration [µmol/mL]		$5{,}05 \cdot 10^{-3}$
Molare Aktivität [GBq/µmol]		19

5.2.4 Trocknungsprozedur für Fluorid-18

Wässriges [^{18}F]F$^-$ wurde von der männlichen Seite auf eine QMA-Kartusche geladen. Zum Entfernen des Restwassers wurde die Kartusche von der männlichen Seite mit trockenem MeOH (1 mL) gespült und anschließend von der weiblichen Seite mit Luft (2 × 10 mL) getrocknet. Die Elution des [^{18}F]F$^-$ erfolgte von der weiblichen Seite mit einer Lösung von Tetraethylammoniumtriflat (Et_4NOTf) in trockenem MeOH in ein Wheaton V-Vial.

5.2.5 Herstellung von 6-[^{18}F]F-FAPI

[^{18}F]F$^-$ (0,1 – 5 GBq) wurde von einer QMA-Kartusche mit Et_4NOTf (1 mg, 4 µmol) in trockenem MeOH (500 µL) eluiert und bei 60 °C unter reduzierten Druck und im Argonstrom abgedampft. Anschließend wurde das V-Vial mit Argon geflutet und mit einem Silikonseptum versiegelt. Eine Lösung von **4** (5,1 mg, 10 µmol) und $Cu(4\text{-}PhPy)_4(ClO_4)_2$ (8,7 mg, 10 µmol) in trockenem DMI (800 µL) wurde mittels einer Kanüle durch das Septum hinzugefügt und die Reaktionslösung wurde bei 90 °C für 10 min erhitzt. Nach Abkühlen auf Raumtemperatur wurde die Reaktionsmischung mit H_2O (15 mL) verdünnt und auf eine StrataX-Kartusche geladen. Die Kartusche wurde mit H_2O (5 mL) gewaschen und das rohe Radioprodukt mit MeCN (500 µL) eluiert. Das Eluat wurde mit H_2O (1 mL) verdünnt und mittels semipräparativer HPLC aufgereinigt. Die Produktfraktion wurde bei einer Retentionszeit von 12,5 – 14,0 min erhalten. Für die Formulierung wurde die Produktfraktion mit H_2O (19 mL) verdünnt und auf eine StrataX-Kartusche geladen. Die Kartusche wurde mit H_2O (5 mL) gewaschen und luftgetrocknet. Der Radiotracer wurde mit EtOH (500 µL) eluiert und das EtOH bei 40 °C unter reduziertem Druck und im Argonstrom entfernt. Der Rückstand wurde in Tween80 aufgenommen um den Radiotracer 6-[^{18}F]F-FAPI als fertige Injektionslösung zu erhalten.

5.2.6 Herstellung von 5-[^{18}F]FMT

[^{18}F]F^- (0,1 – 5 GBq) wurde von einer QMA-Kartusche mit Et_4NOTf (1 mg, 4 µmol) in trockenem MeOH (500 µL) eluiert und bei 60 °C unter reduzierten Druck und im Argonstrom abgedampft. Anschließend wurde eine Lösung von **6** (5,1 mg, 2,5 µmol) und $Cu(4\text{-}PhPy)_4(ClO_4)_2$ (8,7 mg, 10 µmol) in trockenem DMI (800 µL) und *n*BuOH (400 µL) hinzugefügt und bei 110 °C für 10 min erhitzt. Nach Abkühlen auf Raumtemperatur wurde die Reaktionsmischung mit H_2O (15 mL) verdünnt und auf eine C18-Kartusche geladen. Die Kartusche wurde mit H_2O (5 mL) gewaschen und das ^{18}F-markierte Intermediat mit MeOH (500 µL) eluiert. MeOH wurde bei 60 °C unter reduzierten Druck und im Argonstrom abgedampft und anschließend 6 M HCl in 20% MeOH zum Rückstand hinzugegeben. Die Reaktionslösung wurde dann bei 80 °C für 10 min gerührt, nach Abkühlen auf Raumtemperatur mit 6 M NaOH (350 µL) verdünnt und in die HPLC injiziert. Die Produktfraktion wurde bei einer Retentionszeit von 11,5 – 13,0 min erhalten. Für die Formulierung wurde die Produktfraktion mit H_2O (19 mL) verdünnt und auf eine MCX-Kartusche geladen. Die Kartusche wurde mit H_2O (5 mL) gewaschen und mit luftgetrocknet. Der Radiotracer wurde mit 2 M NH_3 in EtOH (1,5 mL) eluiert und das EtOH bei 40 °C unter reduziertem Druck und im Argonstrom entfernt. Der Rückstand wurde in PBS-Puffer aufgenommen um den Radiotracer (S)-5-[^{18}F]FMT als fertige Injektionslösung zu erhalten.

6 Analytische Daten

6.1 NMR-Spektren

^{1}H-NMR Spektrum von Verbindung 3

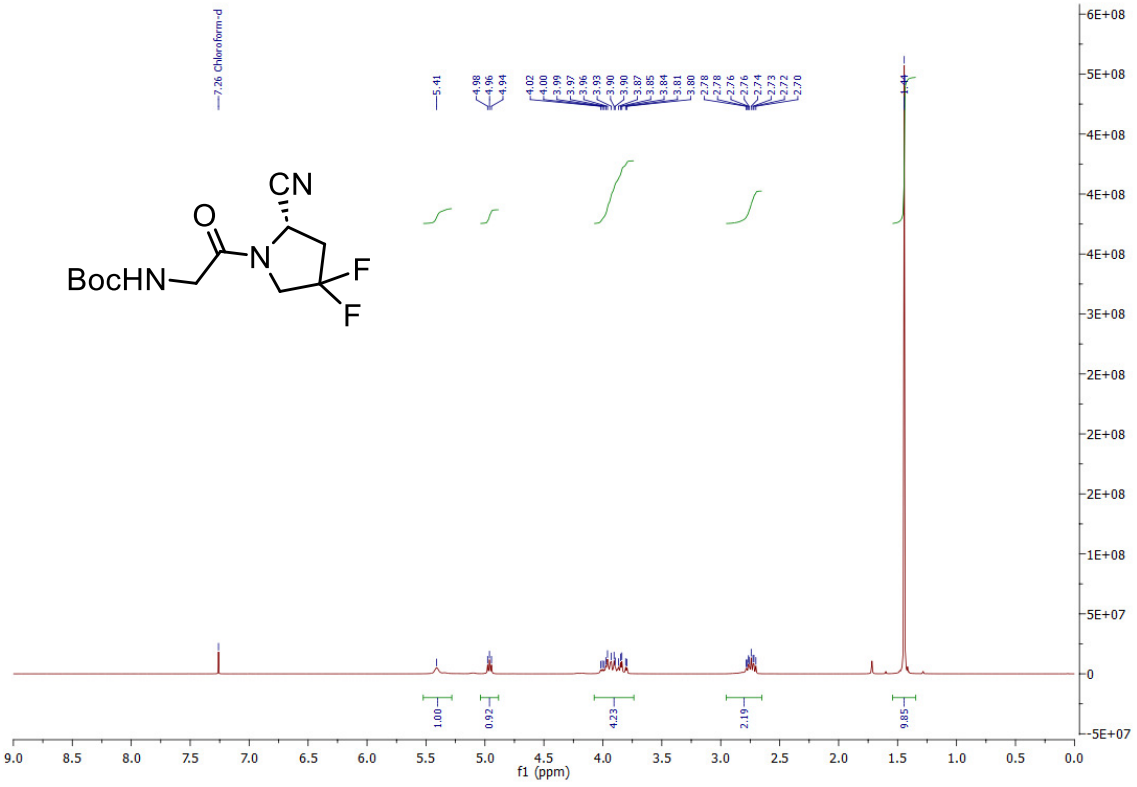

^{13}C-NMR APT Spektrum von Verbindung 3

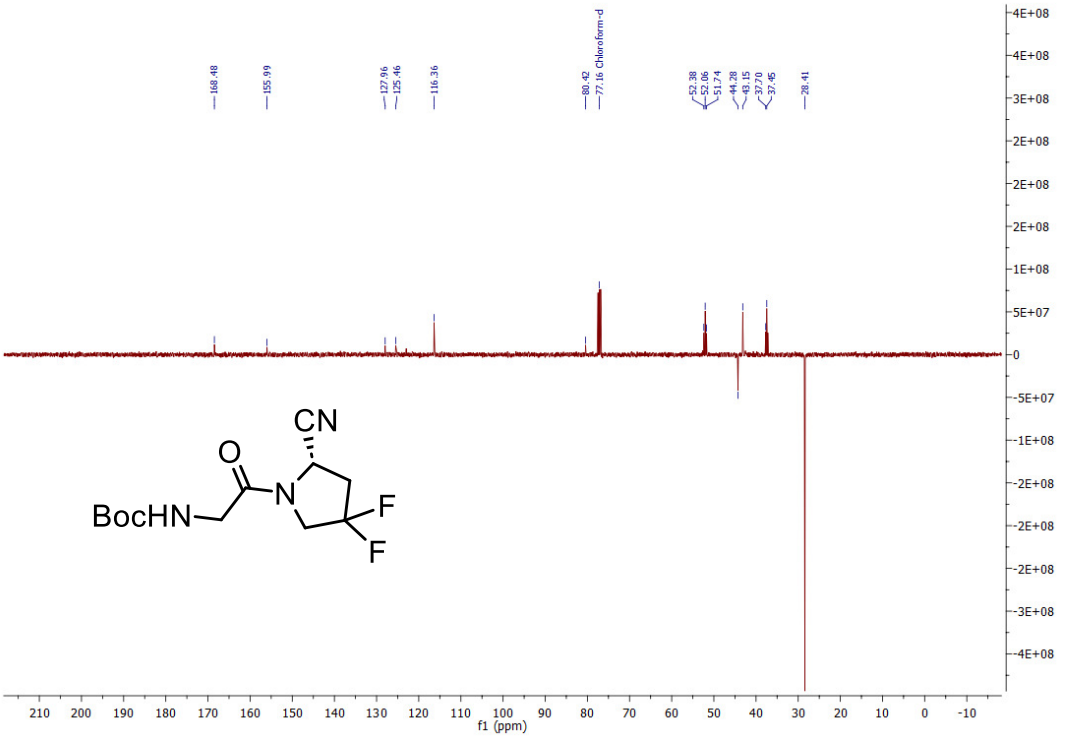

^{19}F-NMR Spektrum von Verbindung 3

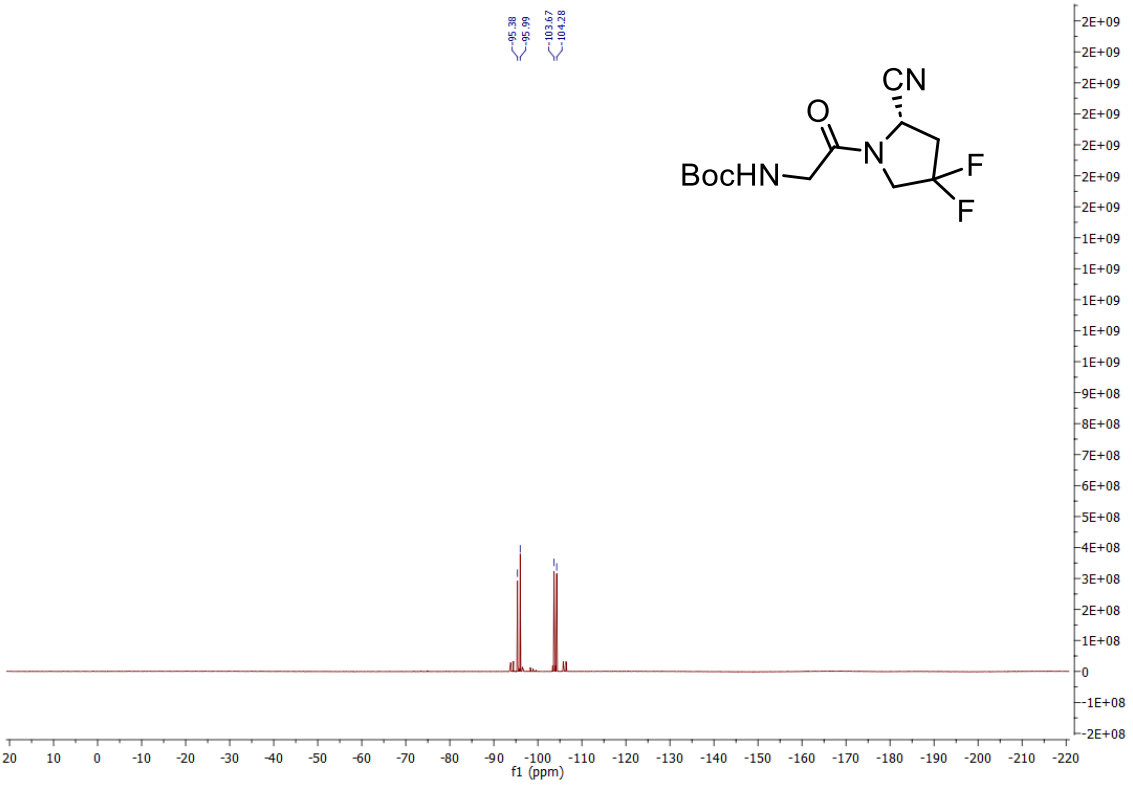

^{1}H-NMR Spektrum von Verbindung 5

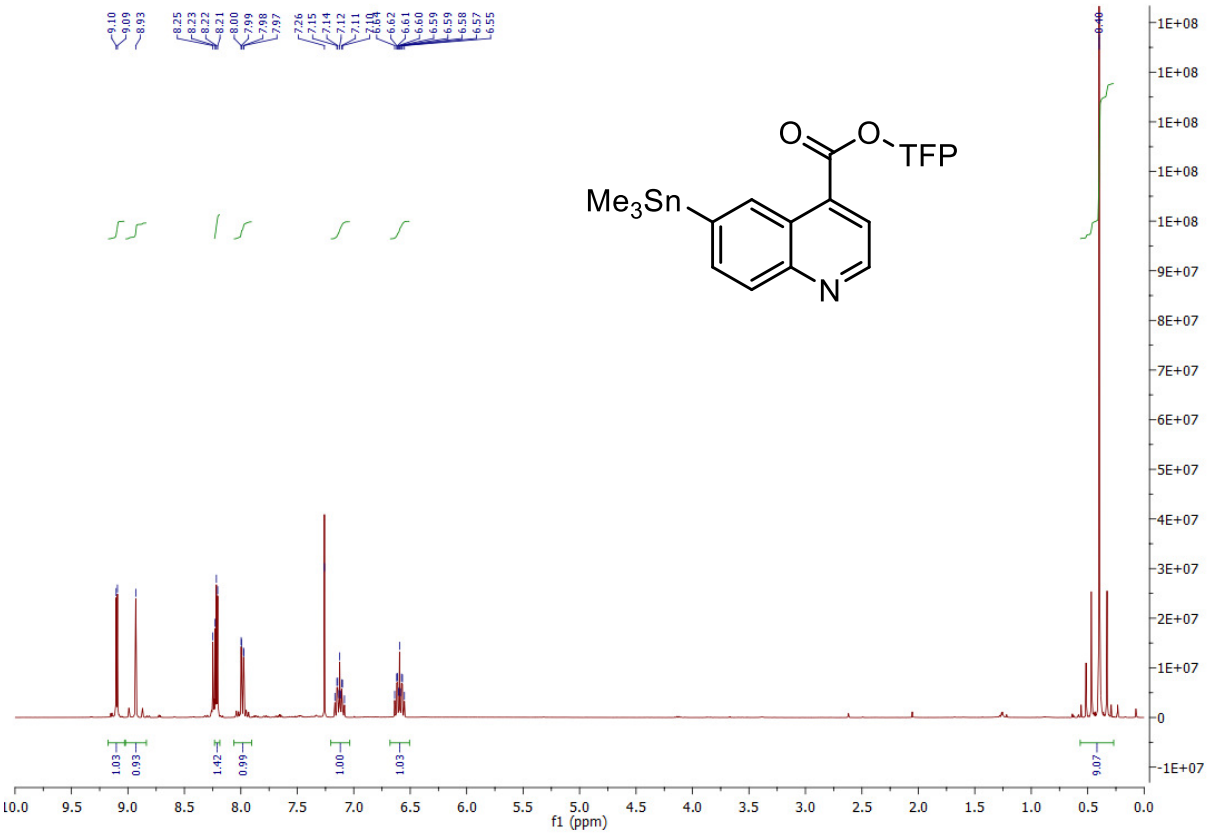

^{13}C-NMR APT Spektrum von Verbindung 5

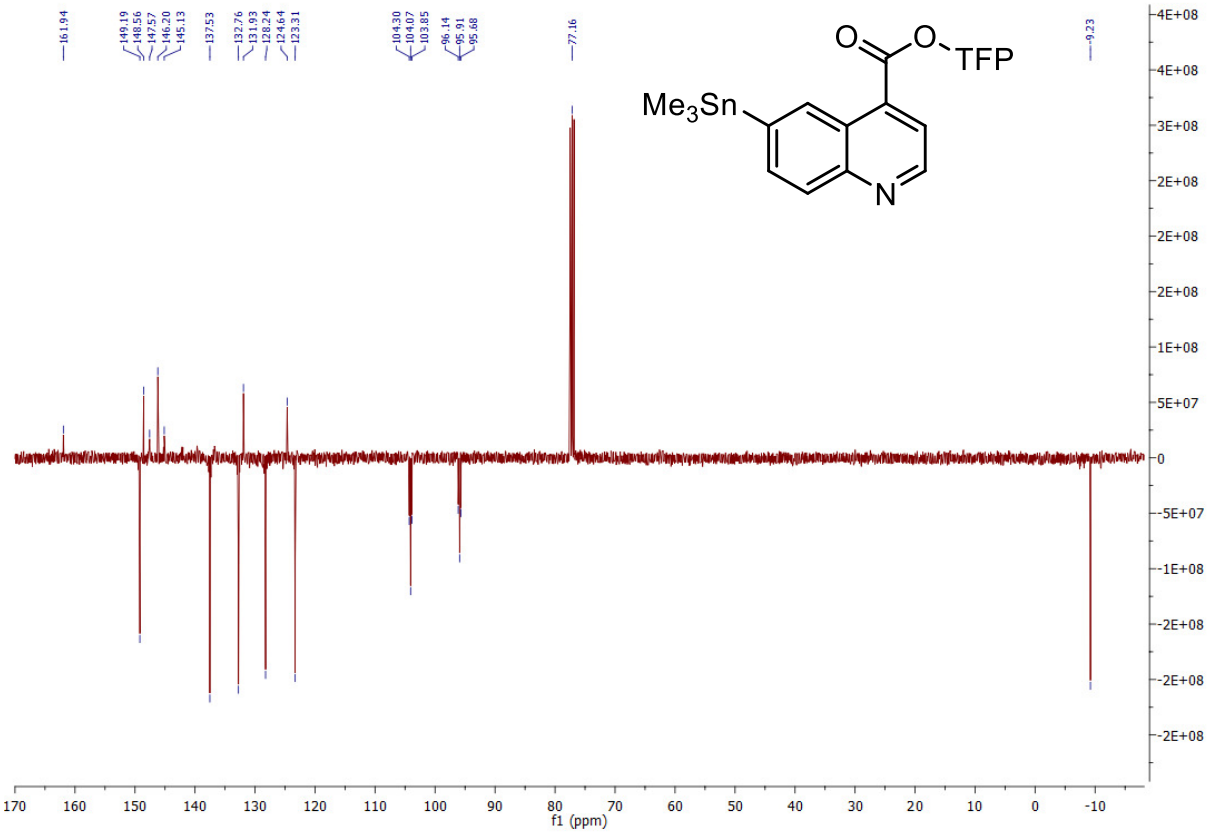

^{19}F-NMR Spektrum von Verbindung 5

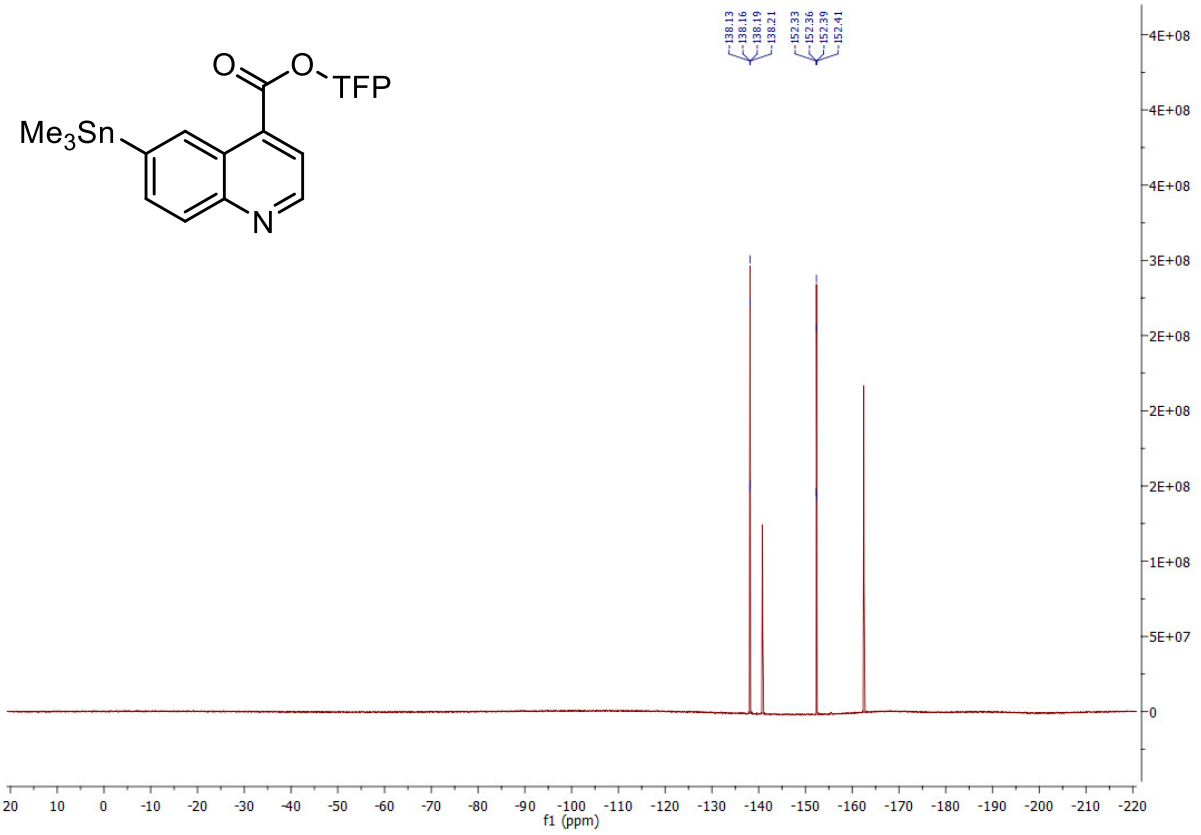

^{1}H-NMR Spektrum von Verbindung 4

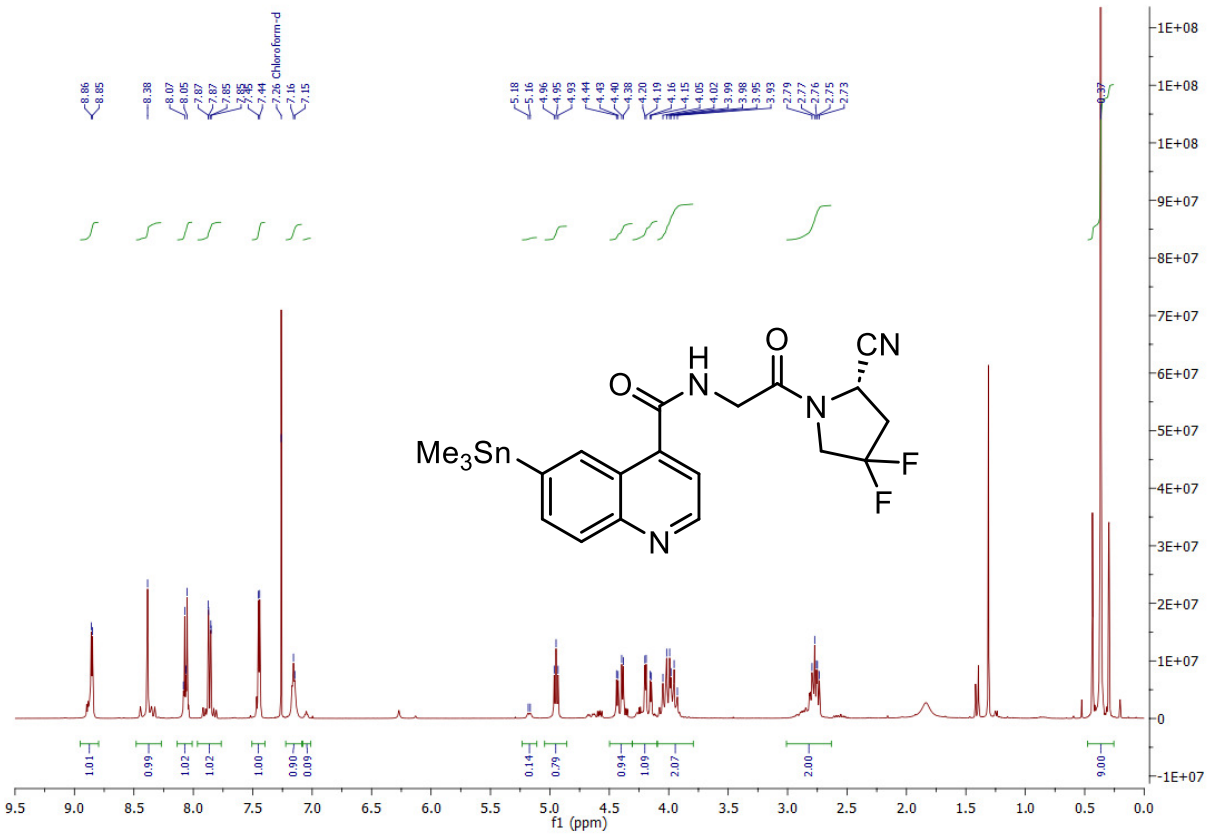

^{13}C-NMR APT Spektrum von Verbindung 4

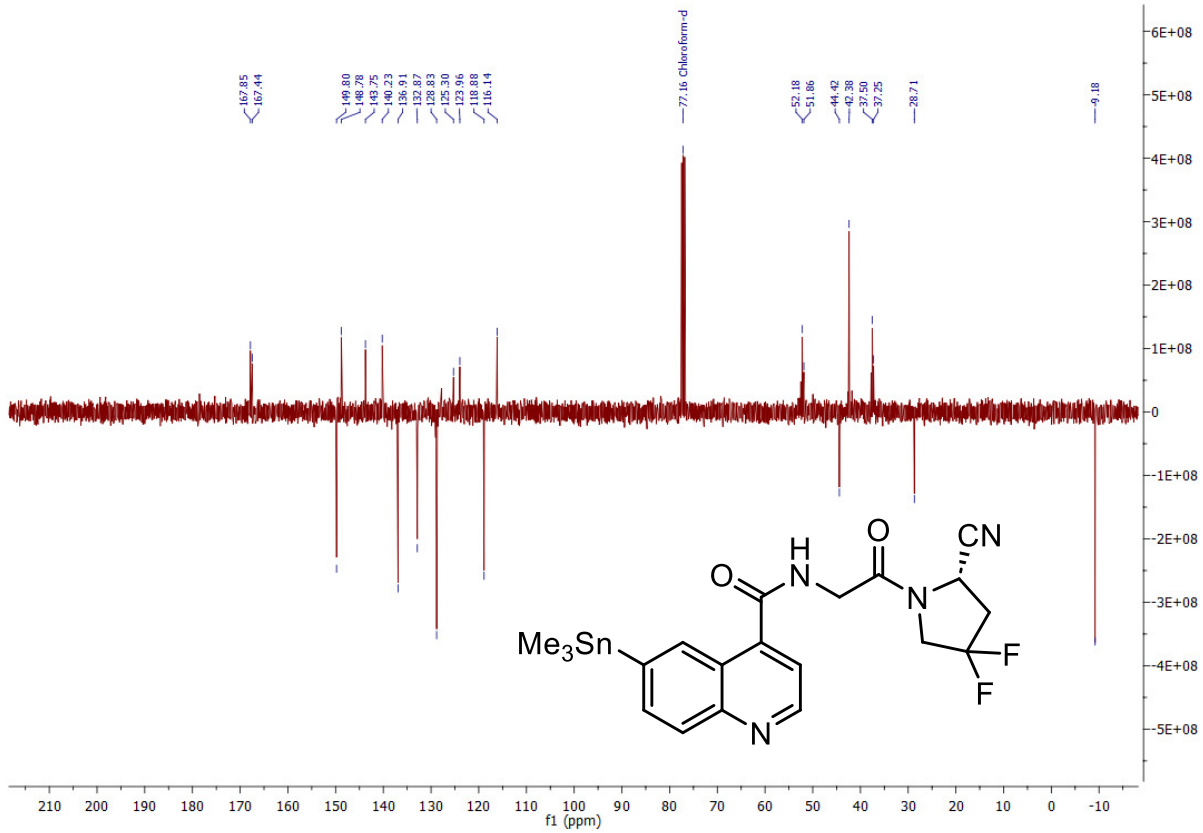

^{19}F-NMR Spektrum von Verbindung 4

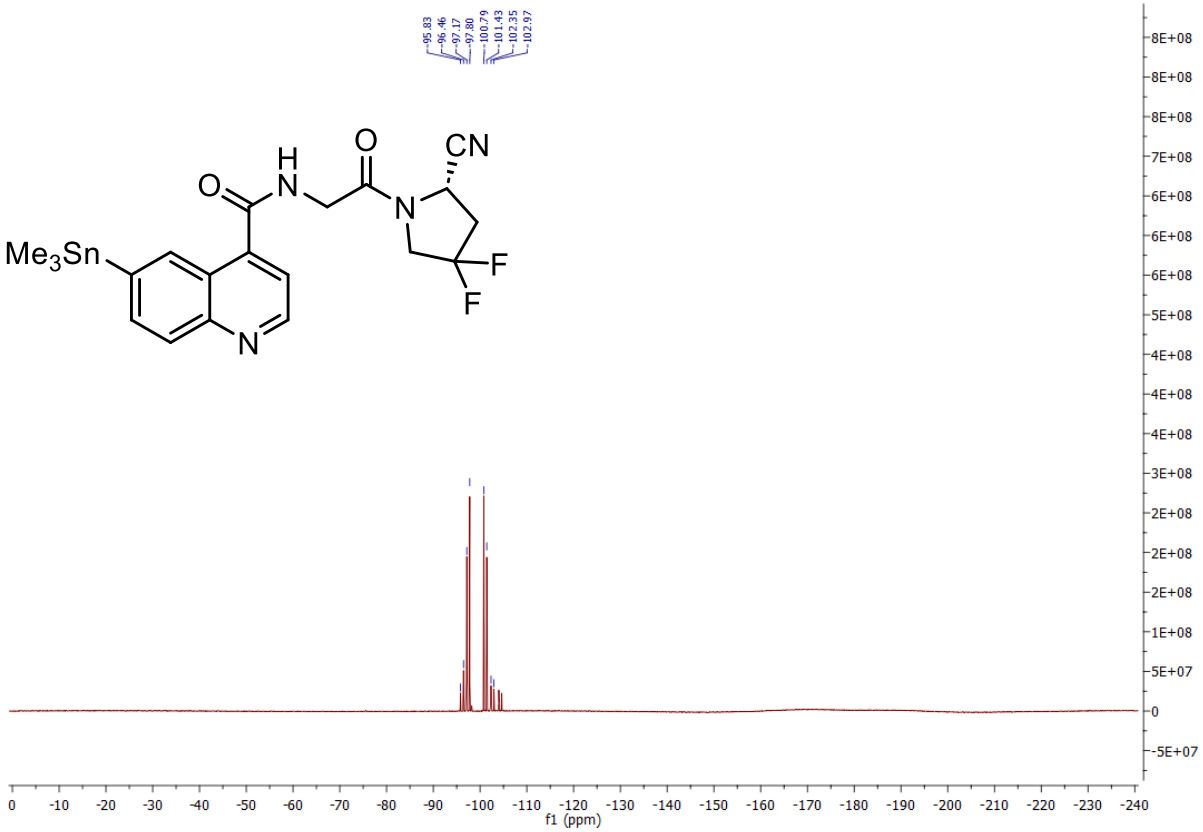

Literatur

[1] W. G. Myers, *J Nucl Med* **1979**, *20*, 590–594.

[2] A. H. Al-Ramadhan, D. W. Gidley, *Phys Rev Lett* **1994**, *72*, 1632–1635.

[3] M. D. Harpen, *Med Phys* **2004**, *31*, 57–61.

[4] P. Moskal, D. Kisielewska, C. Curceanu, E. Czerwiński, K. Dulski, A. Gajos, M. Gorgol, B. Hiesmayr, B. Jasińska, K. Kacprzak, L. Kapłon, G. Korcyl, P. Kowalski, W. Krzemień, T. Kozik, E. Kubicz, M. Mohammed, S. Niedźwiecki, M. Pałka, M. Pawlik-Niedźwiecka, L. Raczyński, J. Raj, S. Sharma, Shivani, R. Y. Shopa, M. Silarski, M. Skurzok, E. Stępień, W. Wiślicki, B. Zgardzińska, *Phys Med Biol* **2019**, *64*, 055017.

[5] R. S. Vallery, P. W. Zitzewitz, D. W. Gidley, *Phys Rev Lett* **2003**, *90*, 203402.

[6] A. THIEL, K. HERHOLZ, H.-M. VON STOCKHAUSEN, G. PAWLIK, W.-D. HEISS, in *Quantitative Functional Brain Imaging with Positron Emission Tomography* (Eds.: R.E. Carson, M.E. Daube-Witherspoon, P. Herscovitch), Academic Press, San Diego, **1998**, pp. 155–158.

[7] M. Diksic, Y. L. Yamamoto, W. Feindel, *Journal of Nuclear Medicine* **1983**, *24*, 603.

[8] G. W. Kabalka, R. M. Lambrecht, M. Sajjad, J. S. Fowler, S. A. Kunda, G. W. McCollum, R. MacGregor, *Int J Appl Radiat Isot* **1985**, *36*, 853–855.

[9] K. Takahashi, M. Murakami, E. Hagami, H. Sasaki, Y. Kondo, S. Mizusawa, H. Nakamichi, H. Iida, S. Miura, I. Kanno, K. Uemura, *J Labelled Comp Radiopharm* **1989**, *27*, 1167–1175.

[10] T. F. Budinger, Y. Yano, B. Hoop, *Journal of Nuclear Medicine* **1975**, *16*, 429.

[11] M. E. Phelps, E. J. Hoffman, R. E. Coleman, M. J. Welch, M. E. Raichle, E. S. Weiss, B. E. Sobel, M. M. Ter-Pogossian, *Journal of Nuclear Medicine* **1976**, *17*, 603.

[12] Y. KISO, S. IINUMA, T. MIMOTO, H. SAJI, A. YOKOYAMA, K. AKAJI, *Chem Pharm Bull (Tokyo)* **1991**, *39*, 2734–2736.

[13] H. Saji, D. Tsutsumi, Y. Kiso, S. Iimuma, T. Mimoto, K. Akaji, Y. Magata, H. Nakamura, A. Kita, J. Konishi, A. Yokoyama, *Int J Rad Appl Instrum B* **1992**, *19*, 455–460.

[14] G. R. Newbery, *Br J Radiol* **1959**, *32*, 633–641.

[15] D. R. Christman, R. D. Finn, K. I. Karlstrom, A. P. Wolf, *Int J Appl Radiat Isot* **1975**, *26*, 435–442.

[16] I. R. Duffy, N. Vasdev, K. Dahl, *ACS Omega* **2020**, *5*, 8242–8250.

[17] J. M. Hooker, A. T. Reibel, S. M. Hill, M. J. Schueller, J. S. Fowler, *Angewandte Chemie International Edition* **2009**, *48*, 3482–3485.

[18] D. Christman, E. J. Crawford, M. Friedkin, A. P. Wolf, *Proceedings of the National Academy of Sciences* **1972**, *69*, 988–992.

[19] J. M. Hooker, M. Schönberger, H. Schieferstein, J. S. Fowler, *Angewandte Chemie International Edition* **2008**, *47*, 5989–5992.

[20] M. Nader, F. Oberdorfer, K. Herrmann, *Applied Radiation and Isotopes* **2019**, *148*, 178–183.

[21] J. E. Jakobsson, S. Lu, S. Telu, V. W. Pike, *Angewandte Chemie International Edition* **2020**, *59*, 7256–7260.

[22] J. E. Jakobsson, S. Telu, S. Lu, S. Jana, V. W. Pike, *Chemistry – A European Journal* **2021**, *27*, 10369–10376.

[23] R. D. Finn, D. R. Christman, H. J. Ache, A. P. Wolf, *Int J Appl Radiat Isot* **1971**, *22*, 735–744.

[24] Y. Xu, W. Qu, *European J Org Chem* **2021**, *2021*, 4653–4682.

[25] Y.-P. Zhou, K. J. Makaravage, P. Brugarolas, *Nucl Med Biol* **2021**, *102–103*, 56–86.

[26] T. Haywood, S. Cesarec, S. Kealey, C. Plisson, P. W. Miller, *Medchemcomm* **2018**, *9*, 1311–1314.

[27] B. Långström, H. Lundqvist, *Int J Appl Radiat Isot* **1976**, *27*, 357–363.

[28] R. Wagner, G. Stöcklin, W. Schaack, *J Labelled Comp Radiopharm* **1981**, *18*, 1557–1566.

[29] P. Larsen, J. Ulin, K. Dahlstrøm, M. Jensen, *Applied Radiation and Isotopes* **1997**, *48*, 153–157.

[30] H. Doi, M. Goto, Y. Sato, *European J Org Chem* **2021**, *2021*, 3970–3979.

[31] D. M. Jewett, *Int J Rad Appl Instrum A* **1992**, *43*, 1383–1385.

[32] K. Någren, L. Müller, C. Halldin, C.-G. Swahn, P. Lehikoinen, *Nucl Med Biol* **1995**, *22*, 235–239.

[33] L. Rischka, C. Vraka, V. Pichler, S. Rasul, L. Nics, G. Gryglewski, P. Handschuh, M. Murgaš, G. M. Godbersen, L. R. Silberbauer, J. Unterholzner, C. Wotawa, A. Haider, H. Ahmed, R. Schibli, T. Mindt, M. Mitterhauser, W. Wadsak, A. Hahn,

R. Lanzenberger, M. Hacker, S. M. Ametamey, *Journal of Nuclear Medicine* **2022**, *63*, 936.

[34] M. R. Brier, M. Hamdi, J. Rajamanikam, H. Zhao, S. Mansor, L. Jones, F. Rahmani, S. Jindal, D. Koudelis, J. Perlmutter, D. F. Wong, M. Nickels, J. Ippolito, R. Gropler, T. H. Schindler, R. Laforest, Z. Tu, T. Benzinger, *Journal of Nuclear Medicine* **2022**, jnumed.121.263189.

[35] I. K. Lee, D. A. Jacome, J. K. Cho, V. Tu, A. J. Young, T. Dominguez, J. D. Northrup, J. M. Etersque, H. S. Lee, A. Ruff, O. Aklilu, K. Bittinger, L. J. Glaser, D. Dorgan, D. Hadjiliadis, R. M. Kohli, R. H. Mach, D. A. Mankoff, R. K. Doot, M. A. Sellmyer, *J Clin Invest* **2023**, *132*, DOI 10.1172/JCI156679.

[36] M. N. Stewart, M. F. L. Parker, S. Jivan, J. M. Luu, T. L. Huynh, B. Schulte, Y. Seo, J. E. Blecha, J. E. Villanueva-Meyer, R. R. Flavell, H. F. Vanbrocklin, M. A. Ohliger, O. Rosenberg, D. M. Wilson, *ACS Infect Dis* **2020**, *6*, 43–49.

[37] M. Szydło, M. Jadwiński, A. Chmura, K. Gorczewski, M. Sokół, *Contemporary Oncology/Współczesna Onkologia* **2016**, *20*, 229–236.

[38] J. Wenz, F. Arndt, S. Samnick, *EJNMMI Radiopharm Chem* **2022**, *7*, DOI 10.1186/S41181-022-00159-Y.

[39] F. Dollé, *J Labelled Comp Radiopharm* **1999**.

[40] H. Alva-Sánchez, C. Quintana-Bautista, A. Martínez-Dávalos, M. A. Ávila-Rodríguez, M. Rodríguez-Villafuerte, *Phys Med Biol* **2016**, *61*, 6307.

[41] G. ; S. Lottes O., *Nuklearmedizin - NuclearMedicine* **2000**, *39*, 72–76.

[42] C. M. Mueller-Platz, G. Kloster, G. Stoecklin, G. Legler, *J Labelled Comp Radiopharm* **1982**, *19*, 1645–1646.

[43] R. L. Williams, F. S. Rowland, *J Phys Chem* **1972**, *76*, 3509–3517.

[44] R. L. Williams, F. S. Rowland, *J Am Chem Soc* **1972**, *94*, 1047–1051.

[45] T. Ido, C.-N. Wan, V. Casella, J. S. Fowler, A. P. Wolf, M. Reivich, D. E. Kuhl, *J Labelled Comp Radiopharm* **1978**, *14*, 175–183.

[46] J. Rong, S. H. Liang, *Fluorination* **2018**, 1–14.

[47] V. M. Vlasov, *J Fluor Chem* **1993**, *61*, 193–216.

[48] S. Preshlock, M. Tredwell, V. Gouverneur, *Chem Rev* **2016**, *116*, 719–766.

[49] K. R. Scroggie, M. V. Perkins, J. M. Chalker, *Front Chem* **2021**, *9*, DOI 10.3389/FCHEM.2021.687678.

[50] R. Richarz, P. Krapf, F. Zarrad, E. A. Urusova, B. Neumaier, B. D. Zlatopolskiy, *Org Biomol Chem* **2014**, *12*, 8094–8099.

[51] O. Jacobson, X. Chen, *Curr Top Med Chem* **2010**, *10*, 1048–1059.

[52] K. Hamacher, H. H. Coenen, G. Stöcklin, *Journal of Nuclear Medicine* **1986**, *27*, 235.

[53] H. J. Wester, M. Herz, W. Weber, P. Heiss, R. Senekowitsch-Schmidtke, M. Schwaiger, G. Stöcklin, *Journal of Nuclear Medicine* **1999**, *40*, 205–212.

[54] J. R. Grierson, A. F. Shields, *Nucl Med Biol* **2000**, *27*, 143–156.

[55] C. K. Hoh, H. A. Burris, J. C. Bendell, J. Tarazi, B. Rosbrook, S. Kim, J. R. Infante, T. R. Reid, *Br J Cancer* **2014**, *110*, 875.

[56] M. Van Kruchten, A. W. J. M. Glaudemans, E. F. J. De Vries, R. G. H. Beets-Tan, C. P. Schröder, R. A. Dierckx, E. G. E. De Vries, G. A. P. Hospers, *Journal of Nuclear Medicine* **2012**, *53*, 182–190.

[57] J. Shi, G. Afari, S. Bhattacharyya, *J Labelled Comp Radiopharm* **2014**, *57*, 730–736.

[58] J. Mukherjee, Z.-Y. Yang, M. K. Das, T. Brown, *Nucl Med Biol* **1995**, *22*, 283–296.

[59] D. W. Kim, Jeong, S. T. Lim, M.-H. Sohn, J. A. Katzenellenbogen, D. Y. Chi, *J Org Chem* **2008**, *73*, 957–962.

[60] D. W. Kim, D.-S. Ahn, Y.-H. Oh, S. Lee, H. S. Kil, S. J. Oh, S. J. Lee, J. S. Kim, J. S. Ryu, D. H. Moon, D. Y. Chi, *J Am Chem Soc* **2006**, *128*, 16394–16397.

[61] K. Bratteby, V. Shalgunov, M. M. Herth, *ChemMedChem* **2021**, *16*, 2612–2622.

[62] V. W. Pike, F. I. Aigbirhio, *J Chem Soc Chem Commun* **1995**, 2215–2216.

[63] M. S. Yusubov, D. Y. Svitich, M. S. Larkina, V. V. Zhdankin, *Arkivoc* **2013**, *2013*, 364–395.

[64] B. H. Rotstein, N. A. Stephenson, N. Vasdev, S. H. Liang, *Nature Communications 2014 5:1* **2014**, *5*, 1–7.

[65] L. Mu, C. R. Fischer, J. P. Holland, J. Becaud, P. A. Schubiger, R. Schibli, S. M. Ametamey, K. Graham, T. Stellfeld, L. M. Dinkelborg, L. Lehmann, *European J Org Chem* **2012**, *2012*, 889–892.

[66] K. Sander, T. Gendron, E. Yiannaki, K. Cybulska, T. L. Kalber, M. F. Lythgoe, E. Årstad, *Scientific Reports 2015 5:1* **2015**, *5*, 1–5.

[67] M. A. Carroll, S. Martín-Santamaría, V. W. Pike, H. S. Rzepa, D. A. Widdowson, *Journal of the Chemical Society, Perkin Transactions 2* **1999**, *0*, 2707–2714.

[68] W. Chen, Z. Huang, N. E. S. Tay, B. Giglio, M. Wang, H. Wang, Z. Wu, D. A. Nicewicz, Z. Li, *Science (1979)* **2019**, *364*, 1170–1174.

[69] L. Wang, A. R. White, W. Chen, Z. Wu, D. A. Nicewicz, Z. Li, *Org Lett* **2020**, *22*, 7971–7975.

[70] W. Entzian, S. Aronow, A. H. Soloway, W. H. Sweet, *Journal of Nuclear Medicine* **1964**, *5*, 542.

[71] R. Ting, M. J. Adam, T. J. Ruth, D. M. Perrin, *J Am Chem Soc* **2005**, *127*, 13094–13095.

[72] R. Ting, C. W. Harwig, J. Lo, Y. Li, M. J. Adam, T. J. Ruth, D. M. Petrin, *Journal of Organic Chemistry* **2008**, *73*, 4662–4670.

[73] Z. Li, K. Chansaenpak, S. Liu, C. R. Wade, P. S. Conti, F. P. Gabbaï, *Medchemcomm* **2012**, *3*, 1305–1308.

[74] Y. Li, J. Guo, S. Tang, L. Lang, X. Chen, D. M. Perrin, *Am J Nucl Med Mol Imaging* **2013**, *3*, 44.

[75] Z. Liu, M. Pourghiasian, M. A. Radtke, J. Lau, J. Pan, G. M. Dias, D. Yapp, K.-S. Lin, F. Bønard, D. M. Perrin, **n.d.**, DOI 10.1002/ange.201406258.

[76] F. An, F. Nurili, H. Sayman, Z. Ozer, H. Cakiroglu, O. Aras, R. Ting, *J Med Chem* **2020**, *63*, 12693–12706.

[77] M. S. Rosenthal, A. L. Bosch, R. J. Nickles, S. J. Gatley, *Int J Appl Radiat Isot* **1985**, *36*, 318–319.

[78] R. Ting, M. J. Adam, T. J. Ruth, D. M. Perrin, *J Am Chem Soc* **2005**, *127*, 13094–13095.

[79] R. Schirrmacher, G. Bradtmöller, E. Schirrmacher, O. Thews, J. Tillmanns, T. Siessmeier, H. G. Buchholz, P. Bartenstein, B. Wängler, C. M. Niemeyer, K. Jurkschat, *Angewandte Chemie International Edition* **2006**, *45*, 6047–6050.

[80] M. Tisseraud, J. Schulz, D. Vimont, M. Berlande, P. Fernandez, P. Hermange, E. Fouquet, *Chemical Communications* **2018**, *54*, 5098–5101.

[81] C. Wängler, B. Waser, A. Alke, L. Iovkova, H. G. Buchholz, S. Niedermoser, K. Jurkschat, C. Fottner, P. Bartenstein, R. Schirrmacher, J. C. Reubi, H. J. Wester, B. Wängler, *Bioconjug Chem* **2010**, *21*, 2289–2296.

[82] J. A. H. Inkster, K. Liu, S. Ait-Mohand, P. Schaffer, B. Guérin, T. J. Ruth, T. Storr, *Chemistry – A European Journal* **2012**, *18*, 11079–11087.

[83] X. Deng, Z. Wang, H. Zhou, J. Liu, B. Yu, X. Zhu, *Org Lett* **2023**, *25*, 1969–1973.

[84] M. K. Nielsen, C. R. Ugaz, W. Li, A. G. Doyle, *J Am Chem Soc* **2015**, *137*, 9571–9574.

[85] B. Zhang, B. H. Fraser, M. A. Klenner, Z. Chen, S. H. Liang, M. Massi, A. J. Robinson, G. Pascali, *Chemistry – A European Journal* **2019**, *25*, 7613–7617.

[86] Q. Zheng, H. Xu, H. Wang, W. G. H. Du, N. Wang, H. Xiong, Y. Gu, L. Noodleman, K. B. Sharpless, G. Yang, P. Wu, *J Am Chem Soc* **2021**, *143*, 3753–3763.

[87] N. Walter, J. Bertram, B. Drewes, V. Bahutski, M. Timmer, M. B. Schütz, F. Krämer, F. Neumaier, H. Endepols, B. Neumaier, B. D. Zlatopolskiy, *Eur J Med Chem* **2022**, *237*, 114383.

[88] M. H. Jeon, Y. Do Kwon, M. P. Kim, G. B. Torres, J. K. Seo, J. Son, Y. H. Ryu, S. Y. Hong, J. H. Chun, *Org Lett* **2021**, *23*, 2766–2771.

[89] W. J. McBride, R. M. Sharkey, H. Karacay, C. A. D'Souza, E. A. Rossi, P. Laverman, C. H. Chang, O. C. Boerman, D. M. Goldenberg, *Journal of Nuclear Medicine* **2009**, *50*, 991–998.

[90] S. C. Ghosh, K. L. Pinkston, H. Robinson, B. R. Harvey, N. Wilganowski, K. Gore, E. M. Sevick-Muraca, A. Azhdarinia, *Nucl Med Biol* **2015**, *42*, 177–183.

[91] C. A. D'Souza, W. J. McBride, R. M. Sharkey, L. J. Todaro, D. M. Goldenberg, *Bioconjug Chem* **2011**, *22*, 1793–1803.

[92] D. Shetty, S. Y. Choi, J. M. Jeong, J. Y. Lee, L. Hoigebazar, Y. S. Lee, D. S. Lee, J. K. Chung, M. C. Lee, Y. K. Chung, *Chemical Communications* **2011**, *47*, 9732–9734.

[93] C. A. D'Souza, W. J. McBride, R. M. Sharkey, L. J. Todaro, D. M. Goldenberg, *Bioconjug Chem* **2011**, *22*, 1793–1803.

[94] C. Da Pieve, A. Makarem, S. Turnock, J. Maczynska, G. Smith, G. Kramer-Marek, *Molecules 2020, Vol. 25, Page 1562* **2020**, *25*, 1562.

[95] R. Bruce Martin, *Biochem Biophys Res Commun* **1988**, *155*, 1194–1200.

[96] W. J. McBride, R. M. Sharkey, D. M. Goldenberg, *EJNMMI Res* **2013**, *3*, 1–11.

[97] T. Tshibangu, C. Cawthorne, K. Serdons, E. Pauwels, W. Gsell, G. Bormans, C. M. Deroose, F. Cleeren, *EJNMMI Radiopharm Chem* **2020**, *5*, 1–23.

[98] T. Liu, C. Liu, X. Xu, F. Liu, X. Guo, N. Li, X. Wang, J. Yang, X. Yang, H. Zhu, Z. Yang, *Journal of Nuclear Medicine* **2019**, *60*, 1284–1292.

[99] K. Hu, L. Wang, H. Wu, S. Huang, Y. Tian, Q. Wang, C. Xiao, Y. Han, G. Tang, *Eur J Nucl Med Mol Imaging* **2022**, *49*, 2833–2843.

[100] L. Russelli, J. Martinelli, F. De Rose, S. Reder, M. Herz, M. Schwaiger, W. Weber, L. Tei, C. D'Alessandria, *ChemMedChem* **2020**, *15*, 284–292.

[101] X. Qin, X. Guo, T. Liu, L. Li, N. Zhou, X. Ma, X. Meng, J. Liu, H. Zhu, B. Jia, Z. Yang, *Eur J Nucl Med Mol Imaging* **2023**, *50*, 302–313.

[102] E. Lee, A. S. Kamlet, D. C. Powers, C. N. Neumann, G. B. Boursalian, T. Furuya, D. C. Choi, J. M. Hooker, T. Ritter, *Science (1979)* **2011**, *334*, 639–642.

[103] E. Lee, J. M. Hooker, T. Ritter, *J Am Chem Soc* **2012**, *134*, 17456–17458.

[104] P. S. Fier, J. F. Hartwig, *J Am Chem Soc* **2012**, *134*, 10795–10798.

[105] P. S. Fier, J. Luo, J. F. Hartwig, *J Am Chem Soc* **2013**, *135*, 2552–2559.

[106] N. Ichiishi, A. F. Brooks, J. J. Topczewski, M. E. Rodnick, M. S. Sanford, P. J. H. Scott, *Org Lett* **2014**, *16*, 3224–3227.

[107] M. Tredwell, S. M. Preshlock, N. J. Taylor, S. Gruber, M. Huiban, J. Passchier, J. Mercier, C. Génicot, V. Gouverneur, *Angewandte Chemie International Edition* **2014**, *53*, 7751–7755.

[108] A. V Mossine, A. F. Brooks, K. J. Makaravage, J. M. Miller, N. Ichiishi, M. S. Sanford, P. J. H. Scott, *Org Lett* **2015**, *17*, 5780–5783.

[109] K. J. Makaravage, A. F. Brooks, A. V Mossine, M. S. Sanford, P. J. H. Scott, *Org Lett* **2016**, *18*, 5440–5443.

[110] N. Ichiishi, A. J. Canty, B. F. Yates, M. S. Sanford, *Org Lett* **2013**, *15*, 5134–5137.

[111] N. Ichiishi, A. J. Canty, B. F. Yates, M. S. Sanford, *Organometallics* **2014**, *33*, 5525–5534.

[112] J. S. Wright, T. Kaur, S. Preshlock, S. S. Tanzey, W. P. Winton, L. S. Sharninghausen, N. Wiesner, A. F. Brooks, M. S. Sanford, P. J. H. Scott, *Clinical and Translational Imaging 2020 8:3* **2020**, *8*, 167–206.

[113] B. D. Zlatopolskiy, J. Zischler, P. Krapf, F. Zarrad, E. A. Urusova, E. Kordys, H. Endepols, B. Neumaier, *Chemistry – A European Journal* **2015**, *21*, 5972–5979.

[114] T. Ishiyama, M. Murata, N. Miyaura, *Journal of Organic Chemistry* **1995**, *60*, 7508–7510.

[115] J. C. Vantourout, H. N. Miras, A. Isidro-Llobet, S. Sproules, A. J. B. Watson, *J Am Chem Soc* **2017**, *139*, 4769–4779.

[116] Q. Zhang, Y. Liu, T. Wang, X. Zhang, C. Long, Y.-D. Wu, M.-X. Wang, *J Am Chem Soc* **2018**, *140*, 5579–5587.

[117] Y. Ye, S. D. Schimler, P. S. Hanley, M. S. Sanford, *J Am Chem Soc* **2013**, *135*, 16292–16295.

[118] F. Zarrad, B. D. Zlatopolskiy, P. Krapf, J. Zischler, B. Neumaier, *Molecules 2017, Vol. 22, Page 2231* **2017**, *22*, 2231.

[119] L. S. Sharninghausen, A. F. Brooks, W. P. Winton, K. J. Makaravage, P. J. H. Scott, M. S. Sanford, *J Am Chem Soc* **2020**, *142*, 7362–7367.

[120] J. R. Pliego, *J Organomet Chem* **2022**, *973–974*, 122397.

[121] M. B. Nodwell, H. Yang, M. Čolović, Z. Yuan, H. Merkens, R. E. Martin, F. Bénard, P. Schaffer, R. Britton, *J Am Chem Soc* **2017**, *139*, 3595–3598.

[122] Z. Yuan, M. B. Nodwell, H. Yang, N. Malik, H. Merkens, F. Bénard, R. E. Martin, P. Schaffer, R. Britton, *Angewandte Chemie International Edition* **2018**, *57*, 12733–12736.

[123] T. Truong, K. Klimovica, O. Daugulis, *J Am Chem Soc* **2013**, *135*, 9342–9345.

[124] S. J. Lee, K. J. Makaravage, A. F. Brooks, P. J. H. Scott, M. S. Sanford, *Angew Chem Int Ed Engl* **2019**, *58*, 3119–3122.

[125] D. Shabashov, O. Daugulis, *J Am Chem Soc* **2010**, *132*, 3965–3972.

[126] J. Zischler, N. Kolks, D. Modemann, B. Neumaier, B. D. Zlatopolskiy, *Chemistry - A European Journal* **2017**, *23*, DOI 10.1002/chem.201604633.

[127] J. W. Newcomer, J. H. Krystal, *Hippocampus* **2001**, *11*, 529–542.

[128] M. Carlsson, A. Carlsson, *Trends Neurosci* **1990**, *13*, 272–276.

[129] J. W. Olney, J. W. Newcomer, N. B. Farber, *J Psychiatr Res* **1999**, *33*, 523–533.

[130] J. Gomeza, K. Ohno, H. Betz, *Current opinion in drug discovery & development* **2003**, *6*, 675–682.

[131] D. C. Javitt, *Hillside J Clin Psychiatry* **1987**, *9*, 12–35.

[132] A. C. Lahti, M. A. Weiler, M. Tamara, A. Parwani, C. A. Tamminga, *Neuropsychopharmacology* **2001**, *25*, 455–467.

[133] D. W. Choi, in *Prog Brain Res* (Ed.: F.E. Bloom), Elsevier, **1994**, pp. 47–51.

[134] K. W. Perry, J. F. Falcone, M. J. Fell, J. W. Ryder, H. Yu, P. L. Love, J. Katner, K. D. Gordon, M. R. Wade, T. Man, G. G. Nomikos, L. A. Phebus, A. J. Cauvin, K. W. Johnson, C. K. Jones, B. J. Hoffmann, G. E. Sandusky, M. W. Walter, W. J. Porter, L. Yang, K. M. Merchant, H. E. Shannon, K. A. Svensson, *Neuropharmacology* **2008**, *55*, 743–754.

[135] H. T. Ravert, W. B. Mathews, M. A. Klitenick, D. F. Wong, R. F. Dannals, *J Labelled Comp Radiopharm* **2001**, *44*, 241–246.

[136] C. Hoffmann, S. Evcüman, F. Neumaier, B. D. Zlatopolskiy, S. Humpert, D. Bier, M. Holschbach, A. Schulze, H. Endepols, B. Neumaier, *ACS Chem Neurosci* **2021**, *12*, 3335–3346.

[137] K. J. Makaravage, A. F. Brooks, A. V Mossine, M. S. Sanford, P. J. H. Scott, *Org Lett* **2016**, *18*, 5440–5443.

[138] D. Antuganov, M. Zykov, V. Timofeev, K. Timofeeva, Y. Antuganova, V. Orlovskaya, O. Fedorova, R. Krasikova, *European J Org Chem* **2019**, *2019*, 918–922.

[139] C. Hoffmann, N. Kolks, D. Smets, A. Haseloer, B. Gröner, E. A. Urusova, H. Endepols, F. Neumaier, U. Ruschewitz, A. Klein, B. Neumaier, B. D. Zlatopolskiy, *Chemistry – A European Journal* **2022**, *n/a*, e202202965.

[140] J. A. J. Schmitt, M. Wingen, J. G. Ramaekers, E. A. T. Evers, W. J. Riedel, *Curr Pharm Des* **2006**, *12*, 2473–2486.

[141] G. Zhang, R. W. Stackman, *Front Pharmacol* **2015**, *6*, 159509.

[142] N. M. Barnes, G. P. Ahern, C. Becamel, J. Bockaert, M. Camilleri, S. Chaumont-Dubel, S. Claeysen, K. A. Cunningham, K. C. Fone, M. Gershon, G. Di Giovanni, N. M. Goodfellow, A. L. Halberstadt, R. M. Hartley, G. Hassaine, K. Herrick-Davis, R. Hovius, E. Lacivita, E. K. Lambe, M. Leopoldo, F. O. Levy, S. C. R. Lummis, P. Marin, L. Maroteaux, A. C. McCreary, D. L. Nelson, J. F. Neumaier, A. Newman-Tancredi, H. Nury, A. Roberts, B. L. Roth, A. Roumier, G. J. Sanger, M. Teitler, T. Sharp, C. M. Villalón, H. Vogel, S. W. Watts, D. Hoyer, *Pharmacol Rev* **2021**, *73*, 310.

[143] M. Naughton\, J. B. [Mulrooney, B. E. [Leonardd, **n.d.**, DOI 10.1002/1099-1077.

[144] B. Dean, W. Hayes, *Schizophr Res* **1996**, *21*, 133–139.

[145] J. J. Rodríguez, H. N. Noristani, A. Verkhratsky, *Prog Neurobiol* **2012**, *99*, 15–41.

[146] E. K. Perry, R. H. Perry, J. M. Candy, A. F. Fairbairn, G. Blessed, D. J. Dick, B. E. Tomlinson, *Neurosci Lett* **1984**, *51*, 353–357.

[147] H. Cohen, *Depress Anxiety* **2005**, *22*, 84–93.

[148] W. K. Kroeze, B. L. Roth, *Biol Psychiatry* **1998**, *44*, 1128–1142.

[149] H. Y. Meltzer, *Neuropsychopharmacology 1999 21:1* **1999**, *21*, 106–115.

[150] H. B. Simpson, M. Slifstein, J. Bender, X. Xu, E. Hackett, M. J. Maher, A. Abi-Dargham, *Biol Psychiatry* **2011**, *70*, 897–904.

[151] Z. Bhagwagar, R. Hinz, M. Taylor, S. Fancy, P. Cowen, P. Grasby, *American Journal of Psychiatry* **2006**, *163*, 1580–1587.

[152] H. Ito, S. Nyberg, C. Halldin, C. Lundkvist, L. Farde, **n.d.**

[153] G. Pauwelyn, L. Vlerick, R. Dockx, J. Verhoeven, A. Dobbeleir, T. Bosmans, K. Peremans, C. Vanhove, I. Polis, F. De Vos, *BMC Vet Res* **2019**, *15*, 1–11.

[154] J. H. Meyer, S. Kapur, S. Houle, J. DaSilva, B. Owczarek, G. M. Brown, A. A. Wilson, S. H. Kennedy, *American Journal of Psychiatry* **1999**, *156*, 1029–1034.

[155] M. Willmann, J. Hegger, B. Neumaier, J. Ermert, *ACS Med Chem Lett* **2021**, *12*, 738–744.

[156] U. Mühlhausen, J. Ermert, H. H. Coenen, *J Labelled Comp Radiopharm* **2009**, *52*, 13–22.

[157] A. A. Fitzgerald, L. M. Weiner, *Cancer and Metastasis Reviews 2020 39:3* **2020**, *39*, 783–803.

[158] E. J. Hamson, F. M. Keane, S. Tholen, O. Schilling, M. D. Gorrell, *Proteomics Clin Appl* **2014**, *8*, 454–463.

[159] A. Loktev, T. Lindner, W. Mier, J. Debus, A. Altmann, D. Jäger, F. Giesel, C. Kratochwil, P. Barthe, C. Roumestand, U. Haberkorn, *Journal of Nuclear Medicine* **2018**, *59*, 1423–1429.

[160] T. Lindner, A. Loktev, A. Altmann, F. Giesel, C. Kratochwil, J. Debus, D. Jäger, W. Mier, U. Haberkorn, *Journal of Nuclear Medicine* **2018**, *59*, 1415–1422.

[161] C. Meyer, M. Dahlbom, T. Lindner, S. Vauclin, C. Mona, R. Slavik, J. Czernin, U. Haberkorn, J. Calais, *Journal of Nuclear Medicine* **2020**, *61*, 1171.

[162] K. Hu, J. Li, L. Wang, Y. Huang, L. Li, S. Ye, Y. Han, S. Huang, H. Wu, J. Su, G. Tang, *Acta Pharm Sin B* **2022**, *12*, 867–875.

[163] N. Zhang, F. Pan, L. Pan, W. Diao, F. Su, R. Huang, B. Yang, Y. Li, Z. Qi, W. Zhang, X. Wu, *Front Bioeng Biotechnol* **2023**, *11*, 1167329.

[164] Z. Yu, Y. Huang, H. Chen, Z. Jiang, C. Li, Y. Xie, Z. Li, X. Cheng, Y. Liu, S. Li, Y. Liang, Z. Wu, *ACS Pharmacol Transl Sci* **2023**, *6*, 1745–1757.

[165] K. Jansen, L. Heirbaut, R. Verkerk, J. D. Cheng, J. Joossens, P. Cos, L. Maes, A.-M. Lambeir, I. De Meester, K. Augustyns, P. Van der Veken, *J Med Chem* **2014**, *57*, 3053–3074.

[166] J. L. Lanciego, N. Luquin, J. A. Obeso, *Cold Spring Harb Perspect Med* **2012**, *2*, DOI 10.1101/CSHPERSPECT.A009621.

[167] O. T. Dejesus, C. J. Endres, S. E. Shelton, R. J. Nickles, J. E. Holden, **n.d.**

[168] P. Cumming, A. Ase, M. Diksic, J. Harrison, D. Jolly, H. Kuwabara, C. Laliberté, A. Gjedde, *Biochem Pharmacol* **1995**, *50*, 943–946.

[169] J. R. Barrio, S.-C. Huang, D.-C. Yu, W. P. Melega, J. Quintana, S. R. Cherry, A. Jacobson, M. Namavari, N. Satyamurthy, M. E. Phelps, *Journal of Cerebral Blood Flow & Metabolism* **1996**, *16*, 667–678.

[170] A. V. Mossine, S. S. Tanzey, A. F. Brooks, K. J. Makaravage, N. Ichiishi, J. M. Miller, B. D. Henderson, T. Erhard, C. Bruetting, M. B. Skaddan, M. S. Sanford, P. J. H. Scott, *Nature Protocols 2020 15:5* **2020**, *15*, 1742–1759.

[171] S. Humpert, C. Hoffmann, F. Neumaier, B. D. Zlatopolskiy, B. Neumaier, *J Chromatogr B Analyt Technol Biomed Life Sci* **2023**, *1228*, DOI 10.1016/J.JCHROMB.2023.123847.

Abkürzungsverzeichnis

[^{11}C]CS1P1	3-((2-Fluor-4-(5-(2′-methyl-2-(trifluormethyl)-[1,1′-biphenyl]-4-yl)-1,2,4-oxadiazol-3-yl)benzyl)-([^{11}C]methyl)amino)-propansäure
(*R*)-[^{11}C]Me-NB1	(1*R*)-2,3,4,5-Tetrahydro-7-methoxy-3-(4-phenylbutyl)-1*H*-3-benzazepin-1-ol
[^{11}C]MET	[^{11}C]Methionin
[^{11}C]TMP	5-(3,5-Dimethoxy-4-([^{11}C]methoxy)benzyl)pyrimidin-2,4-diamin
[^{18}F]AlF	[^{18}F]Aluminiumfluorid
[^{18}F]EFS	Ethylen-[^{18}F]Sulfonylfluorid
[^{18}F]FBAM	*N*-[6-(4-[^{18}F]Fluorbenzyldin)aminooxyhexyl]maleimid
[^{18}F]FBEM	*N*-[2-(4-[^{18}F]Fluorbenzamido)ethyl]maleimid
[^{18}F]FBS	[^{18}F]Fluorbenzoesäure
6-[^{18}F]FDA	6-[^{18}F]Fluor-3,4-hydroxyphenethylamin
[^{18}F]FDAA	*N*-[(2,5-dimethoxyphenyl)methyl]-*N*-(5-[^{18}F]fluor-2-phenoxyphenyl)acetamid
[^{18}F]FDG	[^{18}F]Fluor-D-glucose
[^{18}F]FDM	[^{18}F]Fluor-D-mannose
6-[^{18}F]FDOPA	6-[^{18}F]Fluor-L-3,4-dihydroxyphenylalanin
[^{18}F]FES	[^{18}F]Fluorestradiol
[^{18}F]FET	*O*-(2-[^{18}F]Fluorethyl)-L-tyrosin
[^{18}F]FLT	[^{18}F]Fluor-3-desoxy-L-thymidin
5-[^{18}F]FMT	5-[^{18}F]Fluor-*m*-tyrosin
[^{18}F]FPhe	[^{18}F]Fluorphenylalanin
[^{18}F]FTMS	[^{18}F]Fluortrimethylsilan
[^{18}F]MF	[^{18}F]Metallfluorid
[^{18}F]SFB	*N*-Succinimidyl-4-[^{18}F]fluorbenzoesäurester
[^{18}F]SiFA	[^{18}F]Fluor-di-*tert*-butylphenylsilan
[^{18}F]TBAF	[^{18}F]Tetrabutylammoniumfluorid
[^{18}F]TEAF	[^{18}F]Tetraethylammoniumfluorid
4-PhPy	4-Phenylpyridin
18-Krone-6	1,4,7,10,13,16-Hexaoxacyclooctadecan

AA	Aktivitätsausbeute
AADC	Aromatische Aminosäure-Decarboxylase
2-AMPTA	2-aminomethylpiperidinetriacetate
2-AMPDA-HB	2-(N-(2-Hydroxybenzyl)aminomethyl)piperidine
AG	Abgangsgruppe
A_M	Molare Aktivität
Boc	*tert*-Butyloxycarbonyl
BPin	Boronsäurepinakolester
*n*BuOH	*n*-Butanol
^{t}BuOH	*tert*-Butanol
CAF	engl. „*cancer-assoziated fibroblast*“ – krebsassoziierte Fibroblasten
COMT	Catechol-O-methyltransferase
CVRF	Cu-vermittelte Radiofluorierung
CyHex	Cyclohexan
DABSO	1,4-Diazabicyclo[2.2.2]octan-1,4-diium-1,4-disulfinat
DBU	Diazabyzykloundeken
DMA	*N*-Dimethylacedamid
DMAP	*N*-Dimethylaminopiperidin
DMF	Dimethylformamid
DMI	*N*-1,3-Dimethyl-2-imidazolidion
DMSO	Dimethylsulfoxid
L-DOPA	L-3,4-Dihydroxyphenylalanin
EtOAc	Essigsäureethylester
EtOH	Ethanol
FAP	Fibroblast aktiviertes Protein
FAPI	Fibroblast aktiviertes Proteininhibitor
GlyT1	Glyzintransporter Typ 1
HPLC	engl. „*High-performance liquid chromatography*”
H_3RESCA	2-{[trans-2-[benzyl(carboxymethyl)amino]cyclohexyl]-(carboxymethyl)amino}acetic acid
HRMS	engl. „*high resolution mass spectra*” – Hochaufgelöstes Massenspektrum
$K_{2.2.2}$	Kryptofix®

m	*meta*
MeCN	Acetonitril
MeOH	Methanol
MOM	Methoxymethyl
NextGen	engl. „*next generation*“ – nächste Generation
NHC	*N*-Heterozyklisches Carben
NMDAR	*N*-Methyl-D-Aspartat-Rezeptor
NMM	*N*-Methylmorpholin
NMR	engl. „*nuclear magnetic resonance*“ – Kernspinresonanz
NODA	1,4,7-Triazacyclononan-4,7-diessigsäure
NODAGA	2-[1,4,7-Triazacyclononan-1-yl-4,7-diessigsäure]-1,5-glutarsäure
NOTA	1,4,7-Triazacyclononan-1,4,7-triessigsäure
o	*ortho*
OAc	Acetat
^{t}OBu	*tert*-oxybutyl
OMs	Mesylat
OTf	Triflat
OTs	Tosylat
p	*para*
PBS	engl. „*phosphate-buffered saline*“
PC	Propylencarbonat
PET	Positronen-Emissions-Tomographie
PSMA	Prostata spezifisches Membranantigen
Py	Pyridin
PyFluor	2-Pyridinylsulfonylfluorid
SET	engl. „*single electron transfer*“ – Ein-Elektronen-Transfer
SPE	engl. „*solid phase extraction*“ – Festphasenextraktion
RCA	Radiochemische Ausbeute
RCU	Radiochemischer Umsatz
RT	Raumtemperatur
SPECT	Singe-Photon-Emission-Computer-Tomographie
TBPA	Tertbutylperoxyacetet
TEMPO	2,2,6,6-Tetramethylpiperidinyloxyl

TFA	Trifluoressigsäure
TFAA	Trifluoressigsäureanhydrid
TFP	2,3,5,6-Tetrafluorphenol
THF	Tetrahydrofuran

Abbildungsverzeichnis

Schemaverzeichnis

Anhang

A: Erklärung gemäß § 7 Absatz 8

„Hiermit versichere ich an Eides statt, dass ich die vorliegende Dissertation selbstständig und ohne die Benutzung anderer als der angegebenen Hilfsmittel und Literatur angefertigt habe. Alle Stellen, die wörtlich oder sinngemäß aus veröffentlichten und nicht veröffentlichten Werken dem Wortlaut oder dem Sinn nach entnommen wurden, sind als solche kenntlich gemacht. Ich versichere an Eides statt, dass diese Dissertation noch keiner anderen Fakultät oder Universität zur Prüfung vorgelegen hat; dass sie - abgesehen von unten angegebenen Teilpublikationen und eingebundenen Artikeln und Manuskripten - noch nicht veröffentlicht worden ist sowie, dass ich eine Veröffentlichung der Dissertation vor Abschluss der Promotion nicht ohne Genehmigung des Promotionsausschusses vornehmen werde. Die Bestimmungen dieser Ordnung sind mir bekannt. Darüber hinaus erkläre ich hiermit, dass ich die Ordnung zur Sicherung guter wissenschaftlicher Praxis und zum Umgang mit wissenschaftlichem Fehlverhalten der Universität zu Köln gelesen und sie bei der Durchführung der Dissertation zugrundeliegenden Arbeiten und der schriftlich verfassten Dissertation beachtet habe und verpflichte mich hiermit, die dort genannten Vorgaben bei allen wissenschaftlichen Tätigkeiten zu beachten und umzusetzen. Ich versichere, dass die eingereichte elektronische Fassung der eingereichten Druckfassung vollständig entspricht.“

B: Supporting Information

Supporting Information for

[^{18}F]ALX5406: A Brain-Penetrating Prodrug for GlyT1-Specific PET Imaging

Chris Hoffmann[1,2#], Sibel Evcüman[1#], Felix Neumaier[1,2], Boris D. Zlatopolskiy[1,2,3], Swen Humpert[1], Dirk Bier[1], Marcus Holschbach[1], Annette Schulze[1], Heike Endepols[1,2,4] and Bernd Neumaier[1,2,3*]

[1] Forschungszentrum Jülich GmbH, Institute of Neuroscience and Medicine, Nuclear Chemistry (INM-5), 52425 Jülich, Germany

[2] University of Cologne, Faculty of Medicine and University Hospital Cologne, Institute of Radiochemistry and Experimental Molecular Imaging, 50937 Cologne, Germany

[3] Max Planck Institute of Metabolism Research, 50931 Cologne, Germany

[4] University of Cologne, Faculty of Medicine and University Hospital Cologne, Nuclear Medicine Department, 50937 Cologne, Germany.

[#] contributed equally

Table of contents

1. Determination of enantiomeric excess of compound 1 and 2

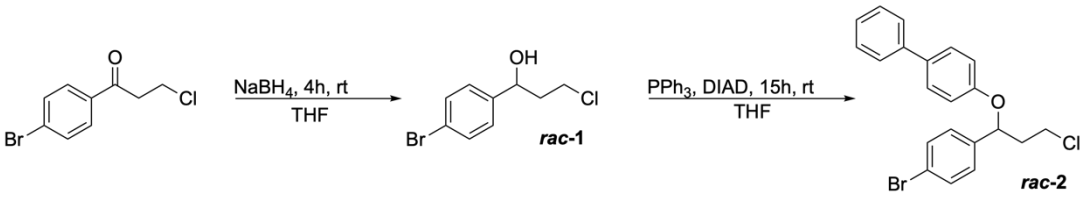

Racemic 1-(4-bromophenyl)-3-chloropropan-1-ol (*rac*-1)[1]

A solution of 4'-bromo-3-chloropropiophenone (500 mg, 2.02 mmol, 1 eq.) in THF (2 mL) was added to a suspension of $NaBH_4$ (76.4 mg, 2.02 mmol, 4 eq.) in THF (2 mL) dropwise at 0 °C under argon. After stirring for 4 h, the reaction mixture was diluted with H_2O (5 mL) and extracted with Et_2O (2 x 10 mL). The combined organic fractions were dried and concentrated under reduced pressure. The residue was purified by column chromatography (petrol ether/EtOAc 9:1), affording the title compound as a colorless solid (416 mg, 1.67 mmol, 83%).

^{1}H NMR (400 MH, $CDCl_3$): δ = 1.86 (br, 1H), 2,03 – 2.12 (m, 1H), 2.18 – 2.26 (m, 1H), 3.56 (dt, *J* = 11.1, 5.8 Hz, 1H), 3.77 (ddd, *J* = 11.1, 8.4, 4.9 Hz, 1H), 4.96 (dd, *J* = 8.4, 4.9 Hz, 1H), 7.26-7.29 (m, 2H), 7.49 – 7.53 (m, 2H). ^{13}C NMR (100 MHz, $CDCl_3$): δ = 41.50, 41.64, 70.81, 121.81, 127.63, 131.89, 142.85.

Racemic 4-[1-(4-bromophenyl)-3-chloropropoxy]-1,1'-biphenyl (*rac*-2)

DIAD (350 µL, 356 mg, 1.76 mmol, 1.1 eq.) was added to an ice-cold solution of *rac*-**1** (400 mg, 1.60 mmol, 1 eq.), 4-phenylphenol (300 mg, 1.76 mmol, 1.1 eq.) and PPh_3 (462 mg, 1.76 mmol, 1 eq.) in anhydrous THF (5 mL) under argon and the reaction mixture was stirred for 15 hours at ambient temperature. Afterwards, the mixture was diluted with H_2O (5 mL) and extracted with Et_2O (3×10 mL). The combined organic fractions were dried and concentrated under reduced pressure. The crude product was purified by column chromatography (petrol ether/EtOAc 49:1) to give the title compound as colorless needles (191 mg, 0.475 mmol, 30%).

^{1}H NMR (400 MHz, $CDCl_3$): δ = 2.23 (dddd, *J* = 14.3, 8.7, 5.7, 4.3 Hz, 1H), 2.49 (ddt, *J* = 14.3, 8.7, 5.3 Hz, 1H), 3.65 (dt, *J* = 11.1, 5.7 Hz, 1H), 3.85 (ddd, *J* = 11.1, 8.7, 5.3 Hz, 1H), 5.42 (dd, *J* = 8.7, 4.3 Hz, 1H), 6.91 – 6.94 (m, 2H), 7.28 – 7.33 (m, 3H), 7.39 – 7.46 (m, 4H), 7.50 – 7.53 (m, 4H). ^{13}C-NMR (100 MHz, $CDCl_3$): δ = 41.24, 41.38, 76.39, 116.33, 121.93, 126.86, 127.82, 128.28, 128.83, 132.14, 134.55, 140.05, 140.74, 149.06, 157.30.

Chiral HPLC was performed on an Ultimate® 3000 HPLC system (Thermo Scientific, Sunnyvale, CA, USA) with Ultimate® 3000 LPG-3400A pump and Ultimate® 3000 VWD-3100 UV/Vis detector.

Column: Lux® 5 µm Cellulose-1, 4.6×250 mm (Phenomenex, Aschaffenburg, Germany)
rac-**1**: 10% *i*PrOH in *n*-hexane; flow rate: 0.5 mL/min; detection: UV, λ=254 nm; t_R [(*S*)-**1**] = 14.1 min, t_R [(*R*)-**1**] = 15.0 min.
rac-2: 5% *i*PrOH in *n*-hexane; flow rate: 0.5 mL/min; detection: UV, λ=254 nm; t_R [(*R*)-**2**] = 10.2 min, t_R [(*S*)-**2**] = 11.0 min.

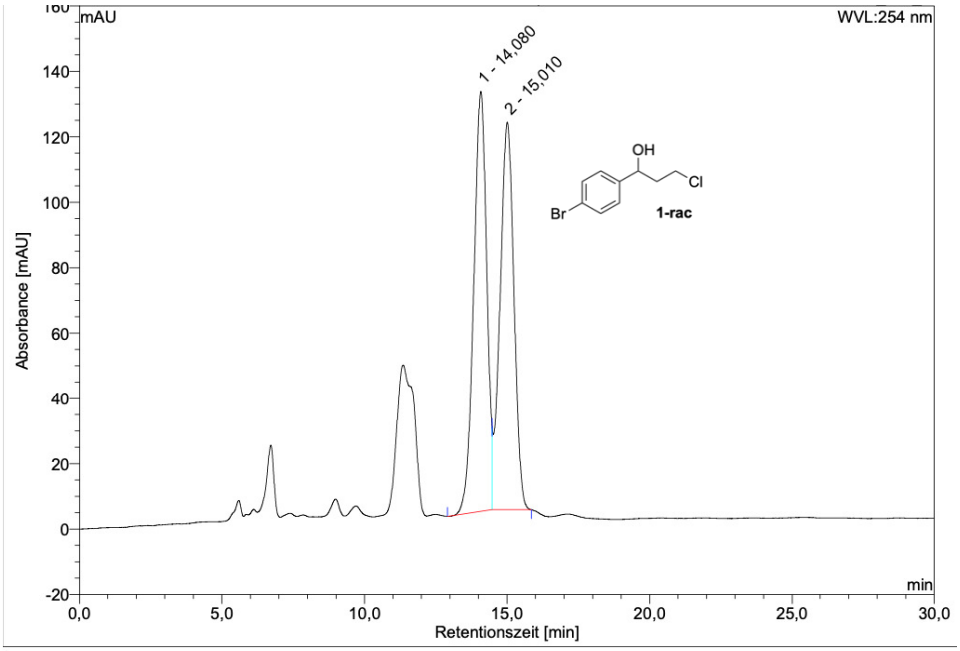

Nr.	Retentionszeit min	Intensität mAU	Integral %
1	14,08	128,496	50,05
2	15,01	118,532	49,95
Total:		247,028	100,00

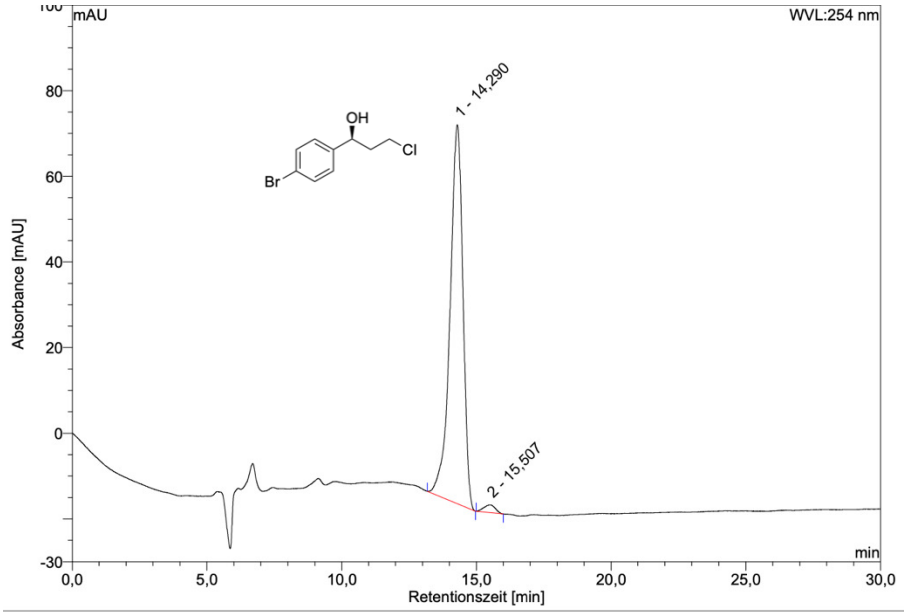

Nr.	Retentionszeit min	Intensität mAU	Integral %
1	14,29	88,517	98,23
2	15,51	1,807	1,77
Total:		90,325	100,00

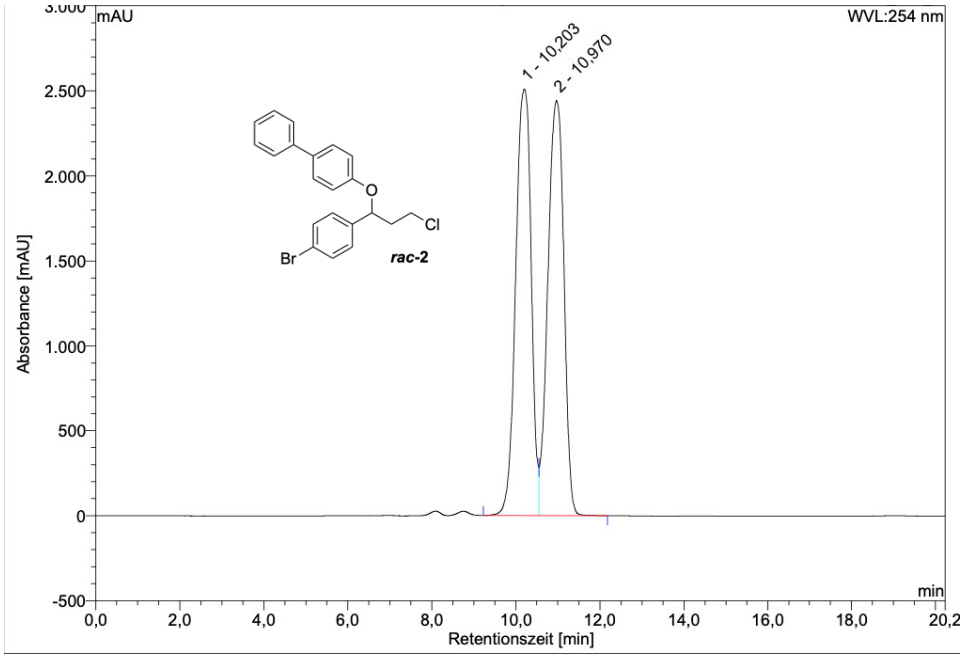

Nr.	Retentionszeit min	Intensität mAU	Integral %
1	10,20	2510,552	49,84
2	10,97	2444,958	50,16
Total:		4955,510	100,00

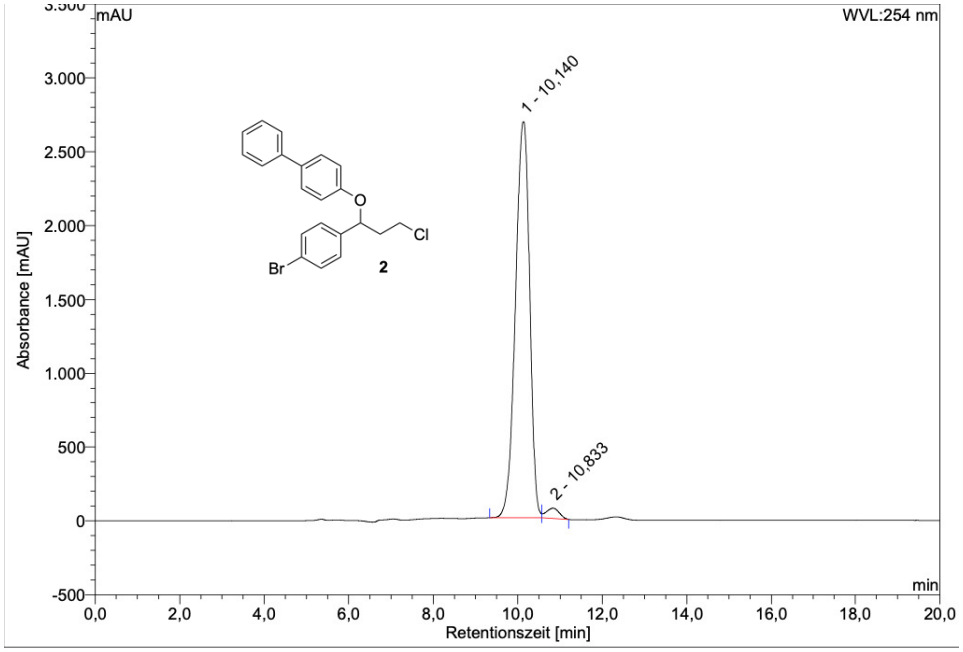

Nr.	Retentionszeit min	Intensität mAU	Integral %
1	10,14	2681,349	97,67
2	10,83	69,448	2,33
Total:		2750,797	100,00

2. NMR Spectra

2.1. ^{1}H NMR of compound 1

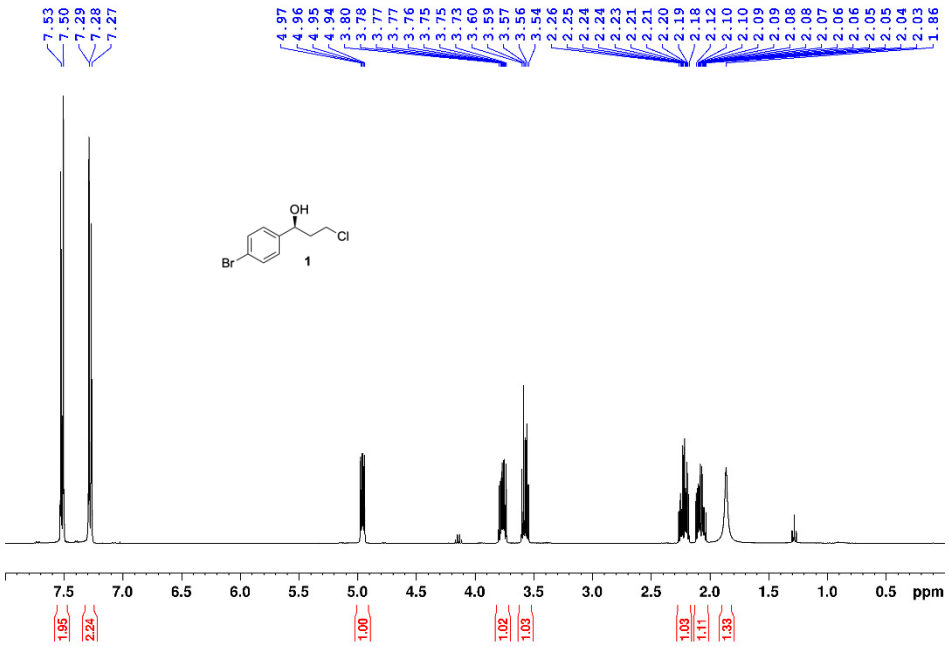

2.2. ^{13}C NMR of compound 1

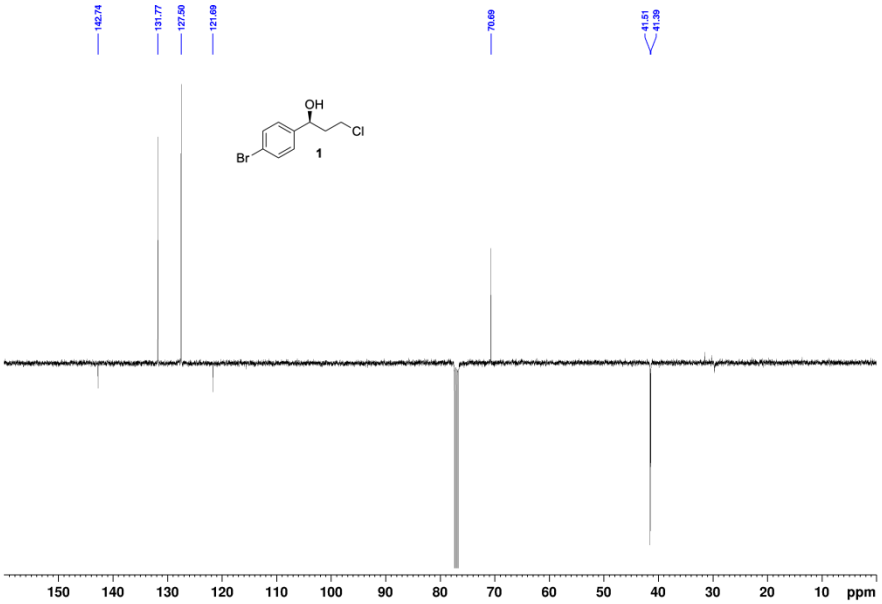

2.3. ^{1}H NMR of compound 2

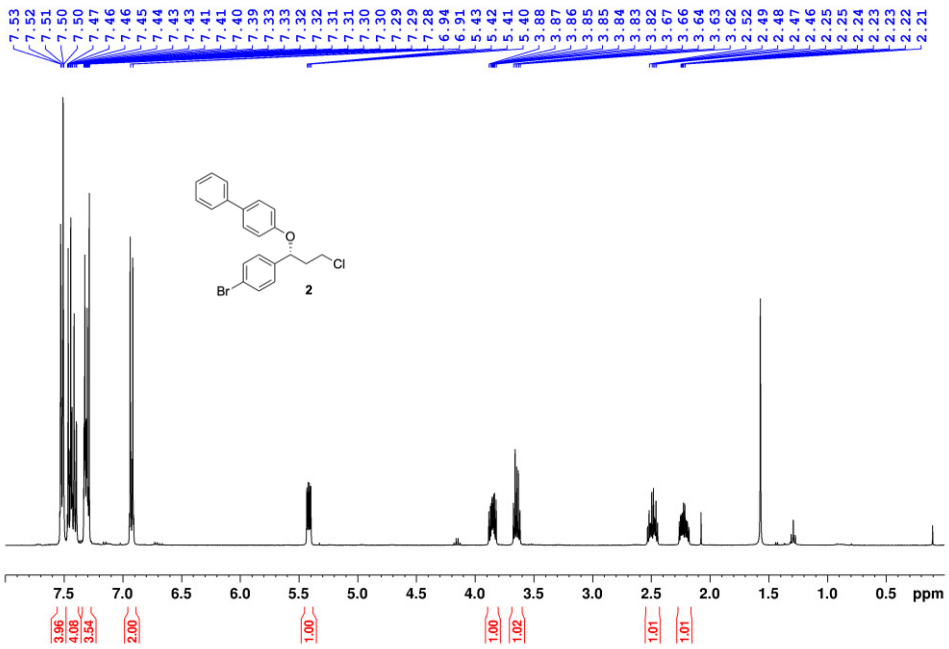

2.4. ^{13}C NMR of compound 2

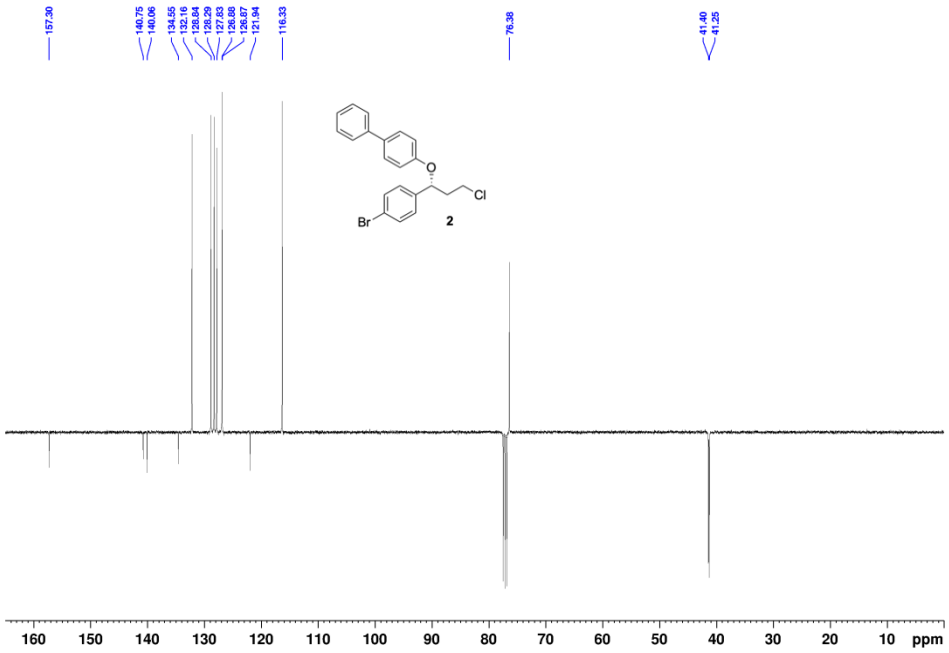

2.5. DEPT135 of compound 2

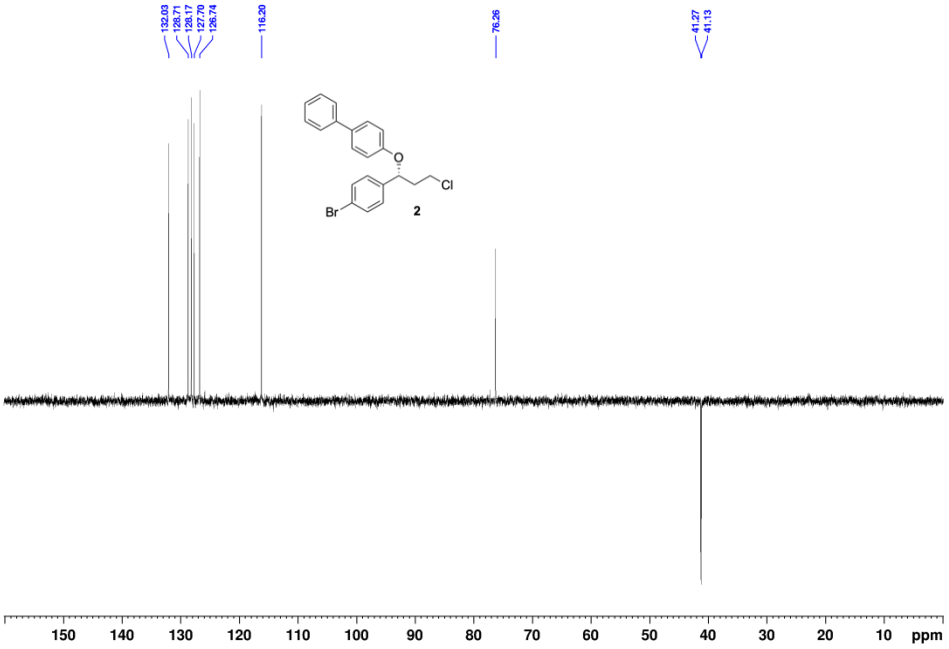

2.6. COSY of compound 2

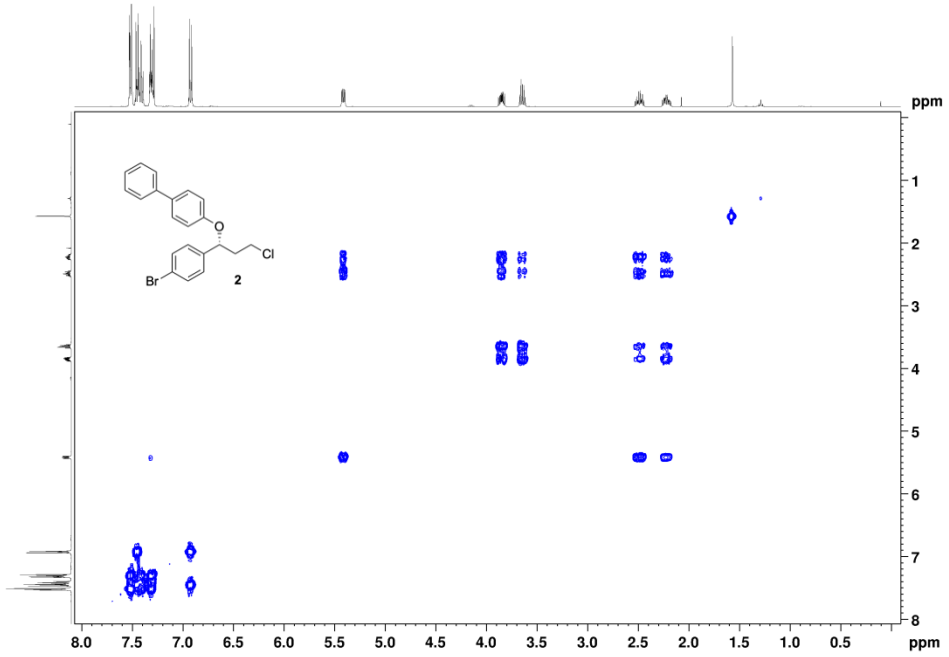

2.7. HSQC of compound 2

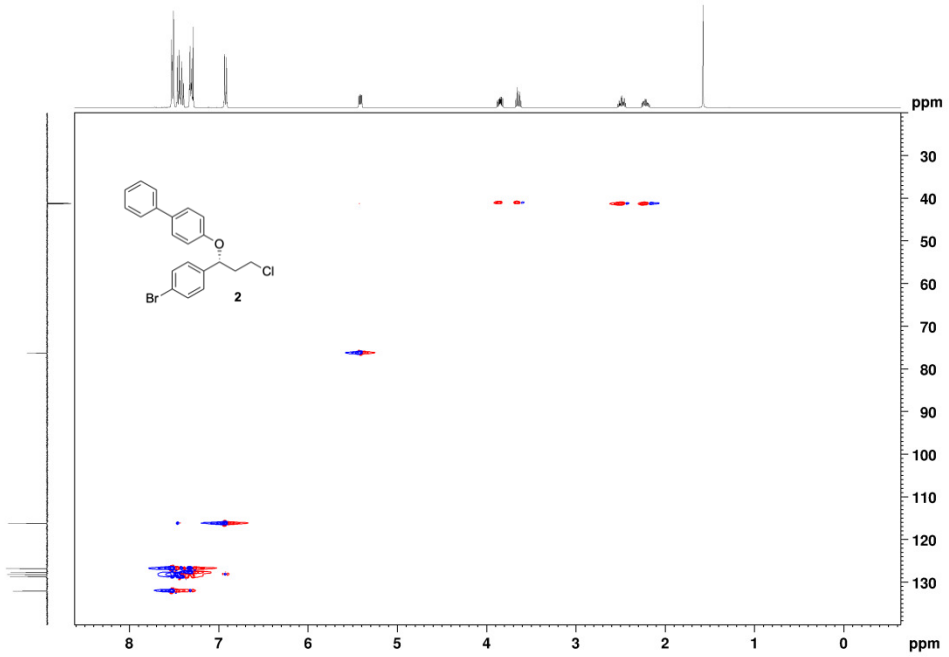

2.8. ^{1}H NMR of compound 3

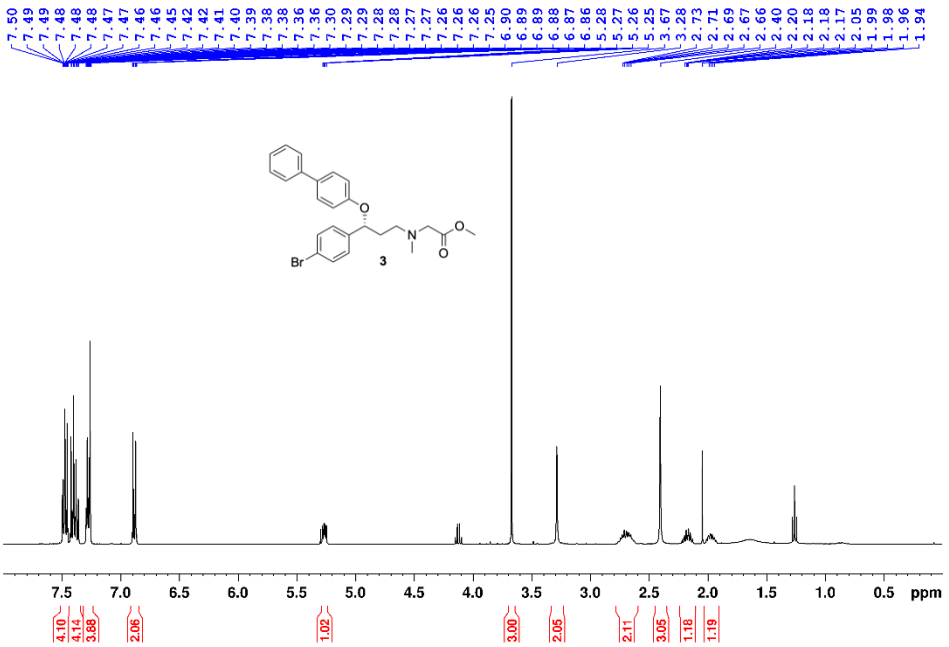

2.9. ^{13}C NMR of compound 3

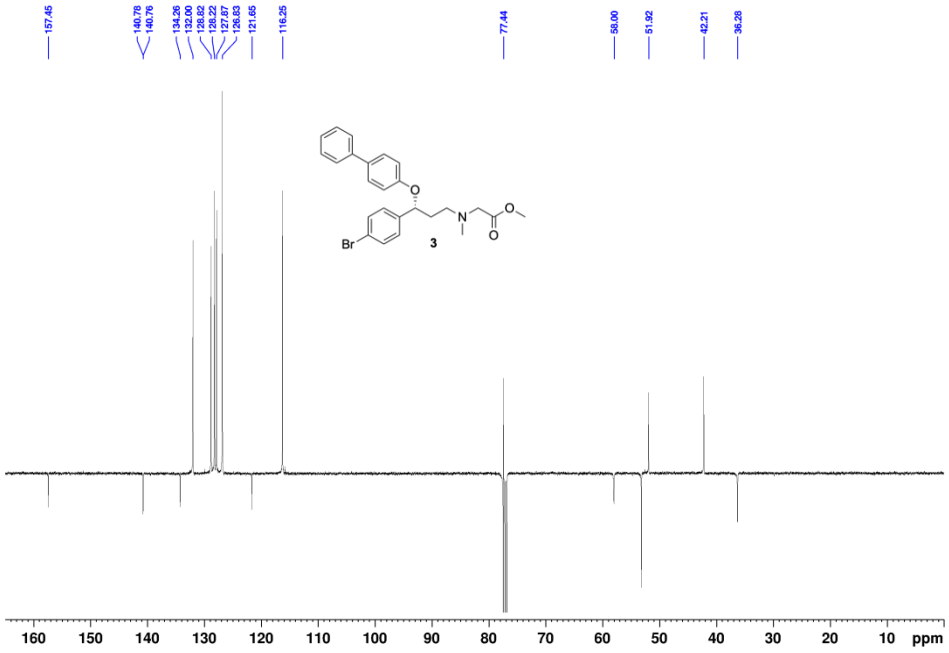

2.10. DEPT135 of compound 3

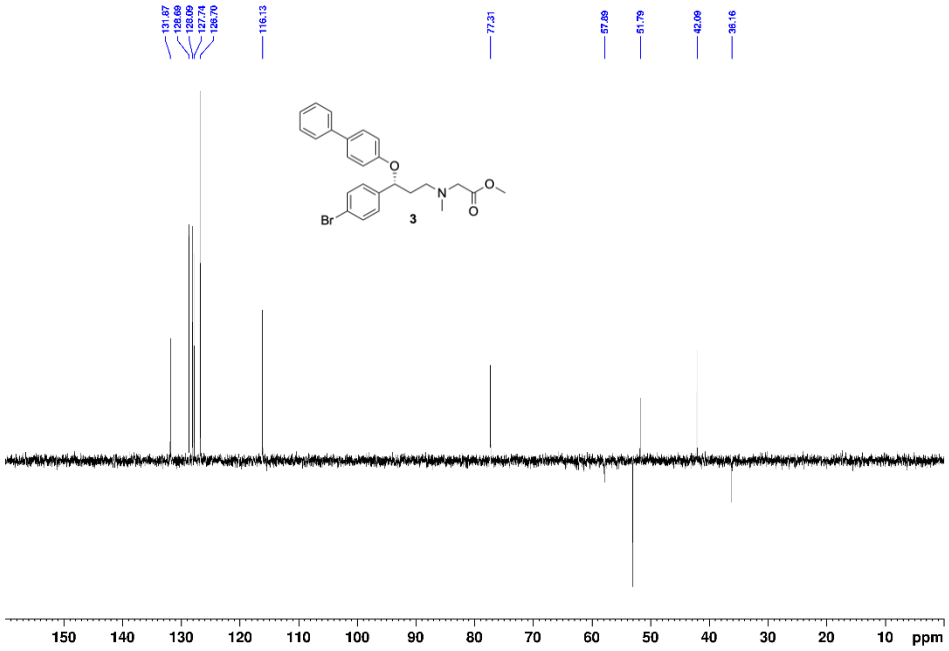

2.11. COSY of compound 3

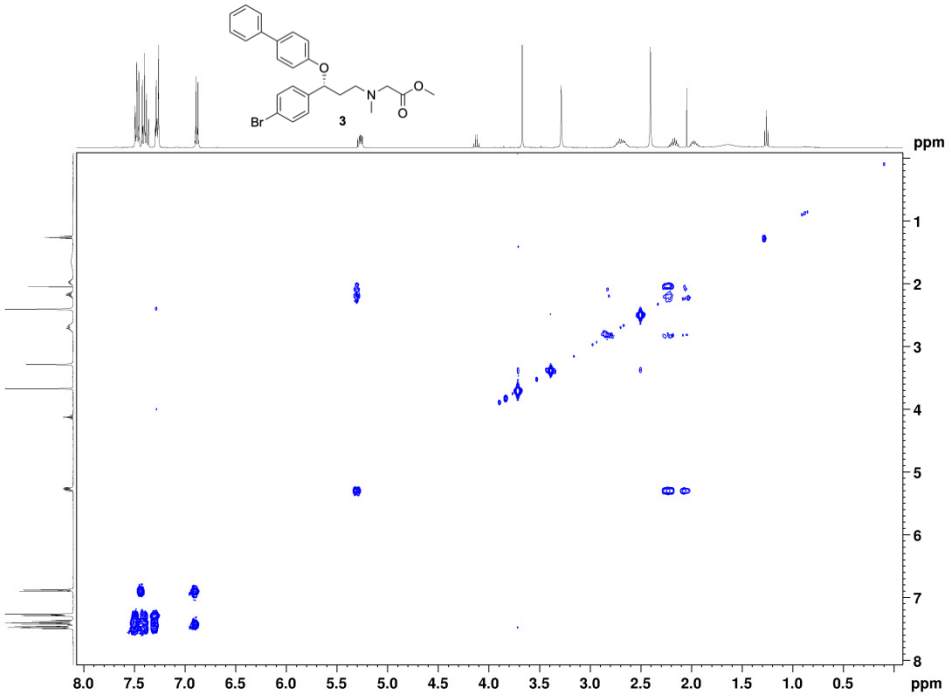

2.12. HSQC of compound 3

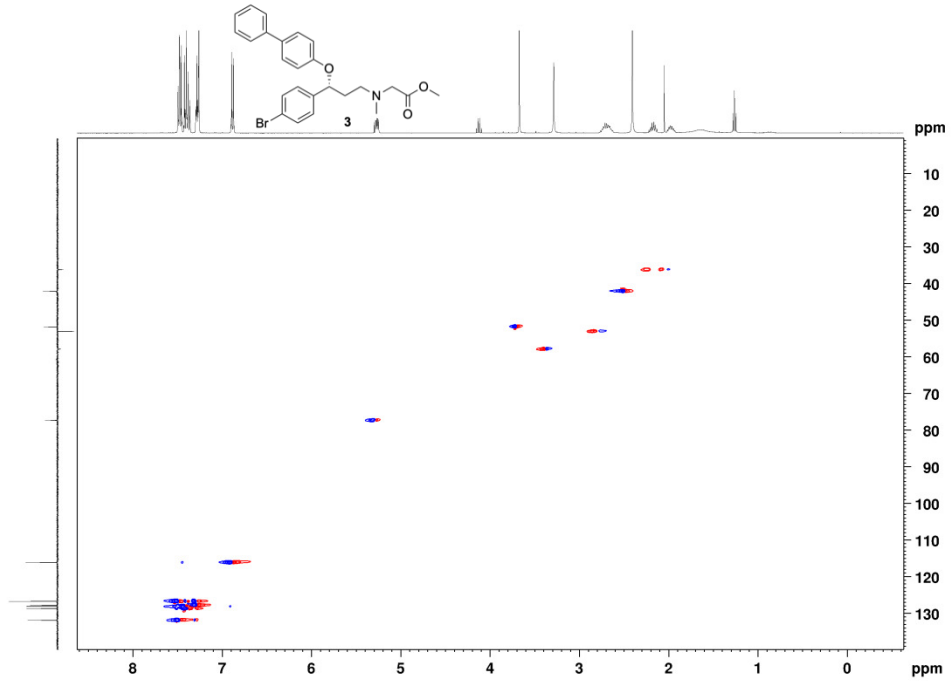

2.13. ^{1}H NMR of compound 4

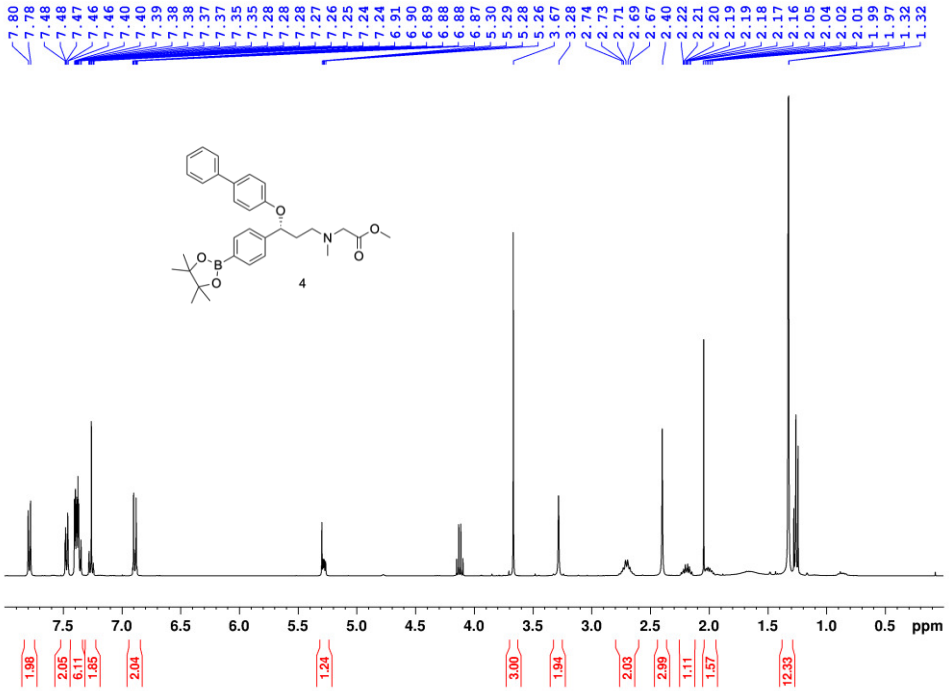

2.14. ^{13}C NMR of compound 4

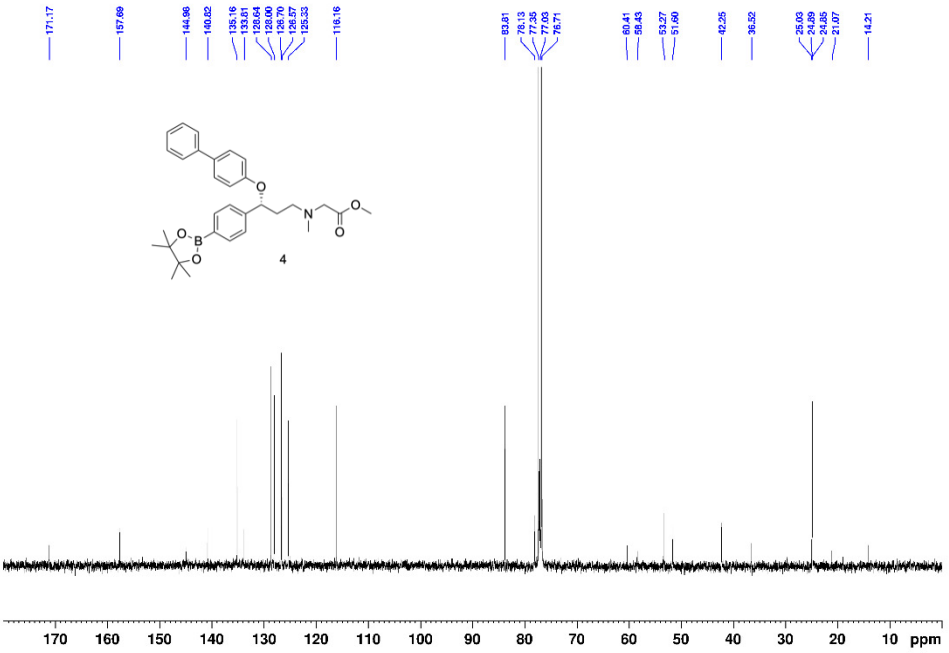

2.15. DEPT135 of compound 4

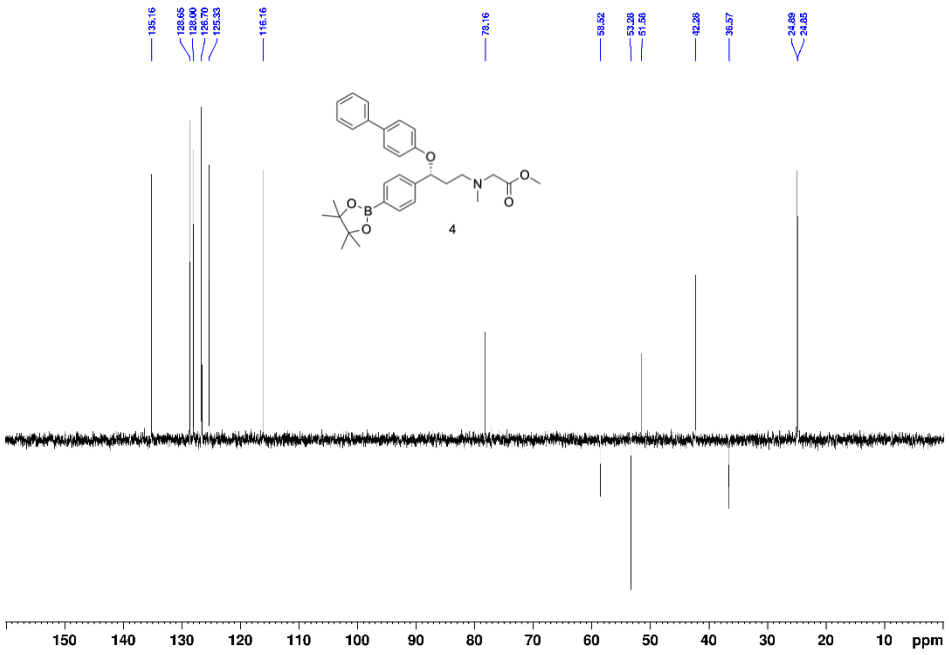

2.16. COSY of compound 4

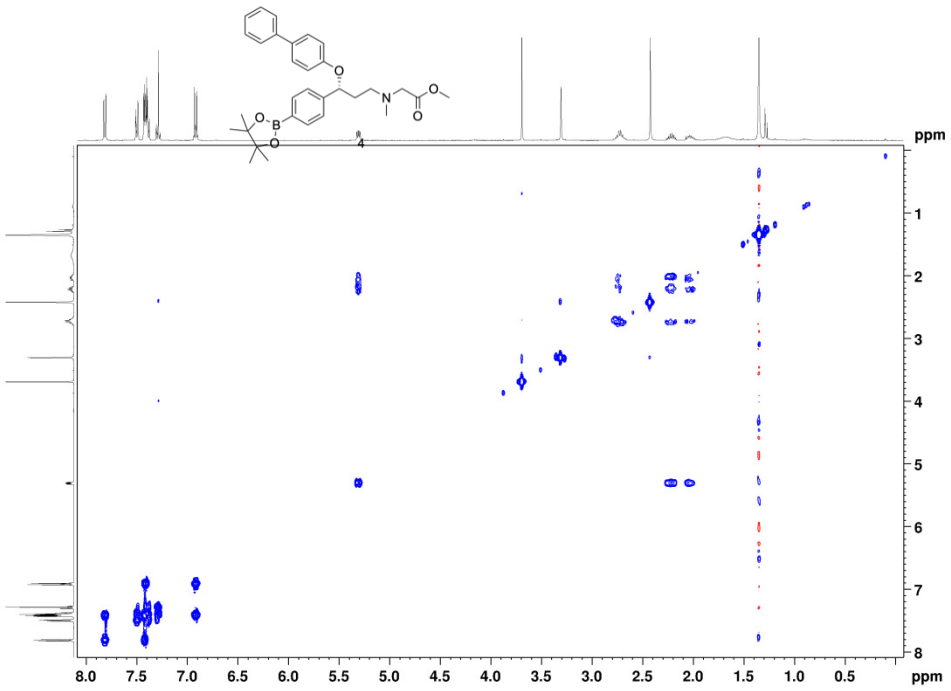

2.17. HSQC of compound 4

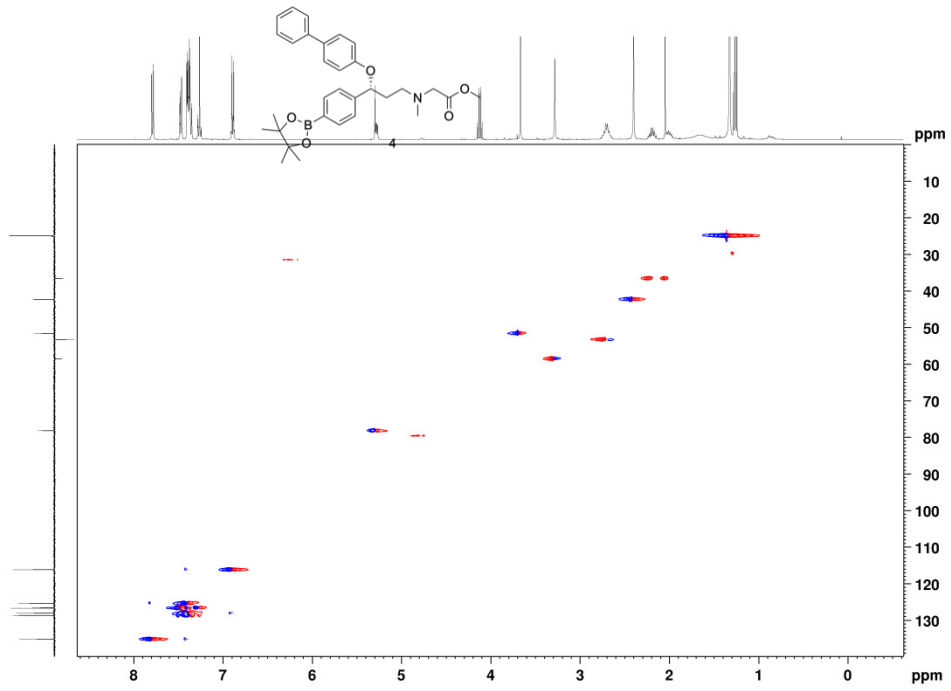

2.18. ^{1}H NMR of compound *rac*-1

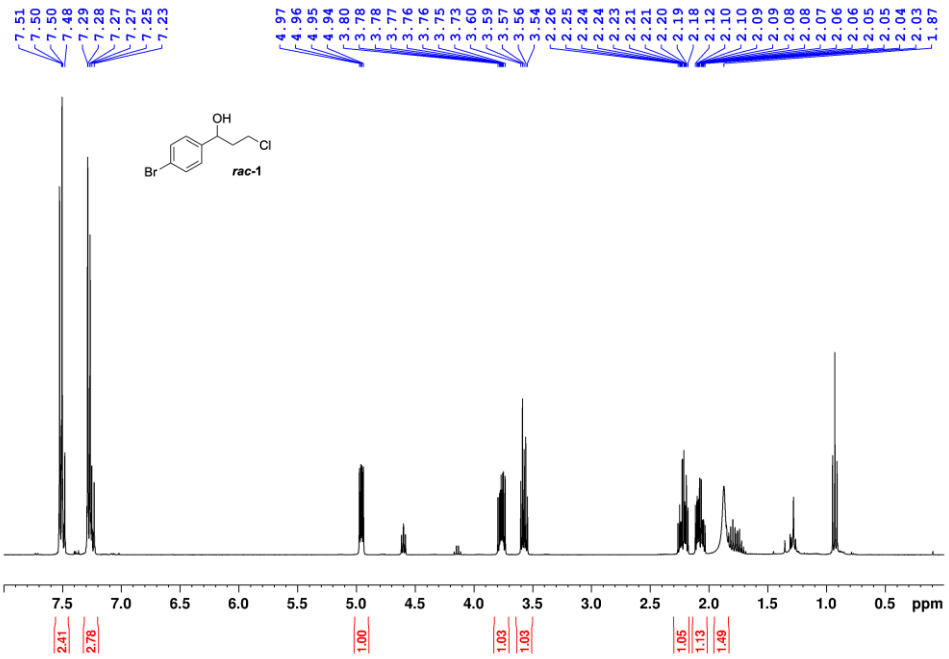

2.19. ^{13}C NMR of compound *rac*-1

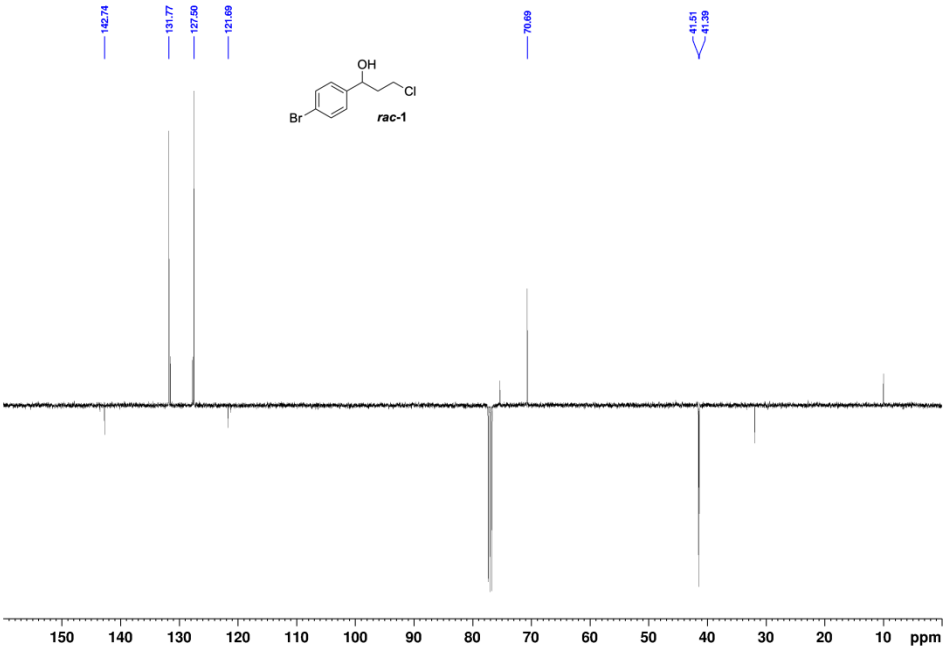

2.20. ^{1}H NMR of compound *rac*-2

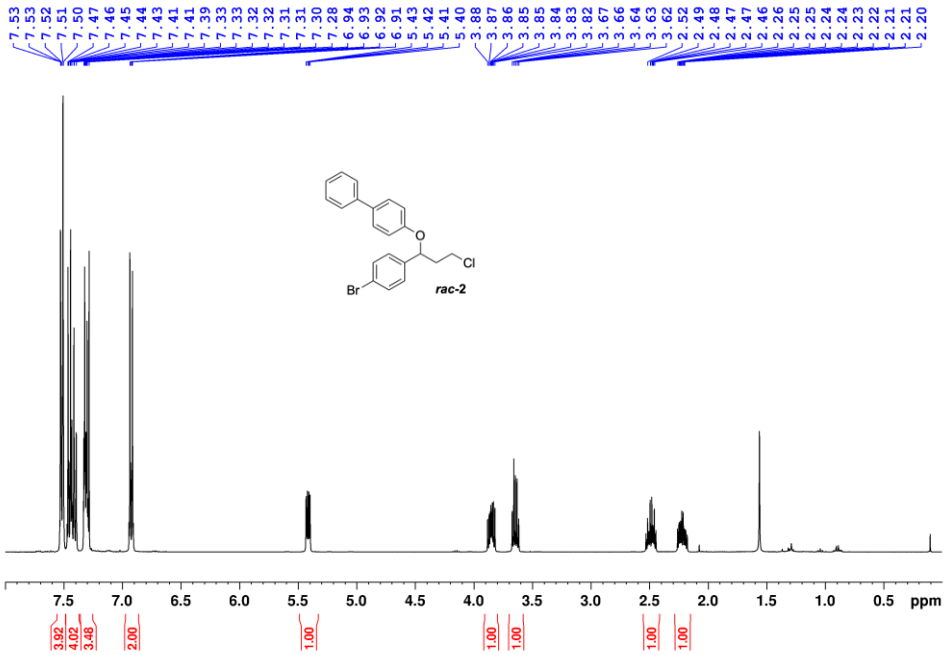

2.21. ^{13}C NMR of compound *rac*-2

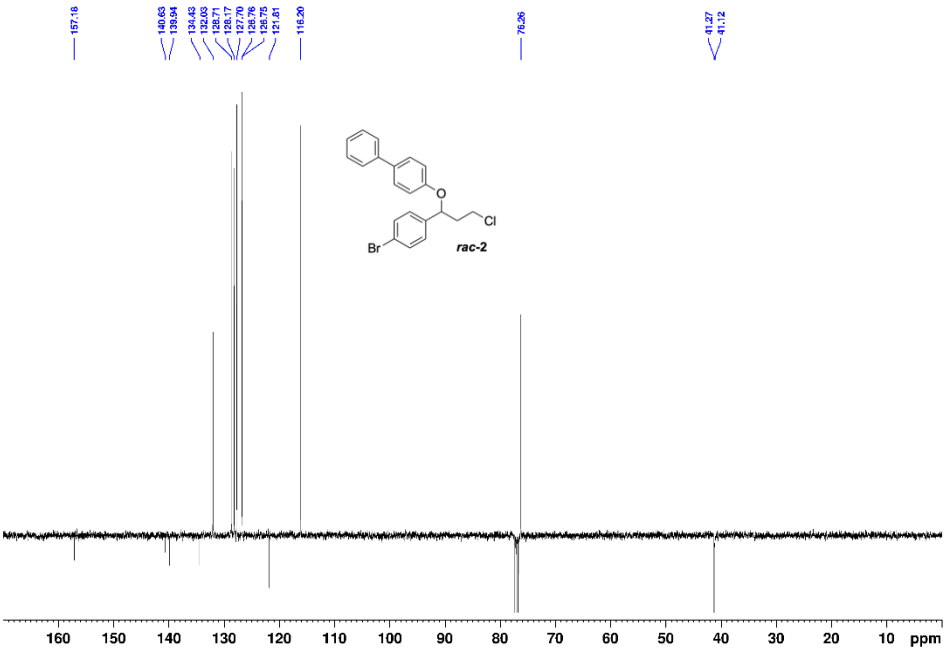

2.22. DEPT135 of compound *rac*-2

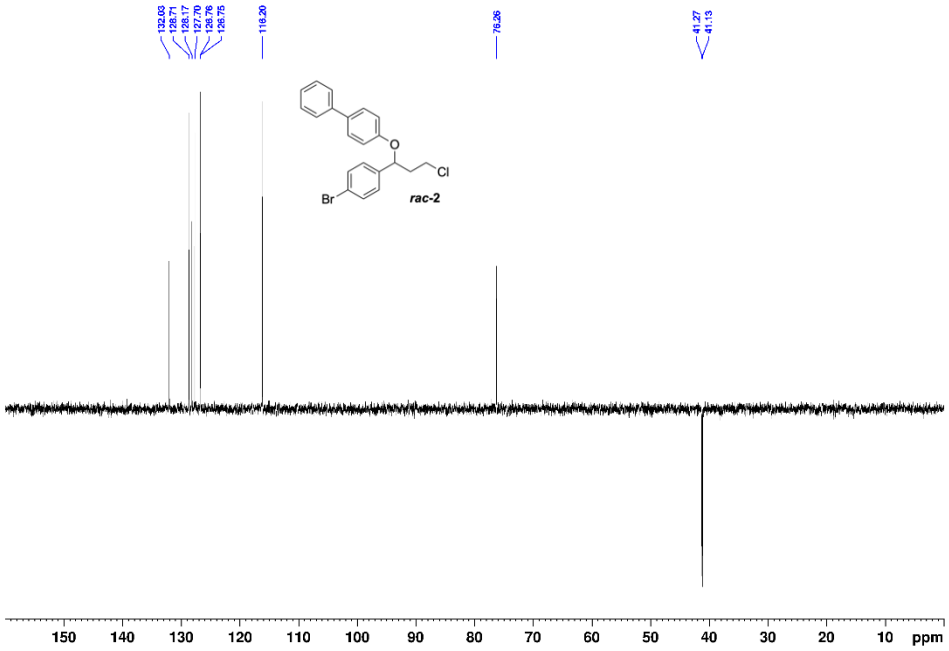

2.23. COSY of compound *rac*-2

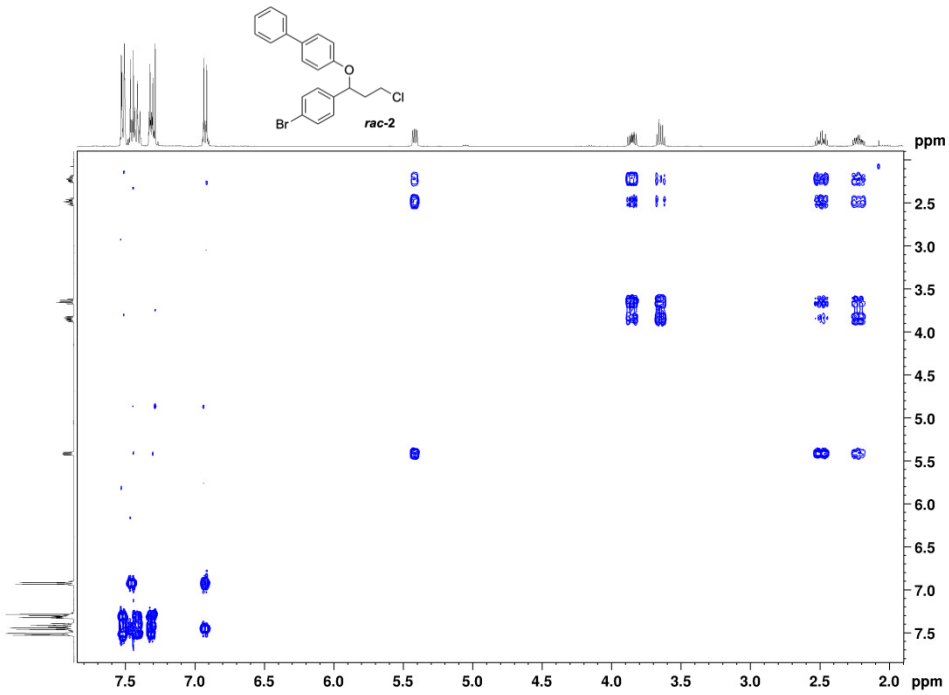

2.24. HSQC of compound *rac*-2

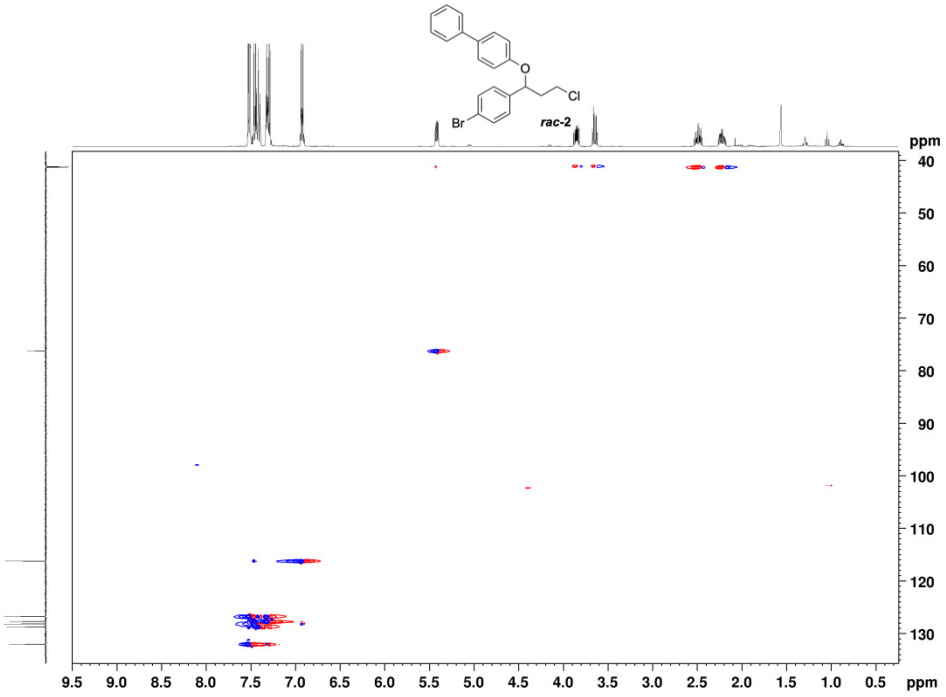

3. Radiosynthesis and Formulation

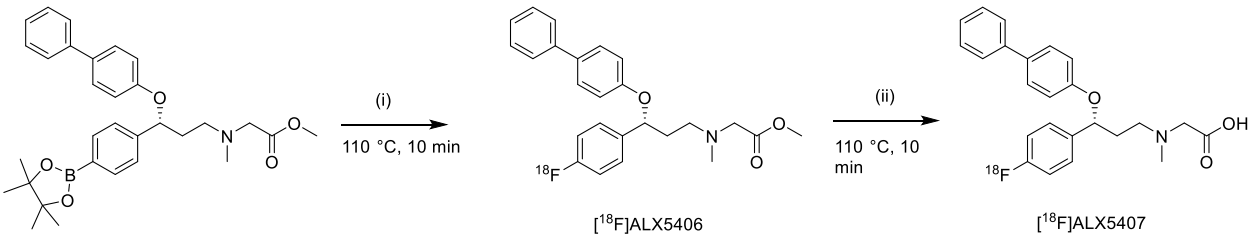

Scheme S1. Radiosynthesis of [^{18}F]ALX5406 and [^{18}F]ALX5407.

Table S1. Summary of the radiofluorination results.

Radiotracer	Radiochemical Yield [%]	Radiochemical Purity [%]	Molar Activity [GBq/µmol]
[^{18}F]ALX5407	55±7 (n=8)	>99	20–137
[^{18}F]ALX5406	60±8 (n=8)	95	14–74

The crude reaction mixtures of [^{18}F]ALX5407 or [^{18}F]ALX5406 were purified via preparative HPLC.

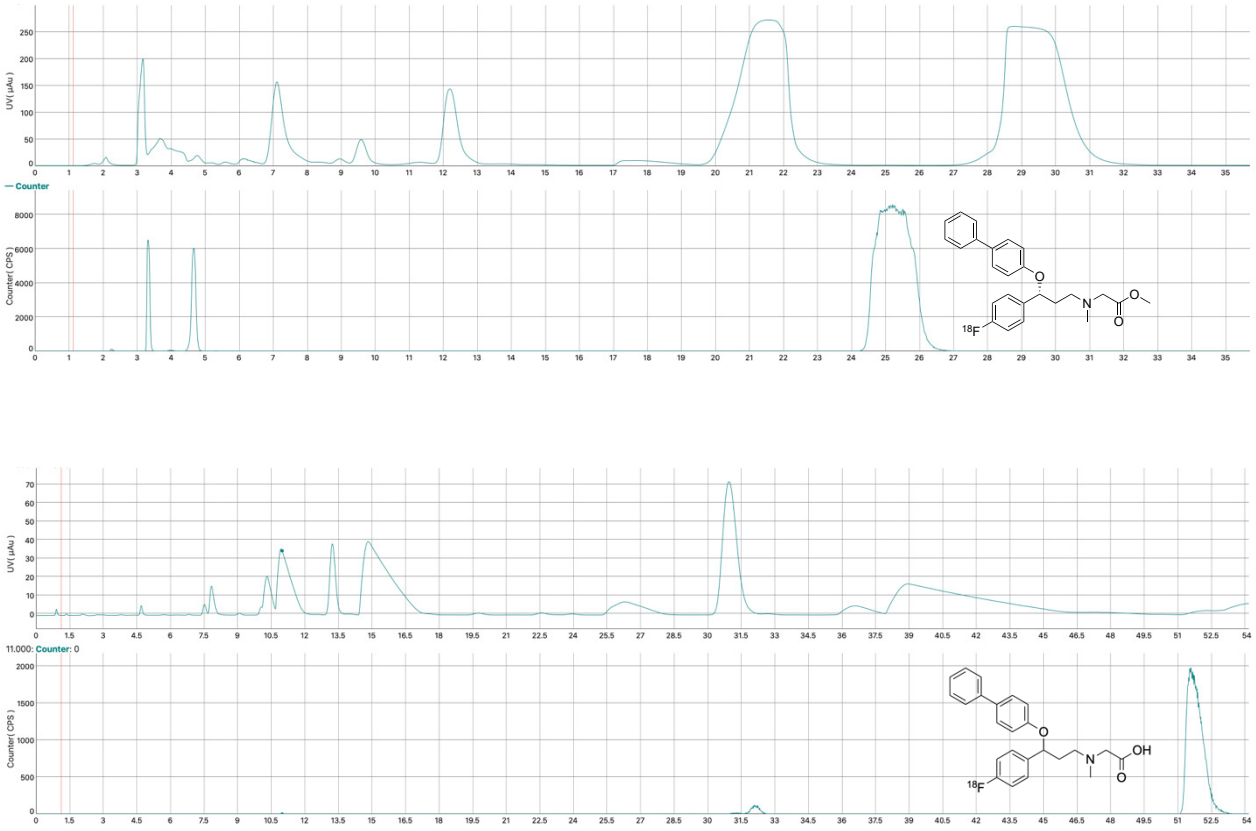

Figure S1. Traces of the purification of [^{18}F]ALX5407 and [^{18}F]ALX5406 by preparative HPLC (Top: UV chromatogram, 254 nm; bottom: radio chromatogram).

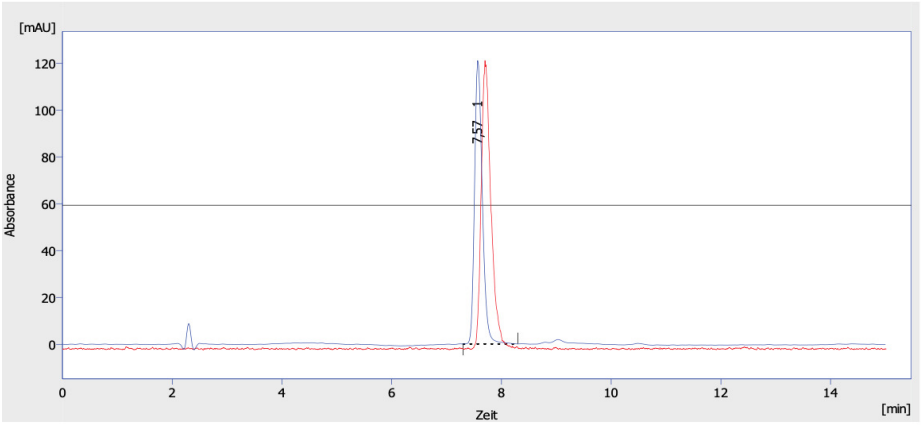

Ergebnistabelle (Nicht kal. - alc-enhanced_246_27_07_2021_[1 DMA]_[18F]ALX5407_spike - IF2/IFU2.1:Channel 1)

	Retentionsz. [min]	Fläche [mV.sek]	Höhe [mV]	Fläche [%]	W05 [min]	Substanzname	Effizienz [th.pl]	Symmetrie/Tailing [-]
1	7,700	1976,306	158,670	100,0	0,18		9773	1,473
	Gesamt	1976,306	158,670	100,0				

Ergebnistabelle (Nicht kal. - alc-enhanced_246_27_07_2021_[1 DMA]_[18F]ALX5407_spike - UV: Channel 1)

	Retentionsz. [min]	Fläche [mAU.sek]	Höhe [mAU]	Fläche [%]	W05 [min]	Substanzname	Effizienz [th.pl]	Symmetrie/Tailing [-]
1	7,567	1191,931	120,973	100,0	0,17		11419	1,313
	Gesamt	1191,931	120,973	100,0				

Figure S2. HPLC trace of [^{18}F]ALX5407 co-injected with the non-radioactive reference compound (Blue: UV chromatogram, 254 nm; red: radio chromatogram).

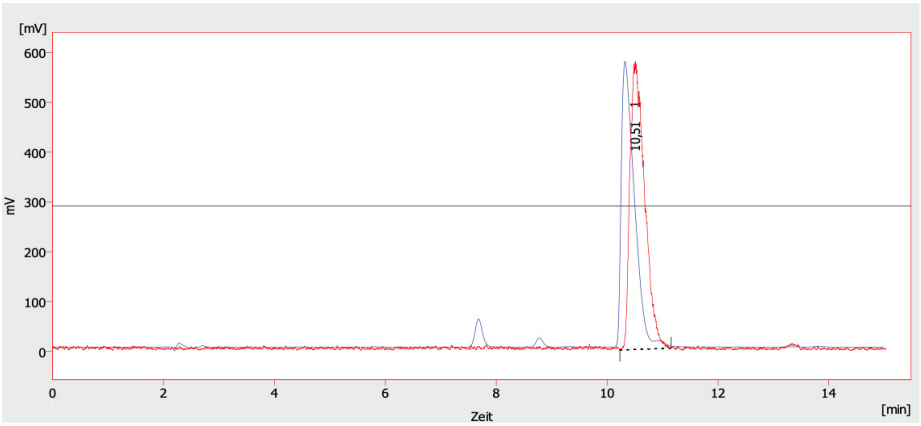

Ergebnistabelle (Nicht kal. - alc-enhanced_269_09_08_2021_[4 DMI]_[18F]ALX5407_spike_sibels_kond - IF2/IFU2.1:Channel 1)

	Retentionsz. [min]	Fläche [mV.sek]	Höhe [mV]	Fläche [%]	W05 [min]	Substanzname	Effizienz [th.pl]	Symmetrie/Tailing [-]
1	10,505	10691,975	578,959	100,0	0,29		7354	1,632
	Gesamt	10691,975	578,959	100,0				

Ergebnistabelle (Nicht kal. - alc-enhanced_269_09_08_2021_[4 DMI]_[18F]ALX5407_spike_sibels_kond - UV: Channel 1)

	Retentionsz. [min]	Fläche [mAU.sek]	Höhe [mAU]	Fläche [%]	W05 [min]	Substanzname	Effizienz [th.pl]	Symmetrie/Tailing [-]
1	10,317	4956,279	306,137	100,0	0,27		8292	2,000
	Gesamt	4956,279	306,137	100,0				

Figure S3. Analytical HPLC profile of [^{18}F]ALX5406 co-injected with the non-radioactive reference compound (Blue: UV chromatogram 254 nm, red: radio chromatogram).

4. Analysis of [^{18}F]ALX5406 radiometabolites in rat and human blood plasma

All experiments were performed with samples obtained after 5, 15, 30 and 60 min incubation of [^{18}F]ALX5406 in rat or human blood plasma at 37°C. For radio-TLC analysis, a sample for each time period was spotted on three lanes and the radio-TLC profile for this time period was determined by averaging the results from all three lanes (for details, see Materials and Methods section in the main article).

4.1. Analysis of [^{18}F]ALX5406 radiometabolites in rat blood plasma

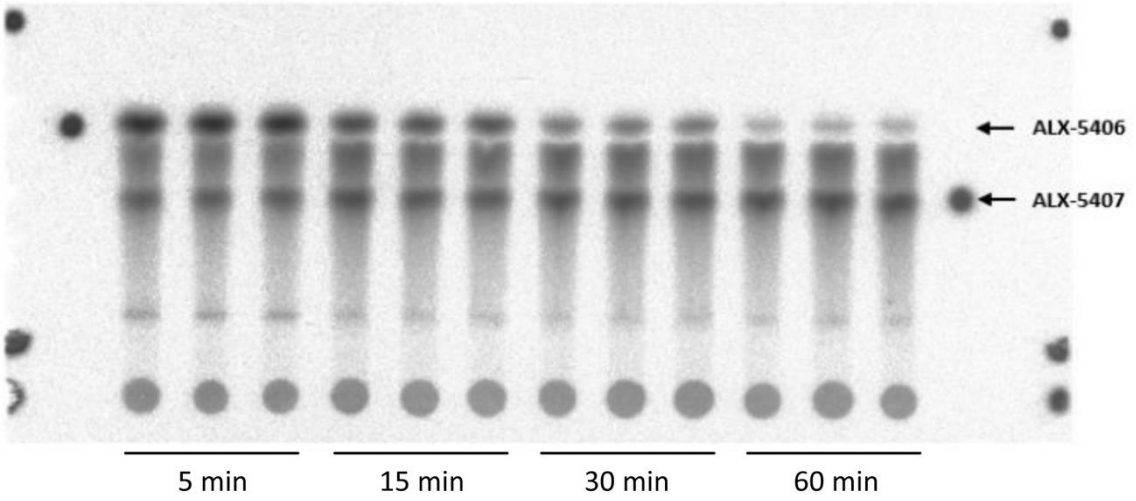

Figure S4: Radio-TLC of [^{18}F]ALX5406 incubated in rat blood plasma at 37 °C for the indicated time (three lanes for each incubation time).

Table S2: Quantitative analysis of the radio-TLC shown in Fig. S4.

Peak #	Identity	% of total activity (mean ± SD)[a]			
		5 min	15 min	30 min	60 min
1	unidentified	7 ± 1%	9 ± 1%	10 ± 1%	10 ± 1%
2	unidentified	1 ± 1%	1 ± 1%	1 ± 1%	1 ± 1%
3	**[^{18}F]ALX5407**	22 ± 1%	36 ± 1%	44 ± 1%	53 ± 2%
4	unidentified	18 ± 1%	30 ± 1%	36 ± 1%	34 ± 2%
5	**[^{18}F]ALX5406**	52 ± 1%	23 ± 1%	8 ± 1%	2 ± 1%
	Recovery rate:	115 ± 10%	113 ± 9%	119 ± 1%	103 ± 12%

[a] all values have been rounded up to the next pre-decimal place

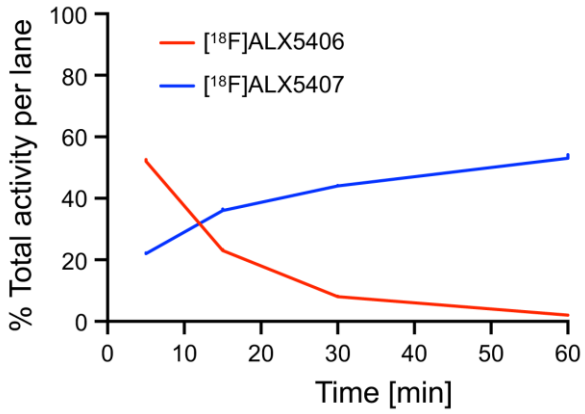

Figure S5: Hydrolysis of [^{18}F]ALX5406 to [^{18}F]ALX5407 in rat blood plasma. Under the assumption of first order kinetics, the half-life of [^{18}F]ALX5406 was approximately 12 min.

4.2. Analysis of [^{18}F]ALX5406 radiometabolites in human blood plasma

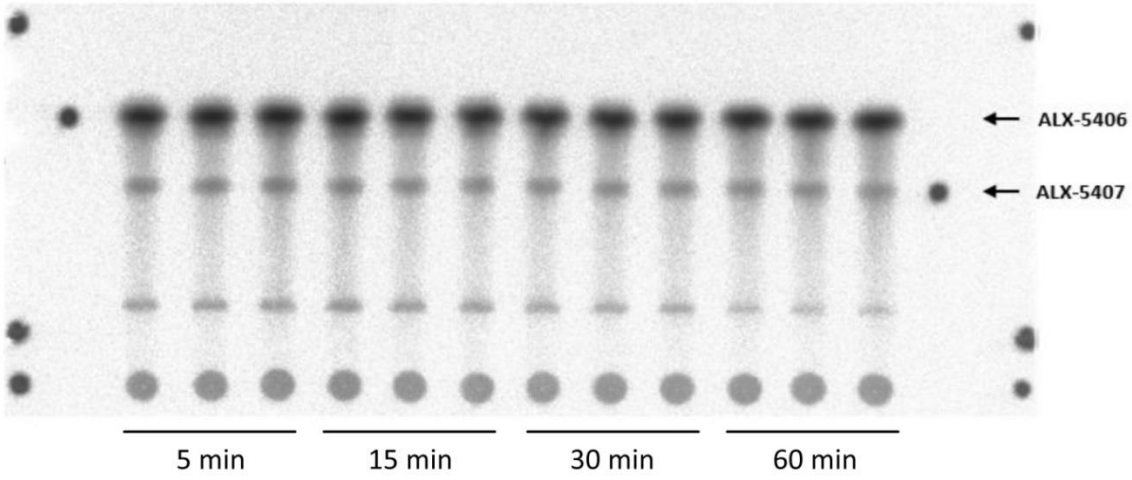

Figure S6: Radio-TLC of [^{18}F]ALX5406 incubated in human blood plasma at 37 °C for the indicated time (three lanes for each incubation time).

Table S3: Quantitative analysis of the radio-TLC shown in Fig. S6.

Peak #	Identity	% of total activity (mean ± SD)[a]			
		5 min	15 min	30 min	60 min
1	unidentified	5 ± 1%	5 ± 1%	5 ± 1%	5 ± 1%
2	unidentified	2 ± 1%	2 ± 1%	1 ± 1%	1 ± 1%
3	**[^{18}F]ALX5407**	5 ± 1%	4 ± 1%	5 ± 1%	7 ± 1%
4	**[^{18}F]ALX5406**	89 ± 1%	88 ± 1%	89 ± 1%	87 ± 1%
	Recovery rate:	98 ± 7%	119 ± 8%	123 ± 7%	133 ± 9%

[a] all values have been rounded up to the next pre-decimal place

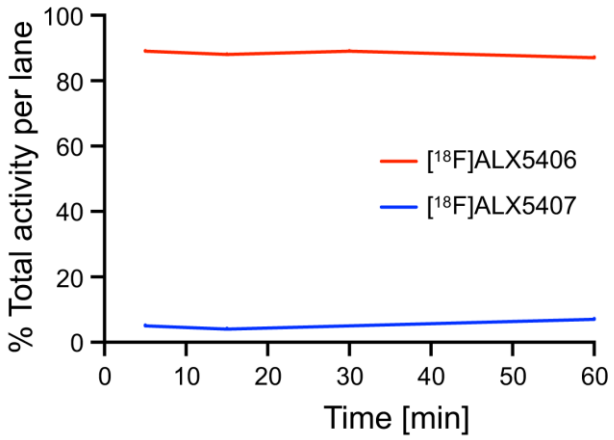

Figure S7: Stability of [^{18}F]ALX5406 in human blood plasma. [^{18}F]ALX5406 was stable for up to 60 min with only minimal demethylation to [^{18}F]ALX5407.

5. Ex vivo analysis of [^{18}F]ALX5406 and [^{18}F]ALX5407 radiometabolites in rat blood and brain, 30 p.i.

All experiments were performed with samples obtained 30 min after tail vein injection of [^{18}F]ALX5406 or [^{18}F]ALX5407 in rats. For radio-TLC analysis, each sample was spotted on five lanes and radio-TLC profiles were determined from the lane with the best resolution (for details, see Materials and Methods section in the main article).

5.1. Analysis of [^{18}F]ALX5406 radiometabolites in rat blood

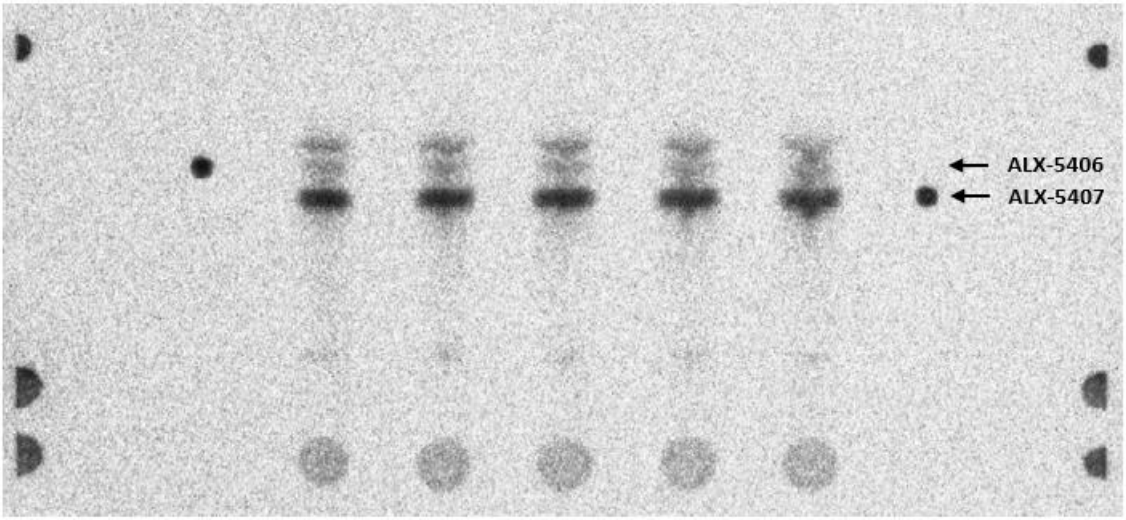

Figure S8: Radio-TLC of rat plasma collected after administration of [^{18}F]ALX5406. The recovery rate after protein precipitation amounted to 93 %.

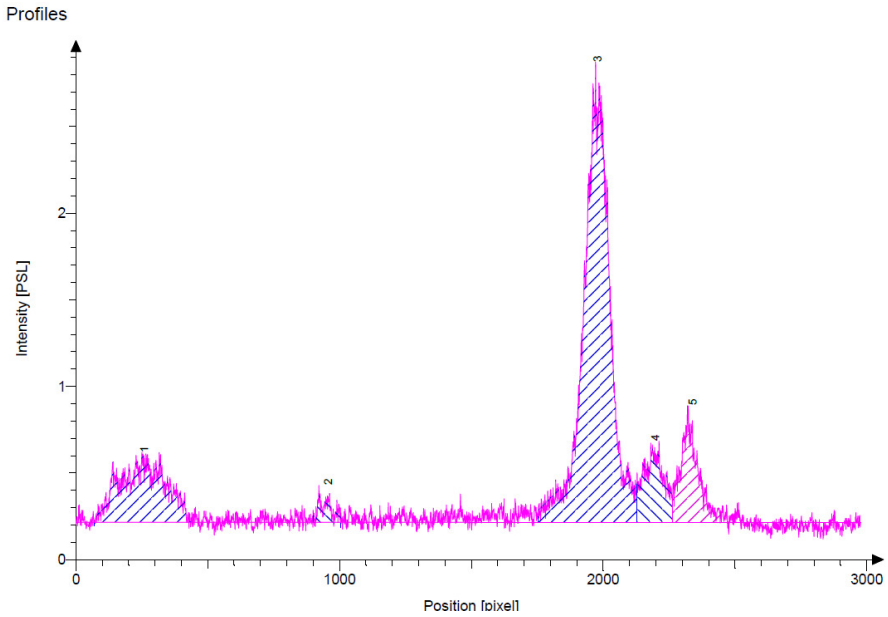

Figure S9: Profile for the best resolved lane on the radio-TLC shown in Fig. S8.

Table S4: Quantitative analysis of the radio-TLC profile shown in Fig. S9.

Peak #	% of total activity	Identity
1	22%	Unidentified metabolite, matrix effect or other artefact
2	4%	Unidentified metabolite, matrix effect or other artefact
3	55%	**[^{18}F]ALX5407**
4	6%	Unidentified metabolite, matrix effect or other artefact
5	13%	**[^{18}F]ALX5406**

5.2. Analysis of [^{18}F]ALX5406 radiometabolites in rat brain tissue extract

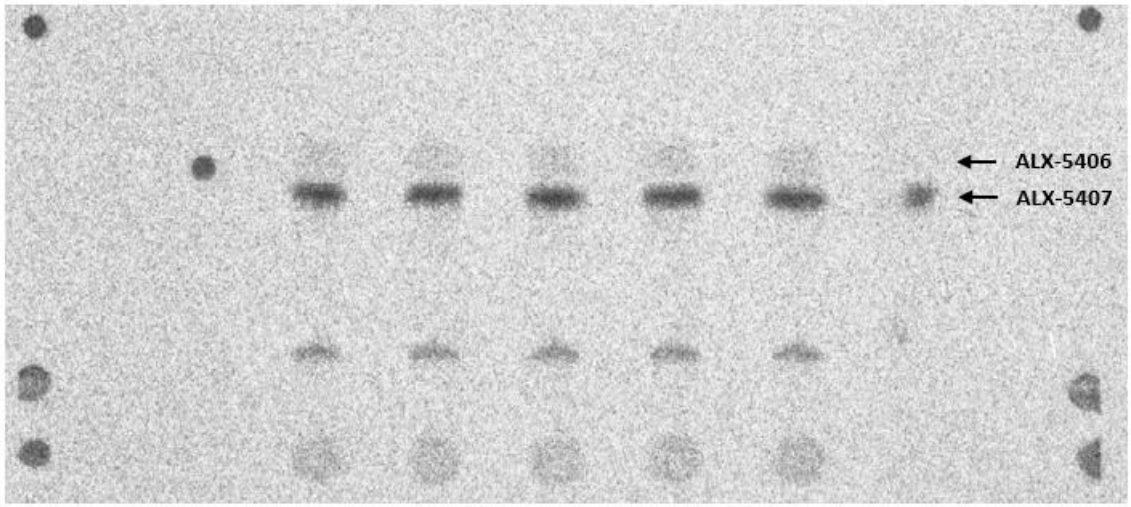

Figure S10: Radio-TLC of rat brain tissue extract obtained after administration of [^{18}F]ALX5406.

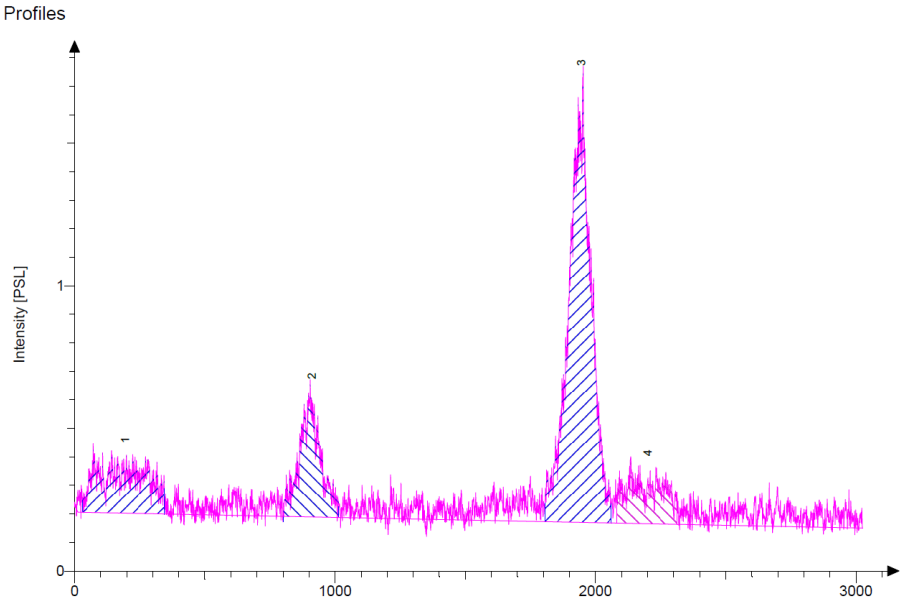

Figure S11: Profile for the best resolved lane on the radio-TLC shown in Fig. S10.

Table S5: Quantitative analysis of the radio-TLC profile shown in Fig. S11

Peak #	% of total activity	Identity
1	23%	Unidentified metabolite, matrix effect or other artefact
2	18%	Unidentified metabolite, matrix effect or other artefact
3	44%	**[^{18}F]ALX5407**
4	15%	**[^{18}F]ALX5406**

5.3. Analysis of [^{18}F]ALX5407 radiometabolites in rat blood

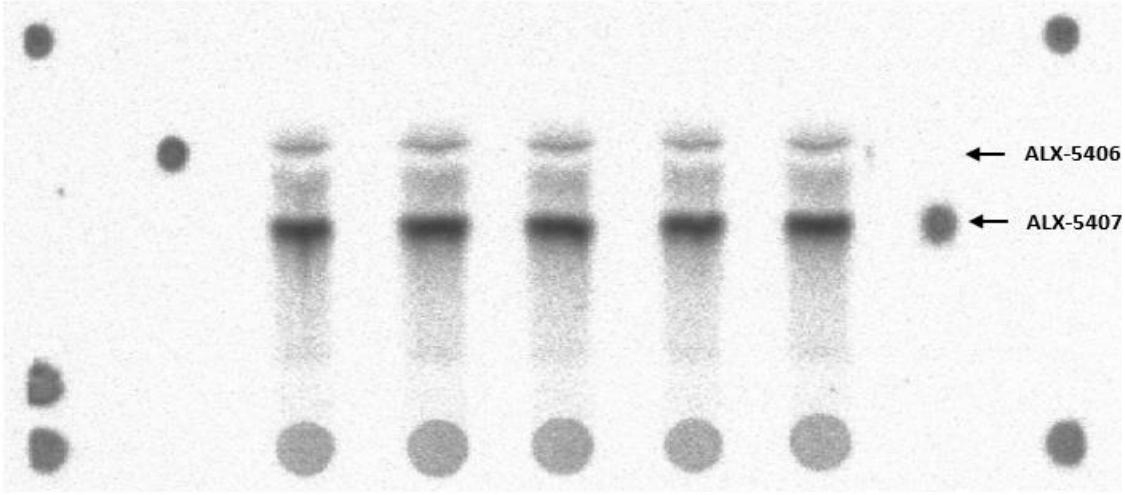

Figure S12: Radio-TLC of rat plasma collected after administration of [^{18}F]ALX5407. The recovery rate after protein precipitation amounted to 96 %.

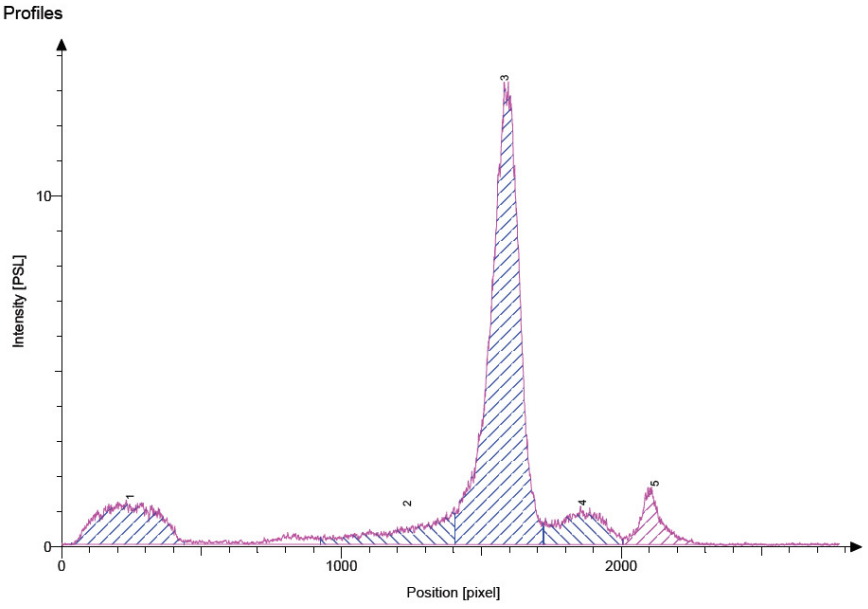

Figure S13: Profile for the best resolved lane on the radio-TLC shown in Fig. S12.

Table S6: Quantitative analysis of the radio-TLC profile shown in Fig. S13.

Peak #	% of total activity	Identity
1	12%	Unidentified metabolite, matrix effect or other artefact
2	9%	Unidentified metabolite, matrix effect or other artefact
3	66%	**[^{18}F]ALX5407**
4	8%	Unidentified metabolite, matrix effect or other artefact
5	5%	Unidentified metabolite, matrix effect or other artefact

6. Small animal PET studies

A summary of the PET studies on healthy rats is provided in Table S7.

Table S7. Summary of small animal PET studies.

Tracer	Additive	n
[^{18}F]ALX5407	none	4
[^{18}F]ALX5407	Elacridar, 4 mg/kg i.v., 30 min pre	1
[^{18}F]ALX5407	ALX5407, 1.5 mg/kg i.v., with tracer	1
[^{18}F]ALX5407	ALX5407, 3 mg/kg i.v., with tracer	1
[^{18}F]ALX5406	none	4
[^{18}F]ALX5406	Elacridar, 4 mg/kg i.v., 30 min pre	1
[^{18}F]ALX5406	ALX5407, 3 mg/kg i.v., 30 min pre	1

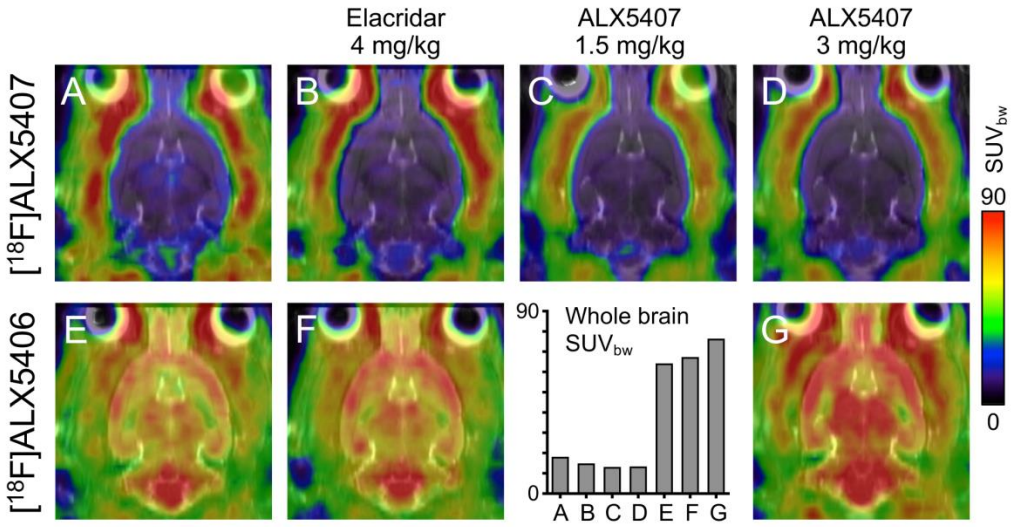

Figure S14. *In vivo* µPET imaging with [^{18}F]ALX5406 and [^{18}F]ALX5407 in healthy rats. µPET images (sum of 60 minutes measurements) were projected onto an MRI template in the horizontal plane. Rats were injected with [^{18}F]ALX5407 (**A**–**D**) or [^{18}F]ALX5406 (**E**–**G**). The tracers were applied alone (**A** and **E**), after pre-treatment with the Pgp inhibitor elacridar (**B** and **F**), together with nonradioactive ALX5407 (**C** and **D**) or after pretreatment with nonradioactive ALX5407 (**G**). Insert: Comparison of whole brain tracer uptake, determined from the same animals as shown in panels **A**–**G** (n=1 rat per experimental condition).

7. References

[1] Varney, M. D.; Romines, W. H.; Boritzki, T.; Margosiak, S. A.; Bartlett, C.; Howland, E. J. Synthesis and Biological Evaluation of -n[4-(2-Trans-[([2,6-Diamino-4(3H)-Oxopyrimidin-5-Yl]Methyl)Thio]Cyclobutyl)Benzoyl]-l-Glutamic Acid a Novel 5-Thiapyrimidinone Inhibitor of Dihydrofolate Reductase. *J. Heterocycl. Chem.* **1995**, *32* (5), 1493–1498. https://doi.org/10.1002/jhet.5570320514.

Chemistry–A European Journal

Supporting Information

Next Generation Copper Mediators for the Efficient Production of ^{18}F-Labeled Aromatics

Chris Hoffmann, Niklas Kolks, Daniel Smets, Alexander Haseloer, Benedikt Gröner, Elizaveta A. Urusova, Heike Endepols, Felix Neumaier, Uwe Ruschewitz, Axel Klein, Bernd Neumaier,* and Boris D. Zlatopolskiy

1 Materials and methods

1.1 General

Unless otherwise stated, all reagents and solvents were purchased from Sigma-Aldrich (Steinheim, Germany), Acros (Fisher Scientific GmbH, Nidderrau, Germany), Alfa Aesar [Thermo Fisher (Kandel) GmbH, Kandel, Germany], BLDPharm (Kaiserslautern, Germany) or Key Organics (Camelford, UK), and used without further purification. Unless otherwise stated, all reactions were carried out with magnetic stirring and, if air or moisture sensitive substrates and/or reagents were handled, in flame-dried glassware under argon. Organic extracts were dried over anhydrous Na_2SO_4 or $MgSO_4$. Solutions were concentrated under reduced pressure (1–900 mbar) at 40–50 °C using a rotary evaporator. Quinoline for the synthesis of copper complexes was purified by vacuum distillation over Na_2SO_4 and stored under argon. Compounds **7**,[1] **8**,[2] **9**,[3] (*S*,*S*)- and (*R*,*R*)-**11**[4] and (*S*,*S*)-**13**,[4] as well as Boc-DOPA-OMe,[5] were prepared according to the literature.

1.2 Nuclear magnetic resonance (NMR) spectroscopy

Proton and carbon nuclear magnetic resonance (^{1}H and ^{13}C NMR) spectra were recorded on a Bruker Avance Neo (400 MHz) spectrometer. Chemical shifts are reported in parts per million (ppm) relative to residual peaks of deuterated solvents. The observed signal multiplicities are characterized as follows: s = singlet, d = doublet, t = triplet, m = multiplet and br = broad. Coupling constants (*J*) are reported in hertz (Hz).

1.3 Mass spectrometry (MS)

Low resolution mass spectra (LR-MS) were measured with an MSQ PlusTM mass spectrometer (Thermo Electron Corporation, San Jose, USA).

High resolution mass spectra (HR-MS) were measured with an LTQ Orbitrap XL (Thermo Fischer Scientific Inc., Bremen, Germany).

1.4 Infrared spectroscopy (IR)

Infrared spectra were recorded as the neat compound using PerkinElmer UATR Two [PerkinElmer LAS (Germany) GmbH, Rodgau, Germany]. Absorptions were reported as wavenumbers (cm^{-1}).

1.5 Elemental analysis

Elemental analyses of the copper complexes were performed by HEKAtech GmbH (Wegberg, Germany).

1.6 Column Chromatography.

Merck silica gel, grade 60, 230–400 mesh, (Merck KGaA, Darmstadt, Germany) was used for column chromatography. Bpin and Me_3Sn derivatives were chromatographed on Sigma-Aldrich silica gel 60 Å, 230–400 mesh, with ca. 0.1% Ca (Sigma-Aldrich, Taufkirchen, Germany). For automated flash chromatography, a Grace Reveleris iES flash chromatography system equipped with RevealX detector, allowing for multisignal (UV/ELSD) collection (Büchi Labortechnik GmbH, Essen, Germany), and Büchi FlashPure (40 µm SiO_2) or Büchi FlashPure Select C_{18} (30 µm, spherical) cartridges (Büchi Labortechnik GmbH, Essen, Germany) were employed. Solvent proportions are indicated in a volume/volume ratio.

1.7 Thin layer chromatography (TLC)

Thin layer chromatography (TLC) was performed using precoated sheets, 0.25 mm Sil G/UV254 from Merck KGaA (Darmstadt, Germany). The chromatograms were visualized under UV light (λ = 254 nm) and/or using either phosphomolybdic acid or $KMnO_4$ stain solutions.

2 Chemistry

2.1 Preparation of Ni(II), Co(II) and Cu(II) complexes – General Procedure 1 (GP1)

The respective Cu, Ni or Co salt (1 eq.) was dissolved in hot *i*PrOH (0.2 M) and *N*-heteroarene (6 eq.) in isopropanol (2 M) was slowly added to the resulting solution. The reaction mixture was allowed to cool to ambient temperature and stirred for another 1 h. The products typically precipitated spontaneously. If no spontaneous precipitation occurred, Et_2O was added until the product had precipitated completely. The solid was filtered off and dried under reduced pressure.

$Co(Py)_4(ClO_4)_2 \cdot 3H_2O$[6]

The title compound was prepared according to GP1 from $Co(ClO_4)_2 \cdot 6H_2O$ (1.0 g, 2.8 mmol, 1 eq.) and pyridine (1.4 mL, 1.3 g, 17 mmol, 6 eq.). The product was obtained as a light red

solid (0.83 g, 1.3 mmol, 47%). IR (ATR): ν = 3391, 1643, 1604, 1489, 1445, 1220, 1126, 1088, 1066, 1042, 1009, 987, 953, 930, 885, 755, 703, 655, 623, 461. Elemental analysis calcd (%) for $C_{20}H_{26}CoCl_2N_4O_{11}$: C 38.23, H 4.17, N 8.92; found C 38.79, H 4.32, N 9.11.

$Ni(Py)_4(OTf)_2 \cdot H_2O$[6]

Anhydrous $Ni(OTf)_2$ (50 mg, 140 µmol, 1 eq.) was suspended in MeOH/H_2O (20 mL, 1:4) and heated gently until the solution became clear. The solvent was removed, and the residue was taken up in 2,2-dimethoxypropane (2 mL). A solution of pyridine (100 µL, 98 mg, 1.2 mmol, 86 eq.) in 2,2-dimethoxypropane (1 mL) was added and a light blue solid precipitated. The solvent was decanted, and the solid was washed with hexane and dried under high vacuum. The title compound was obtained as light blue solid (72 mg, 104 µmol, 74%). IR (ATR): ν = 1605, 1447, 1309, 1233, 1224, 1217, 1180, 1161, 1070, 1033, 1013, 764, 758, 710, 701, 653, 631, 581, 568, 511. Elemental analysis calcd (%) for $C_{22}H_{22}NiF_6N_4O_7S_2$: C 38.23, H 3.21, N 8.11; found C 37.92, H 3.00, N 7.95.

$Cu(Py)_4(OTf)_2$[7]

The title compound was prepared according to GP1 from $Cu(OTf)_2$ (0.50 g, 1.4 mmol, 1 eq.) and pyridine (0.68 mL, 0.67 g, 8.4 mmol, 6 eq.). The product was obtained as a blue solid (0.83 g, 1.2 mmol, 86%). Crystals for structural analysis were obtained by slow evaporation of a diluted solution of $Cu(Py)_4(OTf)_2$ in MeOH at ambient temperature. IR (ATR): ν = 1609, 1489, 1453, 1447, 1290, 1241, 1225, 1156, 1087, 1070, 1031, 1019, 989, 956, 759, 699, 654, 633, 572, 516. Elemental analysis calcd (%) for $C_{22}H_{20}CuF_6N_4O_6S_2$: C 38.97, H 2.97, N 8.26; found C 38.80, H 3.12, N 8.21.

$Cu(Py)_4(ClO_4)_2$[8]

The title compound was prepared according to GP1 from $Cu(ClO_4)_2 \cdot 6H_2O$ (2.0 g, 5.5 mmol, 1 eq.) and pyridine (2.7 mL, 2.65 g, 33 mmol, 6 eq.). The product was obtained as a light violet solid (3.2 g, 4.6 mmol, 85%). IR (ATR): ν = 1609, 1491, 1447, 1238, 1221, 1162, 1109, 1070, 1052, 1043, 1016, 1006, 985, 957, 932, 882, 757, 693, 640, 620. Elemental analysis calcd (%) for $C_{20}H_{20}CuCl_2N_4O_8$: C 41.50, H 3.48, N 9.68; found C 40.80, H 3.45, N 9.49.

$Cu(Py)_2Cl_2$[9]

The title compound was prepared according to GP1 from $CuCl_2$ (1.0 g, 5.9 mmol, 1 eq.) and pyridine (2.8 mL, 2.85 g, 35 mmol, 6 eq.). The product was obtained as a blue solid (1.6 g,

3.5 mmol, 93%). IR (ATR): ν = 3223, 3067, 3042, 3028, 3007, 1606, 1491, 1449, 1366, 1241, 1220, 1153, 1080, 1065, 1044, 1018, 873, 760, 687, 644. Elemental analysis calcd (%) for $C_{10}H_{10}CuCl_2N_2$: C 41.04, H 3.44, N 9.57; found C 40.47, H 3.24, N 9.34.

$Cu(Py)_2Br_2$[10]

The title compound was prepared according to GP1 from $CuBr_2$ (1.0 g, 4.5 mmol, 1 eq.) and pyridine (2.2 mL, 2.17 g, 27 mmol, 6 eq.). The product was obtained as a green solid (216 mg, 0.4 mmol, 13%). IR (ATR): ν = 3113, 3067, 3044, 3027, 3005, 1605, 1490, 1447, 1364, 1220, 1153, 1079, 1043, 1017, 945, 868, 755, 686, 651, 643. Elemental analysis calcd (%) for $C_{10}H_{10}CuBr_2N_2$: C 31.48, H 2.64, N 7.34; found C 30.57, H 2.54, N 7.04.

$Cu(Py)_4(ClO_3)_2$

$Cu(ClO_3)_2$[11] was prepared as follows. $CuSO_4$ (300 mg, 1.2 mmol, 1 eq.) was suspended in MeOH/H_2O (2:1, 30 mL) and heated under reflux until a clear blue solution was obtained. A solution of $Ba(ClO_3)_2$ (380 mg, 1.2 mmol, 1 eq.) in H_2O (3 mL) was added dropwise to the hot reaction mixture. After cooling to room temperature, the precipitated white solid was filtered off, washed with MeOH and the filtrate was concentrated under reduced pressure to afford hydrated $Cu(ClO_3)_2$ as a green solid. $Cu(ClO_3)_2$ was taken up in MeOH (20 mL) and pyridine (0.6 mL, 0.59 g, 7.2 mmol, 6 eq.) was added slowly at 80 °C. Thereafter, the reaction mixture was cooled to room temperature, the volume was reduced by half under reduced pressure and the reaction mixture was placed into the fridge for 16 h. The resulting precipitate was filtered off to afford the title compound as a violet solid (133 mg, 0.2 mmol, 20%). IR (ATR): ν = 3101, 3048, 3030, 1604, 1491, 1449, 1223, 1071, 1043, 994, 953, 902, 819, 777, 760, 707, 697, 640, 600, 472. Elemental analysis calcd (%) for $C_{20}H_{20}CuCl_2N_4O_6$: C 43.93, H 3.69, N 10.25; found C 43.85, H 3.69, N 10.12.

$Cu(Py)_4(OTs)_2 \cdot H_2O$

The title compound was prepared according to GP1 from $Cu(OTs)_2$ (0.50 g, 1.2 mmol, 1 eq.) and pyridine (0.6 mL, 0.57 g, 7.2 mmol, 6 eq.). The product was obtained as a light blue solid (0.76 g, 1.1 mmol, 86%). IR (ATR): ν = 1607, 1450, 1232, 1220, 1172, 1162, 1150, 1117, 1071, 1045, 1030, 1006, 818, 767, 697, 679, 651, 642, 562, 550. Elemental analysis calcd (%) for $C_{34}H_{34}CuN_4O_7S_2$: C 55.16, H 4.90, N 7.57; found C 55.62, H 4.75, N 7.35.

$Cu(Py)_4(OMs)_2$

The title compound was prepared according to GP1 from $Cu(OMs)_2 \cdot 2H_2O$ (1.0 g, 3.5 mmol, 1 eq.) and pyridine (1.7 mL, 1.6 g, 21 mmol, 6 eq.). The product was obtained as a blue solid (1.7 g, 3.0 mmol, 86%). IR (ATR): ν = 1606, 1490, 1448, 1230, 1220, 1206, 1181, 1153, 1145, 1081, 1072, 1042, 1016, 766, 760, 699, 689, 639, 551, 526. Elemental analysis calcd (%) for $C_{22}H_{26}CuN_4O_6S_2$: C 46.35, H 4.60, N 9.83; found C 46.98, H 4.44, N 10.27.

$[Cu(Py)_3SO_4)]_2$[12]

Anhydrous pyridine (12.0 mL, 11.8 g, 149 mmol, 12 eq.) was added to anhydrous $CuSO_4$ (2.00 g, 12.5 mmol, 1 eq.) and the resulting blue suspension was vigorously stirred at 100 ºC for 16 h. *i*PrOH (30 mL) was added to the reaction mixture and stirring was continued at 70 ºC for 1 h. The resulting suspension was cooled to ambient temperature and filtered. The filter cake was washed with *i*PrOH (80 mL) followed by Et_2O (80 mL) and dried to afford the title compound as a blue solid (5.04 g, 12.7 mmol, >99%). IR (ATR): ν = 1449, 1130, 1100, 1083, 1071, 1054, 1041, 1021, 1014, 990, 789, 777, 765, 756, 713, 698, 639, 618, 603, 559. Elemental analysis calcd (%) for $C_{15}H_{15}CuN_3O_4S$: C 45.39, H 3.81, N 10.59; found C 45.90, H 4.33, N 10.62.

$[Cu(Py)(OAc)_2]_2$[13,14]

Anhydrous pyridine (8.0 mL, 7.9 g, 99 mmol, 9 eq.) was added to anhydrous $Cu(OAc)_2$ [2.0 g, 11 mmol, 1 eq.; prepared by drying of $Cu(OAc)_2 \cdot H_2O$ at 140 ºC for 4 h] and the resulting blue suspension was vigorously stirred at 70 ºC for 1 h. *i*PrOH (20 mL) was added to the reaction mixture and stirring was continued for 4 h. The resulting green suspension was cooled to ambient temperature and filtered. The filter cake was washed with *i*PrOH (80 mL) followed by Et_2O (80 mL) and dried to afford the title compound as a green solid (2.54 g, 9.7 mmol ,88%). IR (ATR): ν = 1611, 1597, 1573, 1484, 1445, 1424, 1361, 1350, 1236, 1217, 1153, 1082, 1070, 1049, 1037, 1008, 764, 704, 681, 627. Elemental analysis calcd (%) for $C_9H_{11}CuNO_4$: C 41.46, H 4.25, N 5.37; found C 41.41, H 4.29, N 5.32.

$Cu(4\text{-}PhPy)_4(OTf)_2$[15]

The title compound was prepared according to GP1 from $Cu(OTf)_2$ (1.9 g, 5.4 mmol, 1 eq.) and 4-phenylpyridine (5.0 g, 32 mmol, 6 eq.). The product was obtained as a blue solid (5.2 g, 5.3 mmol, 98%). IR (ATR): ν = 1615, 1421, 1289, 1256, 1241, 1228, 1156, 1072, 1030, 1014, 844, 767, 735, 699, 636, 625, 574, 565, 516, 491. Elemental analysis calcd (%) for $C_{46}H_{36}CuF_6N_4O_6S_2$: C 56.24, H 3.69, N 5.70; found C 55.8, H 3.73, N 5.67.

$Cu(4\text{-}PhPy)_4(ClO_4)_2$

The title compound was prepared according to GP1 from $Cu(ClO_4)_2 \cdot 6H_2O$ (1.0 g, 2.7 mmol, 1 eq.) and 4-phenylpyridine (2.5 g, 16 mmol, 6 eq.). The product was obtained as a violet solid (2.5 g, 2.5 mmol, 93%). IR (ATR): ν = 1615, 1487, 1423, 1225, 1104, 1072, 1045, 1013, 952, 927, 840, 765, 731, 698, 693, 620, 564, 496, 489, 472. Elemental analysis calcd (%) for $C_{44}H_{36}CuCl_2N_4O_8$: C 59.83, H 4.11, N 6.34; found C 59.4, H 4.53, N 5.96.

$Cu(2\text{-}MeOPy)_2(OTf)_2$

The title compound was prepared according to GP1 from $Cu(OTf)_2$ (1.0 g, 2.8 mmol, 1 eq.) and 2-methoxypyridine (1.8 mL, 1.87 g, 17 mmol, 6 eq.). The product was obtained as a violet solid (1.9 g, 2.4 mmol, 84%). IR (ATR): ν = 3118, 1609, 1579, 1486, 1436, 1306, 1263, 1226, 1160, 1120, 1063, 1050, 1029, 1007, 783, 758, 652, 635, 572, 517. Elemental analysis calcd (%) for $C_{26}H_{28}CuF_6N_4O_{10}S_2$: C 39.12, H 3.54, N 7.02; found C 38.64, H 3.53, N 6.89.

$Cu(2\text{-}MeOPy)_2(ClO_4)_2 \cdot 2H_2O$

The title compound was prepared according to GP1 from $Cu(ClO_4)_2 \cdot 6H_2O$ (1.0 g, 2.8 mmol, 1 eq.) and 2-methoxypyridine (1.8 mL, 1.87 g, 17 mmol, 6 eq.). The product was obtained as a violet solid (1.8 g, 2.3 mmol, 84%). IR (ATR): ν = 3117, 1609, 1577, 1485, 1431, 1303, 1289, 1267, 1166, 1078, 1028, 1005, 933, 878, 785, 652, 621, 572, 524, 498. Elemental analysis calcd (%) for $C_{24}H_{32}CuCl_2N_4O_{14}$: C 39.22, H 4.39, N 7.62; found C 39.52, H 4.31, N 7.34.

$Cu(3\text{-}MeOPy)_4(OTf)_2$

The title compound was prepared according to GP1 from $Cu(OTf)_2$ (1.0 g, 2.8 mmol, 1 eq.) and 3-methoxypyridine (1.8 mL, 1.95 g, 17 mmol, 6 eq.). The product was obtained as a violet solid (2.1 g, 2.6 mmol, 92%). IR (ATR): ν = 1580, 1494, 1432, 1282, 1240, 1227, 1197, 1187, 1160, 1112, 1060, 1028, 1012, 823, 807, 700, 634, 574, 562, 516. Elemental analysis calcd (%) for $C_{26}H_{28}CuF_6N_4O_{10}S_2$: C 39.12, H 3.54, N 7.02; found C 38.90, H 3.78, N 7.04.

$Cu(3\text{-}MeOPy)_4(ClO_4)_2$

The title compound was prepared according to GP1 from $Cu(ClO_4)_2 \cdot 6H_2O$ (1.0 g, 2.8 mmol, 1 eq.) and 3-methoxypyridine (1.8 mL, 1.95 g, 17 mmol, 6 eq.). The product was obtained as a violet solid (1.9 g, 2.4 mmol, 85%). IR (ATR): ν = 1575, 1496, 1487, 1430, 1290, 1248, 1197,

1103, 1067, 1058, 1046, 1032, 1010, 930, 909, 808, 700, 649, 620, 577. Elemental analysis calcd (%) for $C_{24}H_{28}CuCl_2N_4O_{12}$: C 41.24, H 4.04, N 8.02; found C 40.50, H 4.11, N 7.93.

Cu(4-MeOPy)$_4$(OTf)$_2$

The title compound was prepared according to GP1 from $Cu(OTf)_2$ (0.6 g, 1.7 mmol, 1 eq.) and 4-methoxypyridine (1.0 mL, 1.08 g, 10 mmol, 6 eq.). The product was obtained as a violet solid (1.3 g, 1.6 mmol, 94%). Crystals for the structural analysis were obtained by slow evaporation of a diluted solution of the complex in MeOH at ambient temperature. IR (ATR): ν = 1616, 1566, 1515, 1441, 1305, 1287, 1241, 1223, 1210, 1154, 1059, 1027, 1005, 836, 828, 812, 635, 572, 541, 516. Elemental analysis calcd (%) for $C_{26}H_{28}CuF_6N_4O_{10}S_2$: C 39.12, H 3.54, N 7.02; found C 38.90, H 3.67, N 7.01.

Cu(4-MeOPy)$_4$(ClO$_4$)$_2$

The title compound was prepared according to GP1 from $Cu(ClO_4)_2 \cdot 6\ H_2O$ (0.6 g, 1.7 mmol, 1 eq.) and 4-methoxypyridine (1.0 mL, 1.08 g, 10 mmol, 6 eq.). The product was obtained as a violet solid (1.1 g, 1.6 mmol, 94%). IR (ATR): ν = 1617, 1567, 1517, 1504, 1441, 1306, 1210, 1111, 1100, 1070, 1057, 1052, 1030, 1010, 984, 838, 832, 813, 620, 539. Elemental analysis calcd (%) for $C_{24}H_{28}CuCl_2N_4O_{12}$: C 41.24, H 4.04, N 8.02; found C 40.90, H 4.02, N 8.03.

Cu[2,4-(MeO)$_2$Py]$_4$(OTf)$_2$

The title compound was prepared according to GP1 from $Cu(OTf)_2$ (1.0 g, 2.8 mmol, 1 eq.) and 2,4-dimethoxypyridine (2.2 mL, 2.34 g, 17 mmol, 6 eq.). The product was obtained as a blue solid (2.1 g, 2.6 mmol, 92%). IR (ATR): ν = 1615, 1575, 1484, 1439, 1341, 1258, 1219, 1186, 1162, 1116, 1044, 1026, 1006, 941, 831, 816, 636, 573, 517, 467. Elemental analysis calcd (%) for $C_{30}H_{36}CuF_6N_4O_{14}S_2$: C 39.24, H 3.95, N 6.10; found C 38.74, H 3.90, N 5.96.

Cu[2,4-(MeO)$_2$Py]$_4$(ClO$_4$)$_2$

The title compound was prepared according to GP1 from $Cu(ClO_4)_2 \cdot 6H_2O$ (1.0 g, 2.8 mmol, 1 eq.) and 2,4-dimethoxypyridine (2.2 mL, 2.34 g, 17 mmol, 6 eq.). The product was obtained as blue solid (1.9 g, 2.4 mmol, 85%). IR (ATR): ν = 1615, 1575, 1504, 1484, 1461, 1440, 1418, 1340, 1271, 1220, 1184, 1079, 1043, 1028, 1007, 941, 828, 664, 622, 464. Elemental analysis calcd (%) for $C_{28}H_{36}CuCl_2N_4O_{16}$: C 41.06, H 4.43, N 6.84; found C 41.03, H 4.78, N 6.78.

$Cu(3,4\text{-}Me_2Py)_4(OTf)_2$

The title compound was prepared according to GP1 from $Cu(OTf)_2$ (1.0 g, 2.8 mmol, 1 eq.) and 3,4-lutidine (1.8 mL, 1.72 g, 17 mmol, 6 eq.). The product was obtained as a violet solid (2.1 g, 2.6 mmol, 94%). Crystals for structural analysis were obtained by slow cooling of a solution of 10 mg of the title compound in 10 mL hot *i*PrOH to ambient temperature. IR (ATR): ν = 1615, 1501, 1451, 1290, 1241, 1223, 1207, 1155, 1086, 1032, 873, 843, 756, 722, 637, 617, 572, 542, 529, 516. Elemental analysis calcd (%) for $C_{30}H_{36}CuF_6N_4O_6S_2$: C 45.59, H 4.59, N 7.09; found C 45.10, H 4.81, N 7.08.

$Cu(3,4\text{-}Me_2Py)_4(ClO_4)_2$

The title compound was prepared according to GP1 from $Cu(ClO_4)_2{\cdot}6H_2O$ (1.0 g, 2.8 mmol, 1 eq.) and 3,4-lutidine (1.8 mL, 1.7 g, 17 mmol, 6 eq.). The product was obtained as a violet solid (1.8 g, 2.6 mmol, 91%). IR (ATR): ν = 2980, 1615, 1502, 1449, 1424, 1383, 1207, 1176, 1111, 1048, 1012, 979, 931, 874, 847, 835, 721, 621, 543, 529. Elemental analysis calcd (%) for $C_{28}H_{36}CuCl_2N_4O_8$: C 48.67, H 5.25, N 8.11; found C 48.3, H 5.34, N 8.09.

$Cu(4,4'\text{-}BiPy)_2(OTf)_2{\cdot}H_2O$

The title compound was prepared according to GP1 from $Cu(OTf)_2$ (1.0 g, 2.8 mmol, 1 eq.) and 4,4'-bipyridine (2.7 g, 17 mmol, 6 eq.). The product was obtained as a light blue solid (1.1 g, 1.6 mmol, 57%). IR (ATR): ν = 1615, 1539, 1493, 1421, 1290, 1241, 1225, 1152, 1073, 1031, 1018, 818, 760, 730, 675, 635, 608, 574, 517, 488. Elemental analysis calcd (%) for $C_{22}H_{18}CuF_6N_4O_7S_2$: C 38.18, H 2.62, N 8.10; found C 37.81, H 2.92, N 7.87.

$Cu(4,4'\text{-}BiPy)_2(ClO_4)_2{\cdot}i$PrOH

The title compound was prepared according to GP1 from $Cu(ClO_4)_2{\cdot}6H_2O$ (1.0 g, 2.7 mmol, 1 eq.) and 4,4'-bipyridine (2.5 g, 16 mmol, 6 eq.). The product was obtained as a light blue solid (2.1 g, >99%). IR (ATR): ν = 1612, 1600, 1419, 1408, 1076, 1064, 1019, 1004, 992, 833, 828, 813, 802, 729, 642, 623, 611, 571, 516, 476. Elemental analysis calcd (%) for $C_{23}H_{24}CuCl_2N_4O_9$: C 43.51, H 3.81, N 8.82; found C 44.58, H 3.25, N 10.27.

$Cu(Pz)_4(OTf)_2{\cdot}2H_2O$[7]

The title compound was prepared according to GP1 from $Cu(OTf)_2$ (1.9 g, 5.4 mmol, 1 eq.) and pyrazine (2.6 g, 32 mmol, 6 eq.). The product was obtained as a light blue solid (3.7 g, 5.4 mmol, 95%). IR (ATR): ν = 1418, 1283, 1247, 1225, 1175, 1149, 1125, 1084, 1055, 1033,

1027, 805, 760, 749, 701, 633, 573, 515, 494, 455. Elemental analysis calcd (%) for $C_{18}H_{20}CuF_6N_8O_8S_2$: C 30.11, H 2.81, N 15.61; found C 29.52, H 2.45, N 14.69.

Cu(4-F$_3$CPy)$_4$(OTf)$_2$·2H$_2$O

The title compound was prepared according to GP1 from $Cu(OTf)_2$ (2.9 g, 8.0 mmol, 1 eq.) and 4-(trifluoromethyl)pyridine (7.0 g, 48 mmol, 6 eq.). The product was obtained as a light blue solid (7.1 g, 7.4 mmol, 90%). IR (ATR): ν = 1425, 1326, 1298, 1241, 1215, 1168, 1137, 1108, 1089, 1061, 1029, 841, 759, 678, 665, 637, 610, 574, 517, 502. Elemental analysis calcd (%) for $C_{26}H_{20}CuF_{18}N_4O_8S_2$: C 31.67, H 2.04, N 5.68; found C 31.33, H 1.65, N 5.52.

Cu(Quin)$_3$(OTf)$_2$·MeOH

$Cu(OTf)_2$ (500 mg, 1.4 mmol, 1 eq.) was suspended in degassed anhydrous MeOH (14 mL) and heated gently until the solution became clear. A solution of freshly distilled quinoline (1 mL, 1.1 g, 8.4 mmol, 6 eq.) in degassed anhydrous MeOH (17 mL) was added slowly at room temperature and the green solution placed in the freezer at –20 °C for 2 h. The solvent was decanted, and the precipitated solid was washed with hexane and dried over high vacuum. The title compound was obtained as dark green solid (425 mg, 0.54 mmol, 42%). IR (ATR): ν = 1510, 1289, 1251, 1235, 1224, 1166, 1146, 1133, 1057, 1032, 822, 808, 780, 756, 736, 635, 572, 556, 515, 489. Elemental analysis calcd (%) for $C_{30}H_{25}CuF_6N_3O_7S_2$: C 46.13, H 3.23, N 5.38; found C 46.90, H 3.40, N 5.55.

Cu(Quin)$_3$(ClO$_4$)$_2$·MeOH

$Cu(ClO_4)_2$·6H$_2$O (500 mg, 1.3 mmol, 1 eq.) was suspended in degassed anhydrous MeOH (14 mL) and heated gently until the solution became clear. A solution of freshly distilled quinoline (0.9 mL, 1.0 g, 7.8 mmol, 6 eq.) in degassed anhydrous MeOH (17 mL) was added slowly at room temperature and the green solution placed in the freezer at –20 °C for 2 h. The solvent was decanted, and the precipitated solid was washed with hexane and dried over high vacuum. The title compound was obtained as dark green solid (355 mg, 0.52 mmol, 40%). IR (ATR): ν = 1509, 1312, 1095, 1083, 1067, 1047, 960, 824, 808, 788, 779, 746, 738, 640, 621, 559, 531, 500, 488, 467. Elemental analysis calcd (%) for $C_{28}H_{25}CuCl_2N_3O_9$: C 49.31, H 3.70, N 6.16; found C 49.04, H 3.82, N 6.10.

Cu(Isoq)$_4$(OTf)$_2$[16]

The title compound was prepared according to GP1 from $Cu(OTf)_2$ (1.0 g, 2.8 mmol, 1 eq.) and isoquinoline (2.2 g, 17 mmol, 6 eq.). The product was obtained as a light blue solid (2.5 g,

2.8 mmol, 99%). IR (ATR): ν = 1634, 1389, 1291, 1239, 1222, 1183, 1158, 1149, 1045, 1029, 1017, 962, 873, 830, 748, 632, 573, 516, 484, 471. Elemental analysis calcd (%) for $C_{38}H_{28}CuF_6N_4O_6S_2$: C 51.96, H 3.21, N 6.38; found C 51.80, H 3.61, N 6.25.

Cu(Isoq)$_4$(ClO$_4$)$_2$

The title compound was prepared according to GP1 from $Cu(ClO_4)_2 \cdot 6H_2O$ (1.0 g, 2.8 mmol, 1 eq.) and isoquinoline (2.2 g, 17 mmol, 6 eq.). The product was obtained as a light blue solid (2.2 g, 2.4 mmol, 98%). IR (ATR): ν = 1633, 1389, 1281, 1112, 1055, 1044, 1037, 1016, 998, 962, 931, 872, 835, 827, 745, 639, 620, 542, 484, 470. Elemental analysis calcd (%) for $C_{36}H_{28}CuCl_2N_4O_8$: C 55.50, H 3.62, N 7.19; found C 54.70, H 3.69, N 7.16.

Cu(Pyr)$_4$(OTf)$_2$[17]

The title compound was prepared according to GP1 from $Cu(OTf)_2$ (1.0 g, 2.8 mmol, 1 eq.) and *N*-methylpyrazole (1.4 mL, 1.38 g, 17 mmol, 6 eq.). The product was obtained as a blue solid (0.9 g, 1.3 mmol, 47%). IR (ATR): ν = 1526, 1434, 1413, 1274, 1241, 1223, 1175, 1152, 1114, 1083, 1056, 1028, 1000, 788, 766, 678, 633, 607, 573, 516. Elemental analysis calcd (%) for $C_{18}H_{24}CuF_6N_8O_6S_2$: C 31.33, H 3.51, N 16.24; found C 30.68, H 3.48, N 15.75.

Cu(Triaz)$_4$(OTf)$_2$

The title compound was prepared according to GP1 from $Cu(OTf)_2$ (1.0 g, 2.8 mmol, 1 eq.) and 1-methyl-1,2,4-triazole (1.3 mL, 1.4 g, 17 mmol, 6 eq.). The product was obtained as a light blue solid (1.7 g, 2.4 mmol, 85%). IR (ATR): ν = 1543, 1295, 1280, 1248, 1227, 1171, 1157, 1129, 1077, 1034, 994, 905, 883, 853, 691, 681, 672, 634, 573, 517. Elemental analysis calcd (%) for $C_{14}H_{20}CuF_6N_{12}O_6S_2$: C 24.23, H 2.90, N 24.22; found C 24.00, H 2.91, N 23.85.

Cu(Impdz)$_4$(OTf)$_2$[18]

The title compound was prepared according to GP1 from $Cu(OTf)_2$ (1.9 g, 5.4 mmol, 1 eq.) and imidazo(1,2-b)pyridazine (3.8 g, 32 mmol, 6 eq.). The product was obtained as a blue solid (4.4 g, 5.2 mmol, 96%). IR (ATR): ν = 1541, 1503, 1373, 1352, 1307, 1280, 1239, 1220, 1149, 1069, 1026, 878, 804, 754, 731, 632, 582, 572, 514, 457. Elemental analysis calcd (%) for $C_{26}H_{20}CuF_6N_{12}O_6S_2$: C 37.26, H 2.41, N 20.05; found C 36.80, H 2.36, N 19.80.

$Cu(Impdz)_4(ClO_4)_2 \cdot H_2O$

The title compound was prepared according to GP1 from $Cu(ClO_4)_2 \cdot 6H_2O$ (2.0 g, 5.5 mmol, 1 eq.) and imidazo(1,2-b)pyridazine (3.9 g, 33 mmol, 6 eq.). The product was obtained as a light violet solid (4.4 g, >99%). IR (ATR): ν = 1541, 1504, 1372, 1348, 1301, 1270, 1151, 1088, 1068, 1023, 991, 806, 784, 758, 744, 637, 621, 583, 573, 459. Elemental analysis calcd (%) for $C_{24}H_{22}CuCl_2N_{12}O_9$: C 38.08, H 2.93, N 22.21; found C 38.10, H 3.06, N 22.20.

$Cu(Impdz)_4(ClO_3)_2 \cdot 2H_2O$

$Cu(ClO_3)_2$[11] was prepared as follows. $CuSO_4$ (1.2 g, 7.4 mmol, 1 eq.) was suspended in $MeOH/H_2O$ (2:1, 186 mL) and heated under reflux until a clear blue solution was obtained. A solution of $Ba(ClO_3)_2$ (2.4 g, 7.4 mmol, 1 eq.) in H_2O (19 mL) was added dropwise to the hot reaction mixture. After cooling to room temperature, the precipitated white solid was filtered off, washed with MeOH and the filtrate was concentrated under reduced pressure to afford $Cu(ClO_3)_2$ as a green solid. $Cu(ClO_3)_2$ was taken up in MeOH (124 mL) and imidazo(1,2-b)pyridazine (5.3 g, 44 mmol, 6 eq.) was added slowly at 80 °C. Thereafter, the reaction mixture was cooled to room temperature, the volume was reduced by half under reduced pressure and the reaction mixture was placed into the fridge for 16 h. The resulting precipitate was filtered off to afford the title compound as a blue solid (1.9 g, 2.7 mmol, 36%). IR (ATR): ν = 1620, 1537, 1500, 1372, 1350, 1303, 1270, 1149, 956, 927, 913, 793, 756, 731, 636, 604, 581, 573, 471, 458. Elemental analysis calcd (%) for $C_{24}H_{24}CuCl_2N_{12}O_8$: C 38.80, H 3.26, N 22.62; found C 39.12, H 3.27, N 22.33.

$Cu(Impdz)_4(OTs)_2 \cdot 2H_2O$

The title compound was prepared according to GP1 from $Cu(OTs)_2$ (1.1 g, 2.7 mmol, 1 eq.) and imidazo(1,2-b)pyridazine (1.9 g, 16 mmol, 6 eq.). The product was obtained as a dark turquoise solid (1.7 g, 1.9 mmol, 69%). IR (ATR): ν = 1539, 1371, 1349, 1303, 1230, 1186, 1174, 1151, 1119, 1035, 1010, 808, 798, 753, 717, 679, 634, 566, 549, 456. Elemental analysis calcd (%) for $C_{38}H_{38}CuN_{12}O_8S_2$: C 49.69, H 4.17, N 18.30; found C 50.03, H 4.11, N 17.91.

$[Cu(Impdz)_3(OMs)_2]_2$

The title compound was prepared according to GP1 from $Cu(OMs)_2$ (1.7 g, 6.8 mmol, 1 eq.) and imidazo(1,2-b)pyridazine (4.9 g, 41 mmol, 6 eq.). The product was obtained as a turquoise solid (4.3 g, 5.8 mmol, 85%). IR (ATR): ν = 1349, 1303, 1206, 1186, 1149, 1137, 1040, 808,

800, 793, 772, 757, 749, 727, 572, 550, 528, 516, 467, 455. Elemental analysis calcd (%) for $C_{20}H_{21}CuN_9O_6S_2$: C 39.31, H 3.46, N 20.63; found C 39.35, H 3.48, N 21.32.

2.2 Crystallography

Crystallographic tables for $Cu(Py)_4(OTf)_2$

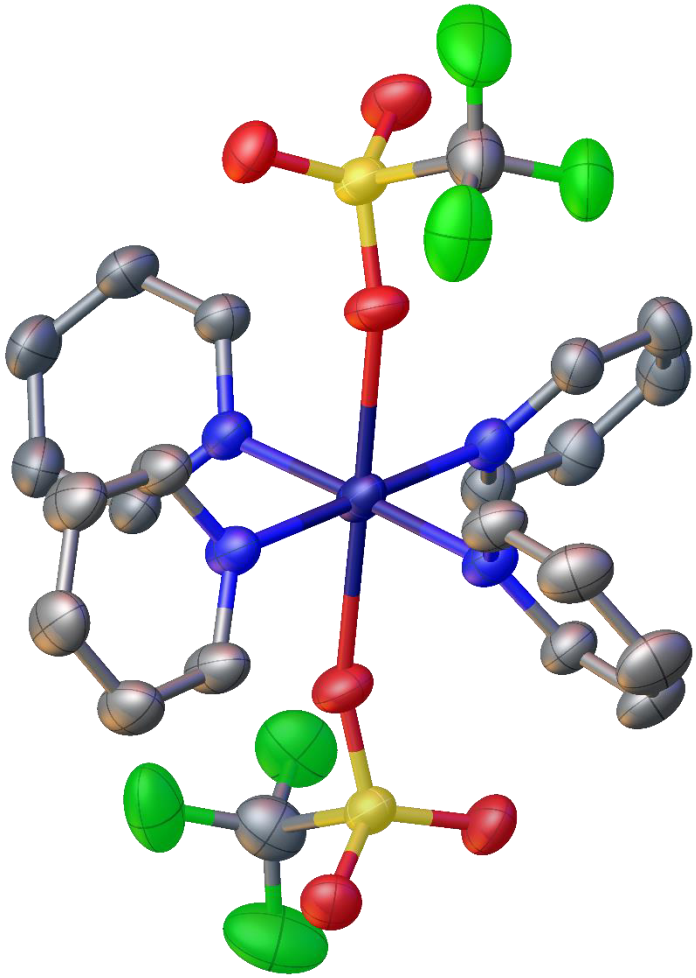

Figure S1: Crystal structure of $Cu(Py)_4(OTf)_2$.

Table S1: Crystal data and structure refinement for $Cu(Py)_4(OTf)_2$.

Identification code	$Cu(Py)_4(OTf)_2$
CCDC number:	2202867
Empirical formula	$C_{11}H_{10}Cu_{0.5}F_3N_2O_3S$
Formula weight	339.048
Temperature/K	293(2)
Crystal system	orthorhombic
Space group	Pbcn
a/Å	10.461(5)
b/Å	16.152(5)

c/Å	16.556(5)
α/°	90.000(5)
β/°	90.000(5)
γ/°	90.000(5)
Volume/Å^3	2797.4(18)
Z	8
ρ_{calc}g/cm^3	1.610
μ/mm^{-1}	1.014
F(000)	1375.3
Radiation	Mo Kα (λ = 0.71073)
2Θ range for data collection/°	4.64 to 53.6
Index ranges	-13 ≤ h ≤ 13, -20 ≤ k ≤ 20, -20 ≤ l ≤ 20
Reflections collected	39891
Independent reflections	2978 [R_{int} = 0.0796, R_{sigma} = 0.0298]
Data/restraints/parameters	2978/0/189
Goodness-of-fit on F^2	1.042
Final R indexes [I>=2σ (I)]	R_1 = 0.0352, wR_2 = 0.0878
Final R indexes [all data]	R_1 = 0.0552, wR_2 = 0.0979
Largest diff. peak/hole / e Å^{-3}	0.49/-0.44

Table S2: Fractional atomic coordinates (×10^4) and equivalent isotropic displacement parameters (Å^2×10^3) for Cu(Py)$_4$(OTf)$_2$. U_{eq} is defined as 1/3 of the trace of the orthogonalized U_{IJ} tensor.

Atom	*x*	*y*	*z*	U(eq)
C1	2478(2)	789.7(15)	8237.0(16)	41.5(5)
C2	1491(2)	851.1(19)	8778.2(19)	54.0(7)
C3	1670(3)	1297(2)	9476(2)	60.2(8)
C4	2835(3)	1662.0(18)	9613.2(19)	55.1(7)
C5	3779(2)	1583.5(15)	9041.6(17)	45.0(6)
C6	6032(3)	2819.0(16)	7730.9(19)	49.7(7)
C7	6064(3)	3667.2(17)	7749(2)	55.1(7)
C8	5000	4099(2)	7500	54.7(10)
C9	4764(2)	-564.0(14)	6818.4(17)	41.5(6)
C10	4750(3)	-1415.4(16)	6802.6(19)	48.8(7)
C11	5000	-1847(2)	7500	49.8(9)
C12	7242(3)	1013.5(18)	10020.3(19)	57.6(7)
N1	3618.1(18)	1153.4(11)	8354.1(13)	37.9(4)
N2	5000	2390.1(16)	7500	40.1(7)
N3	5000	-134.5(16)	7500	36.2(6)
O1	6530.8(16)	1141.7(11)	8564.3(12)	46.6(4)
O2	8498.3(17)	1823.2(11)	8947.9(12)	47.2(4)
O3	8414.7(18)	324.5(11)	8827.5(14)	53.9(5)
F1	6533(2)	338.4(11)	10147.6(12)	71.4(5)
F2	6516(2)	1668.0(12)	10219.8(12)	77.1(6)
F3	8223(2)	993.3(15)	10521.1(13)	91.0(7)

Atom	*x*	*y*	*z*	U(eq)
S1	7748.1(5)	1083.6(3)	8974.8(4)	36.84(16)
Cu1	5000	1128.3(2)	7500	36.47(14)

Table S3: Anisotropic displacement parameters ($Å^2×10^3$) for $Cu(Py)_4(OTf)_2$. The anisotropic displacement factor exponent takes the form: $-2\pi^2[h^2a^{*2}U_{11}+2hka^*b^*U_{12}+\ldots]$.

Atom	U_{11}	U_{22}	U_{33}	U_{12}	U_{13}	U_{23}
C1	31.0(11)	42.1(12)	51.4(15)	-3.0(9)	0.1(11)	-3.0(11)
C2	30.1(13)	66.6(17)	65.2(19)	-2.5(12)	2.9(12)	-8.5(14)
C3	40.2(14)	77(2)	63.8(19)	6.9(13)	12.2(14)	-16.5(16)
C4	44.7(15)	56.9(16)	63.6(19)	9.7(12)	-1.1(14)	-18.3(14)
C5	33.1(12)	40.5(12)	61.5(17)	4.0(10)	-3.3(12)	-10.8(12)
C6	36.1(13)	37.0(12)	76(2)	-2.2(10)	-9.8(13)	4.0(12)
C7	43.2(15)	39.3(13)	83(2)	-7.2(11)	-6.8(15)	-3.0(13)
C8	54(2)	29.5(16)	80(3)	-0	0(2)	0
C9	38.7(13)	37.8(12)	47.9(15)	-0.7(9)	4.5(11)	-2.4(10)
C10	50.1(16)	40.4(13)	55.8(17)	-3.6(11)	7.0(13)	-8.8(11)
C11	50(2)	31.9(16)	67(3)	-0	13(2)	0
C12	65.6(19)	53.3(17)	53.9(17)	-12.9(14)	-0.5(15)	4.8(13)
N1	27.8(9)	33.0(10)	53.0(12)	1.2(7)	-0.1(9)	-4.6(8)
N2	32.1(14)	28.8(13)	59.5(19)	-0	-4.4(14)	0
N3	29.2(13)	29.8(12)	49.4(16)	-0	4.9(13)	0
O1	30.3(9)	51.6(10)	58.0(11)	4.6(7)	-8.1(8)	-0.2(8)
O2	40.8(10)	42.9(10)	57.9(11)	-9.4(7)	3.7(9)	-1.7(8)
O3	37.9(10)	42.7(10)	81.1(15)	9.0(7)	0.5(10)	-8.2(9)
F1	79.5(13)	62.8(11)	71.8(13)	-19.3(9)	11.0(10)	15.4(9)
F2	94.6(15)	64.8(11)	71.9(12)	-10.2(10)	35.4(11)	-16.4(9)
F3	104.5(17)	110.2(17)	58.2(12)	-32.5(14)	-28.0(12)	17.5(11)
S1	28.3(3)	35.1(3)	47.1(3)	0.5(2)	-1.1(2)	-1.6(2)
Cu1	25.8(2)	27.8(2)	55.8(3)	-0	2.27(17)	0

Table S4: Bond lengths for $Cu(Py)_4(OTf)_2$.

Atom	Atom	Length/Å	Atom	Atom	Length/Å
C1	C2	1.371(4)	C12	F1	1.336(3)
C1	N1	1.343(3)	C12	F2	1.343(4)
C2	C3	1.374(4)	C12	F3	1.320(4)
C3	C4	1.373(4)	C12	S1	1.813(3)
C4	C5	1.373(4)	N1	$Cu1^1$	2.023(2)
C5	N1	1.344(3)	N2	Cu1	2.038(3)
C6	C7	1.371(4)	N3	Cu1	2.040(3)
C6	N2	1.338(3)	O1	S1	1.4465(18)
C7	C8	1.377(3)	O1	Cu1	2.3811(19)

Atom	Atom	Length/Å	Atom	Atom	Length/Å
C9	C10	1.376(3)	O2	S1	1.4300(18)
C9	N3[1]	1.347(3)	O3	S1	1.4314(18)
C10	C11[1]	1.374(4)			

[1]1-X,+Y,3/2-Z

Table S5: Bond angles for $Cu(Py)_4(OTf)_2$.

Atom	Atom	Atom	Angle/°	Atom	Atom	Atom	Angle/°
N1	C1	C2	122.9(2)	Cu1	N3	C9[1]	120.99(14)
C3	C2	C1	119.0(3)	Cu1	N3	C9	120.99(14)
C4	C3	C2	119.0(3)	Cu1	O1	S1	159.91(12)
C5	C4	C3	119.0(3)	O1	S1	C12	101.29(14)
N1	C5	C4	122.8(2)	O2	S1	C12	104.00(13)
N2	C6	C7	122.9(3)	O2	S1	O1	114.48(11)
C8	C7	C6	118.7(3)	O3	S1	C12	104.55(14)
C7[1]	C8	C7	119.1(3)	O3	S1	O1	113.85(11)
N3[1]	C9	C10	122.2(3)	O3	S1	O2	116.29(11)
C11[1]	C10	C9	119.3(3)	N1	Cu1	N1[1]	177.70(11)
C10	C11	C10[1]	119.0(3)	N2	Cu1	N1[1]	88.85(5)
F2	C12	F1	106.8(3)	N2	Cu1	N1	88.85(5)
F3	C12	F1	108.2(2)	N3	Cu1	N1[1]	91.15(5)
F3	C12	F2	107.7(3)	N3	Cu1	N1	91.15(5)
S1	C12	F1	111.3(2)	N3	Cu1	N2	180.0
S1	C12	F2	110.5(2)	O1	Cu1	N1	87.89(7)
S1	C12	F3	112.0(2)	O1[1]	Cu1	N1[1]	87.89(7)
C5	N1	C1	117.3(2)	O1	Cu1	N1[1]	92.09(7)
Cu1[1]	N1	C1	121.66(17)	O1[1]	Cu1	N1	92.09(7)
Cu1[1]	N1	C5	120.88(16)	O1[1]	Cu1	N2	89.48(4)
C6[1]	N2	C6	117.6(3)	O1	Cu1	N2	89.48(4)
Cu1	N2	C6	121.18(15)	O1[1]	Cu1	N3	90.52(4)
Cu1	N2	C6[1]	121.18(15)	O1	Cu1	N3	90.52(4)
C9	N3	C9[1]	118.0(3)	O1[1]	Cu1	O1	178.96(9)

[1]1-X,+Y,3/2-Z

Crystallographic tables for $Cu(4\text{-}MeOPy)_4(ClO_4)_2$

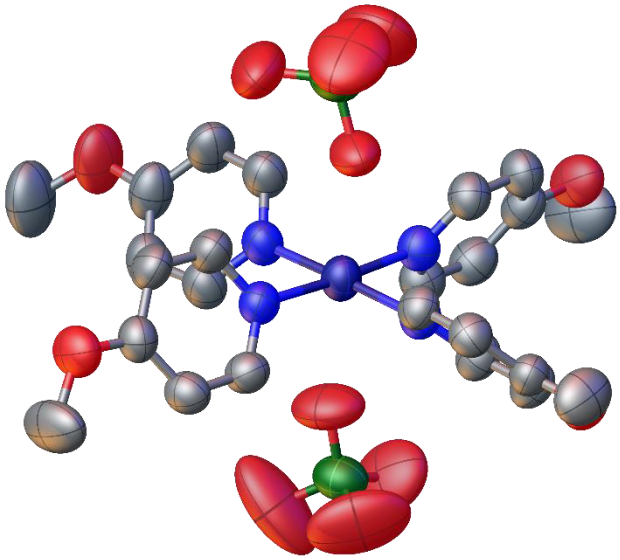

Figure S2: Crystal structure of $Cu(4\text{-}MeOPy)_4(ClO_4)_2$.

Table S6: Crystal data and structure refinement for $Cu(4\text{-}MeOPy)_4(ClO_4)_2$.

Identification code	$Cu(4\text{-}OMePy)_4(ClO_4)_2$
CCDC number:	2202868
Empirical formula	$C_{24}H_{28}N_4O_{12}Cl_2Cu$
Formula weight	698.960
Temperature/K	293(2)
Crystal system	orthorhombic
Space group	Pbca
a/Å	10.849(5)
b/Å	15.715(5)
c/Å	36.036(5)
α/°	90.000(5)
β/°	90.000(5)
γ/°	90.000(5)
Volume/$Å^3$	6144(4)
Z	8
$\rho_{calc}g/cm^3$	1.511
μ/mm^{-1}	0.950
F(000)	2878.8
Radiation	Mo Kα (λ = 0.71073)
2Θ range for data collection/°	4.38 to 49.3
Index ranges	$-12 \leq h \leq 11$, $-18 \leq k \leq 18$, $-42 \leq l \leq 42$
Reflections collected	97722
Independent reflections	5169 [R_{int} = 0.0883, R_{sigma} = 0.0280]
Data/restraints/parameters	5169/0/389
Goodness-of-fit on F^2	1.032
Final R indexes [I>=2σ (I)]	R_1 = 0.0509, wR_2 = 0.1418

Final R indexes [all data] $R_1 = 0.0791$, $wR_2 = 0.1615$
Largest diff. peak/hole / e $Å^{-3}$ 0.67/-0.49

Table S7: Fractional atomic coordinates ($\times 10^4$) and equivalent isotropic displacement parameters ($Å^2 \times 10^3$) for $Cu(4\text{-}MeOPy)_4(ClO_4)_2$. U_{eq} is defined as 1/3 of the trace of the orthogonalized U_{IJ} tensor.

Atom	*x*	*y*	*z*	U(eq)
C1	9245(4)	744(3)	873.5(12)	78.8(12)
C2	8759(4)	373(3)	558.9(14)	84.2(13)
C3	8879(5)	784(4)	230.4(13)	89.5(14)
C4	9488(5)	1550(4)	222.9(13)	95.1(15)
C5	9947(4)	1882(3)	545.1(13)	79.8(12)
C6	7621(7)	-216(5)	-94(2)	144(3)
C7	12766(4)	1524(3)	988.3(12)	76.9(11)
C8	13889(4)	1590(3)	817.9(12)	79.5(12)
C9	14351(4)	2386(3)	752.6(12)	74.9(11)
C10	13689(4)	3092(3)	869.2(13)	79.8(12)
C11	12580(4)	2964(3)	1039.5(12)	72.8(11)
C12	16159(6)	1854(5)	450(2)	140(3)
C13	12231(4)	2331(3)	1939.0(12)	73.7(11)
C14	12705(4)	2646(3)	2258.8(13)	75.1(11)
C15	12022(4)	3195(3)	2474.0(11)	65.8(10)
C16	10857(4)	3416(3)	2349.6(12)	67.7(10)
C17	10450(4)	3081(3)	2022.9(12)	67.6(10)
C18	11853(6)	4037(4)	3019.0(15)	106.9(18)
C19	7734(4)	2243(3)	1388.0(12)	76.2(12)
C20	6563(4)	2101(3)	1505.2(13)	79.1(12)
C21	6353(4)	1573(3)	1802.8(12)	69.0(10)
C22	7356(4)	1238(3)	1983.6(12)	71.1(11)
C23	8523(4)	1417(3)	1852.0(11)	69.3(10)
C24	4933(6)	784(5)	2162(2)	138(3)
N1	9829(3)	1492(2)	871.6(9)	70.7(9)
N2	12096(3)	2193(2)	1098.6(9)	67.9(8)
N3	11103(3)	2542(2)	1812.7(9)	65.5(8)
N4	8726(3)	1906(2)	1556.7(9)	66.6(8)
O1	148(7)	4416(6)	668(2)	227(4)
O2	-189(3)	3567(2)	1157.5(13)	111.6(13)
O3	-1704(5)	3741(3)	718.3(18)	168(2)
O4	-1173(7)	4872(4)	1100(2)	210(3)
O5	983(5)	581(3)	1583.1(13)	134.6(16)
O6	904(8)	-836(4)	1662(3)	244(4)
O7	1392(8)	-2(5)	2133.9(13)	219(4)
O8	2697(4)	-214(4)	1638.0(19)	178(2)
O9	8402(4)	519(3)	-96.0(10)	130.2(15)

Atom	*x*	*y*	*z*	U(eq)
O10	15444(3)	2560(3)	587.2(10)	100.9(11)
O11	12550(3)	3475(2)	2787.4(8)	82.8(8)
O12	5170(3)	1442(2)	1900.0(10)	93.2(10)
Cl1	-716.6(14)	4157.8(9)	913.0(5)	107.9(5)
Cl2	1511.9(12)	-101.4(7)	1762.2(4)	86.4(4)
Cu01	10444.0(5)	2042.4(3)	1341.48(13)	68.0(2)

Table S8: Anisotropic displacement parameters ($Å^2 \times 10^3$) for $Cu(4\text{-}MeOPy)_4(ClO_4)_2$. The anisotropic displacement factor exponent takes the form: $-2\pi^2[h^2a^{*2}U_{11}+2hka^*b^*U_{12}+\ldots]$.

Atom	U_{11}	U_{22}	U_{33}	U_{12}	U_{13}	U_{23}
C1	74(3)	90(3)	73(3)	-14(2)	5(2)	5(2)
C2	73(3)	93(3)	87(3)	-13(2)	7(2)	-18(3)
C3	73(3)	128(4)	68(3)	-12(3)	2(2)	-19(3)
C4	94(3)	129(4)	63(3)	-23(3)	-6(2)	9(3)
C5	75(3)	95(3)	70(3)	-14(2)	2(2)	6(2)
C6	137(6)	175(7)	119(5)	-48(5)	-10(4)	-53(5)
C7	78(3)	76(3)	76(3)	-2(2)	3(2)	-5(2)
C8	73(3)	90(3)	76(3)	13(2)	0(2)	-4(2)
C9	57(2)	101(3)	66(2)	7(2)	-0.5(19)	7(2)
C10	64(3)	88(3)	88(3)	-9(2)	2(2)	7(2)
C11	62(2)	77(3)	80(3)	0(2)	0(2)	-4(2)
C12	94(4)	181(7)	144(6)	45(5)	50(4)	25(5)
C13	59(2)	93(3)	70(2)	7(2)	1(2)	-2(2)
C14	58(2)	93(3)	74(3)	11(2)	-5(2)	2(2)
C15	61(2)	73(2)	63(2)	-5(2)	-4.4(18)	4.8(19)
C16	64(2)	65(2)	74(2)	2.9(19)	4(2)	-2(2)
C17	53(2)	75(3)	74(2)	5(2)	-3.3(19)	2(2)
C18	130(5)	91(3)	100(4)	15(3)	-18(3)	-28(3)
C19	67(3)	90(3)	72(3)	-7(2)	-8(2)	11(2)
C20	58(3)	97(3)	82(3)	-2(2)	-12(2)	11(2)
C21	57(2)	75(3)	75(2)	-7(2)	1.2(19)	-2(2)
C22	67(3)	72(3)	74(2)	2(2)	8(2)	9(2)
C23	66(3)	76(3)	66(2)	4(2)	-1.7(19)	8(2)
C24	80(4)	167(6)	167(6)	-2(4)	34(4)	75(5)
N1	66(2)	81(2)	65(2)	-12.8(18)	1.4(16)	4.4(17)
N2	64(2)	74(2)	66(2)	-2.0(17)	2.5(16)	-3.6(16)
N3	51.5(18)	77(2)	67.4(19)	0.6(16)	2.2(15)	4.3(17)
N4	62.3(19)	72(2)	65.8(19)	-4.1(16)	-5.0(16)	2.4(16)
O1	216(7)	266(8)	198(6)	-56(6)	28(5)	117(6)
O2	88(2)	92(2)	155(3)	0.8(19)	-26(2)	42(2)
O3	139(4)	139(4)	225(6)	-17(3)	-88(4)	50(4)
O4	220(7)	130(4)	278(9)	78(4)	-38(6)	-24(5)

Atom	U_{11}	U_{22}	U_{33}	U_{12}	U_{13}	U_{23}
O5	143(4)	115(3)	146(4)	49(3)	8(3)	47(3)
O6	281(9)	134(5)	316(10)	-91(5)	130(8)	-82(6)
O7	311(9)	272(8)	75(3)	100(7)	32(4)	20(4)
O8	96(3)	241(6)	197(6)	63(4)	25(3)	14(5)
O9	128(3)	183(4)	80(2)	-50(3)	-7(2)	-30(2)
O10	63.5(19)	139(3)	100(2)	10(2)	17.6(18)	22(2)
O11	82(2)	91(2)	75.1(18)	1.2(16)	-13.7(16)	-7.4(16)
O12	62.6(19)	111(2)	106(2)	-2.7(17)	13.3(17)	16.3(19)
Cl1	89.7(9)	88.9(9)	144.9(13)	1.7(7)	-8.2(9)	37.5(9)
Cl2	90.2(8)	75.4(7)	93.7(8)	13.5(6)	14.5(6)	11.3(6)
Cu01	58.5(3)	82.3(4)	63.2(3)	-7.7(2)	0.1(2)	0.1(2)

Table S9: Bond lengths for $Cu(4\text{-}MeOPy)_4(ClO_4)_2$.

Atom	Atom	Length/Å	Atom	Atom	Length/Å
C1	C2	1.379(6)	C17	N3	1.338(5)
C1	N1	1.335(6)	C18	O11	1.432(6)
C2	C3	1.355(7)	C19	C20	1.357(6)
C3	C4	1.374(8)	C19	N4	1.345(5)
C3	O9	1.351(6)	C20	C21	1.375(6)
C4	C5	1.367(7)	C21	C22	1.373(6)
C5	N1	1.333(6)	C21	O12	1.347(5)
C6	O9	1.433(7)	C22	C23	1.381(6)
C7	C8	1.369(6)	C23	N4	1.331(5)
C7	N2	1.339(5)	C24	O12	1.423(7)
C8	C9	1.368(7)	N1	Cu01	2.015(3)
C9	C10	1.387(7)	N2	Cu01	2.009(3)
C9	O10	1.355(5)	N3	Cu01	2.003(3)
C10	C11	1.366(6)	N4	Cu01	2.030(3)
C11	N2	1.337(5)	O1	Cl1	1.351(6)
C12	O10	1.442(7)	O2	Cl1	1.403(4)
C13	C14	1.356(6)	O3	Cl1	1.438(5)
C13	N3	1.348(5)	O4	Cl1	1.401(6)
C14	C15	1.377(6)	O5	Cl2	1.377(4)
C15	C16	1.385(6)	O6	Cl2	1.378(6)
C15	O11	1.341(5)	O7	Cl2	1.355(5)
C16	C17	1.363(6)	O8	Cl2	1.373(5)

Table S10: Bond angles for $Cu(4\text{-}MeOPy)_4(ClO_4)_2$.

Atom	Atom	Atom	Angle/°	Atom	Atom	Atom	Angle/°
N1	C1	C2	123.3(4)	C11	N2	C7	116.9(4)
C3	C2	C1	118.7(5)	Cu01	N2	C7	121.4(3)
C4	C3	C2	118.8(4)	Cu01	N2	C11	121.8(3)
O9	C3	C2	125.3(5)	C17	N3	C13	116.4(4)
O9	C3	C4	115.9(5)	Cu01	N3	C13	120.9(3)
C5	C4	C3	119.5(5)	Cu01	N3	C17	122.6(3)
N1	C5	C4	122.6(5)	C23	N4	C19	117.1(4)
N2	C7	C8	123.8(4)	Cu01	N4	C19	121.4(3)
C9	C8	C7	118.2(4)	Cu01	N4	C23	121.3(3)
C10	C9	C8	119.4(4)	C6	O9	C3	118.0(5)
O10	C9	C8	125.5(4)	C12	O10	C9	117.8(5)
O10	C9	C10	115.1(4)	C18	O11	C15	117.8(4)
C11	C10	C9	118.3(4)	C24	O12	C21	117.1(4)
N2	C11	C10	123.4(4)	O2	Cl1	O1	109.1(4)
N3	C13	C14	122.8(4)	O3	Cl1	O1	109.6(5)
C15	C14	C13	120.2(4)	O3	Cl1	O2	108.0(3)
C16	C15	C14	117.8(4)	O4	Cl1	O1	108.6(5)
O11	C15	C14	116.7(4)	O4	Cl1	O2	111.9(4)
O11	C15	C16	125.5(4)	O4	Cl1	O3	109.7(4)
C17	C16	C15	118.5(4)	O6	Cl2	O5	109.3(5)
N3	C17	C16	124.2(4)	O7	Cl2	O5	109.5(4)
N4	C19	C20	122.9(4)	O7	Cl2	O6	108.1(5)
C21	C20	C19	119.8(4)	O8	Cl2	O5	109.7(4)
C22	C21	C20	118.0(4)	O8	Cl2	O6	104.8(4)
O12	C21	C20	117.0(4)	O8	Cl2	O7	115.3(5)
O12	C21	C22	124.9(4)	N2	Cu01	N1	88.85(14)
C23	C22	C21	119.0(4)	N3	Cu01	N1	177.38(15)
N4	C23	C22	123.0(4)	N3	Cu01	N2	90.28(13)
C5	N1	C1	117.1(4)	N4	Cu01	N1	88.39(13)
Cu01	N1	C1	122.1(3)	N4	Cu01	N2	176.52(13)
Cu01	N1	C5	120.8(3)	N4	Cu01	N3	92.57(13)

Crystallographic tables for Cu(3,4-Me$_2$Py)$_4$(OTf)$_2$

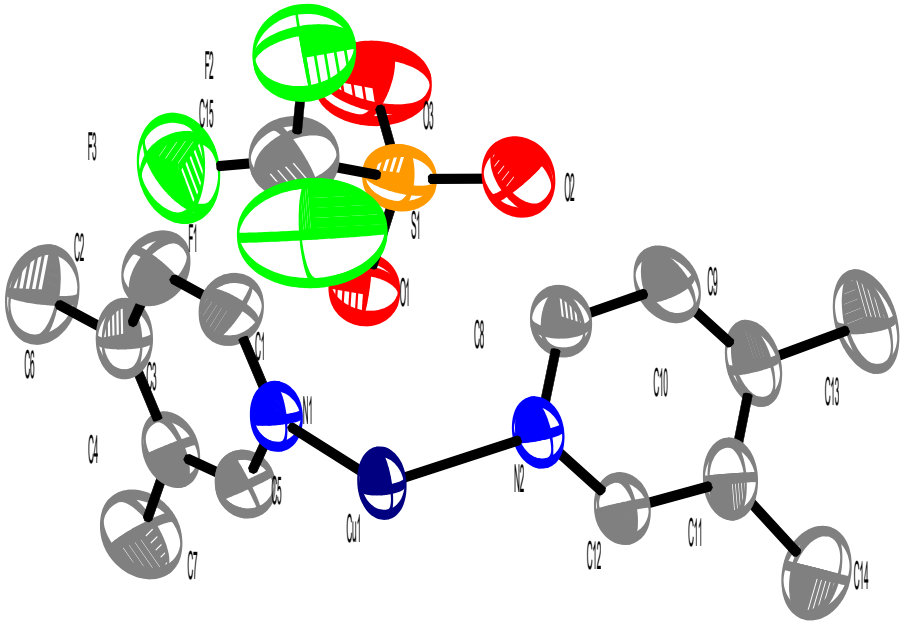

Figure S3: Asymmetric unit of Cu(3,4-Me$_2$Py)$_4$(OTf)$_2$ and naming scheme.

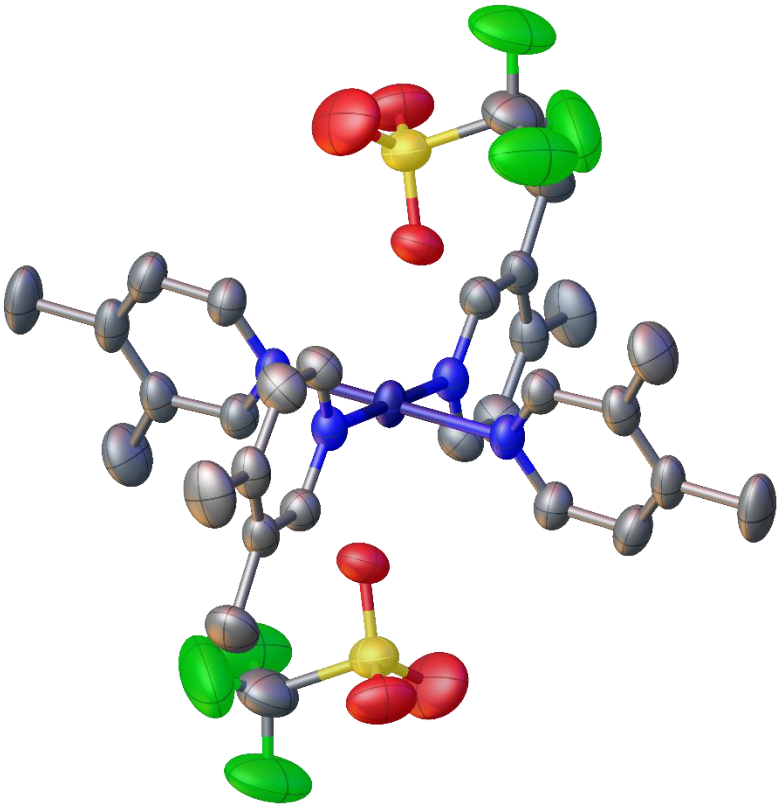

Figure S4: Crystal structure of Cu(3,4-Me$_2$Py)$_4$(OTf)$_2$.

Table S11: Crystal data and structure refinement for $Cu(3,4\text{-}Me_2Py)_4(OTf)_2$.

Identification code	$Cu(3,4\text{-}Me_2Py)_4(OTf)_2$
CCDC number	2202858
Empirical formula	$C_{30}H_{36}N_4O_6F_6S_2Cu$
Formula weight	790.31
Temperature/K	100.0(2)
Crystal system	monoclinic
Space group	$P2_1/n$
a/Å	10.1196(6)
b/Å	10.4414(5)
c/Å	17.5274(10)
α/°	90
β/°	106.280(2)
γ/°	90
Volume/Å^3	1777.73(17)
Z	2
ρ_{calc}g/cm^3	1.4766
μ/mm^{-1}	0.809
F(000)	815.9
Crystal size/mm^3	0.827 × 0.452 × 0.433
Radiation	Mo Kα (λ = 0.71073)
2Θ range for data collection/°	5.74 to 67.7
Index ranges	$-15 \leq h \leq 15$, $-16 \leq k \leq 14$, $-27 \leq l \leq 27$
Reflections collected	64608
Independent reflections	7126 [R_{int} = 0.0335, R_{sigma} = 0.0152]
Data/restraints/parameters	7126/0/227
Goodness-of-fit on F^2	1.023
Final R indexes [I>=2σ (I)]	R_1 = 0.0439, wR_2 = 0.1382
Final R indexes [all data]	R_1 = 0.0519, wR_2 = 0.1453
Largest diff. peak/hole / e Å^{-3}	0.60/-0.51

Table S12: Fractional atomic coordinates ($\times 10^4$) and equivalent isotropic displacement parameters ($Å^2 \times 10^3$) for $Cu(3,4\text{-}Me_2Py)_4(OTf)_2$. U_{eq} is defined as 1/3 of the trace of the orthogonalized U_{IJ} tensor.

Atom	*x*	*y*	*z*	U(eq)
Cu1	5000	5000	5000	40.12(8)
S1	4702.4(5)	4082.0(5)	2769.2(3)	56.44(11)
N1	3005.9(11)	5614.3(10)	4678.9(7)	40.0(2)
N2	5628.7(12)	6825.7(10)	4916.4(8)	41.3(2)
O1	4832.8(16)	4717.0(14)	3517.7(8)	58.6(3)
O2	5590(2)	2998.2(16)	2836.4(10)	84.4(5)
C12	5271.9(16)	7463.1(13)	4228.2(9)	45.6(3)
C1	2224.4(16)	5710.8(16)	3927.9(9)	49.6(3)
C5	2438.3(15)	5995.8(13)	5246.6(9)	44.7(3)
C2	898.5(18)	6180.0(19)	3727.9(11)	56.7(4)
C11	5686.2(16)	8709.4(13)	4132.6(11)	50.1(3)
C3	315.6(15)	6568.4(14)	4317.7(11)	49.9(3)
C9	6848.2(18)	8684.6(15)	5512.2(12)	57.2(4)
C10	6495.6(17)	9338.5(13)	4795.7(12)	53.4(4)
C8	6416.5(16)	7439.0(14)	5551.4(10)	49.4(3)
C4	1114.0(15)	6470.3(12)	5099.4(10)	46.2(3)
O3	3322(2)	3918(3)	2281.3(15)	116.0(8)
F2	5272(4)	4873(2)	1491.9(11)	136.7(11)
F3	4804(4)	6352.9(19)	2198.0(12)	152.0(11)
C14	5242(3)	9312(2)	3321.0(15)	78.6(6)
F1	6715(3)	5431(4)	2582.1(18)	168.4(13)
C13	7026(3)	10677.2(17)	4759.7(19)	81.4(7)
C7	607(3)	6884(2)	5788.2(15)	74.5(6)
C6	-1125(2)	7082(2)	4105.1(18)	78.1(6)
C15	5438(4)	5242(3)	2235.9(15)	88.9(8)

Table S13: Anisotropic displacement parameters ($Å^2 \times 10^3$) for $Cu(3,4\text{-}Me_2Py)_4(OTf)_2$. The anisotropic displacement factor exponent takes the form: $-2\pi^2[h^2a^{*2}U_{11}+2hka^*b^*U_{12}+\ldots]$.

Atom	U_{11}	U_{22}	U_{33}	U_{12}	U_{13}	U_{23}
Cu1	35.19(11)	27.06(11)	59.92(16)	0.15(6)	16.29(9)	4.48(7)
S1	55.9(2)	63.2(2)	50.0(2)	-0.11(17)	14.42(16)	-9.19(16)
N1	37.7(5)	32.0(4)	52.9(6)	0.9(3)	17.0(4)	3.7(4)
N2	41.1(5)	29.1(4)	56.7(6)	-1.7(3)	18.9(4)	1.9(4)
O1	71.6(8)	60.6(6)	50.3(6)	6.7(6)	28.0(6)	-2.7(5)
O2	112.8(14)	68.2(9)	70.0(9)	25.3(9)	22.2(9)	-10.5(7)
C12	49.1(7)	35.1(5)	55.5(7)	-1.7(5)	19.4(6)	2.7(5)
C1	46.8(7)	54.5(7)	50.7(7)	7.5(6)	19.1(6)	5.4(6)
C5	44.8(6)	41.0(6)	50.2(7)	-0.8(5)	16.2(5)	-1.6(5)
C2	48.2(7)	64.3(9)	56.6(8)	9.6(7)	13.1(6)	9.9(7)
C11	51.5(7)	35.3(6)	71.0(9)	1.9(5)	29.6(7)	9.9(6)
C3	39.4(6)	40.3(6)	73.3(9)	3.9(5)	21.2(6)	8.3(6)
C9	53.2(8)	42.5(7)	76.6(11)	-11.6(6)	19.6(7)	-8.8(7)
C10	46.7(7)	31.5(5)	90.1(12)	-4.2(5)	32.6(7)	0.4(6)
C8	47.5(7)	41.1(6)	59.7(8)	-5.8(5)	15.0(6)	0.7(5)
C4	47.6(6)	34.6(5)	64.2(8)	-2.3(5)	28.5(6)	-2.8(5)
O3	63.4(10)	158(2)	112.0(17)	-12.9(12)	-0.1(10)	-32.5(15)
F2	234(3)	133.1(18)	62.0(9)	21.0(15)	72.4(15)	8.1(8)
F3	298(4)	78.5(11)	98.4(14)	21.0(17)	86.4(18)	14.9(10)
C14	91.9(16)	63.6(11)	85.4(15)	-0.1(10)	33.2(12)	28.8(10)
F1	142(2)	241(3)	137(2)	-94(2)	62.7(19)	1(2)
C13	75.5(13)	37.5(7)	140(2)	-15.3(8)	44.6(14)	1.9(10)
C7	79.3(14)	73.4(12)	87.2(14)	3.2(10)	50.4(12)	-13.4(10)
C6	46.1(8)	78.7(14)	113.5(19)	17.3(9)	28.9(10)	19.6(13)
C15	125(3)	94.1(16)	57.8(12)	-4.6(17)	41.5(15)	2.5(11)

[1]1-X,1-Y,1-Z

Table S14: Bond lengths for $Cu(3,4\text{-}Me_2Py)_4(OTf)_2$.

Atom	Atom	Length/Å	Atom	Atom	Length/Å
Cu1	N1[1]	2.0405(11)	C5	C4	1.384(2)
Cu1	N1	2.0405(11)	C2	C3	1.387(3)
Cu1	N2[1]	2.0279(10)	C11	C10	1.386(3)
Cu1	N2	2.0279(10)	C11	C14	1.504(3)
S1	O1	1.4426(13)	C3	C4	1.386(2)
S1	O2	1.4289(16)	C3	C6	1.499(2)
S1	O3	1.4288(18)	C9	C10	1.385(3)
S1	C15	1.813(3)	C9	C8	1.380(2)
N1	C1	1.3359(19)	C10	C13	1.505(2)
N1	C5	1.3412(18)	C4	C7	1.502(2)
N2	C12	1.3356(19)	F2	C15	1.324(3)
N2	C8	1.337(2)	F3	C15	1.318(4)
C12	C11	1.3916(19)	F1	C15	1.279(4)
C1	C2	1.378(2)			

[1]1-X,1-Y,1-Z

Table S15: Bond angles for $Cu(3,4\text{-}Me_2Py)_4(OTf)_2$.

Atom	Atom	Atom	Angle/°	Atom	Atom	Atom	Angle/°
N1[1]	Cu1	N1	180.0	C3	C2	C1	120.11(16)
N2[1]	Cu1	N1[1]	89.46(4)	C10	C11	C12	118.00(15)
N2[1]	Cu1	N1	90.54(4)	C14	C11	C12	119.00(17)
N2	Cu1	N1[1]	90.54(4)	C14	C11	C10	123.00(15)
N2	Cu1	N1	89.46(4)	C4	C3	C2	117.62(14)
N2[1]	Cu1	N2	180.0	C6	C3	C2	120.44(18)
O2	S1	O1	113.20(9)	C6	C3	C4	121.95(18)
O3	S1	O1	115.11(13)	C8	C9	C10	120.32(16)
O3	S1	O2	116.15(14)	C9	C10	C11	117.92(13)
C15	S1	O1	102.46(11)	C13	C10	C11	122.63(18)
C15	S1	O2	103.42(15)	C13	C10	C9	119.44(18)
C15	S1	O3	104.20(18)	C9	C8	N2	122.24(16)
C1	N1	Cu1	124.19(10)	C3	C4	C5	118.47(13)
C5	N1	Cu1	119.00(10)	C7	C4	C5	118.98(17)
C5	N1	C1	116.76(12)	C7	C4	C3	122.54(16)
C12	N2	Cu1	121.52(10)	F2	C15	S1	110.9(2)
C8	N2	Cu1	121.07(10)	F3	C15	S1	110.5(2)
C8	N2	C12	117.41(12)	F3	C15	F2	106.3(3)
C11	C12	N2	124.09(14)	F1	C15	S1	111.4(2)
C2	C1	N1	122.86(15)	F1	C15	F2	110.2(3)
C4	C5	N1	124.18(14)	F1	C15	F3	107.5(3)

[1]1-X,1-Y,1-Z

In all three crystal structures, Cu(II) is coordinated by four *N*-donor systems in a planar fashion (Figs. S1–4). The coordination sphere surrounding the Cu(II) ion can best be described as an elongated octahedron, which is most distorted for the pyridine structure and symmetrical in the case of Cu(3,4-lutidine)$_4$(OTf)$_2$ due to the characteristics of the crystal refinement.

The crystal structures of the pyridine and 3,4-lutidine complexes exhibit similar Cu–N bond distances, yet the axial triflate coligand is 3.7% and 9.6% further away from the metal center, leading to a more distorted coordination sphere. The 4-methoxy substitution at the pyridine ring leads to a small (about 2%) shortening of the Cu–N bond distance in comparison to the complex with the unsubstituted pyridine. The tilt of the pyridine rings out of the Cu(II) coordination plane remains similar when comparing the pyridine and 4-methoxy pyridine ligands, while the lutidine ligands are almost perpendicular to the plane.

2.3 Preparation of aryl trimethylstannanes – General Procedure 2 (GP2)

Sn_2Me_6 (1.5 eq.) was added slowly at ambient temperature to a solution of the respective aryl iodide or bromide (1 eq.) and $Pd(PPh_3)_4$ (0.2 eq) in a suspension of LiCl (5 eq.) in anhydrous toluene. The reaction mixture was stirred at 110 ºC until TLC indicated complete conversion of the aryl halogenide (typically 4 h). After cooling to ambient temperature, the mixture was diluted with EtOAc and filtered through a plug of Celite®. All volatiles were removed under reduced pressure and the residue was purified by flash column chromatography to afford the desired aryl trimethyl stannane.

4-Ph-Ph-$SnMe_3$ (5)[19]

The title compound was obtained as a colorless solid (382 mg, 1.20 mmol, 67%) according to GP2 from 4-iodobiphenyl (500 mg, 1.8 mmol, 1 eq.) and Sn_2Me_6 (0.60 mL, 0.95 g, 2.7 mmol, 1.5 eq.) using $Pd(PPh_3)_4$ (0.42 g, 0.36 mmol, 0.2 eq) and LiCl (0.38 g, 9 mmol, 5 eq) in anhydrous toluene (25 mL). The crude product was purified by flash chromatography (petrol ether, R_f = 0.49). ^{1}H NMR (400 MHz, $CDCl_3$): δ = 7.67 – 7.54 (m, 6H), 7.48 – 7.44 (m, 2H), 7.39 – 7.34 (m, 1H), 0.34 (s, 9H). ^{13}C NMR (100 MHz, $CDCl_3$): δ = 141.4, 141.3, 141.2, 136.4, 128.9, 127.4, 127.3, 126.3, –9.4.

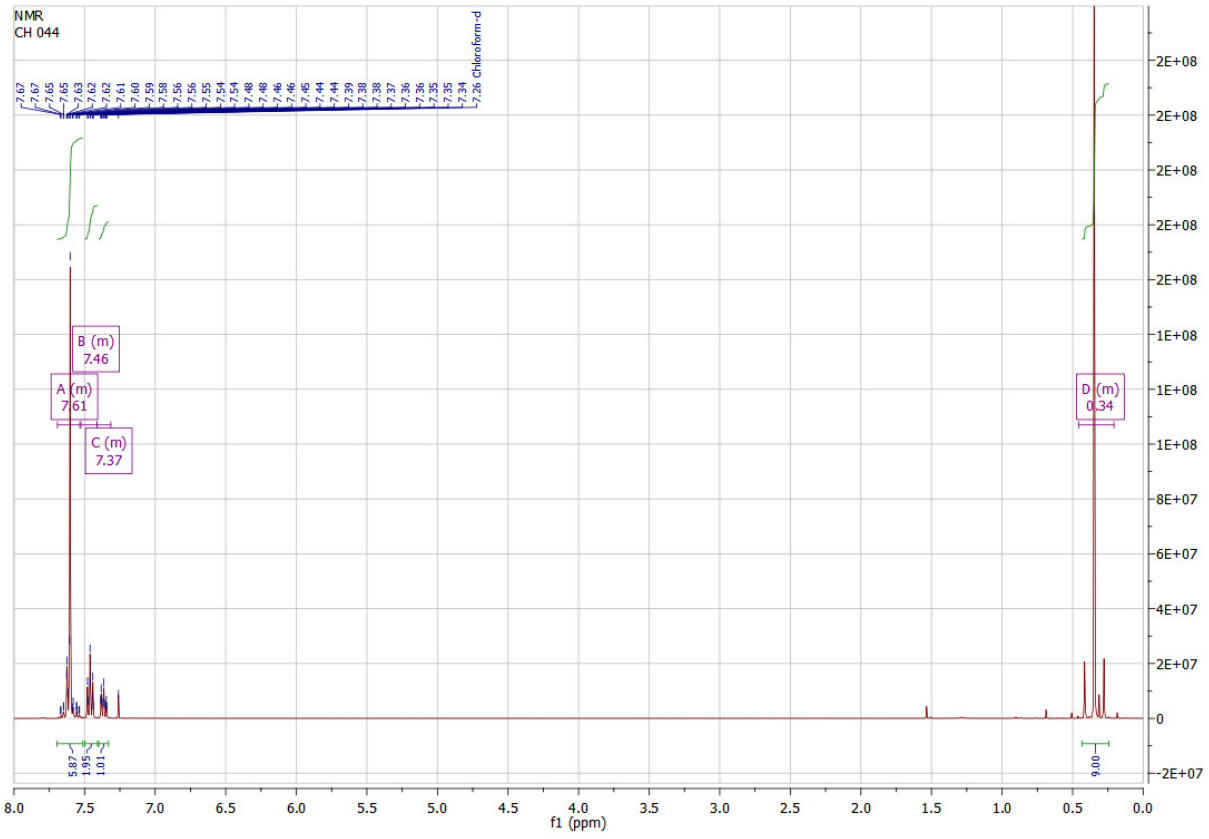

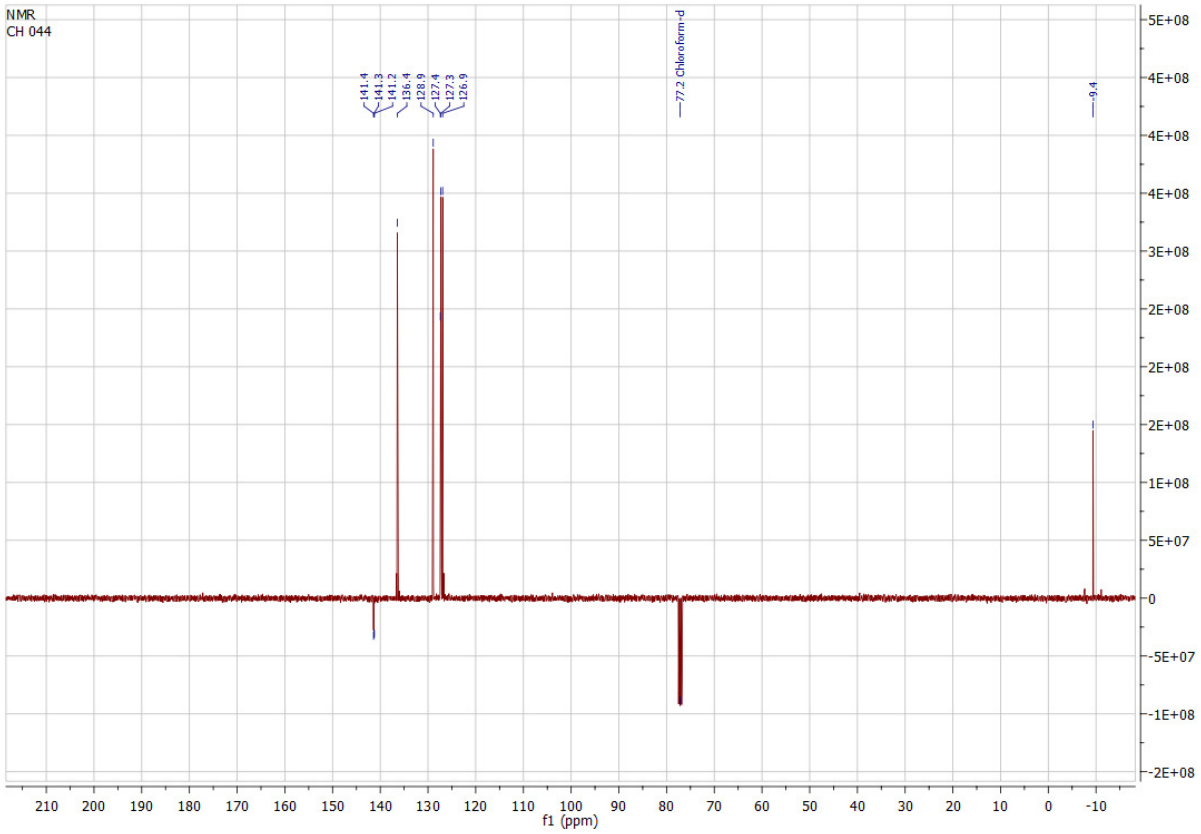

4-Ac-Ph-SnMe$_3$ (6)[20]

The title compound was obtained as a colorless oil (1.0 g, 3.6 mmol, 89%) according to GP2 from 4-iodoacetophenone (1.0 g, 4.1 mmol, 1 eq.) and Sn_2Me_6 (1.3 mL, 2.1 g, 6.1 mmol, 1.5 eq.) using $Pd(PPh_3)_4$ (0.94 g, 0.82 mmol, 0.2 eq) and LiCl (0.87 g, 21 mmol, 5 eq) in anhydrous toluene (30 mL). The crude product was purified by flash chromatography (petrol ether/EtOAc = 9:1, R_f = 0.48). ^{1}H NMR (400 MHz, $CDCl_3$): δ = 7.89 (d, J = 8.19 Hz, 2H), 7.61(d, J = 8.10 Hz, 2H), 2.59 (s, 3H), 0.33 (s, 9H). ^{13}C NMR (100 MHz, $CDCl_3$): δ = 198.6, 150.3, 136.9, 136.1, 127.4, 26.7, –9.4.

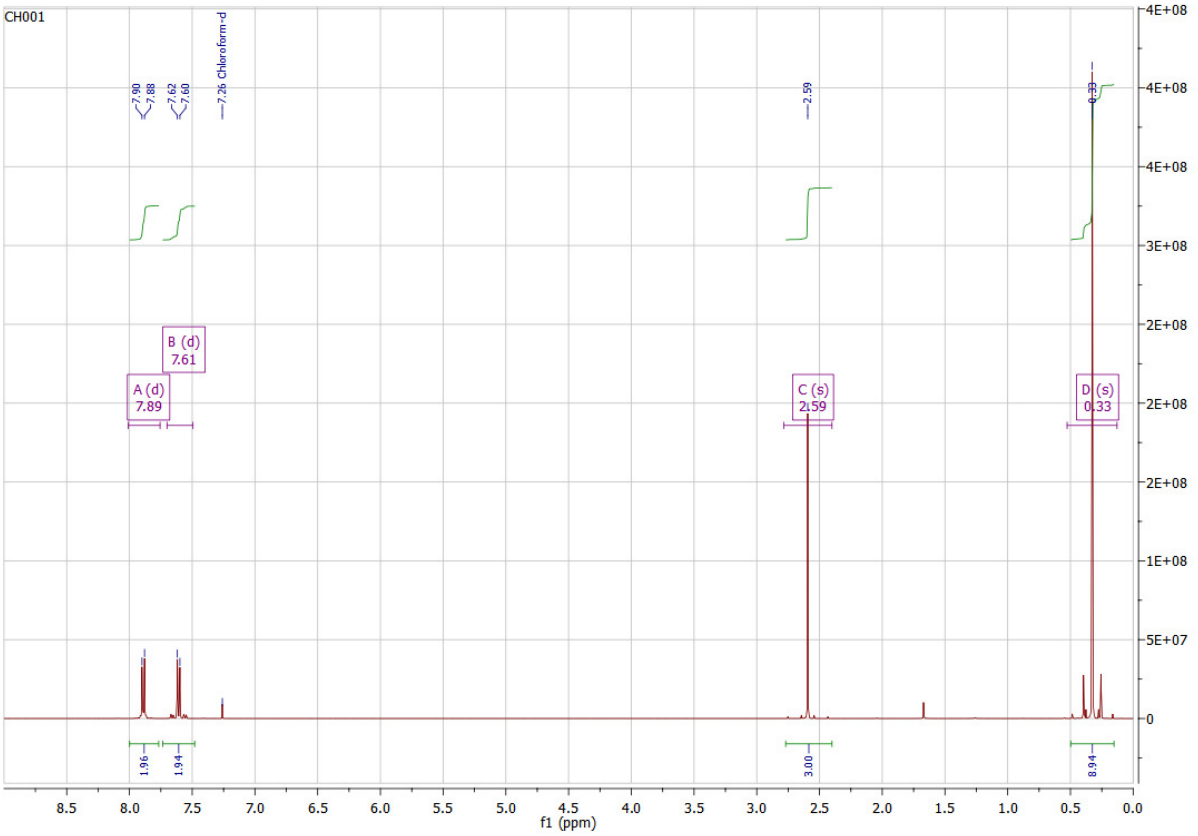
CH001
7.90
7.88
7.62
7.60
7.26 Chloroform-d
2.59
0.33
B (d)
7.61
A (d)
7.89
C (s)
2.59
D (s)
0.33
1.96
1.94
3.00
8.94
f1 (ppm)

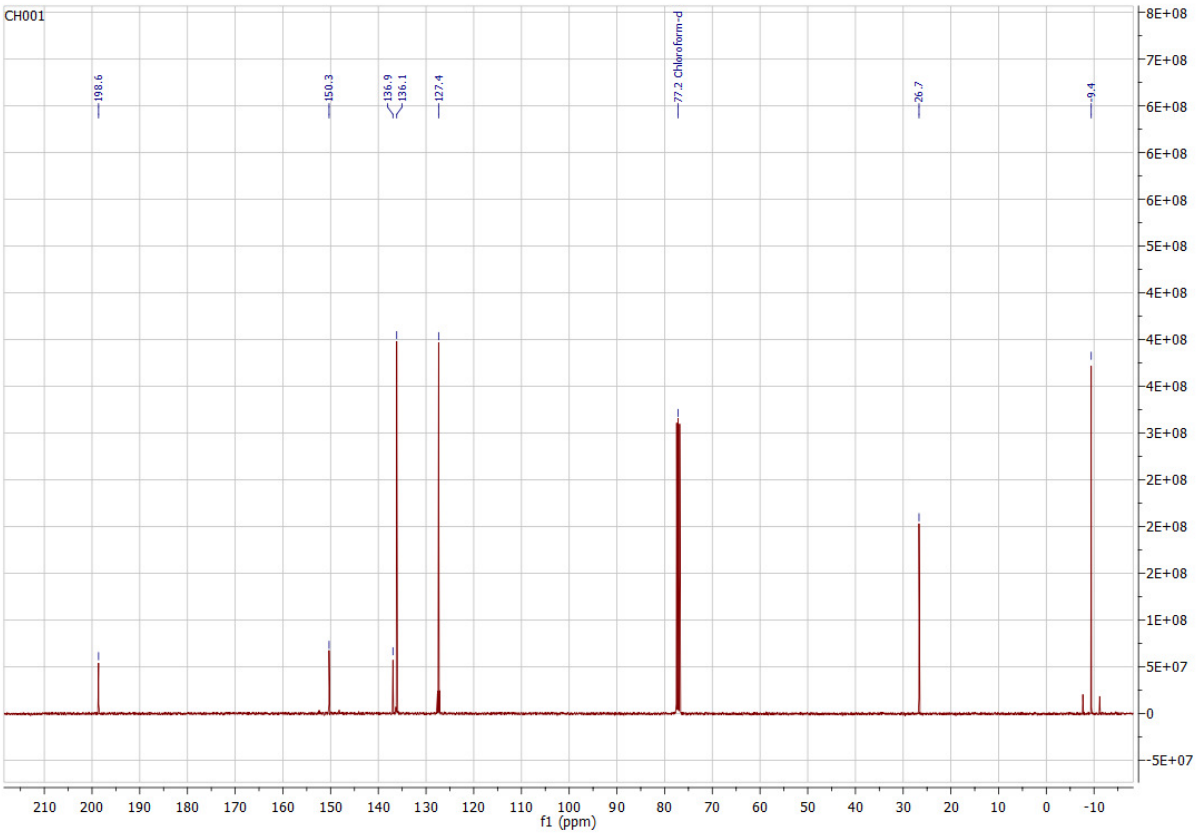
CH001
198.6
150.3
136.9
136.1
127.4
77.2 Chloroform-d
26.7
9.4
f1 (ppm)

2.4 Preparation of aryl neopentyl glycol boronates – General Procedure 3 (GP3)

Anhydrous $MgSO_4$ (3–4 eq.; dried at 300 ºC for 16 h and cooled to ambient temperature under Ar before use) was added to a solution of the respective aryl boronic acid (1 eq.) and 2,2-dimethyl-1,3-propandiol (1 eq.) in anhydrous Et_2O (0.3 M) and the reaction mixture was vigorously stirred for 16 h. Thereafter, the mixture was filtered through a pad of silica gel (0.1% Ca) and concentrated under reduced pressure. The residue was dried at 1 mbar and 50 ºC and purified by recrystallization from hexane to afford the desired aryl boronate.

4-Ph-Ph-Bneo[21]

The title compound was obtained as a colorless solid (1.0 g, 3.8 mmol, 74%) according to GP3 from 4-Ph-Ph-$B(OH)_2$ (1.0 g, 5.1 mmol, 1 eq.) and 2,2-dimethyl-1,3-propandiol (0.53 g, 5.1 mmol, 1 eq.) using $MgSO_4$ (2.2 g, 18 mmol, 3.6 eq). R_f = 0.50 (hexane/EtOAc = 6:1). ^{1}H NMR (400 MHz, $CDCl_3$): δ = 7.93 – 7.87 (m, 2H), 7.68 – 7.59 (m, 4H), 7.49 – 7.42 (m, 2H), 7.40 – 7.33 (m, 1H), 3.81 (s, 4H), 1.05 (s, 6H). ^{13}C NMR(101 MHz, $CDCl_3$): δ = 143.4, 141.4, 134.5, 128.9, 127.5, 127.4, 126.5, 72.5, 32.1, 22.1. *C*-Bneo was not observed.

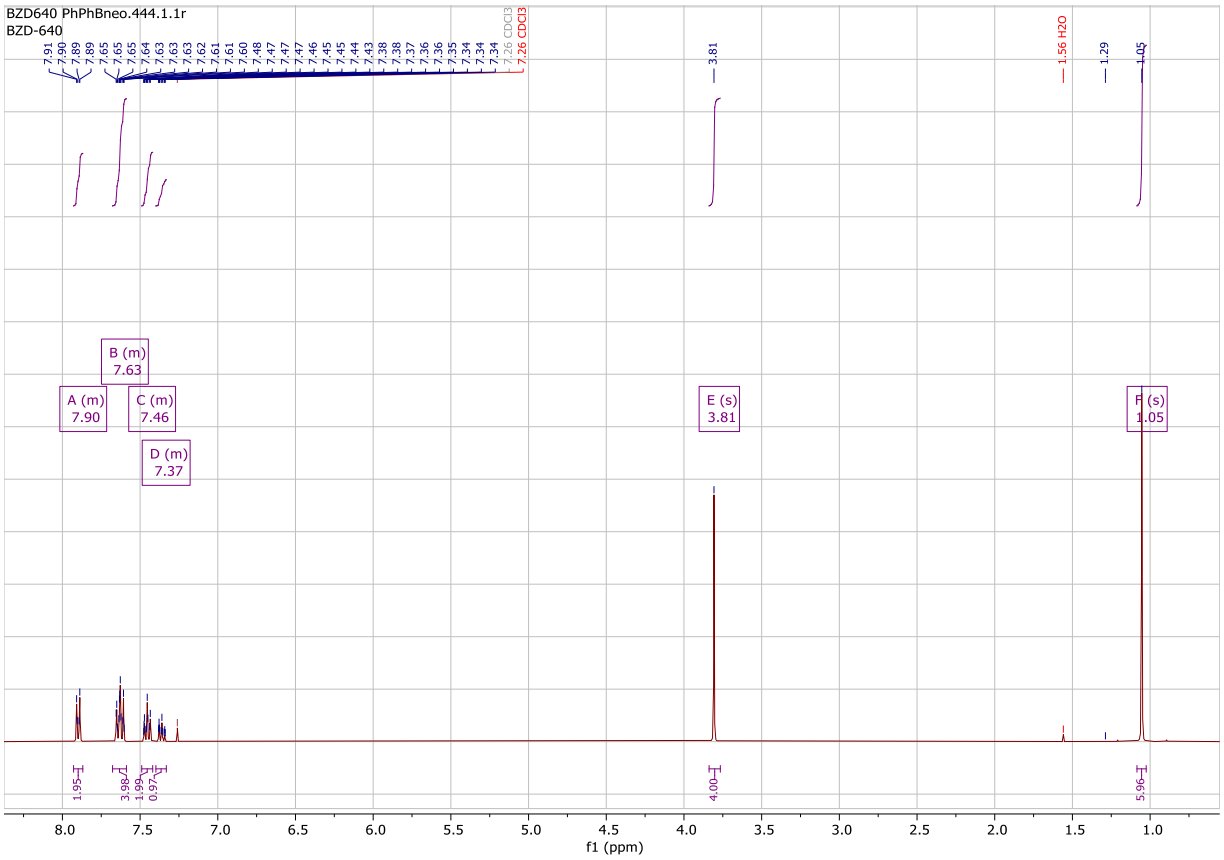
BZD640 PhPhBneo.444.1.1r
BZD-640
B (m)
7.63
A (m)
7.90
C (m)
7.46
D (m)
7.37
E (s)
3.81
F (s)
1.05
f1 (ppm)

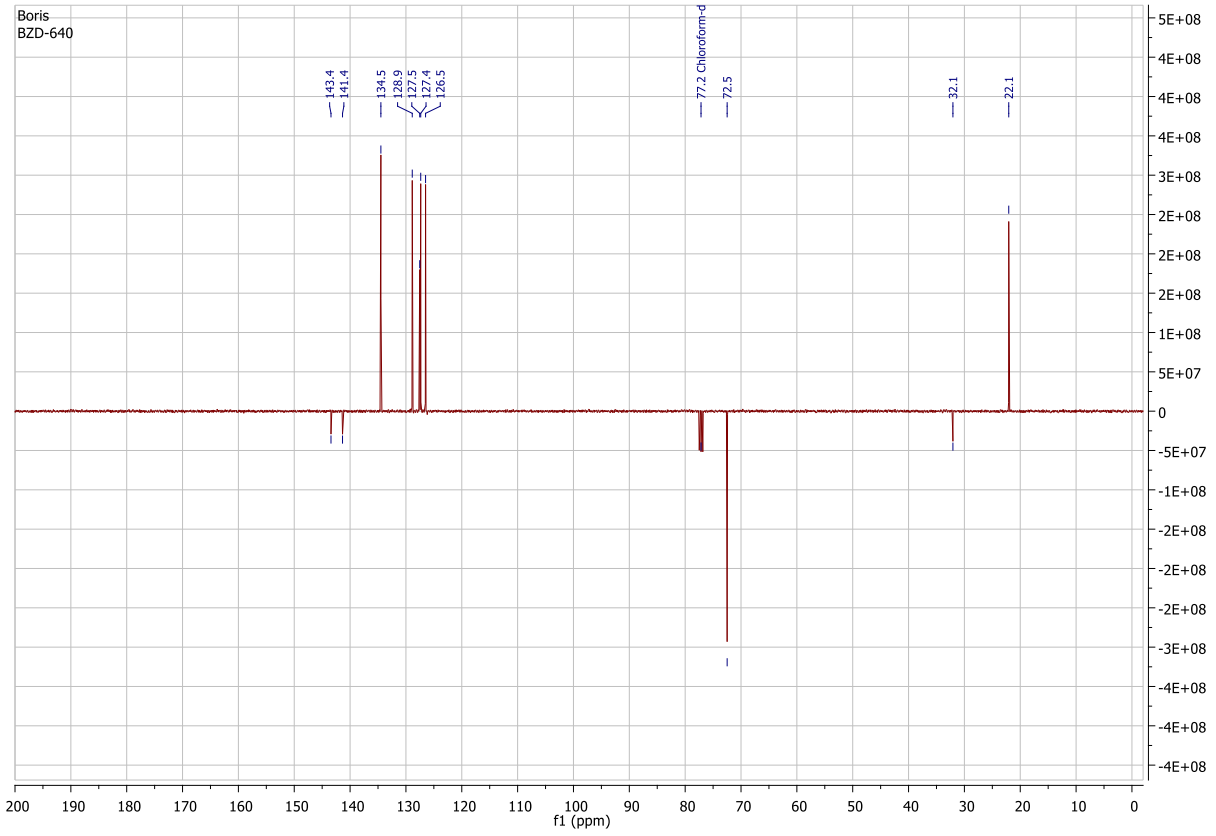
Boris
BZD-640
77.2 Chloroform-d
f1 (ppm)

4-Ac-Ph-Bneo[22]

The title compound was obtained as a colorless solid (1.0 g, 4.4 mmol, 72%) according to GP3 from 4-Ac-Ph-B(OH)$_2$ (1.0 g, 6.1 mmol, 1 eq.) and 2,2-dimethyl-1,3-propandiol (0.64 g, 6.1 mmol) using $MgSO_4$ (2.3 g, 19 mmol, 3.1 eq.). R_f = 0.28 (hexane/EtOAc = 6:1). ^{1}H NMR (400 MHz, $CDCl_3$): δ = 7.96 – 7.84 (m, 4H), 3.78 (s, 4H), 2.61 (s, 3H), 1.03 (s, 6H). ^{13}C NMR (101 MHz, $CDCl_3$): δ = 198.7, 138.7, 134.1, 127.3, 72.5, 32.0, 26.9, 22.0. *C*-Bneo was not observed. LR-MS: m/z $[M+H]^+$ calculated for $[C_{13}H_{17}BO_3+H]^+$ = 233.13, found: 233.23.

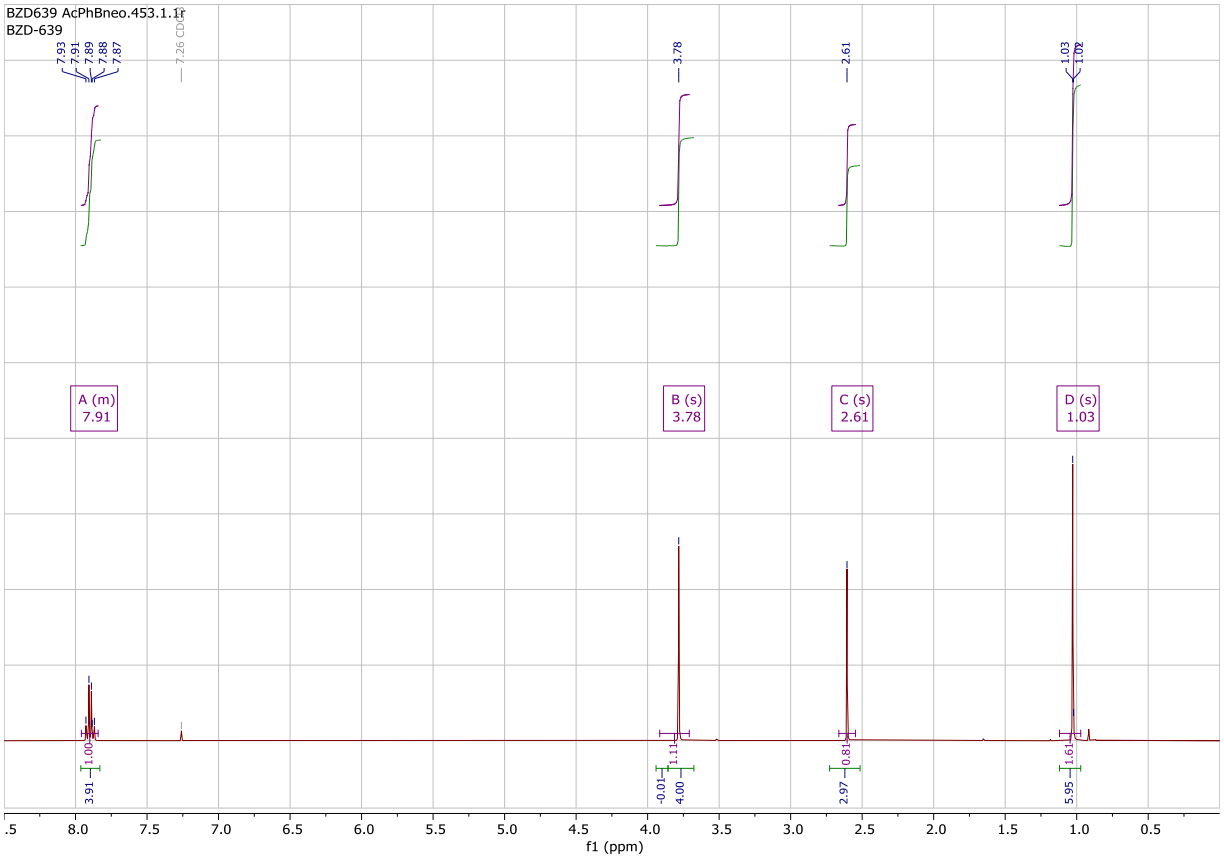

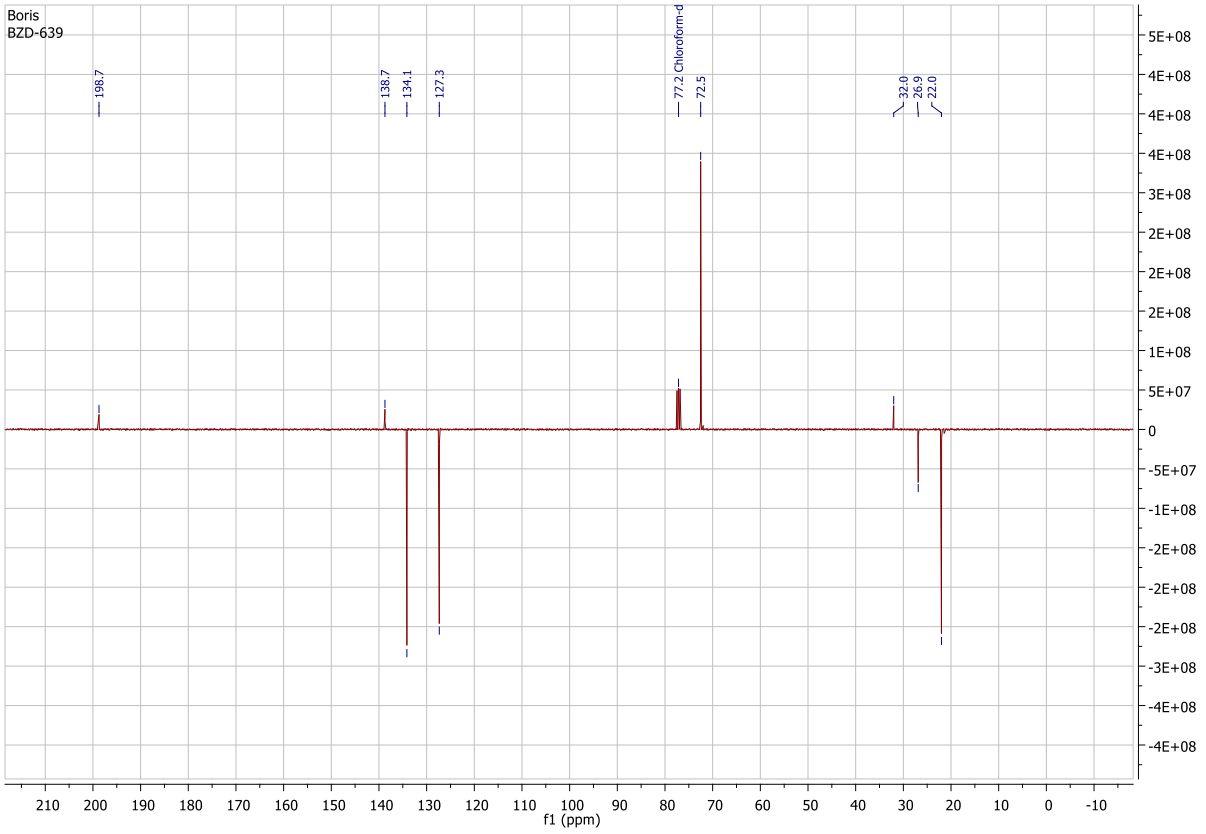

2.5 **Preparation of (Boc)$_2$-6-BpinDOPA(MOM)$_2$-OMe (S4)**

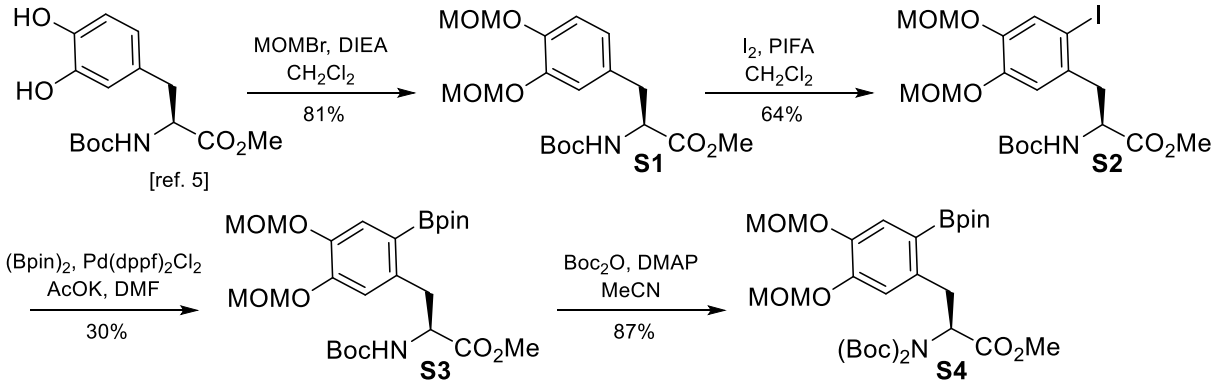

Scheme S1: Preparation of (Boc)$_2$-6-BpinDOPA(MOM)$_2$-OMe (**S4**). (Bpin)$_2$ – bis-(pinacolato)-diborane; DMAP – (4-dimethylamino)pyridine; MOMBr – methoxymethyl bromide; Pd(dppf)$_2$Cl$_2$ – [1,1'-bis-(diphenylphosphino)-ferrocene]-dichloropalladium; PIFA – [bis(trifluoroacetoxy)iodo]benzene.

Boc-DOPA(MOM)$_2$-OMe (S1)

MOMBr (13.8 mL, 21.9 g, 175 mmol, 3.5 eq.) was added dropwise to a solution of Boc-DOPA-OMe (15.7 g, 50.0 mmol, 1 eq.) and DIEA (30.5 mL, 22.6 g, 175 mmol, 3.5 eq.) in CH_2Cl_2 (120 mL) and the reaction mixture was stirred for 2 h. Thereafter, additional DIEA (15.3 mL, 11.3 g, 87.5 mmol, 1.75 eq.) followed by MOMBr (6.40 mL, 10.9 g, 87.4 mmol, 1.75 eq.) was added and the mixture was stirred for 16 h. Afterwards, all volatiles were removed under reduced pressure and the residue was taken up in Et_2O/H_2O (200 mL of each). The organic layer was separated, successively washed with 1 M $NaHSO_4$ (3×50 mL), H_2O (50 mL), 10% $NaHCO_3$ (3×50 mL), H_2O (3×50 mL), and brine (2×30 mL), dried, filtered and concentrated under reduced pressure. The resulting crude product was purified by column chromatography (EtOAc:hexane 1:1.5; R_f=0.41) to afford the title compound as a colorless oil (16.3 g, 40.8 mmol, 82%). ^{1}H NMR (400 MHz, $CDCl_3$) δ = 7.10 – 7.02 (m, 1H), 6.91 (d, J = 1.9 Hz, 1H), 6.70 (dd, *J* = 8.2, 1.7 Hz, 1H), 5.22 – 5.16 (m, 4H), 5.01 – 4.91 (m, *J* = 7.6 Hz, 1H), 4.62 – 4.48 (m, 1H), 3.73 (s, 3H), 3.50 (s, 6H), 1.42 (s, 9H). ^{13}C NMR (101 MHz, $CDCl_3$): δ = 172.4, 155.2, 147.4, 146.4, 130.3, 123.4, 117.8, 116.8, 95.6 (×2), 80.0, 56.3, 56.2, 54.5, 52.3, 37.8, 28.4. LR-MS: m/z $[M+H]^+$ calculated for $[C_{19}H_{29}NO_8+H]^+$ = 400.2, found: 399.98.

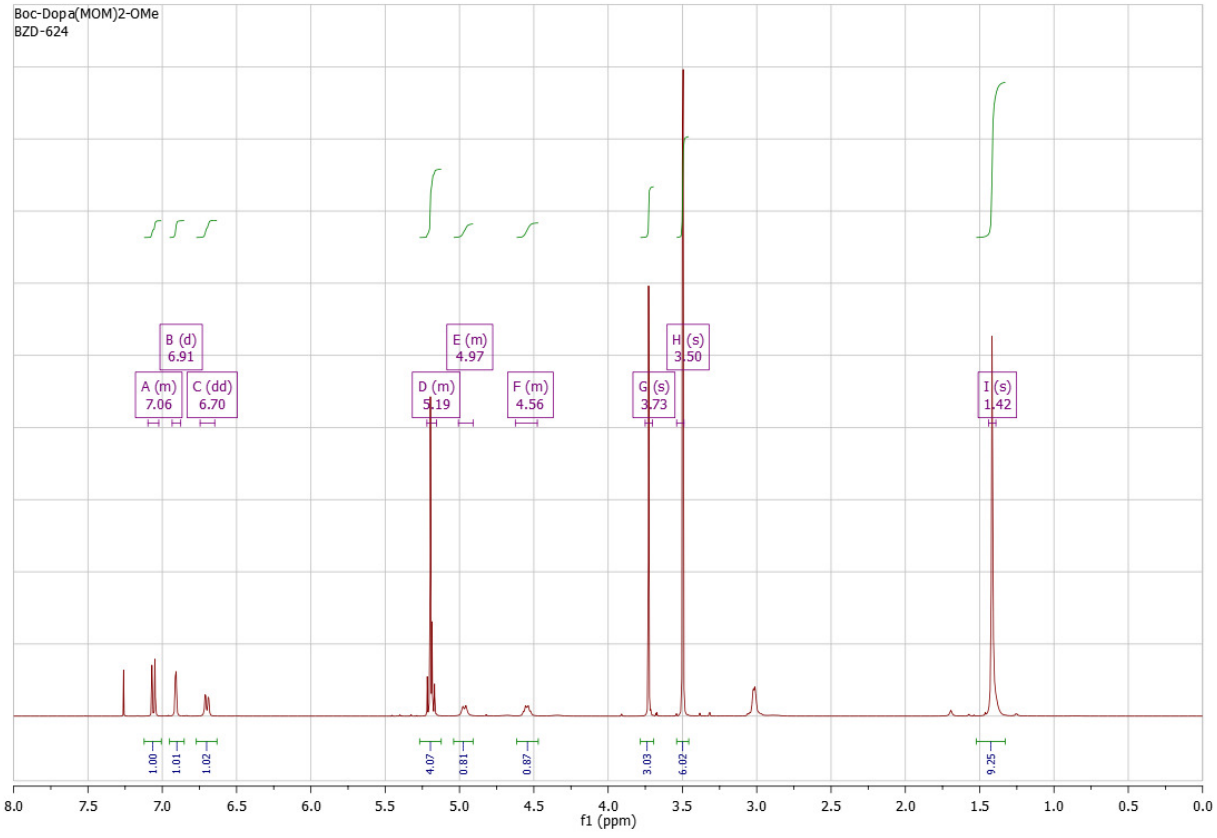

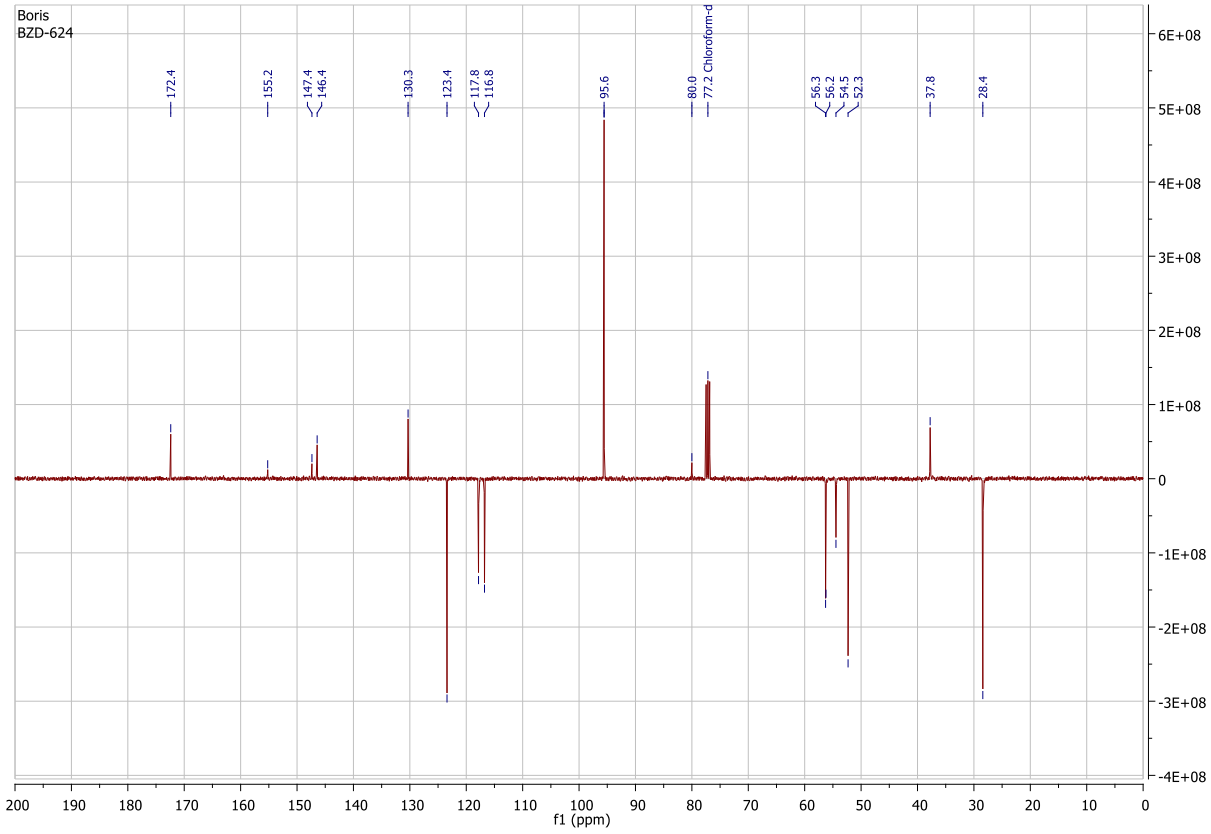

Boc-6-IDOPA(MOM)$_2$-OMe (S2)

Iodine (8.63 g, 34.0 mmol, 1 eq.) was added to an ice-cold solution of **S1** (13.6 g, 34.0 mmol, 1 eq.) in anhydrous CH_2Cl_2 (160 mL) and the mixture was stirred until the iodine was completely dissolved. Thereafter, PIFA (17.5 g, 40.7 mmol, 1.2 eq.) was added and the reaction mixture was stirred for 15 min. Afterwards, the cooling bath was removed, and the mixture was stirred for 90 min. A saturated solution of $Na_2S_2O_3$ (100 mL) was added and stirring continued for 10 min. The organic layer was separated, washed with 10% $NaHCO_3$ (3×50 mL) and brine (2×30 mL), dried, filtered and concentrated under reduced pressure. The residue was purified by column chromatography (EtOAc:hexane 1:1; R_f=0.57) followed by recrystallization from Et_2O/hexane to afford the title compound as a colorless solid (8.5 g, 16.2 mmol, 48%). The mother liquor was concentrated under reduced pressure and the residue was purified by column chromatography followed by recrystallization from Et_2O/hexane to afford a second crop of the title compound (2.2 g, overall 56%). Noteworthy, **S1** and **S2** were inseparable from each other on silica gel TLC plates or columns. ^{1}H NMR (400 MHz, $CDCl_3$; mixture of two rotamers) δ = 7.53 (s, 1H), 6.98 (s, 1H), 5.18 (s, 4H), 5.08 – 4.95 (m, 1H), 4.70 – 4.42 (m, 1H), 3.75 (s, 3H), 3.51 (s, 3H), 3.49 (s, 3H), 3.21 (dd, J = 14.0, 5.7 Hz, 1H), 3.10 – 2.70 (m, 1H), 1.47 – 1.19 (m, 9H). ^{13}C NMR (101 MHz, $CDCl_3$) δ 172.4, 155.1, 147.6, 146.9, 133.5, 127.0, 118.1, 95.6, 95.6, 91.2, 80.0, 56.5, 56.4, 53.9, 52.5, 42.5, 28.4. LR-MS: m/z $[M+Na]^+$ calculated for

$[C_{19}H_{28}INO_8+Na]^+$ = 548.08, found: 547.92 $[M+H]^+$; calculated for $[C_{19}H_{28}INO_8+H]^+$ = 526.1, found: 525.92.

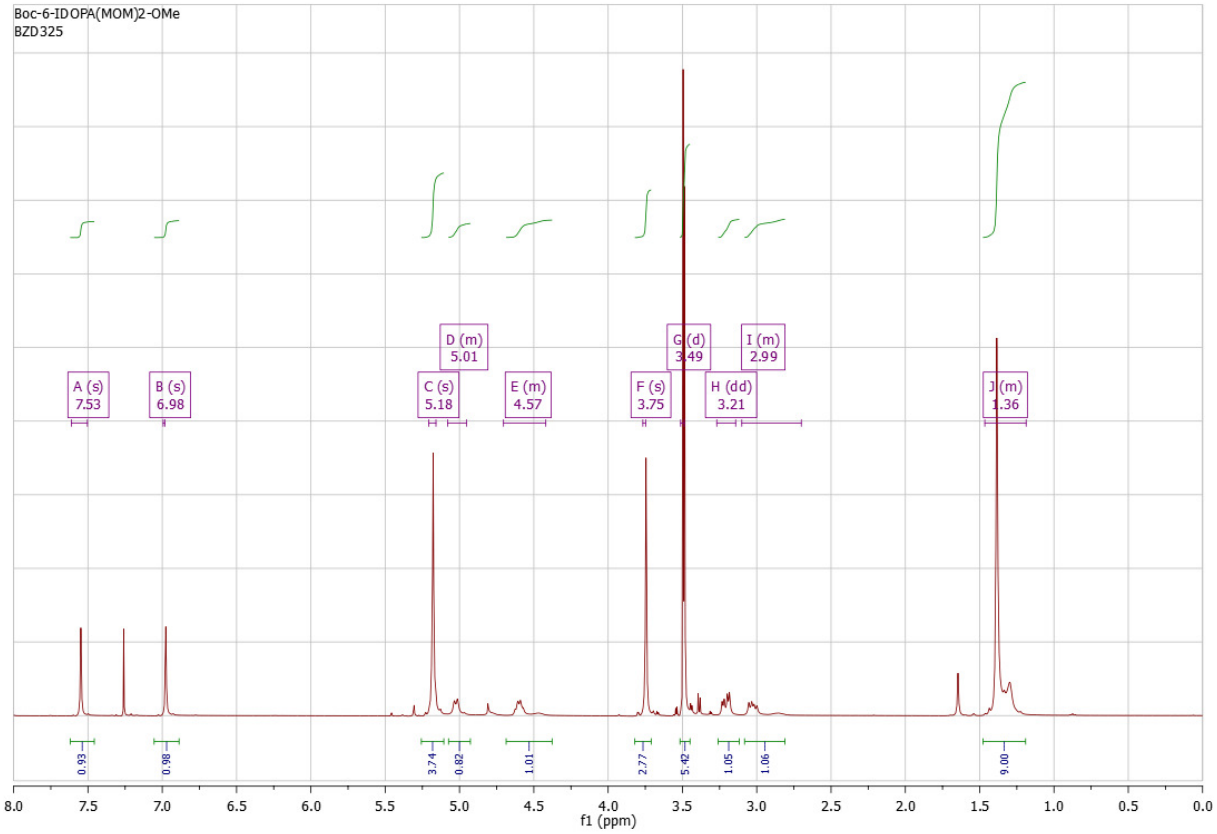

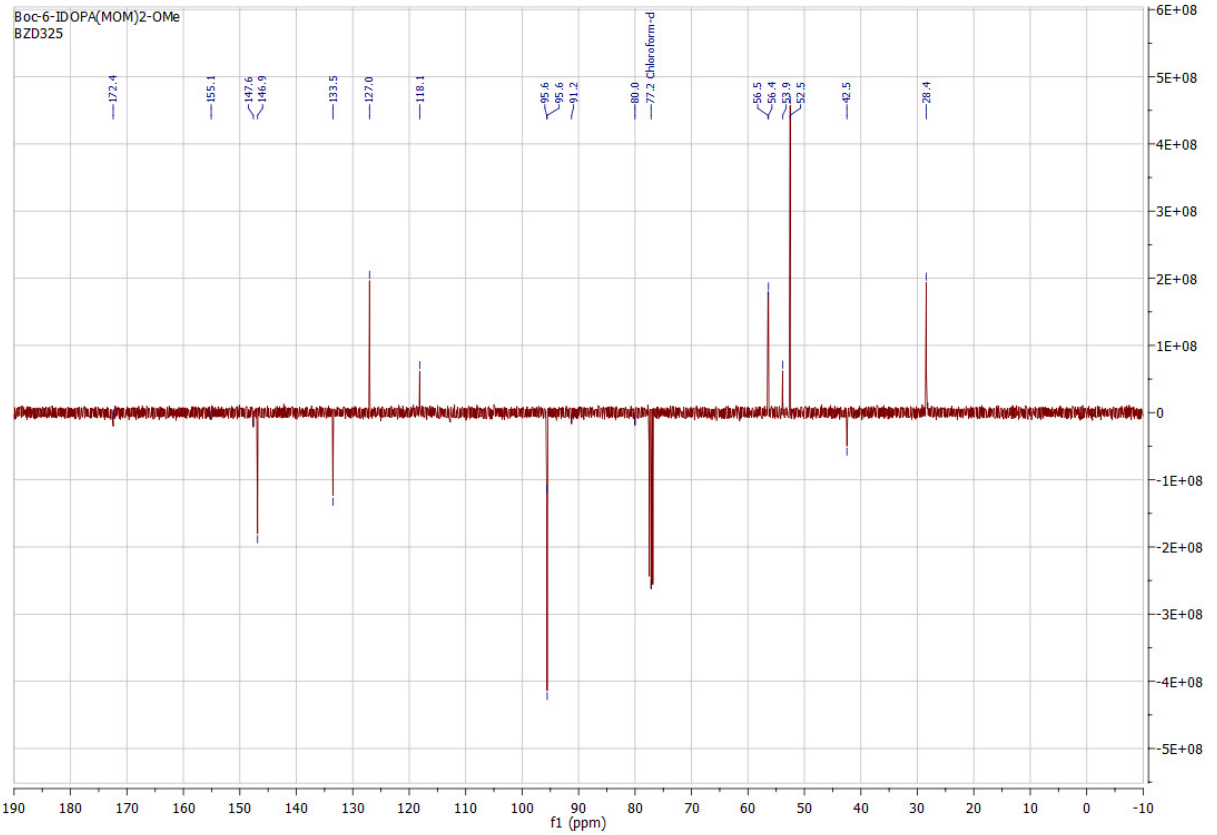

Boc-6-BpinDOPA(MOM)$_2$-OMe (S3)

A suspension of AcOK (1.68 g, 17.1mmol, 3 eq.) in a solution of **S2** (3.00 g, 5.71 mmol, 1 eq.), Pd(dppf)Cl_2 (0.37 g, 0.46 mmol, 0.08 eq.) and $(Bpin)_2$ (5.08 g, 10.0 mmol, 1.75 eq.) in anhydrous DMF (12 mL) was placed into an oil bath preheated to 65 ºC and the reaction mixture was stirred for 4 days. All volatiles were removed under reduced pressure, the residue was dried at 1 mbar and 60 ºC, taken up in EtOAc/hexane = 1:6, and the resulting suspension was purified by column chromatography on silica gel (EtOAc:hexane 1:1; R_f=0.57) followed by column chromatography on C_{18} phase (dry loading; 20% → 100% MeCN) to afford the title compound (0.9 g, 30%; contained ca. 20 mol.% MeCN according to its ^{1}H-NMR spectrum) as a colorless oil. Noteworthy, **S1**, **S2** and **S3** were inseparable from each other on normal phase silica gel TLC plates or columns. ^{1}H NMR (400 MHz, $CDCl_3$; mixture of two rotamers) δ = 7.51 (s, 1H), 7.01 (s, 1H), 5.98 (d, *J* = 7.9 Hz, 1H), 5.34 – 5.18 (m, 4H), 4.32 (ddd, *J* = 10.4, 8.1, 4.2 Hz, 1H), 3.75 (s, 3H), 3.52 (s, 3H), 3.50 (s, 3H), 3.30 – 3.08 (m, 2H), 1.36 (s, 9H), 1.35 (s, 6H), 1.34 (s, 6H). ^{13}C NMR (101 MHz, $CDCl_3$): δ = 173.4, 155.9, 150.1, 145.3, 139.2, 124.0, 117.8, 95.6, 95.1, 84.2, 79.4, 56.5, 56.4, 52.2, 36.6, 28.4, 25.1, 24.8. *C*-Bpin was not observed. LR-MS: m/z $[M+Na]^+$ calculated for $[C_{25}H_{40}BNO_{10}+Na]^+$ = 548.26, found: 548.16; $[M+H]^+$ calculated for $[C_{25}H_{41}BNO_{10}+H]^+$ = 526.28, found: 526.1.

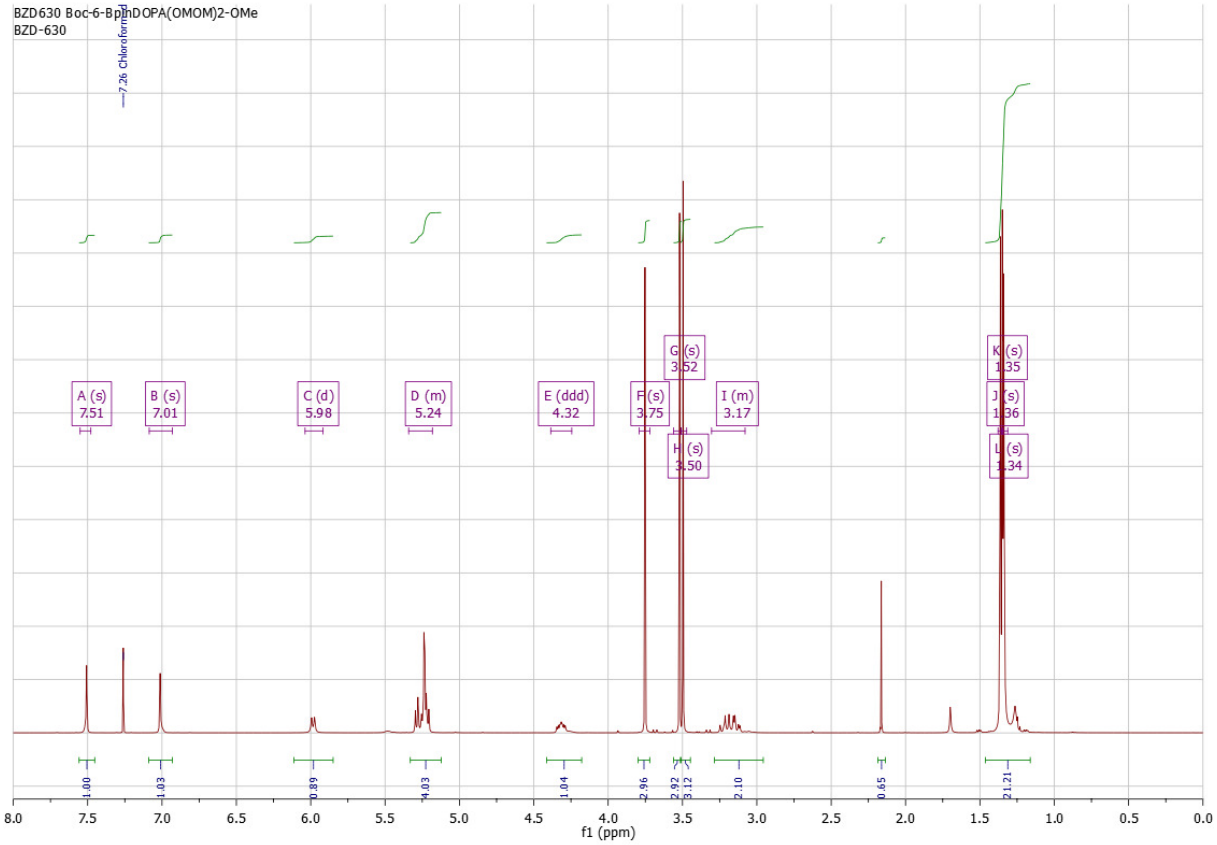
BZD630 Boc-6-Bpin-DOPA(OMOM)2-OMe
BZD-630
7.26 Chloroform
A (s) 7.51
B (s) 7.01
C (d) 5.98
D (m) 5.24
E (ddd) 4.32
F (s) 3.75
G (s) 3.52
H (s) 3.50
I (m) 3.17
K (s) 1.35
J (s) 1.36
L (s) 1.34
1.00
1.03
0.89
1.04
2.96
2.92
3.12
2.10
0.65
21.21
f1 (ppm)

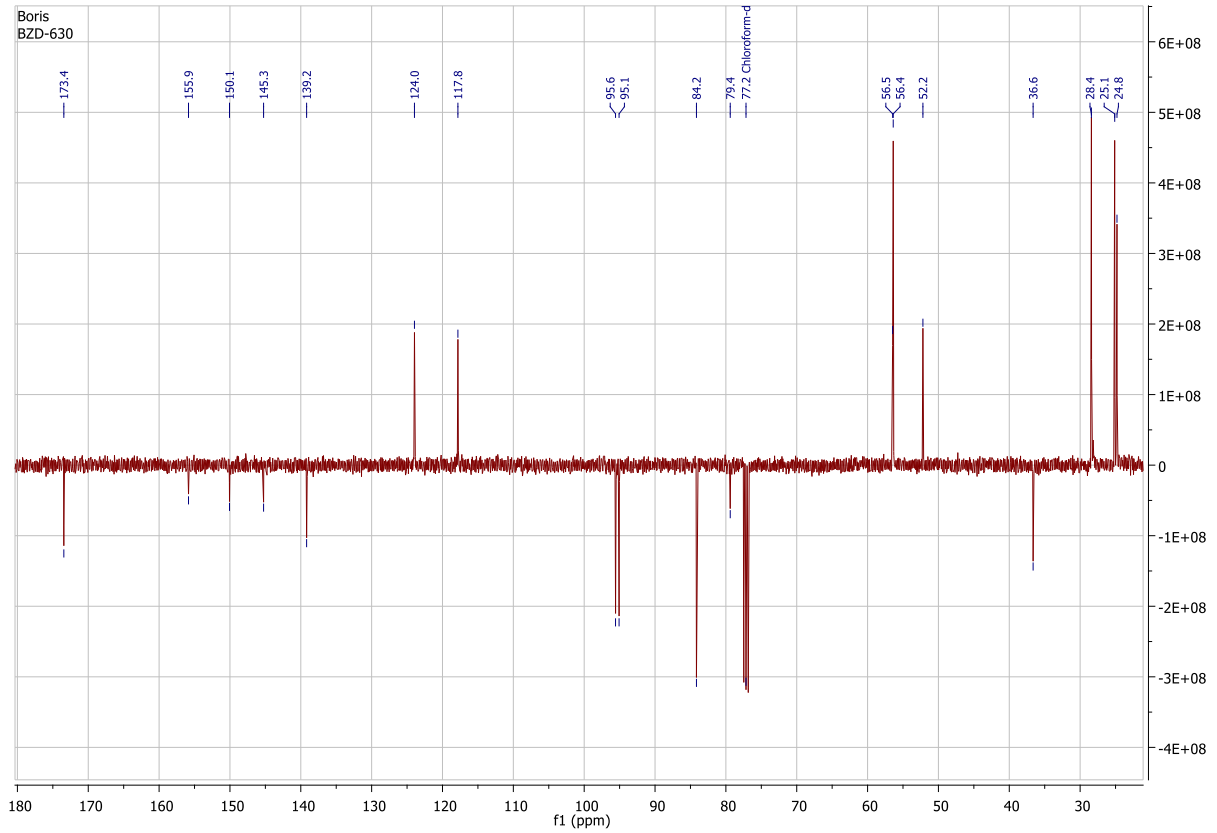
Boris
BZD-630
173.4
155.9
150.1
145.3
139.2
124.0
117.8
95.6
95.1
84.2
79.4
77.2 Chloroform-d
56.5
56.4
52.2
36.6
28.4
25.1
24.8
6E+08
5E+08
4E+08
3E+08
2E+08
1E+08
0
-1E+08
-2E+08
-3E+08
-4E+08
f1 (ppm)

$(Boc)_2$-6-BpinDOPA$(MOM)_2$-OMe (S4)

DMAP (30 mg, 0.25 mmol, 0.1 eq.) was added to a solution of **S3** (1.2 g, 2.3 mmol, 1 eq.) and Boc_2O (2.2 g, 10 mmol, 4.3 eq.) in anhydrous MeCN (7 mL) and the reaction mixture was manually stirred until the DMAP had dissolved. Thereafter, the mixture was left to stay at ambient temperature for 4 days. All volatiles were removed under reduced pressure and the residue was purified by column chromatography (EtOAc/hexane = 1:3, R_f = 0.35) followed by low-temperature recrystallization from pentane (–25 ºC) to afford the title compound as a colorless solid (1.2 g, 1.9 mmol, 83%). ^{1}H NMR (400 MHz, $CDCl_3$) δ = 7.49 (s, 1H), 6.87 (s, 1H), 5.28 (dd, *J* = 11.4, 3.9 Hz, 1H), 5.24 (dd, *J* = 6.5, 3.8 Hz, 2H), 5.16 (dd, *J* = 12.9, 6.5 Hz, 2H), 3.97 (dd, *J* = 13.5, 3.9 Hz, 1H), 3.75 (s, 3H), 3.49 (s, 3H), 3.46 (s, 3H), 3.04 (dd, *J* = 13.5, 11.4 Hz, 1H), 1.33 (s, 18H), 1.31 (s, 6H), 1.29 (s, 6H). ^{13}C NMR (101 MHz, $CDCl_3$): δ = 171.1, 151.7, 149.7, 144.9, 140.1, 124.3, 119.1, 95.5, 95.3, 83.6, 82.6, 60.1, 56.3, 56.1, 52.1, 35.5, 27.9, 25.1, 24.9. *C*-Bpin was not observed. LR-MS: m/z $[M+Na]^+$ calculated for $[C_{30}H_{48}BNO_{12}+Na]^+$ = 648.33, found: 648.38; $[M+H]^+$ calculated for $[C_{30}H_{48}BNO_{12}+H]^+$ = 626.34, found: 626.38. HR-MS: m/z $[M+Na]^+$ calculated for $[C_{30}H_{48}BNO_{12}+Na]^+$ = 648.31618, found: 648.31687.

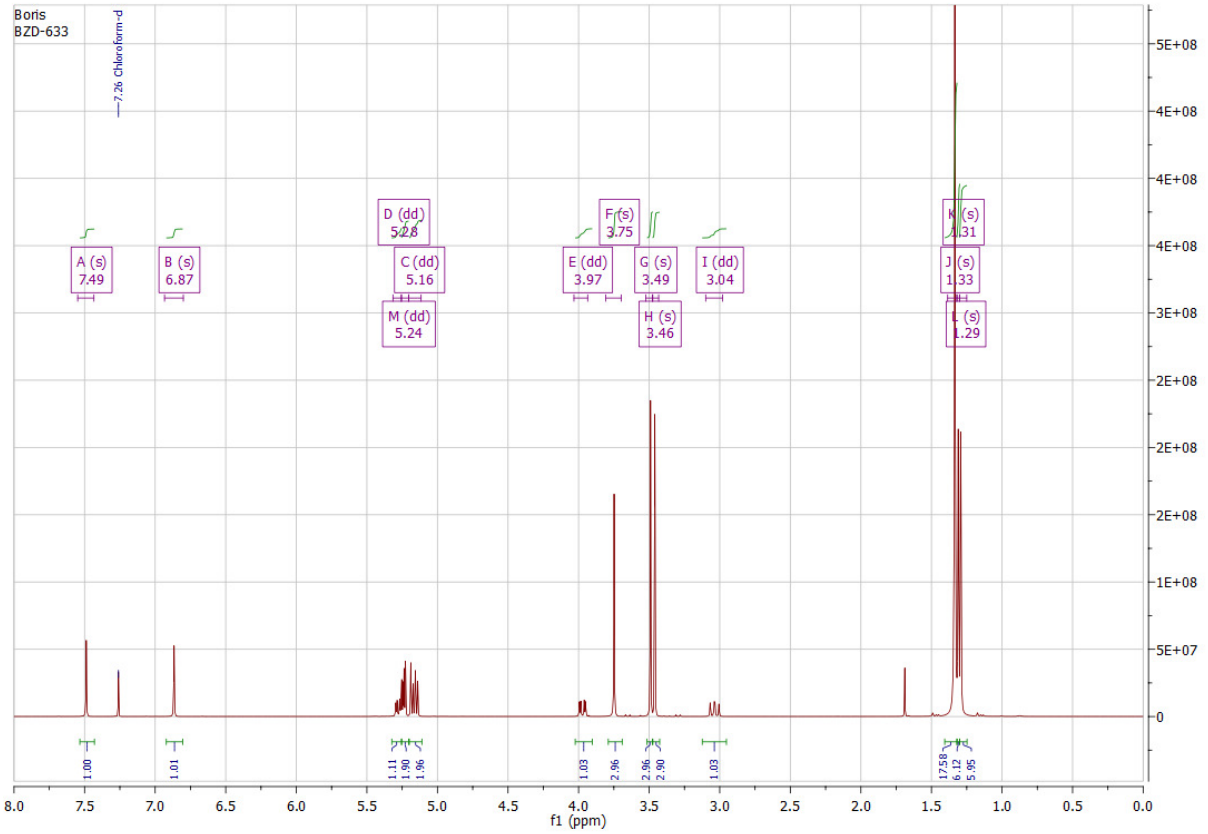
Boris
BZD-633
7.26 Chloroform-d
A (s) 7.49
B (s) 6.87
D (dd) 5.28
C (dd) 5.16
M (dd) 5.24
E (dd) 3.97
F (s) 3.75
G (s) 3.49
H (s) 3.46
I (dd) 3.04
K (s) 1.31
J (s) 1.33
L (s) 1.29
f1 (ppm)

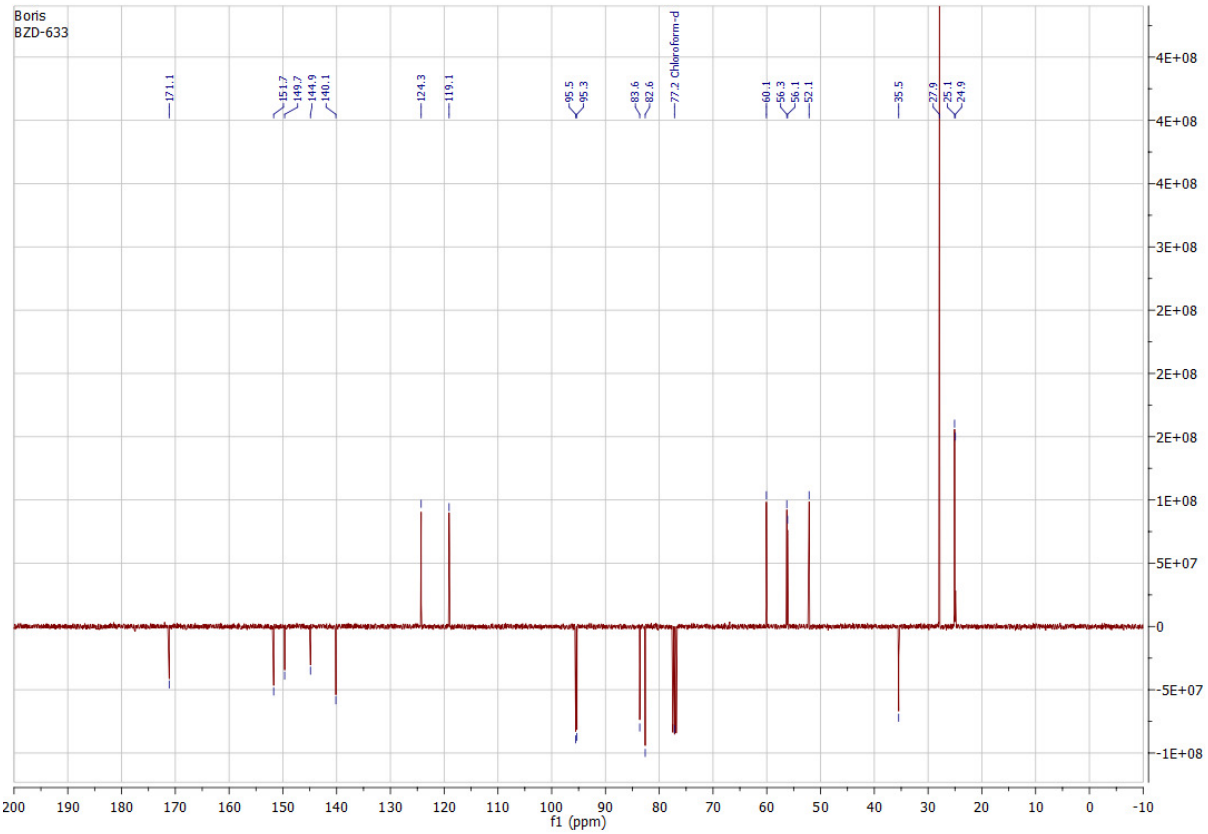
Boris
BZD-633
171.1
151.7
149.7
144.9
140.1
124.3
119.1
95.5
95.3
83.6
82.6
77.2 Chloroform-d
60.1
56.3
56.1
52.1
35.5
27.9
25.1
24.9
f1 (ppm)

2.6 **Preparation of (Boc)$_2$-6-SnMe$_3$DOPA(MOM)$_2$-OMe (S6)**

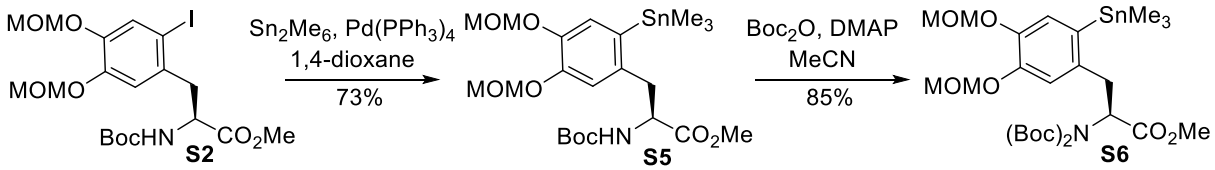

Scheme S2: Preparation of (Boc)$_2$-6-SnMe$_3$DOPA(MOM)$_2$-OMe (**S6**).

Boc-6-SnMe$_3$DOPA(MOM)$_2$-OMe (S5)

A solution of **S2** (2.3 g, 4.3 mmol, 1 eq.), Sn_2Me_6 (3.5 g, 11 mmol, 2.6 eq.) and $Pd(PPh_3)_4$ (0.50 g, 0.43 mmol, 0.1 eq.) in anhydrous 1,4-dioxane (10 mL) was stirred at 70 ºC for 24 h and thereafter at 90 ºC for 3 h. The reaction mixture was concentrated under reduced pressure and the residue was dried at 1 mbar and 60 ºC for 2 h. Thereafter, the crude product was purified by column chromatography (EtOAc:hexane = 1:3, R_f = 0.26) to afford the title compound (1.8 g, 73%) as a yellow oil, which was directly used for the next step without further purification and characterization.

(Boc)$_2$-6-SnMe$_3$DOPA(MOM)$_2$-OMe (S6)

DMAP (38 mg, 0.31 mmol, 0.1 eq.) was added to a solution of **S5** (1.8 g, 3.1 mmol, 1 eq.) and Boc_2O (2.2 g, 9.4 mmol, 3 eq.) in anhydrous MeCN (8 mL) and the reaction mixture was manually stirred until DMAP had dissolved. Thereafter, the mixture was left to stay at ambient temperature for 4 days. All volatiles were removed under reduced pressure and the residue was purified by column chromatography (EtOAc/hexane = 1:3, R_f = 0.54) to afford the title compound (1.7 g, 2.6 mmol, 84%) as a yellow oil. ^{1}H NMR (400 MHz, $CDCl_3$) δ = 7.15 (s, 1H), 6.93 (s, 1H), 5.26 (d, J = 6.6 Hz, 1H), 5.21 – 5.11 (m, 3H), 4.94 (td, J = 7.8, 4.9 Hz, 1H), 3.75 (s, 3H), 3.49 (s, 3H), 3.47 (s, 3H), 3.32 – 3.25 (m, 2H), 1.37 (s, 18H), 0.31 (s, 9H). ^{13}C NMR (101 MHz, $CDCl_3$): δ = 170.8, 151.7, 147.9, 145.4, 139.1, 135.3, 124.7, 118.2, 95.8, 95.4, 83.1, 60.0, 56.2, 56.1, 52.4, 38.1, 27.9, –8.1. HR-MS: m/z $[M+H]^+$ calculated for $[C_{27}H_{45}SnNO_{10}+H]^+$ = 664.21382, found: 664.21345. Correct isotopic pattern.

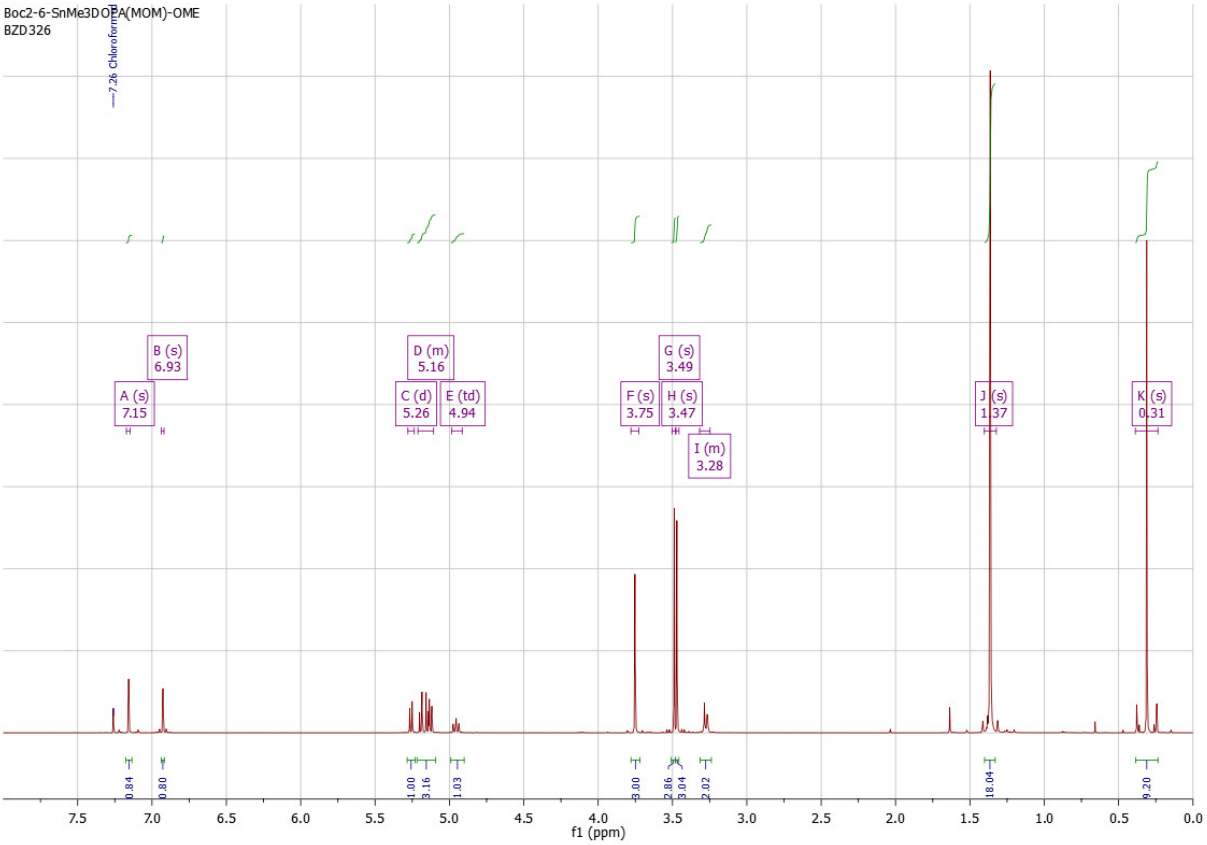
Boc2-6-SnMe3DOPA(MOM)-OME
BZD326
7.26 Chloroform
B (s) 6.93
A (s) 7.15
D (m) 5.16
C (d) 5.26
E (td) 4.94
G (s) 3.49
F (s) 3.75
H (s) 3.47
I (m) 3.28
J (s) 1.37
K (s) 0.31
0.84
0.80
1.00
3.16
1.03
3.00
2.86
3.04
2.02
18.04
9.20
f1 (ppm)

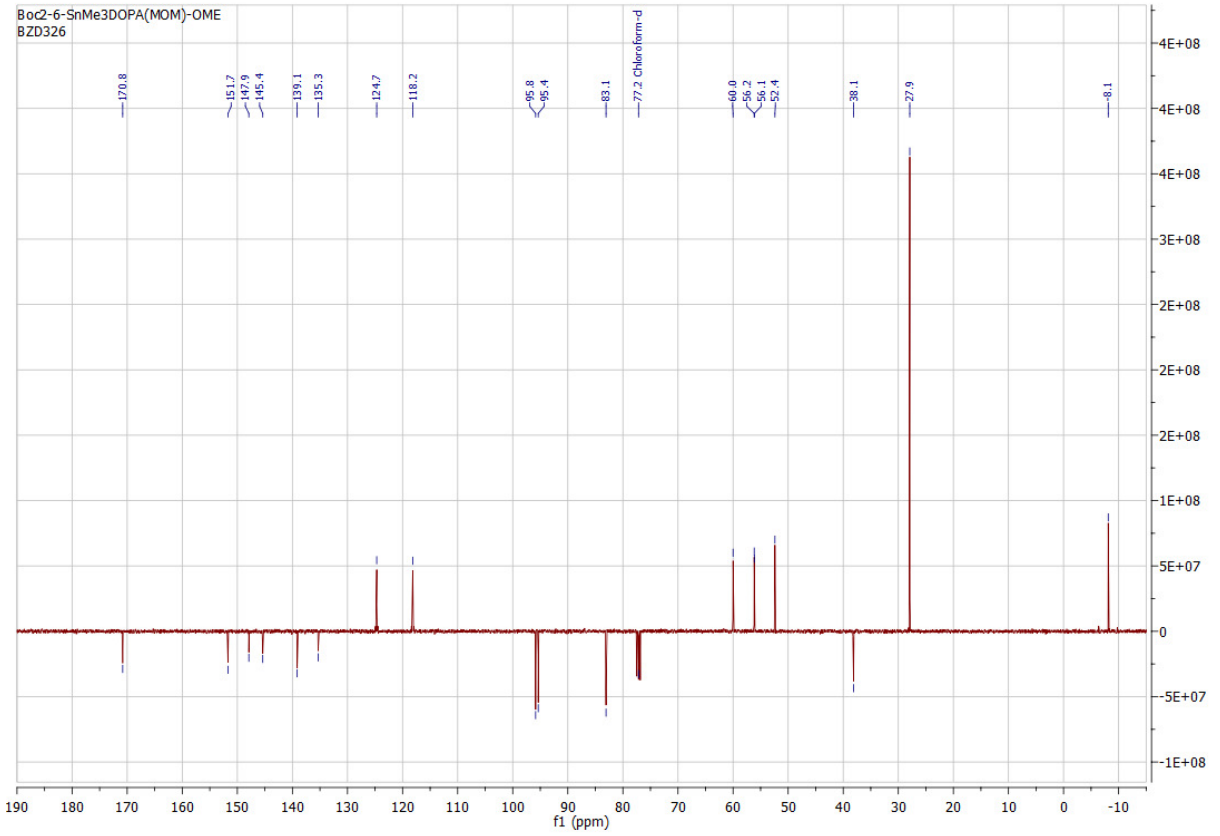
Boc2-6-SnMe3DOPA(MOM)-OME
BZD326
170.8
151.7
147.9
145.4
139.1
135.3
124.7
118.2
95.8
95.4
83.1
77.2 Chloroform-d
60.0
56.2
56.1
52.4
30.1
27.9
8.1
f1 (ppm)

2.7 Preparation of $B(OH)_2$ substituted Ni(II)-BPX complexes – General Procedure 4 (GP4)

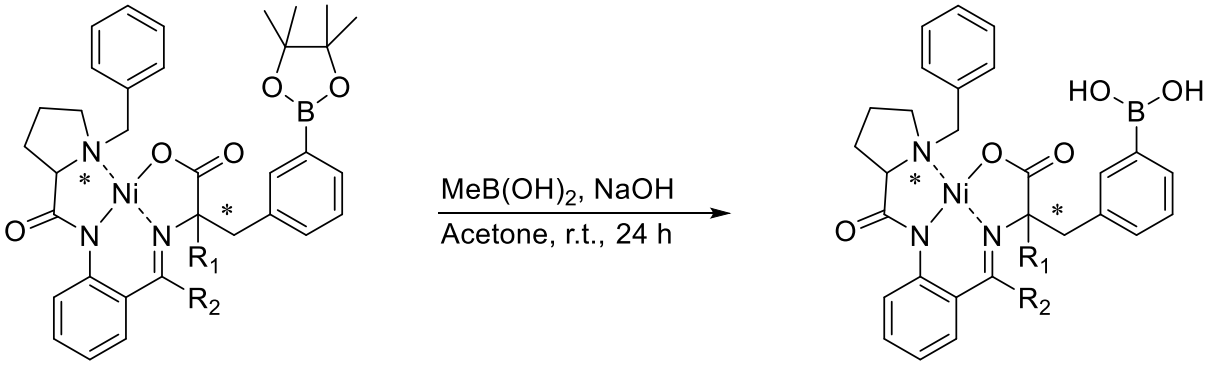

R_1 = H, R_2 = Ph [(*S*,*S*)-**11**]
R_1 = H, R_2 = Ph [(*R*,*R*)-**11**]
R_1 = Me, R_2 = H [(*R*,*R*)-**13**]

R_1 = H, R_2 = Ph [(*S*,*S*)-**10**]
R_1 = H, R_2 = Ph [(*R*,*R*)-**10**]
R_1 = Me, R_2 = H [(*S*,*S*)-**12**]

Scheme 3: Preparation of $B(OH)_2$ substituted Ni(II)-BPX complexes.

$B(OH)_2$-substituted Ni(II)-BPX complexes were prepared according to the literature.[23] 0.1 M NaOH (0.2 eq.) was added to a solution of the respective BPin substituted Ni-BPX complex (0.6 M, 1 eq.) and methylboronic acid (10 eq.) in acetone and the reaction mixture was stirred for 24 h. Afterwards, the mixture was neutralized by addition of 0.1 M HCl (0.15 eq.) and all volatiles were removed under reduced pressure. The crude product was purified by reversed phase flash column chromatography ($MeCN/H_2O$).

(*S*,*S*)-Ni-BPB-3-$B(OH)_2$Phe [(*S*,*S*)-10]

The title compound was obtained as a red solid (337 mg, 0.53 mmol, 85%) according to GP4 from (*S,S*)-Ni-BPB-3-BPinPhe[4] (450 mg, 0.63 mmol). ^{1}H NMR (400 MHz, THF-d_8) δ = 8.40 (dd, *J* = 8.8, 1.0 Hz, 1H), 8.14 – 8.04 (m, 2H), 7.86 (d, *J* = 7.4 Hz, 1H), 7.69 (s, 1H), 7.62 – 7.42 (m, 4H), 7.37 – 7.20 (m, 6H), 7.10 (ddd, *J* = 7.4, 2.8, 1.5 Hz, 2H), 7.02 (ddd, *J* = 8.7, 6.8, 1.8 Hz, 1H), 6.65 (dd, *J* = 8.3, 1.7 Hz, 1H), 6.56 (ddd, *J* = 8.2, 6.8, 1.2 Hz, 1H), 4.13 (dd, *J* = 11.0, 6.6 Hz, 2H), 3.42 (d, *J* = 12.5 Hz, 1H), 3.23 (t, *J* = 8.3 Hz, 1H), 3.00 (ddd, *J* = 17.5, 11.4, 4.2 Hz, 2H), 2.79 (dd, *J* = 13.5, 5.6 Hz, 1H), 2.20 – 2.13 (m, 3H), 2.02 – 1.92 (m, 1H), 1.58 – 1.49 (m, 1H). ^{13}C NMR (101 MHz, THF-d_8) δ = 181.1, 178.0, 171.8, 145.2, 137.2, 136.2 (×2), 135.4, 134.4, 134.1, 133.4, 132.7, 132.4, 130.4, 130.0, 129.8, 129.4 (×2), 129.3, 128.5 (×2), 127.1, 124.5, 120.3, 72.6, 71.1, 63.9, 58.5, 40.4, 31.7, 24.2. HR-MS: m/z $[M+H]^+$ calculated for $[C_{34}H_{31}BN_3NiO_5+H]^+$ = 631.18976, found: 631.19052 $[M+H^+]$. Correct isotopic pattern.

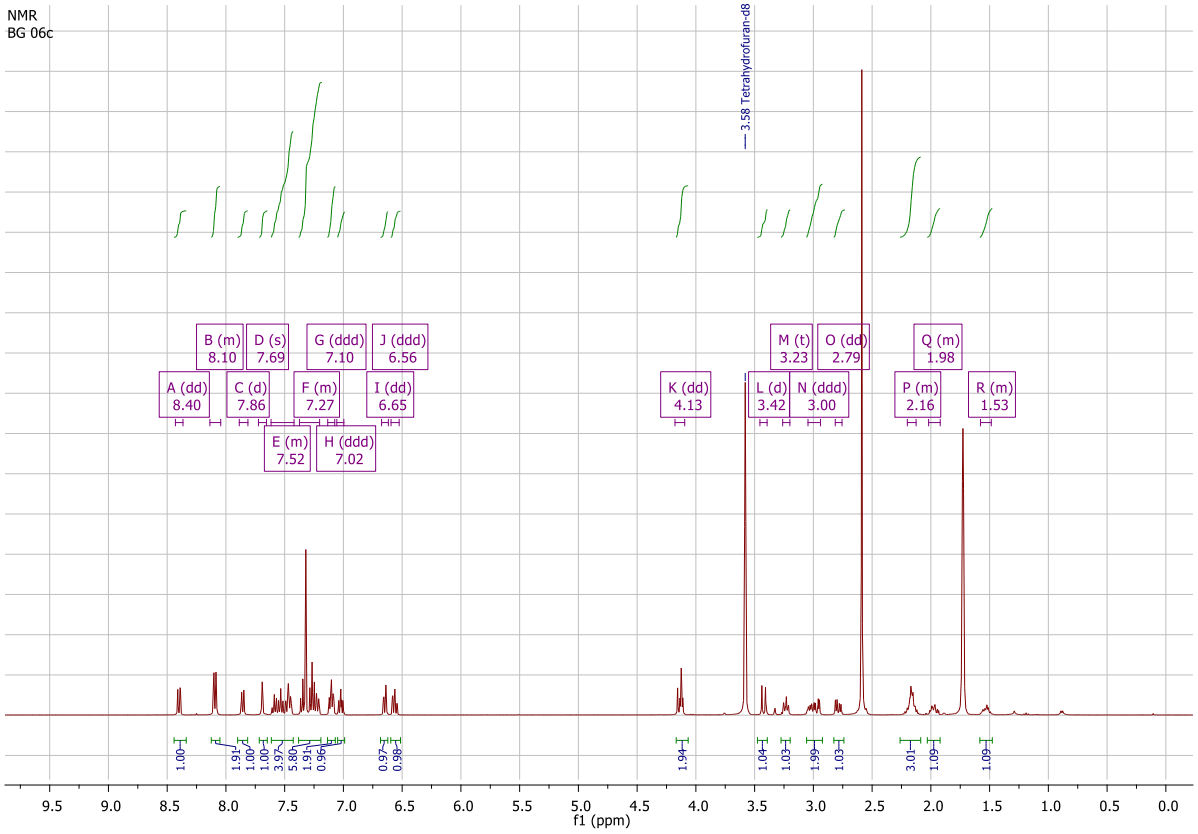
NMR
BG 06c
3.58 Tetrahydrofuran-d8
A (dd) 8.40
B (m) 8.10
C (d) 7.86
D (s) 7.69
E (m) 7.52
F (m) 7.27
G (ddd) 7.10
H (ddd) 7.02
I (dd) 6.65
J (ddd) 6.56
K (dd) 4.13
L (d) 3.42
M (t) 3.23
N (ddd) 3.00
O (dd) 2.79
P (m) 2.16
Q (m) 1.98
R (m) 1.53
f1 (ppm)

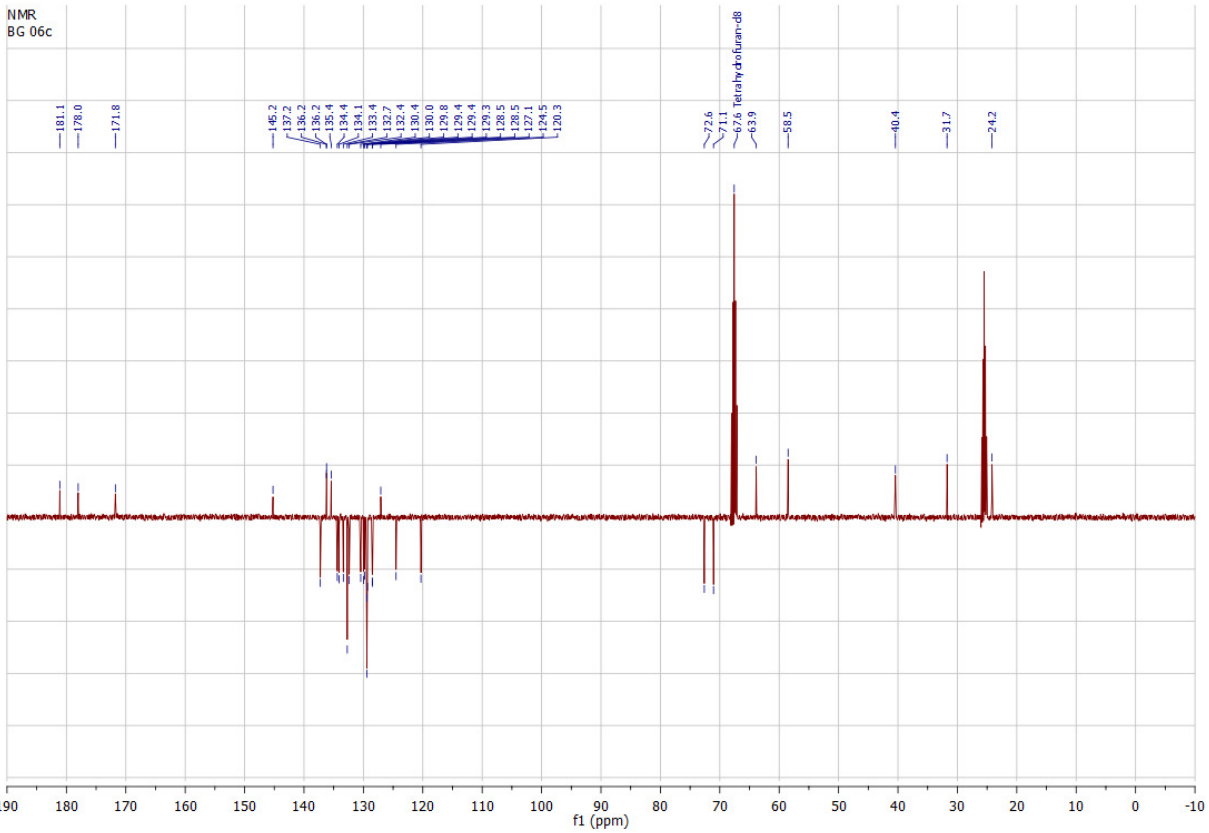
NMR
BG 06c
Tetrahydrofuran-d8
f1 (ppm)

(*R*,*R*)-Ni-BPB-3-B(OH)$_2$Phe [(*R*,*R*)-10]

The title compound was obtained as a red solid (357 mg, 0.63 mmol, 90%) according to GP4 from (*R,R*)-Ni-BPB-3-BPinPhe[4] (450 mg, 0.63 mmol). ^{1}H NMR (400 MHz, THF-d_8) δ = 8.40 (dd, *J* = 8.8, 0.9 Hz, 1H), 8.12 – 8.06 (m, 2H), 7.85 (t, *J* = 9.5 Hz, 1H), 7.68 (d, *J* = 12.9 Hz, 1H), 7.61 – 7.43 (m, 4H), 7.38 – 7.18 (m, 6H), 7.14 – 7.08 (m, 2H), 7.02 (ddd, *J* = 8.7, 6.8, 1.8 Hz, 1H), 6.65 (dd, *J* = 8.3, 1.7 Hz, 1H), 6.56 (ddd, *J* = 8.2, 6.8, 1.2 Hz, 1H), 4.17 – 4.09 (m, 2H), 3.42 (d, *J* = 12.5 Hz, 1H), 3.22 (d, *J* = 7.2 Hz, 1H), 3.06 – 2.94 (m, 2H), 2.79 (dd, *J* = 13.5, 5.6 Hz, 1H), 2.24 – 2.11 (m, 3H), 1.98 (ddd, *J* = 16.4, 11.1, 5.7 Hz, 1H), 1.53 (td, *J* = 11.0, 5.3 Hz, 1H). ^{13}C NMR (101 MHz, THF-d_8) δ = 181.1, 178.1, 171.8, 145.2, 137.3, 136.2 (×2), 135.4, 134.4, 134.1, 133.4, 132.7, 132.4, 130.5, 130.0, 129.8, 129.7, 129.4, 129.3, 128.5 (×2), 127.1, 124.5, 120.3, 72.6, 71.1, 63.9, 58.5, 40.4, 31.7, 24.2. HR-MS: m/z $[M+H]^+$ calculated for $[C_{34}H_{31}BN_3NiO_5+H]^+$ = 631.18976, found: 631.19045 $[M+H^+]$. Correct isotopic pattern.

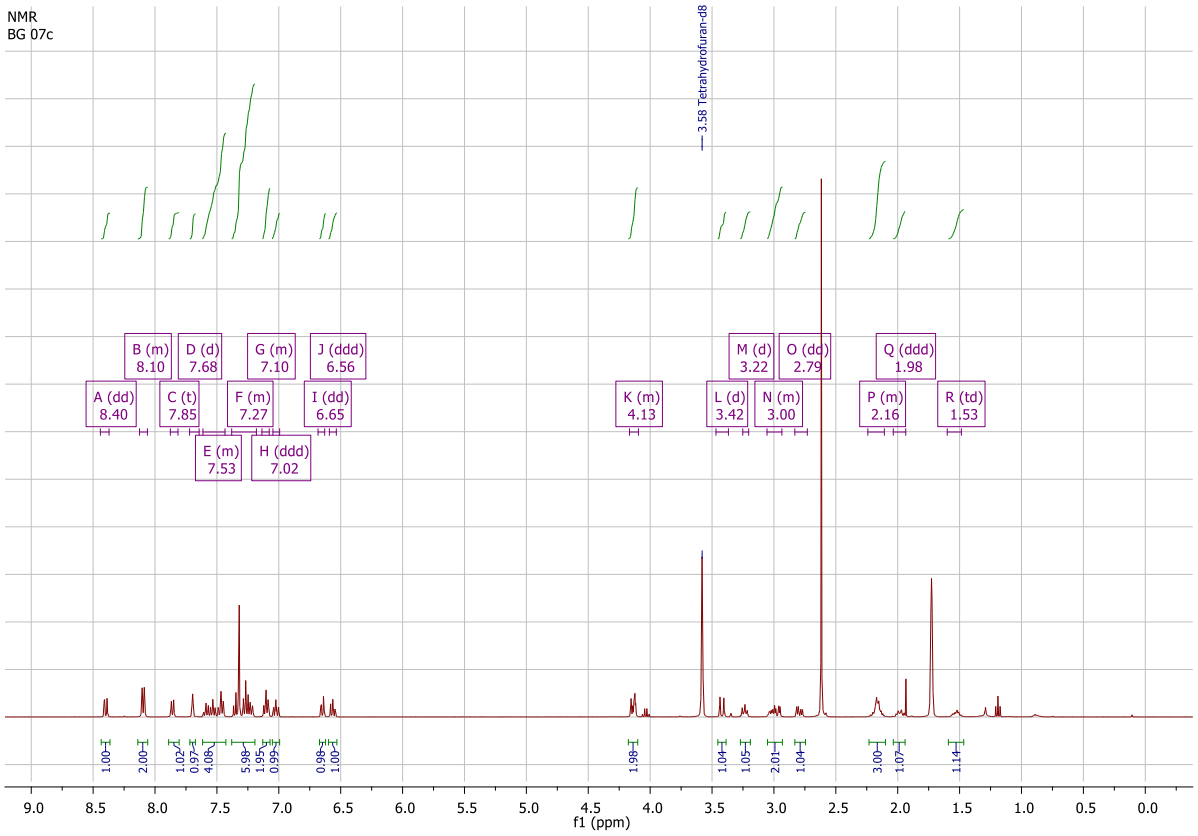

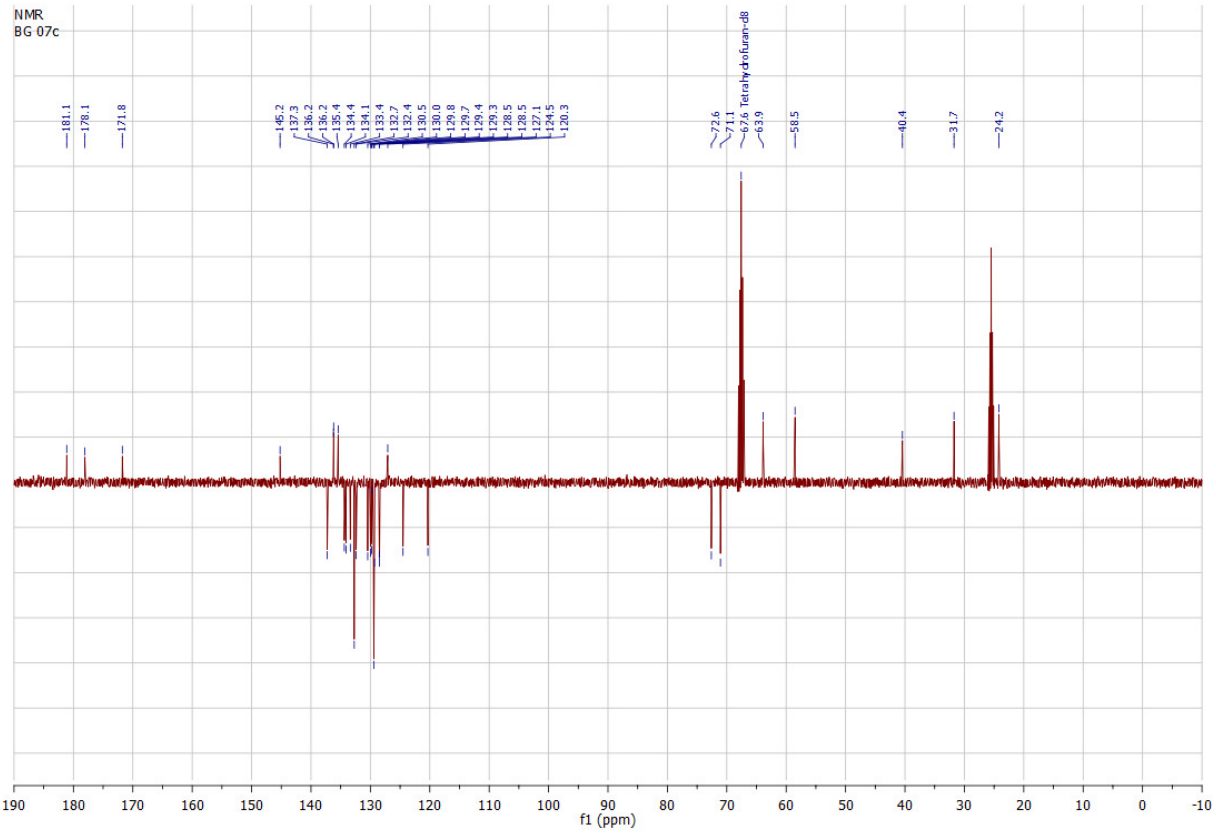

Synthesis of (*S,S*)-Ni-BPA-α-methyl-3-B(OH)$_2$Phe [(*S,S*)-12]

The title compound was obtained as a red solid (370 mg, 0.65 mmol, 83%) according to GP4 from (*S,S*)-Ni-BPA-α-methyl-3-BPinPhe[4] (510 mg, 0.78 mmol). ^{1}H NMR (400 MHz, $CDCl_3$) δ = 8.48 (d, *J* = 8.6 Hz, 1H), 8.03 – 7.90 (m, 3H), 7.72 (d, *J* = 19.9 Hz, 1H), 7.62 – 7.54 (m, 1H), 7.47 – 7.16 (m, 7H), 7.14 (t, *J* = 8.2 Hz, 1H), 7.01 – 6.84 (m, 1H), 4.20 – 4.07 (m, 2H), 3.48 (d, *J* = 12.7 Hz, 1H), 3.35 (d, *J* = 13.4 Hz, 1H), 3.23 (dd, *J* = 9.4, 6.6 Hz, 1H), 2.98 (dd, *J* = 10.1, 5.8 Hz, 1H), 2.86 (d, *J* = 13.5 Hz, 1H), 2.29 – 1.99 (m, 2H), 1.92 – 1.78 (m, 1H), 1.68 – 1.56 (m, 4H), 1.50 – 1.40 (m, 1H), 1.31 – 1.21 (m, 3H), 0.89 (ddt, *J* = 46.7, 43.1, 19.6 Hz, 1H). ^{13}C NMR (101 MHz, $CDCl_3$) δ = 182.2, 181.8, 161.4, 142.8, 136.3, 134.4, 134.1, 133.9, 133.7, 133.3, 132.9, 131.8, 129.1, 128.9, 128.1, 124.0, 123.5, 121.6, 74.9, 70.4, 63.2, 60.5, 60.0, 57.4, 48.3, 30.9, 29.8, 25.4, 23.2, 21.2, 14.3 (×2). HR-MS: m/z $[M+H]^+$ calculated for $[C_{29}H_{29}BN_3NiO_5+H]^+$ = 569.17411, found: 569.17416. Correct isotopic pattern.

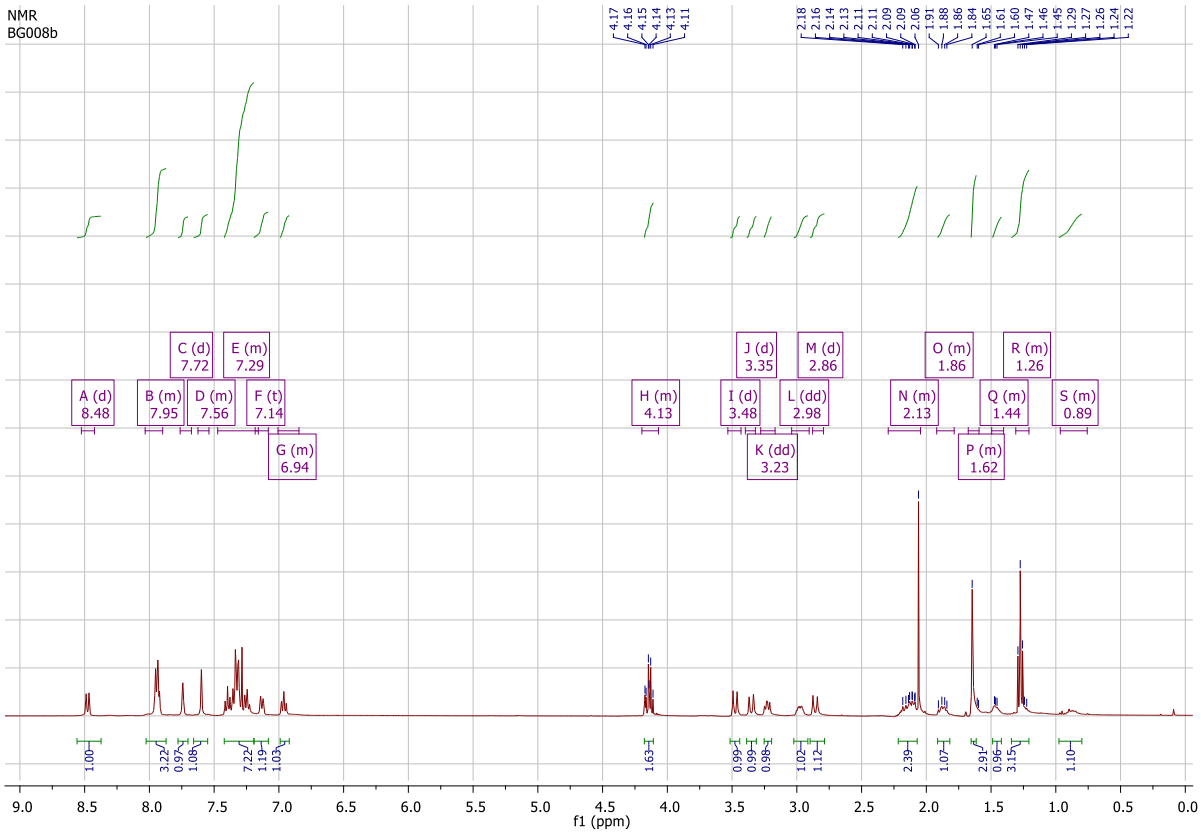
NMR
BG008b
A (d) 8.48
B (m) 7.95
C (d) 7.72
D (m) 7.56
E (m) 7.29
F (t) 7.14
G (m) 6.94
H (m) 4.13
I (d) 3.48
J (d) 3.35
K (dd) 3.23
L (dd) 2.98
M (d) 2.86
N (m) 2.13
O (m) 1.86
P (m) 1.62
Q (m) 1.44
R (m) 1.26
S (m) 0.89
f1 (ppm)

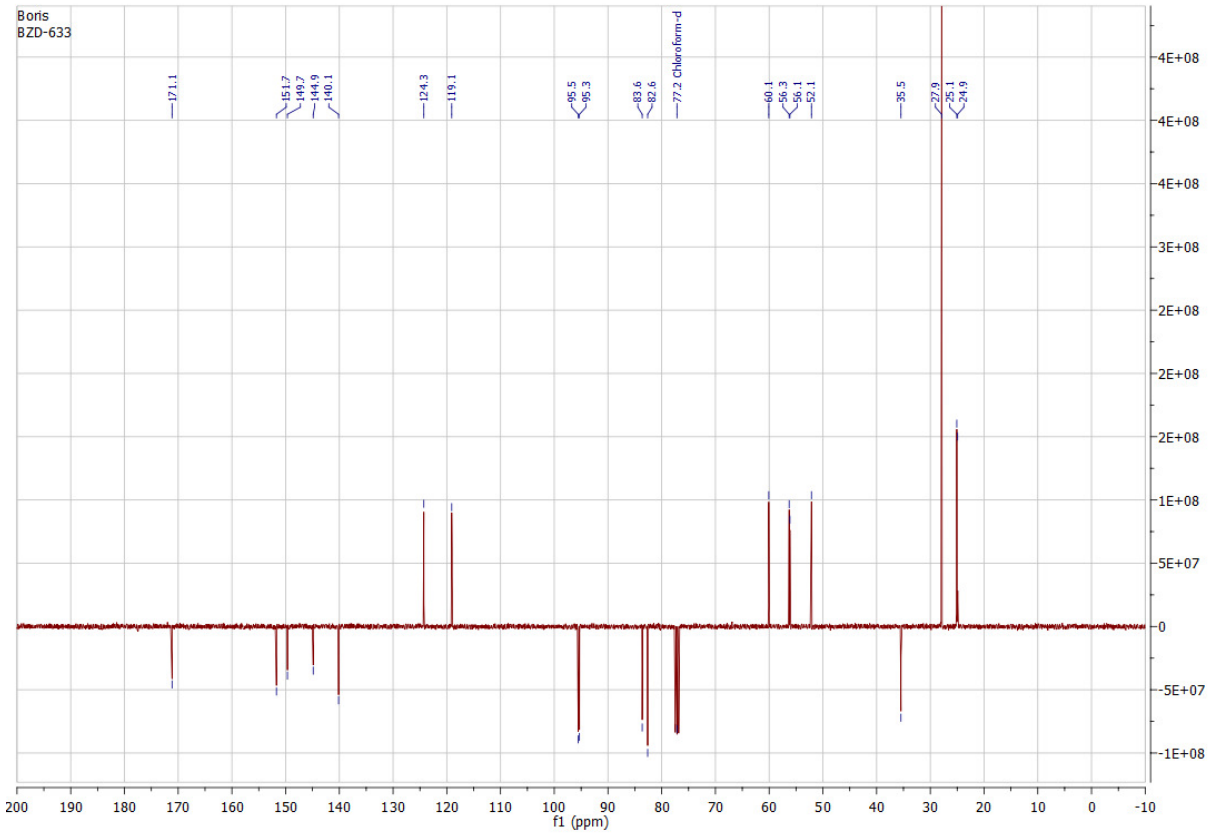
Boris
BZD-633
171.1
151.7
149.7
144.9
140.1
124.3
119.1
95.5
95.3
83.6
82.6
77.2 Chloroform-d
60.1
56.3
56.1
52.1
35.5
27.9
25.1
24.9
f1 (ppm)

3 Radiochemistry

3.1 General conditions

[^{18}F]Fluoride ([^{18}F]F$^-$) was produced via the ^{18}O(p,n)^{18}F nuclear reaction by bombardment of enriched [^{18}O]H_2O with 16.5 MeV protons using a BC1710 cyclotron (The Japan Steel Works Ltd., Shinagawa, Japan) at the INM-5 (Forschungszentrum Jülich). All radiosyntheses were carried out in 5 mL Wheaton V-Vials equipped with PTFE wing coated stir bars. Anhydrous solvents (DMA, DMI, PC, *n*BuOH and MeOH, dried over molecular sieves) were purchased from Sigma-Aldrich (Steinheim, Germany) or Acros (Fisher Scientific GmbH, Nidderrau, Germany). Anion exchange resins (Sep-Pak Accell Plus QMA carbonate plus light cartridges 40 mg sorbent per cartridge) and solid phase extraction Sep-Pak C18 and HLB short cartridges (360 mg per cartridge) were obtained from Waters GmbH (Eschborn, Germany). The polymeric-based StrataX cartridge (30 mg) was obtained from Phenomenex (Aschaffenburg, Deutschland).

3.2 Analytical HPLC

Analytical radio-HPLC was performed on a Dionex Ultimate® 3000 HPLC systems (Thermo Fisher Scientific GmbH, Dreieich, Germany) or a HPLC system (Knauer Wissenschaftliche Geräte GmbH, Berlin, Germany) with Azura P 6.1L pump and Azura UVD 2.1S UV/Vis detector. For monitoring absorbance at 254 nm and radioactivity, the UV/Vis detector was coupled in series with a Berthold NaI detector, giving a time of delay of 0.1–0.3 min between the corresponding responses, depending on the flow rate. RCCs were determined by radio-HPLC after dilution of the reaction mixture with H_2O (2 mL) or 20% MeCN (2 mL), through comparison of the peak areas for the radiolabeled product and a post-column injection of the reaction mixture.[24] The identity of radiolabeled products was confirmed by co-injection of the corresponding non-radiolabeled reference compound. Activity yields (AY) were determined by comparing the initial activity on the QMA cartridge and the activity of the radiolabeled product.

HPLC conditions for radiolabeled model compounds: column: Chromolith SpeedROD®, 130 Å, 1.6 µm, 4.6×50 mm (Merck Millipore, Darmstadt, Germany) flow rate: 1.5 mL/min, injection loop: 20 µL.

Radiolabeled product	Mobile phase	t_R [min]
[^{18}F]F-Ph-Ph	50% MeCN	3.5
[^{18}F]F-Ac-Ph	20% MeCN	3.7
[^{18}F]**14**	40% MeCN	5.5
[^{18}F]**15**	10% MeCN	3.5
[^{18}F]**16**	30% MeCN	4.7
[^{18}F]**17**	30% MeCN	4.0
[^{18}F]**18**	30% MeCN	3.5
[^{18}F]**19**	10% MeCN	2.1
[^{18}F]**20**	40% MeCN	4.7
[^{18}F]**21**	20% MeCN	3.6
[^{18}F]**22**	20% MeCN	3.2
[^{18}F]**23**	10% MeCN	4.5
[^{18}F]**24**	10% MeCN	3.9
[^{18}F]**25**	30% MeCN	3.2
[^{18}F]**26**	50% MeCN	4.4

HPLC conditions for radiolabeled tracer

[^{18}F]7: Column: Synergi Hydro-RP, 4 µm, 4.6×250 mm (Phenomenex, Aschaffenburg, Germany); eluent: 60% MeCN (0.1% TFA); flow rate: 1.5 mL/min; injection loop: 20 µL. t_R = 3.1 min.

[^{18}F]ALX5407: Column: Synergi Hydro-RP, 4 µm, 4.6×250 mm (Phenomenex, Aschaffenburg, Germany); eluent: 45% MeCN (0.1% TFA); flow rate: 1.5 mL/min; injection loop: 20 µL. t_R = 8.3 min.

[^{18}F]MNI1126: Column: Chromolith SpeedROD®, 4.6×50 mm (Merck Millipore, Darmstadt, Germany); eluent: 25% MeCN; flow rate: 1.5 mL/min; injection loop: 20 µL. t_R = 5.6 min.

(*S*,*S*)-**Ni-BPB-3-[^{18}F]FPhe**: Column: Synergi Hydro-RP, 4 µm, 4.6×250 mm (Phenomenex, Aschaffenburg, Germany); eluent: 75% MeCN; flow rate: 1.5 mL/min; injection loop: 20 µL. t_R = 5.0 min.

(*R*,*R*)-**Ni-BPB-3-[^{18}F]FPhe**: Column: Synergi Hydro-RP, 4 µm, 4.6×250 mm (Phenomenex, Aschaffenburg, Germany); eluent: 75% MeCN; flow rate: 1.5 mL/min; injection loop: 20 µL. t_R = 5.0 min.

(*S*,*S*)-**Ni-BPA-αMe-[^{18}F]FPhe**: Column: Synergi Hydro-RP, 4 µm, 4.6×250 mm (Phenomenex, Aschaffenburg, Germany); eluent: 75% MeCN; flow rate: 1.5 mL/min; injection loop: 20 µL. t_R = 3.8 min.

6-[^{18}F]FDOPA: Column: Synergi Hydro-RP, 4 µm, 4.6×250 mm (Phenomenex, Aschaffenburg, Germany); eluent: 60% MeCN; flow rate: 1.5 mL/min; injection loop: 20 µL. t_R = 10.9 min.

HPLC conditions for quality control

[^{18}F]R91150: Column: Synergi Hydro-RP, 4 µm, 4.6×250 mm (Phenomenex, Aschaffenburg, Germany); eluent: 30% MeCN (0.1% TFA); flow rate: 1.0 mL/min; injection loop: 20 µL. t_R = 6.4 min

[^{18}F]ALX5407: Column, Kinetex EVO C18, 5 µm, 4.6×250 mm (Phenomenex, Aschaffenburg, Germany); eluent, 35% MeCN (0.1% TFA); flow rate, 1.5 mL/min; injection loop: 20 µL. t_R = 12.0 min.

3-(*S*)**-[^{18}F]FPhe**: Column: Synergi Hydro-RP, 4 µm, 4.6×100 mm (Phenomenex, Aschaffenburg, Germany); eluent: 5% EtOH (0.1% H_3PO_4); flow rate: 1.0 mL/min; injection loop: 20 µL. t_R = 9.8 min.

3-(*R*)**-[^{18}F]FPhe**: Column: Synergi Hydro-RP, 4 µm, 4.6×100 mm (Phenomenex, Aschaffenburg, Germany); eluent: 10% EtOH (0.1% H_3PO_4); flow rate: 1.0 mL/min; injection loop: 20 µL. t_R = 7.8 min.

6-[^{18}F]FDOPA: Column: Synergi Hydro-RP, 4 µm, 4.6×250 mm (Phenomenex, Aschaffenburg, Germany); eluent: 1% EtOH (0.1% H_3PO_4); flow rate: 1.0 mL/min; injection loop: 20 µL. t_R = 7.1 min

3.3 Preparative HPLC

The HPLC system used for purification of crude PET-tracers comprised a Merck Hitachi L-6000 pump, a Knauer K-2500 detector, a Rheodyne 6-way valve and a Geiger-Müller counter.

[^{18}F]R91150: Column: Hydro-RP, 10 µm, 10×250 mm (Phenomenex, Aschaffenburg); eluent: 30% MeCN (0.1% TFA); flow rate: 7.1 mL/min; t_R= 7.5–9.0 min.

[^{18}F]ALX5407: Column: Gemini C18 110A, 5 µm, 10×250 mm (Phenomenex, Aschaffenburg, Germany); eluent: 35% MeCN (0.1% AcOH); flow rate: 7.4 mL/min. t_R = 20.5–22.5 min.

3-(*S*)-[^{18}F]FPhe: Column: Hydro-RP, 10 µm, 10×250 mm (Phenomenex, Aschaffenburg); eluent: 5% EtOH (0.1% H_3PO_4); flow rate: 7.4 mL/min; t_R= 8.0–9.2 min.

3-(*R*)-[^{18}F]FPhe: The same as for 3-(*S*)-[^{18}F]FPhe.

3-(*S*)-αMe-[^{18}F]FPhe: Column: Hydro-RP, 10 µm, 10×250 mm (Phenomenex, Aschaffenburg); eluent: 5% EtOH (0.1% H_3PO_4); flow rate: 7.4 mL/min. t_R = 17.1 min.

6-[^{18}F]FDOPA: Column: Hydro-RP, 10 µm, 10×250 mm (Phenomenex, Aschaffenburg); eluent, 1% EtOH (0.1% H_3PO_4); flow rate: 7.1 mL/min. t_R = 9–11 min.

3.4 Processing of fluoride-18

Aqueous [^{18}F]F^- was loaded onto a QMA cartridge (preconditioned with 1 mL H_2O) from the female to the male side. The cartridge was washed (from the male side) with anhydrous MeOH (1 mL) to remove residual H_2O and dried (from the female side) with air (2×10 mL). [^{18}F]F^- was eluted (from the female to the male side) with a solution of Et_4NOTf in *n*BuOH or MeOH.

3.5 Statistical analysis

All statistical analyses were performed with GraphPad Prism 8.4.3 for macOS, using one-way and two-way ANOVAs followed by appropriate Dunnett's, Tukey's or Sidak's multiple comparison tests. Statistical significance was defined as a *p*-value of less than 0.05.

3.6 General procedures for radiolabeling

"Alcohol enhanced" Cu-mediated radiofluorination of boranyl precursors – General Procedure 5 (GP5)

[^{18}F]F$^-$ (500 µL, 20–5000 MBq) was loaded onto a QMA cartridge and eluted with a solution of Et_4NOTf (1 mg, 3.6 µmol) in *n*BuOH (400 µL) into a solution of the respective Cu complex and precursor (10 µmol of each if not otherwise noted) in the corresponding solvent (800 µL). The reaction mixture was heated at 110 °C for 10 min under atmospheric or synthetic air, cooled to ambient temperature and diluted with H_2O (2 mL). RCCs were determined by radio-HPLC as described above. At high atmospheric humidity (e.g., during the midsummer), a significant drop of the RCCs was sometimes observed, presumably owing to the hygroscopicity of Et_4NOTf. In such cases [^{18}F]F$^-$ should preferably be eluted with a solution of Et_4NOTf in MeOH, as described above. MeOH was removed at 60 °C for 2–3 min under reduced pressure in a stream of argon and the residue was taken up into a solution of the respective Cu complex and precursor (10 µmol of each if not otherwise noted) in a mixture of the corresponding solvent and *n*BuOH (1200 µL; 2:1).

"Alcohol enhanced" Cu-mediated radiofluorination of stannyl precursors – General Procedure 6 (GP6)

Air conditions (GP6-A): [^{18}F]F$^-$ was loaded onto a QMA carbonate cartridge and eluted with Et_4NOTf (1 mg, 3.6 µmol) in *n*BuOH (400 µL) as described above directly into a solution of the corresponding stannyl precursor and copper(II) complex (10 µmol of each if not otherwise noted) in DMI (800 µL). The reaction mixture was heated at 110 °C for 10 min. RCCs were determined by radio-HPLC as described above.

Argon conditions (GP6-B): [^{18}F]F$^-$ was loaded onto a QMA carbonate cartridge. The V-Vial was evacuated using an oil pump, filled with argon and sealed with a silicone septum. Thereafter, [^{18}F]F$^-$ was eluted with Et_4NOTf (1 mg. 3.6 µmol) in *n*BuOH (400 µL) as described above with a cannula through the septum into the V-Vial, the cartridge was purged with argon and a solution of the corresponding precursor and copper(II) complex (10 µmol of each if not

otherwise noted) in DMI (800 µL) was added via a cannula. The reaction mixture was heated at 110 °C for 10 min. RCCs were determined by radio-HPLC as described above.

Cu-mediated radiofluorination of stannyl precursors in pure DMI – General Procedure 7 (GP7)

Air conditions (GP7-A): [^{18}F]F$^-$ was loaded onto a QMA carbonate cartridge and eluted with Et_4NOTf (1 mg, 3.6 µmol) in MeOH (500 µL) as described above. MeOH was evaporated at 60 °C for 2–3 min under reduced pressure in a stream of argon. The V-Vial was opened and a solution of the respective precursor and copper(II) complex (10 µmol of each if not otherwise noted) in DMI (800 µL) was added. The reaction mixture was heated at 110 °C for 10 min. RCCs were determined by radio-HPLC as described above.

Argon conditions (GP7-B): [^{18}F]F$^-$ was loaded onto a QMA carbonate cartridge and eluted with Et_4NOTf (1 mg, 3.6 µmol) in MeOH (500 µL) as described above, followed by evaporation of MeOH at 60 °C under reduced pressure in a stream of argon. The V-Vial was filled with argon, sealed with a silicon septum and a solution of the appropriate precursor and copper(II) complex (10 µmol of each if not otherwise noted) in DMI (800 µL) was added via a cannula through the septum. The reaction mixture was heated at 90 or 110 °C for 10 min. RCCs were determined by radio HPLC as described above.

3.7 Optimization studies

Elution efficiency

The dependency of $[^{18}F]F^-$ elution efficiency and RCC on the amount of Et_4NOTf used was assessed according to GP5 with **1** and $Cu(Py)_4(OTf)_2$ in *n*BuOH/DMA (n = 3). RCCs were determined by radio-HPLC as described above.

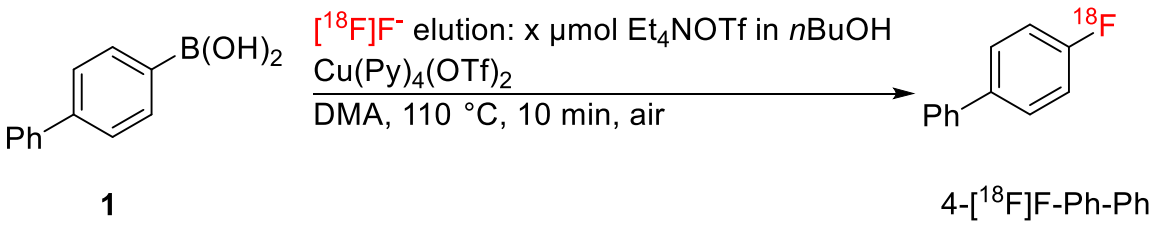

1 4-[^{18}F]F-Ph-Ph

Table S16: Dependency of $[^{18}F]F^-$ recovery and RCCs on the amount of Et_4NOTf.

Entry	m [mg]	x [µmol]	Elution Efficiency [%]	RCC [%]
1	7.7	28	98 ± 0.4	28 ± 3
2	3.5	13	97 ± 0.3	35 ± 3
3	1.0	3.6	95 ± 1	38 ± 2
4	0.1	0.36	53 ± 7	19 ± 1

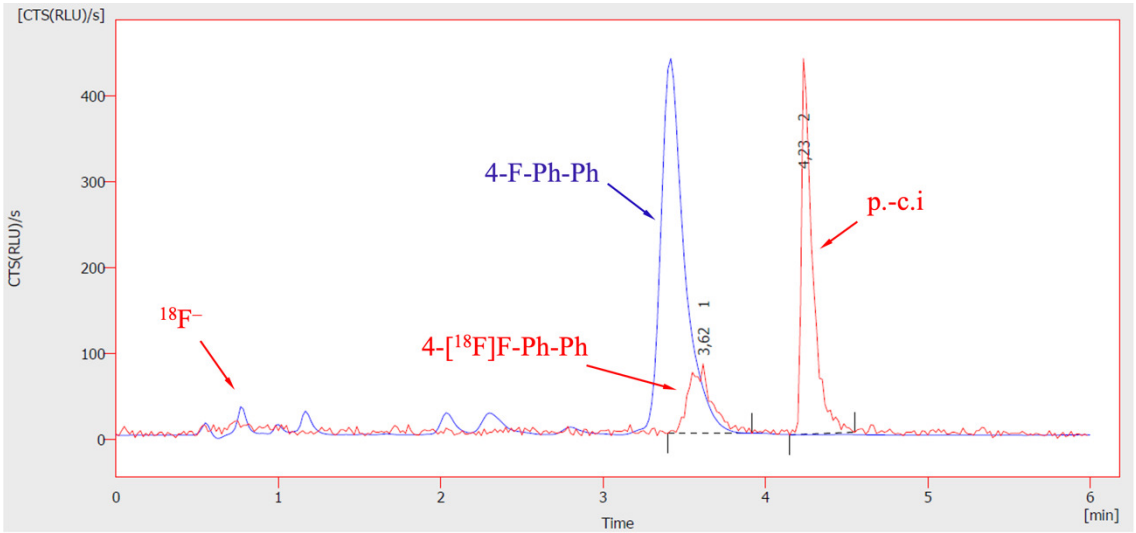

Result Table (Uncal - Data\alc-enhanced_393_19_01_2022_[1 DMA]_biphenyl_b(OH)2 - HERM)

	Reten. Time [min]	Area [CTS(RLU)/s.s]	Height [CTS(RLU)/s]	Area [%]
1	3,617	799,000	81,000	27,4
2	4,233	2117,000	438,375	72,6
	Total	2916,000	519,375	100,0

Figure S5: HPLC traces of crude 4-[^{18}F]F-Ph-Ph (spiked with 4-F-Ph-Ph) prepared in *n*BuOH/DMA from **1** using $Cu(Py)_4(OTf)_2$ as mediator and 1 mg Et_4NOTf for the elution of $[^{18}F]F^-$. Blue trace: UV, λ = 254 nm; red trace: radioactivity. Abbreviation: p.-c.i – post-column injection.

Screening of nickel(II), cobalt(II) and copper(II) complexes

The screening of nickel(II), cobalt(II) and copper(II) complexes was performed according to GP5 with aryl boronates **1 – 4** and stannanes **5** and **6** in *n*BuOH/DMA (n=3). RCCs were determined by radio-HPLC as described above. Representative radio-HPLC chromatograms of radiolabeled products are shown in Figure **S6**–**S12** and Figure **S14**–**S18**.

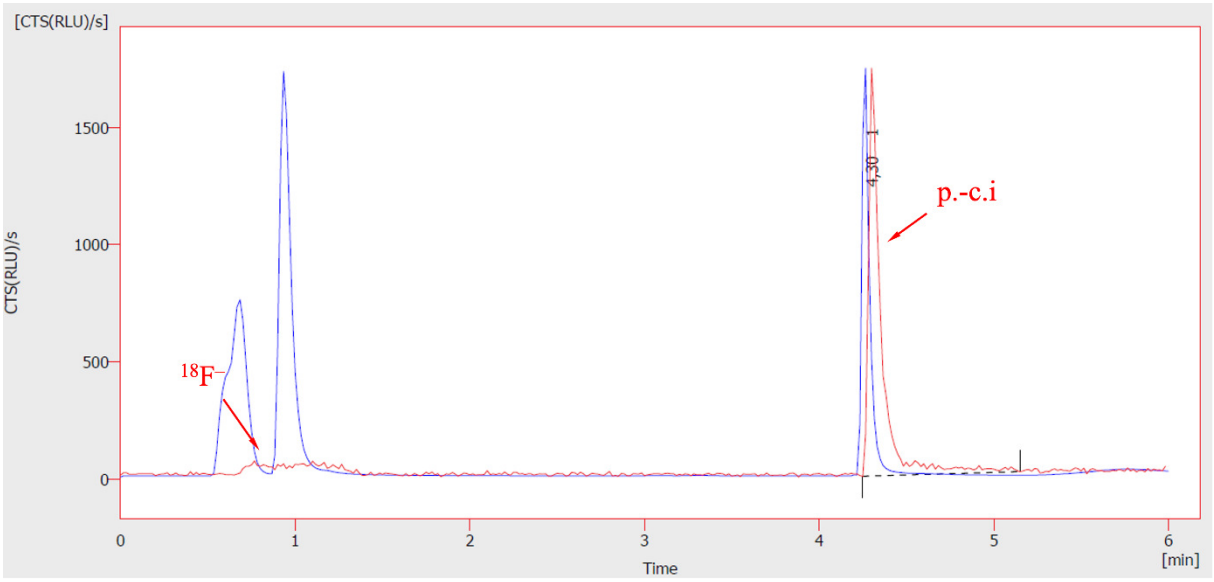

Result Table (Uncal - Data|alc-enhanced_855_01_08_2022_[31 DMA]biphenyl-B(OH)2 - HERM)

	Reten. Time [min]	Area [CTS(RLU)/s.s]	Height [CTS(RLU)/s]	Area [%]
1	4,300	8598,000	1741,944	100,0
	Total	8598,000	1741,944	100,0

Figure S6: HPLC traces of radiolabeling of **1** in *n*BuOH/DMA using $Ni(Py)_4(OTf)_2 \cdot H_2O$ as mediator and 1 mg Et_4NOTf for the elution of $[^{18}F]F^-$. Blue trace: UV, λ = 254 nm; red trace: radioactivity. Abbreviation: p.-c.i – post-column injection.

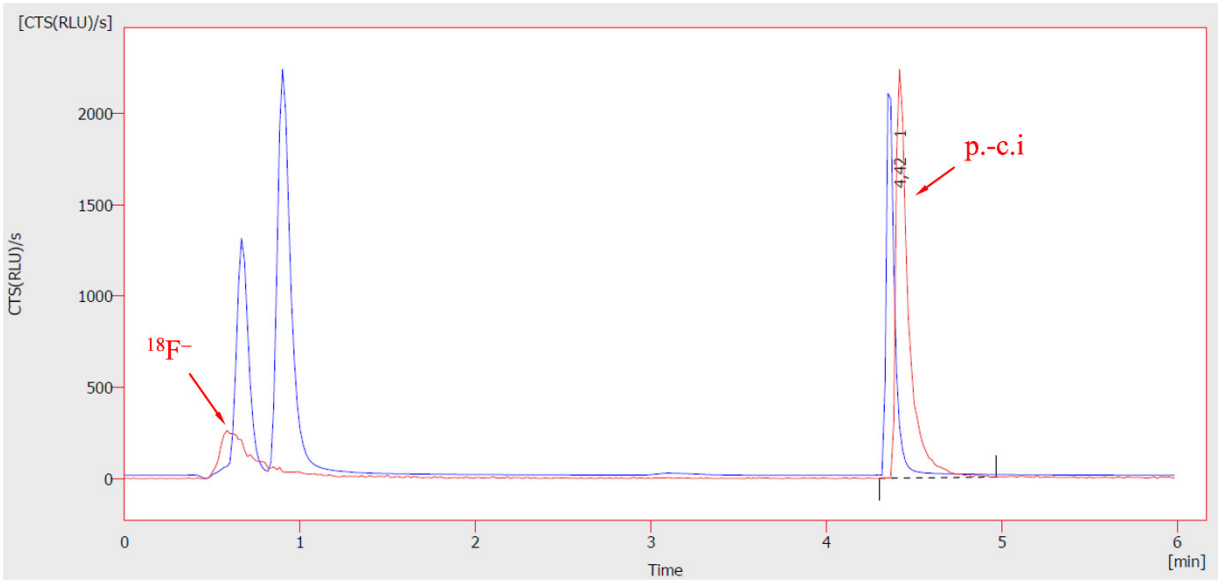

Result Table (Uncal - Data|alc-enhanced_916_20_09_2022_[32 DMA]biphenyl-B(OH)2 - HERM)

	Reten. Time [min]	Area [CTS(RLU)/s.s]	Height [CTS(RLU)/s]	Area [%]
1	4,417	11166,000	2239,775	100,0
	Total	11166,000	2239,775	100,0

Figure S7: HPLC traces of radiolabeling of **1** in *n*BuOH/DMA using $Co(Py)_4(ClO_4)_2 \cdot 3H_2O$ as mediator and 1 mg Et_4NOTf for the elution of $[^{18}F]F^-$. Blue trace: UV, $\lambda = 254$ nm; red trace: radioactivity. Abbreviation: p.-c.i – post-column injection.

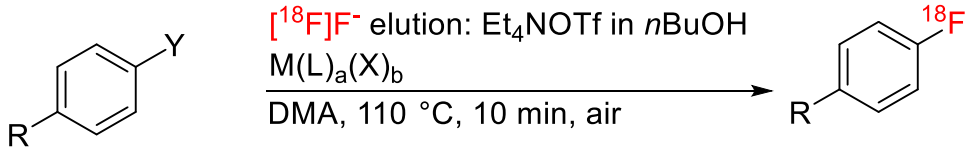

Y = $B(OH)_2$ R = Ph (**1**), Ac (**3**)
Bpin R = Ph (**2**), Ac (**4**)

R = Ph 4-[^{18}F]F-Ph-Ph
R = Ac 4-[^{18}F]F-Ac-Ph

Table S17: Dependency of RCCs in *n*BuOH/DMA on the applied nickel, cobalt or copper mediator.

				RCC [%]			
Entry	**M**	**L**	**X**	**1**	**2**	**3**	**4**
1	Ni	Py	OTf	0	–	–	–
2	Co	Py	ClO_4	0	–	–	–
3	Cu	Py	OTf	30 ± 6	21 ± 8	15 ± 2	8 ± 2
4			ClO_4	34 ± 4	22 ± 4	17 ± 1	11 ± 3
5			ClO_3	13 ± 5	–	–	–
6			OTs	4 ± 1	3 ± 2	2 ± 0.4	–
7			OMs	0	–	–	–
8			Cl	0	–	–	–
9			SO_4	0	–	–	–
10			OAc	0	–	–	–
11			Br	0	–	–	–
12		2-MeOPy	OTf	2 ± 1	1 ± 0.4	0	0
13			ClO_4	4 ± 1	3 ± 1	0	0
14		3-MeOPy	OTf	20 ± 4	10 ± 2	5 ± 2	3 ± 1
15			ClO_4	30 ± 2	27 ± 5	13 ± 4	7 ± 1
16		4-MeOPy	OTf	46 ± 3	50 ± 4	27 ± 9	16 ± 3
17			ClO_4	36 ± 3	30 ± 6	34 ± 2	29 ± 5
18		2,4-$(MeO)_2$Py	OTf	0	0	3 ± 1	2 ± 1
19			ClO_4	0	0	3 ± 1	2 ± 1
20		4-PhPy	OTf	29 ± 2	21 ± 2	12 ± 1	7 ± 1
21			ClO_4	39 ± 10	35 ± 4	30 ± 4	19 ± 1
22		3,4-Me_2Py	OTf	58 ± 8	52 ± 7	26 ± 1	18 ± 2
23			ClO_4	26 ± 7	54 ± 4	19 ± 5	26 ± 1
24		4-F_3Cpy	OTf	2 ± 2	1 ± 0.2	0	0
25		Pz	OTf	6 ± 2	5 ± 0.3	0	0
26		4,4'-BiPy	OTf	1 ± 1	3 ± 0.4	0	0
27			ClO_4	14 ± 2	13 ± 4	6 ± 2	3 ± 1
28		Triaz	OTf	10 ± 2	9 ± 1	6 ± 1	2 ± 0.3
29		Pyr	OTf	4 ± 1	2 ± 0.3	0	1 ± 1
30		Quin	OTf	8 ± 3	2 ± 1	0	0

Entry	M	L	X	RCC [%] 1	2	3	4
31			ClO_4	3 ± 1	5 ± 1	0	1 ± 1
32		Isoq	OTf	29 ± 5	19 ± 5	12 ± 2	5 ± 2
33			ClO_4	48 ± 3	26 ± 8	16 ± 3	15 ± 3
34		Impdz	OTf	17 ± 3	13 ± 1	5 ± 1	7 ± 1
35			ClO_4	30 ± 5	39 ± 5	44 ± 5	26 ± 4
36			ClO_3	13 ± 6	–	–	–
37			OMs	0	0	0	0
38			OTs	36 ± 5	5 ± 3	1 ± 1	4 ± 1

Conditions: i) elution of [^{18}F]F$^-$ (10–50 MBq) with Et_4NOTf (1 mg, 4 µmol) in *n*BuOH (400 µL) into a solution of substrates **1**–**4** (10 µmol, 1 eq.) and $M(L)_a(X)_b$ (10 µmol, 1 eq.) in DMA (800 µL); ii) 110 °C for 10 min under air; iii) addition of H_2O (1 mL). Radiochemical conversions (RCCs) were determined by HPLC as described in the supporting information and are provided in the following format: mean RCC ± standard deviation (%). All experiments were carried out at least in triplicate. Py – pyridine, 2-MeOPy – 2-methoxypyridine, 3-MeOPy – 3-methoxypyridine, 4-MeOPy – 4-methoxypyridine, 2,4-$(MeO)_2$Py – 2,4-dimethoxypyridine, 4,4'-BiPy – 4,4'-bipyridine, 4-PhPy – 4-phenylpyridine, 3,4-Me_2Py – 3,4-lutidine, 4-F_3CPy – 4-trifluoromethylpyridine, Pz – pyrazine, Triaz – *N*-methyl-1,2,4-triazole, Pyr – *N*-methylpyrazole, Quin – quinoline, Isoq – isoquinoline, Impdz – imidazo(1,2-b)pyridazine.

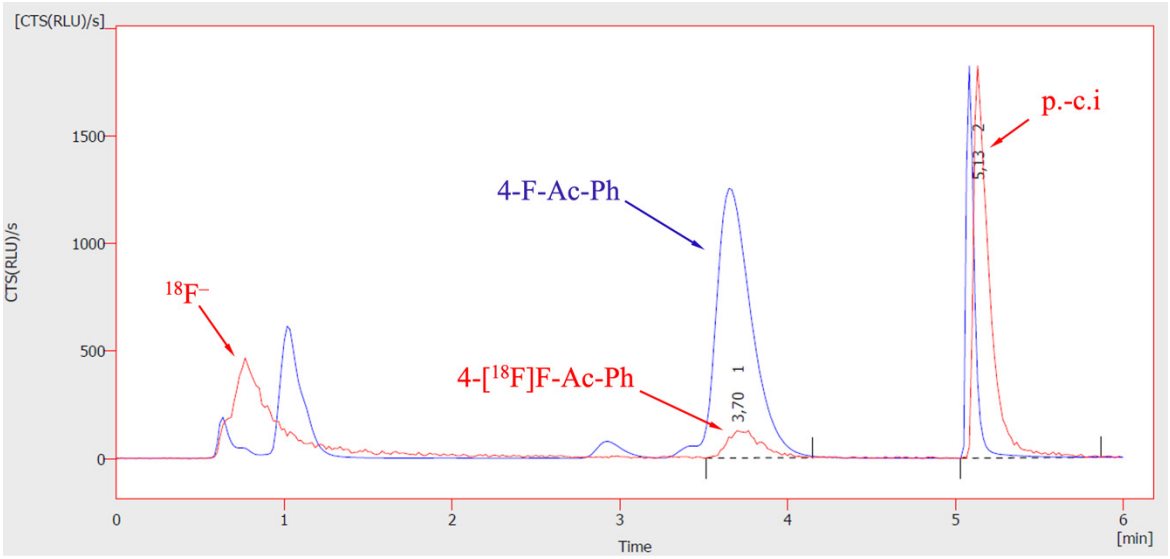

Result Table (Uncal - Data|alc-enhanced_824_28_06_2022_[1 DMA]4-acetylphenyl_B(OH)2_spike - HERM)

	Reten. Time [min]	Area [CTS(RLU)/s.s]	Height [CTS(RLU)/s]	Area [%]
1	3,700	1816,000	126,711	13,3
2	5,133	11853,000	1823,520	86,7
	Total	13669,000	1950,231	100,0

Figure S8: HPLC traces of crude 4-[^{18}F]F-Ac-Ph (spiked with 4-F-Ac-Ph) prepared in *n*BuOH/DMA from **3** using $Cu(Py)_4(OTf)_2$ as mediator. Blue trace: UV, λ = 254 nm; red trace: radioactivity. Abbreviation: p.-c.i – post-column injection.

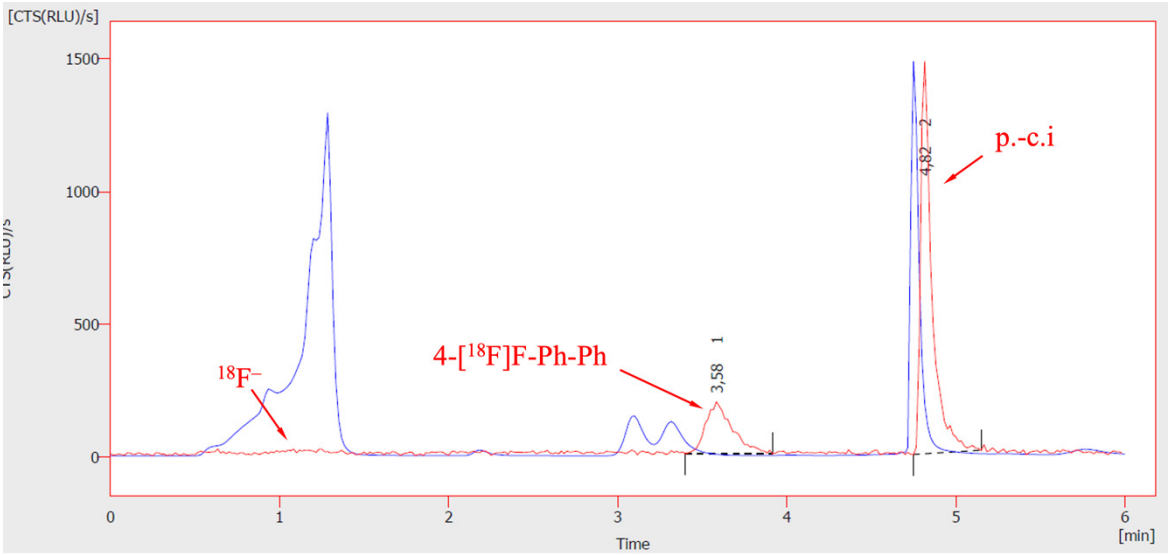

Result Table (Uncal - Data|alc-enhanced_400_19_01_2022_[3 DMA]_biphenyl_b(OH)2 - HERM)

	Reten. Time [min]	Area [CTS(RLU)/s.s]	Height [CTS(RLU)/s]	Area [%]
1	3,583	2122,000	196,000	23,5
2	4,817	6916,000	1478,333	76,5
	Total	9038,000	1674,333	100,0

Figure S9: HPLC traces of crude 4-[^{18}F]F-Ph-Ph prepared in *n*BuOH/DMA from **1** using Cu(4-PhPy)$_4$(OTf)$_2$ as mediator. Blue trace: UV, λ = 254 nm; red: radioactivity. Abbreviation: p.-c.i – post-column injection.

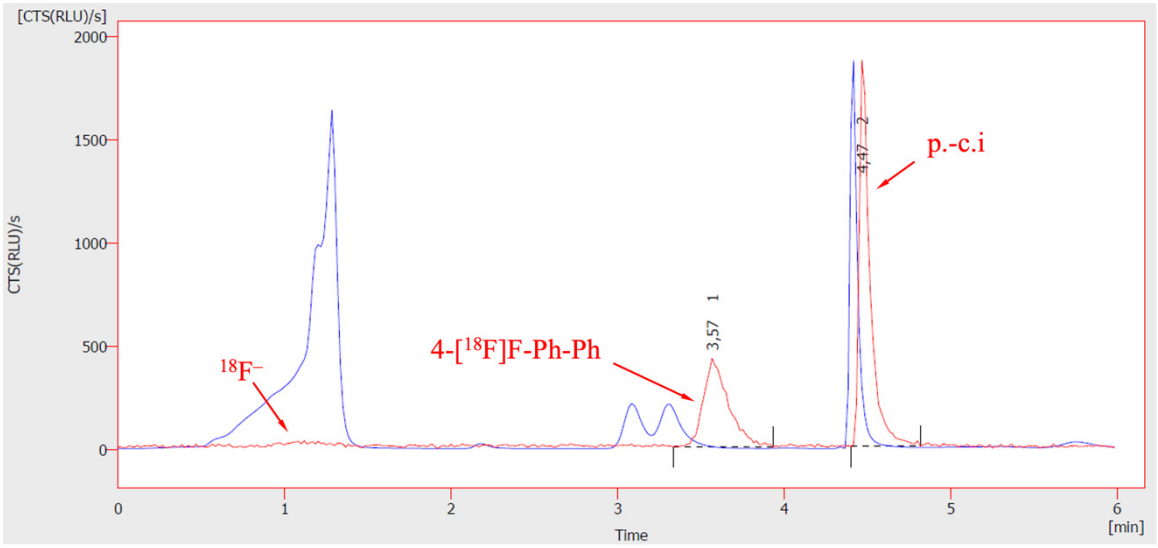

Result Table (Uncal - Data|alc-enhanced_403_19_01_2022_[4 DMA]_biphenyl_b(OH)2 - HERM)

	Reten. Time [min]	Area [CTS(RLU)/s.s]	Height [CTS(RLU)/s]	Area [%]
1	3,567	4500,000	428,389	34,6
2	4,467	8494,000	1866,680	65,4
	Total	12994,000	2295,069	100,0

Figure S10: HPLC traces of crude 4-[^{18}F]F-Ph-Ph prepared in *n*BuOH//DMA from **1** using Cu(4-PhPy)$_4$(ClO$_4$)$_2$ as mediator. Blue trace: UV, λ = 254 nm; red trace: radioactivity. Abbreviation: p.-c.i – post-column injection.

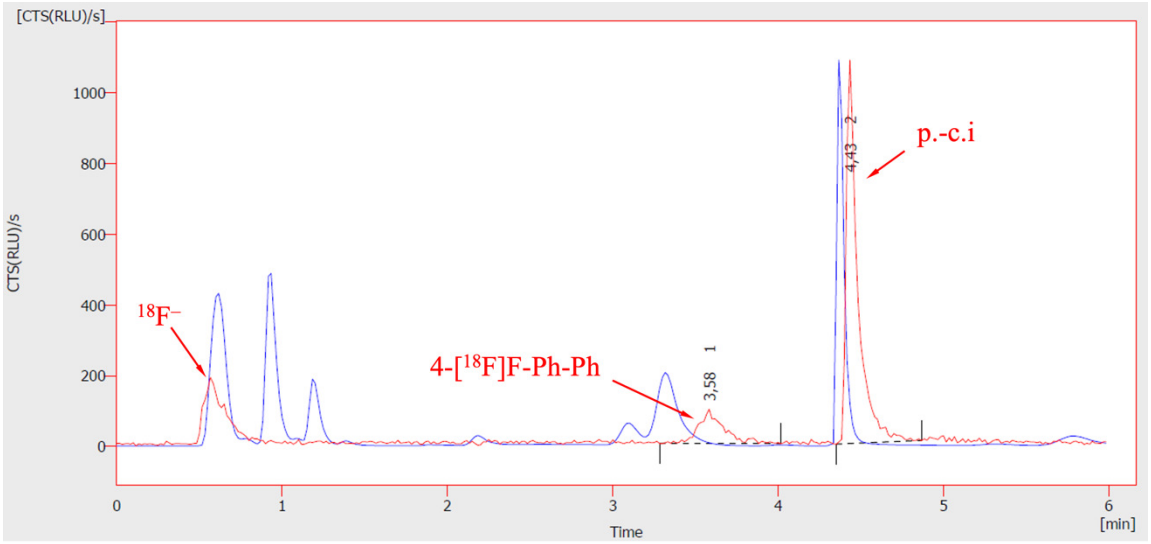

Result Table (Uncal - Data\alc-enhanced_405_19_01_2022_[17 DMA]_biphenyl_b(OH)2 - HERM)

	Reten. Time [min]	Area [CTS(RLU)/s.s]	Height [CTS(RLU)/s]	Area [%]
1	3,583	1027,000	97,409	16,2
2	4,433	5318,000	1085,387	83,8
	Total	6345,000	1182,796	100,0

Figure S11: HPLC traces of crude 4-[^{18}F]F-Ph-Ph prepared in *n*BuOH/DMA from **1** using Cu(Impdz)$_4$(OTf)$_2$ as mediator. Blue trace: UV, λ = 254 nm; red trace: radioactivity. Blue: UV chromatogram, λ = 254 nm; red: radio-chromatogram. Abbreviation: p.-c.i – post-column injection.

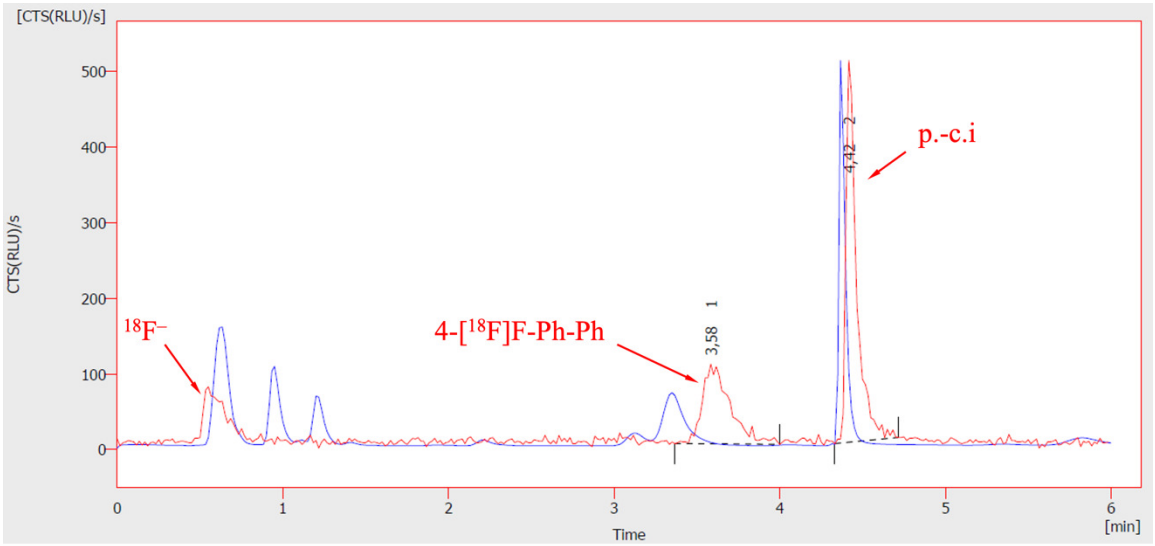

Result Table (Uncal - Data\alc-enhanced_410_19_01_2022_[18 DMA]_biphenyl_b(OH)2 - HERM)

	Reten. Time [min]	Area [CTS(RLU)/s.s]	Height [CTS(RLU)/s]	Area [%]
1	3,583	1225,000	105,342	34,9
2	4,417	2287,000	505,261	65,1
	Total	3512,000	610,603	100,0

Figure S12: HPLC traces of crude 4-[^{18}F]F-Ph-Ph prepared in *n*BuOH/DMA from **1** using Cu(Impdz)$_4$(ClO$_4$)$_2$ as mediator. Blue trace: UV, λ = 254 nm; red trace: radioactivity. Abbreviation: p.-c.i – post-column injection.

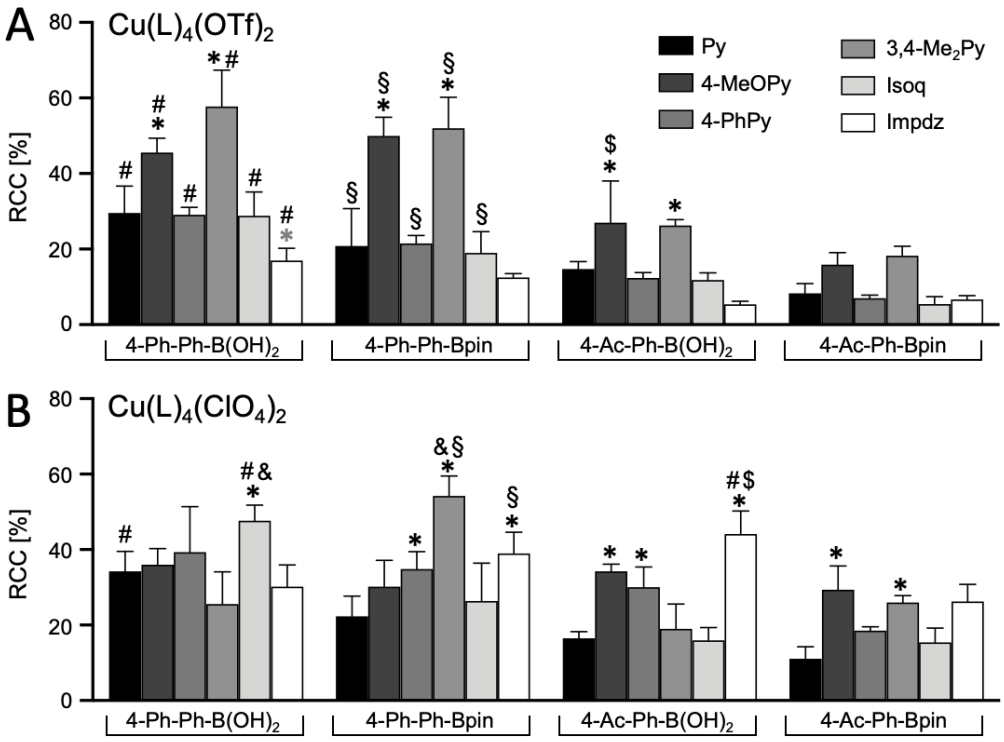

Figure S13: Dependency of RCCs on the precursor and applied Cu complex in *n*BuOH/DMA. Significant differences are indicated by the following symbols: *: $p<0.05$ for comparison of the different ligands to Py; &: $p<0.05$ for 4-Ph-Ph-B(OH)$_2$ vs. 4-Ph-Ph-Bpin; #: $p<0.05$ for 4-Ph-Ph-B(OH)$_2$ vs. 4-Ac-Ph-B(OH)$_2$; §: $p<0.05$ for 4-Ph-Ph-Bpin vs. 4-Ac-Ph-Bpin; $: $p<0.05$ for 4-Ac-Ph-B(OH)$_2$ vs. 4-Ac-Ph-Bpin (two-way ANOVA).

Statistical data corresponding to Figure S13:

Table S18: RCCs (mean values ± standard deviation in %) for radiosyntheses with different Cu mediators, Cu(L)$_4$(OTf)$_2$, in *n*BuOH/DMA. 2-way ANOVA: Main effect of factor "**ligand**": $F(5,48)=60.23$, $p<0.0001$. Dunnett's multiple comparisons test with Cu(Py)$_4$(OTf)$_2$ as control with n=3 per group.

	4-Ph-Ph-B(OH)$_2$	4-Ph-Ph-Bpin	4-Ac-Ph-B(OH)$_2$	4-Ac-Ph-Bpin
Py	29.55 ± 7.14	20.82 ± 9.91	14.75 ± 1.93	8.29 ± 2.55
4-MeOPy	45.53 ± 3.81 p=0.0014*	49.96 ± 4.93 p<0.0001*	27.01 ± 11.05 p=0.0187*	15.88 ± 3.17 p=0.2415
4-PhPy	29.09 ± 1.98 p=0.9999	21.48 ± 2.11 p=0.9997	12.37 ± 1.42 p=0.9669	7.00 ± 0.85 p=0.9979
3,4-Me$_2$Py	57.76 ± 9.63 p<0.0001*	51.96 ± 8.26 p<0.0001*	26.23 ± 1.57 p=0.0305*	18.24 ± 2.52 p=0.0744
Isoq	28.80 ± 6.35 p=0.9997	19.00 ± 5.63 p=0.9896	11.80 ± 1.91 p=0.9240	5.43 ± 1.96 p=0.9329
Impdz	16.98 ± 3.27 p=0.0153*	12.51 ± 1.02 p=0.1729	5.37 ± 0.80 p=0.1012	6.70 ± 0.96 p=0.9944

green: significantly higher RCCs compared to Cu(Py)$_4$(OTf)$_2$; red: significantly lower RCCs compared to Cu(Py)$_4$(OTf)$_2$.

Table S19: RCCs (mean values ± standard deviation in %) for radiosyntheses with different Cu mediators, $Cu(L)_4(OTf)_2$, in *n*BuOH/DMA. Main effect of factor "**precursor**": F(3,48)=91.01, p<0.0001. Tukey's multiple comparisons test, n=3 per group.

	4-Ph-Ph-$B(OH)_2$ vs. 4-Ph-Ph-Bpin	4-Ph-Ph-$B(OH)_2$ vs. 4-Ac-Ph-$B(OH)_2$	4-Ph-Ph-Bpin vs. 4-Ac-Ph-Bpin	4-Ac-Ph-$B(OH)_2$ vs. 4-Ac-Ph-Bpin
Py	29.55 ± 7.14	29.55 ± 7.14	20.82 ± 9.91	14.75 ± 1.93
	20.82 ± 9.91	14.75 ± 1.93	8.29 ± 2.55	8.29 ± 2.55
	p=0.1582	p=0.0039#	p=0.0183§	p=0.4007
4-MeOPy	45.53 ± 3.81	45.53 ± 3.81	49.96 ± 4.93	27.01 ± 11.05
	49.96 ± 4.93	27.01 ± 11.05	15.88 ± 3.17	15.88 ± 3.17
	p=0.7029	p=0.0002#	p<0.0001§	p=0.0438$
4-PhPy	29.09 ± 1.98	29.09 ± 1.98	21.48 ± 2.11	12.37 ± 1.42
	21.48 ± 2.11	12.37 ± 1.42	7.00 ± 0.85	7.00 ± 0.85
	p=0.2594	p=0.0009#	p=0.0049§	p=0.5612
3,4-Me_2Py	57.76 ± 9.63	57.76 ± 9.63	51.96 ± 8.26	26.23 ± 1.57
	51.96 ± 8.26	26.23 ± 1.57	18.24 ± 2.52	18.24 ± 2.52
	p=0.4959	p<0.0001#	p<0.0001§	p=0.2209
Isoq	28.80 ± 6.35	28.80 ± 6.35	19.00 ± 5.63	11.80 ± 1.91
	19.00 ± 5.63	11.80 ± 1.91	5.43 ± 1.96	5.43 ± 1.96
	p=0.0922	p=0.0008#	p=0.0093§	p=0.4141
Impdz	16.98 ± 3.27	16.98 ± 3.27	12.51 ± 1.02	5.37 ± 0.80
	12.51 ± 1.02	5.37 ± 0.80	6.70 ± 0.96	6.70 ± 0.96
	p=0.6956	p=0.0327#	p=0.4949	p=0.9879

red: significantly lower RCCs for Bpin compared to $B(OH)_2$ precursors; green: significantly higher RCCs for 4-Ph-Ph compared to 4-Ac-Ph precursors.

Table S20: RCCs (mean values ± standard deviation in %) for radiosyntheses with different Cu mediators, $Cu(L)_4(ClO_4)_2$, in *n*BuOH/DMA. 2-way ANOVA: Main effect of factor "**ligand**": $F(5,48)=9.02$, $p<0.0001$. Dunnett's multiple comparisons test with $Cu(Py)_4(ClO_4)_2$ as control with n=3 per group.

	4-Ph-Ph-B(OH)$_2$	4-Ph-Ph-Bpin	4-Ac-Ph-B(OH)$_2$	4-Ac-Ph-Bpin
Py	34.21 ± 5.32	22.33 ± 5.31	16.51 ± 1.73	11.08 ± 3.17
4-MeOPy	36.03 ± 4.24 p=0.9944	30.17 ± 6.96 p=0.3291	34.23 ± 1.92 p=0.0020*	29.33 ± 6.35 p=0.0014*
4-PhPy	39.32 ± 12.07 p=0.7135	34.88 ± 4.59 p=0.0414*	30.04 ± 5.39 p=0.0244*	18.55 ± 1.09 p=0.3736
3,4-Me$_2$Py	25.57 ± 8.53 p=0.2446	54.26 ± 5.24 p<0.0001*	19.00 ± 6.56 p=0.9772	25.97 ± 1.82 p=0.0114*
Isoq	47.62 ± 4.19 p=0.0262*	26.37 ± 10.07 p=0.8575	15.97 ± 3.35 p=0.9999	15.43 ± 3.77 p=0.8187
Impdz	30.21 ± 5.73 p=0.8613	39.00 ± 5.60 p=0.0039*	44.15 ± 6.10 p<0.0001*	26.24 ± 4.58 p=0.0097*

green: significantly higher RCCs compared to $Cu(Py)_4(ClO_4)_2$; red: significantly lower RCC compared to $Cu(Py)_4(ClO_4)_2$.

Table S21: RCCs (mean values ± standard deviation in %) for radiosyntheses with different Cu mediators, $Cu(L)_4(ClO_4)_2$, in *n*BuOH/DMA. 2-way ANOVA: Main effect of factor "**precursor**": F(3,48)=25.45, p<0.0001. Tukey's multiple comparisons test, n=3 per group.

	4-Ph-Ph-$B(OH)_2$ vs. 4-Ph-Ph-Bpin	4-Ph-Ph-$B(OH)_2$ vs. 4-Ac-Ph-$B(OH)_2$	4-Ph-Ph-Bpin vs. 4-Ac-Ph-Bpin	4-Ac-Ph-$B(OH)_2$ vs. 4-Ac-Ph-Bpin
Py	34.21 ± 5.32 22.33 ± 5.31 p=0.0669	34.21 ± 5.32 16.51 ± 1.73 p=0.0024[#]	22.33 ± 5.31 11.08 ± 3.17 p=0.0904	16.51 ± 1.73 11.08 ± 3.17 p=0.6556
4-MeOPy	36.03 ± 4.24 30.17 ± 6.96 p=0.5972	36.03 ± 4.24 34.23 ± 1.92 p=0.9805	30.17 ± 6.96 29.33 ± 6.35 p=0.9980	34.23 ± 1.92 29.33 ± 6.35 p=0.7235
4-PhPy	39.32 ± 12.07 34.88 ± 4.59 p=0.7797	39.32 ± 12.07 30.04 ± 5.39 p=0.2094	34.88 ± 4.59 18.55 ± 1.09 p=0.0056[§]	30.04 ± 5.39 18.55 ± 1.09 p=0.0807
3,4-Me_2Py	25.57 ± 8.53 54.26 ± 5.24 p<0.0001[&]	25.57 ± 8.53 19.00 ± 6.56 p=0.5045	54.26 ± 5.24 25.97 ± 1.82 p<0.0001[§]	19.00 ± 6.56 25.97 ± 1.82 p=0.4531
Isoq	47.62 ± 4.19 26.37 ± 10.07 p=0.0002[&]	47.62 ± 4.19 15.97 ± 3.35 p<0.0001[#]	26.37 ± 10.07 15.43 ± 3.77 p=0.1046	15.97 ± 3.35 15.43 ± 3.77 p=0.9995
Impdz	30.21 ± 5.73 39.00 ± 5.60 p=0.2517	30.21 ± 5.73 44.15 ± 6.10 p=0.0229[#]	39.00 ± 5.60 26.24 ± 4.58 p=0.0430[§]	44.15 ± 6.10 26.24 ± 4.58 p=0.0021[$]

red: significantly lower RCCs for Bpin compared to $B(OH)_2$ precursors; blue: significantly higher RCCs for Bpin compared to $B(OH)_2$ precursors; green: significantly higher RCCs for 4-Ph-Ph compared to 4-Ac-Ph substituted precursors; pink: significantly lower RCCs for 4-Ph-Ph compared to 4-Ac-Ph precursors.

Statistical data corresponding to Figure 2 in the main article:

Table S22: RCCs (mean values ± standard deviation in %) for radiolabeling of 4-Ph-Ph-$B(OH)_2$ using different $Cu(Py)_4X_2$ complexes in *n*BuOH/DMA. 1-way ANOVA: Main effect of factor "**counter ion**": F(4,10)=29.30, p<0.0001. Tukey's multiple comparisons test, n=3 per group.

	RCC (%)	comparison	
$Cu(Py)_4(OTf)_2$	29.55 ± 7.14	vs. $Cu(Py)_4(ClO_4)_2$	p=0.7659
		vs. $Cu(Py)_4(ClO_3)_2$	p=0.0108*
		vs. $Cu(Py)_4(OTs)_2$	p=0.0006*
		vs. $Cu(Py)_4(OMs)_2$	p=0.0002*
$Cu(Py)_4(ClO_4)_2$	34.21 ± 5.32	vs. $Cu(Py)_4(ClO_3)_2$	p=0.0020*
		vs. $Cu(Py)_4(OTs)_2$	p=0.0001*
		vs. $Cu(Py)_4(OMs)_2$	p<0.0001*
$Cu(Py)_4(ClO_3)_2$	12.50 ± 6.05	vs. $Cu(Py)_4(OTs)_2$	p=0.2824
		vs. $Cu(Py)_4(OMs)_2$	p=0.0628
$Cu(Py)_4(OTs)_2$	4.06 ± 1.65	vs. $Cu(Py)_4(OMs)_2$	p=0.8402
$Cu(Py)_4(OMs)_2$	0.00 ± 0.00		

Table S23: RCCs (mean values ± standard deviation in %) for radiolabeling of 4-Ph-Ph-$B(OH)_2$ in *n*BuOH/DMA using different $Cu(Impdz)_4X_2$ complexes as mediators. 1-way ANOVA: Main effect of factor "**counter ion**": F(4,10)=23.64, p<0.0001. Tukey's multiple comparisons test, n=3 per group.

	RCC (%)	comparison	
$Cu(Impdz)_4(OTf)_2$	16.98 ± 3.27	vs. $Cu(Impdz)_4(ClO_4)_2$	p=0.0586
		vs. $Cu(Impdz)_4(ClO_3)_2$	p=0.8865
		vs. $Cu(Impdz)_4(OTs)_2$	p=0.0069*
		vs. $Cu(Impdz)_4(OMs)_2$	p=0.0145*
$Cu(Impdz)_4(ClO_4)_2$	30.21 ± 5.73	vs. $Cu(Impdz)_4(ClO_3)_2$	p=0.0144*
		vs. $Cu(Impdz)_4(OTs)_2$	p=0.6407
		vs. $Cu(Impdz)_4(OMs)_2$	p=0.0002*
$Cu(Impdz)_4(ClO_3)_2$	13.21 ± 7.21	vs. $Cu(Impdz)_4(OTs)_2$	p=0.0019*
		vs. $Cu(Impdz)_4(OMs)_2$	p=0.0590
$Cu(Impdz)_4(OTs)_2$	36.02 ± 5.80	vs. $Cu(Impdz)_4(OMs)_2$	p<0.0001*
$Cu(Impdz)_4(OMs)_2$	0.00 ± 0.00		

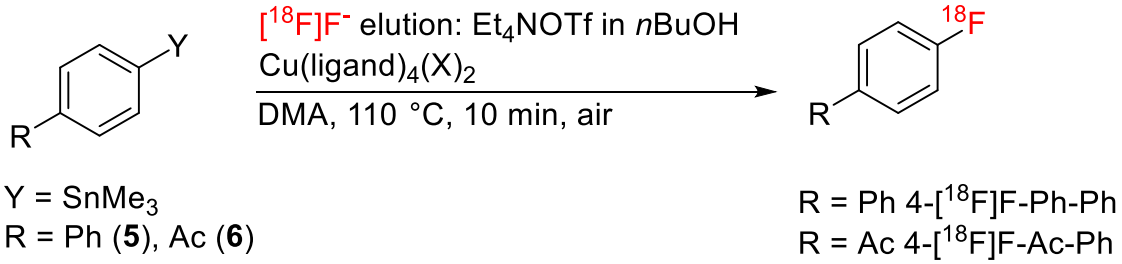

Y = $SnMe_3$
R = Ph (**5**), Ac (**6**)

R = Ph 4-[^{18}F]F-Ph-Ph
R = Ac 4-[^{18}F]F-Ac-Ph

Table S24: Dependency of RCCs for radiolabeling of 4-Ph- and 4-Ac-Ph-$SnMe_3$ in *n*BuOH/DMA on the applied copper mediators.

			RCC [%]	
Entry	**Ligand**	**X**	**5**	**6**
1	Py	OTf	14 ± 2	2 ± 1
2		ClO_4	10 ± 2	3 ± 1
3	3-MeOPy	OTf	4 ± 1	5 ± 1
4		ClO_4	5 ± 1	7 ± 2
5	4-MeOPy	OTf	4 ± 2	13 ± 6
6		ClO_4	5 ± 2	12 ± 2
7	4-PhPy	OTf	9 ± 1	3 ± 0.3
8		ClO_4	14 ± 5	9 ± 1
9	3,4-Me_2Py	OTf	10 ± 4	11 ± 2
10		ClO_4	8 ± 3	5 ± 1
11	Isoq	OTf	7 ± 2	7 ± 1
12		ClO_4	20 ± 4	9 ± 2
13	Impdz	OTf	7 ± 3	13 ± 3
14		ClO_4	20 ± 4	23 ± 2

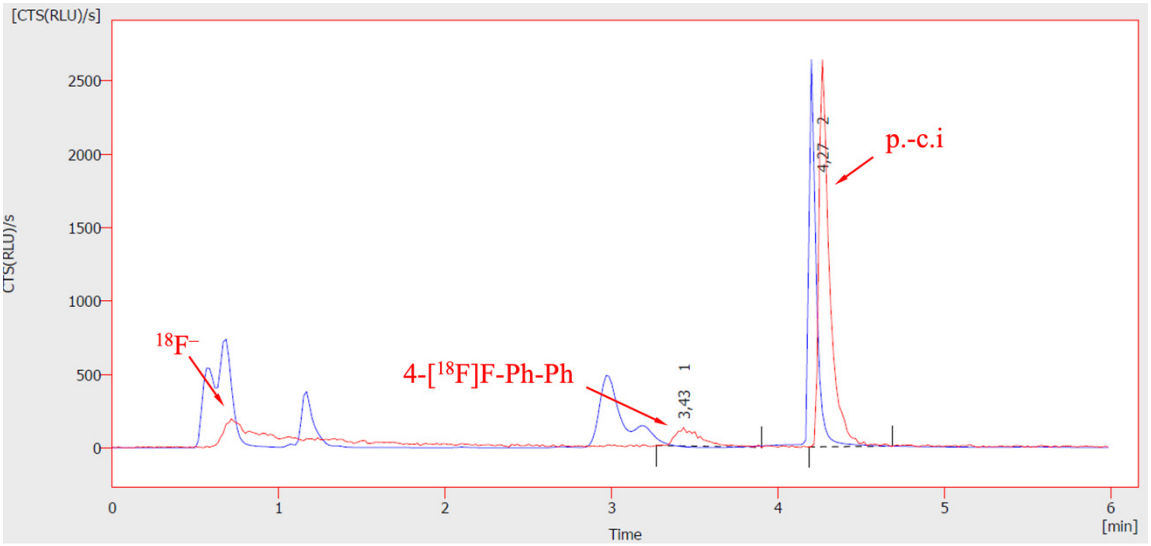

Result Table (Uncal - Data\alc-enhanced_637_29_03_2022_[1 DMA]biphenyl-SnMe3 - HERM)

	Reten. Time [min]	Area [CTS(RLU)/s.s]	Height [CTS(RLU)/s]	Area [%]
1	3,433	1339,000	125,421	10,2
2	4,267	11813,000	2636,000	89,8
	Total	13152,000	2761,421	100,0

Figure S14: HPLC traces of crude 4-[^{18}F]F-Ph-Ph prepared in *n*BuOH/DMA from **5** using $Cu(Py)_4(OTf)_2$ as mediator. Blue trace: UV, λ = 254 nm; red trace: radioactivity. Abbreviation: p.-c.i – post-column injection.

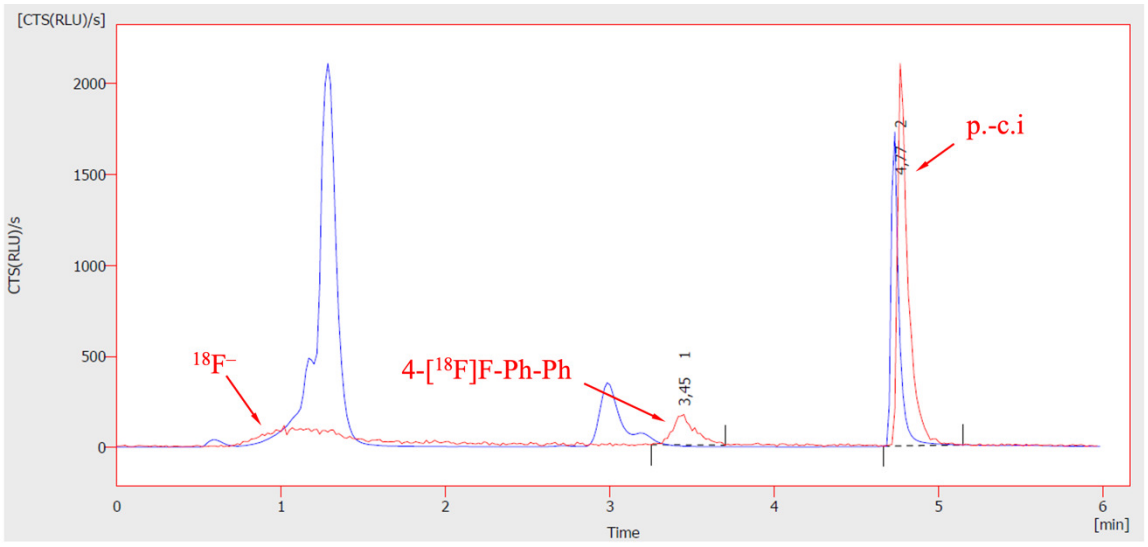

Result Table (Uncal - Data\alc-enhanced_640_29_03_2022_[4 DMA]biphenyl-SnMe3 - HERM)

	Reten. Time [min]	Area [CTS(RLU)/s.s]	Height [CTS(RLU)/s]	Area [%]
1	3,450	1599,000	166,889	14,6
2	4,767	9387,500	2104,552	85,4
	Total	10986,500	2271,441	100,0

Figure S15: HPLC traces of crude 4-[^{18}F]F-Ph-Ph prepared in *n*BuOH/DMA from **5** using $Cu(4\text{-}PhPy)_4(ClO_4)_2$ as mediator. Blue trace: UV, λ = 254 nm; red trace: radioactivity. Abbreviation: p.-c.i – post-column injection.

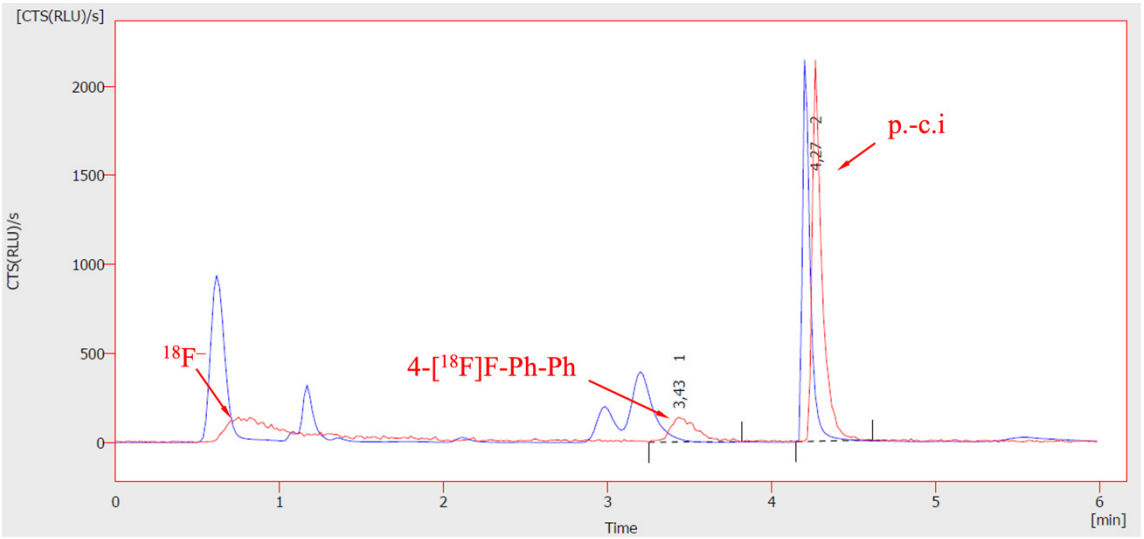

Result Table (Uncal - Data\alc-enhanced_642_29_03_2022_[18 DMA]biphenyl-SnMe3 - HERM)

	Reten. Time [min]	Area [CTS(RLU)/s.s]	Height [CTS(RLU)/s]	Area [%]
1	3,433	1614,000	139,029	15,5
2	4,267	8798,000	2141,500	84,5
	Total	10412,000	2280,529	100,0

Figure S16: HPLC traces of crude 4-[^{18}F]F-Ph-Ph prepared in *n*BuOH/DMA from **5** using Cu(Impdz)$_4$(ClO$_4$) as mediator. Blue trace: UV, λ = 254 nm; red trace: radioactivity. Abbreviation: p.-c.i – post-column injection.

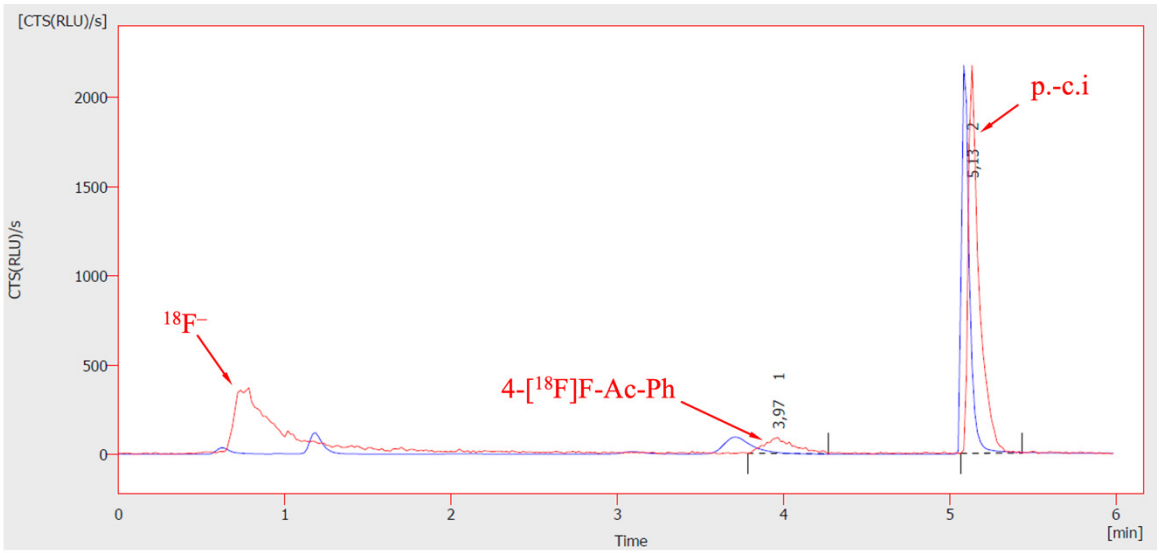

Result Table (Uncal - Data\alc-enhanced_644_29_03_2022_[4 DMA]4-acetylphenyl-SnMe3 - HERM)

	Reten. Time [min]	Area [CTS(RLU)/s.s]	Height [CTS(RLU)/s]	Area [%]
1	3,967	1098,500	89,138	10,1
2	5,133	9748,000	2175,636	89,9
	Total	10846,500	2264,774	100,0

Figure S17: HPLC traces of crude 4-[^{18}F]F-Ac-Ph prepared in *n*BuOH/DMA from **6** using Cu(4-PhPy)$_4$(ClO$_4$)$_2$ as mediator. Blue trace: UV, λ = 254 nm; red trace: radioactivity. Abbreviation: p.-c.i – post-column injection.

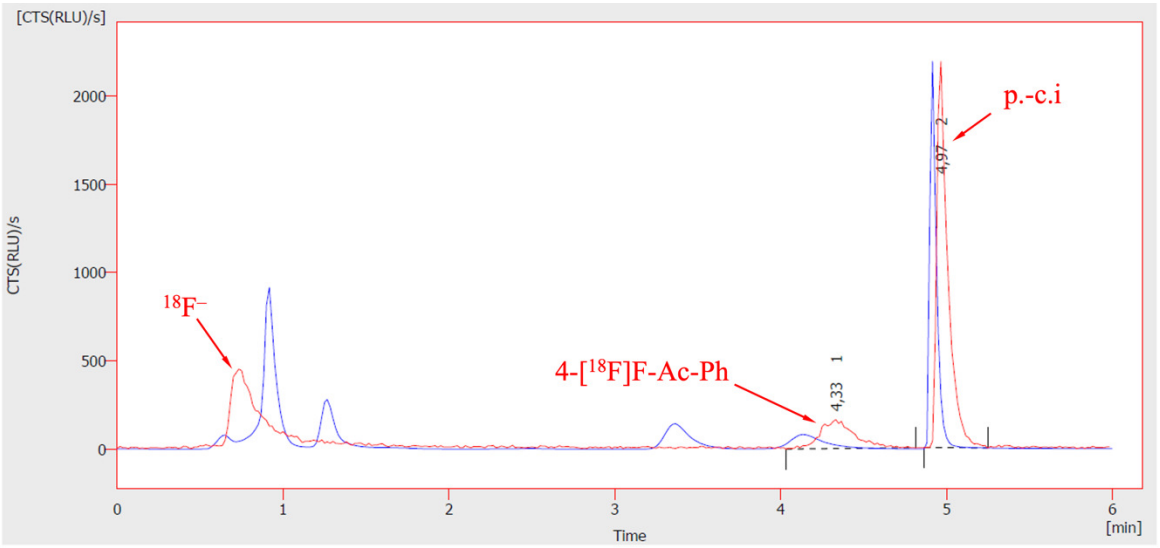

Result Table (Uncal - Data|alc-enhanced_657_30_03_2022_[18 DMA]4-acetylphenyl-SnMe3 - HERM)

	Reten. Time [min]	Area [CTS(RLU)/s.s]	Height [CTS(RLU)/s]	Area [%]
1	4,333	2391,500	164,319	19,1
2	4,967	10157,500	2187,261	80,9
	Total	12549,000	2351,580	100,0

Figure S18: HPLC traces of crude 4-[^{18}F]F-Ac-Ph prepared in *n*BuOH/DMA from **6** using $Cu(Impdz)_4(ClO_4)_2$ as mediator. Blue trace: UV, λ = 254 nm; red trace: radioactivity. Abbreviation: p.-c.i – post-column injection.

Screening of aprotic co-solvents

Radiosyntheses were performed according to GP5 with different copper(II) complexes and **1**–**4** in PC or DMI (n=3). RCCs were determined by radio-HPLC as described above. Representative radio-HPLC chromatograms of radiolabeled products are shown in Figure **S19** and Figure **S20**.

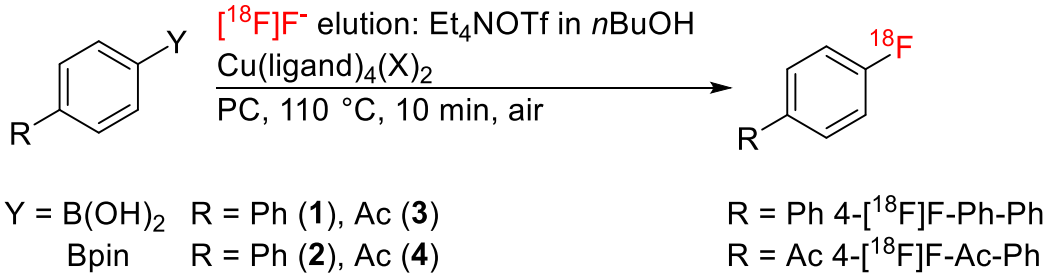

Table S25: Dependency of RCCs in *n*BuOH/PC on the applied copper mediator.

			RCC (%)			
Entry	**Ligand**	**X**	**1**	**2**	**3**	**4**
1	Py	OTf	46 ± 5	45 ± 5	66 ± 5	30 ± 7
2		ClO_4	99 ± 1	40 ± 7	76 ± 1	55 ± 9
3	2-MeOPy	OTf	17 ± 8	38 ± 8	16 ± 2	8 ± 3
4		ClO_4	49 ± 16	43 ± 8	39 ± 6	6 ± 1
5	3-MeOPy	OTf	90 ± 1	57 ± 4	72 ± 19	70 ± 16
6		ClO_4	67 ± 10	45 ± 10	73 ± 14	48 ± 15
7	4-MeOPy	OTf	27 ± 5	32 ± 1	25 ± 2	18 ± 2
8		ClO_4	57 ± 15	49 ± 12	50 ± 3	31 ± 6
9	4-PhPy	OTf	86 ± 9	73 ± 5	89 ± 4	68 ± 6
10		ClO_4	71 ± 4	80 ± 4	86 ± 5	80 ± 4
11	3,4-Me_2Py	OTf	68 ± 4	25 ± 3	53 ± 1	32 ± 8
12		ClO_4	53 ± 5	22 ± 6	71 ± 4	37 ± 8
13	Quin	OTf	20 ± 4	11 ± 2	3 ± 0.4	7 ± 3
14		ClO_4	4 ± 6	8 ± 2	3 ± 0.4	9 ± 4
15	Isoq	OTf	86 ± 2	52 ± 6	75 ± 6	51 ± 7
16		ClO_4	83 ± 6	53 ± 4	99 ± 1	67 ± 21
17	Impdz	OTf	41 ± 13	10 ± 1	29 ± 2	14 ± 3
18		ClO_4	55 ± 5	35 ± 1	78 ± 2	62 ± 6

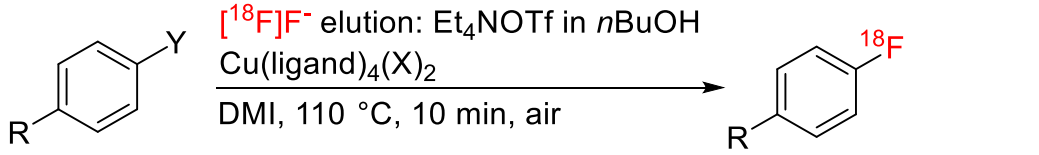

Y = $B(OH)_2$ R = Ph (**1**), Ac (**3**)
Bpin R = Ph (**2**), Ac (**4**)

R = Ph 4-[^{18}F]F-Ph-Ph
R = Ac 4-[^{18}F]F-Ac-Ph

Table S26: Dependency of RCCs in *n*BuOH/DMI on the applied copper mediator.

			RCC (%)			
Entry	**Ligand**	**X**	**1**	**2**	**3**	**4**
1	Py	OTf	93 ± 9	94 ± 7	45 ± 5	30 ± 7
2		ClO_4	82 ± 5	82 ± 5	56 ± 10	47 ± 10
3	2-MeOPy	OTf	9 ± 1	5 ± 0.4	2 ± 0.2	0
4		ClO_4	32 ± 8	13 ± 1	5 ± 2	1 ± 2
5	3-MeOPy	OTf	87 ± 2	71 ± 4	51 ± 8	35 ± 2
6		ClO_4	98 ± 1	78 ± 7	53 ± 6	39 ± 3
7	4-MeOPy	OTf	67 ± 1	69 ± 4	67 ± 6	51 ± 4
8		ClO_4	91 ± 3	86 ± 4	77 ± 4	64 ± 5
9	4-PhPy	OTf	86 ± 0.4	81 ± 4	57 ± 5	39 ± 6
10		ClO_4	98 ± 2	95 ± 5	86 ± 8	67 ± 3
11	3,4-Me_2Py	OTf	91 ± 1	93 ± 2	83 ± 6	81 ± 6
12		ClO_4	92 ± 3	89 ± 3	93 ± 2	84 ± 5
13	Quin	OTf	17 ± 3	12 ± 3	8 ± 1	7 ± 1
14		ClO_4	20 ± 2	23 ± 5	6 ± 1	7 ± 2
15	Isoq	OTf	93 ± 2	89 ± 3	79 ± 1	39 ± 1
16		ClO_4	95 ± 1	88 ± 2	80 ± 8	55 ± 4
17	Impdz	OTf	52 ± 2	37 ± 7	41 ± 3	24 ± 2
18		ClO_4	91 ± 2	67 ± 6	88 ± 1	64 ± 5

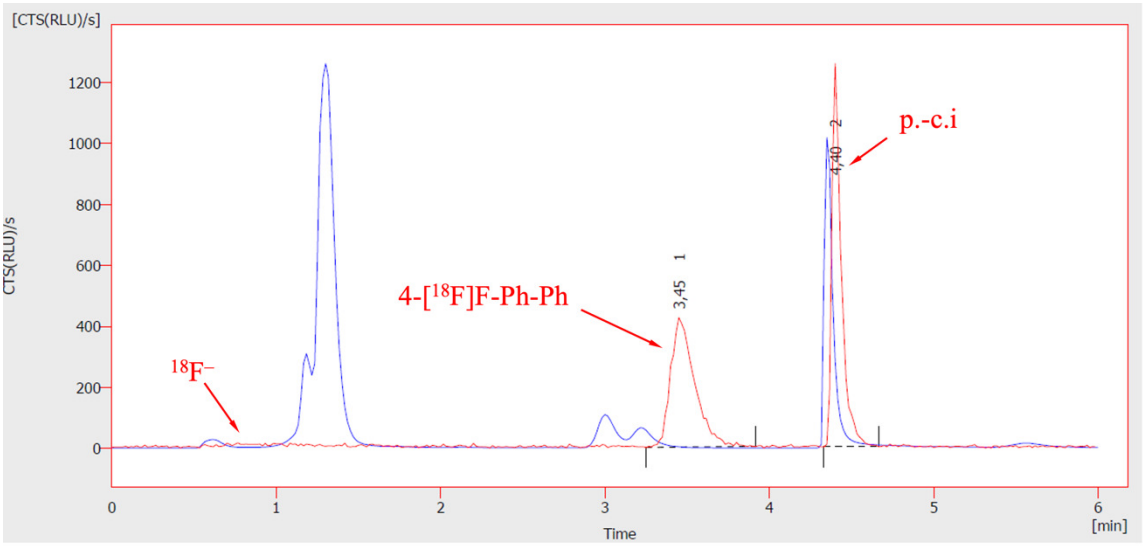

Result Table (Uncal - Data|alc-enhanced_536_21_02_2022_[4 DMI]_biphenyl-B(OH)2 - HERM)

	Reten. Time [min]	Area [CTS(RLU)/s.s]	Height [CTS(RLU)/s]	Area [%]
1	3,450	4338,000	425,100	46,2
2	4,400	5058,000	1257,000	53,8
	Total	9396,000	1682,100	100,0

Figure S19: HPLC traces of crude 4-[^{18}F]F-Ph-Ph prepared in *n*BuOH/DMI from **1** using Cu(4-PhPy)$_4$(ClO$_4$)$_2$ as mediator. Blue trace: UV, λ = 254 nm; red trace: radioactivity. Abbreviation: p.-c.i – post-column injection.

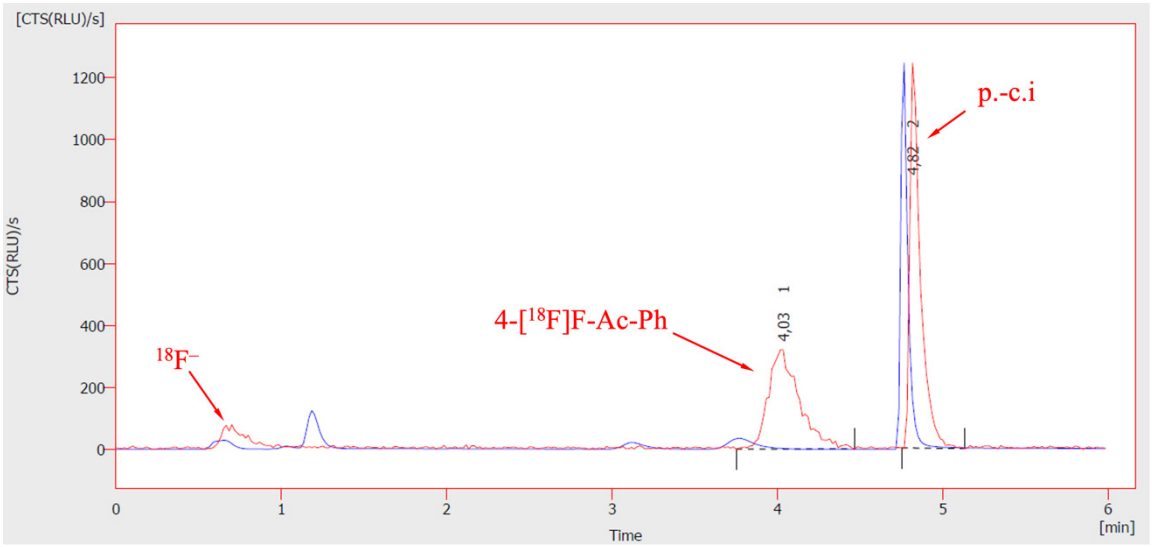

Result Table (Uncal - Data|alc-enhanced_538_21_02_2022_[4 DMI]_4-acetylphenyl-B(OH)2 - HERM)

	Reten. Time [min]	Area [CTS(RLU)/s.s]	Height [CTS(RLU)/s]	Area [%]
1	4,033	4179,500	320,605	42,7
2	4,817	5600,000	1242,348	57,3
	Total	9779,500	1562,952	100,0

Figure S20: HPLC traces of crude 4-[^{18}F]F-Ac-Ph prepared in *n*BuOH/DMI from **3** using Cu(4-PhPy)$_4$(ClO$_4$)$_2$ as mediator. Blue trace: UV, λ = 254 nm; red trace: radioactivity. Abbreviation: p.-c.i – post-column injection.

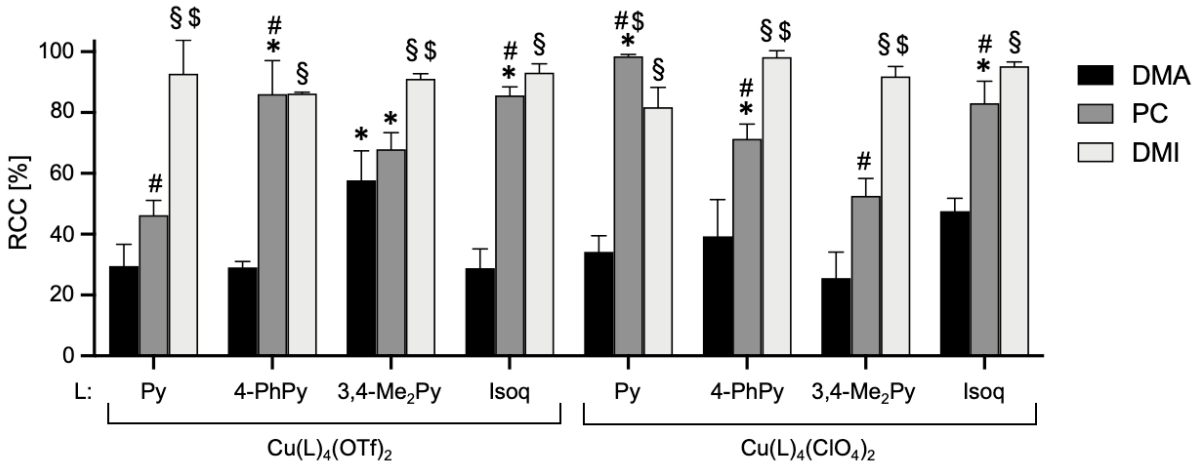

Figure S21: Dependency of RCCs on the aprotic co-solvent. Ph-Ph-$B(OH)_2$ was used as substrate for radiolabeling. Radiosyntheses were carried out according to GP5. Statistics: RCCs were compared using 2-way ANOVA with factors "solvent" and "Cu complex", using selected Cu complexes with the highest RCCs. Using Dunnett's post-hoc test, Cu complexes were compared to $Cu(Py)_4(OTf)_2$ (*$p<0.05$). Solvents were compared with Tukey's post-hoc test. Significant differences are labeled with the following symbols: #: $p<0.05$ for DMA vs. PC; §: $p<0.05$ for DMA vs. DMI; $: $p<0.05$ for DMI vs. PC.

Statistical data corresponding to Figure S21:

Table S27: RCCs (mean values ± standard deviation in %) for radiolabeling of 4-Ph-Ph-B(OH)$_2$ in *n*BuOH/DMA, *n*BuOH/PC or *n*BuOH/DMI using different mediators. 2-way ANOVA: Main effect of factor "**solvent**": F(2,48)=482.7, p<0.0001. Tukey's multiple comparisons test with n=3 per group.

	DMA *vs.* DMI	DMA *vs.* PC	DMI *vs.* PC
Cu(Py)$_4$(OTf)$_2$	DMA: 29.55 ± 7.14 DMI: 92.70 ± 11.01 p<0.0001[§]	DMA: 29.55 ± 7.14 PC: 46.30 ± 4.79 p=0.0053[#]	DMI: 92.70 ± 11.01 PC: 46.30 ± 4.79 p<0.0001[$]
Cu(4-PhPy)$_4$(OTf)$_2$	DMA: 29.09 ± 1.98 DMI: 86.08 ± 0.50 p<0.0001[§]	DMA: 29.09 ± 1.98 PC: 86.06 ± 11.03 p<0.0001[#]	DMI: 86.08 ± 0.50 PC: 86.06 ± 11.03 p=0.9996
Cu(3,4-Me$_2$Py)$_4$(OTf)$_2$	DMA: 57.76 ± 9.63 DMI: 91.04 ± 1.64 p<0.0001[§]	DMA: 57.76 ± 9.63 PC: 67.93 ± 5.44 p=0.1237	DMI: 91.04 ± 1.64 PC: 67.93 ± 5.44 p=0.0001[$]
Cu(Isoq)$_4$(OTf)$_2$	DMA: 28.80 ± 6.35 DMI: 93.05 ± 2.91 p<0.0001[§]	DMA: 28.80 ± 6.35 PC: 85.64 ± 2.84 p<0.0001[#]	DMI: 93.05 ± 2.91 PC: 85.64 ± 2.84 p=0.3216
Cu(Py)$_4$(ClO$_4$)$_2$	DMA: 34.21 ± 5.3 DMI: 81.68 ± 6.53 p<0.0001[§]	DMA: 34.21 ± 5.3 PC: 98.51 ± 0.57 p<0.0001[#]	DMI: 81.68 ± 6.53 PC: 98.51 ± 0.57 p=0.0050[$]
Cu(4-PhPy)$_4$(ClO$_4$)$_2$	DMA: 39.32 ± 12.07 DMI: 98.12 ± 2.14 p<0.0001[§]	DMA: 39.32 ± 12.07 PC: 71.42 ± 4.80 p<0.0001[#]	DMI: 98.12 ± 2.14 PC: 71.42 ± 4.80 p<0.0001[$]
Cu(3,4-Me$_2$Py)$_4$(ClO$_4$)$_2$	DMA: 25.57 ± 8.53 DMI: 91.78 ± 3.25 p<0.0001[§]	DMA: 25.57 ± 8.53 PC: 52.65 ± 5.65 p<0.0001[#]	DMI: 91.78 ± 3.25 PC: 52.65 ± 5.65 p<0.0001[$]
Cu(Isoq)$_4$(ClO$_4$)$_2$	DMA: 47.62 ± 4.19 DMI: 95.18 ± 1.38 p<0.0001[§]	DMA: 47.62 ± 4.19 PC: 83.08 ± 7.22 p<0.0001[#]	DMI: 95.18 ± 1.38 PC: 83.08 ± 7.22 p=0.0550

[§]green: RCCs in *n*BuOH/DMI were significantly higher than in *n*BuOH/DMA; [#] red: RCCs in *n*BuOH/PC were significantly higher than *n*BuOH DMA, [$] blue: RCCs in *n*BuOH/DMI were significantly higher than in *n*BuOH/PC, [$] pink: RCCs in *n*BuOH/PC were significantly higher than in *n*BuOH/DMI.

Table S28: RCCs (mean values ± standard deviation in %) for radiolabeling of 4-Ph-Ph-$B(OH)_2$ in *n*BuOH/DMA, *n*BuOH/PC or *n*BuOH/DMI using different mediators. 2-way ANOVA: Main effect of factor "**Cu-complex**": $F(7,48)=11.60$, $p<0.0001$. Dunnett's multiple comparisons test with $Cu(Py)_4(OTf)_2$ as control with n=3 per group.

	DMA	DMI	PC
$Cu(Py)_4(OTf)_2$	29.55 ± 7.14	92.70 ± 11.01	46.30 ± 4.79
$Cu(4\text{-}PhPy)_4(OTf)_2$	29.09 ± 1.98 p=0.9999	86.08 ± 0.50 p=0.6720	86.06 ± 11.03 p<0.0001*
$Cu(3,4\text{-}Me_2Py)_4(OTf)_2$	57.76 ± 9.63 p<0.0001*	91.04 ± 1.64 p=0.9995	67.93 ± 5.44 p=0.0007*
$Cu(Isoq)_4(OTf)_2$	28.80 ± 6.35 p=0.9998	93.05 ± 2.91 p=0.9999	85.64 ± 2.84 p<0.0001*
$Cu(Py)_4(ClO_4)_2$	34.21 ± 5.3 p=0.8988	81.68 ± 6.53 p=0.1671	98.51 ± 0.57 p<0.0001*
$Cu(4\text{-}PhPy)_4(ClO_4)_2$	39.32 ± 12.07 p=0.2659	98.12 ± 2.14 p=0.8187	71.42 ± 4.80 p<0.0001*
$Cu(3,4\text{-}Me_2Py)_4(ClO_4)_2$	25.57 ± 8.53 p=0.9502	91.78 ± 3.25 p=0.9997	52.65 ± 5.65 p=0.6954
$Cu(Isoq)_4(ClO_4)_2$	47.62 ± 4.19 p=0.0054*	95.18 ± 1.38 p=0.9952	83.08 ± 7.22 p<0.0001*

green: significantly higher RCCs compared to $Cu(Py)_4(OTf)_2$

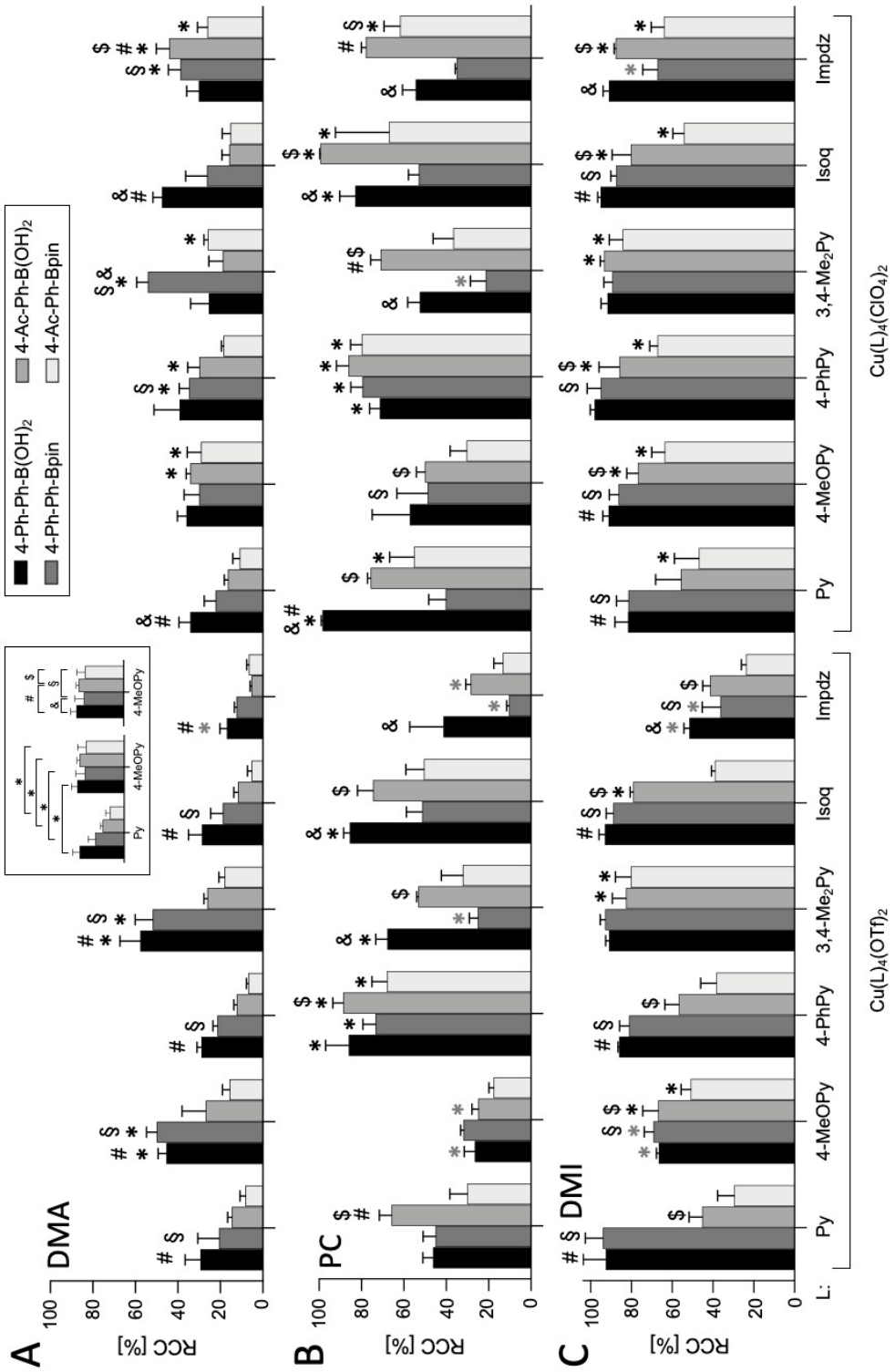

Figure S22: Dependency of RCCs in different solvents on radiolabeling substrates and Cu-complexes. A: Cu complexes in *n*BuOH/DMA. B: Cu complexes in *n*BuOH /PC. C: Cu complexes in *n*BuOH/DMI. Statistics: RCCs were compared using two-way ANOVA with factors "precursor" and "Cu complex". Using Dunnett's post-hoc test, Cu complexes were compared to $Cu(Py)_4(OTf)_2$ (*$p<0.05$). Precursors were compared with Tukey's post-hoc test. Significant differences are labeled with the following symbols: &: $p<0.05$ for 4-Ph-Ph-$B(OH)_2$ vs. 4-Ph-Ph-Bpin; #: $p<0.05$ for 4-Ph-Ph-$B(OH)_2$ vs. 4-Ac-Ph-$B(OH)_2$; §: $p<0.05$ for 4-Ph-Ph-Bpin vs. 4-Ac-Ph-Bpin; $: $p<0.05$ for 4-Ac-Ph-$B(OH)_2$ vs. 4-Ac-Ph-Bpin (for example, see insert).

Statistical data corresponding to Figure S22:

Table S29: RCCs (mean values ± standard deviation in %) in *n*BuOH/DMA. 2-way ANOVA: Main effect of factor "**Cu-complex**": $F(11,96)=33.63$, $p<0.0001$. Dunnett's multiple comparisons test with $Cu(Py)_4(OTf)_2$ as control with n=3 per group.

	4-Ph-Ph-B(OH)$_2$	4-Ph-Ph-Bpin	4-Ac-Ph-B(OH)$_2$	4-Ac-Ph-Bpin
$Cu(Py)_4(OTf)_2$	29.55 ± 7.14	20.82 ± 9.91	14.75 ± 1.93	8.29 ± 2.55
$Cu(4\text{-}MeOPy)_4(OTf)_2$	45.53 ± 3.81 p=0.0043*	49.96 ± 4.93 p<0.0001*	27.01 ± 11.05 p=0.0515	15.88 ± 3.17 p=0.4609
$Cu(4\text{-}PhPy)_4(OTf)_2$	29.09 ± 1.98 p=0.9999	21.48 ± 2.11 p=0.9998	12.37 ± 1.42 p=0.9991	7.00 ± 0.85 p=0.9996
$Cu(3,4\text{-}Me_2Py)_4(OTf)_2$	57.76 ± 9.63 p<0.0001*	51.96 ± 8.26 p<0.0001*	26.23 ± 1.57 p=0.0799	18.24 ± 2.52 p=0.1747
$Cu(Isoq)_4(OTf)_2$	28.80 ± 6.35 p=0.9998	19.00 ± 5.63 p=0.9994	11.80 ± 1.91 p=0.9957	5.43 ± 1.96 p=0.9960
$Cu(Impdz)_4(OTf)_2$	16.98 ± 3.27 p=0.0429*	12.51 ± 1.02 p=0.3535	5.37 ± 0.80 p=0.2271	6.70 ± 0.96 p=0.9995
$Cu(Py)_4(ClO_4)_2$	34.21 ± 5.3 p=0.9137	22.33 ± 5.31 p=0.9995	16.51 ± 1.73 p=0.0004	11.08 ± 3.17 p=0.9961
$Cu(4\text{-}MeOPy)_4(ClO_4)_2$	36.03 ± 4.24 p=0.6465	30.17 ± 6.96 p=0.2310	34.23 ± 1.92 p=0.0003*	29.33 ± 6.35 p<0.0001*
$Cu(4\text{-}PhPy)_4(ClO_4)_2$	39.32 ± 12.07 p=0.1905	34.88 ± 4.59 p=0.0167*	30.04 ± 5.39 p=0.0071*	18.55 ± 1.09 p=0.1508
$Cu(3,4\text{-}Me_2Py)_4(ClO_4)_2$	25.57 ± 8.53 p=0.9663	54.26 ± 5.24 p<0.0001*	19.00 ± 6.56 p=0.9494	25.97 ± 1.82 p=0.0112*
$Cu(Isoq)_4(ClO_4)_2$	47.62 ± 4.19 p=0.0009*	26.37 ± 10.07 p=0.8015	15.97 ± 3.35 p=0.9996	15.43 ± 3.77 p=0.5330
$Cu(Impdz)_4(ClO_4)_2$	30.21 ± 5.73 p=0.9998	39.00 ± 5.60 p=0.0008*	44.15 ± 6.10 p<0.0001*	26.24 ± 4.58 p=0.0009*

green: significantly higher RCCs compared to $Cu(Py)_4(OTf)_2$; red: significantly lower RCCs compared to $Cu(Py)_4(OTf)_2$.

Table S30: RCCs (mean values ± standard deviation in %) in *n*BuOH/DMA. 2-way ANOVA: Main effect of factor "**precursor**": F(3,96)=100.8, p<0.0001. Tukey's multiple comparisons test, n=3 per group.

	4-Ph-Ph-B(OH)$_2$ vs. 4-Ph-Ph-Bpin	4-Ph-Ph-B(OH)$_2$ vs. 4-Ac-Ph-B(OH)$_2$	4-Ph-Ph-Bpin vs. 4-Ac-Ph-Bpin	4-Ac-Ph-B(OH)$_2$ vs. 4-Ac-Ph-Bpin
Cu(Py)$_4$(OTf)$_2$	29.55 ± 7.14 20.82 ± 9.91 p=0.2015	29.55 ± 7.14 14.75 ± 1.93 p=0.0060$^{\#}$	20.82 ± 9.91 8.29 ± 2.55 p=0.0271§	14.75 ± 1.93 8.29 ± 2.55 p=0.4603
Cu(4-MeOPy)$_4$(OTf)$_2$	45.53 ± 3.81 49.96 ± 4.93 p=0.7463	45.53 ± 3.81 27.01 ± 11.05 p=0.0003$^{\#}$	49.96 ± 4.93 15.88 ± 3.17 p<0.0001§	27.01 ± 11.05 15.88 ± 3.17 p=0.0617
Cu(4-PhPy)$_4$(OTf)$_2$	29.09 ± 1.98 21.48 ± 2.11 p=0.3139	29.09 ± 1.98 12.37 ± 1.42 p=0.0014$^{\#}$	21.48 ± 2.11 7.00 ± 0.85 p=0.0075§	12.37 ± 1.42 7.00 ± 0.85 p=0.6160
Cu(3,4-Me$_2$Py)$_4$(OTf)$_2$	57.76 ± 9.63 51.96 ± 8.26 p=0.5538	57.76 ± 9.63 26.23 ± 1.57 p<0.0001$^{\#}$	51.96 ± 8.26 18.24 ± 2.52 p<0.0001§	26.23 ± 1.57 18.24 ± 2.52 p=0.2720
Cu(Isoq)$_4$(OTf)$_2$	28.80 ± 6.35 19.00 ± 5.63 p=0.1233	28.80 ± 6.35 11.80 ± 1.91 p=0.0011$^{\#}$	19.00 ± 5.63 5.43 ± 1.96 p=0.0140§	11.80 ± 1.91 5.43 ± 1.96 p=0.4736
Cu(Impdz)$_4$(OTf)$_2$	16.98 ± 3.27 12.51 ± 1.02 p=0.7397	16.98 ± 3.27 5.37 ± 0.80 p=0.0469$^{\#}$	12.51 ± 1.02 6.70 ± 0.96 p=0.5528	5.37 ± 0.80 6.70 ± 0.96 p=0.9903
Cu(Py)$_4$(ClO$_4$)$_2$	34.21 ± 5.32 22.33 ± 5.31 p=0.0402$^{\&}$	34.21 ± 5.32 16.51 ± 1.73 p=0.0007$^{\#}$	22.33 ± 5.31 11.08 ± 3.17 p=0.0578	16.51 ± 1.73 11.08 ± 3.17 p=0.6074
Cu(4-MeOPy)$_4$(ClO$_4$)$_2$	36.03 ± 4.24 30.17 ± 6.96 p=0.5442	36.03 ± 4.24 34.23 ± 1.92 p=0.9768	30.17 ± 6.96 29.33 ± 6.35 p=0.9976	34.23 ± 1.92 29.33 ± 6.35 p=0.6821
Cu(4-PhPy)$_4$(ClO4)2	39.32 ± 12.07 34.88 ± 4.59 p=0.7450	39.32 ± 12.07 30.04 ± 5.39 p=0.1576	34.88 ± 4.59 18.55 ± 1.09 p=0.0019§	30.04 ± 5.39 18.55 ± 1.09 p=0.0503

$Cu(3,4\text{-}Me_2Py)_4(ClO_4)_2$	25.57 ± 8.53	25.57 ± 8.53	54.26 ± 5.24	19.00 ± 6.56
	54.26 ± 5.24	19.00 ± 6.56	25.97 ± 1.82	25.97 ± 1.82
	$p<0.0001^{*}$	p=0.4461	$p<0.0001^{\S}$	p=0.3930
$Cu(Isoq)_4(ClO_4)_2$	47.62 ± 4.19	47.62 ± 4.19	26.37 ± 10.07	15.97 ± 3.35
	26.37 ± 10.07	15.97 ± 3.35	15.43 ± 3.77	15.43 ± 3.77
	$p<0.0001^{\&}$	$p<0.0001^{\#}$	p=0.0688	p=0.9994
$Cu(Impdz)_4(ClO_4)_2$	30.21 ± 5.73	30.21 ± 5.73	39.00 ± 5.60	44.15 ± 6.10
	39.00 ± 5.60	44.15 ± 6.10	26.24 ± 4.58	26.24 ± 4.58
	p=0.1961	$p=0.0109^{\#}$	$p=0.0236^{\S}$	$p=0.0006^{\$}$

red: significantly lower RCCs for Bpin compared to $B(OH)_2$ precursors; blue: significantly higher RCCs for Bpin compared to $B(OH)_2$ precursors; green: significantly higher RCCs for 4-Ph-Ph compared to 4-Ac-Ph substituted precursors; pink: significantly lower RCCs for 4-Ph-Ph compared to 4-Ac-Ph precursors.

Table S31: RCCs (mean values ± standard deviation in %) in *n*BuOH/PC. 2-way ANOVA: Main effect of factor "**Cu-complex**": $F(11,96)=72.21$, $p<0.0001$. Dunnett's multiple comparisons test with $Cu(Py)_4(OTf)_2$ as control with n=3 per group.

	4-Ph-Ph-B(OH)$_2$	4-Ph-Ph-Bpin	4-Ac-Ph-B(OH)$_2$	4-Ac-Ph-Bpin
$Cu(Py)_4(OTf)_2$	46.30 ± 4.79	45.24 ± 5.77	65.90 ± 5.74	30.13 ± 8.30
$Cu(4\text{-}MeOPy)_4(OTf)_2$	26.69 ± 4.98 p=0.0246*	31.98 ± 1.28 p=0.2563	25.08 ± 2.94 p<0.0001*	17.75 ± 2.19 p=0.3289
$Cu(4\text{-}PhPy)_4(OTf)_2$	86.06 ± 11.03 p<0.0001*	73.44 ± 6.00 p=0.0003*	88.80 ± 4.88 p=0.0052*	68.20 ± 6.98 p<0.0001*
$Cu(3,4\text{-}Me_2Py)_4(OTf)_2$	67.93 ± 5.44 p=0.0097*	25.14 ± 4.00 p=0.0198*	53.37 ± 0.74 p=0.3162	32.40 ± 10.02 p=0.9995
$Cu(Isoq)_4(OTf)_2$	85.64 ± 2.84 p<0.0001*	51.55 ± 7.39 p=0.9432	74.71 ± 7.32 p=0.7209	50.67 ± 8.55 p=0.0163*
$Cu(Impdz)_4(OTf)_2$	41.41 ± 15.93 p=0.9897	10.44 ± 1.13 p<0.0001*	28.61 ± 2.32 p<0.0001*	13.51 ± 4.16 p=0.0832
$Cu(Py)_4(ClO_4)_2$	98.51 ± 0.57 p<0.0001*	40.30 ± 8.05 p=0.9892	75.83 ± 1.46 p=0.5886	55.39 ± 11.40 p=0.0015*
$Cu(4\text{-}MeOPy)_4(ClO_4)_2$	57.31 ± 17.79 p=0.4666	48.98 ± 14.43 p=0.9991	50.21 ± 3.95 p=0.1165	30.55 ± 7.72 p=0.9999
$Cu(4\text{-}PhPy)_4(ClO_4)_2$	71.42 ± 4.80 p=0.0016*	79.66 ± 5.46 p<0.0001*	86.39 ± 5.56 p=0.0166*	80.06 ± 5.20 p<0.0001*
$Cu(3,4\text{-}Me_2Py)_4(ClO_4)_2$	52.65 ± 5.65 p=0.9411	21.52 ± 7.15 p=0.0034*	71.01 ± 4.78 p=0.9868	36.87 ± 9.40 p=0.9173
$Cu(Isoq)_4(ClO_4)_2$	83.08 ± 7.22 p<0.0001*	53.08 ± 4.86 p=0.8250	99.39 ± 0.55 p<0.0001*	67.13 ± 25.26 p<0.0001*
$Cu(Impdz)_4(ClO_4)_2$	54.58 ± 6.19 p=0.7800	35.24 ± 0.59 p=0.5808	78.09 ± 2.05 p=0.3462	61.96 ± 7.53 p<0.0001*

green: significantly higher RCCs compared to $Cu(Py)_4(OTf)_2$; red: significantly lower RCCs compared to $Cu(Py)_4(OTf)_2$.

Table S32: RCCs (mean values ± standard deviation in %) in *n*BuOH/PC: 2-way ANOVA: Main effect of factor "**precursor**": F(3,96)=88.15, p<0.0001. Tukey's multiple comparisons test, n=3 per group.

	4-Ph-Ph-B(OH)$_2$ vs. 4-Ph-Ph-Bpin	4-Ph-Ph-B(OH)$_2$ vs. 4-Ac-Ph-B(OH)$_2$	4-Ph-Ph-Bpin vs. 4-Ac-Ph-Bpin	4-Ac-Ph-B(OH)$_2$ vs. 4-Ac-Ph-Bpin
Cu(Py)$_4$(OTf)$_2$	46.30 ± 4.79 45.24 ± 5.7 p=0.9984	46.30 ± 4.79 65.90 ± 5.74 p=0.0151$^{\#}$	45.24 ± 5.77 30.13 ± 8.30 p=0.0926	65.90 ± 5.74 30.13 ± 8.30 p<0.0001$^{\$}$
Cu(4-MeOPy)$_4$(OTf)$_2$	26.69 ± 4.98 31.98 ± 1.28 p=0.8426	26.69 ± 4.98 25.08 ± 2.94 p=0.9944	31.98 ± 1.28 17.75 ± 2.19 p=0.1253	25.08 ± 2.94 17.75 ± 2.19 p=0.6636
Cu(4-PhPy)$_4$(OTf)$_2$	86.06 ± 11.03 73.44 ± 6.00 p=0.1070	86.06 ± 11.03 88.80 ± 4.88 p=0.9735	73.44 ± 6.00 68.20 ± 6.98 p=0.8465	88.80 ± 4.88 68.20 ± 6.98 p=0.0095$^{\$}$
Cu(3,4-Me$_2$Py)$_4$(OTf)$_2$	67.93 ± 5.44 25.14 ± 4.00 p<0.0001$^{\&}$	67.93 ± 5.44 53.37 ± 0.74 p=0.1120	25.14 ± 4.00 32.40 ± 10.02 p=0.6706	53.37 ± 0.74 32.40 ± 10.02 p=0.0079$^{\$}$
Cu(Isoq)$_4$(OTf)$_2$	85.64 ± 2.84 51.55 ± 7.39 p<0.0001$^{\&}$	85.64 ± 2.84 74.71 ± 7.32 p=0.3263	51.55 ± 7.39 50.67 ± 8.55 p=0.9991	74.71 ± 7.32 50.67 ± 8.55 p=0.0017$^{\$}$
Cu(Impdz)$_4$(OTf)$_2$	41.41 ± 15.93 10.44 ± 1.13 p<0.0001$^{\&}$	41.41 ± 15.93 28.61 ± 2.32 p=0.1965	10.44 ± 1.13 13.51 ± 4.16 p=0.9636	28.61 ± 2.32 13.51 ± 4.16 p=0.0929
Cu(Py)$_4$(ClO$_4$)$_2$	98.51 ± 0.57 40.30 ± 8.05 p<0.0001$^{\&}$	98.51 ± 0.57 75.83 ± 1.46 p=0.0034$^{\#}$	40.30 ± 8.05 55.39 ± 11.40 p=0.0931	75.83 ± 1.46 55.39 ± 11.40 p=0.0102$^{\$}$
Cu(4-MeOPy)$_4$(ClO$_4$)$_2$	57.31 ± 17.79 48.98 ± 14.43 p=0.5654	57.31 ± 17.79 50.21 ± 3.95 p=0.6857	48.98 ± 14.43 30.55 ± 7.72 p=0.0252§	50.21 ± 3.95 30.55 ± 7.72 p=0.0147$^{\$}$
Cu(4-PhPy)$_4$(ClO$_4$)2	71.42 ± 4.80 79.66 ± 5.46 p=0.5740	71.42 ± 4.80 86.39 ± 5.56 p=0.0970	79.66 ± 5.46 80.06 ± 5.20 p=0.9999	86.39 ± 5.56 80.06 ± 5.20 p=0.7565

$Cu(3,4\text{-}Me_2Py)_4(ClO_4)_2$	52.65 ± 5.65	52.65 ± 5.65	21.52 ± 7.15	71.01 ± 4.78
	21.52 ± 7.15	71.01 ± 4.78	36.87 ± 9.40	36.87 ± 9.40
	$p<0.0001^{\&}$	$p=0.0260^{\#}$	p=0.0849	$p<0.0001^{\$}$
$Cu(Isoq)_4(ClO_4)_2$	83.08 ± 7.22	83.08 ± 7.22	53.08 ± 4.86	99.39 ± 0.55
	53.08 ± 4.86	99.39 ± 0.55	67.13 ± 25.26	67.13 ± 25.26
	$p<0.0001^{\&}$	p=0.0593	p=0.1328	$p<0.0001^{\$}$
$Cu(Impdz)_4(ClO_4)_2$	54.58 ± 6.19	54.58 ± 6.19	35.24 ± 0.59	78.09 ± 2.05
	35.24 ± 0.59	78.09 ± 2.05	61.96 ± 7.53	61.96 ± 7.53
	$p=0.0169^{\&}$	$p=0.0022^{\#}$	$p=0.0004^{\S}$	p=0.0636

red: significantly lower RCCs for Bpin compared to $B(OH)_2$ precursors; green: significantly higher RCCs for 4-Ph-Ph compared to 4-Ac-Ph substituted precursors; pink: significantly lower RCCs for 4-Ph-Ph compared to 4-Ac-Ph precursors.

Table S33: RCCs (mean values ± standard deviation in %) in *n*BuOH/DMI. 2-way ANOVA: Main effect of factor "**Cu-complex**": $F(11,96)=68.60$, $p<0.0001$. Dunnett's multiple comparisons test with $Cu(Py)_4(OTf)_2$ as control with n=3 per group.

	4-Ph-Ph-B(OH)$_2$	4-Ph-Ph-Bpin	4-Ac-Ph-B(OH)$_2$	4-Ac-Ph-Bpin
$Cu(Py)_4(OTf)_2$	92.70 ± 11.01	94.05 ± 8.57	45.39 ± 6.48	29.74 ± 8.00
$Cu(4\text{-}MeOPy)_4(OTf)_2$	66.74 ± 1.09 p<0.0001*	69.40 ± 4.34 p<0.0001*	67.00 ± 7.53 p=0.0002*	51.06 ± 4.71 p=0.0003*
$Cu(4\text{-}PhPy)_4(OTf)_2$	86.08 ± 0.50 p=0.7251	81.23 ± 4.60 p=0.0724	56.91 ± 6.73 p=0.1350	38.57 ± 7.56 p=0.3933
$Cu(3,4\text{-}Me_2Py)_4(OTf)_2$	91.04 ± 1.64 p=0.9995	92.93 ± 2.43 p=0.9997	82.70 ± 6.77 p<0.0001*	80.51 ± 7.39 p<0.0001*
$Cu(Isoq)_4(OTf)_2$	93.05 ± 2.91 p=0.9999	89.07 ± 3.38 p=0.9268	79.21 ± 1.50 p<0.0001*	39.23 ± 1.62 p=0.3125
$Cu(Impdz)_4(OTf)_2$	51.67 ± 2.71 p<0.0001*	36.58 ± 8.83 p<0.0001*	41.44 ± 3.65 p=0.9839	23.86 ± 2.27 p=0.8307
$Cu(Py)_4(ClO_4)_2$	81.68 ± 6.53 p=0.1688	81.63 ± 5.73 p=0.0885	55.82 ± 12.36 p=0.2165	46.98 ± 12.00 p=0.0054*
$Cu(4\text{-}MeOPy)_4(ClO_4)_2$	91.27 ± 2.82 p=0.9996	86.41 ± 4.57 p=0.5669	76.95 ± 5.34 p<0.0001*	63.81 ± 6.33 p<0.0001*
$Cu(4\text{-}PhPy)_4(ClO_4)_2$	98.12 ± 2.14 p=0.8851	95.15 ± 6.67 p=0.9997	86.04 ± 9.90 p<0.0001*	67.29 ± 3.82 p<0.0001*
$Cu(3,4\text{-}Me_2Py)_4(ClO_4)_2$	91.78 ± 3.25 p=0.9997	89.44 ± 4.16 p=0.9523	93.47 ± 1.89 p<0.0001*	84.41 ± 6.50 p<0.0001*
$Cu(Isoq)_4(ClO_4)_2$	95.18 ± 1.38 p=0.9992	87.62 ± 2.54 p=0.7535	80.31 ± 9.19 p<0.0001*	54.51 ± 5.24 p<0.0001*
$Cu(Impdz)_4(ClO_4)_2$	91.16 ± 2.84 p=0.9996	67.31 ± 7.17 p<0.0001*	87.79 ± 0.79 p<0.0001*	64.15 ± 6.21 p<0.0001*

green: significantly higher RCCs compared to $Cu(Py)_4(OTf)_2$; red: significantly lower RCCs compared to $Cu(Py)_4(OTf)_2$.

Table S34: RCCs (mean values ± standard deviation in %) in *n*BuOH/DMI. 2-way ANOVA: Main effect of factor "**precursor**": F(3,96)=155.4, p<0.0001. Tukey's multiple comparisons test, n=3 per group.

	4-Ph-Ph-B(OH)$_2$ *vs.* 4-Ph-Ph-Bpin	4-Ph-Ph-B(OH)$_2$ *vs.* 4-Ac-Ph-B(OH)$_2$	4-Ph-Ph-Bpin *vs.* 4-Ac-Ph-Bpin	4-Ac-Ph-B(OH)$_2$ *vs.* 4-Ac-Ph-Bpin
Cu(Py)$_4$(OTf)$_2$	92.70 ± 11.01	92.70 ± 11.01	94.05 ± 8.57	45.39 ± 6.48
	94.05 ± 8.57	45.39 ± 6.48	29.74 ± 8.00	29.74 ± 8.00
	p=0.9924	p<0.0001$^{\#}$	p<0.0001§	p=0.0089$^{\$}$
Cu(4-MeOPy)$_4$(OTf)$_2$	66.74 ± 1.09	66.74 ± 1.09	69.40 ± 4.34	67.00 ± 7.53
	69.40 ± 4.34	67.00 ± 7.53	51.06 ± 4.71	51.06 ± 4.71
	p=0.9464	p=0.9999	p=0.0015§	p=0.0074$^{\$}$
Cu(4-PhPy)$_4$(OTf)$_2$	86.08 ± 0.50	86.08 ± 0.50	81.23 ± 4.60	56.91 ± 6.73
	81.23 ± 4.60	56.91 ± 6.73	38.57 ± 7.56	38.57 ± 7.56
	p=0.7475	p<0.0001$^{\#}$	p<0.0001§	p=0.0015$^{\$}$
Cu(3,4-Me$_2$Py)$_4$(OTf)$_2$	91.04 ± 1.64	91.04 ± 1.64	92.93 ± 2.43	82.70 ± 6.77
	92.93 ± 2.43	82.70 ± 6.77	80.51 ± 7.39	80.51 ± 7.39
	p=0.9795	p=0.3174	p=0.0562	p=0.9688
Cu(Isoq)$_4$(OTf)$_2$	93.05 ± 2.91	93.05 ± 2.91	89.07 ± 3.38	79.21 ± 1.50
	89.07 ± 3.38	79.21 ± 1.50	39.23 ± 1.62	39.23 ± 1.62
	p=0.8439	p=0.0263$^{\#}$	p<0.0001§	p<0.0001$^{\$}$
Cu(Impdz)$_4$(OTf)$_2$	51.67 ± 2.71	51.67 ± 2.71	36.58 ± 8.83	41.44 ± 3.65
	36.58 ± 8.83	41.44 ± 3.65	23.86 ± 2.27	23.86 ± 2.27
	p=0.0126$^{\&}$	p=0.1554	p=0.0483§	p=0.0025$^{\$}$
Cu(Py)$_4$(ClO$_4$)$_2$	81.68 ± 6.53	81.68 ± 6.53	81.63 ± 5.73	55.82 ± 12.36
	81.63 ± 5.73	55.82 ± 12.36	46.98 ± 12.00	46.98 ± 12.00
	p=0.9999	p<0.0001$^{\#}$	p<0.0001§	p=0.2667
Cu(4-MeOPy)$_4$(ClO$_4$)$_2$	91.27 ± 2.82	91.27 ± 2.82	86.41 ± 4.57	76.95 ± 5.34
	86.41 ± 4.57	76.95 ± 5.34	63.81 ± 6.33	63.81 ± 6.33
	p=0.7475	p=0.0200$^{\#}$	p<0.0001§	p=0.0386$^{\$}$
Cu(4-PhPy)$_4$(ClO$_4$)2	98.12 ± 2.14	98.12 ± 2.14	95.15 ± 6.67	86.04 ± 9.90
	95.15 ± 6.67	86.04 ± 9.90	67.29 ± 3.82	67.29 ± 3.82
	p=0.9272	p=0.0669	p<0.0001§	p=0.0011$^{\$}$

$Cu(3,4\text{-}Me_2Py)_4(ClO_4)_2$	91.78 ± 3.25	91.78 ± 3.25	89.44 ± 4.16	93.47 ± 1.89
	89.44 ± 4.16	93.47 ± 1.89	84.41 ± 6.50	84.41 ± 6.50
	p=0.9624	p=0.9854	p=0.7262	p=0.2463
$Cu(Isoq)_4(ClO_4)_2$	95.18 ± 1.38	95.18 ± 1.38	87.62 ± 2.54	80.31 ± 9.19
	87.62 ± 2.54	80.31 ± 9.19	54.51 ± 5.24	54.51 ± 5.24
	p=0.4044	p=0.0143[#]	p<0.0001[§]	p<0.0001[$]
$Cu(Impdz)_4(ClO_4)_2$	91.16 ± 2.84	91.16 ± 2.84	67.31 ± 7.17	87.79 ± 0.79
	67.31 ± 7.17	87.79 ± 0.79	64.15 ± 6.21	64.15 ± 6.21
	p<0.0001[&]	p=0.8982	p=0.9137	p<0.0001[$]

red: significantly lower RCCs for Bpin compared to $B(OH)_2$ precursors; green: significantly higher RCCs for 4-Ph-Ph compared to 4-Ac-Ph substituted precursors.

$Cu(Impdz)_4(OTf)_2$ *vs.* $Cu(Impdz)_4(ClO_4)_2$

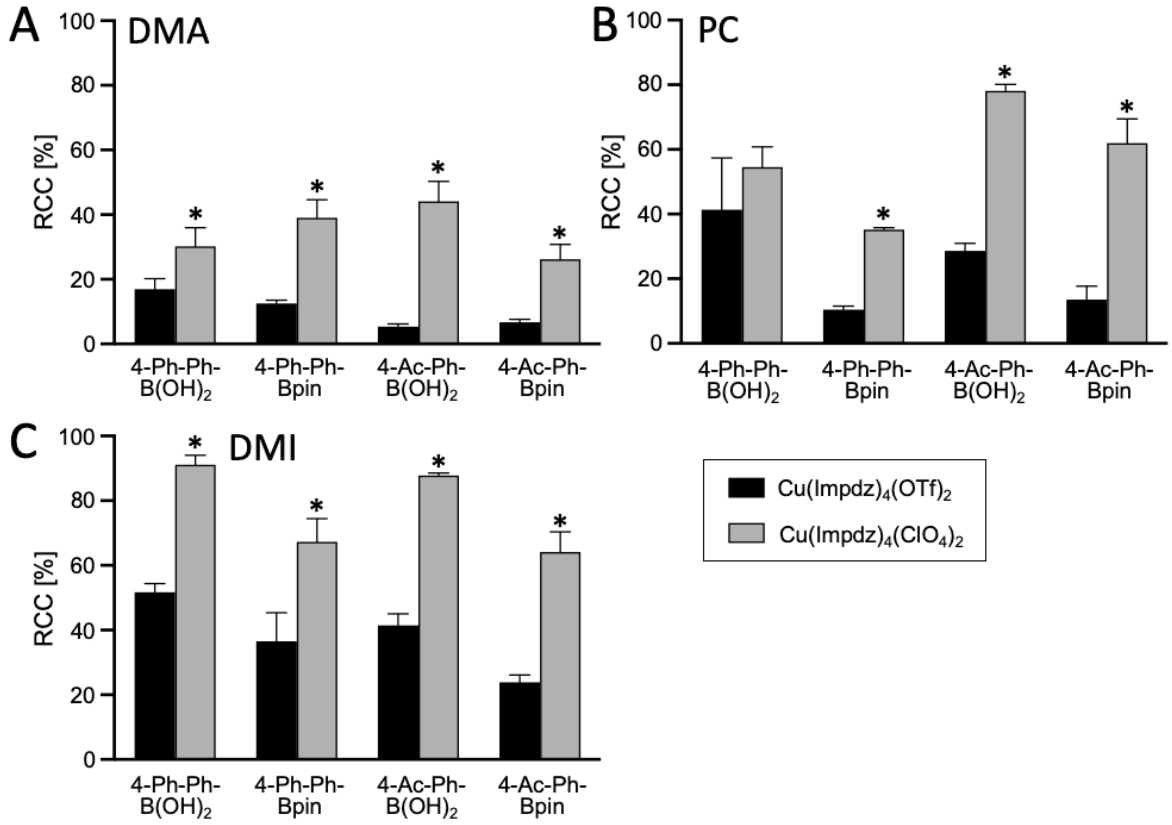

Figure S23: $Cu(Impdz)_4(OTf)_2$ *vs.* $Cu(Impdz)_4(ClO_4)_2$. * $p<0.05$. For full statistics, see Table S35.

Table S35: RCCs (mean values ± standard deviation in %) obtained using $Cu(Impdz)_4(OTf)_2$ and $Cu(Impdz)_4(ClO_4)_2$ as radiofluorination mediators. Comparison was carried out using 2-way ANOVA followed by Sidak's multiple comparison test (n=3 per group). Main effects (F-values) of the factor "**counter ion**" are given.

		$Cu(Impdz)_4(OTf)_2$	$Cu(Impdz)_4(ClO_4)_2$	
DMA	4-Ph-Ph-$B(OH)_2$	16.98 ± 3.27	30.21 ± 5.73	p=0.0047*
F(1,16)=212.6	4-Ph-Ph-Bpin	12.51 ± 1.02	39.00 ± 5.60	p<0.0001*
p<0.0001	4-Ac-Ph-$B(OH)_2$	5.37 ± 0.80	44.15 ± 6.10	p<0.0001*
	4-Ac-Ph-Bpin	6.70 ± 0.96	26.24 ± 4.58	p=0.0001*
PC	4-Ph-Ph-$B(OH)_2$	41.41 ± 15.93	54.58 ± 6.19	p=0.1219
F(1,16)=146.8	4-Ph-Ph-Bpin	10.44 ± 1.13	35.24 ± 0.59	p=0.0017*
p<0.0001	4-Ac-Ph-$B(OH)_2$	28.61 ± 2.32	78.09 ± 2.05	p<0.0001*
	4-Ac-Ph-Bpin	13.51 ± 4.16	61.96 ± 7.53	p<0.0001*
DMI	4-Ph-Ph-$B(OH)_2$	51.65 ± 2.71	91.16 ± 2.84	p<0.0001*
F(1,16)=364.4	4-Ph-Ph-Bpin	36.58 ± 8.83	67.31 ± 7.17	p<0.0001*
p<0.0001	4-Ac-Ph-$B(OH)_2$	41.44 ± 3.65	87.79 ± 0.79	p<0.0001*
	4-Ac-Ph-Bpin	23.86 ± 2.27	64.15 ± 6.21	p<0.0001*

Screening of reaction temperatures

The screening of reaction temperatures was performed in *n*BuOH/DMI according to GP5 using **1** as model substrate and $Cu(4\text{-}PhPy)_4(ClO_4)_2$ as mediator (n=3). RCCs were determined by radio-HPLC as described above. Representative HPLC chromatograms of the crude radiolabeled products are shown in Figure **S25**–**S27**.

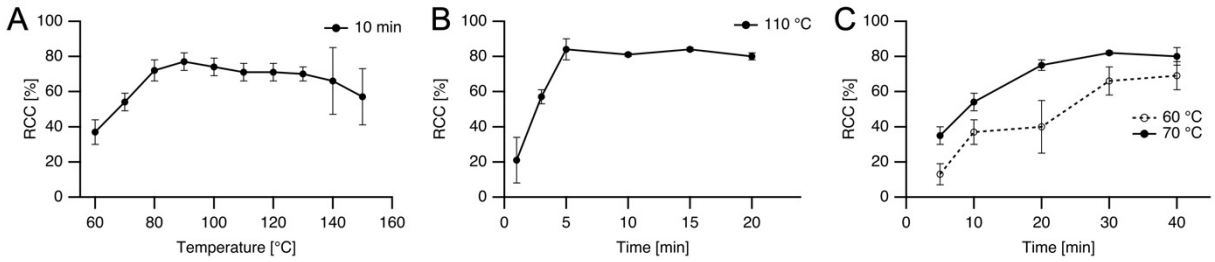

Figure S24: Temperature (A) and reaction time studies (B and C) for $Cu(4\text{-}PhPy)_4(ClO_4)_2$-mediated radiofluorination of 4-Ph-Ph-$B(OH)_2$. Conditions: $[^{18}F]F^-$ (10–50 MBq) was eluted with Et_4NOTf (1 mg, 4 µmol) in *n*BuOH (400 µL) into a solution of 4-Ph-Ph-$B(OH)_2$ (10 µmol, 1 eq.) and $Cu(4\text{-}PhPy)_4(ClO_4)_2$ (10 µmol, 1 eq.) in DMI (800 µL),; (A) 60–150 °C as indicated for 10 min. (B) 1–20 min as indicated at 110 °C (C) 10–40 min at 60 or 70 °C as indicated. All radiosyntheses were carried out in triplicate.

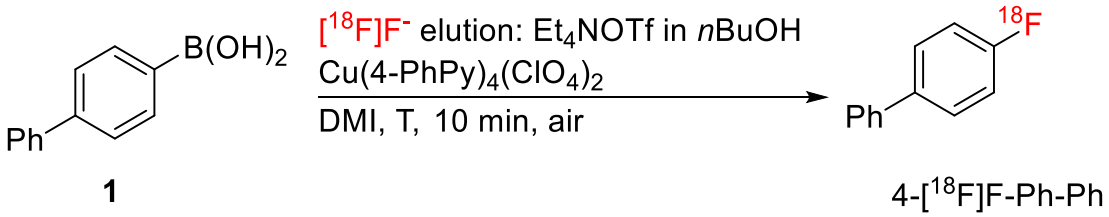

1

4-[^{18}F]F-Ph-Ph

Table S36: Screening of temperature.

Entry	T [°C]	RCC [%]
1	rt	0
2	60	37 ± 7
3	70	54 ± 5
4	80	72 ± 6
5	90	77 ± 5
6	100	74 ± 5
7	110	71 ± 5
8	120	71 ± 5
9	130	70 ± 4
10	140	66 ± 19
11	150	57 ± 16

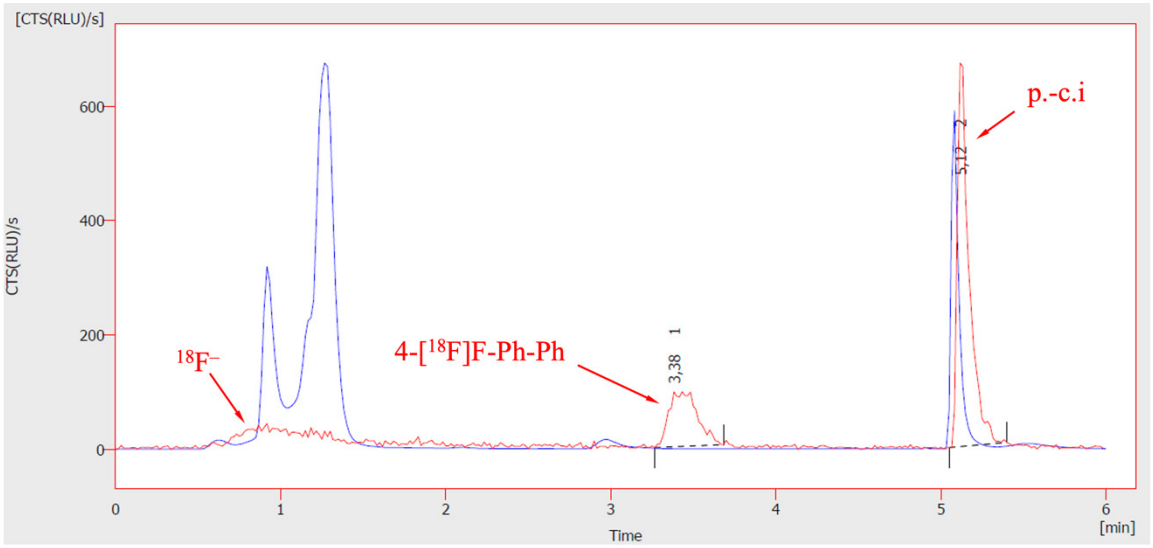

Result Table (Uncal - Data|alc-enhanced_328_03_11_2021_[4 DMI]_biphenyl-B(OH)2_60 - HERM)

	Reten. Time [min]	Area [CTS(RLU)/s.s]	Height [CTS(RLU)/s]	Area [%]
1	3,383	1164,500	96,600	25,6
2	5,117	3377,500	671,286	74,4
	Total	4542,000	767,886	100,0

Figure S25: HPLC traces of crude 4-[^{18}F]F-Ph-Ph prepared from **1** using Cu(4-PhPy)$_4$(ClO$_4$)$_2$ as mediator in *n*BuOH/DMI at 60 °C for 10 min. Blue trace: UV, λ = 254 nm; red trace: radioactivity. Abbreviation: p.-c.i – post-column injection.

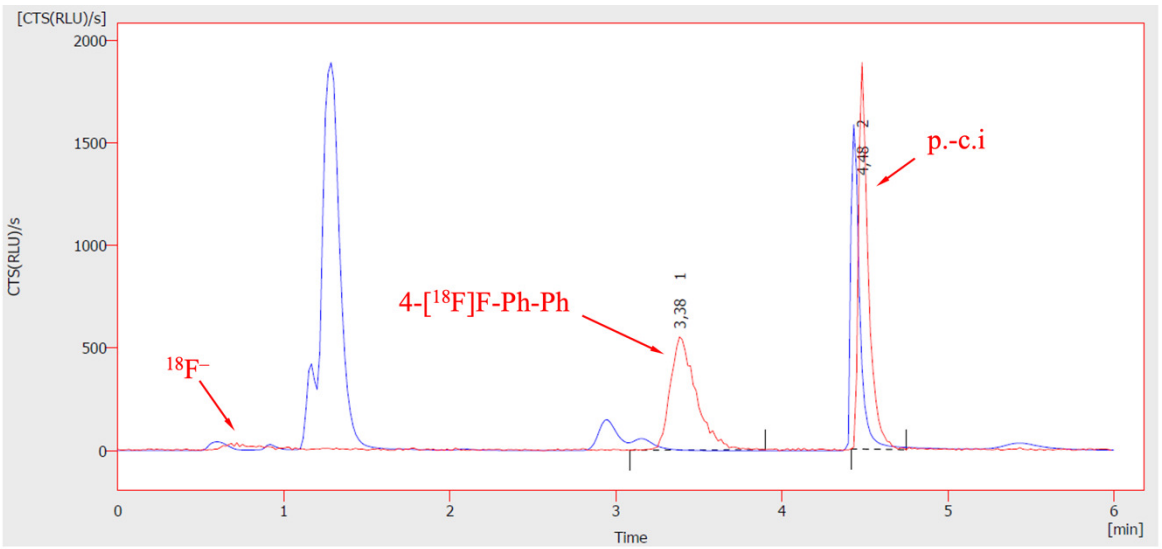

Result Table (Uncal - Data|alc-enhanced_678_08_04_2022_[4 DMI]biphenyl-B(OH)2_90°C - HERM)

	Reten. Time [min]	Area [CTS(RLU)/s.s]	Height [CTS(RLU)/s]	Area [%]
1	3,383	5980,000	551,265	43,5
2	4,483	7767,000	1884,600	56,5
	Total	13747,000	2435,865	100,0

Figure S26: HPLC traces of crude 4-[^{18}F]F-Ph-Ph prepared from **1** using Cu(4-PhPy)$_4$(ClO$_4$)$_2$ as mediator in *n*BuOH/DMI at 90 °C for 10 min. Blue trace: UV, λ = 254 nm; red trace: radioactivity. Abbreviation: p.-c.i – post-column injection.

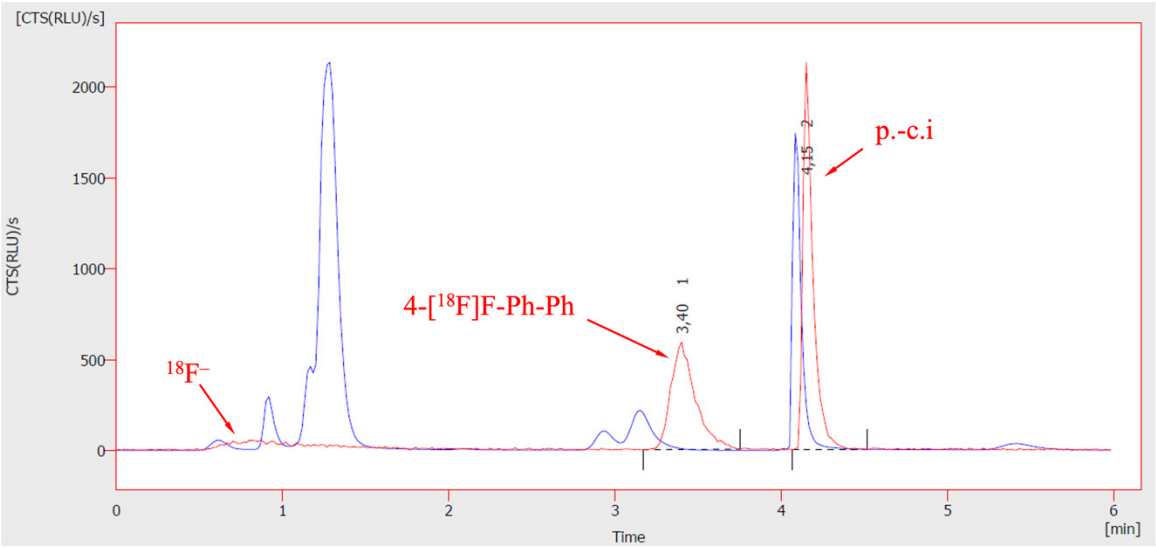

Result Table (Uncal - Data|alc-enhanced_698_11_04_2022_[4 DMI]biphenyl-B(OH)2_150°C - HERM)

	Reten. Time [min]	Area [CTS(RLU)/s.s]	Height [CTS(RLU)/s]	Area [%]
1	3,400	6051,500	591,800	40,1
2	4,150	9030,000	2134,000	59,9
	Total	15081,500	2725,800	100,0

Figure S27: HPLC traces of crude 4-[^{18}F]F-Ph-Ph prepared from **1** using $Cu(4\text{-}PhPy)_4(ClO_4)_2$ as mediator in *n*BuOH/DMI at 150 °C for 10 min. Blue trace: UV, λ = 254 nm; red trace: radioactivity. Abbreviation: p.-c.i – post-column injection.

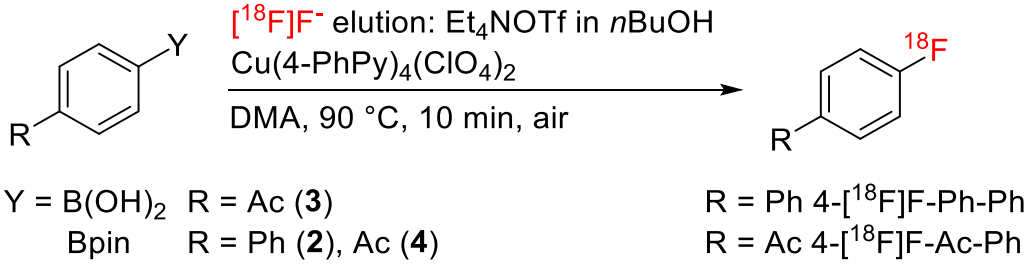

Table S37: Radiolabeling of precursors **2**–**4** at 90 °C for 10 min.

Entry	Precursor	RCC [%]
1	**2**	39 ± 10
2	**3**	44 ± 2
3	**4**	21 ± 2

Screening of reaction times

The screening of various reaction times at different temperatures was performed according to GP5 using **1** as model radiolabeling substrate and $Cu(4\text{-}PhPy)_4(ClO_4)_2$ as mediator in *n*BuOH/DMI. RCCs were determined by radio-HPLC as described above. Representative HPLC chromatograms of the crude radiolabeled products are shown in Figure **S28**–**S36**.

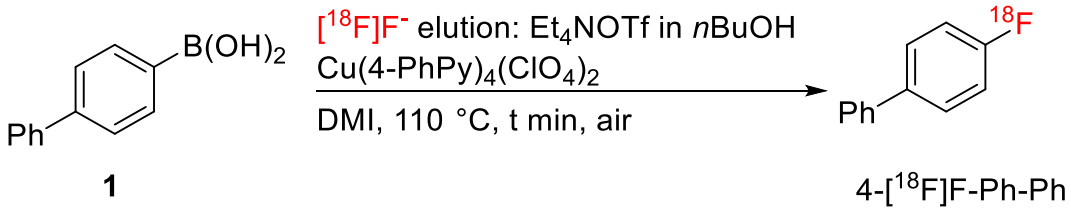

1 4-[^{18}F]F-Ph-Ph

Table S38: Screening of reaction time at 110 °C.

Entry	t [min]	RCC [%]
1	1	21 ± 13
2	3	57 ± 4
3	5	84 ± 6
4	10	81 ± 1
5	15	84 ± 1
6	20	80 ± 2
7	30	59 ± 5
8	40	63 ± 13

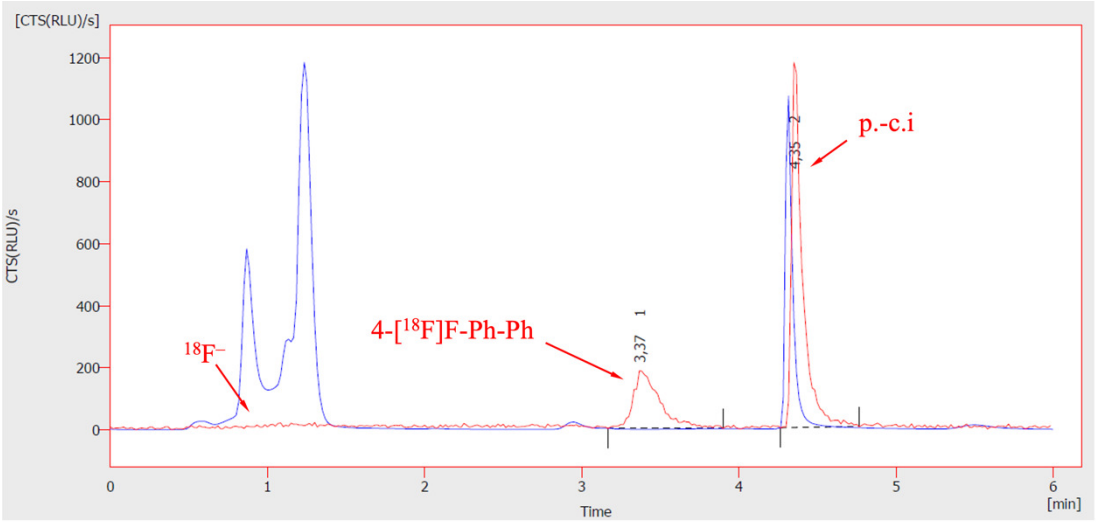

Result Table (Uncal - Data|alc-enhanced_480_04_02_2022_[4 DMI]_biphenyl_B(OH)2_rkt_1min - HERM)

	Reten. Time [min]	Area [CTS(RLU)/s.s]	Height [CTS(RLU)/s]	Area [%]
1	3,367	2204,000	186,000	27,7
2	4,350	5744,000	1177,333	72,3
	Total	7948,000	1363,333	100,0

Figure S28: HPLC traces of crude 4-[^{18}F]F-Ph-Ph prepared from **1** using Cu(4-PhPy)$_4$(ClO$_4$)$_2$ as mediator in *n*BuOH/DMI at 110 °C for 1 min. Blue trace: UV, λ = 254 nm; red trace: radioactivity. Abbreviation: p.-c.i – post-column injection.

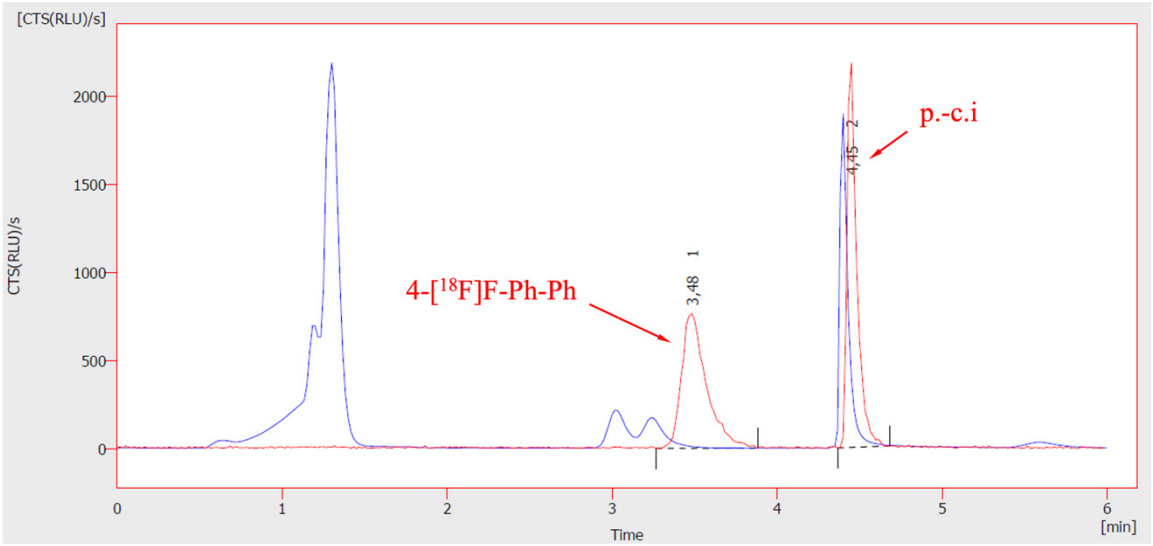

Result Table (Uncal - Data|alc-enhanced_474_04_02_2022_[4 DMI]_biphenyl_B(OH)2_rkt_15min - HERM)

	Reten. Time [min]	Area [CTS(RLU)/s.s]	Height [CTS(RLU)/s]	Area [%]
1	3,483	8086,000	765,297	47,2
2	4,450	9039,500	2181,105	52,8
	Total	17125,500	2946,403	100,0

Figure S29: HPLC traces of crude 4-[^{18}F]F-Ph-Ph prepared from **1** using Cu(4-PhPy)$_4$(ClO$_4$)$_2$ as mediator in *n*BuOH/DMI at 110 °C for 15 min. Blue trace: UV, λ = 254 nm; red trace: radioactivity. Abbreviation: p.-c.i – post-column injection.

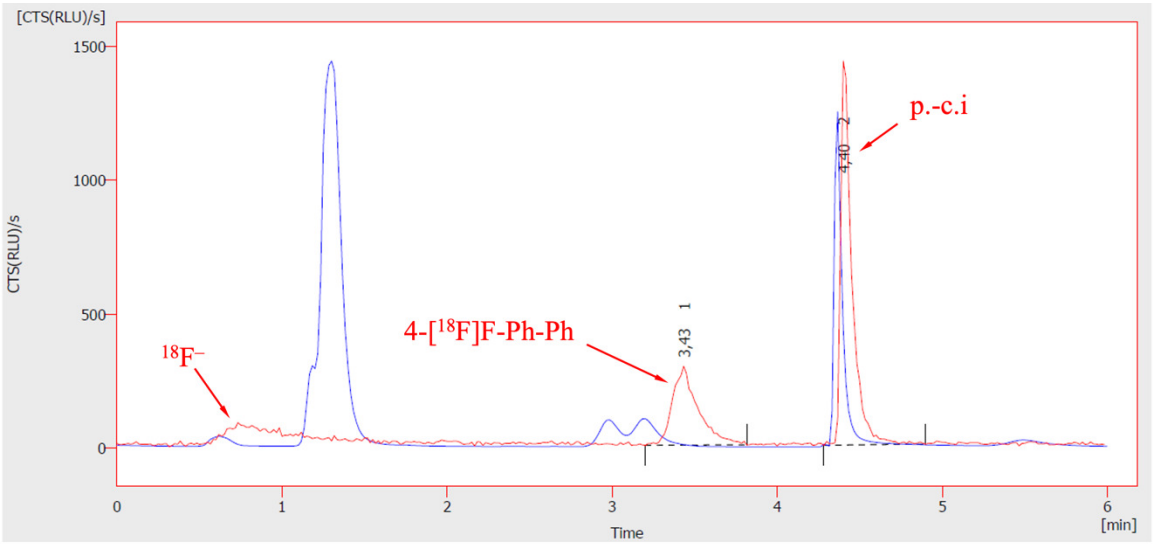

Result Table (Uncal - Data|alc-enhanced_756_12_05_2022_[4 DMI]biphenyl-B(OH)2_110°C_40min - HERM)

	Reten. Time [min]	Area [CTS(RLU)/s.s]	Height [CTS(RLU)/s]	Area [%]
1	3,433	3195,500	295,622	31,6
2	4,400	6913,000	1435,243	68,4
	Total	10108,500	1730,865	100,0

Figure S30: HPLC traces of crude 4-[^{18}F]F-Ph-Ph prepared from **1** using Cu(4-PhPy)$_4$(ClO$_4$)$_2$ as mediator in *n*BuOH/DMI at 110 °C for 40 min. Blue trace: UV, λ = 254 nm; red trace: radioactivity. Abbreviation: p.-c.i – post-column injection.

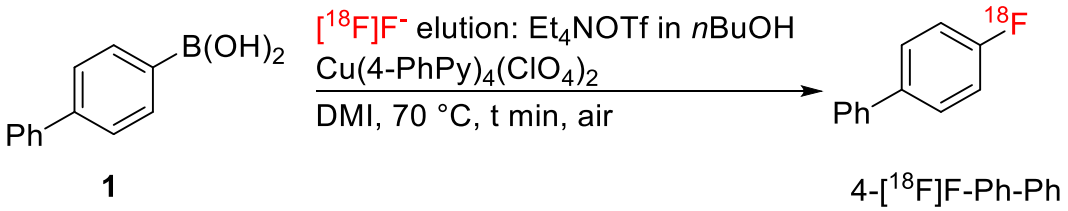

Table S39: Screening of reaction times at 70 °C.

Entry	t [min]	RCC [%]
1	5	35 ± 5
2	10	54 ± 5
3	20	75 ± 3
4	30	82 ± 1
5	40	80 ± 5

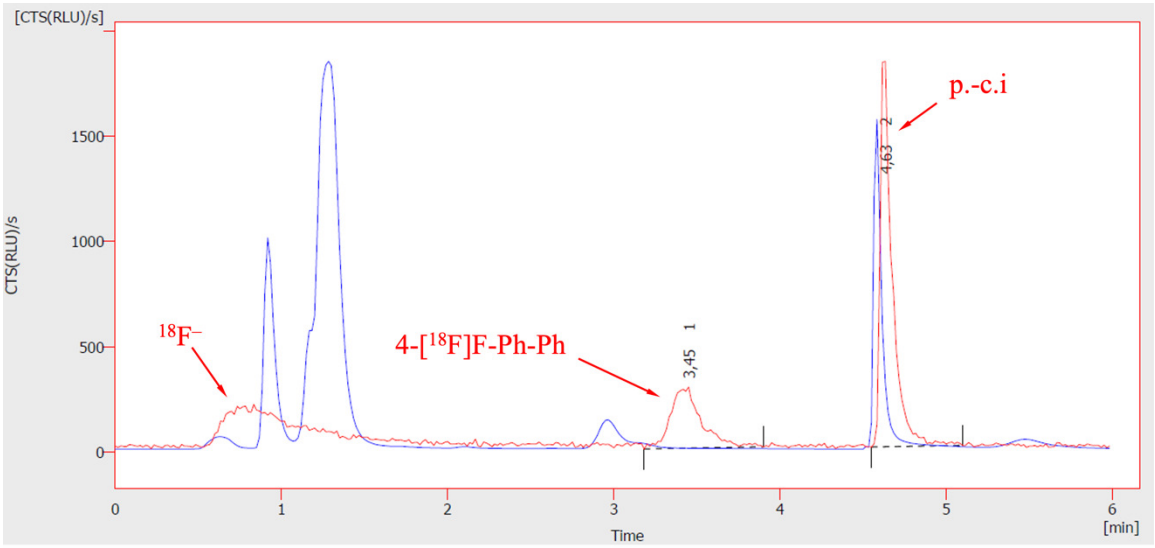

Result Table (Uncal - Data|alc-enhanced_762_12_05_2022_[4 DMI]biphenyl-B(OH)2_70°C_5min - HERM)

	Reten. Time [min]	Area [CTS(RLU)/s.s]	Height [CTS(RLU)/s]	Area [%]
1	3,450	3775,500	290,907	28,7
2	4,633	9400,500	1829,939	71,3
	Total	13176,000	2120,846	100,0

Figure S31: HPLC traces of crude 4-[^{18}F]F-Ph-Ph prepared from **1** using Cu(4-PhPy)$_4$(ClO$_4$)$_2$ as mediator in *n*BuOH/DMI at 70 °C for 5 min. Blue trace: UV, λ = 254 nm; red trace: radioactivity. Abbreviation: p.-c.i – post-column injection.

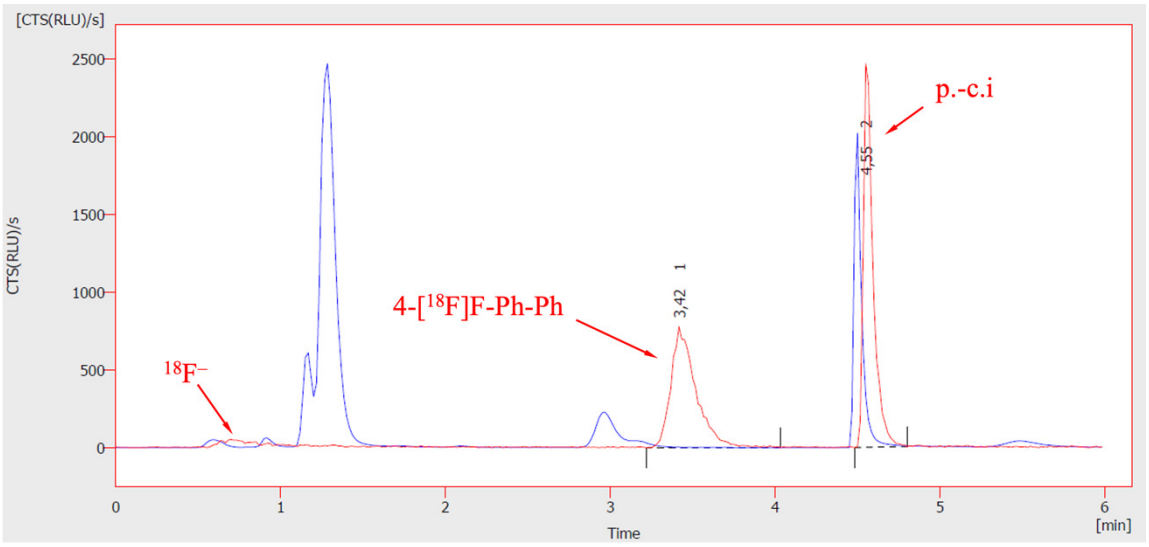

Result Table (Uncal - Data|alc-enhanced_675_08_04_2022_[4 DMI]biphenyl-B(OH)2_70_20min - HERM)

	Reten. Time [min]	Area [CTS(RLU)/s.s]	Height [CTS(RLU)/s]	Area [%]
1	3,417	8122,000	778,000	44,2
2	4,550	10250,500	2469,947	55,8
	Total	18372,500	3247,947	100,0

Figure S32: HPLC traces of crude 4-[^{18}F]F-Ph-Ph prepared from **1** using Cu(4-PhPy)$_4$(ClO$_4$)$_2$ as mediator in *n*BuOH/DMI at 70 °C for 20 min. Blue trace: UV, λ = 254 nm; red trace: radioactivity. Abbreviation: p.-c.i – post-column injection.

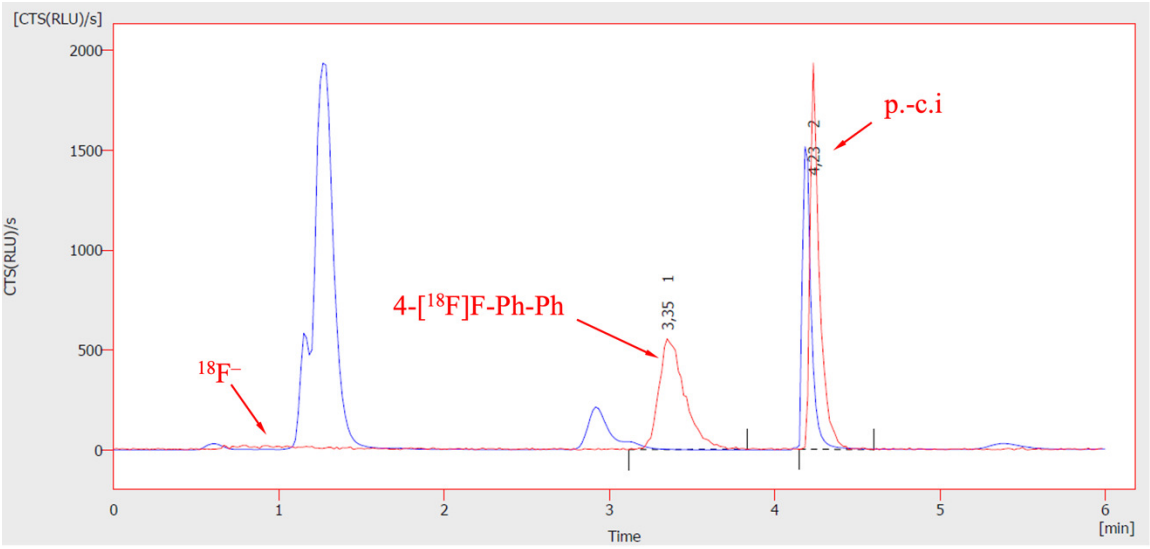

Result Table (Uncal - Data|alc-enhanced_712_14_04_2022_[4 DMI]biphenyl-B(OH)2_70°C_40min - HERM)

	Reten. Time [min]	Area [CTS(RLU)/s.s]	Height [CTS(RLU)/s]	Area [%]
1	3,350	6062,000	553,349	44,4
2	4,233	7591,000	1931,370	55,6
	Total	13653,000	2484,719	100,0

Figure S33: HPLC traces of crude 4-[^{18}F]F-Ph-Ph prepared from **1** using Cu(4-PhPy)$_4$(ClO$_4$)$_2$ as mediator in *n*BuOH/DMI at 70 °C for 30 min. Blue trace: UV, λ = 254 nm; red trace: radioactivity. Abbreviation: p.-c.i – post-column injection.

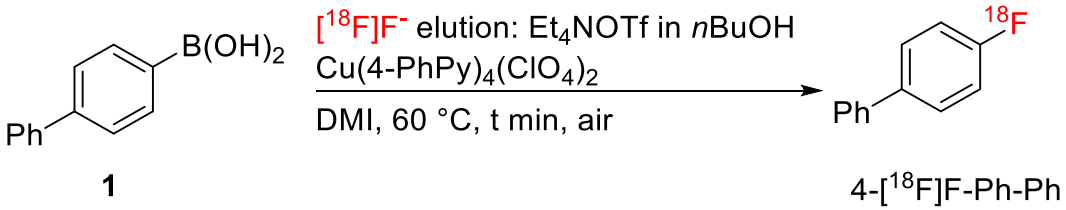

Table S40: Screening of reaction times at 60 °C.

Entry	t [min]	RCC [%]
1	5	13 ± 6
2	10	37 ± 7
3	20	40 ± 15
4	30	66 ± 8
5	40	69 ± 8

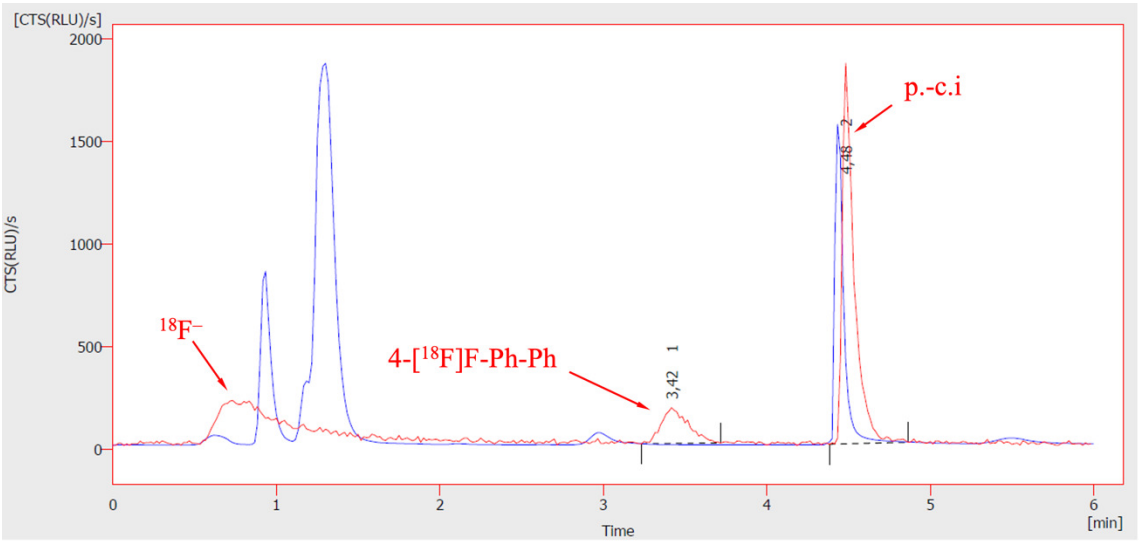

Result Table (Uncal - Data\alc-enhanced_760_12_05_2022_[4 DMI]biphenyl-B(OH)2_60°C_5min - HERM)

	Reten. Time [min]	Area [CTS(RLU)/s.s]	Height [CTS(RLU)/s]	Area [%]
1	3,417	1993,000	174,483	17,4
2	4,483	9441,500	1854,138	82,6
	Total	11434,500	2028,621	100,0

Figure S34: HPLC traces of crude 4-[^{18}F]F-Ph-Ph prepared from **1** using Cu(4-PhPy)$_4$(ClO$_4$)$_2$ as mediator in *n*BuOH/DMI at 60 °C for 5 min. Blue trace: UV, λ = 254 nm; red trace: radioactivity. Abbreviation: p.-c.i – post-column injection.

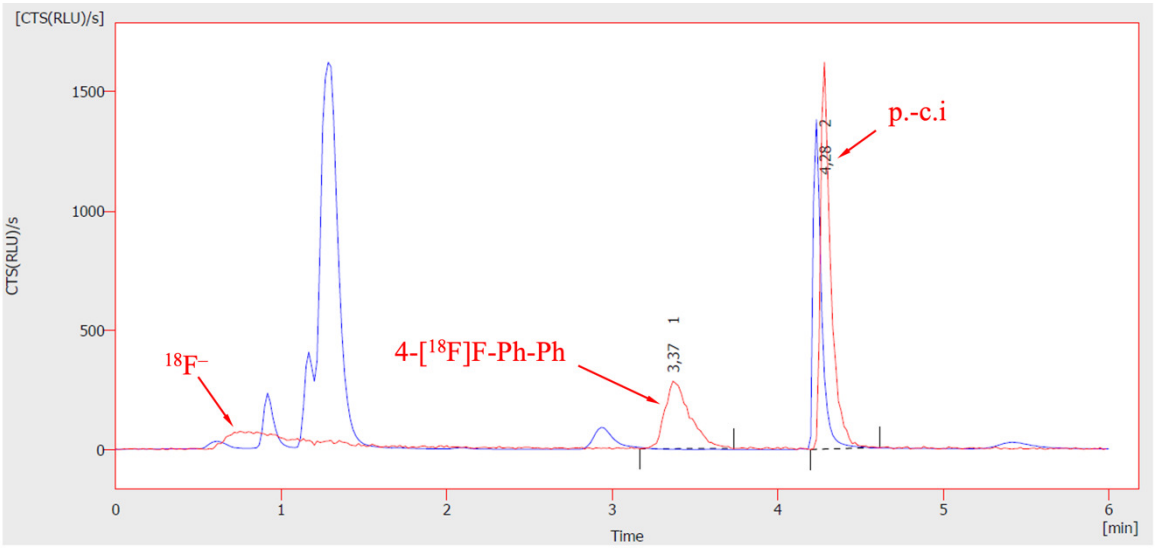

Result Table (Uncal - Data\alc-enhanced_687_08_04_2022_[4 DMI]biphenyl-B(OH)2_60°C_20min - HERM)

	Reten. Time [min]	Area [CTS(RLU)/s.s]	Height [CTS(RLU)/s]	Area [%]
1	3,367	3005,000	283,647	29,9
2	4,283	7052,000	1621,400	70,1
	Total	10057,000	1905,047	100,0

Figure S35: HPLC traces of crude 4-[^{18}F]F-Ph-Ph prepared from **1** using Cu(4-PhPy)$_4$(ClO$_4$)$_2$ as mediator in *n*BuOH/DMI at 60 °C for 20 min. Blue trace: UV, λ = 254 nm; red trace: radioactivity. Abbreviation: p.-c.i – post-column injection.

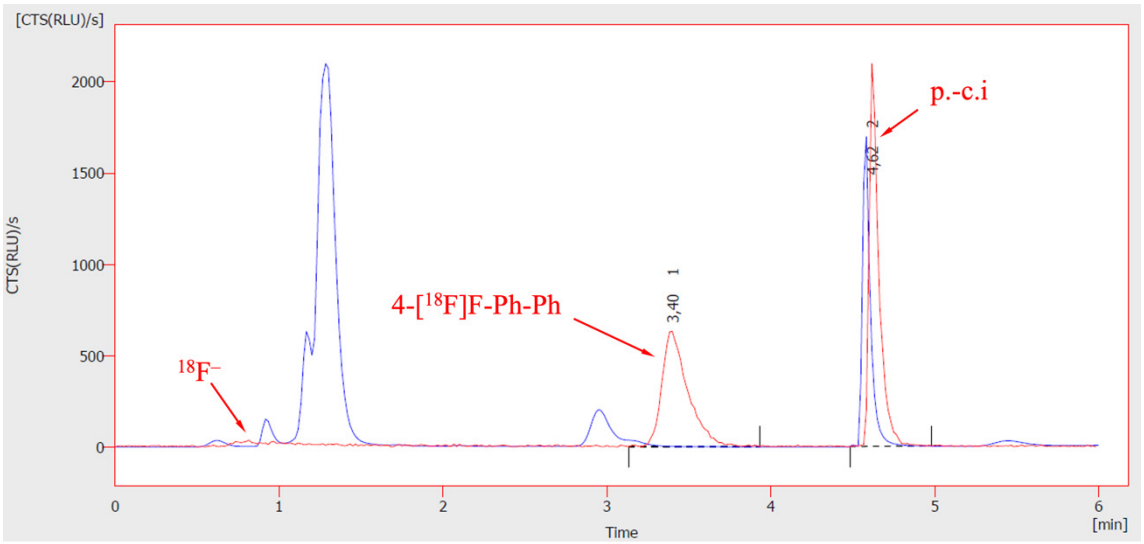

Result Table (Uncal - Data|alc-enhanced_710_14_04_2022_[4 DMI]biphenyl-B(OH)2_60°C_40min - HERM)

	Reten. Time [min]	Area [CTS(RLU)/s.s]	Height [CTS(RLU)/s]	Area [%]
1	3,400	7010,000	630,333	44,6
2	4,617	8693,000	2096,200	55,4
	Total	15703,000	2726,533	100,0

Figure S36: HPLC trace of crude 4-[^{18}F]F-Ph-Ph prepared from **1** using Cu(4-PhPy)$_4$(ClO$_4$)$_2$ as mediator in *n*BuOH/DMI at 60 °C for 40 min. Blue trace: UV, λ = 254 nm; red trace: radioactivity. Abbreviation: p.-c.i – post-column injection.

3.8 Radiolabeling of model stannyl precursors 5 and 6

Screening of radiofluorination mediator

Radiolabeling of stannyl precursors **5** and **6** was performed according to GP6-A in *n*BuOH/DMI (n = 3). RCCs were determined by radio-HPLC as described above.

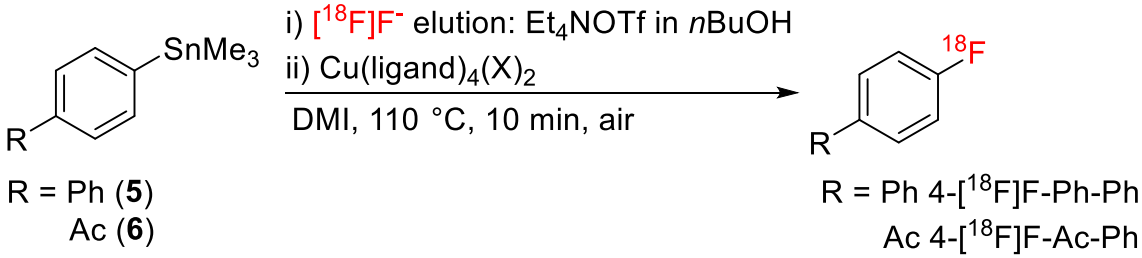

Table S41: Screening of radiofluorination mediators.

			RCC [%]	
Entry	**Ligand**	**X**	**5**	**6**
1	Py	OTf	27 ± 8	22 ± 5
2	4-PhPy	ClO_4	26 ± 8	44 ± 3
3	3,4-Me_2Py	OTf	25 ± 6	31 ± 9
4	3,4-Me_2Py	ClO_4	24 ± 1	41 ± 5
5	Impdz	OTf	16 ± 2	26 ± 3
6	Impdz	ClO_4	28 ± 6	41 ± 3

Optimization of radiolabeling of stannyl precursors 5 and 6 with regard to the presence/absence of *n*BuOH and reaction atmosphere

Radiosyntheses were performed according to GP6-B, GP7-A and GP7-B with Cu(4-PhPy)$_4$(ClO$_4$)$_2$ in DMI (n=3). RCCs were determined by radio-HPLC as described above. Representative HPLC chromatograms of the crude radiolabeled products are shown in Figure **S37**–**S42**.

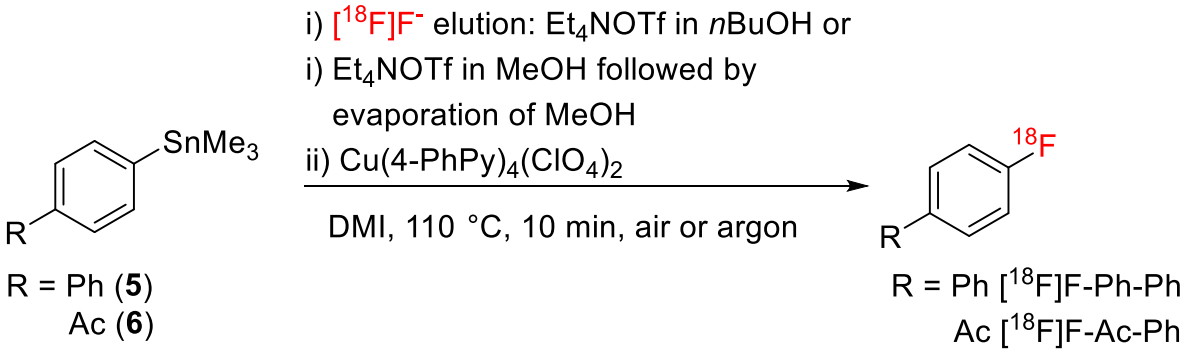

Table S42: Influence of *n*BuOH and reaction atmosphere on radiolabeling of **5** and **6**.

Entry	**Precursor**	**Elution**	**Conditions**	**RCC [%]**
1	**5**	*n*BuOH	argon	22 ± 6
2		MeOH	air	38 ± 2
3		MeOH	argon	57 ± 3
4	**6**	*n*BuOH	argon	33 ± 11
5		MeOH	air	45 ± 3
6		MeOH	argon	47 ± 6

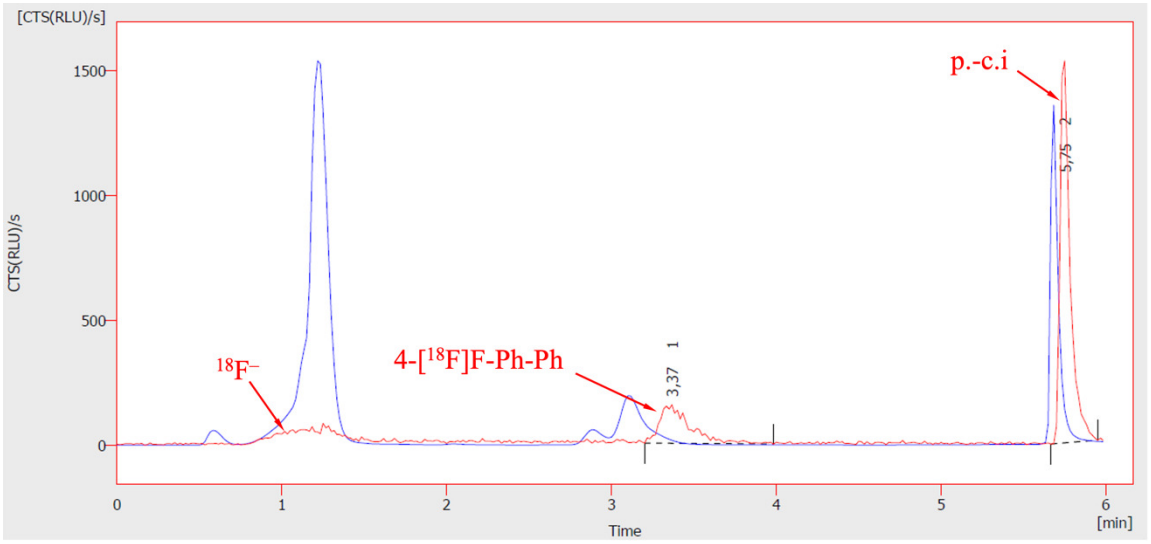

Result Table (Uncal - Data|alc-enhanced_372_24_11_2021_[4 DMI]_biphenyl-SnMe3_nBuOH_argon_110 - HERM)

	Reten. Time [min]	Area [CTS(RLU)/s.s]	Height [CTS(RLU)/s]	Area [%]
1	3,367	2017,000	154,851	23,4
2	5,750	6604,000	1529,294	76,6
	Total	8621,000	1684,145	100,0

Figure S37: HPLC traces of crude 4-[^{18}F]F-Ph-Ph prepared from **5** using Cu(4-PhPy)$_4$(ClO$_4$)$_2$ as mediator in *n*BuOH/DMI at 110 °C for 10 min under Ar. Blue trace: UV, λ = 254 nm; red trace: radioactivity. Abbreviation: p.-c.i – post-column injection.

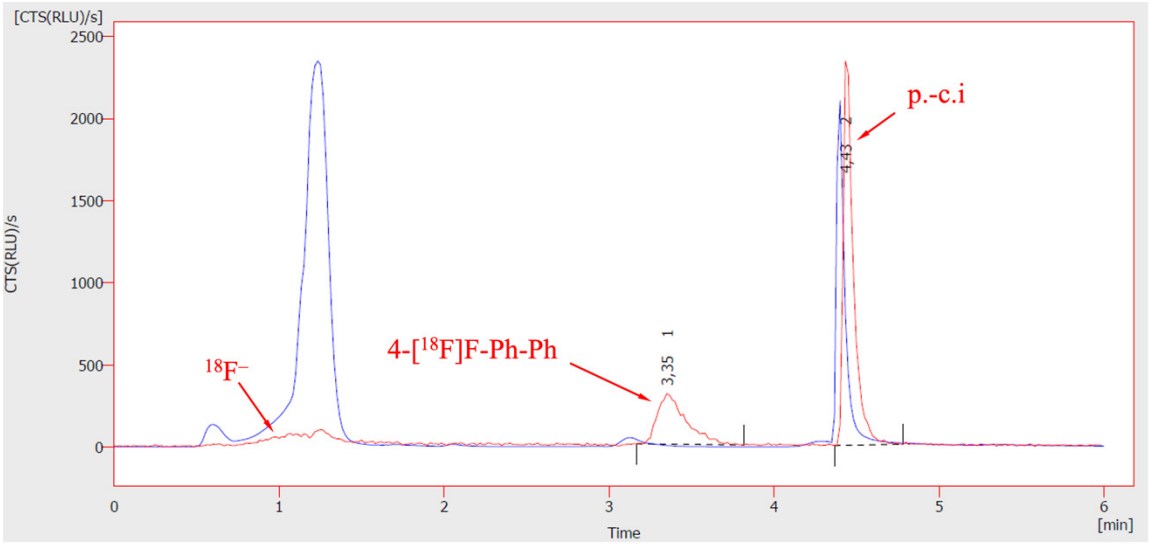

Result Table (Uncal - Data|alc-enhanced_369_24_11_2021_[4 DMI]_biphenyl-SnMe3_MeOH_air_110 - HERM)

	Reten. Time [min]	Area [CTS(RLU)/s.s]	Height [CTS(RLU)/s]	Area [%]
1	3,350	3746,000	308,256	26,9
2	4,433	10203,500	2340,880	73,1
	Total	13949,500	2649,136	100,0

Figure S38: HPLC traces of crude 4-[^{18}F]F-Ph-Ph prepared from **5** using Cu(4-PhPy)$_4$(ClO$_4$)$_2$ as mediator in DMI at 110 °C for 10 min under air. Blue trace: UV, λ = 254 nm; red trace: radioactivity. Abbreviation: p.-c.i – post-column injection.

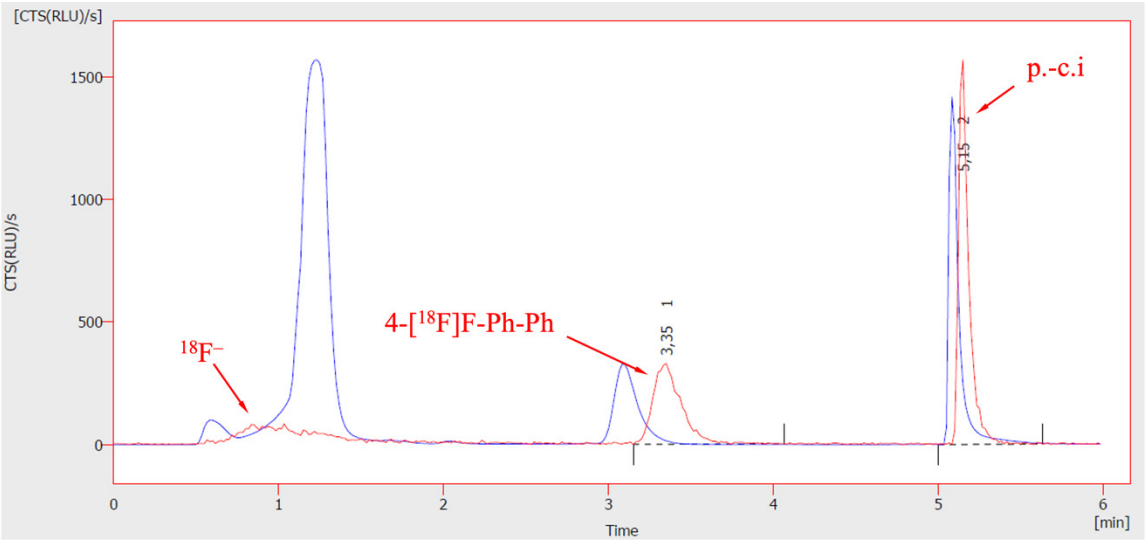

Result Table (Uncal - Data|alc-enhanced_332_03_11_2021_[4 DMI]_biphenyl-Sn(Me)3_argon - HERM)

	Reten. Time [min]	Area [CTS(RLU)/s.s]	Height [CTS(RLU)/s]	Area [%]
1	3,350	3970,000	329,564	36,5
2	5,150	6914,000	1569,526	63,5
	Total	10884,000	1899,090	100,0

Figure S39: HPLC traces of crude 4-[^{18}F]F-Ph-Ph prepared from **5** using Cu(4-PhPy)$_4$(ClO$_4$)$_2$ as mediator in DMI at 110 °C for 10 min under Ar. Blue trace: UV, λ = 254 nm; red trace: radioactivity. Abbreviation: p.-c.i – post-column injection.

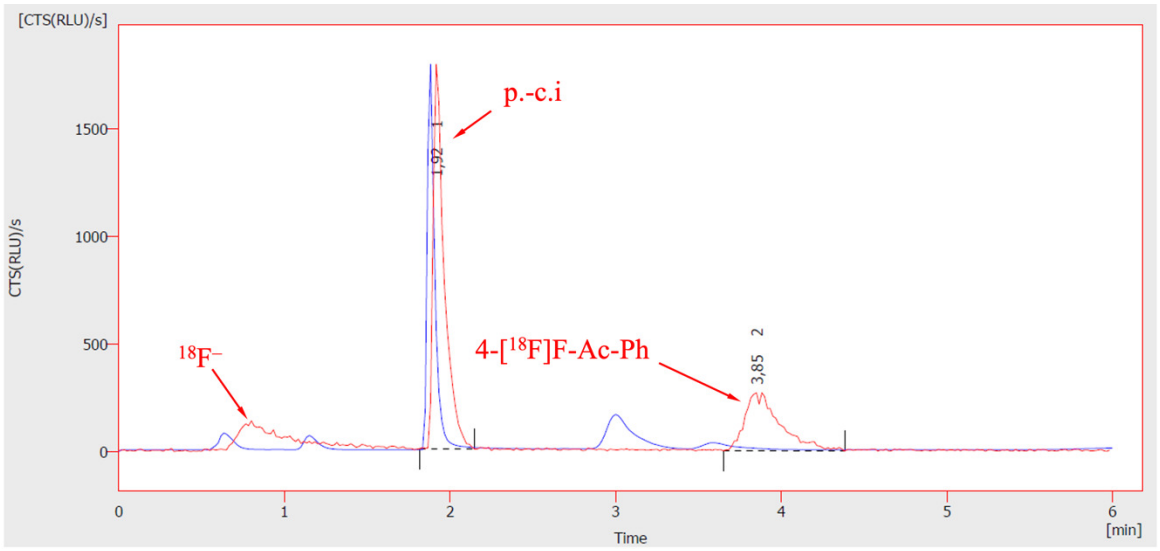

Result Table (Uncal - Data|alc-enhanced_351_16_11_2021_[4 DMI]_4-acetylphenyl-SnMe3_argon_nBuOH - HERM)

	Reten. Time [min]	Area [CTS(RLU)/s.s]	Height [CTS(RLU)/s]	Area [%]
1	1,917	8384,000	1788,300	67,7
2	3,850	4005,000	269,273	32,3
	Total	12389,000	2057,573	100,0

Figure S40: HPLC traces of crude 4-[^{18}F]F-Ac-Ph prepared from **6** using Cu(4-PhPy)$_4$(ClO$_4$)$_2$ as mediator in nBuOH/DMI at 110 °C for 10 min under argon. Blue trace: UV, λ = 254 nm; red trace: radioactivity. Abbreviation: p.-c.i – post-column injection.

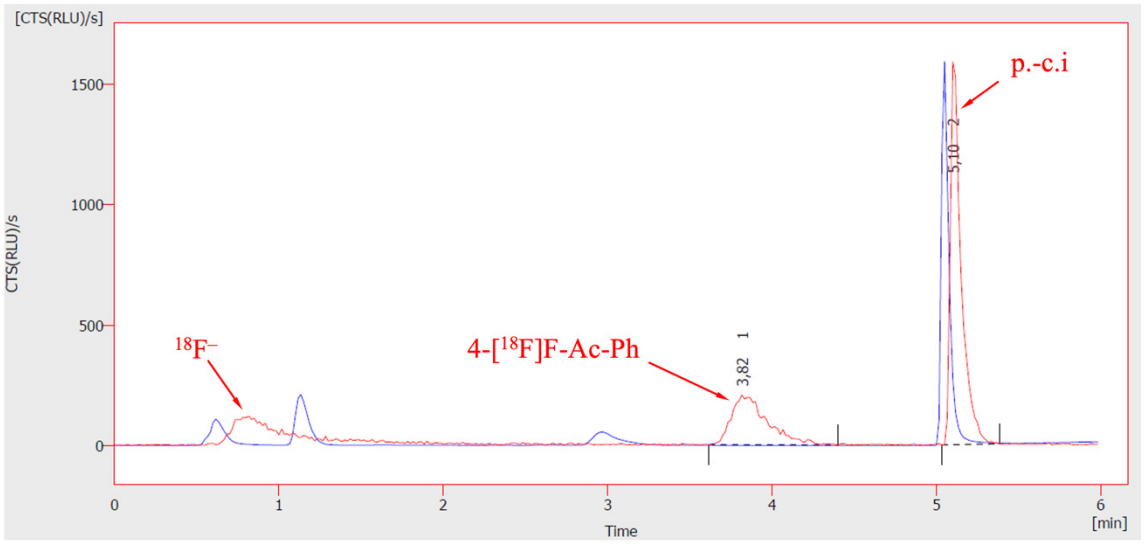

Result Table (Uncal - Data|alc-enhanced_344_15_11_2021_[4 DMI]_4-acetylphenyl-SnMe3_air_MeOH_evap - HERM)

	Reten. Time [min]	Area [CTS(RLU)/s.s]	Height [CTS(RLU)/s]	Area [%]
1	3,817	3147,000	207,511	29,9
2	5,100	7390,000	1590,238	70,1
	Total	10537,000	1797,749	100,0

Figure S41: HPLC traces of crude 4-[^{18}F]F-Ac-Ph prepared from **6** using Cu(4-PhPy)$_4$(ClO$_4$)$_2$ as mediator in DMI at 110 °C for 10 min under air. Blue trace: UV, λ = 254 nm; red trace: radioactivity. Abbreviation: p.-c.i – post-column injection.

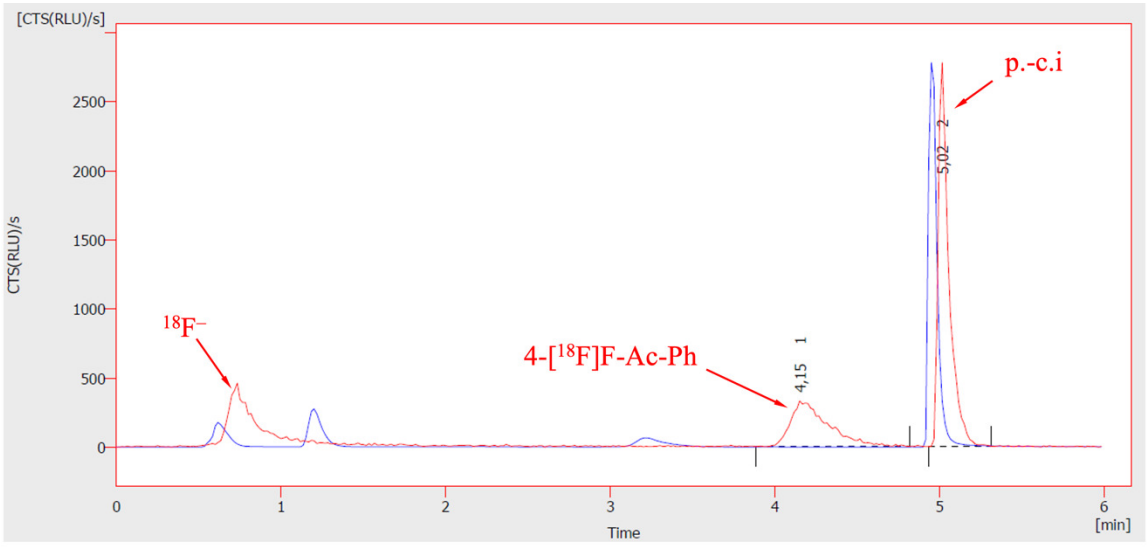

Result Table (Uncal - Data|alc-enhanced_336_05_11_2021_[4 DMI]_4-acetylphenyl-Sn(Me)3_argon - HERM)

	Reten. Time [min]	Area [CTS(RLU)/s.s]	Height [CTS(RLU)/s]	Area [%]
1	4,150	5188,000	331,143	29,0
2	5,017	12719,500	2778,783	71,0
	Total	17907,500	3109,925	100,0

Figure S42: HPLC traces of crude 4-[^{18}F]F-Ac-Ph prepared from **6** using Cu(4-PhPy)$_4$(ClO$_4$)$_2$ as mediator in DMI at 110 °C for 10 min under argon. Blue trace: UV, λ = 254 nm; red trace: radioactivity. Abbreviation: p.-c.i. – post-column injection.

Radiolabeling of stannanes 5 and 6 under optimized conditions

Radiolabeling of stannyl precursors **5** and **6** was performed according to GP7-B with Cu(4-PhPy)$_4$(ClO$_4$)$_2$ in DMI at 90 °C for 10 min (n=3). RCCs were determined by radio-HPLC as described above. Representative radio-HPLC chromatograms of radiolabeled products are shown in Figure **S43** and Figure **S44**.

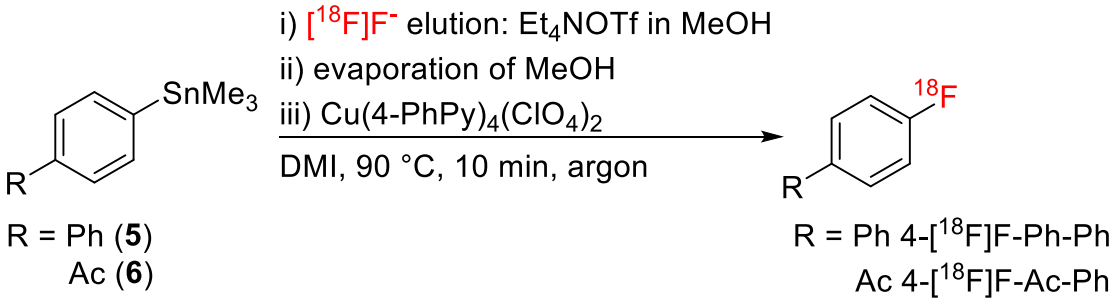

Table S43: Radiolabeling of stannyl precursors under optimized conditions.

Entry	Precursor	RCC [%]
1	**5**	60 ± 6
2	**6**	63 ± 10

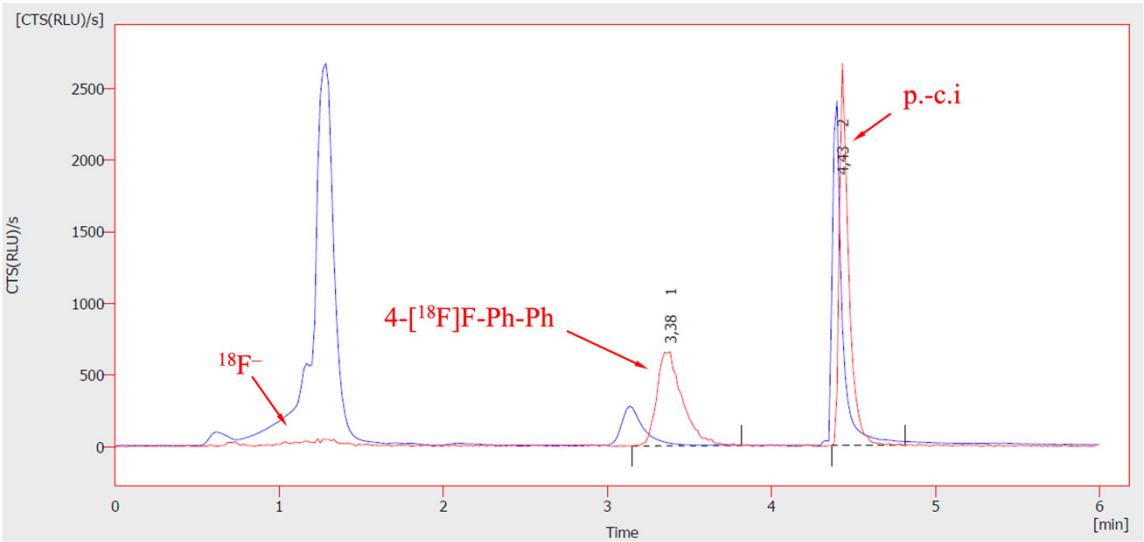

Result Table (Uncal - Data\alc-enhanced_576_02_03_2022_[4 DMI]biphenyl-SnMe3_90°C_argon_MeOH - HERM)

	Reten. Time [min]	Area [CTS(RLU)/s.s]	Height [CTS(RLU)/s]	Area [%]
1	3,383	7179,000	656,950	40,4
2	4,433	10597,000	2665,000	59,6
	Total	17776,000	3321,950	100,0

Figure S43: HPLC traces of crude 4-[^{18}F]F-Ph-Ph prepared from **5** using Cu(4-PhPy)$_4$(ClO$_4$)$_2$ as mediator in DMI at 90 °C for 10 min under argon. Blue trace: UV, λ = 254 nm; red trace: radioactivity. Abbreviation: p.-c.i. – post-column injection.

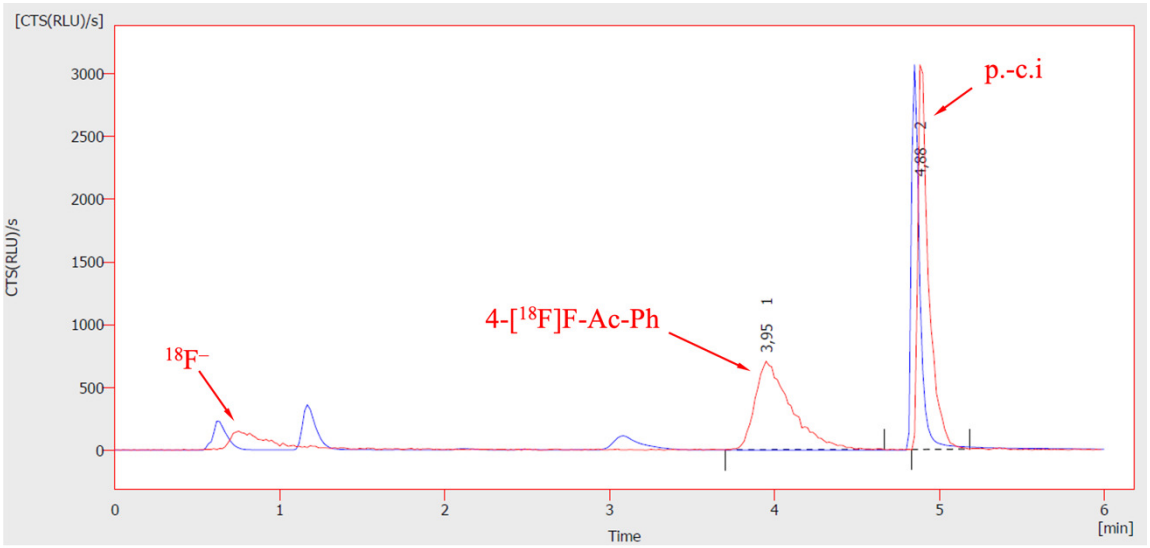

Result Table (Uncal - Data\alc-enhanced_353_19_11_2021_[4 DMI]_4-acetylphenyl-SnMe3_90_MeOH_argon - HERM)

	Reten. Time [min]	Area [CTS(RLU)/s.s]	Height [CTS(RLU)/s]	Area [%]
1	3,950	10640,000	705,224	43,2
2	4,883	14008,500	3067,286	56,8
	Total	24648,500	3772,510	100,0

Figure S44: HPLC traces of crude 4-[^{18}F]F-Ac-Ph prepared from **6** using Cu(4-PhPy)$_4$(ClO$_4$)$_2$ as mediator in DMI at 90 °C for 10 min under argon. Blue trace: UV, λ = 254 nm; red trace: radioactivity. Abbreviation: p.-c.i. – post-column injection.

Statistical evaluation of the influence of *n*BuOH, reaction atmosphere and temperature on radiolabeling of stannyl precursors 5 and 6

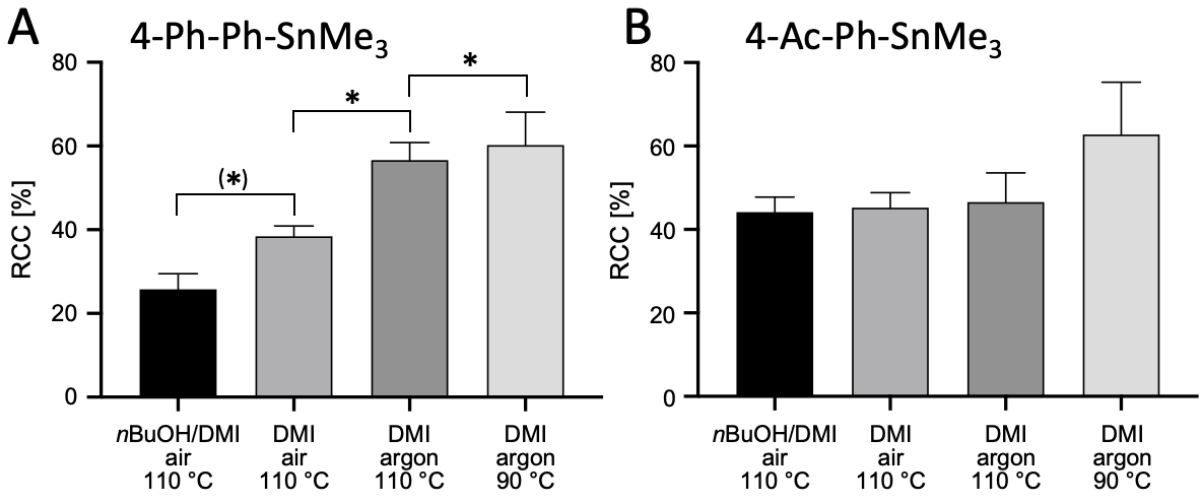

Figure S45: Statistical evaluation of the influence of *n*BuOH, reaction atmosphere and temperature on radiolabeling of stannyl precursors **5** and **6**. Solvent: *n*BuOH/DMI or DMI; radiolabeling mediator: Cu(4-PhPy)$_4$(ClO$_4$)$_2$. Statistics: 1-way ANOVA followed by Tukey's multiple comparison test. * $p<0.05$; (*) $p=0.0552$

Table S44: Comparison of RCCs (mean ± standard deviation in %) under different reaction conditions using 1-way ANOVA followed by Tukey's multiple comparison test (n=3 per group). Solvent: DMI; radiolabeling mediator: $Cu(4\text{-}PhPy)_4(ClO_4)_2$. p-values refer to the respective previous condition.

		atmosph.	temp.	RCCs [%]	
4-Ph-Ph-$SnMe_3$	nBuOH	air	110 °C	25.7 ± 3.69	
F(3,8)=31.43	MeOH	air	110 °C	38.46 ± 2.45	p=0.0552
p<0.0001	MeOH	argon	110 °C	56.60 ± 4.25	p=0.0091*
	MeOH	argon	90 °C	60.22 ± 7.85	p=0.0031*
4-Ac-Ph-$SnMe_3$	nBuOH	air	110 °C	44.15 ± 3.60	
F(3,8)=31.43	MeOH	air	110 °C	45.25 ± 3.58	p=0.9979
p<0.0001	MeOH	argon	110 °C	46.54 ± 7.01	p=0.9966
	MeOH	argon	90 °C	62.80 ± 12.53	p=0.1145

3.9 Radiosynthesis of [^{18}F]R91150

[^{18}F]F^{-} (30–500 MBq) was eluted from the QMA cartridge with a solution of Et_4NOTf (1 mg, 3.6 µmol) in anhydrous MeOH (500 µL). MeOH was evaporated at 60 °C under reduced pressure in a stream of argon. The reactor was opened, a solution of **7** (6.2 mg, 10 µmol) and $Cu(4\text{-PhPy})_4(ClO_4)_2$ (8.8 mg, 10 µmol) in anhydrous DMI/*n*BuOH (1.2 mL, 2:1) was added and the reaction mixture was heated at 110 °C for 10 min. That followed, the reaction mixture was diluted with H_2O (18 mL) and loaded onto a preconditioned (2 mL EtOH, 10 mL H_2O) HLB short cartridge (300 mg). The cartridge was washed with H_2O (5 mL) and the radiolabeled intermediate was eluted with acetone (2 mL). The acetone was evaporated at 80 °C under reduced pressure in a stream of argon, 6 M HCl (500 µL) was added to the residue and the mixture was heated at 110 °C for 10 min. Thereafter, 6 M NaOH (350 µL) followed by 0.1% TFA (600 µL) were added to the mixture, and the resulting solution was loaded onto a preparative HPLC column. The product fraction was eluted at 7.5–9.0 min.

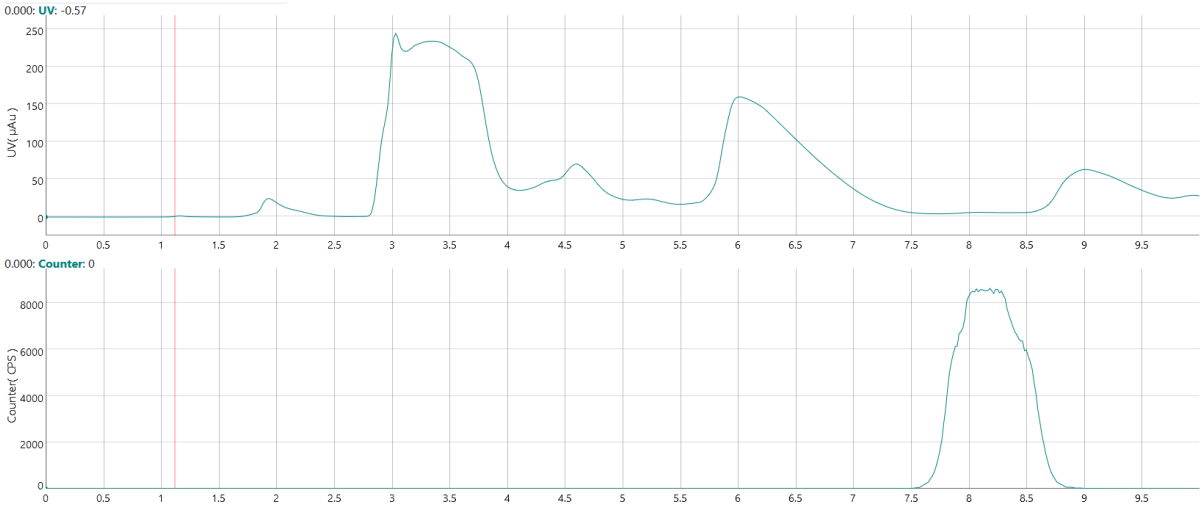

Figure S46: Purification of [^{18}F]R91150 by preparative HPLC (top: UV trace, λ=254 nm; bottom: radioactivity trace).

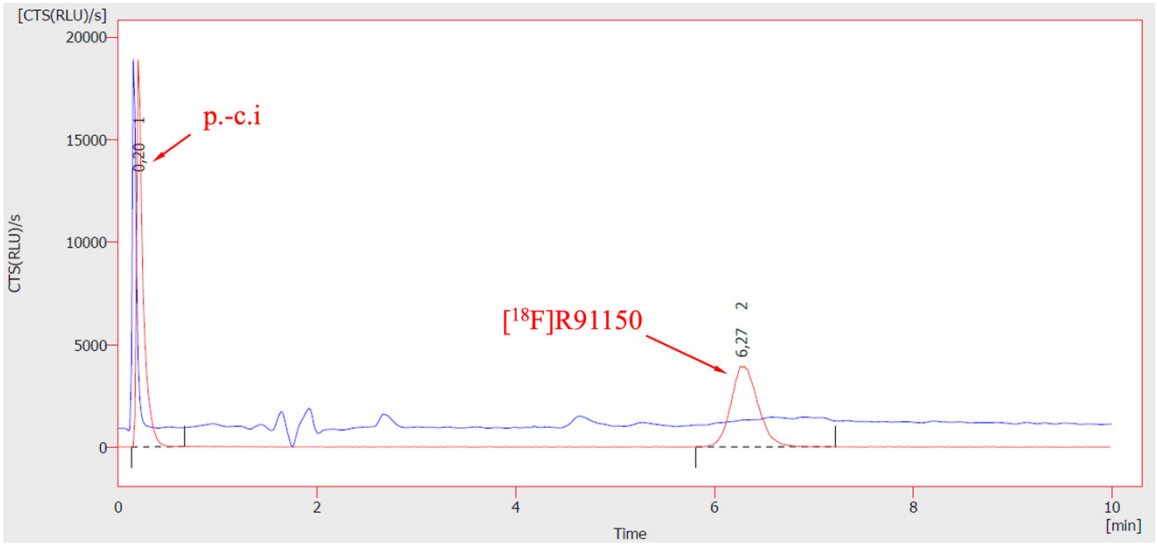

Result Table (Uncal - Data|alc-enhanced_890_08_08_2022_[4 DMI][18F]R91150-Bpin_MeOH_elution_hplc - HERM)

	Reten. Time [min]	Area [CTS(RLU)/s.s]	Height [CTS(RLU)/s]	Area [%]
1	0,200	84242,000	18896,875	52,9
2	6,267	74967,000	3942,786	47,1
	Total	159209,000	22839,661	100,0

Figure S47: HPLC chromatogram of purified [^{18}F]R91150 for quality control. Blue trace: UV channel, λ=254 nm; red trace: radioactivity channel. Abbreviation: p.-c.i. – post-column injection.

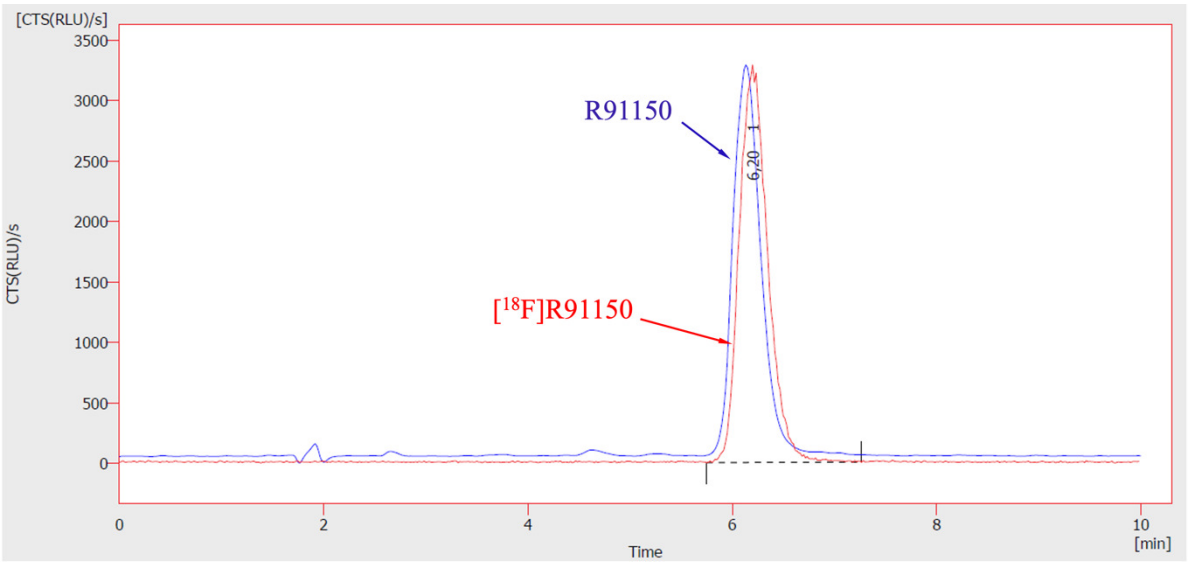

Result Table (Uncal - Data|alc-enhanced_891_08_08_2022_[4 DMI][18F]R91150-Bpin_MeOH_elution_spiked - HERM)

	Reten. Time [min]	Area [CTS(RLU)/s.s]	Height [CTS(RLU)/s]	Area [%]
1	6,200	63849,500	3291,110	100,0
	Total	63849,500	3291,110	100,0

Figure S48: HPLC chromatogram of purified [^{18}F]R91150 spiked with the non-radioactive reference compound. Blue trace: UV channel, λ=254 nm; red trace: radioactivity channel.

3.10 Radiosynthesis of [^{18}F]ALX5407

[^{18}F]F^{-} was eluted from the QMA cartridge directly into a solution of **8** (8.8 mg, 10 µmol) and Cu(4-PhPy)$_4$(ClO$_4$)$_2$ (8.8 mg, 10 µmol) in anhydrous DMI (800 µL) with a solution of Et$_4$NOTf (1 mg) in anhydrous *n*BuOH (400 µL), and the reaction mixture was stirred for 10 min at 110 °C. That followed, 6 M NaOH (250 µL) was added and the mixture was stirred for another 10 min at 110 °C. The reaction mixture was cooled to ambient temperature, diluted with 6 M HCl (400 µL) followed by H$_2$O (20 mL) and loaded onto a Strata-X cartridge. The cartridge was washed with H$_2$O (5 mL) and the crude [^{18}F]ALX5407 was eluted with MeCN (500 µL). The resulting solution was diluted with 0.1% AcOH (1 mL) and loaded onto a preparative HPLC column. The product fraction, which eluted at 20.5–22.5 min, was taken up into H$_2$O (100 mL) and loaded onto a Strata-X cartridge. The cartridge was washed with H$_2$O (5 mL) and dried for 2 min in a flow of argon. [^{18}F]ALX5407 was eluted with EtOH (800 µL), and the solvent was removed under reduced pressure at 70 °C. The residue was taken up into a sterile filtered 1% Tween 80 solution (500 µL) to afford [^{18}F]ALX5407 in a ready-to-use form.

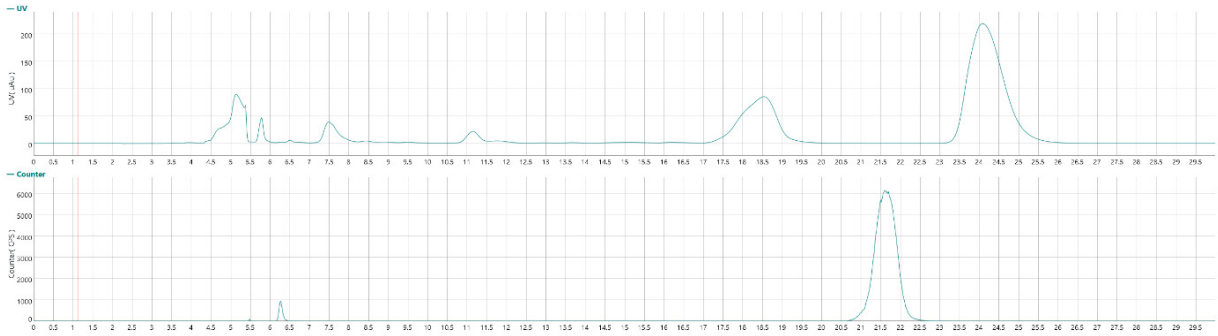

Figure S49: Purification of [^{18}F]ALX5407 by preparative HPLC (top: UV trace, λ=254 nm; bottom: radioactivity trace).

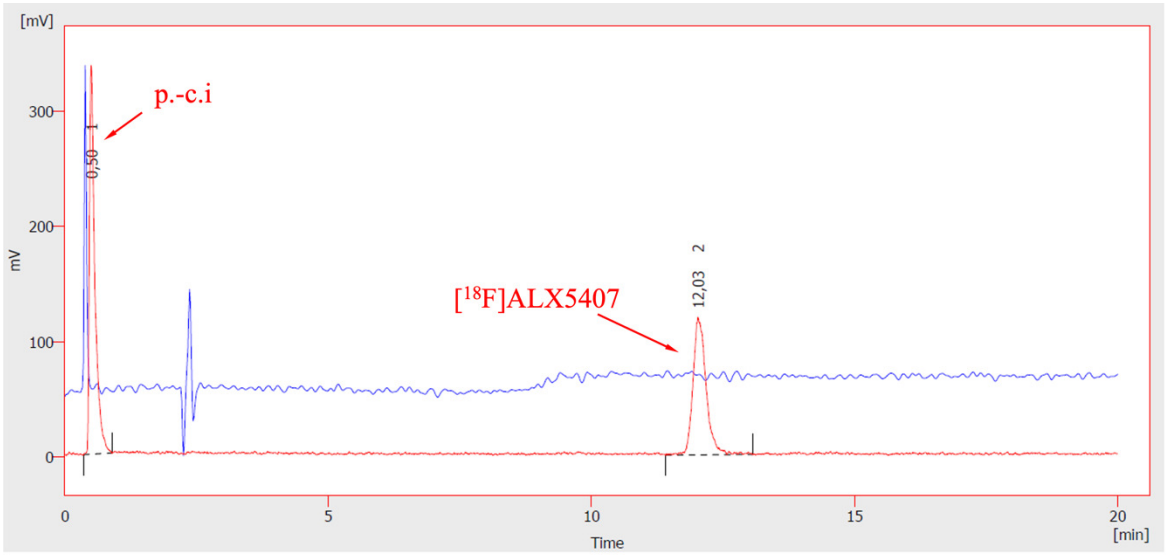

Result Table (Uncal - Data|alc-enhanced_205_23_06_2021_[4 DMI]_[18F]ALX5407_radio_purity - IF2/IFU2.1:Channel 1)

	Reten. Time [min]	Area [mV.s]	Height [mV]	Area [%]
1	0,498	2455,282	336,988	54,1
2	12,025	2081,980	119,362	45,9
	Total	4537,262	456,350	100,0

Figure S50: HPLC chromatogram of purified [^{18}F]ALX5407 for quality control. Blue trace: UV channel, λ=254 nm; red trace: radioactivity channel. Abbreviation: p.-c.i. – post-column injection.

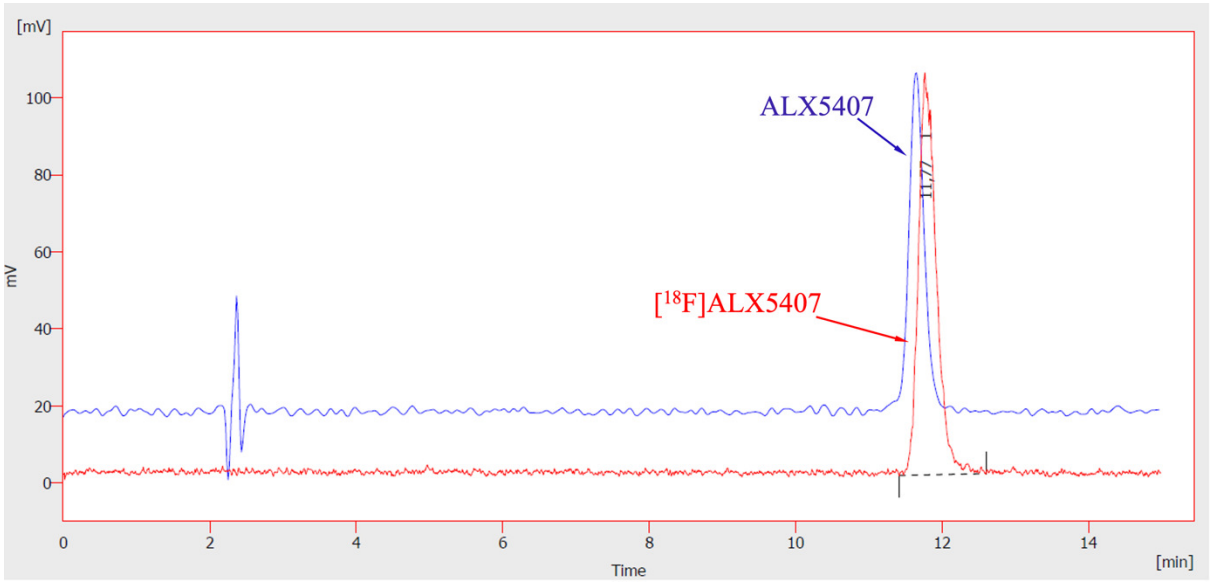

Result Table (Uncal - Data|alc-enhanced_206_23_06_2021_[4 DMI]_[18F]ALX5407_gespiked - IF2/IFU2.1:Channel 1)

	Reten. Time [min]	Area [mV.s]	Height [mV]	Area [%]
1	11,767	1766,430	104,502	100,0
	Total	1766,430	104,502	100,0

Figure S51: HPLC chromatogram of purified [^{18}F]ALX5407 spiked with the non-radioactive reference compound. Blue trace: UV channel, λ=254 nm; red trace: radioactivity channel.

3.11 Radiosynthesis of [^{18}F]MNI1126

[^{18}F]F^{-} was eluted from the QMA cartridge into a reaction vial with a solution of Et_4NOTf (1 mg, 3.6 µmol) in anhydrous MeOH (500 µL) and all volatiles were removed at 80 °C. Thereafter, a solution of **9** (10 µmol) and copper complex (10 µmol) in anhydrous DMI (800 µL) was added, and the reaction mixture was stirred for 10 min at 110 °C (n=3). RCCs were determined by radio-HPLC.

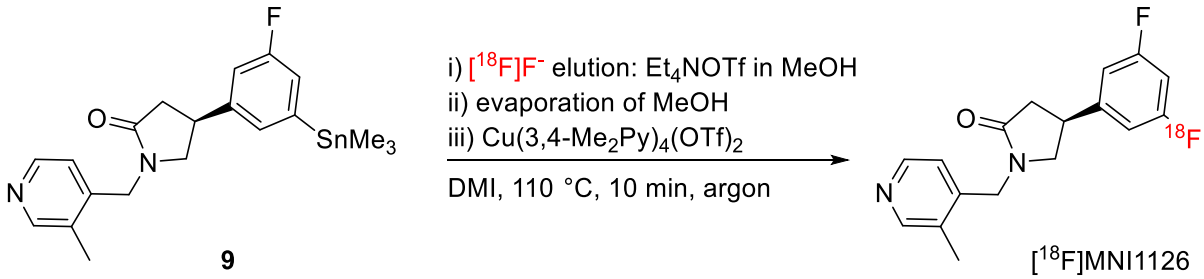

Table S45: Screening of radiolabeling mediator

entry	Cu(II) complex	RCC [%]
1	$Cu(Py)_4(OTf)_2$	26 ± 15
2	$Cu(4\text{-}PhPy)_4(ClO_4)_2$	34 ± 10
3	$Cu(3,4\text{-}Me_2Py)_4(OTf)_2$	47 ± 5
4	$Cu(3,4\text{-}Me_2Py)_4(ClO_4)_2$	37 ± 7

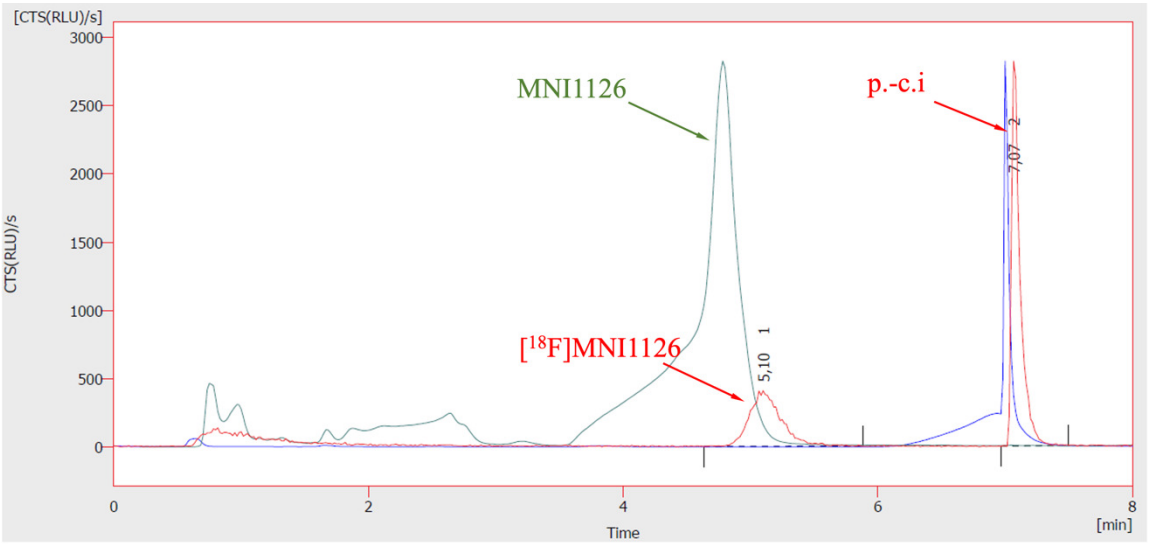

Result Table (Uncal - Data\alc-enhanced_844_14_07_2022_[4 DMI]MNI1126-SnMe3 - HERM)

	Reten. Time [min]	Area [CTS(RLU)/s.s]	Height [CTS(RLU)/s]	Area [%]	RCC [%]
1	5,100	7116,500	408,627	34,6	100,000
2	7,067	13465,000	2823,500	65,4	189,208
	Total	20581,500	3232,127	100,0	289,208

Figure S52: Overlay of HPLC traces of crude [^{18}F]MNI1126 prepared from **9** using $Cu(4\text{-}PhPy)_4(ClO_4)_2$ as mediator in DMI at 110 °C for 10 min under argon and the corresponding non-radioactive reference compound. Blue trace: UV, λ = 254 nm; green trace: MNI1126; red trace: radioactivity. Abbreviation: p.-c.i. – post-column injection.

3.12 Preparation of 3-[^{18}F]FPhes and (*S*)-αMe-3-[^{18}F]FPhe – General Procedure (GP8)

[^{18}F]F$^-$ was eluted from the QMA cartridge with a solution of Et_4NOTf (1 mg, 3.6 µmol) in anhydrous *n*BuOH (400 µL) into a solution of $B(OH)_2$ or Bpin substituted [Ni(II)-BPB] or [Ni(II)-BPA] complex (10 µmol of each) in the corresponding anhydrous solvent (800 µL). The reaction mixture was heated at 110 °C for 10 min under air. After cooling to ambient temperature, the reaction mixture was diluted with 5 ml H_2O, loaded onto a ChromaFix C18 ec cartridge (preconditioned with 1 mL EtOH and 5 mL H_2O), and washed with H_2O (5 mL). The labeled intermediate was eluted with EtOH (1 mL) and the resulting solution was concentrated under reduced pressure at 80 °C for 5 min in a stream of argon. Thereafter, 2 M HCl (500 µl) was added and the resulting mixture was stirred for another 10 min at 110 °C. After cooling to ambient temperature, the mixture was purified by preparative HPLC. The fraction containing the radiolabeled amino acid was collected and neutralized with $NaHCO_3$ to afford the desired PET tracer in a ready-to-use form.

Radiosynthesis of 3-[^{18}F]FPhes and (*S*)-αMe-3-[^{18}F]FPhe under optimized conditions

Radiosynthesis of 3-[^{18}F]FPhes was performed according to GP8 in *n*BuOH/DMI using Cu(3,4-$Me_2Py)_4(OTf)_2$ as radiolabeling mediator (n=3).

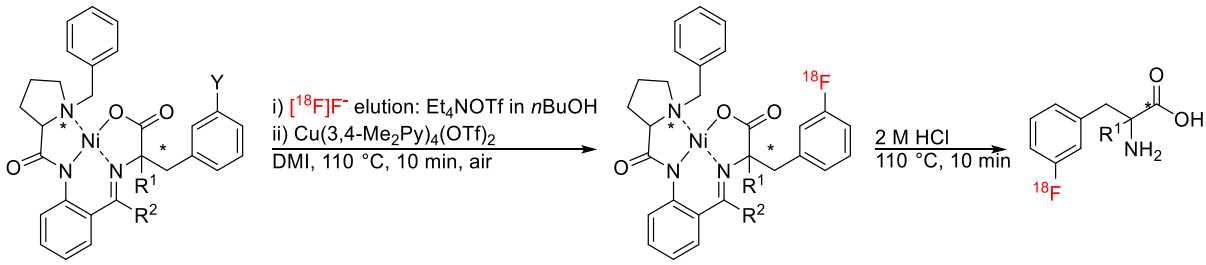

R^1 = H, R^2 = Ph, Y = $B(OH)_2$ [(*S*,*S*)-**10**]
R^1 = H, R^2 = Ph, Y = Bpin [(*S*,*S*)-**11**]

R^1 = H, R^2 = Ph, Y = $B(OH)_2$ [(*R*,*R*)-**10**]
R^1 = H, R^2 = Ph, Y = Bpin [(*R*,*R*)-**11**]

R^1 = Me, R^2 = H, Y = $B(OH)_2$ [(*S*,*S*)-**12**]
R^1 = Me, R^2 = H, Y = Bpin [(*R*,*R*)-**13**]

(*S*)-3-[^{18}F]FPhe

(*R*)-3-[^{18}F]FPhe

(*S*)-αMe-3-[^{18}F]FPhe

Table S46: Radiosynthesis of [^{18}F]FPhes and (*S*)-αMe-3-[^{18}F]FPhe under optimized conditions.

Entry	PET tracer	Y	RCC [%]	AY [%]
1	(*S*)-3-[^{18}F]FPhes	$B(OH)_2$	91 ± 4	41 ± 2
2		Bpin	74 ± 1	
3	(*R*)-3-[^{18}F]FPhes	$B(OH)_2$	78 ± 3	33 ± 0.5
4		Bpin	70 ± 7	
5	(*S*)-αMe-3-[^{18}F]FPhe	$B(OH)_2$	69 ± 11	
6		Bpin	76 ± 2	

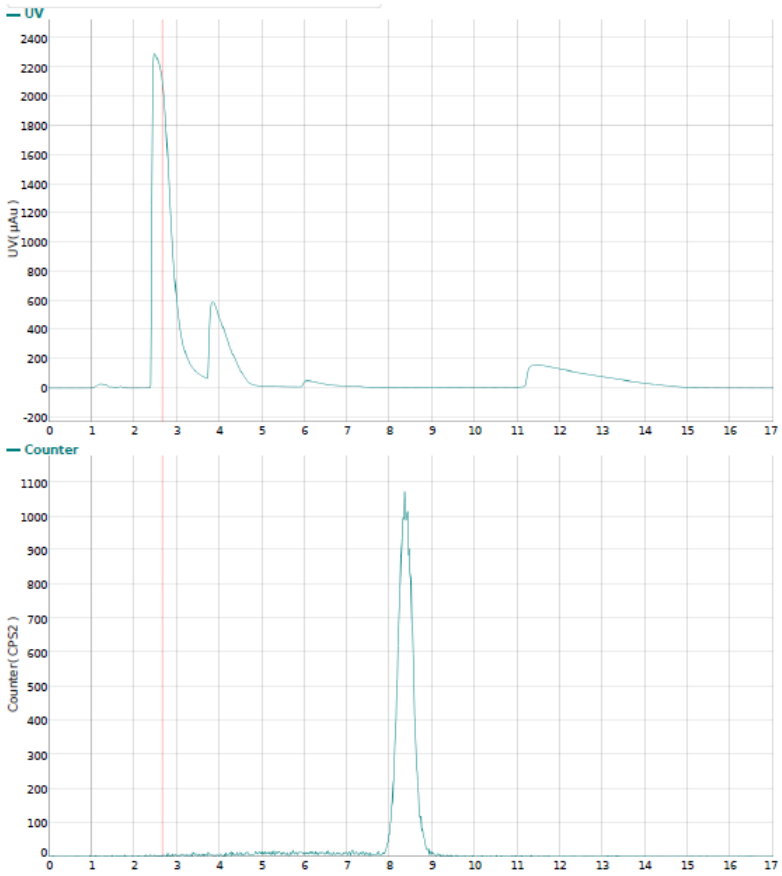

Figure S53: Purification of (*S*)-3-[^{18}F]FPhe by preparative HPLC (top: UV chromatogram, λ=254 nm, bottom: radio-chromatogram).

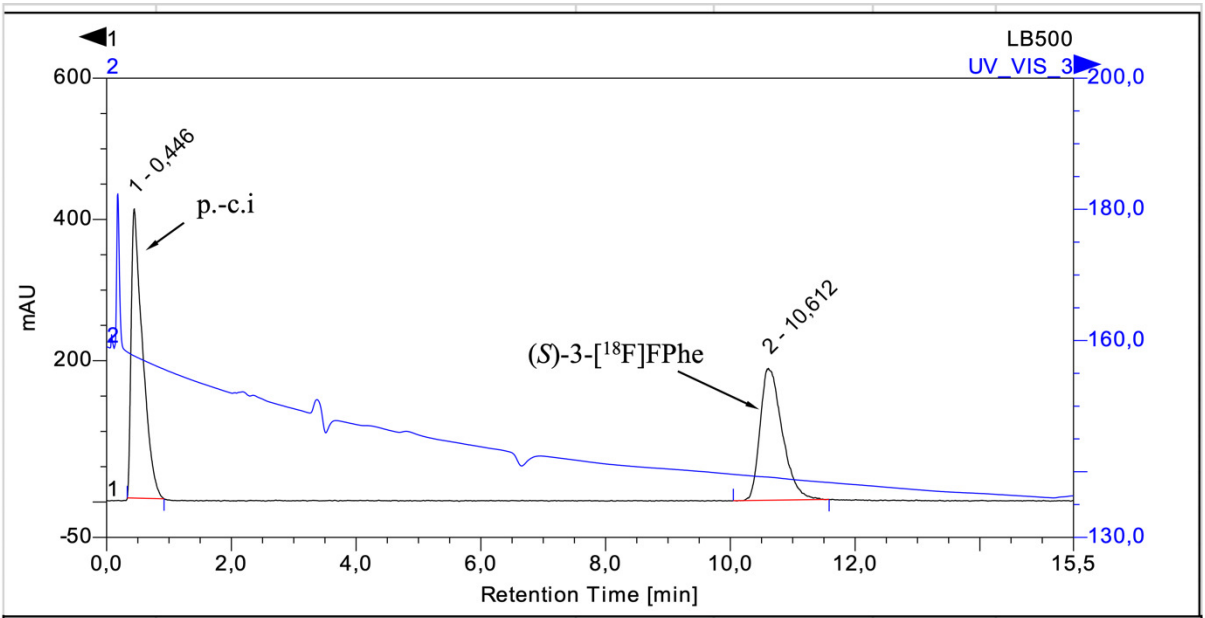

Nr.	R(t)	Intensity	Plates(EP)	Area	Resolution(EP)
	min	mAU		mV*min	
1	0,45	409,415	29	86,525	21,06
2	10,61	186,633	4456	78,819	n.a.

Figure S54: HPLC chromatogram of purified (*S*)-3-[^{18}F]FPhe for quality control. Blue trace: UV channel, λ=254 nm; red trace: radioactivity channel.

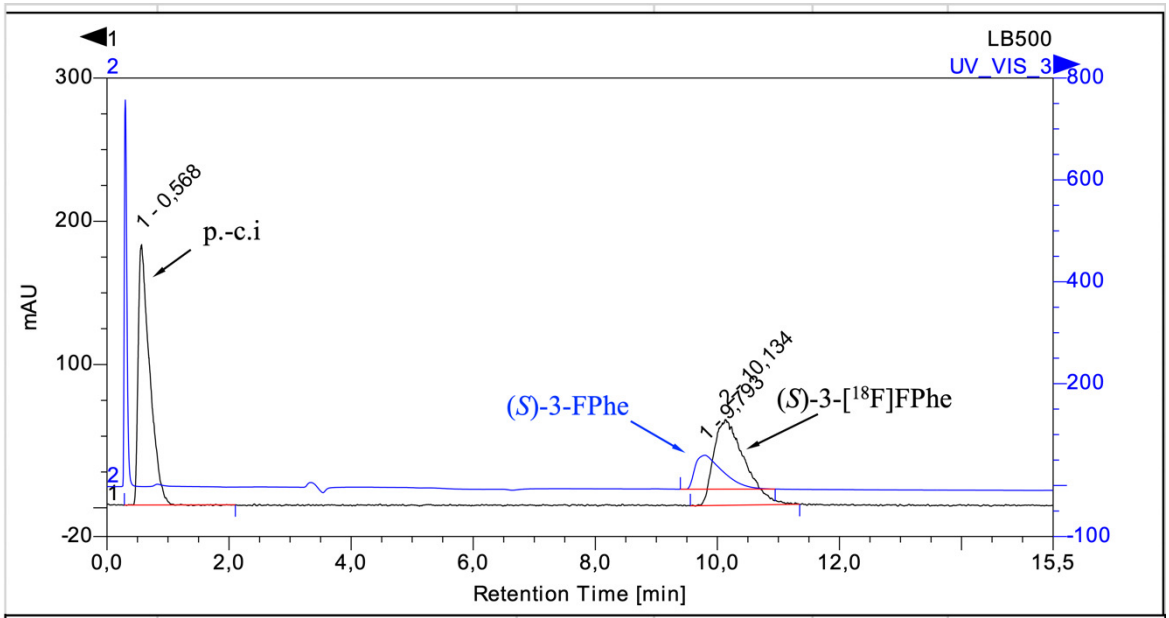

Nr.	R(t)	Intensity	Plates(EP)	Area	Resolution(EP)
	min	mAU		mV*min	
1	0,57	181,798	43	39,482	14,89
2	10,13	59,951	1846	34,966	n.a.

Figure S55: Co-injection of (*S*)-3-[^{18}F]FPhe with the non-radioactive reference compound. Blue trace: UV channel, λ=254 nm; black trace: radioactivity channel.

Determination of carrier amount and molar activity for (*S*)-3-[^{18}F]FPhe

An aliquot of the tracer solution (20 µL) was analyzed by analytical HPLC as described above. The carrier amount was determined from the peak area and the molar activity was calculated according to a calibration curve (Figure **S56**), which was obtained using different concentrations of 3-FPhe (Table **S47**).

$$A_M = \frac{A\ \left[\frac{GBq}{mL}\right]}{c\ \left[\frac{\mu mol}{mL}\right]}$$

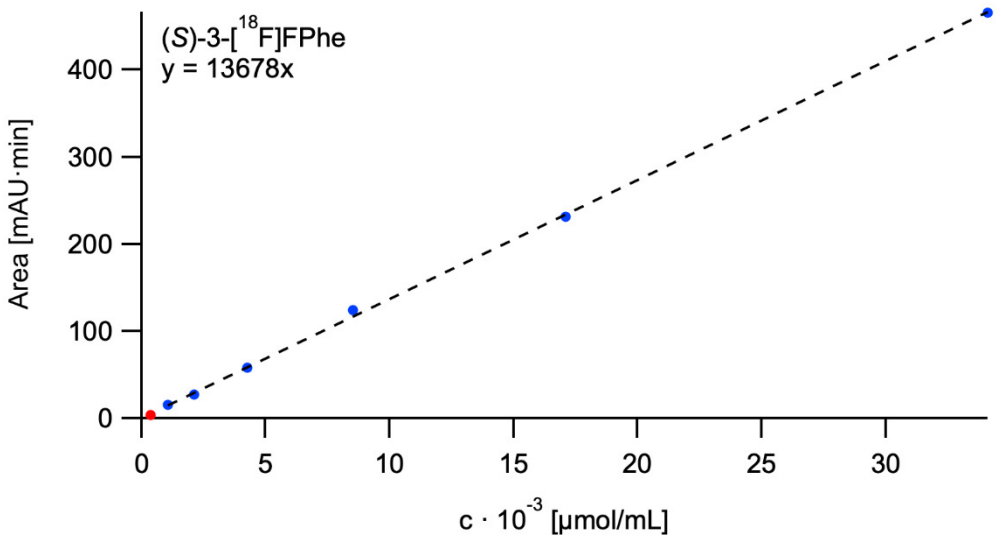

Figure S56: Calibration curve of 3-fluorophenylalanine for calculation of the molar activity of (*S*)-3-[^{18}F]FPhe. Raw data are shown in Table **S47**.

Table S47: Calibration data (measured at 254 nm) for determination of molar activity of (*S*)-3-[^{18}F]FPhe.

Concentration [µmol/mL]	**Amount [µg]**	**Peak area [mAU·min]**
0.0683	12.5	1178.8
0.0341	6.25	685.3
0.0171	3.13	347.9
0.00853	1.56	192.2
0.00427	0.781	130.1
0.00213	0.390	58.9
Measured sample:		
0.000249	0.046	3.4

Volume [mL]	13.4
Activity [GBq]	1.8
Carrier amount (µg)	0.62
Carrier concentration [µmol/mL]	$2.49 \cdot 10^{-4}$
Molar activity [GBq/µmol]	538

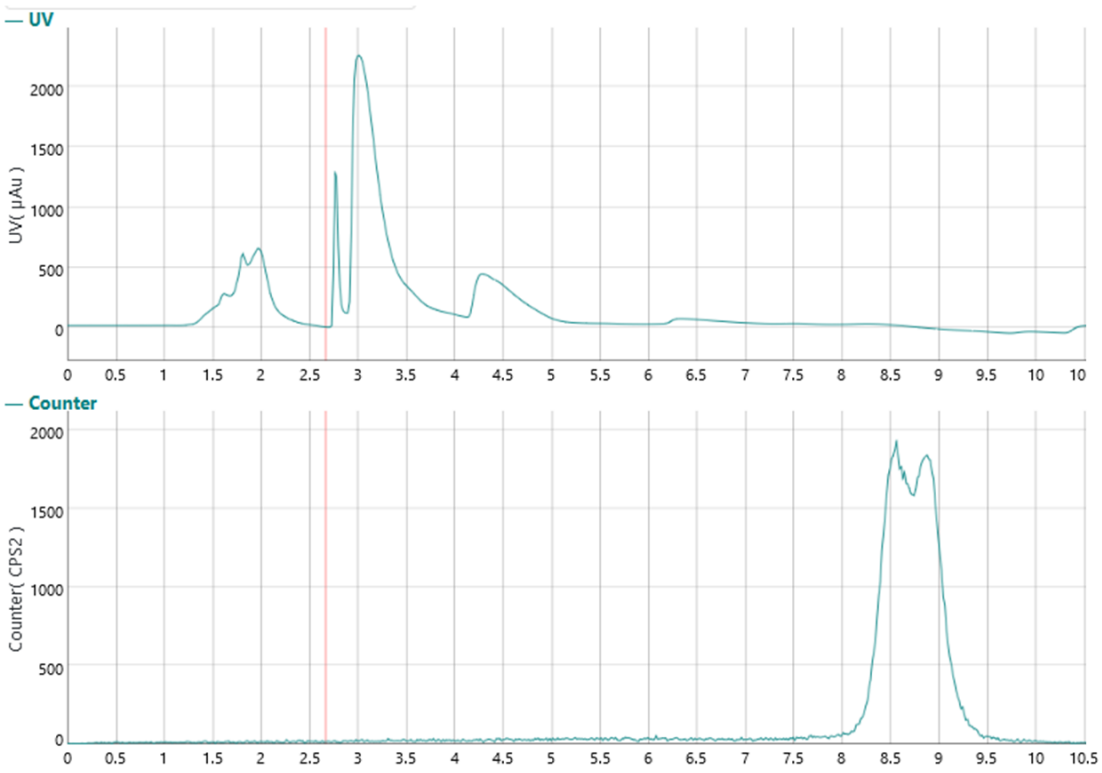

Figure S57: Purification of (*R*)-3-[^{18}F]FPhe by preparative HPLC (top: UV trace, λ=254 nm; bottom: radioactivity trace).

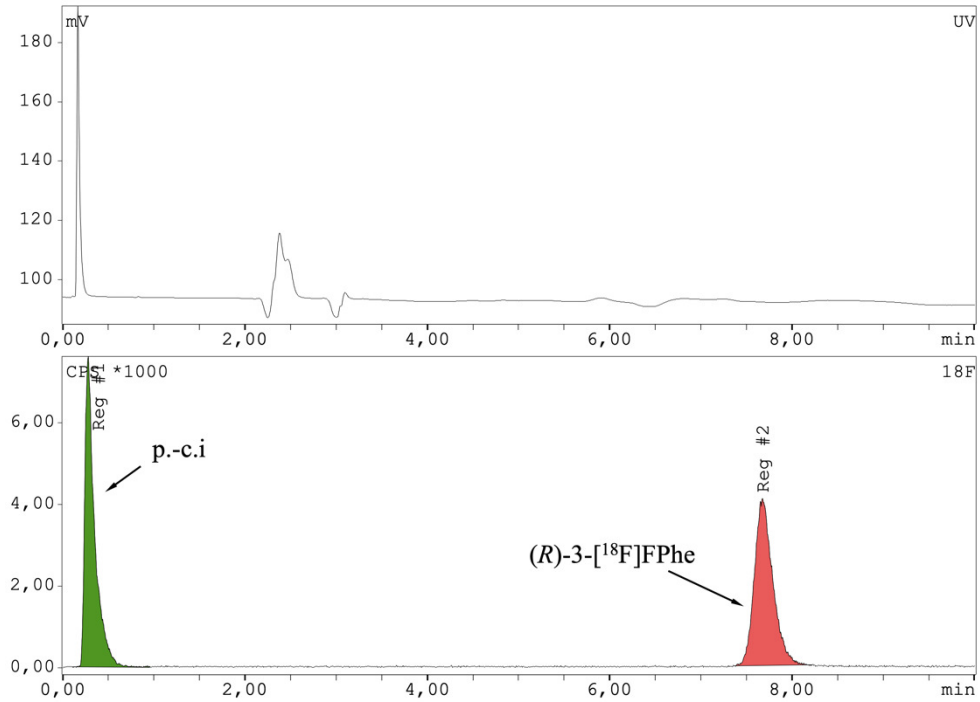

Name	Channel	Start, min	End, min	Area
Reference Injection	^{18}F	0.1	1.0	57223,19
3-(*R*)-[^{18}F]FPhe	^{18}F	7.4	8.2	57433,21

Figure S58: HPLC chromatogram of purified (*R*)-3-[^{18}F]FPhe for quality control. Top: UV trace, λ=254 nm; bottom: radioactivity trace.

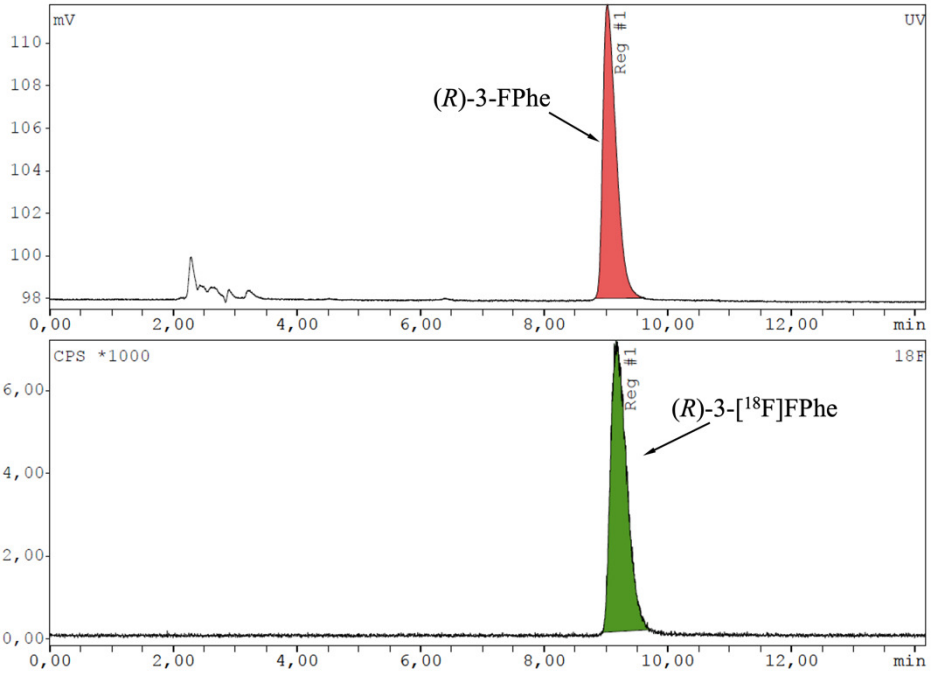

Name	Channel	t_R, min	Area
Non-reference compound	UV	0.1	203.1 mV·min
3-(*R*)-[^{18}F]FPhe	^{18}F	9.2	125296.0 counts·min

Figure S59: Co-injection of (*R*)-3-[^{18}F]FPhe with the non-radioactive reference compound. Top trace: UV channel, λ=254 nm; bottom trace: radioactivity channel.

Radiosynthesis of 3-[^{18}F]FPhes and (*S*)-αMe-3-[^{18}F]FPhe under standard conditions

Radiosynthesis of 3-[^{18}F]FPhes and (*S*)-αMe-3-[^{18}F]FPhe was performed according to GP5 in *n*BuOH/DMA using $Cu(Py)_4(OTf)_2$ as mediator (n=3).

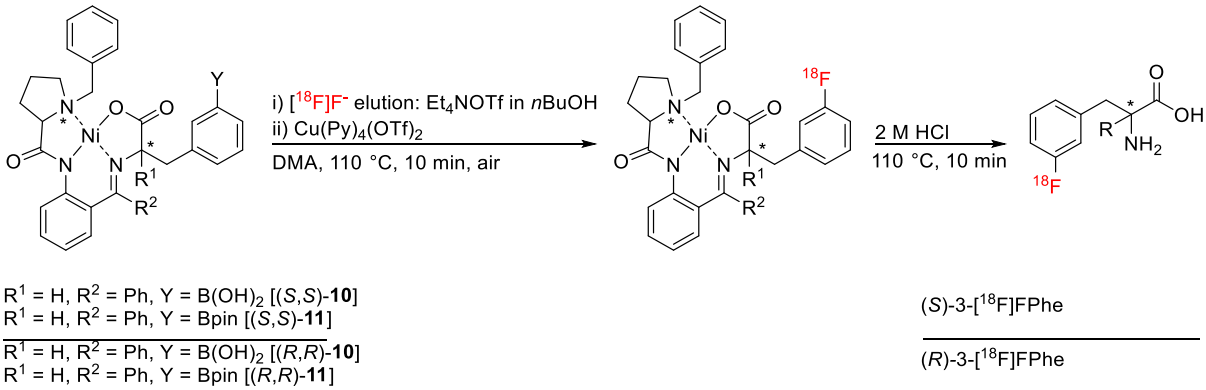

Table S48: Radiosynthesis of [^{18}F]FPhes under standard conditions.

Entry	PET tracer	Y	RCC [%]	AY [%]
1	(*S*)-3-[^{18}F]FPhe	$B(OH)_2$	9 ± 4	17 ± 6
2		Bpin	8 ± 1	
3	(*R*)-3-[^{18}F]FPhe	$B(OH)_2$	21 ± 2	14 ± 4
4		Bpin	11 ± 2	
5	(*S*)-αMe-3-[^{18}F]FPhe	$B(OH)_2$	14 ± 3	
6		Bpin	9 ± 2	

3.13 Automated radiosynthesis of 3-(*S*)-[^{18}F]FPhe in an AllInOne synthesis module (Trasis)

Cassette layout is depicted in Figure **S60**. Aqueous [^{18}F]F^- was loaded (from the male side) onto an anion-exchange resin (QMA-cartridge), washed with MeCN (1 mL, Vial 2) and subsequently eluted (from the female side) into reactor 1 using Bu_4NOH solution (25 mg $Bu_4NOH \cdot 30\ H_2O$ in 0.5 mL MeCN, Vial 1). All volatiles were removed under reduced pressure in a stream of N_2 at 95 °C for 5 min. That followed, a solution of the precursor and catalyst (10 µmol precursor and 15.8 mg catalyst in 0.25 mL *n*BuOH and 0.5 mL DMI, Vial 3) was added and the reaction mixture was heated at 110 °C for 15 min. The reaction mixture was diluted with H_2O (5 mL) and loaded onto a Chromafix C_{18} SPE cartridge which was subsequently washed with H_2O (5 mL) and dried in a stream of N_2 for 1 min. The radiolabeled intermediate was eluted with EtOH (1 mL) into reactor 2 and all volatiles were removed under reduced pressure in a stream of N_2 at 100 °C for 10 min. Afterwards, 1 M HCl (0.5 mL, Vial 4) was added and deprotection was carried out at 110 °C for 10 min. The resulting mixture was diluted with H_2O (5 mL) and 3-(*S*)-[^{18}F]FPhe was isolated by HPLC [column: Hydro RP, 250×10 mm, 5 µm/100 Å, Phenomenex; eluent: 10% EtOH (0.1% H_3PO_4), flow rate: 7.4 mL/min]. The product was collected through a sterile filter directly into the product vial.

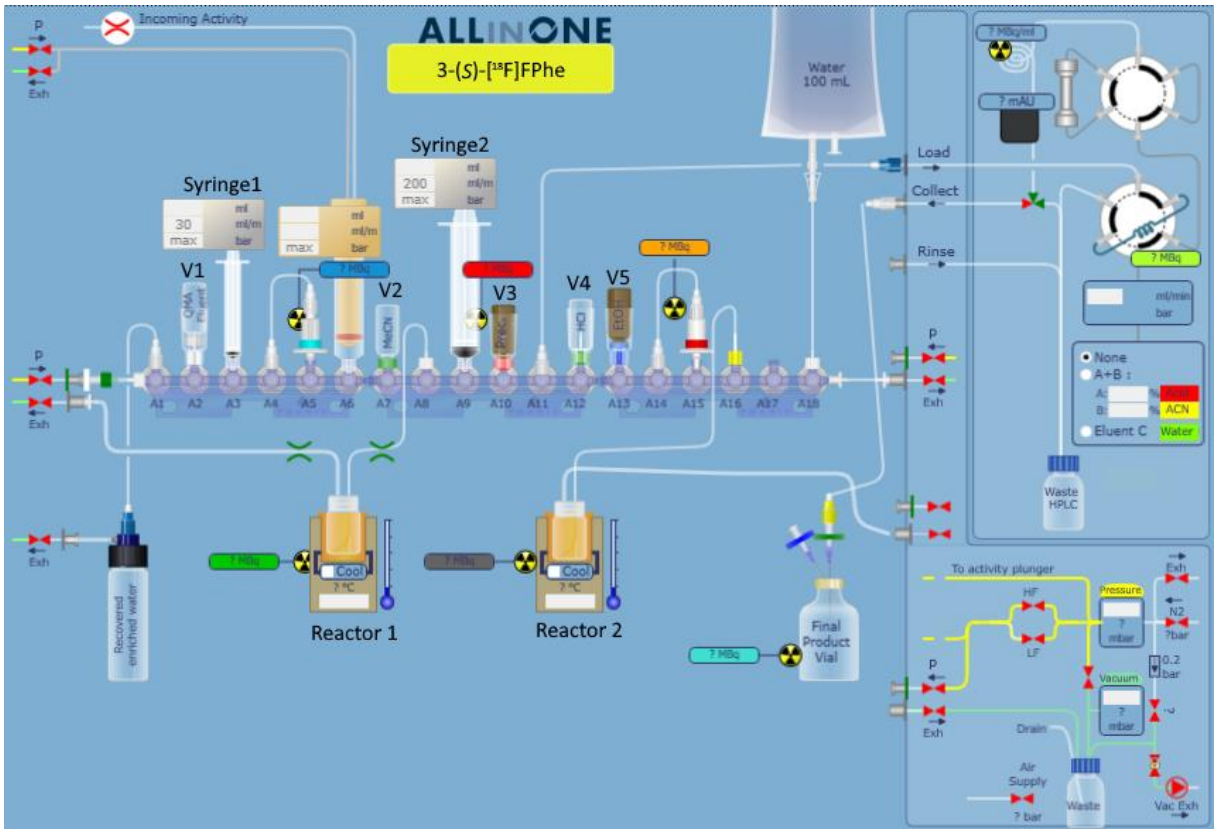

Figure S60: Schematic diagram of the Trasis AIO module with the custom made cassette for preparation of 3-(S)-[^{18}F]FPhe. A2: V1 QMA eluent (25 mg $Bu_4NOH{\cdot}30\ H_2O$ in 0.5 mL MeCN) (4 mL Vial); A5: Sep-Pak Acell Plus QMA Carbonate Plus Light cartridge (130 mg); A7: V2 0.5 mL MeCN (4 mL Vial); A10: V3 Precursor solution: 10 µmol precursor and 15.8 mg $Cu(3,4\text{-}Me_2Py)_4(OTf)_2$ in 0.25 mL nBuOH and 0.5 mL DMI (4 mL Vial); A12: V4 0.5 mL 0.5 M HCl (4 mL Vial); A13: V5 1 mL EtOH (4 ml Vial); A15: Macherey-Nagel Chromafix C18 ec (s) cartridge (270 mg).

Table S49: Process sequence for the automated synthesis of 3-(S)-[^{18}F]FPhe using the Trasis AIO module.

Entry	Process	Activated Path/Function
1	Loading of [^{18}F]fluoride onto the QMA cartridge	A6-A5-QMA-A4-A1
2	Washing of QMA with MeCN (1 mL)	V2-A7-A5-QMA-A4-A3-syringe 1
3	Elution of [^{18}F]fluoride from the cartridge into reactor 1	A2-A3-syringe 1-A4-QMA-A5-A8-reactor 1
4	Drying, reactor 1, 95 °C, 5 min, N_2 flow, vacuum	P-A8-R1-Exh
5	Addition of precursor and $Cu(3,4\text{-}Me_2Py)_4(OTf)_2$	V3-A10-A8-reactor1
6	Radiofluorination, 110 °C, 15 min	-
7	Dilution with H_2O (5 mL)	A18-A9-syringe 2, then R1-A8-A9-syringe 2
8	Loading onto SPE cartridge	Syringe 2-A9-A14-cartridge-A15-exh
9	Washing of SPE cartridge with H_2O (5 mL)	A18-A9-syringe 2, then syringe 2-A9- A14-cartridge-A15-exh
10	Drying of SPE cartridge with N_2 (1 min)	P- A14-cartridge-A15-exh
11	Elution of intermediate compound from SPE cartridge into reactor 2	V5-A13-A9-syringe 2, then syringe 2-A9-A14-SPE-A15-A16-reactor 2
12	Drying, reactor 2, 100 °C, 10 min, N_2 flow, vacuum	P-A16-exh
13	Addition of 0.5 M HCl (0.5 mL)	V4-A12-A16-reactor 2
14	Deprotection, 110 °C, 10 min	-
15	Dilution with H_2O (5 mL)	A18-A9-syringe 2, then reactor2-A16-A9-syringe 2
16	Transfer to HPLC system	Syringe-A9-A11-Load
17	Collection of 3-(*S*)-[^{18}F]FPhe into the product vial	Collect-sterile filter-final product vial

3.14 Radiolabeling at 2.5 µmol precursor loading. Initial experiments

The initial experiments were performed according to GP5 in *n*BuOH/DMI using **1** (2.5 µmol) as model substrate with four different radiolabeling mediators. RCCs were determined by radio-HPLC as described above. Representative HPLC chromatograms of the corresponding reaction mixtures are shown in Figure **S61** and Figure **S62**.

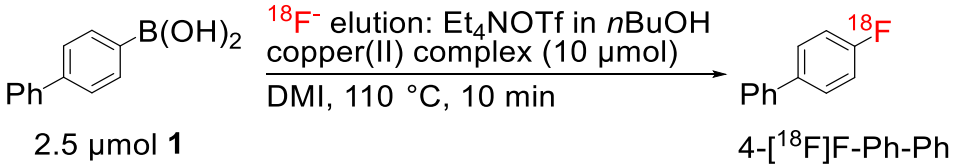

Table S50: Dependency of RCCs for ^{18}F-fluorination of **1** (2.5 µmol) on the applied copper complex.

Entry	Cu(II) complex	RCC [%]
1	$Cu(Py)_4(OTf)_2$	37 ± 2
2	$Cu(4\text{-}PhPy)_4(ClO_4)_2$	56 ± 2
3	$Cu(3,4\text{-}Me_2Py)_4(OTf)_2$	40 ± 2
4	$Cu(3,4\text{-}Me_2Py)_4(ClO_4)_2$	33 ± 2

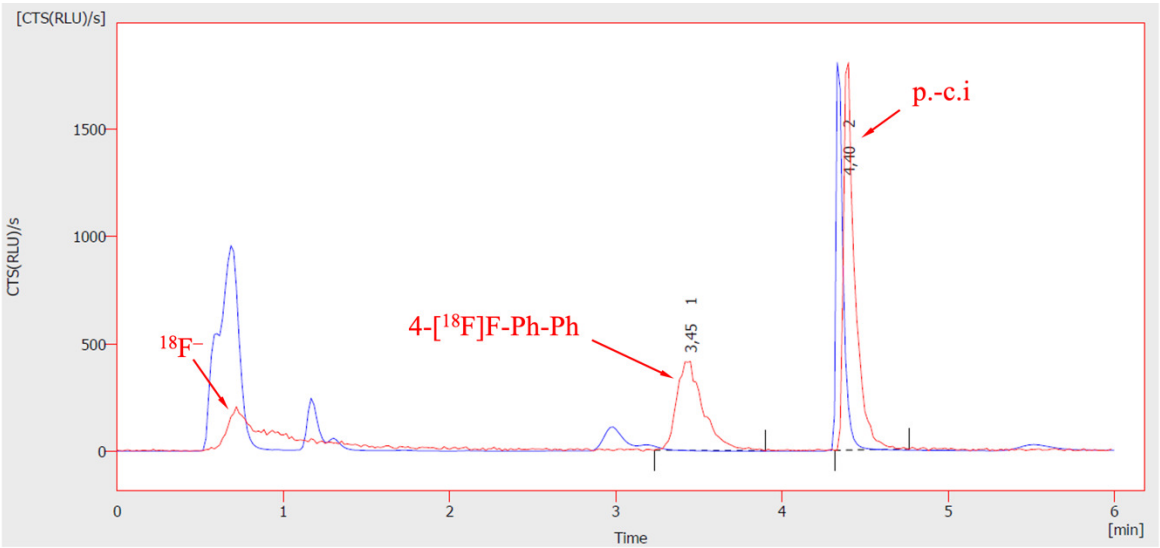

Result Table (Uncal - Data\alc-enhanced_667_07_04_2022_[1 DMI]biphenyl-B(OH)2_2,5umol - HERM)

	Reten. Time [min]	Area [CTS(RLU)/s.s]	Height [CTS(RLU)/s]	Area [%]
1	3,450	4621,000	413,300	35,1
2	4,400	8550,500	1803,074	64,9
	Total	13171,500	2216,374	100,0

Figure S61: HPLC traces of crude 4-[^{18}F]F-Ph-Ph prepared from **1** (2.5 µmol) using $Cu(Py)_4(OTf)_2$ as mediator. Blue trace: UV, λ = 254 nm; red trace: radioactivity. Abbreviation: p.-c.i – post-column injection.

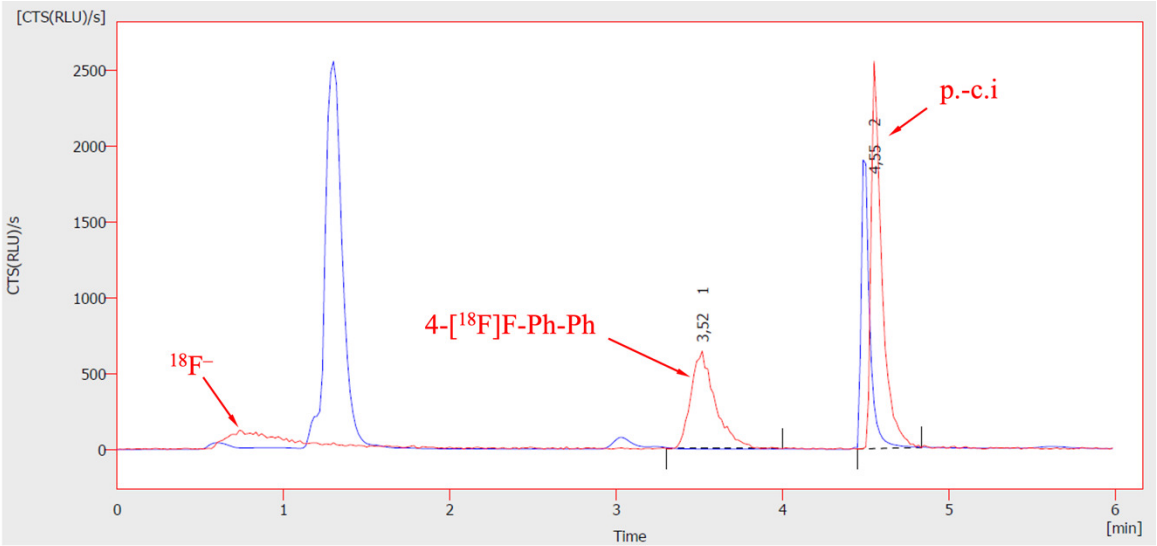

Result Table (Uncal - Data|alc-enhanced_527_18_02_2022_[4 DMI]_biphenyl-B(OH)2_10umol-2.5umol - HERM)

	Reten. Time [min]	Area [CTS(RLU)/s.s]	Height [CTS(RLU)/s]	Area [%]
1	3,517	6550,000	644,000	36,2
2	4,550	11555,000	2554,391	63,8
	Total	18105,000	3198,391	100,0

Figure S62: HPLC traces of crude 4-[^{18}F]F-Ph-Ph prepared from **1** (2.5 µmol) using $Cu(4\text{-}PhPy)_4(ClO_4)_2$ as mediator. Blue trace: UV, λ = 254 nm; red trace: radioactivity. Abbreviation: p.-c.i – post-column injection.

Statistical evaluation of the dependency of RCCs for radiolabeling of 1 (2.5 µmol) on the applied Cu-complex

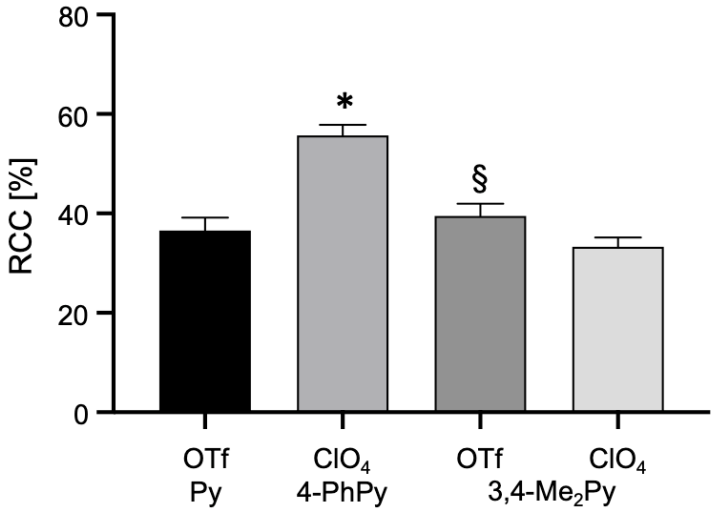

Figure S63: Dependency of RCCs for radiolabeling of **1** (2.5 µmol) on the applied Cu-complex (10 µmol). Solvent: *n*BuOH/DMI; conditions: 110 °C for 10 min. Statistics: 1-way ANOVA followed by Tukey's multiple comparison test. * $p<0.05$ for comparison of $Cu(4\text{-}PhPy)_4(ClO_4)_2$ with all other Cu-complexes. § $p<0.05$ for $Cu(3,4\text{-}Me_2Py)_4(OTf)_2$ *vs.* $Cu(3,4\text{-}Me_2Py)_4(ClO_4)_2$.

Table S51: Screening of Cu mediators for radiolabeling of **1** (2.5 µmol); n=3 per group. 1-way ANOVA followed by Tukey's multiple comparison test. Main effect: $F(3,8)=56.99$, $p<0.0001$.

	RCC (%)	comparison	
$Cu(Py)_4(OTf)_2$	36.55 ± 2.61	vs. $Cu(4\text{-}PhPy)_4(ClO_4)_2$	p<0.0001*
		vs. $Cu(3,4\text{-}Me_2Py)_4(OTf)_2$	p=0.4367
		vs. $Cu(3,4\text{-}Me_2Py)_4(ClO_4)_2$	p=0.3661
$Cu(4\text{-}PhPy)_4(ClO_4)_2$	55.73 ± 2.13	vs. $Cu(3,4\text{-}Me_2Py)_4(OTf)_2$	p=0.0001*
		vs. $Cu(3,4\text{-}Me_2Py)_4(ClO_4)_2$	p<0.0001*
$Cu(3,4\text{-}Me_2Py)_4(OTf)_2$	39.51 ± 2.46	vs. $Cu(3,4\text{-}Me_2Py)_4(ClO_4)_2$	p=0.0421§
$Cu(3,4\text{-}Me_2Py)_4(ClO_4)_2$	33.31 ± 1.88		

* $p<0.05$

Scope of the novel radiolabeling protocol at ≤2.5 µmol precursor loading (Tables S52, S53)

Radiolabeling experiments were performed according to GP5 (boronate precursors) in *n*BuOH/DMI or GP7-B at 110 ºC (stannane precursors) using $Cu(4\text{-}PhPy)_4(ClO_4)_2$ (10 µmol) as radiolabeling mediator (n=3). RCCs were determined by radio-HPLC as described above. Representative HPLC chromatograms of radiolabeled products are shown in Figure **S64**–**S87**.

Table S52: Radiolabeled compounds prepared using the novel ^{18}F-fluorination protocol at ≤2.5 µmol precursor loading.

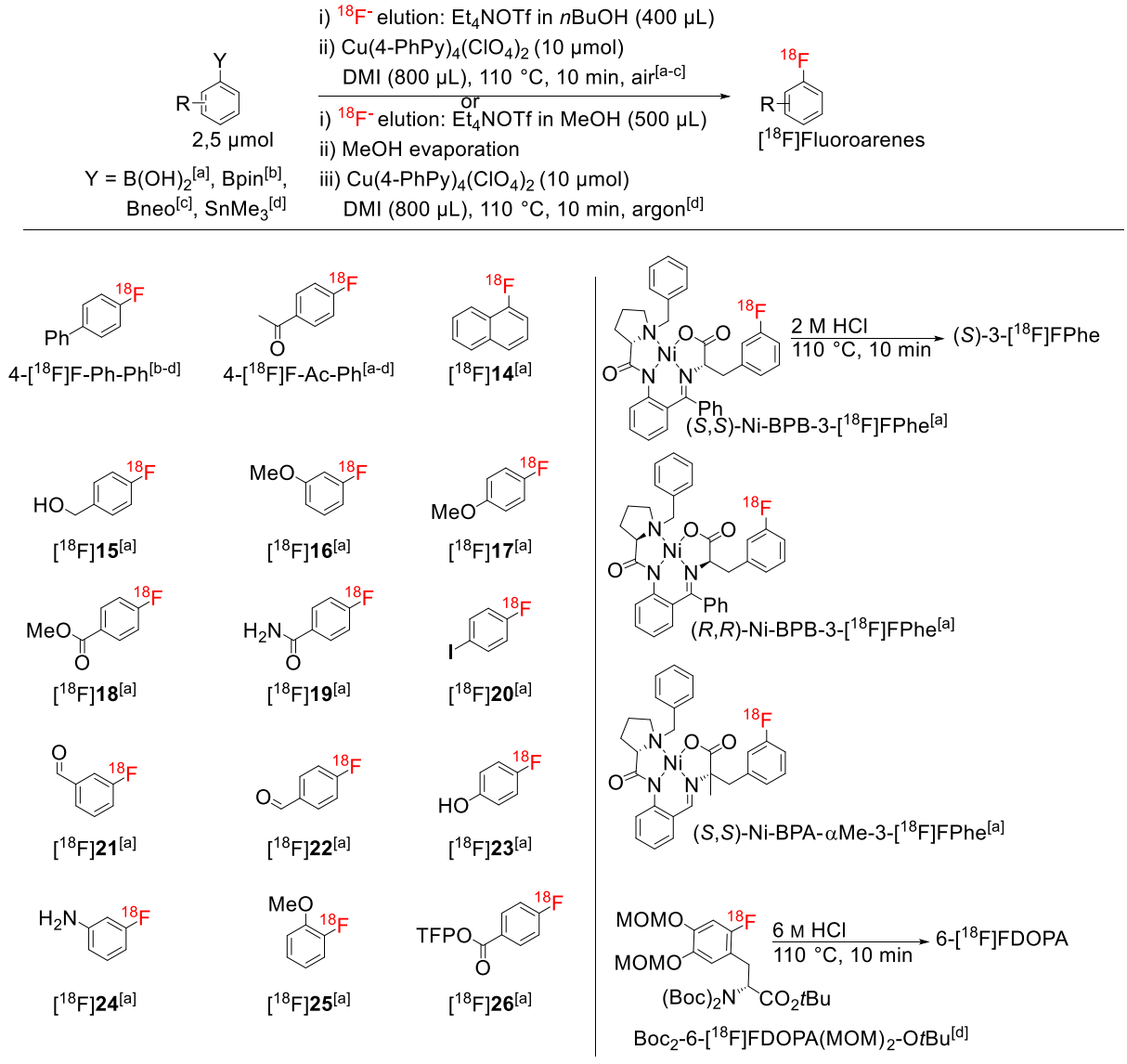

Table S53: Scope of the novel radiolabeling protocol at ≤2.5 µmol precursor loading.

Entry	Radiolabeled product	RCC [%]
1	[^{18}F]F-Ph-Ph	56 ± 2[a]
2		48 ± 6[b]
3		63 ± 12[c]
4		30 ± 0.2[d]
5	[^{18}F]F-Ac-Ph	53 ± 3[a]
6		25 ± 2[b]
7		28 ± 4[c]
8		37 ± 3[d]
9	[^{18}F]**14**	76 ±5[a]
10		62 ± 17[e]
11		29 ± 8[f]
12	[^{18}F]**15**	76 ± 8[a]
13	[^{18}F]**16**	44 ± 2[a]
14	[^{18}F]**17**	28 ± 3[a]
15	[^{18}F]**18**	51 ± 5[a]
16	[^{18}F]**19**	54 ± 14[a]
17	[^{18}F]**20**	29 ± 5[a]
18	[^{18}F]**21**	30 ± 6[a]
19	[^{18}F]**22**	34 ± 6[a]
20	[^{18}F]**23**	39 ± 2[a]
21	[^{18}F]**24**	19 ± 2[a]
22	[^{18}F]**25**	18 ± 3[a]
23	[^{18}F]**26**	6 ± 1[a]
24		28 ± 3[g] (n=2)
25		63 ± 2[g, h]
26	(*S*,*S*)-Ni-BPB-3-[^{18}F]FPhe	62 ± 5[a] (AY = 23 ± 1)
27	(*R*,*R*)-Ni-BPB-3-[^{18}F]FPhe	46 ± 9[a]
28	(*S*,*S*)-Ni-BPB-αMe-3-[^{18}F]FPhe	53 ± 2[a]
29	Boc_2-6-[^{18}F]FDOPA$(MOM)_2$-O*t*Bu	60 ± 5[d]
30		10 ± 3[d,e]

Radiolabeled products were prepared from the respective [a]aryl boronic acid, [b]pinacol boronate, [c]neopentyl glycol boronate or [d]trimethyl stannyl precursor. [e]Prepared from 1 µmol precursor. [f]Prepared from 0.5 µmol precursor. [g]Radiosyntheses were performed according to GP7A. [h]Prepared from 10 µmol precursor.

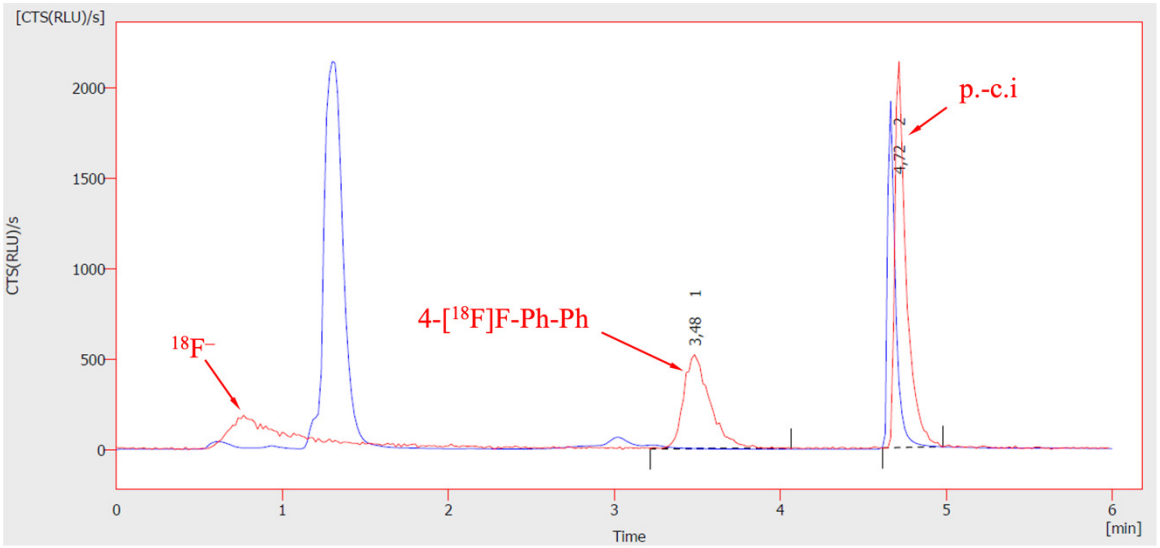

Result Table (Uncal - Data|alc-enhanced_529_18_02_2022_[4 DMI]_biphenyl-Bpin_10umol-2.5umol - HERM)

	Reten. Time [min]	Area [CTS(RLU)/s.s]	Height [CTS(RLU)/s]	Area [%]
1	3,483	5801,000	520,000	36,3
2	4,717	10177,000	2133,091	63,7
	Total	15978,000	2653,091	100,0

Figure S64: HPLC traces of crude 4-[^{18}F]F-Ph-Ph prepared from **2** (2.5 µmol). Blue trace: UV, λ = 254 nm; red trace: radioactivity. Abbreviation: p.-c.i – post-column injection.

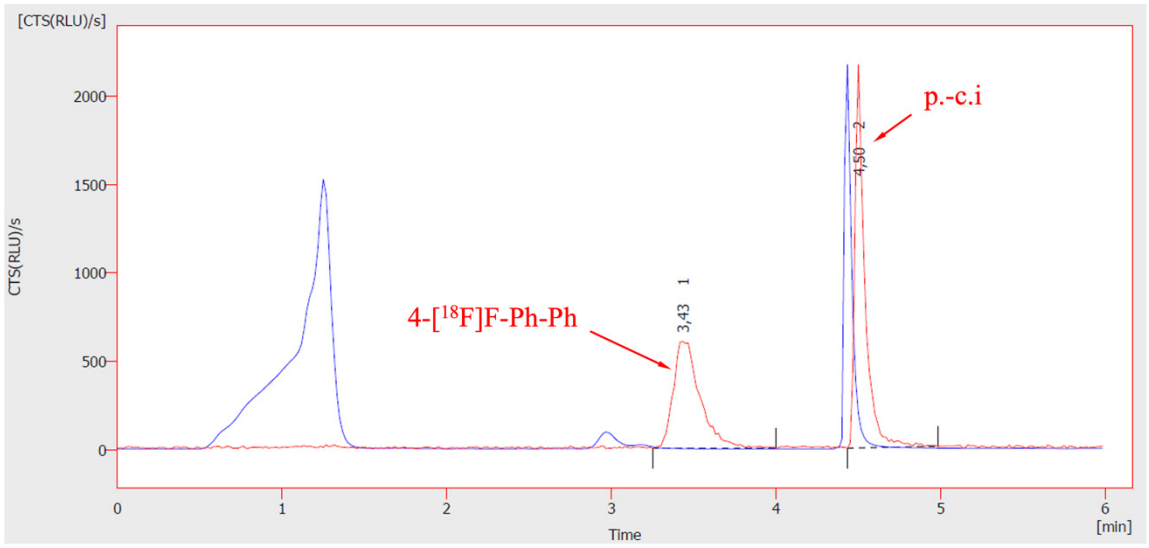

Result Table (Uncal - Data|alc-enhanced_561_01_03_2022_[4 DMI]biphenyl-Bneo_2.5umol - HERM)

	Reten. Time [min]	Area [CTS(RLU)/s.s]	Height [CTS(RLU)/s]	Area [%]
1	3,433	6861,500	603,756	42,9
2	4,500	9120,500	2167,909	57,1
	Total	15982,000	2771,665	100,0

Figure S65: HPLC traces of crude 4-[^{18}F]F-Ph-Ph prepared from 4-Ph-Ph-Bneo (2.5 µmol). Blue trace: UV, λ = 254 nm; red trace: radioactivity. Abbreviation: p.-c.i – post-column injection.

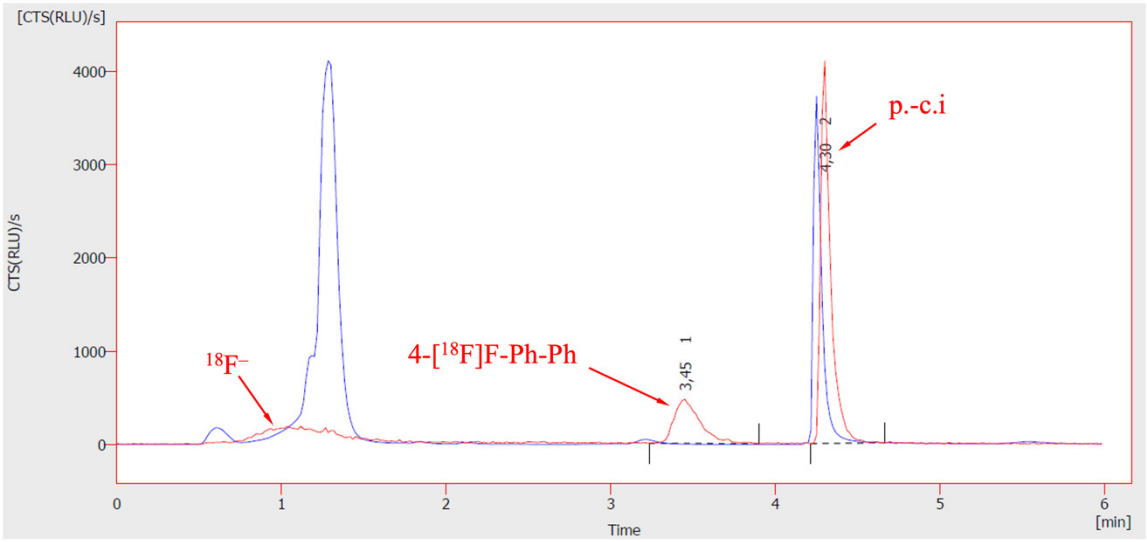

Result Table (Uncal - Data|alc-enhanced_661_04_04_2022_[4 DMI]biphenyl-SnMe3_2,5umol - HERM)

	Reten. Time [min]	Area [CTS(RLU)/s.s]	Height [CTS(RLU)/s]	Area [%]
1	3,450	5255,000	474,650	23,2
2	4,300	17404,000	4102,519	76,8
	Total	22659,000	4577,169	100,0

Figure S66: HPLC traces of crude 4-[^{18}F]F-Ph-Ph prepared from **5** (2.5 µmol). Blue trace: UV, λ = 254 nm; red trace: radioactivity. Abbreviation: p.-c.i – post-column injection.

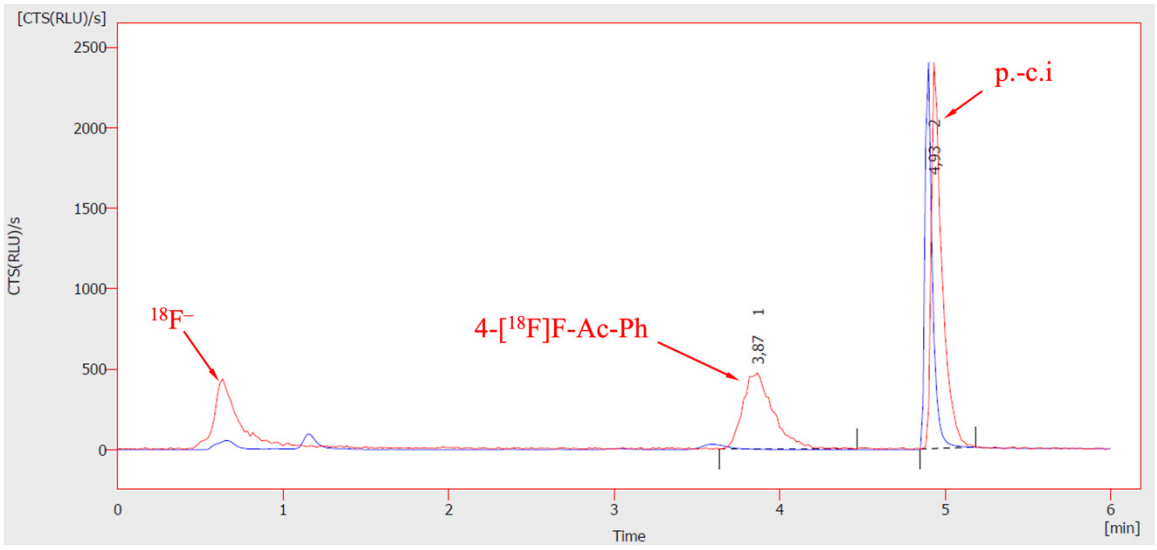

Result Table (Uncal - Data|alc-enhanced_530_18_02_2022_[4 DMI]_4-acetylphenyl-B(OH)2_10umol-2.5umol - HERM)

	Reten. Time [min]	Area [CTS(RLU)/s.s]	Height [CTS(RLU)/s]	Area [%]
1	3,867	6089,000	474,720	36,3
2	4,933	10699,000	2400,000	63,7
	Total	16788,000	2874,720	100,0

Figure S67: HPLC traces of crude 4-[^{18}F]F-Ac-Ph prepared from **3** (2.5 µmol). Blue trace: UV, λ = 254 nm; red trace: radioactivity. Abbreviation: p.-c.i – post-column injection.

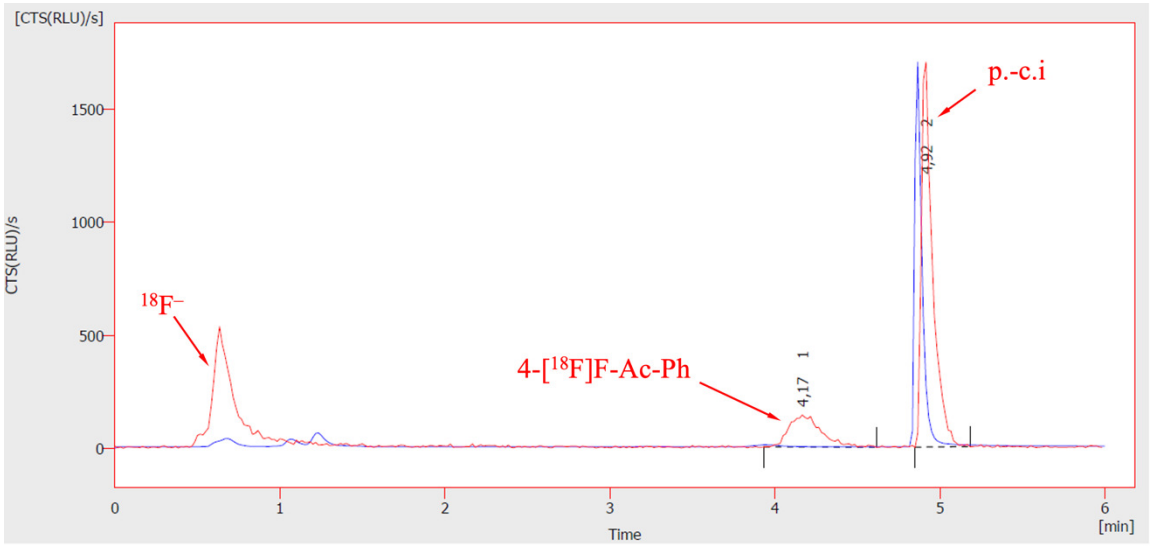

Result Table (Uncal - Data|alc-enhanced_533_18_02_2022_[4 DMI]_4-acetylphenyl-Bpin_10umol-2.5umol - HERM)

	Reten. Time [min]	Area [CTS(RLU)/s.s]	Height [CTS(RLU)/s]	Area [%]
1	4,167	1944,000	141,683	19,4
2	4,917	8087,000	1701,600	80,6
	Total	10031,000	1843,283	100,0

Figure S68: HPLC traces of crude 4-[^{18}F]F-Ac-Ph prepared from **4** (2.5 µmol). Blue trace: UV, λ = 254 nm; red trace: radioactivity. Abbreviation: p.-c.i – post-column injection.

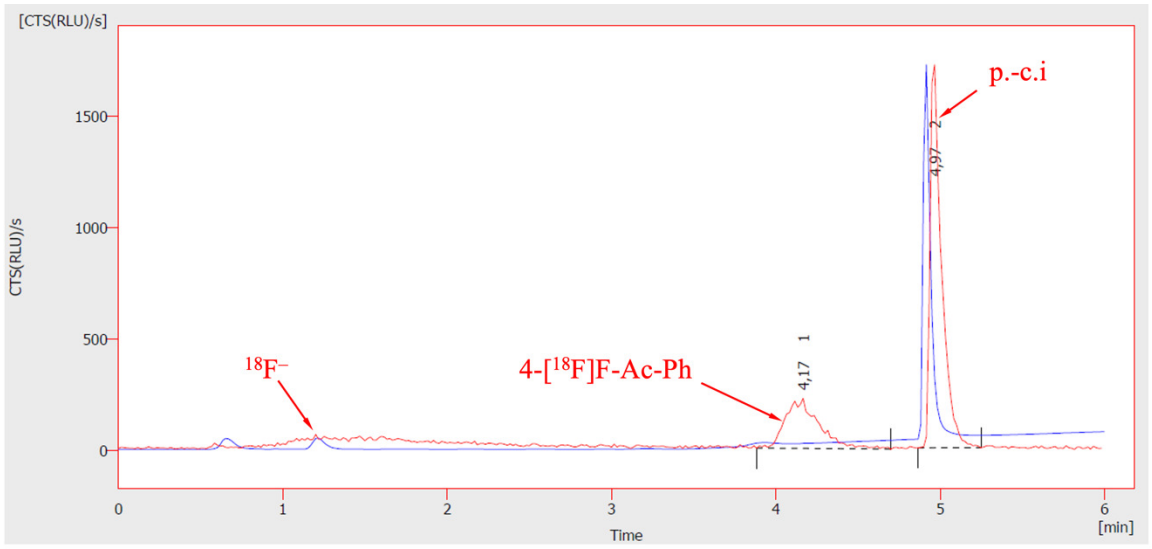

Result Table (Uncal - Data|alc-enhanced_562_01_03_2022_[4 DMI]4-acetylphenyl-Bneo_2.5umol - HERM)

	Reten. Time [min]	Area [CTS(RLU)/s.s]	Height [CTS(RLU)/s]	Area [%]
1	4,167	3191,500	225,735	27,5
2	4,967	8423,500	1720,739	72,5
	Total	11615,000	1946,474	100,0

Figure S69: HPLC traces of crude 4-[^{18}F]F-Ac-Ph prepared from 4-Ac-Ph-Bneo (2.5 µmol). Blue trace: UV, λ = 254 nm; red trace: radioactivity. Abbreviation: p.-c.i – post-column injection.

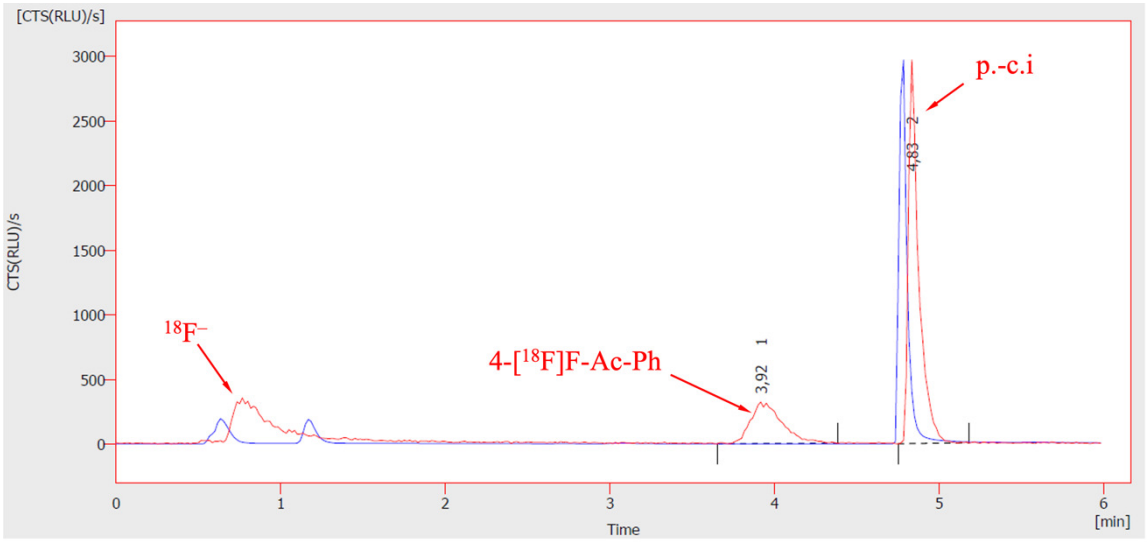

Result Table (Uncal - Data|alc-enhanced_662_04_04_2022_[4 DMI]4-acetylphenyl-SnMe3_2,5umol - HERM)

	Reten. Time [min]	Area [CTS(RLU)/s.s]	Height [CTS(RLU)/s]	Area [%]
1	3,917	4278,000	322,909	24,6
2	4,833	13090,000	2971,846	75,4
	Total	17368,000	3294,755	100,0

Figure S70: HPLC traces of crude 4-[^{18}F]F-Ac-Ph prepared from **6** (2.5 µmol). Blue trace: UV, λ = 254 nm; red trace: radioactivity. Abbreviation: p.-c.i – post-column injection.

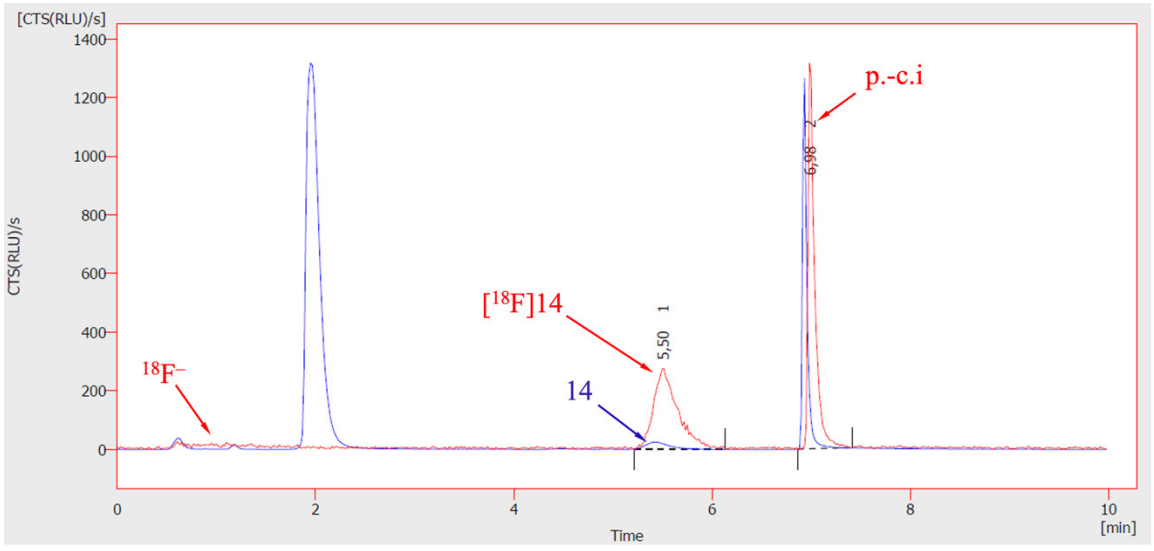

Result Table (Uncal - Data|alc-enhanced_820_27_06_2022_[4 DMI][18F]14_spike - HERM)

	Reten. Time [min]	Area [CTS(RLU)/s.s]	Height [CTS(RLU)/s]	Area [%]
1	5,500	4664,000	275,000	42,8
2	6,983	6230,500	1315,939	57,2
	Total	10894,500	1590,939	100,0

Figure S71: HPLC traces of crude 1-[^{18}F]fluoronaphthalene ([^{18}F]**14**) prepared from the corresponding boronic acid precursor (2.5 µmol) and spiked with 1-fluoronaphthalene (**14**). Blue trace: UV, λ = 254 nm; red trace: radioactivity. Abbreviation: p.-c.i – post-column injection.

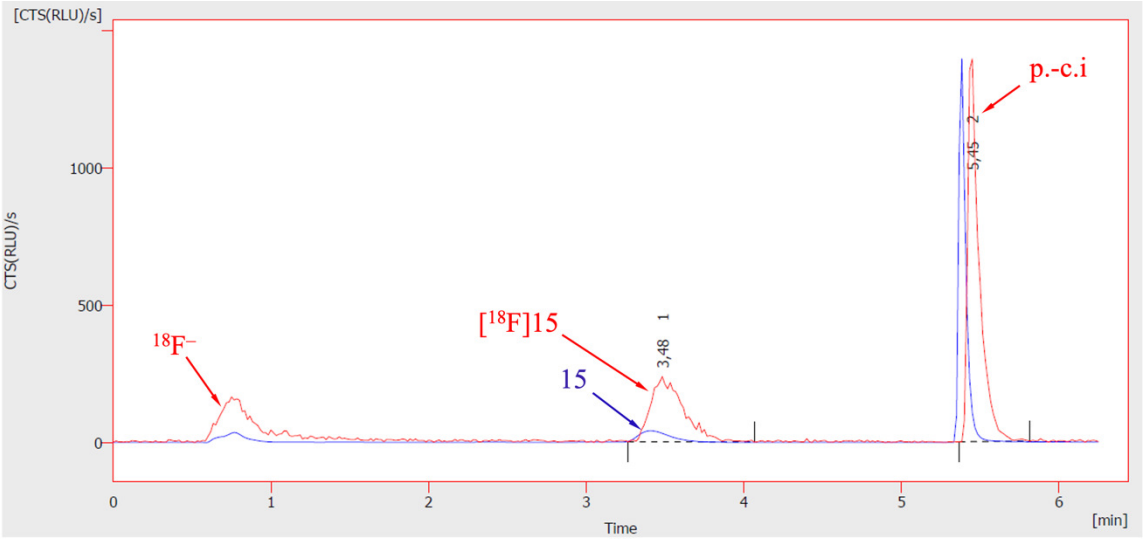

Result Table (Uncal - Data\alc-enhanced_810_27_06_2022_[4 DMI][18F]15_spike - HERM)

	Reten. Time [min]	Area [CTS(RLU)/s.s]	Height [CTS(RLU)/s]	Area [%]
1	3,483	3426,000	237,271	32,4
2	5,450	7132,000	1393,630	67,6
	Total	10558,000	1630,900	100,0

Figure S72: HPLC trace of crude 4-[^{18}F]fluorobenzyl alcohol ([^{18}F]**15**) prepared from the respective boronic acid precursor (2.5 µmol) and spiked with 4-fluorobenzyl alcohol (**15**). Blue trace: UV, λ = 254 nm; red trace: radioactivity. Abbreviation: p.-c.i – post-column injection.

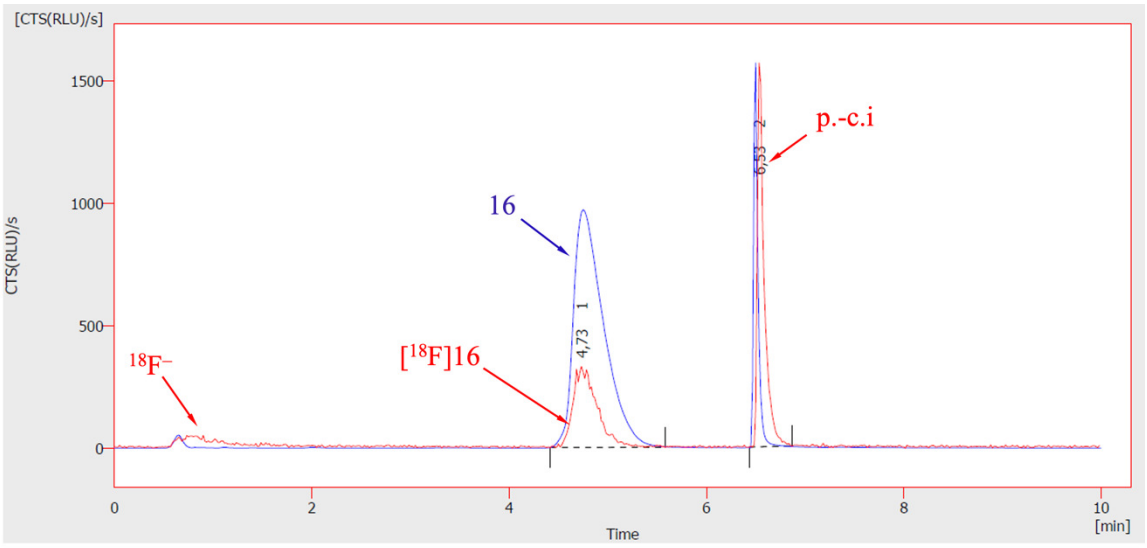

Result Table (Uncal - Data\alc-enhanced_816_27_06_2022_[4 DMI][18F]16_spike - HERM)

	Reten. Time [min]	Area [CTS(RLU)/s.s]	Height [CTS(RLU)/s]	Area [%]
1	4,733	5671,000	331,729	42,9
2	6,533	7543,000	1568,077	57,1
	Total	13214,000	1899,805	100,0

Figure S73: HPLC traces of crude 3-[^{18}F]fluoroanisole ([^{18}F]**16**) prepared from the corresponding boronic acid precursor (2.5 µmol) and spiked with 3-fluoroanisole (**16**). Blue trace: UV, λ = 254 nm; red trace: radioactivity. Abbreviation: p.-c.i – post-column injection.

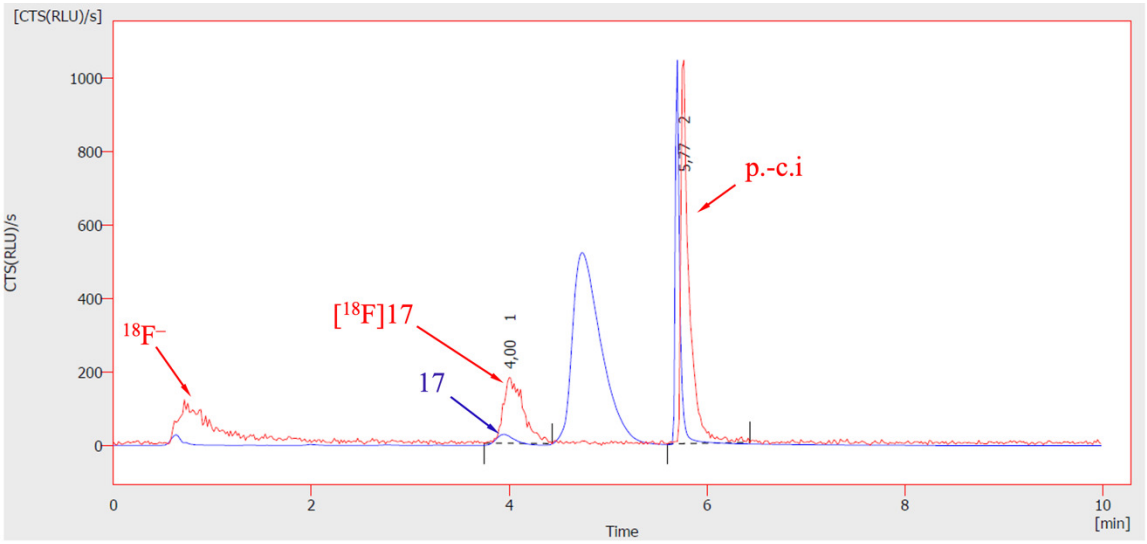

Result Table (Uncal - Data\alc-enhanced_817_27_06_2022_[4 DMI][18F]17_spike - HERM)

	Reten. Time [min]	Area [CTS(RLU)/s.s]	Height [CTS(RLU)/s]	Area [%]
1	4,000	2535,500	179,366	29,3
2	5,767	6110,000	1045,200	70,7
	Total	8645,500	1224,566	100,0

Figure S74: HPLC traces of crude 4-[^{18}F]fluoroanisole ([^{18}F]**17**) prepared from the corresponding boronic acid precursor (2.5 µmol) and spiked with 4-fluoroanisole (**17**). Blue: UV chromatogram, λ = 254 nm; red: radio chromatogram. Abbreviations: p.-c.i – post-column injection.

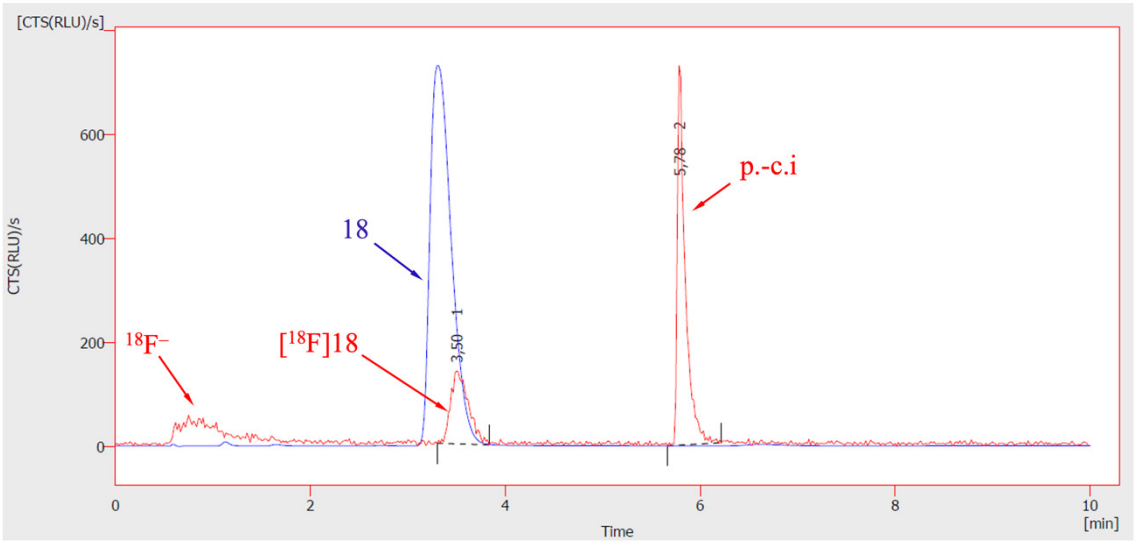

Result Table (Uncal - Data\alc-enhanced_818_27_06_2022_[4 DMI][18F]18_spike - HERM)

	Reten. Time [min]	Area [CTS(RLU)/s.s]	Height [CTS(RLU)/s]	Area [%]
1	3,500	1807,000	140,125	30,3
2	5,783	4162,000	729,727	69,7
	Total	5969,000	869,852	100,0

Figure S75: HPLC traces of crude methyl 4-[^{18}F]fluorobenzoate ([^{18}F]**18**) prepared from the corresponding boronic acid precursor (2.5 µmol) and spiked with methyl 4-flourobenzoate (**18**). Blue trace: UV, λ = 254 nm; red trace: radioactivity. Abbreviation: p.-c.i – post-column injection.

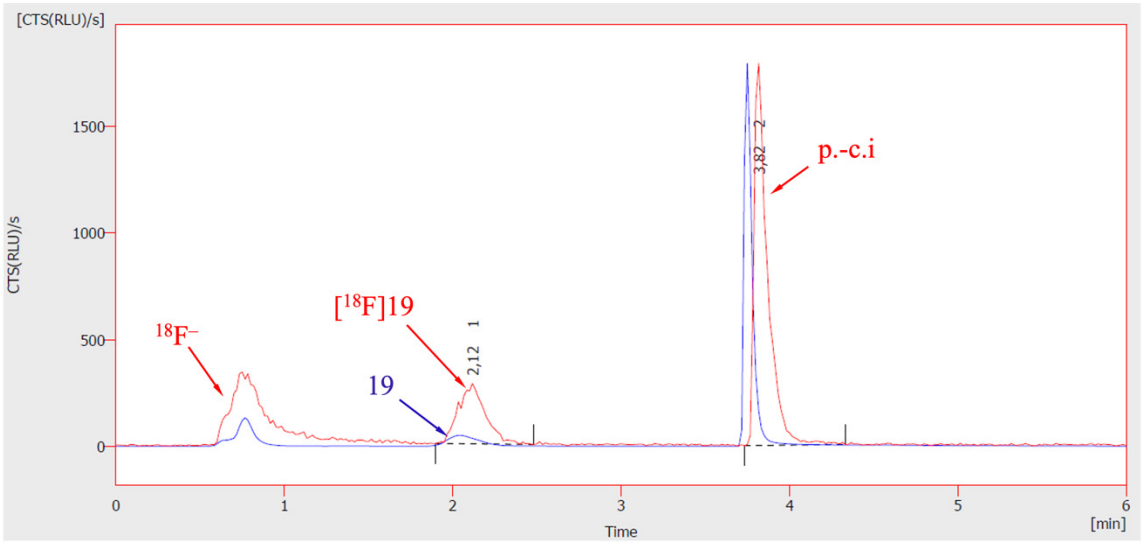

Result Table (Uncal - Data|alc-enhanced_811_27_06_2022_[4 DMI][18F]19_spike - HERM)

	Reten. Time [min]	Area [CTS(RLU)/s.s]	Height [CTS(RLU)/s]	Area [%]
1	2,117	3164,500	282,857	24,1
2	3,817	9988,000	1792,167	75,9
	Total	13152,500	2075,024	100,0

Figure S76: HPLC traces of crude 4-[^{18}F]fluorobenzamide ([^{18}F]**19**) prepared from the corresponding boronic acid precursor (2.5 µmol) and spiked with 4-fluorobenzamide (**19**). Blue trace: UV, λ = 254 nm; red trace: radioactivity. Abbreviation: p.-c.i – post-column injection.

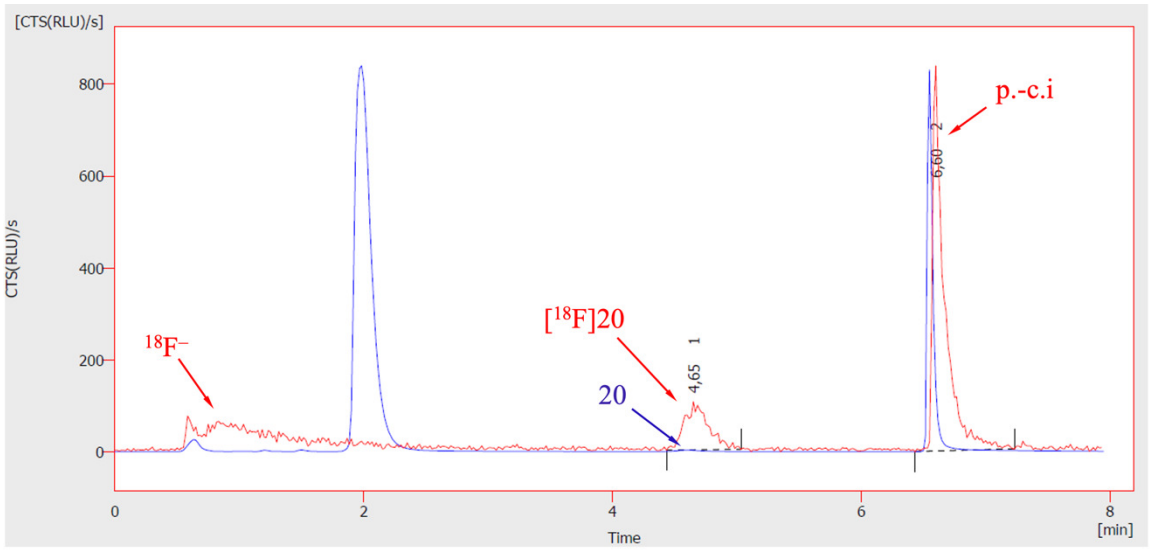

Result Table (Uncal - Data|alc-enhanced_821_27_06_2022_[4 DMI][18F]20_spike - HERM)

	Reten. Time [min]	Area [CTS(RLU)/s.s]	Height [CTS(RLU)/s]	Area [%]
1	4,650	1391,000	105,278	20,0
2	6,600	5570,000	837,750	80,0
	Total	6961,000	943,028	100,0

Figure S77: HPLC traces of crude 4-[^{18}F]fluoroiodobenzene ([^{18}F]**20**) prepared from the corresponding boronic acid precursor (2.5 µmol) and spiked with 4-fluoroiodobenzene (**20**). Blue trace: UV, λ = 254 nm; red trace: radioactivity. Abbreviation: p.-c.i – post-column injection.

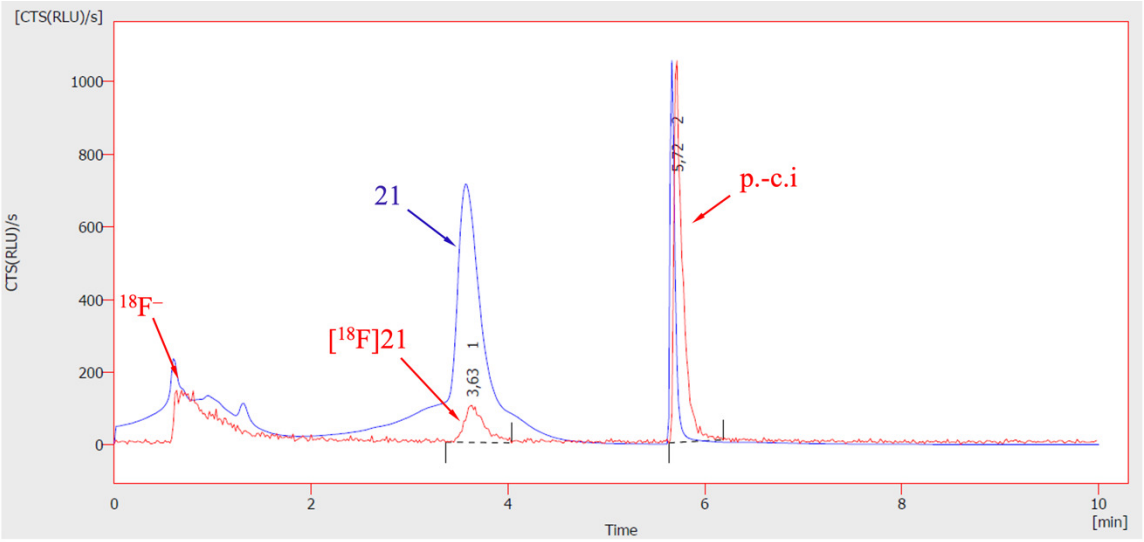

Result Table (Uncal - Data|alc-enhanced_814_27_06_2022_[4 DMI][18F]21_spike - HERM)

	Reten. Time [min]	Area [CTS(RLU)/s.s]	Height [CTS(RLU)/s]	Area [%]
1	3,633	1471,000	101,800	18,7
2	5,717	6395,000	1051,788	81,3
	Total	7866,000	1153,588	100,0

Figure S78: HPLC traces of crude 3-[^{18}F]fluorobenzaldehyde ([^{18}F]**21**) prepared from the corresponding boronic acid precursor (2.5 µmol) and spiked with 3-fluorobenzaldehyde (**21**). Blue trace: UV, λ = 254 nm; red trace: radioactivity. Abbreviation: p.-c.i – post-column injection.

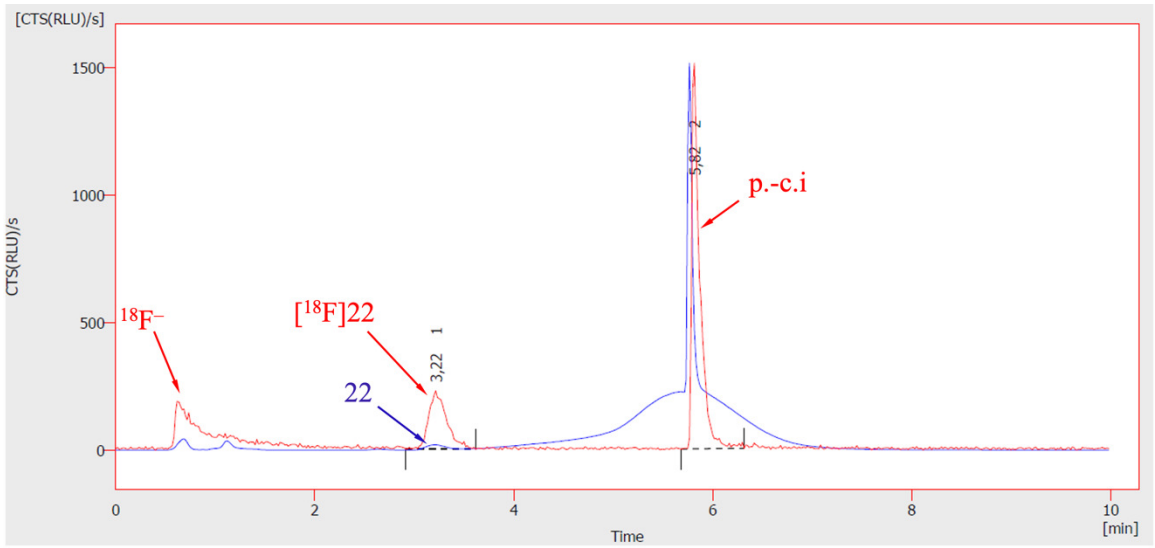

Result Table (Uncal - Data|alc-enhanced_815_27_06_2022_[4 DMI][18F]22_spike - HERM)

	Reten. Time [min]	Area [CTS(RLU)/s.s]	Height [CTS(RLU)/s]	Area [%]
1	3,217	2867,000	228,000	25,0
2	5,817	8623,000	1512,368	75,0
	Total	11490,000	1740,368	100,0

Figure S79: HPLC traces of crude 4-[^{18}F]fluorobenzaldehyde ([^{18}F]**22**) prepared from the corresponding boronic acid precursor (2.5 µmol) and spiked with 4-fluorobenzaldehyde (**22**). Blue trace: UV, λ = 254 nm; red trace: radioactivity. Abbreviation: p.-c.i – post-column injection.

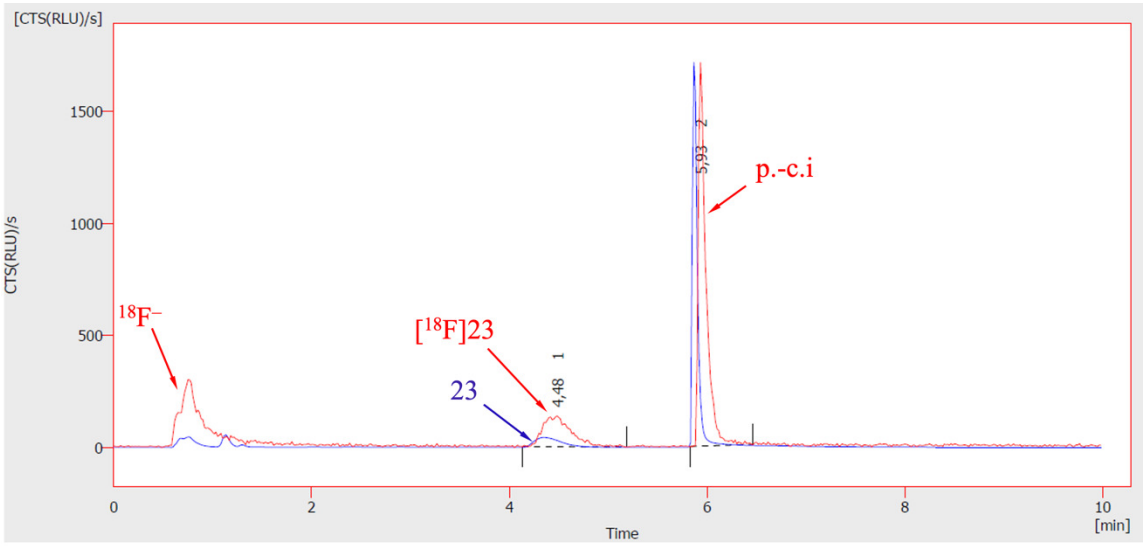

Result Table (Uncal - Data|alc-enhanced_812_27_06_2022_[4 DMI][18F]23_spike - HERM)

	Reten. Time [min]	Area [CTS(RLU)/s.s]	Height [CTS(RLU)/s]	Area [%]
1	4,483	2820,500	138,333	23,3
2	5,933	9288,000	1712,579	76,7
	Total	12108,500	1850,912	100,0

Figure S80: HPLC traces of crude 4-[^{18}F]fluorophenol ([^{18}F]**23**) prepared from the corresponding boronic acid precursor (2.5 µmol) and spiked with 4-fluorophenol (**23**). Blue trace: UV, λ = 254 nm; red trace: radioactivity. Abbreviation: p.-c.i – post-column injection.

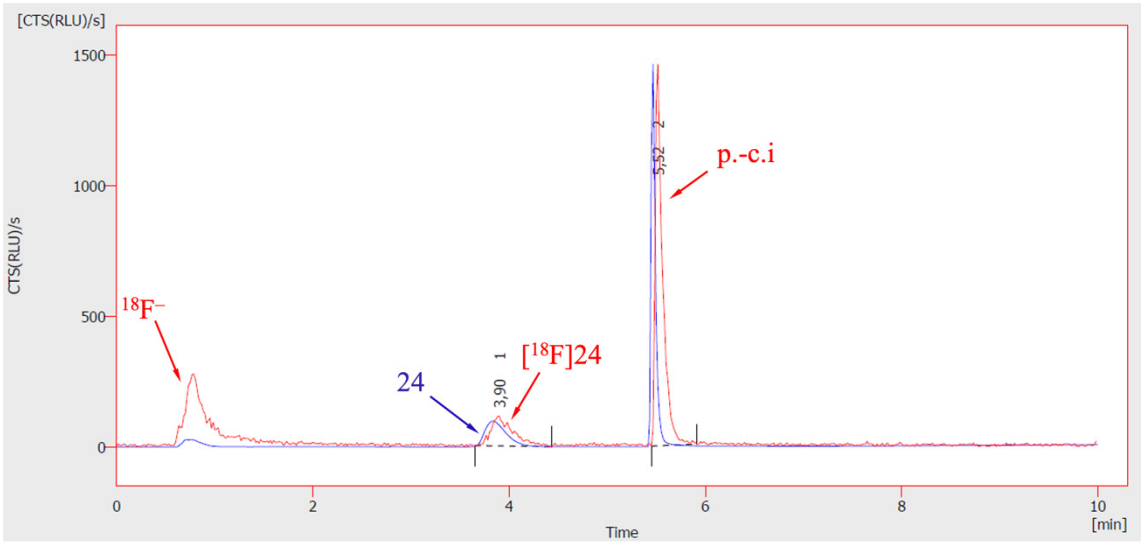

Result Table (Uncal - Data|alc-enhanced_813_27_06_2022_[4 DMI][18F]24_spike - HERM)

	Reten. Time [min]	Area [CTS(RLU)/s.s]	Height [CTS(RLU)/s]	Area [%]
1	3,900	1801,000	114,277	18,9
2	5,517	7704,000	1461,000	81,1
	Total	9505,000	1575,277	100,0

Figure S81: HPLC traces of crude 3-[^{18}F]fluoroaniline ([^{18}F]**24**) prepared from the corresponding boronic acid precursor (2.5 µmol) and spiked with 3-fluoroaniline (**24**). Blue trace: UV, λ = 254 nm; red trace: radioactivity. Abbreviation: p.-c.i – post-column injection.

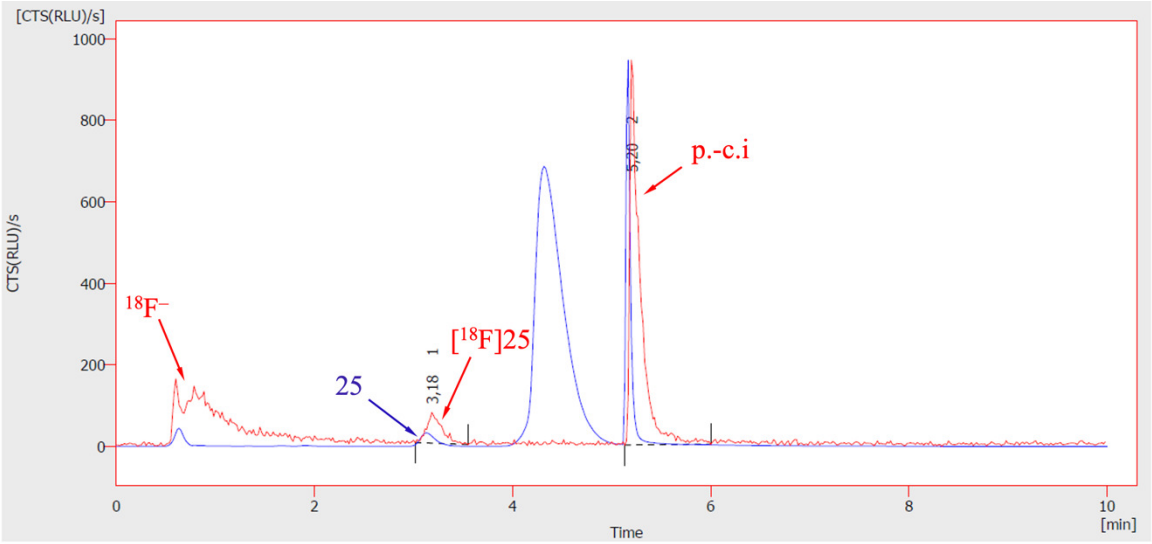

Result Table (Uncal - Data|alc-enhanced_819_27_06_2022_[4 DMI][18F]25_spike - HERM)

	Reten. Time [min]	Area [CTS(RLU)/s.s]	Height [CTS(RLU)/s]	Area [%]
1	3,183	807,000	75,563	10,5
2	5,200	6865,000	943,846	89,5
	Total	7672,000	1019,409	100,0

Figure S82: HPLC traces of crude 2-[^{18}F]fluoroanisole ([^{18}F]**25**) prepared from the corresponding boronic acid precursor (2.5 µmol) and spiked with 2-[^{18}F]fluoroanisole (**25**). Blue trace: UV, λ = 254 nm; red trace: radioactivity. Abbreviation: p.-c.i – post-column injection.

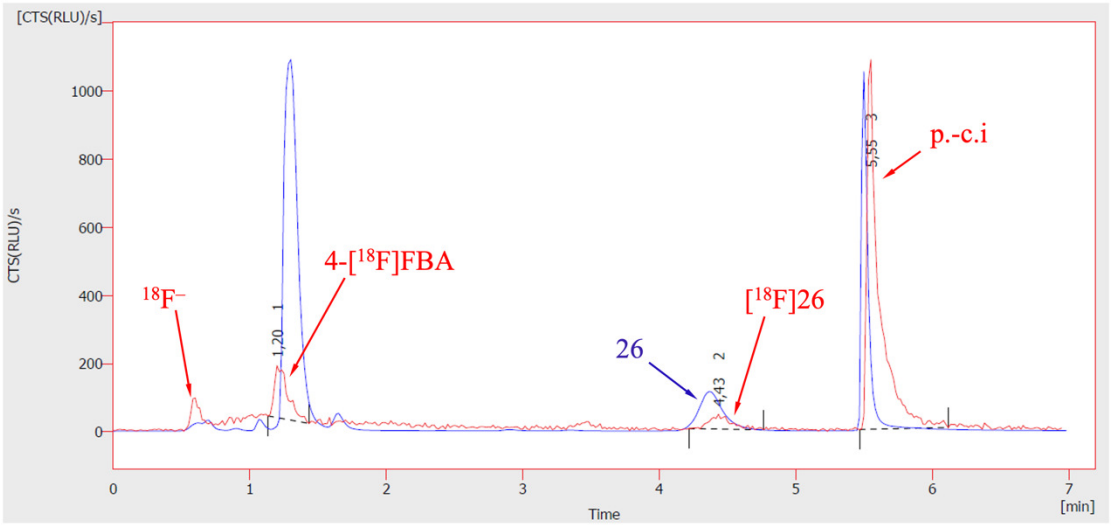

Result Table (Uncal - Data|alc-enhanced_822_27_06_2022_[4 DMI][18F]26_spike - HERM)

	Reten. Time [min]	Area [CTS(RLU)/s.s]	Height [CTS(RLU)/s]	Area [%]	RCC [%]
1	1,200	1085,000	152,889	13,0	100,000
2	4,433	478,000	43,576	5,7	44,055
3	5,550	6804,000	1086,231	81,3	627,097
	Total	8367,000	1282,695	100,0	771,152

Figure S83: HPLC traces of crude 2,3,5,6-tetrafluorophenyl 4-[^{18}F]fluorobenzoate ([^{18}F]**26**) prepared from the corresponding boronic acid precursor (2.5 µmol) in *n*BuOH/DMI and spiked with 2,3,5,6-tretrafluorophenyl 4-fluorobenzoate (**26**). Blue trace: UV, λ = 254 nm; red trace: radioactivity. Abbreviations: 4-[^{18}F]FBA – 4-[^{18}F]fluorobenzoic acid; p.-c.i – post-column injection.

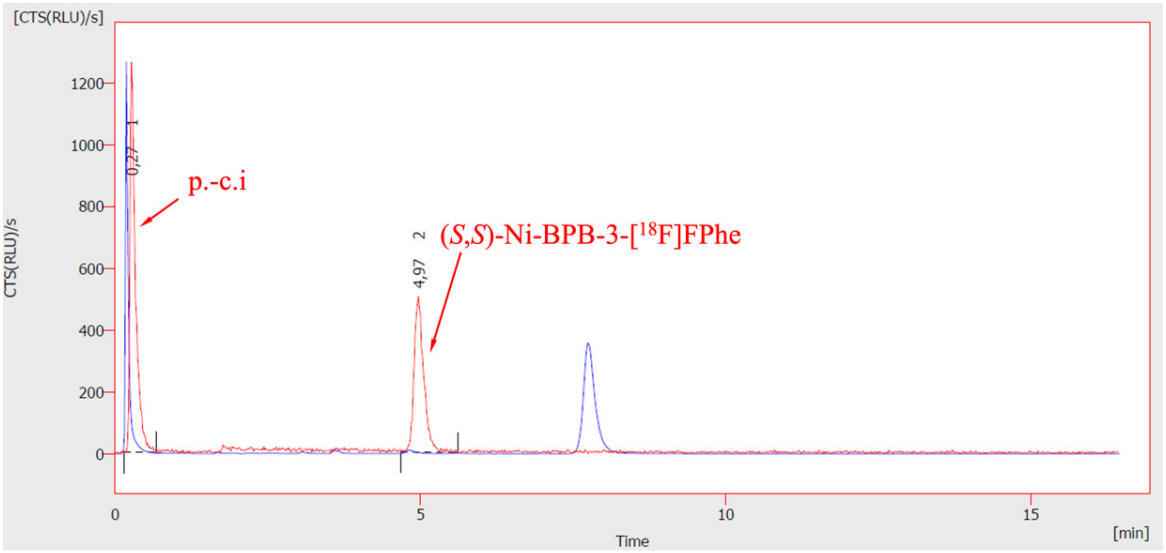

Result Table (Uncal - Data|alc-enhanced_718_20_04_2022_[4 DMI]L-[18F]FPhe - HERM)

	Reten. Time [min]	Area [CTS(RLU)/s.s]	Height [CTS(RLU)/s]	Area [%]
1	0,267	8140,000	1263,000	59,3
2	4,967	5583,000	502,911	40,7
	Total	13723,000	1765,911	100,0

Figure S84: HPLC traces of crude (*S*,*S*)-Ni-BPB-3-[^{18}F]FPhe prepared from (*S*,*S*)-**10** (2.5 µmol). Blue trace: UV, λ = 254 nm; red trace: radioactivity. Abbreviation: p.-c.i – post-column injection.

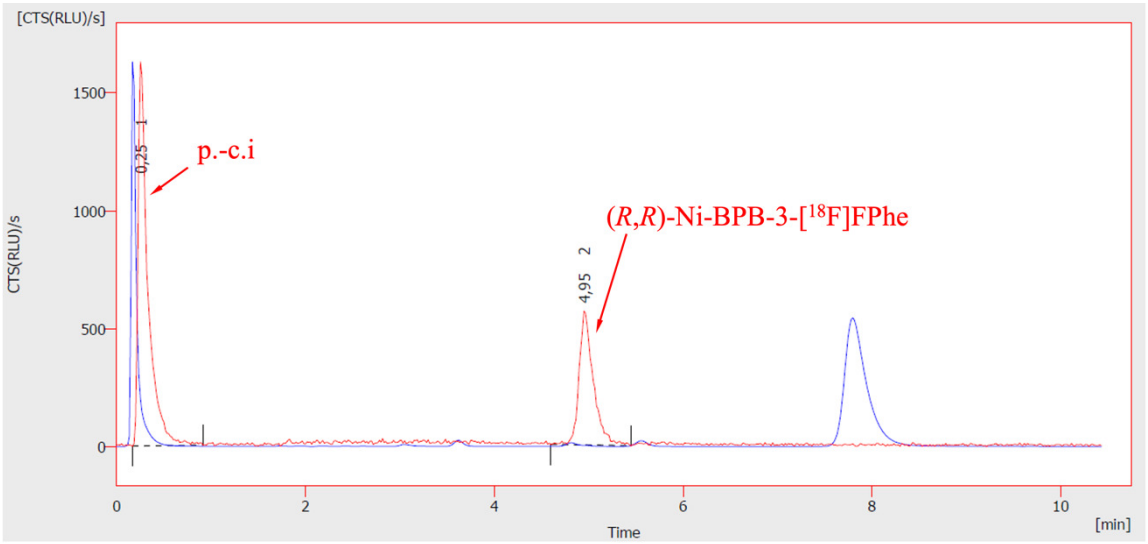

Result Table (Uncal - Data|alc-enhanced_721_20_04_2022_[4 DMI]D-[18F]FPhe - HERM)

	Reten. Time [min]	Area [CTS(RLU)/s.s]	Height [CTS(RLU)/s]	Area [%]
1	0,250	11845,500	1626,667	66,3
2	4,950	6025,000	566,471	33,7
	Total	17870,500	2193,137	100,0

Figure S85: HPLC traces of crude (*R*,*R*)-Ni-BPB-3-[^{18}F]FPhe prepared from (*R*,*R*)-**10** (2.5 µmol). Blue trace: UV, λ = 254 nm; red trace: radioactivity. Abbreviation: p.-c.i – post-column injection.

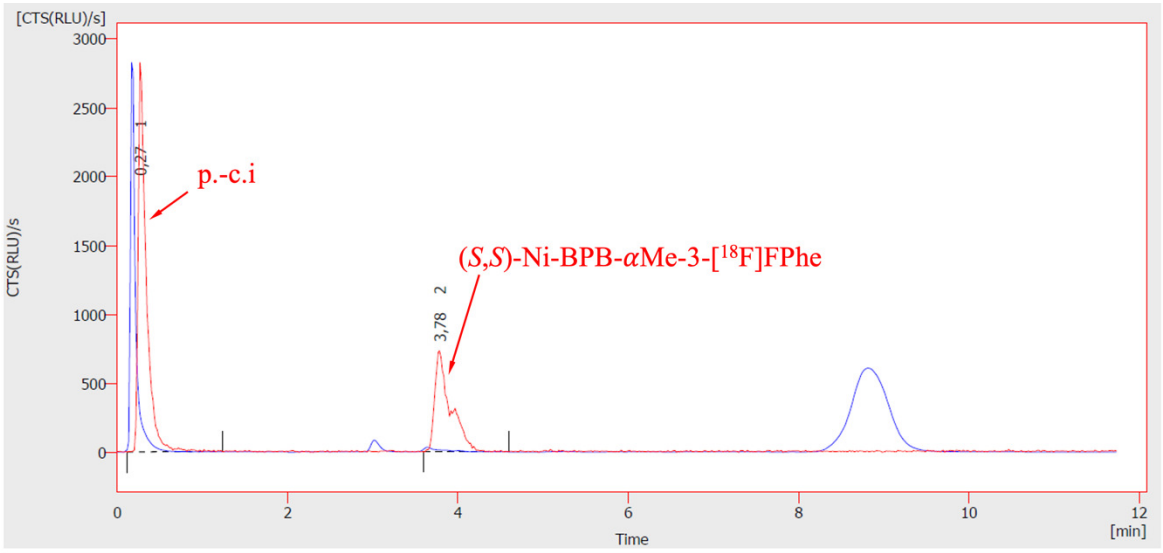

Result Table (Uncal - Data|alc-enhanced_731_21_04_2022_[4 DMI]L-alpha_Me_[18F]FPhe - HERM)

	Reten. Time [min]	Area [CTS(RLU)/s.s]	Height [CTS(RLU)/s]	Area [%]
1	0,267	18735,500	2825,597	66,3
2	3,783	9534,000	733,817	33,7
	Total	28269,500	3559,414	100,0

Figure S86: HPLC traces of crude (*S*,*S*)-Ni-BPB-αMe-3-[^{18}F]FPhe prepared from (*S*,*S*)-**12** (2.5 µmol). Blue trace: UV, λ = 254 nm; red trace: radioactivity. Abbreviation: p.-c.i – post-column injection.

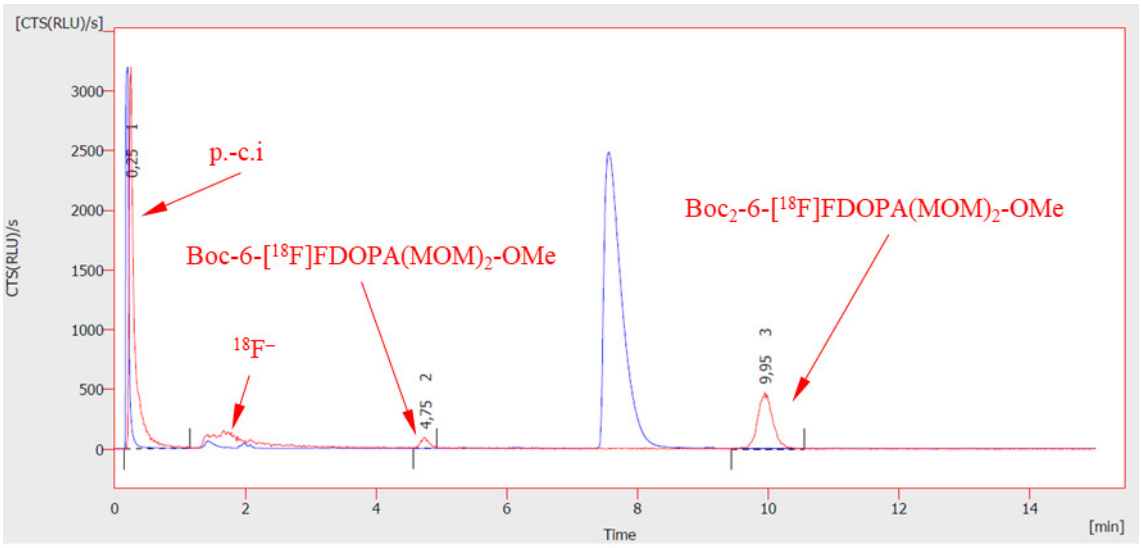

Result Table (Uncal - Data|alc-enhanced_825_28_06_2022_[4 DMI]FDOPA-SnMe3_90°C_MeOH - HERM)

	Reten. Time [min]	Area [CTS(RLU)/s.s]	Height [CTS(RLU)/s]	Area [%]
1	0,250	17861,000	3199,400	68,1
2	4,750	829,000	94,500	3,2
3	9,950	7530,500	476,537	28,7
	Total	26220,500	3770,437	100,0

Figure S87: HPLC traces of crude Boc_2-6-[^{18}F]FDOPA$(MOM)_2$-OMe prepared from **S6** (2.5 µmol). Partial deprotection of the radiolabeled product to Boc-6-[^{18}F]FDOPA$(MOM)_2$-OMe was observed.[25] Blue trace: UV, λ = 254 nm; red trace: radioactivity. Abbreviation: p.-c.i – post-column injection.

3.15 Preparation of 6-[^{18}F]FDOPA

[^{18}F]F^- (0.2–3 GBq) was eluted from the QMA cartridge with a solution of Et_4NOTf (1 mg, 3.6 µmol) in anhydrous MeOH (500 µL). MeOH was evaporated at 60 °C under reduced pressure in a stream of argon. The reactor was filled with argon and sealed with a silicone septum. Thereafter, a solution of **S6** (1.7 mg, 2.5 µmol) and $Cu(4\text{-}PhPy)_4(ClO_4)_2$ (8.8 mg, 10 µmol) in anhydrous DMI (800 µL) was added via a cannula through the septum and the reaction mixture was heated at 90 °C for 10 min. That followed, the reaction mixture was diluted with H_2O (15 mL) and loaded onto a C18 cartridge. The cartridge was washed with H_2O (5 mL) and the radiolabeled intermediate was eluted with MeOH (500 µL). The MeOH was evaporated at 60 °C under reduced pressure in a stream of argon, 6 M HCl (500 µL) was added to the residue and the mixture was heated at 110 °C for 10 min. Thereafter, 6 M NaOH (400 µL) followed by H_2O (600 µL) were added to the mixture, and the resulting solution was loaded onto a preparative HPLC column. The product fraction eluting at 9–11 min was collected.

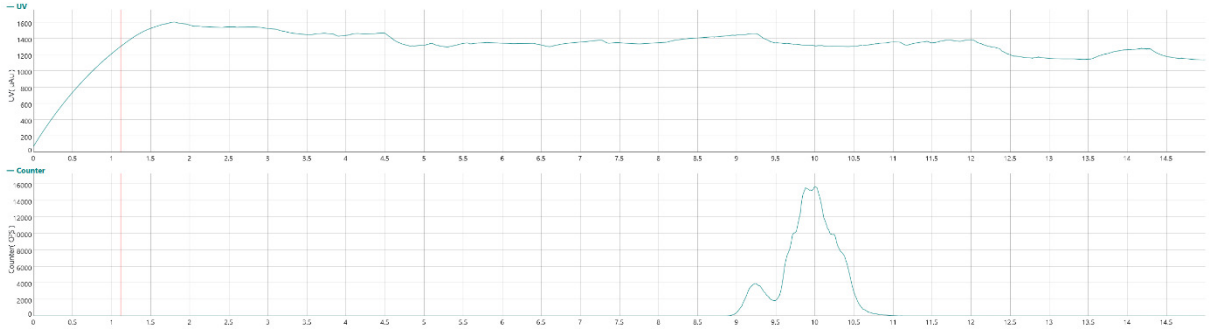

Figure S88: Purification of 6-[^{18}F]FDOPA by preparative HPLC (top: UV trace, λ=254 nm; bottom: radioactivity trace).

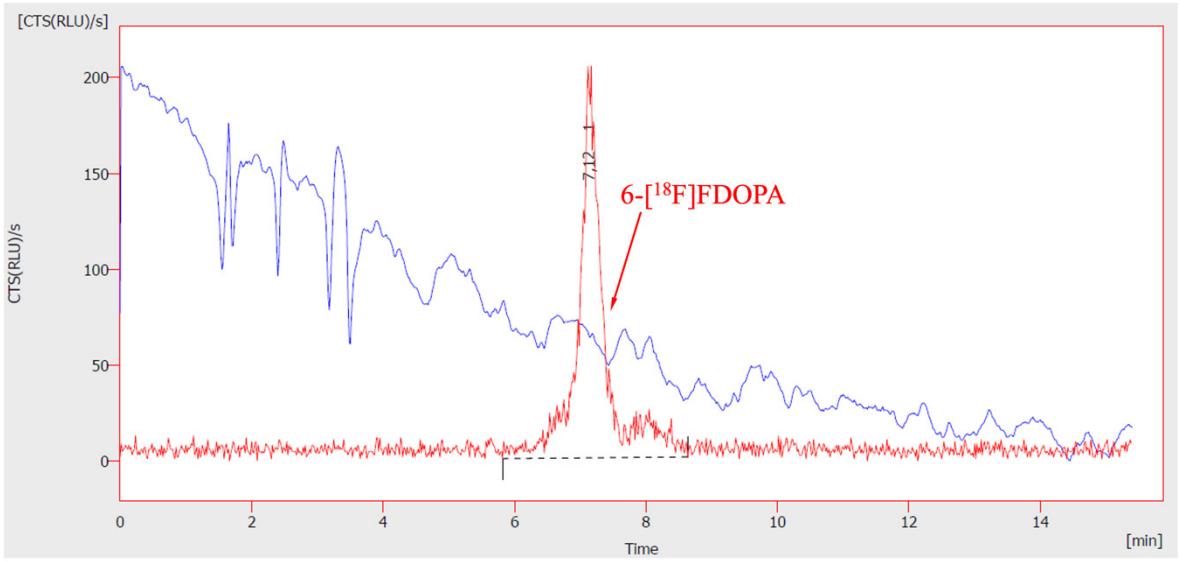

Result Table (Uncal - Data|alc-enhanced_600_09_03_2022_[4 DMI][18F]FDOPA_hplc - HERM)

	Reten. Time [min]	Area [CTS(RLU)/s.s]	Height [CTS(RLU)/s]	Area [%]
1	7,117	5387,500	204,538	100,0
	Total	5387,500	204,538	100,0

Figure S89: HPLC traces of purified 6-[^{18}F]FDOPA for quality control. Blue trace: UV channel, λ=254 nm; red trace: radioactivity channel

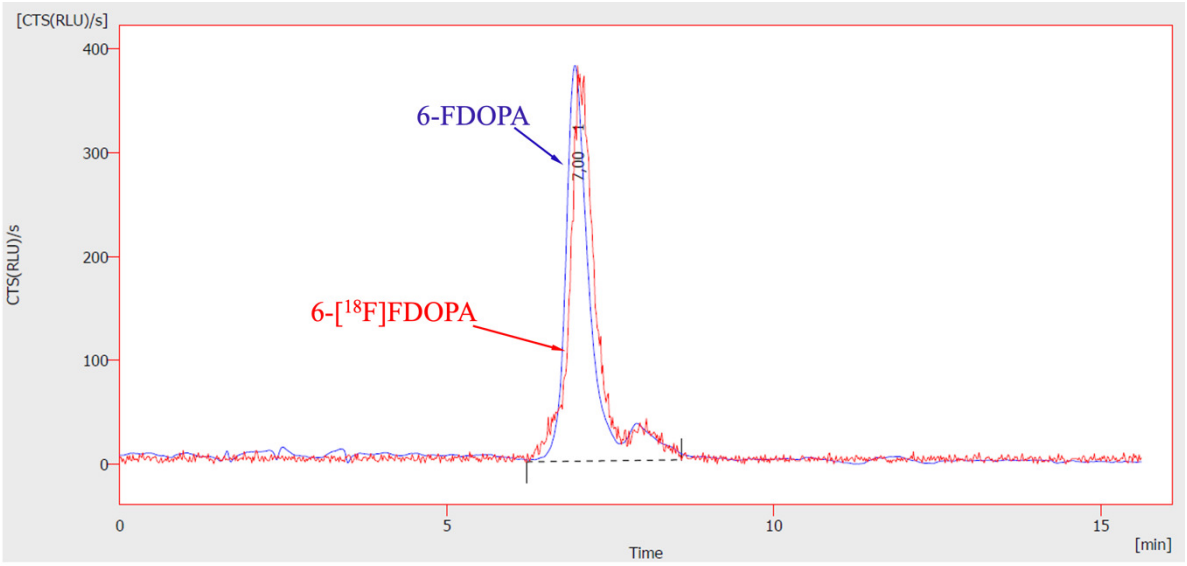

Result Table (Uncal - Data|alc-enhanced_601_09_03_2022_[4 DMI][18F]FDOPA_hplc_spike - HERM)

	Reten. Time [min]	Area [CTS(RLU)/s.s]	Height [CTS(RLU)/s]	Area [%]
1	7,000	10902,000	381,338	100,0
	Total	10902,000	381,338	100,0

Figure S90: HPLC traces of purified 6-[^{18}F]FDOPA spiked with an authentic sample of 6-FDOPA. Blue trace: UV channel, λ=254 nm; red trace: radioactivity channel.

4 References

[1] M. Willmann, J. Hegger, B. Neumaier, J. Ermert, *ACS Med. Chem. Lett.* **2021**, *12*, 738–744.

[2] C. Hoffmann, S. Evcüman, F. Neumaier, B. D. Zlatopolskiy, S. Humpert, D. Bier, M. Holschbach, A. Schulze, H. Endepols, B. Neumaier, *ACS Chem. Neurosci.* **2021**, *12*, 3335–3346.

[3] S. Li, Z. Cai, X. Wu, D. Holden, R. Pracitto, M. Kapinos, H. Gao, D. Labaree, N. Nabulsi, R. E. Carson, Y. Huang, *ACS Chem. Neurosci.* **2019**, *10*, 1544–1554.

[4] A. Craig, N. Kolks, E. A. Urusova, J. Zischler, M. Brugger, H. Endepols, B. Neumaier, B. D. Zlatopolskiy, *Chem. Commun.* **2020**, *56*, 9505–9508.

[5] A. Gaucher, L. Dutot, O. Barbeau, W. Hamchaoui, M. Wakselman, J.-P. Mazaleyrat, *Tetrahedron: Asymmetry* **2005**, *16*, 857–864.

[6] A. R. Byington, W. E. Bull, *Inorganica Chim. Acta* **1977**, *21*, 239–244.

[7] J. S. Haynes, S. J. Rettig, J. R. Sams, J. Trotter, R. C. Thompson, *Inorg. Chem.* **1988**, *27*, 1237–1241.

[8] Y. Agnus, M. Labarelle, R. Louis, B. Metz, *Acta Crystallogr. Sect. C Cryst. Struct. Commun.* **1994**, *50*, 536–538.

[9] W. Libug, I. Uruska, *Inorg. Chem.* **1966**, *5*, 256–264.

[10] G. A. Bowmaker, C. Di Nicola, C. Pettinari, B. W. Skelton, N. Somers, A. H. White, *Dalt. Trans.* **2011**, *40*, 5102.

[11] M. H. H. Wurzenberger, N. Szimhardt, J. Stierstorfer, *J. Am. Chem. Soc.* **2018**, *140*, 3206–3209.

[12] M. Roy, D. N. K. Pham, A. Kreider-Mueller, J. A. Golen, D. R. Manke, *Acta Crystallogr. Sect. C Struct. Chem.* **2018**, *74*, 263–268.

[13] G. A. Barclay, C. H. L. Kennard, *J. Chem. Soc.* **1961**, 5244.

[14] F. Hanic, D. Štempelová, K. Hanicová, *Acta Crystallogr.* **1964**, *17*, 633–639.

[15] A. M. Kałuża, S. Mukherjee, S.-Q. Wang, D. J. O'Hearn, M. J. Zaworotko, *Chem. Commun.* **2020**, *56*, 1940–1943.

[16] K. Al Sarraj, J. Gouteron, S. Jeannin, Y. Jeannin, *Acta Crystallogr. Sect. C Cryst. Struct. Commun.* **1987**, *43*, 1261–1264.

[17] V. Raab, M. Merz, J. Sundermeyer, *J. Mol. Catal. A Chem.* **2001**, *175*, 51–63.

[18] N. J. Taylor, E. Emer, S. Preshlock, M. Schedler, M. Tredwell, S. Verhoog, J. Mercier, C. Genicot, V. Gouverneur, *J. Am. Chem. Soc.* **2017**, *139*, 8267–8276.

[19] P. Luo, J. P. Dinnocenzo, *J. Org. Chem.* **2015**, *80*, 9240–9246.

[20] K. Komeyama, R. Asakura, K. Takaki, *Org. Biomol. Chem.* **2015**, *13*, 8713–8716.

[21] A. Hofer, G. Kovacs, A. Zappatini, M. Leuenberger, M. A. Hediger, M. Lochner, *Bioorg. Med. Chem.* **2013**, *21*, 3202–3213.

[22] B. Shi, R. W. Boyle, *J. Chem. Soc. Perkin Trans. 1* **2002**, 1397–1400.

[23] S. P. A. Hinkes, C. D. P. Klein, *Org. Lett.* **2019**, *21*, 3048–3052.

[24] N. Walter, J. Bertram, B. Drewes, V. Bahutski, M. Timmer, M. B. Schütz, F. Krämer, F. Neumaier, H. Endepols, B. Neumaier, B. D. Zlatopolskiy, *Eur. J. Med. Chem.* **2022**, *237*, 114383.

[25] J. Zischler, N. Kolks, D. Modemann, B. Neumaier, B. D. Zlatopolskiy, *Chem. - Eur. J.* **2017**, *23*, 3251–3256.

Supporting Information for

[^{18}F]R91150: Improved radiosynthesis and in vivo evaluation as imaging probe for 5-HT$_{2A}$ receptors

Chris Hoffmann[1,2], Heike Endepols[1,2,3], Elizaveta A. Urusova[1,2], Dominik Elchine[1], Felix Neumaier[1,2], Bernd Neumaier[1,2]*, Boris D. Zlatopolskiy[1,2]

[1] *Forschungszentrum Jülich GmbH, Institute of Neuroscience and Medicine, Nuclear Chemistry (INM-5), Wilhelm-Johnen-Straße, 52428 Jülich, Germany.*

[2] *University of Cologne, Faculty of Medicine and University Hospital Cologne, Institute of Radiochemistry and Experimental Molecular Imaging, Kerpener Straße 62, 50937 Cologne, Germany.*

[3] *University of Cologne, Faculty of Medicine and University Hospital Cologne, Department of Nuclear Medicine, Kerpener Straße 62, 50937 Cologne, Germany.*

[*] *Corresponding author; e-mail: b.neumaier@fz-juelich.de*

Table of contents

1 NMR spectra

1.1 Compound **3a**

^{1}H-NMR spectrum of **3a**

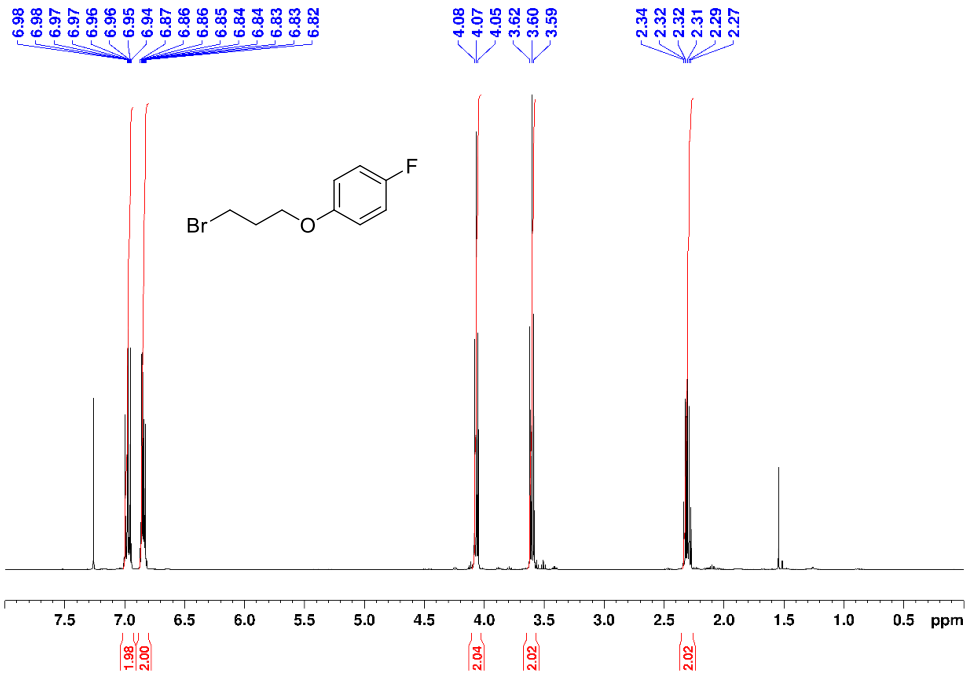

^{13}C-NMR APT spectrum of **3a**

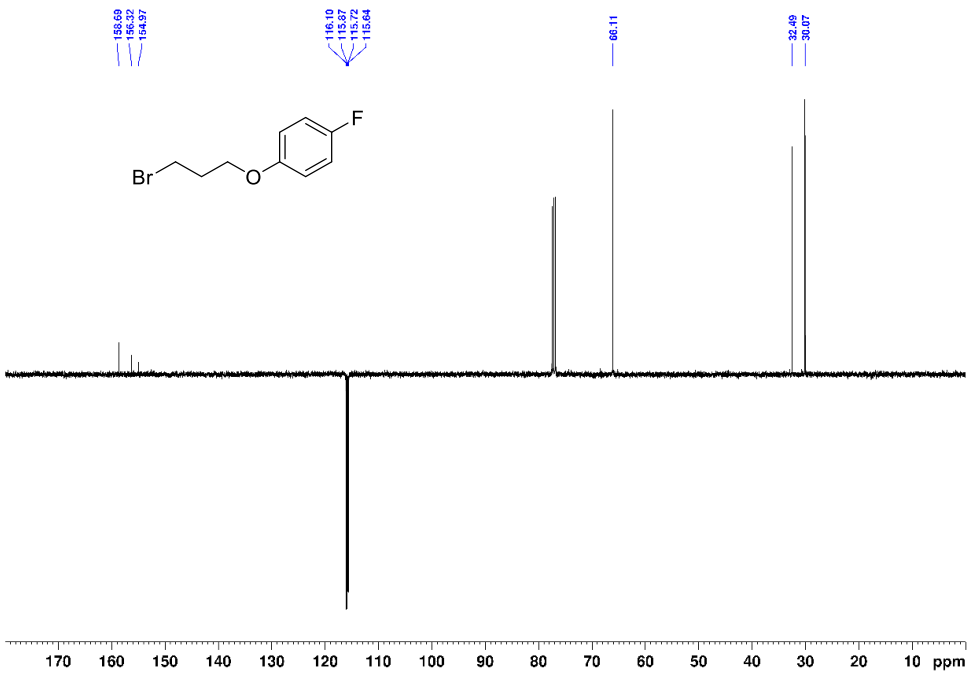

^{19}F-NMR spectrum of **3a**

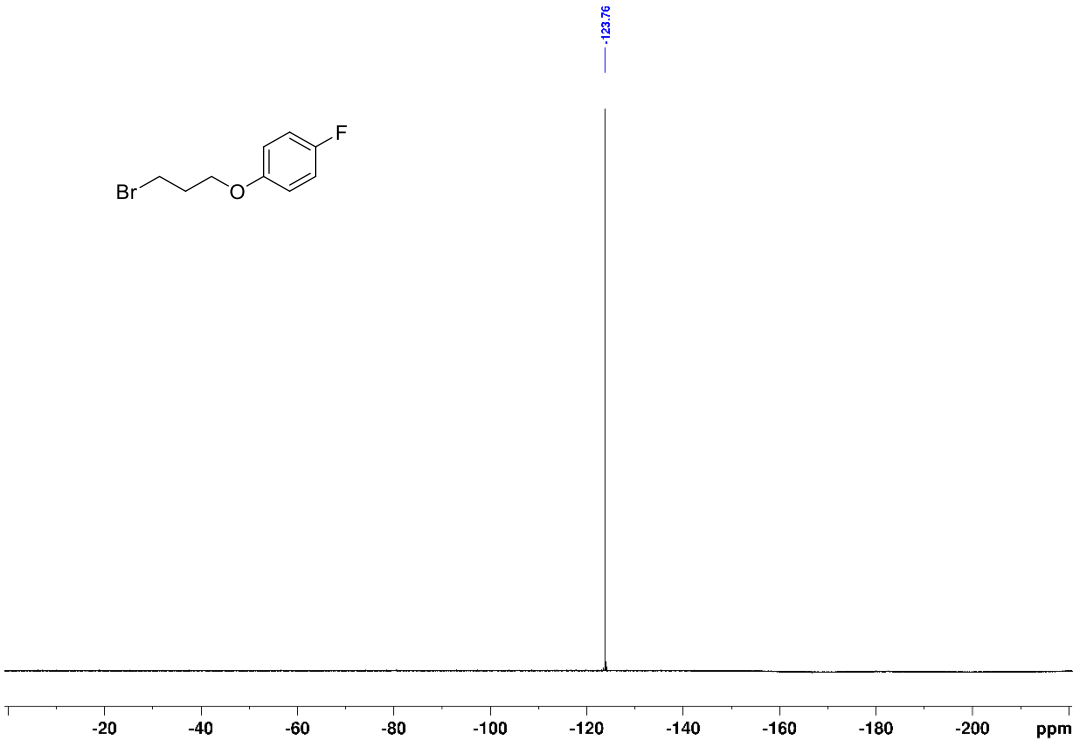

1.2 Compound **3b**

^{1}H-NMR spectrum of **3b**

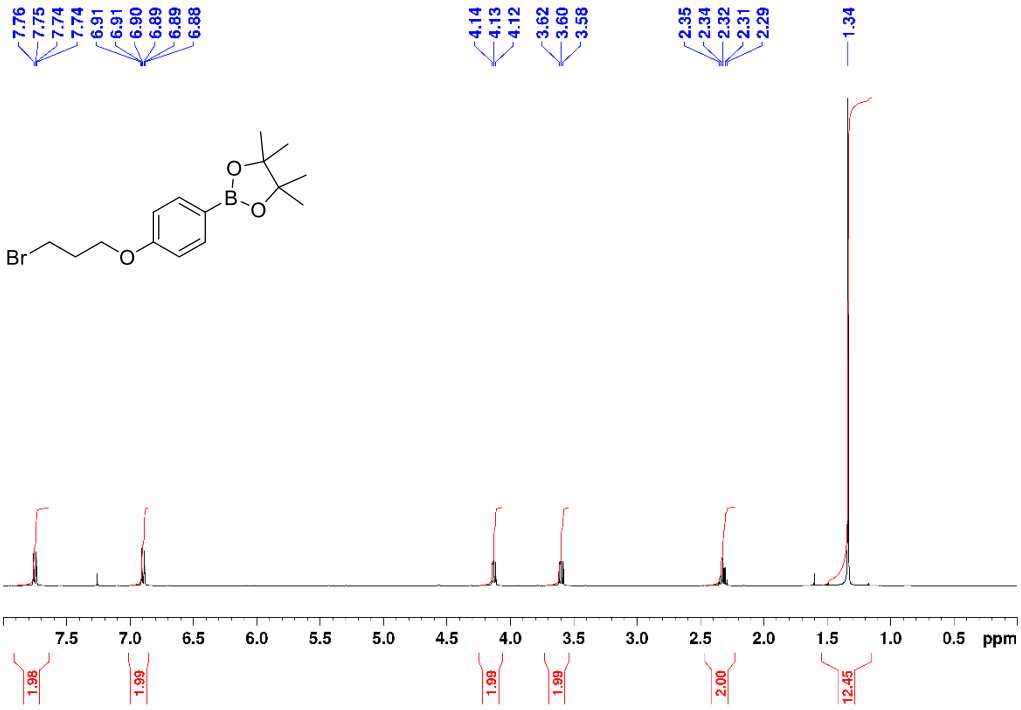

^{13}C-NMR APT spectrum of **3b**

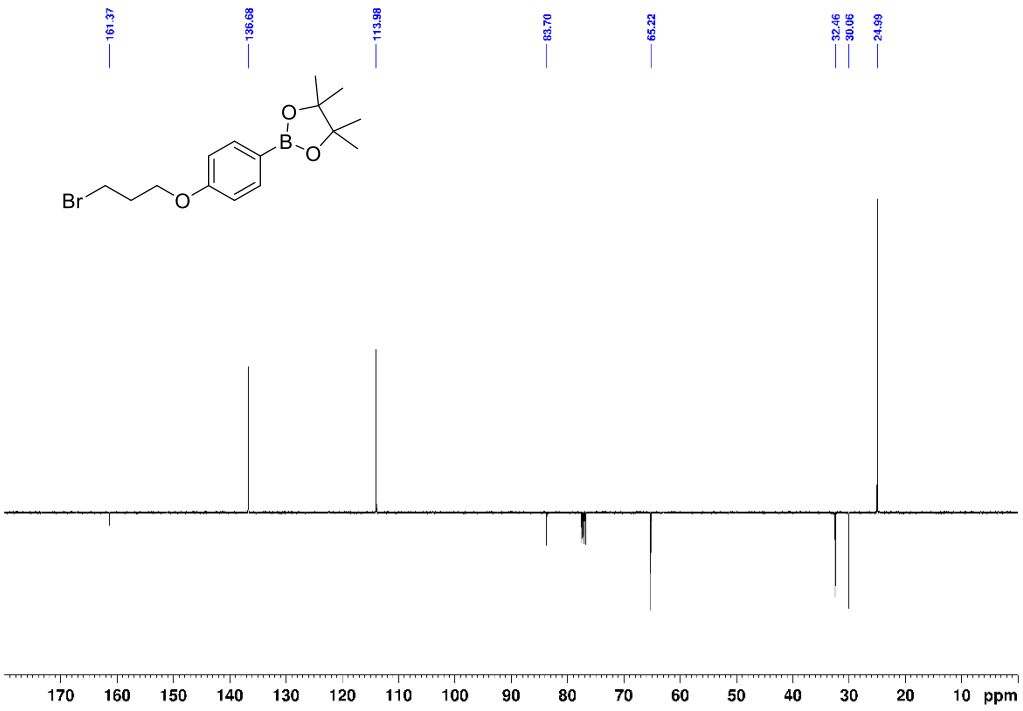

1.3 Compound **5**

^{1}H-NMR spectrum of **5**

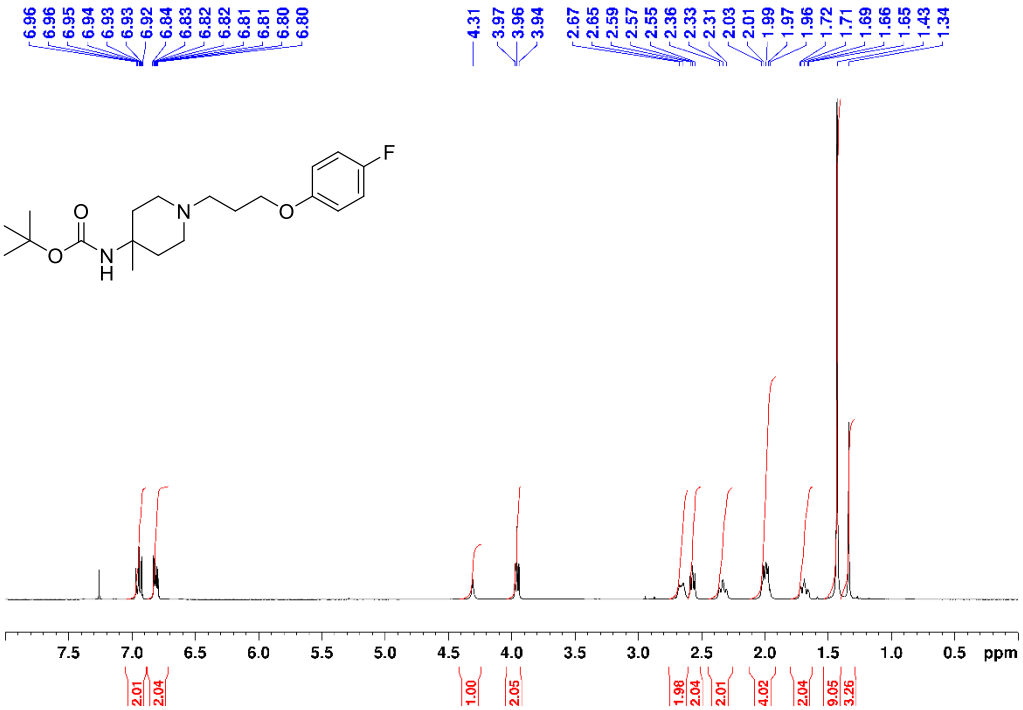

^{13}C-NMR spectrum of **5**

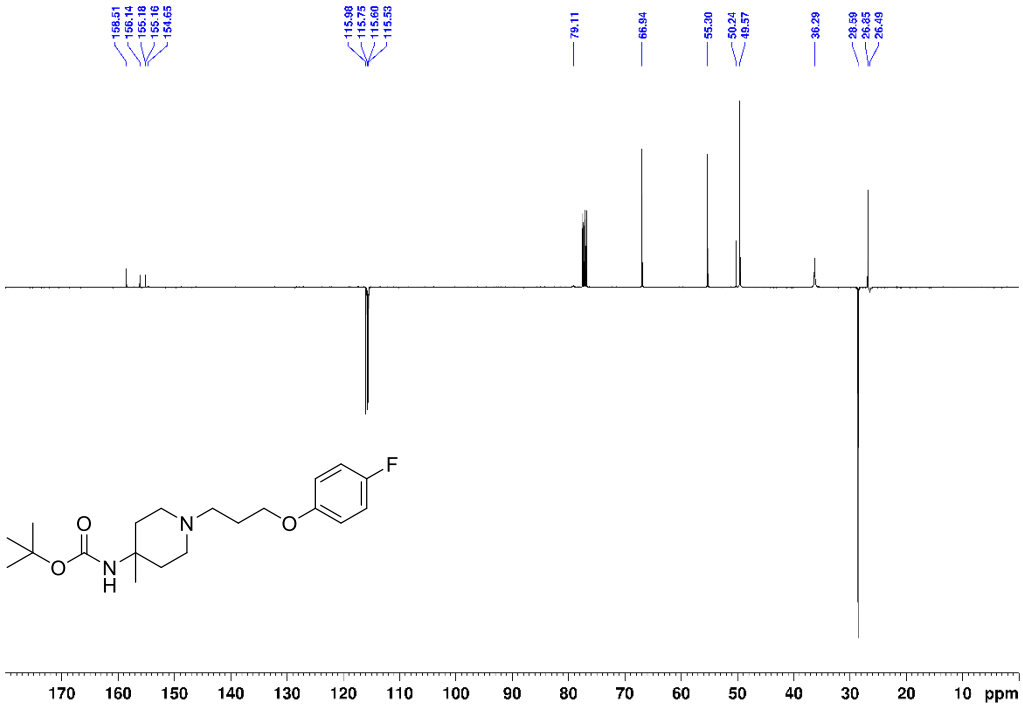

^{19}F-NMR spectrum of **5**

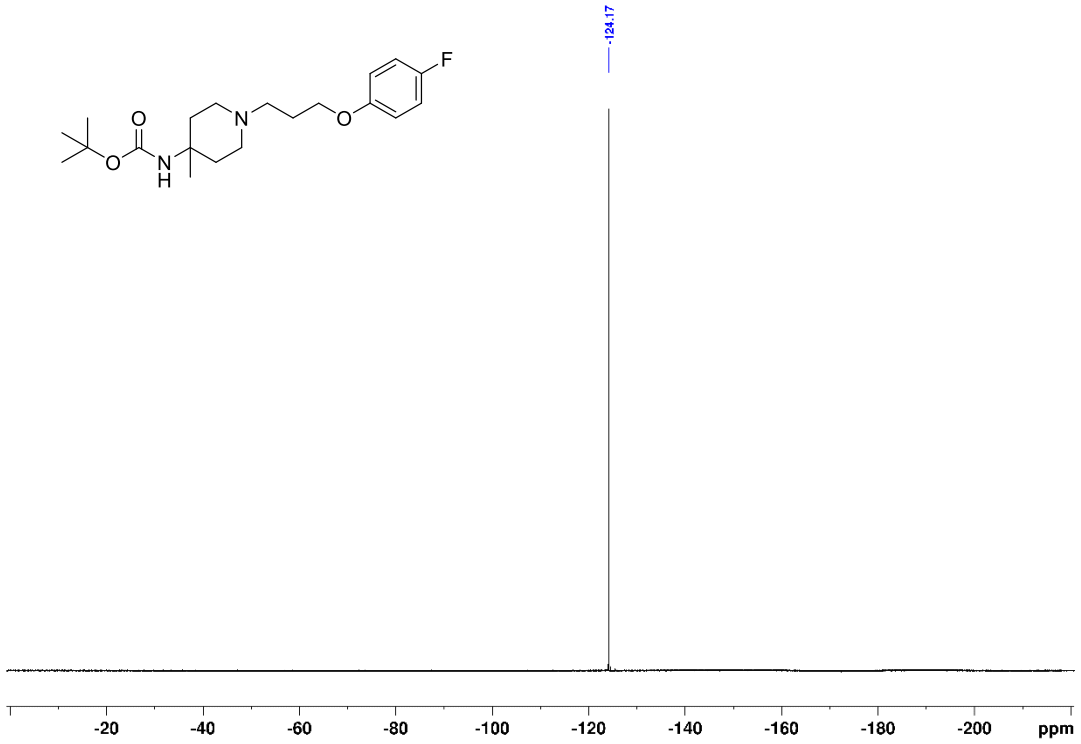

1.4 Compound **6a**

^{1}H-NMR spectrum of **6a**

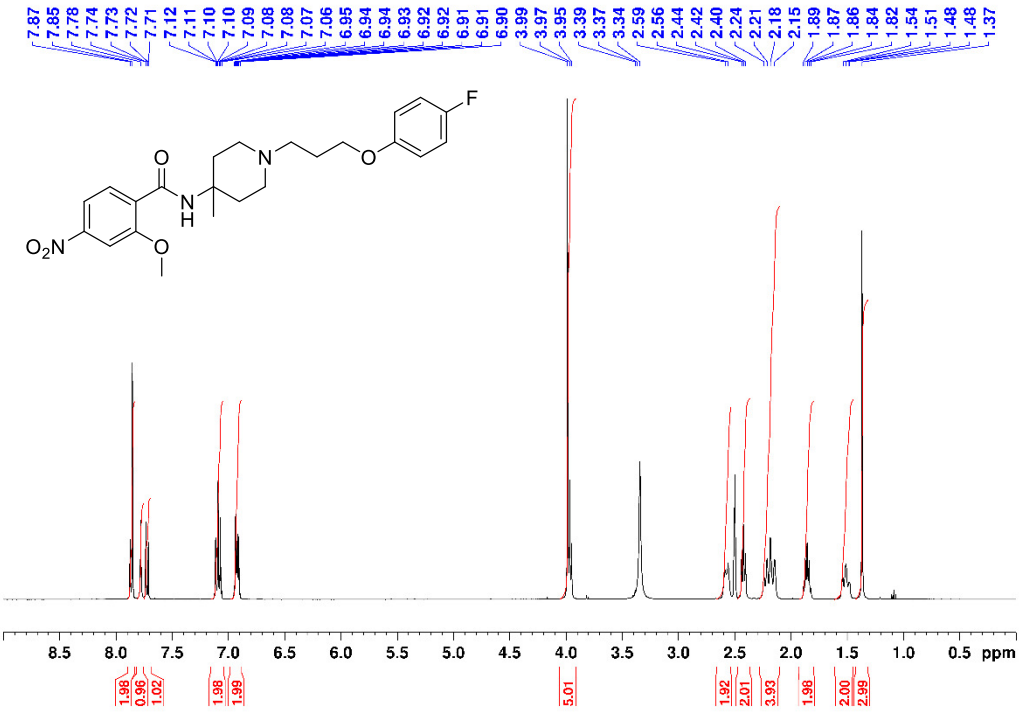

^{13}C-NMR APT spectrum of **6a**

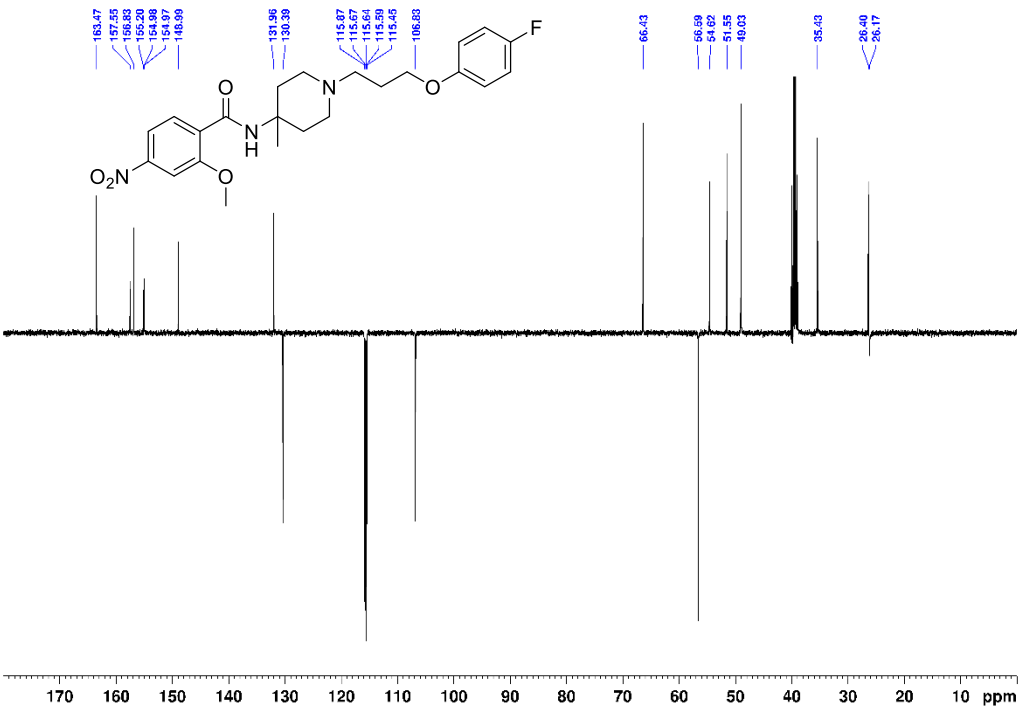

^{19}F-NMR spectrum of **6a**

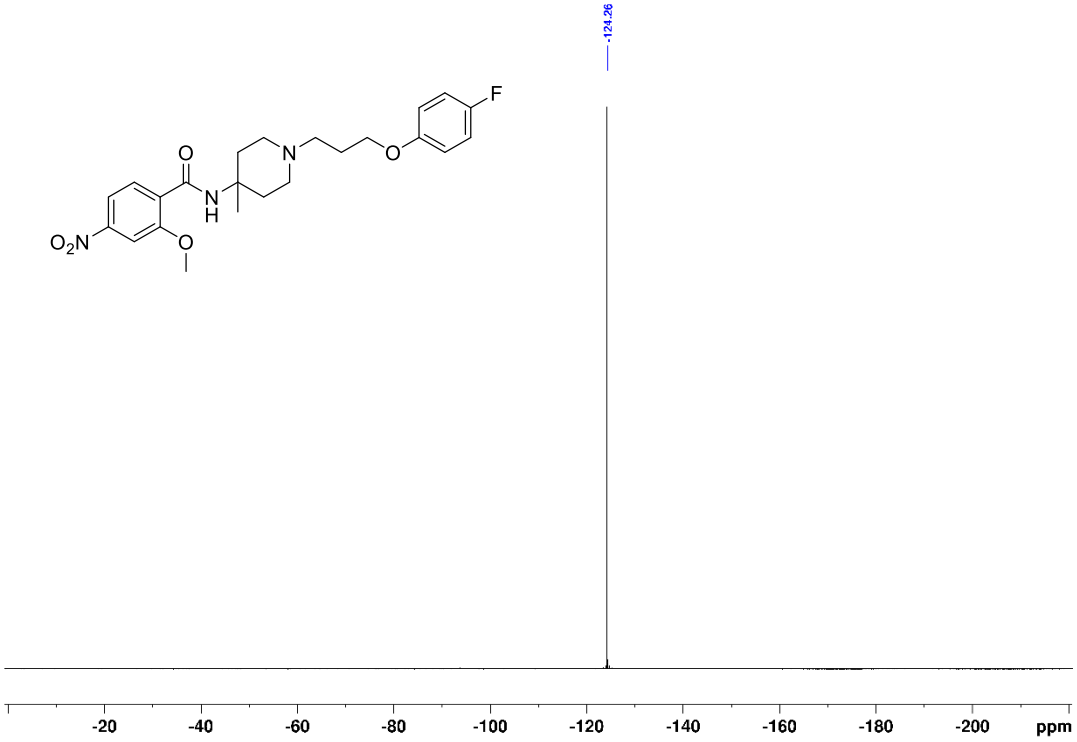

1.5 R91150

^{1}H-NMR spectrum of R91150

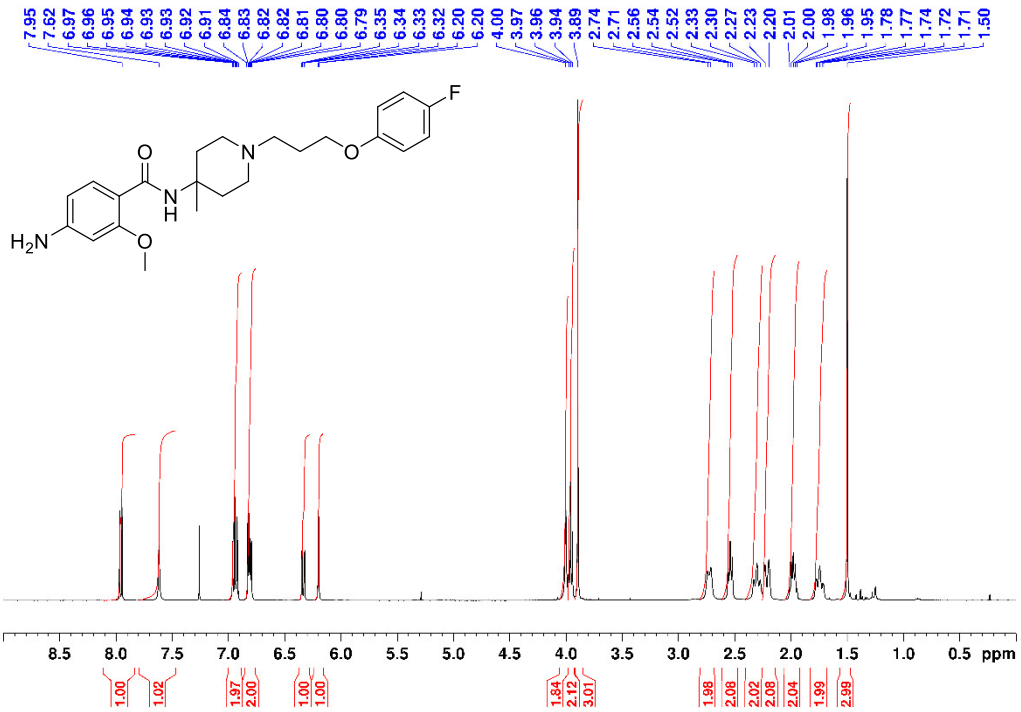

^{13}C-NMR APT spectrum of R91150

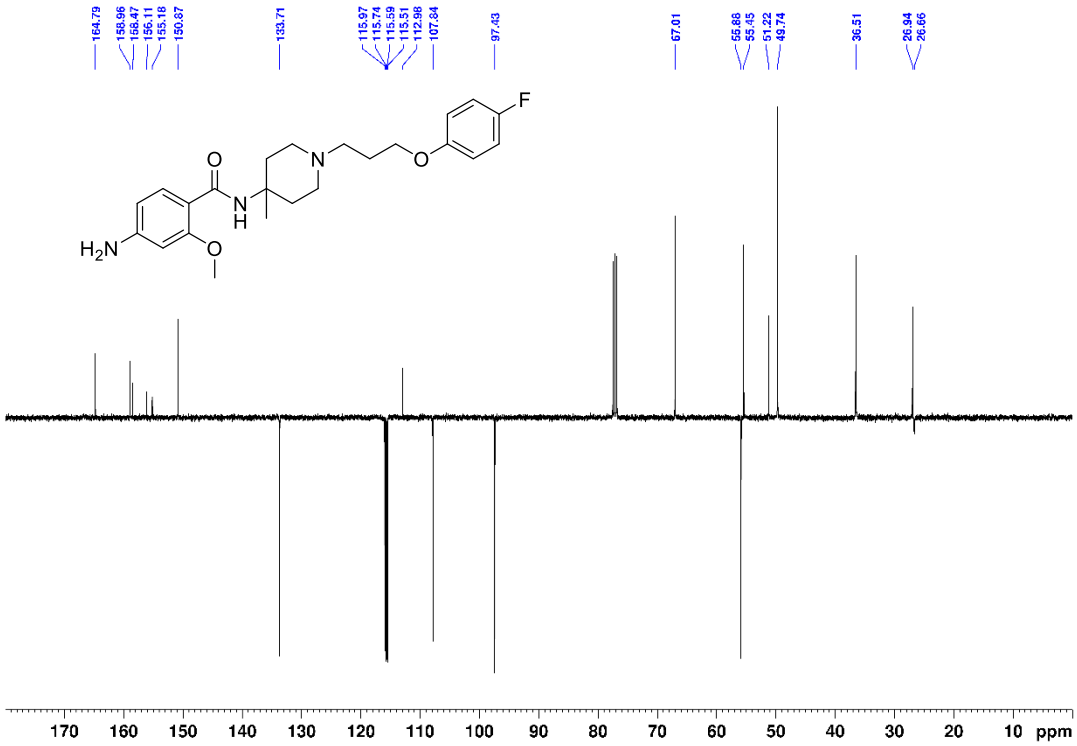

^{19}F-NMR spectrum of R91150

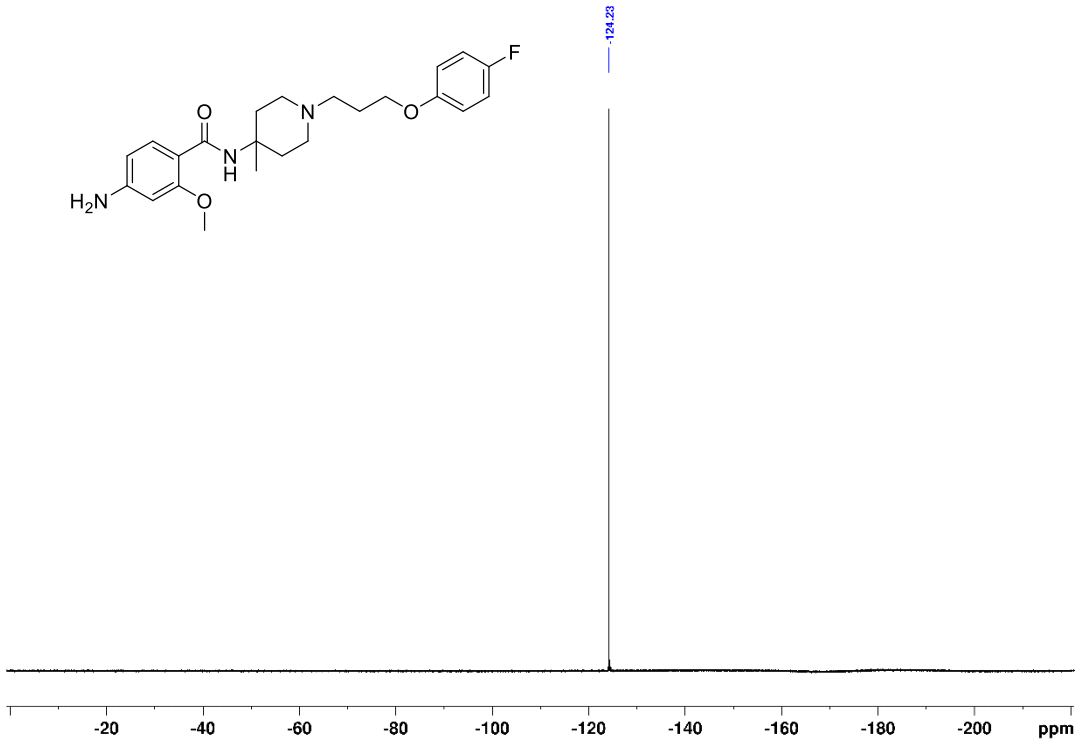

1.6 Compound **8**

^{1}H-NMR spectrum of **8**

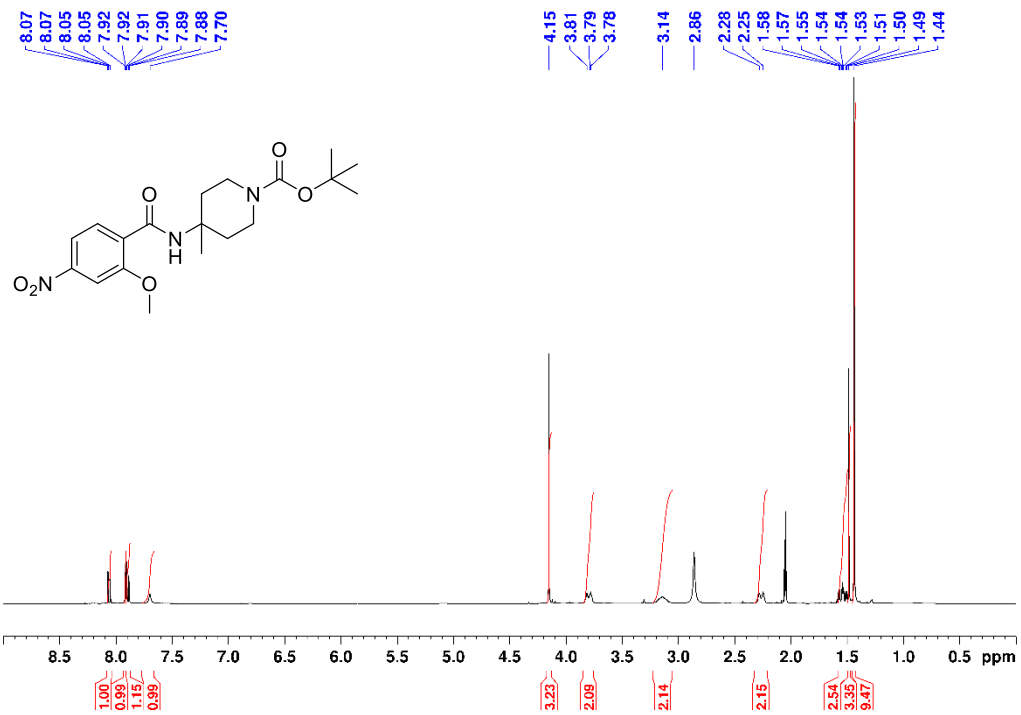

^{13}C-NMR spectrum of **8**

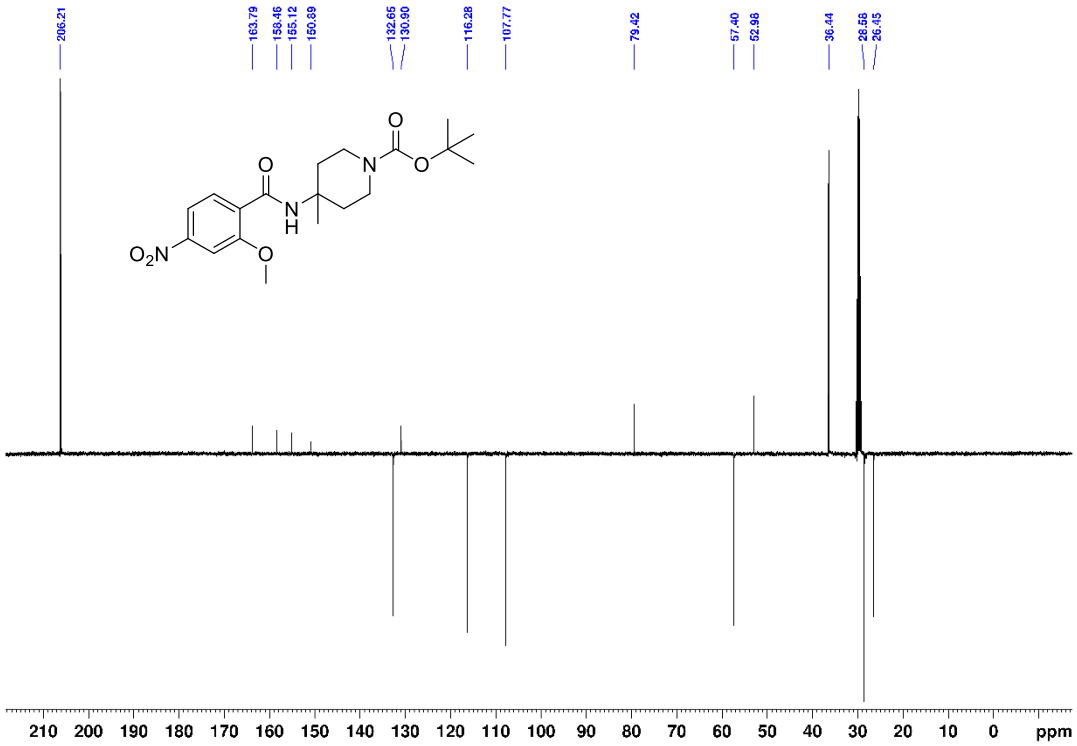

1.7 Compound **9**

^{1}H-NMR spectrum of **9**

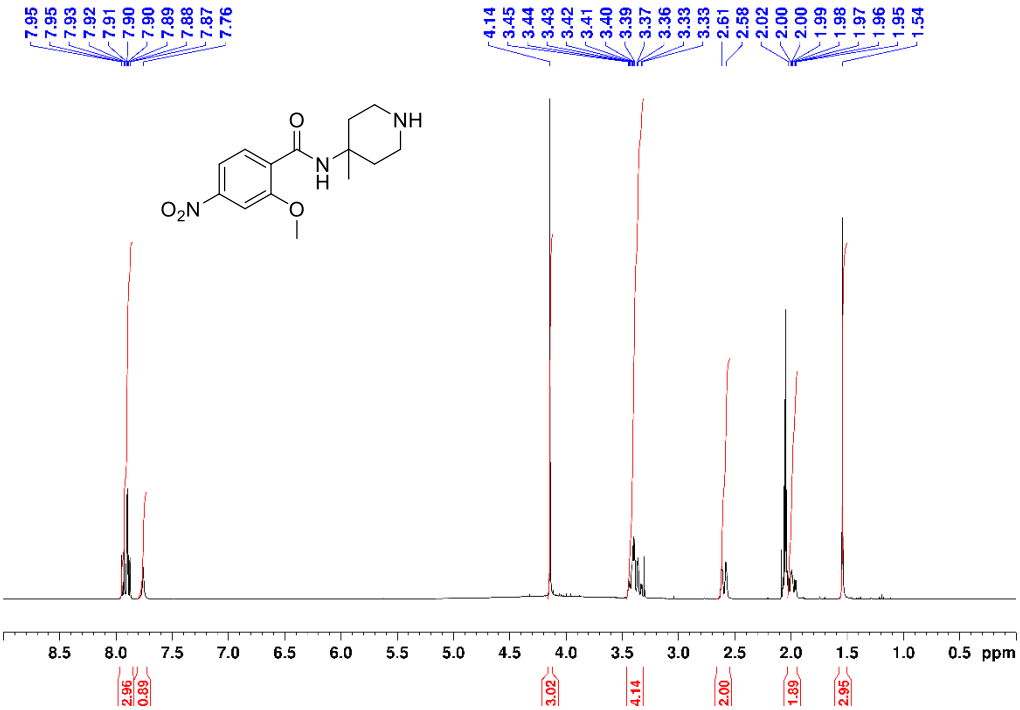

^{13}C-NMR APT spectrum of **9**

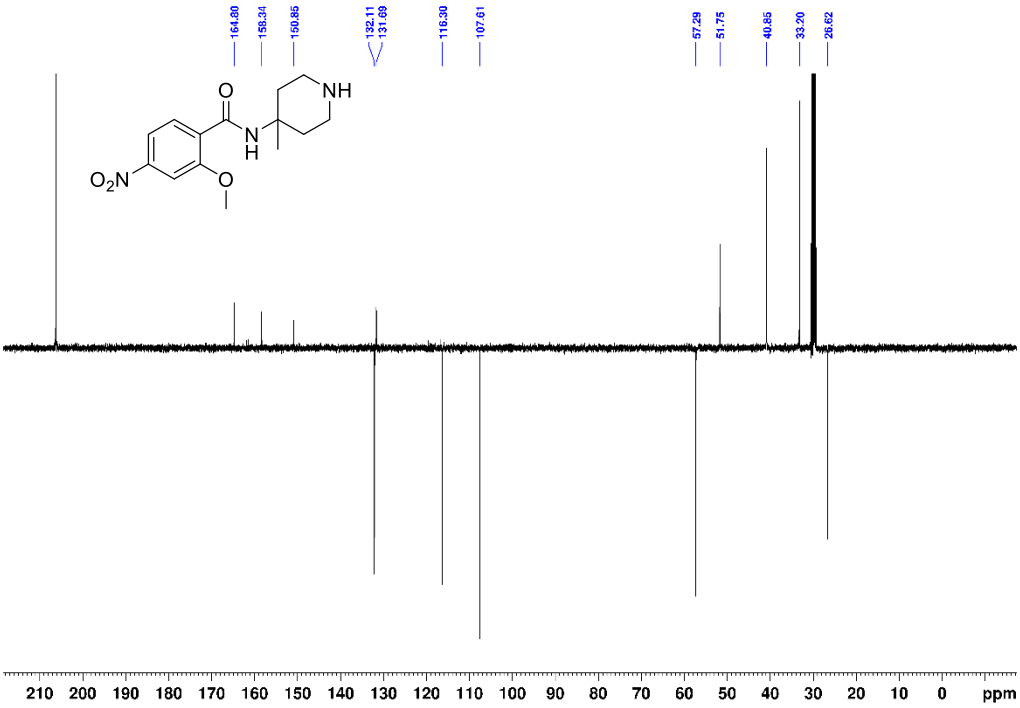

1.8 Compound **6b**

^{1}H-NMR spectrum of **6b**

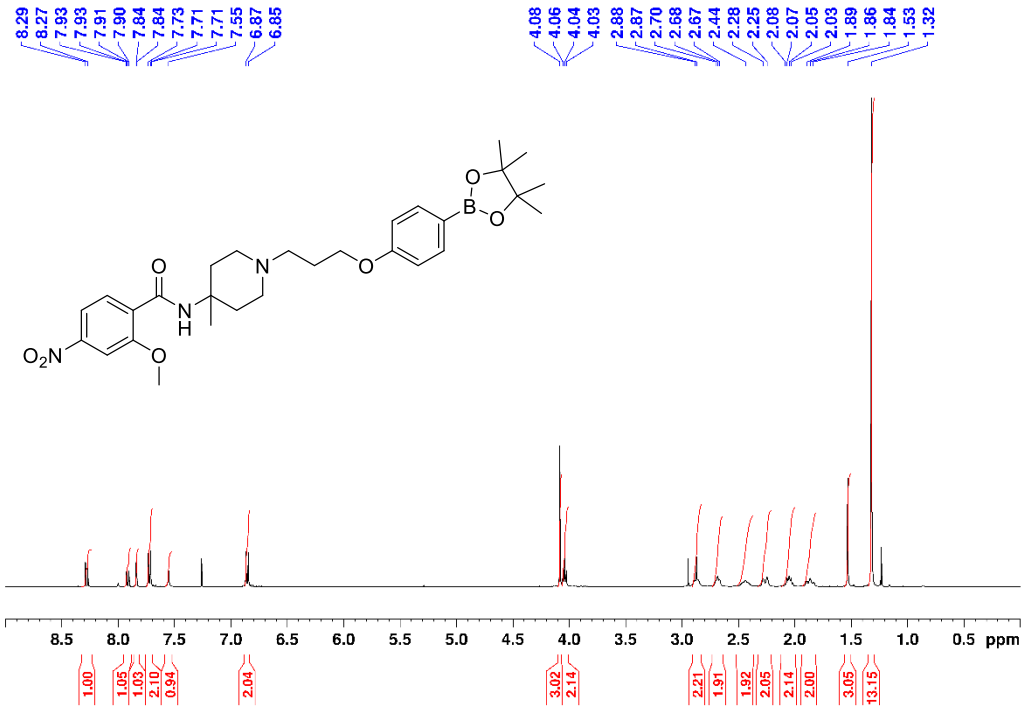

^{13}C-NMR APT spectrum of **6b**

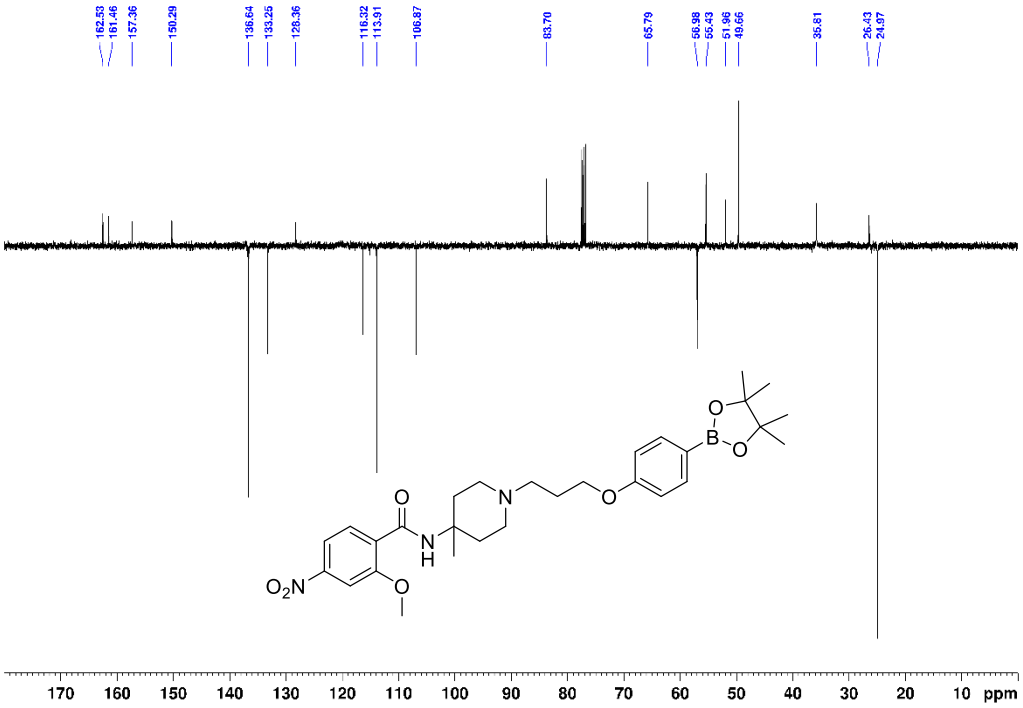

1.9 Compound **1**

^{1}H-NMR spectrum of **1**

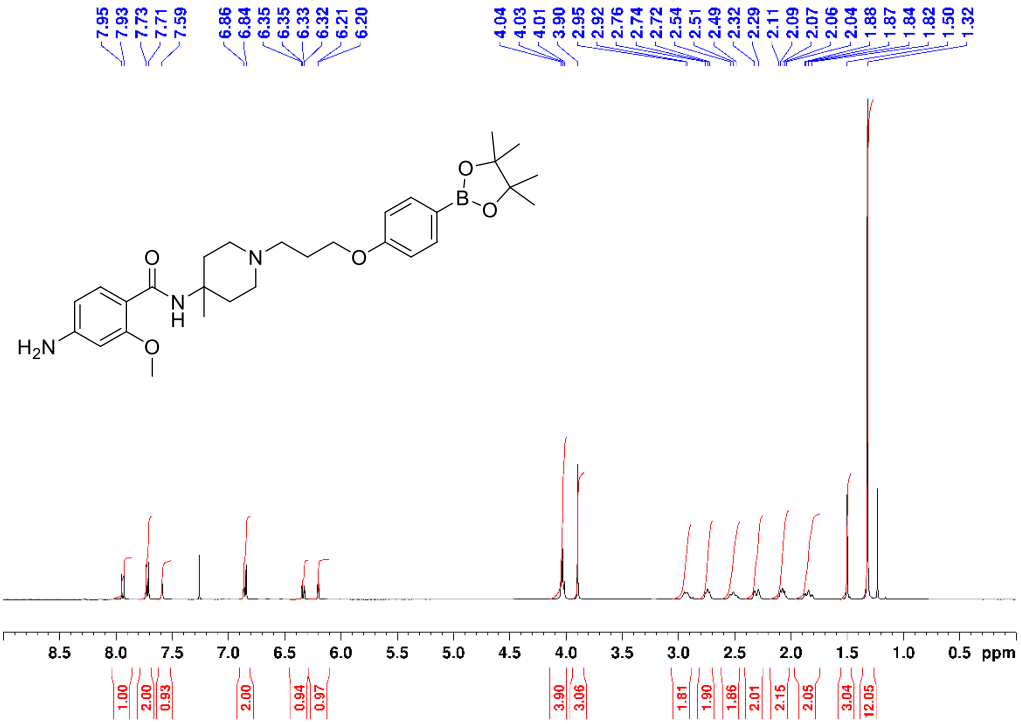

^{13}C-NMR APT spectrum of **1**

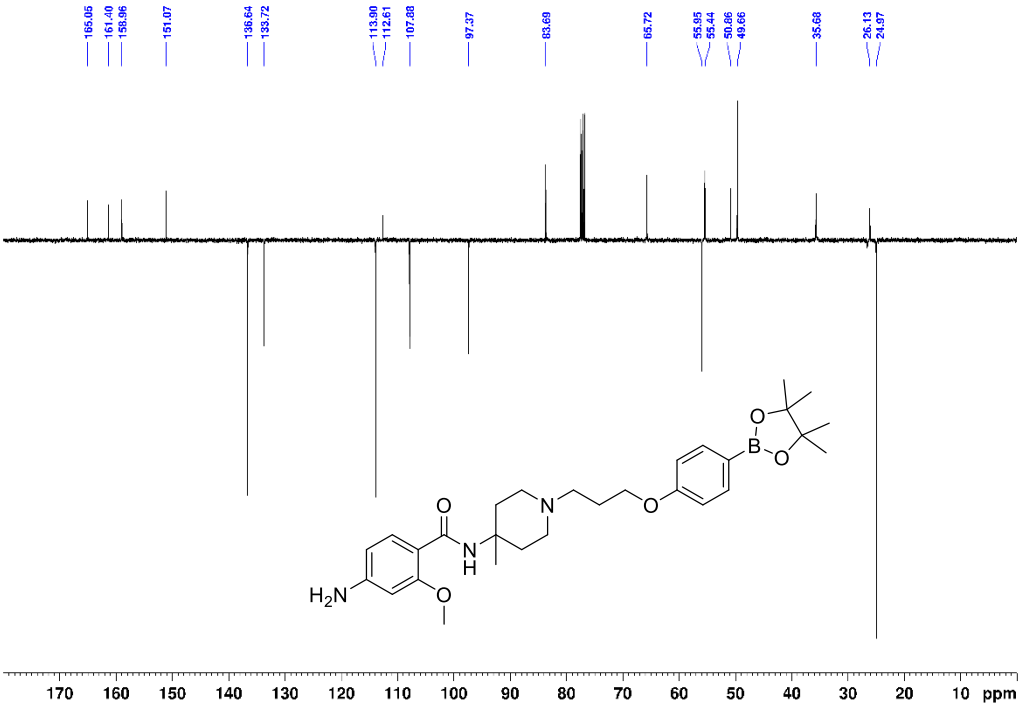

1.10 Benzyl 4-[(*tert*-butoxycarbonyl)amino]-4-methylpiperidine-1-carboxylate

^{1}H-NMR spectrum of benzyl 4-[(*tert*-butoxycarbonyl)amino]-4-methylpiperidine-1-carboxylate

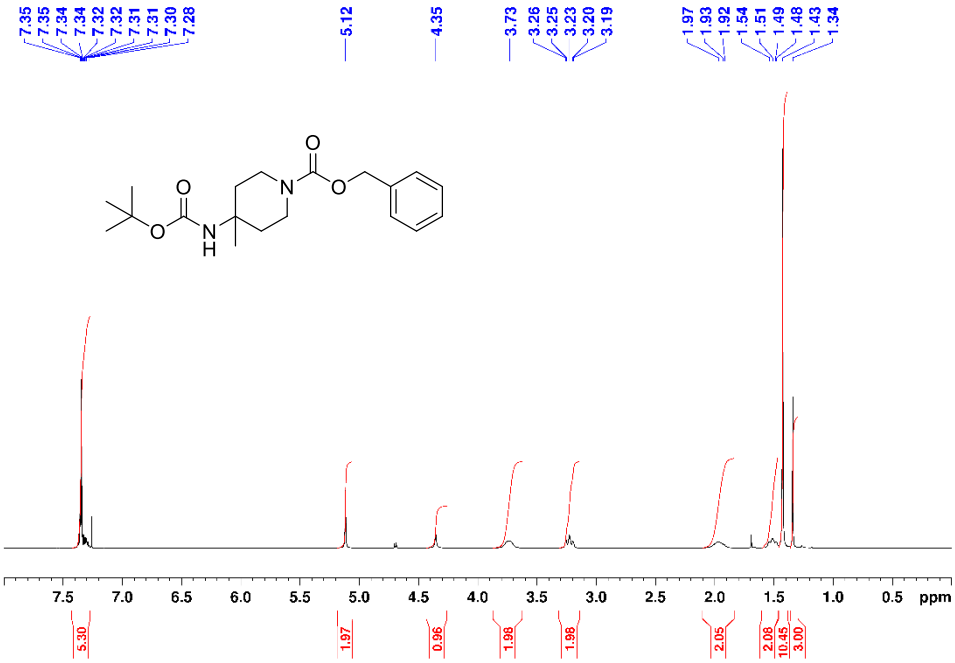

^{13}C-NMR APT spectrum of benzyl 4-[(*tert*-butoxycarbonyl)amino]-4-methylpiperidine-1-carboxylate

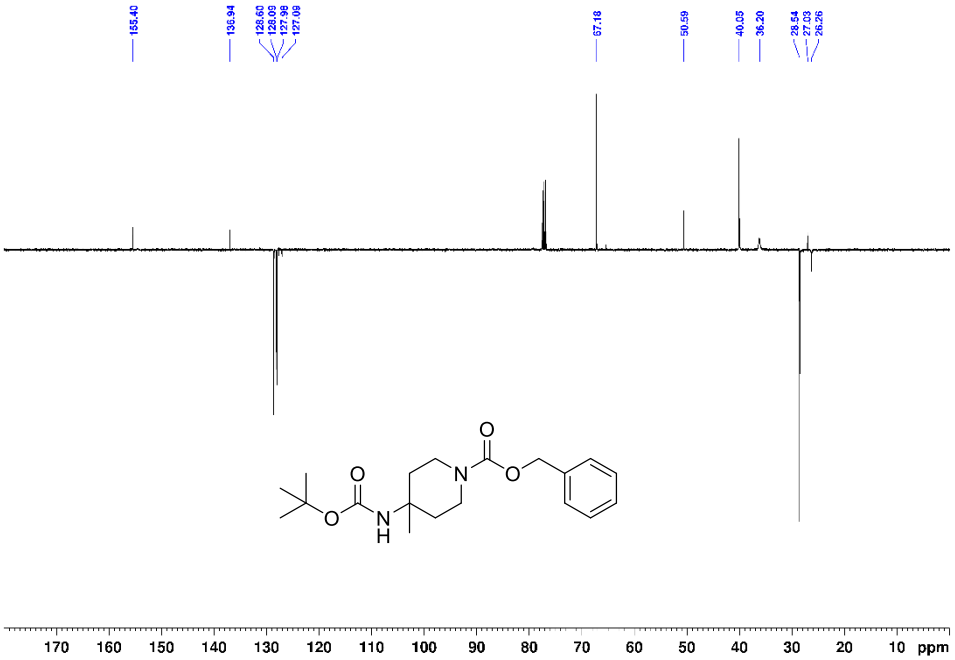

1.11 Compound **11**

^{1}H-NMR spectrum of **11**

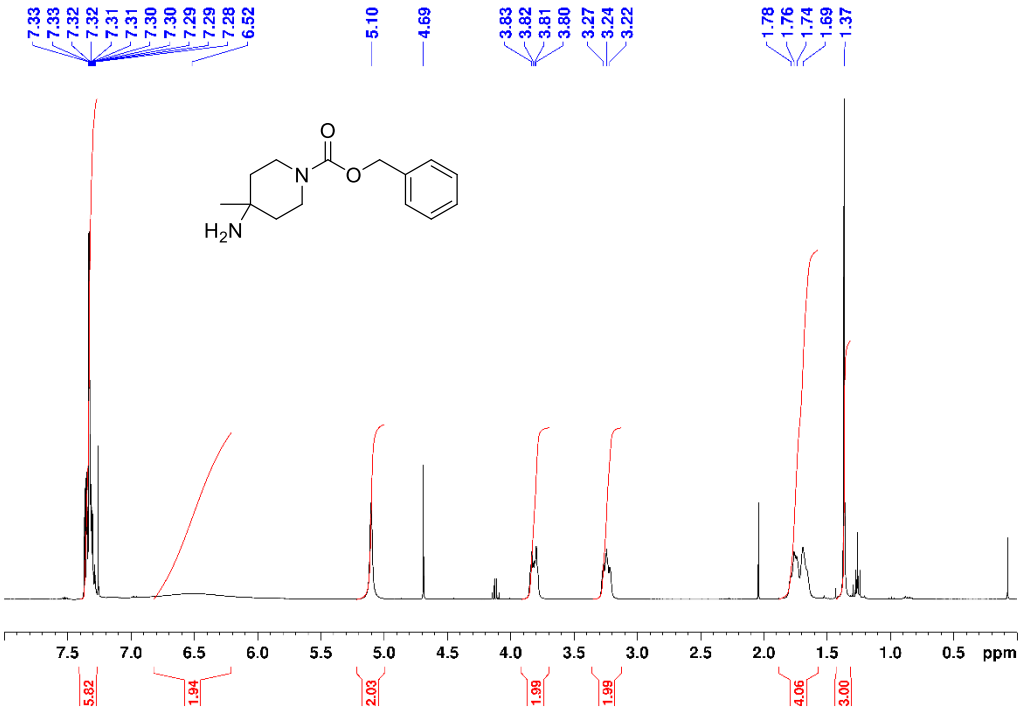

^{13}C-NMR APT spectrum of **11**

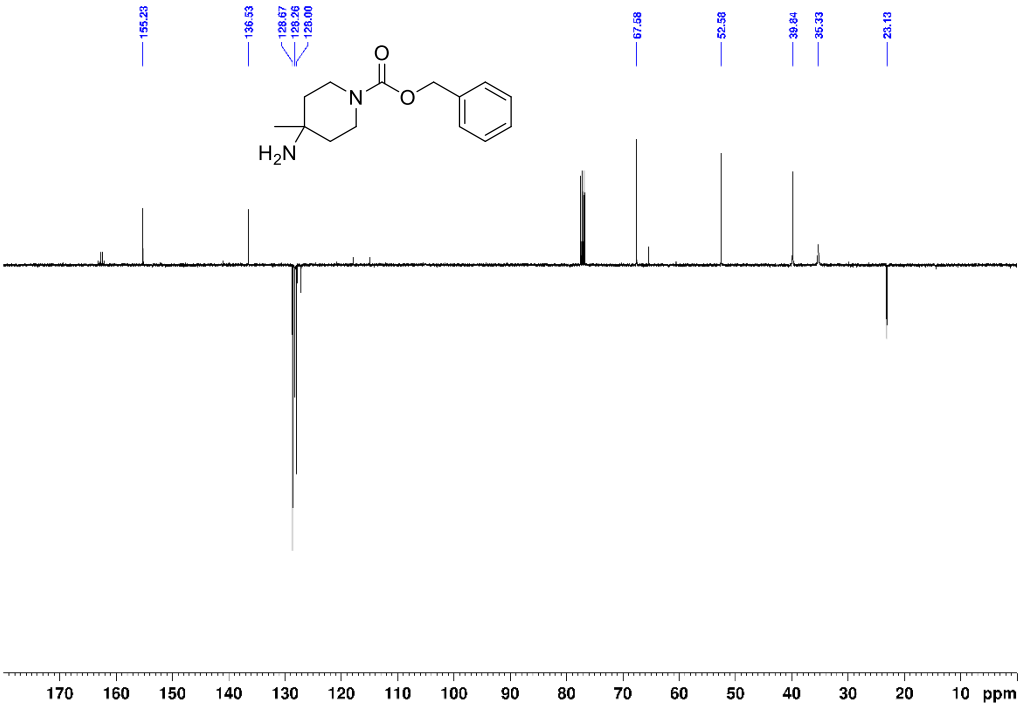

1.12 Compound **12**

^{1}H-NMR spectrum of **12**

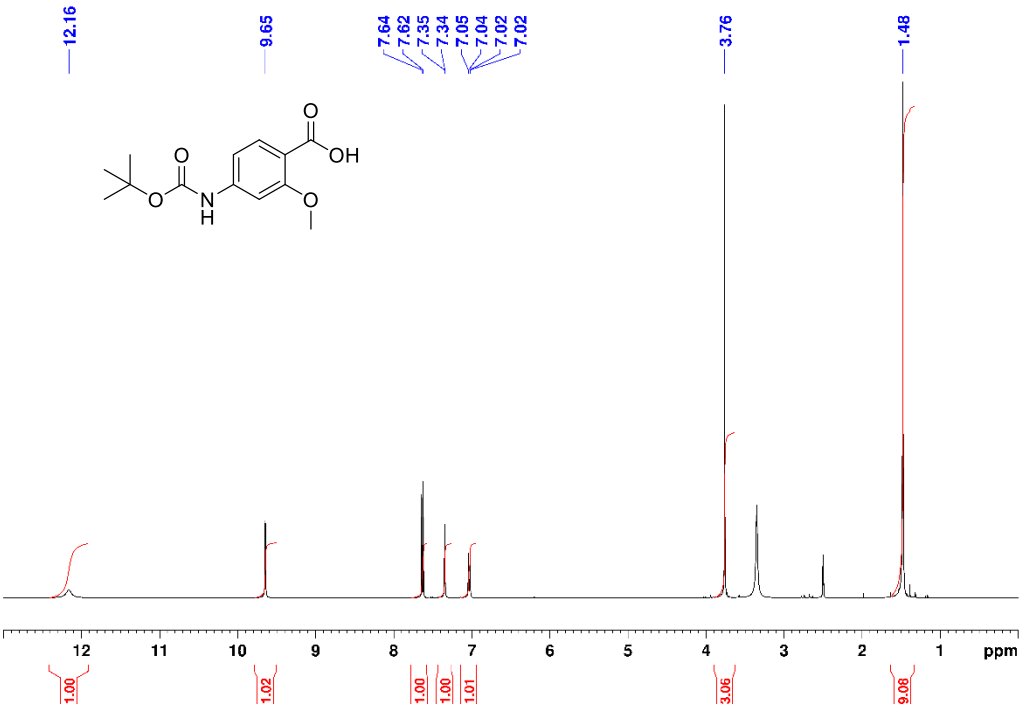

^{13}C-NMR APT spectrum of **12**

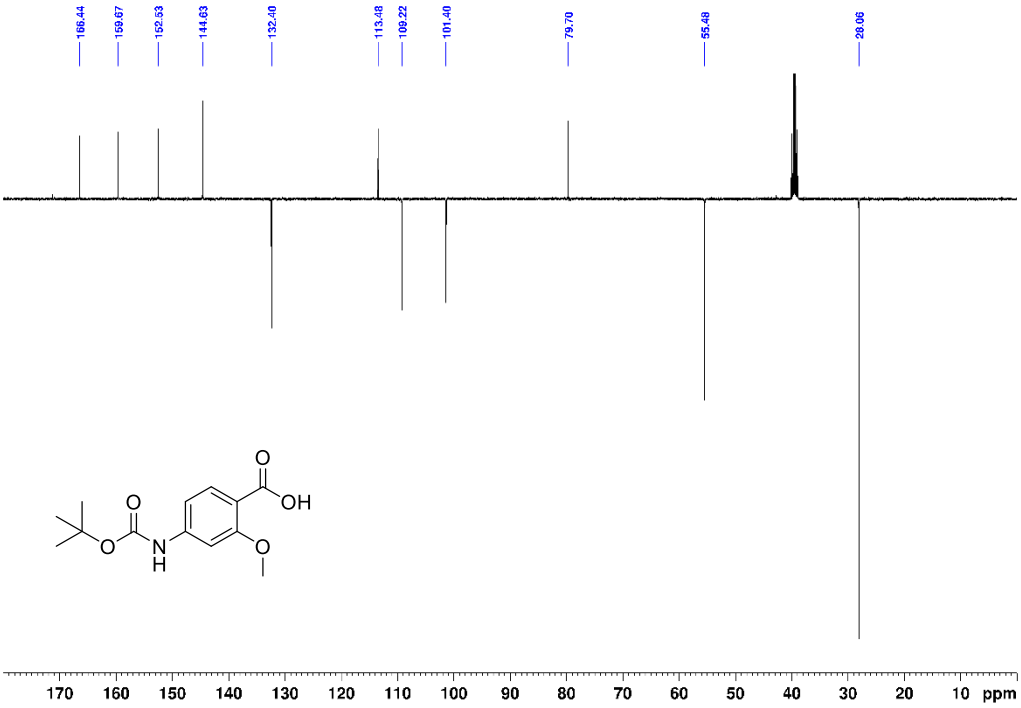

1.13 Compound **13**

^{1}H-NMR spectrum of **13**

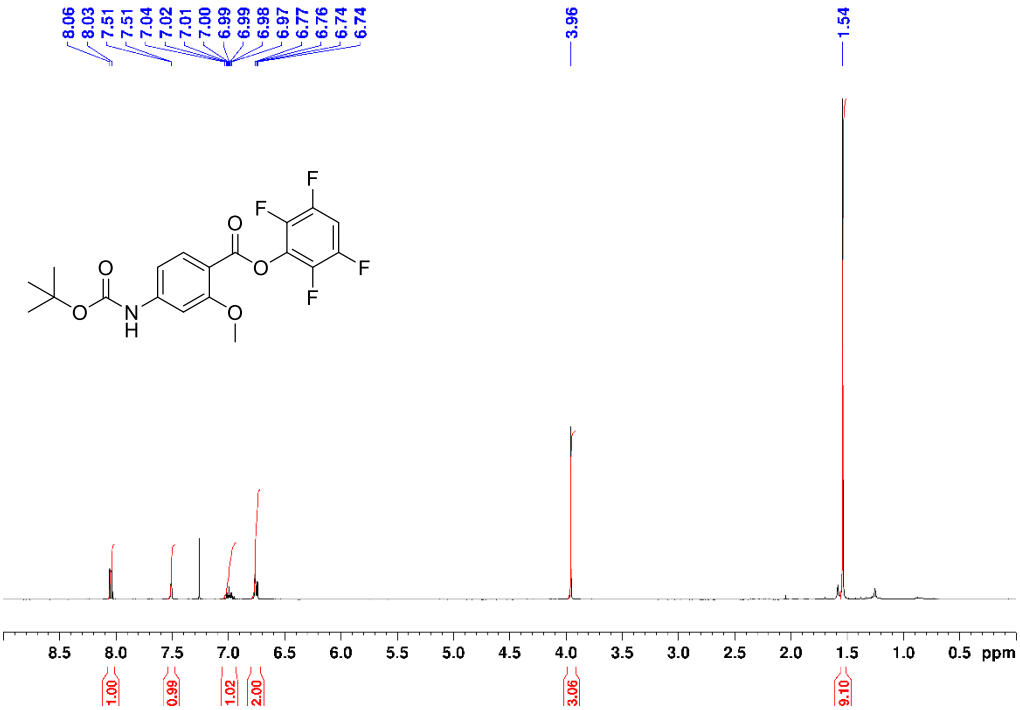

^{13}C-NMR APT spectrum of **13**

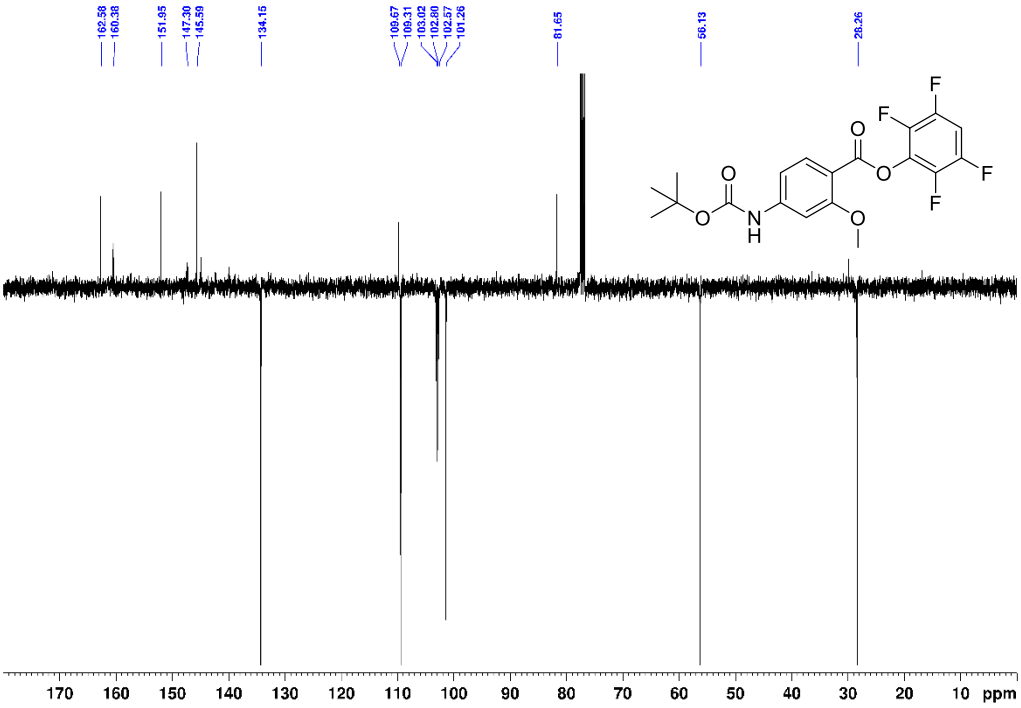

^{19}F-NMR spectrum of **13**

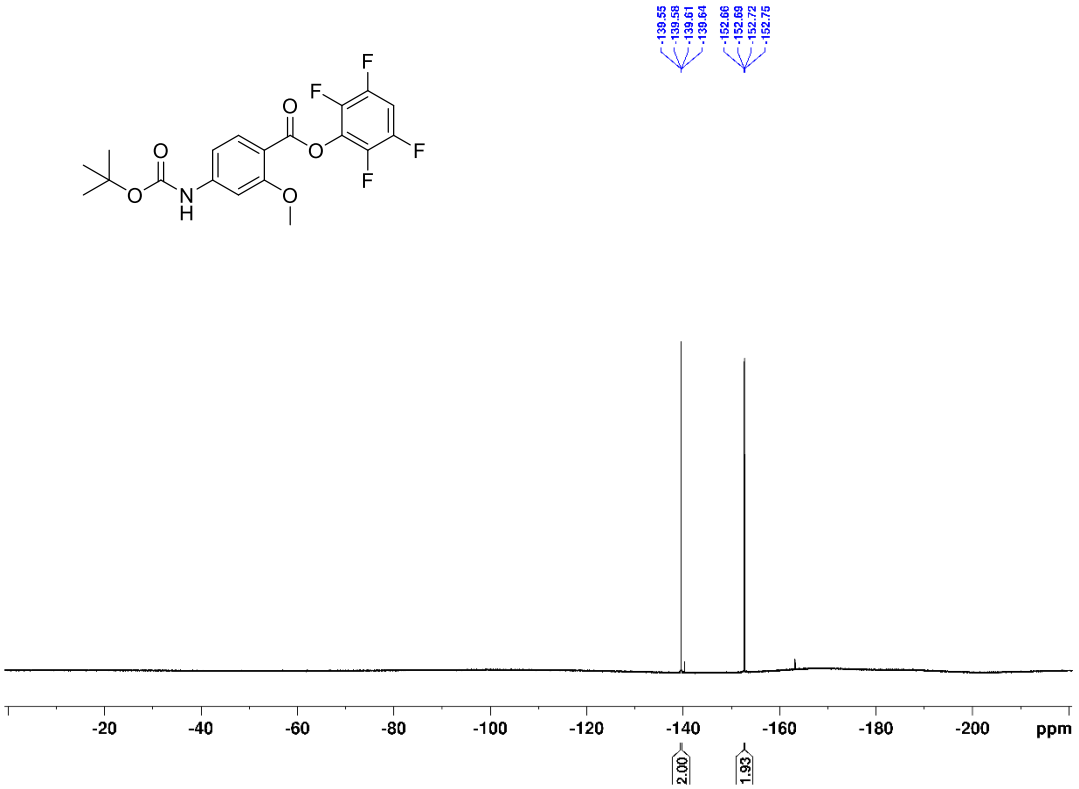

1.14 Compound **14**

^{1}H-NMR spectrum of **14**

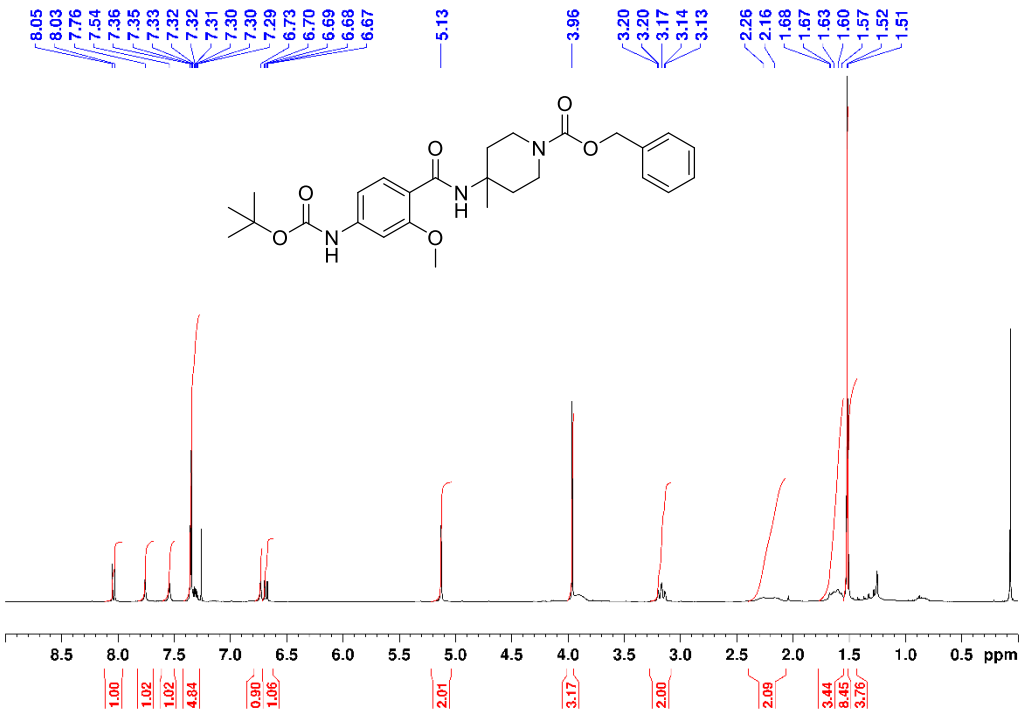

^{13}C-NMR APT spectrum of **14**

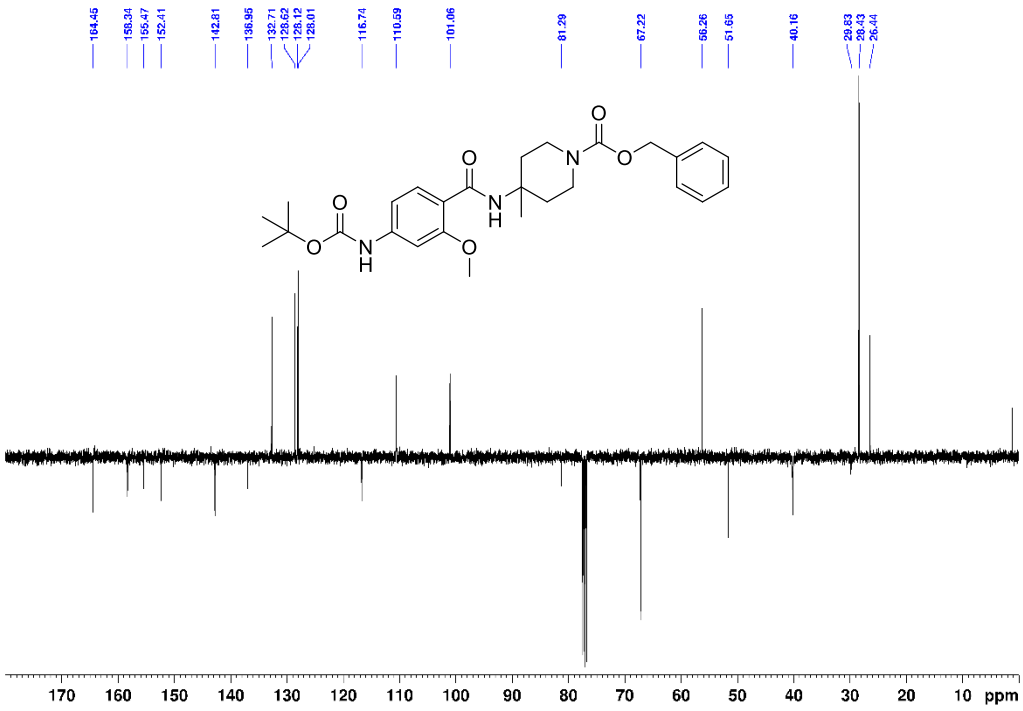

1.15 4-[(*tert*-Butoxycarbonyl)amino]-2-methoxy-*N*-(4-methyl-piperidine-4-yl)benzamide

^{1}H-NMR spectrum of 4-[(*tert*-butoxycarbonyl)amino]-2-methoxy-*N*-(4-methyl-piperidine-4-yl)benzamide

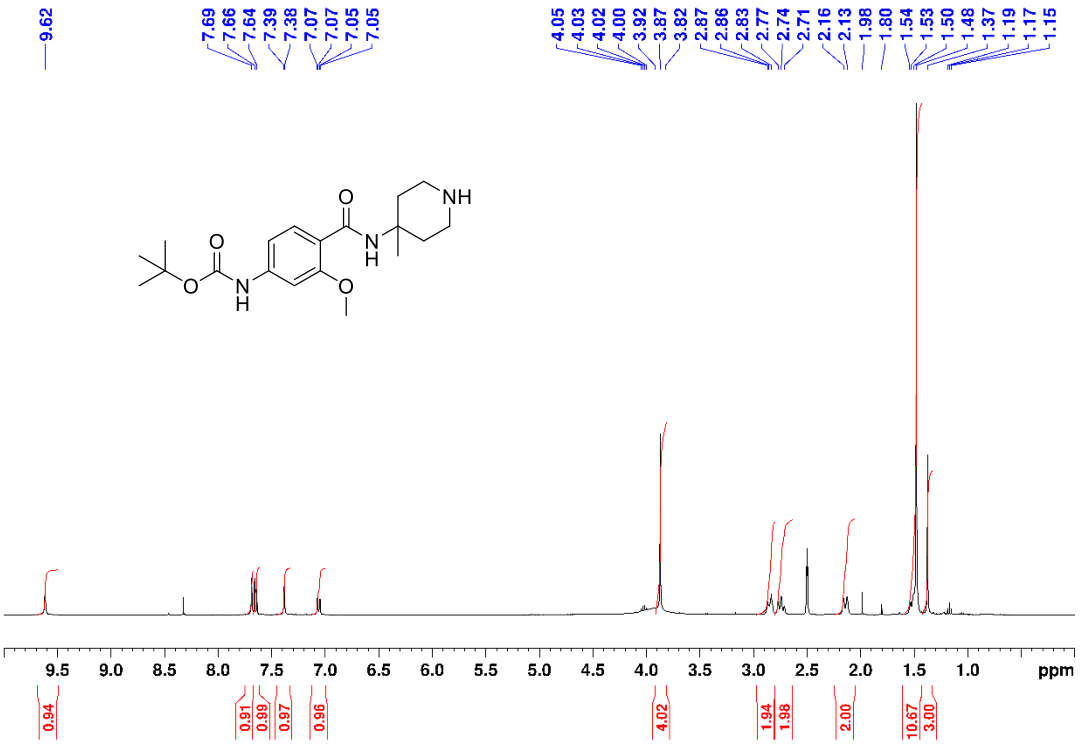

1.17 Compound **10**

^{1}H-NMR spectrum of **10**

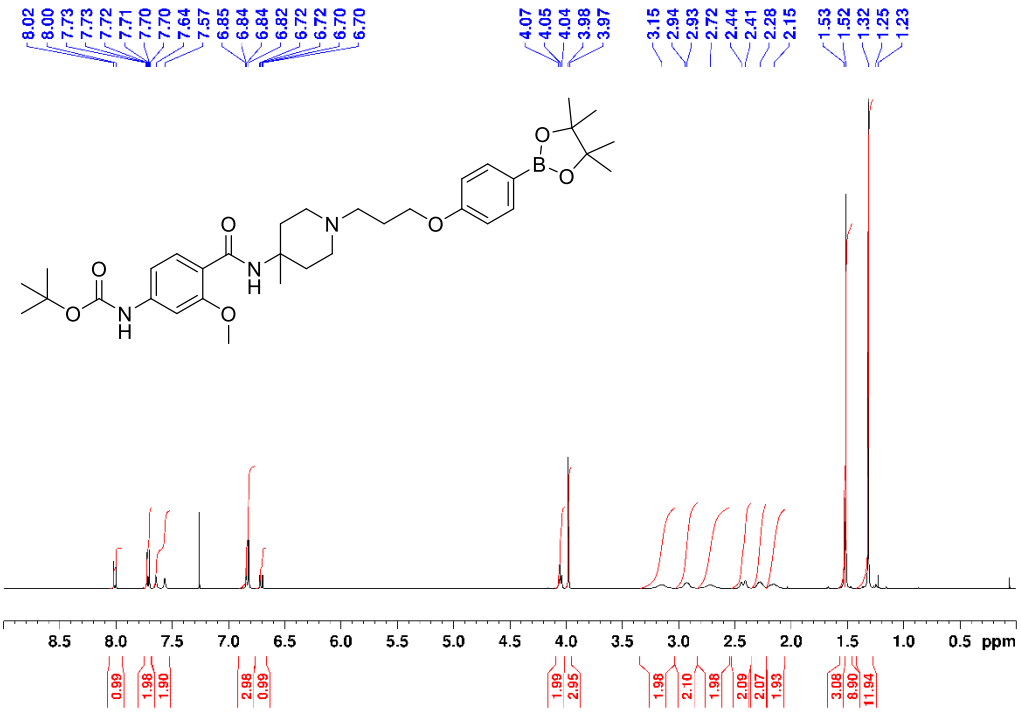

^{13}C-NMR APT spectrum of **10**

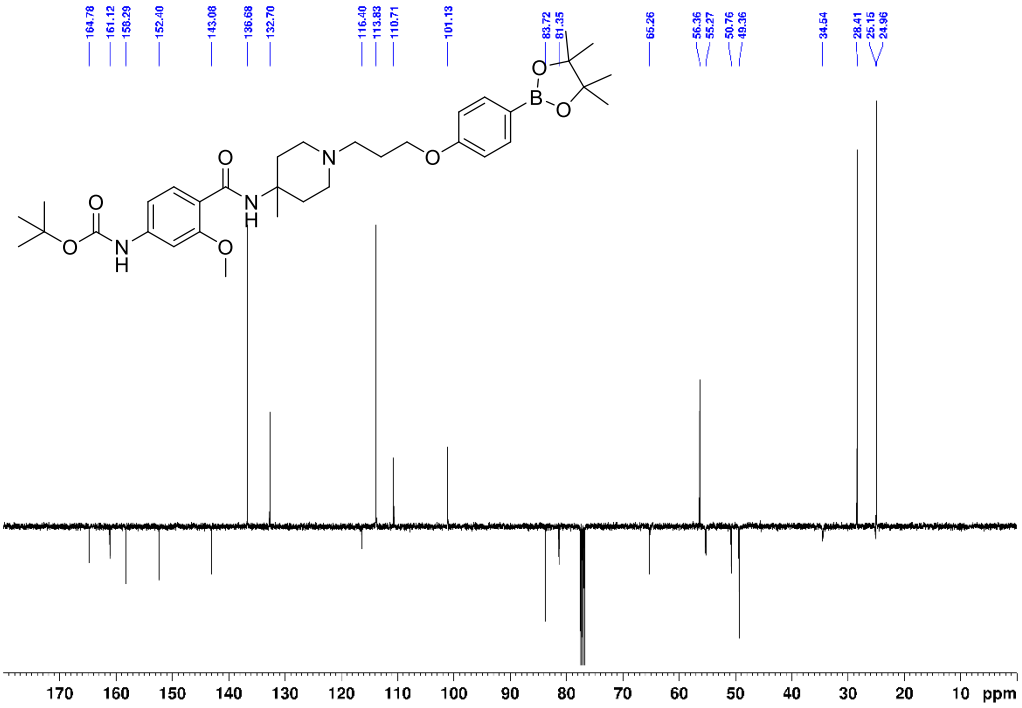

2 Radiochemistry

General conditions

[^{18}F]Fluoride ([^{18}F]F$^-$) was produced via the ^{18}O(p,n)^{18}F nuclear reaction by bombardment of enriched [^{18}O]H_2O with 16.5 MeV protons using a BC1710 cyclotron (The Japan Steel Works Ltd., Shinagawa, Japan) at the INM-5 (Forschungszentrum Jülich). All radiosyntheses were carried out in 5 mL Wheaton V-Vials equipped with PTFE-coated wing stir bars. Anhydrous solvents (DMI, *n*BuOH and MeOH, dried over molecular sieves) were purchased from Sigma-Aldrich (Steinheim, Germany). Anion exchange resin cartridges (Sep-Pak Accell Plus QMA carbonate plus light cartridges with 40 mg sorbent per cartridge) were obtained from Waters (Eschborn, Deutschland).

Processing of [^{18}F]F$^-$

Aqueous [^{18}F]F$^-$ was loaded (from the female side) onto a QMA cartridge (preconditioned with 1 mL H_2O) and the cartridge was washed (from the male side) with anhydrous MeOH (1 mL) to remove residual H_2O and dried (from the female side) with air (2×10 mL). [^{18}F]F$^-$ was eluted (from the female to the male side) with a solution of Et_4NOTf in MeOH (500 µL), and the MeOH was evaporated at 80 °C under reduced pressure in a stream of argon to give Et_4N[^{18}F]F/Et_4NOTf, which was used for the optimizations studies described below.

High-Performance Liquid Chromatography (HPLC)

Analytical radio-HPLC was performed on a HPLC system (Knauer Wissenschaftliche Geräte GmbH, Berlin, Germany) with Azura P 6.1L pump and Azura UVD 2.1S UV/Vis detector. For monitoring UV absorbance and radioactivity, the UV/Vis detector was coupled in series with a Berthold NaI detector, giving a time of delay of 0.1–0.3 min (depending on the flow rate) between the corresponding responses. Radiochemical conversions (RCCs) were determined by radio-HPLC with post-column injection[1] after dilution of the reaction mixtures with H_2O (1 mL) or 20% MeCN (1 mL). Column: MultoKrom® 100-5, 5 µm, 250×4.6 mm (CS-Chromatography Service GmbH, Langerwehe, Germany); eluent: 30% MeCN (0.1% TFA).

2.1 Radiosynthesis of [^{18}F]R91150 from **1**

Dependence of RCCs on reaction time

[^{18}F]F^{-} was eluted from the QMA cartridge with a solution of Et_4NOTf (1 mg, 4 µmol) in MeOH (500 µL), and the MeOH was evaporated at 80 °C under reduced pressure in a stream of argon. A solution of **1** and $Cu(4\text{-}PhPy)_4(ClO_4)_2$ (10 µmol of each) in anhydrous DMI/*n*BuOH (1.2 mL, 2:1 ratio) was then added, the reaction mixture was stirred at 110 °C for indicated time, and the RCC was determined by analytical HPLC as described above.

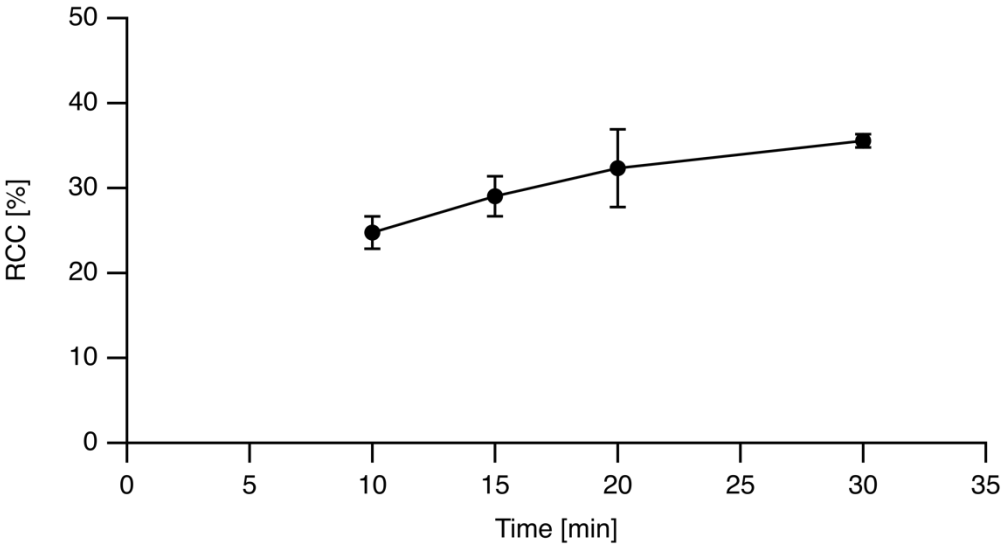

Figure S1: Time screening for the radiosynthesis of [^{18}F]R91150 from precursor **1**.

Table S1: RCCs of [^{18}F]R91150 from precursor **1** after different reaction times.

Time [min]	RCC [%]
10	25 ± 2
15	29 ± 2
20	32 ± 5
30	36 ± 0.8

Dependence of RCCs on precursor amount

[^{18}F]F^{-} was eluted from the QMA cartridge with a solution of Et_4NOTf (1 mg, 4 µmol) in MeOH (500 µL), and the MeOH was evaporated at 80 °C under reduced pressure in a stream of argon. A solution of the indicated amount of precursor **1** and $Cu(4\text{-}PhPy)_4(ClO_4)_2$ (10 µmol) in anhydrous DMI/*n*BuOH (1.2 mL, 2:1 ratio) was then added, the reaction mixture was stirred at 110 °C for 10 min, and the RCC was determined by analytical HPLC as described above.

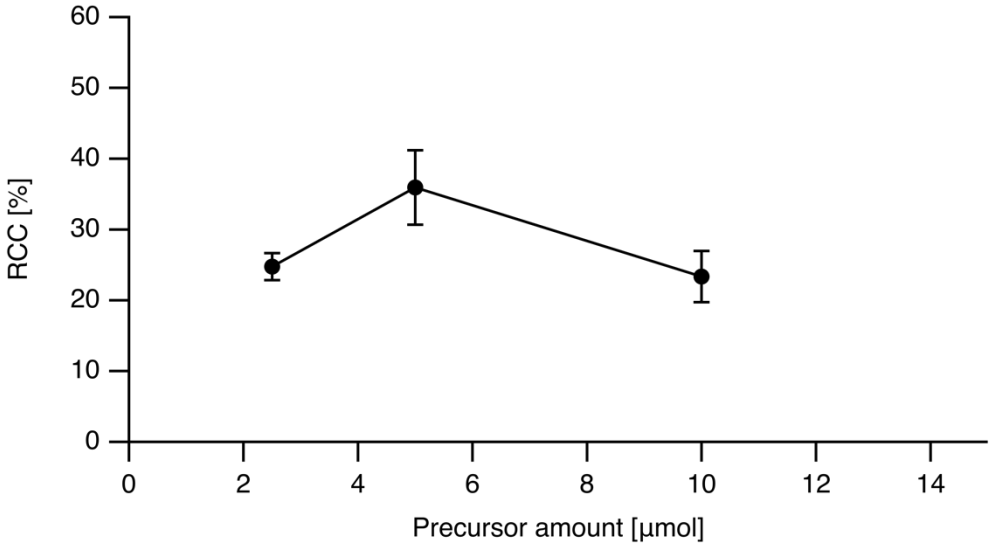

Figure S2: Precursor amount screening for the radiosynthesis of [^{18}F]R91150 from precursor **1**.

Table S2: RCCs of [^{18}F]R91150 from different amounts of precursor **1**.

Amount [µmol]	RCC [%]
10	25 ± 2
5	36 ± 5
2.5	23 ± 4

Dependence of RCCs on precursor purity

Boronate precursor **1** was stored in the fridge under argon for five months and either used without purification or purified by column chromatography (silica gel with 0.1% Ca, CH_2Cl_2/MeOH, 19:1). The radiosyntheses were performed as followed: [^{18}F]F^- was eluted from the QMA cartridge with a solution of Et_4NOTf (1 mg, 4 µmol) in MeOH (500 µL) and the MeOH was evaporated at 60 °C under reduced pressure in a stream of argon. A solution of the indicated amount of (non-purified or purified) precursor **1** and $Cu(4\text{-PhPy})_4(ClO_4)_2$ (10 µmol) in anhydrous DMI/*n*BuOH (1.2 mL, 2:1 ratio) was then added, the reaction mixture was stirred at 110 °C for 10 min, and the RCC was determined by analytical HPLC.

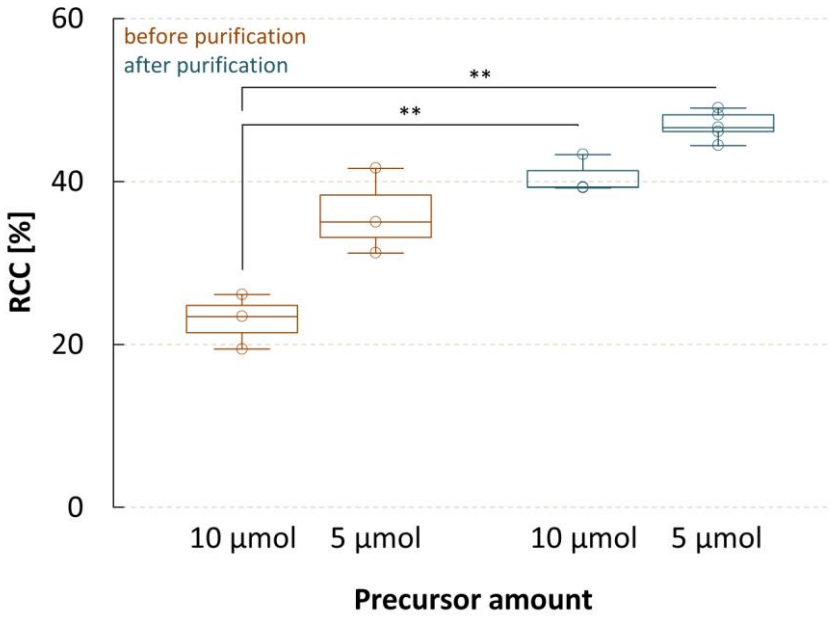

Figure S3: RCCs of [^{18}F]R91150 from 5 or 10 µmol unpurified and purified precursor **1**. Boxplots indicate median, 25th and 75th percentile (box), minimum and maximum values (whiskers) and individual data points (circles). Statistically significant differences between RCC values were identified by Welch's ANOVA with Games-Howell post-hoc test and are indicated by asterisks (**, $p<0.01$).

Table S3: RCCs (%) of [^{18}F]R91150 obtained from unpurified and purified precursor **1**.

Amount [µmol]	Before purification	After purification
10	23 ± 3 (n=3)	41 ± 2 (n=3)
5	36 ± 5 (n=3)	47 ± 2 (n=5)

2.2 Determination of carrier amount and molar activity of [^{18}F]R91150

An aliquot of the purified tracer solution (20 µL) was analyzed by analytical HPLC as described above. The carrier amount was determined from the peak area and the molar activity was calculated according to a calibration curve (Figure S4; λ=254 nm) obtained with different concentrations of R91150 (Table S4).

$$A_M = \frac{A\ \left[\frac{GBq}{mL}\right]}{c\ \left[\frac{\mu mol}{mL}\right]}$$

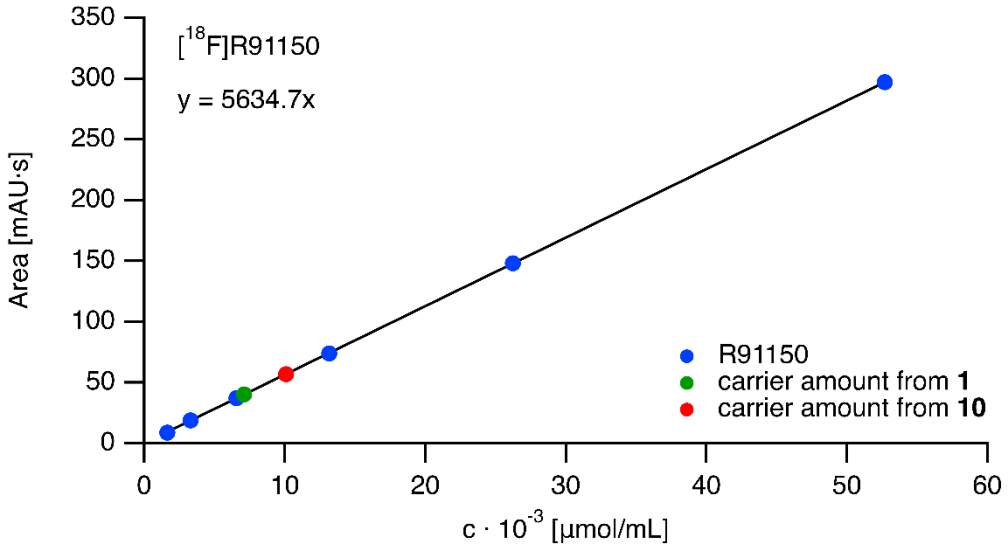

Figure S4: Calibration curve for determination of the molar activity of [^{18}F]R91150. Raw data are shown in Table S4.

Table S4: Calibration data (measured at 254 nm) for determination of the molar activity of [^{18}F]R91150.

Concentration [µmol/mL]	**Amount [µg]**	**Peak area [mAU·min]**
0.0219	21.9	297
0.0109	10.9	148
0.00547	5.47	73.8
0.00273	2.73	37.0
0.00137	1.37	18.7
0.000684	0.684	8.62
Measured sample ([^{18}F]R91150 prepared from **1**):		40.082
Volume [mL]		0.6
Activity [MBq]		1023

Carrier amount [µg]	2.9557
Carrier concentration [µmol/mL]	$7.1134 \cdot 10^{-3}$
Molar activity [GBq/µmol]	240
Measured sample ([^{18}F]R91150 prepared from **10**):	56.665
Volume [mL]	0.67
Activity [MBq]	1460
Carrier amount [µg]	4.1785
Carrier concentration [µmol/mL]	$10.056 \cdot 10^{-3}$
Molar activity [GBq/µmol]	217

2.3 HPLC chromatograms

HPLC chromatograms of [^{18}F]R91150 prepared from non-protected precursor 1

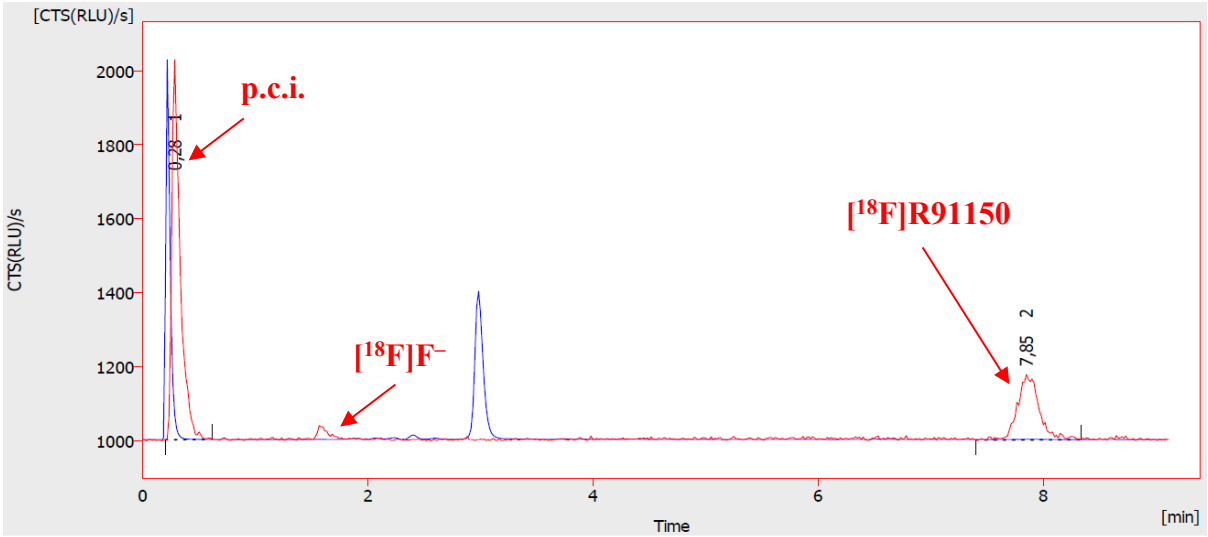

Result Table (Uncal - Data\alc-enhanced_1334_22_08_2023_[4 DMI][18F]R91150_opt_dominik_rcc - HERM)

	Reten. Time [min]	Area [CTS(RLU)/s.s]	Height [CTS(RLU)/s]	Area [%]
1	0,283	5298,500	1026,800	69,2
2	7,850	2354,000	176,518	30,8
	Total	7652,500	1203,318	100,0

Figure S5: HPLC traces of the crude [^{18}F]R91150 prepared from **1** using Cu(4-PhPy)$_4$(ClO$_4$)$_2$ in DMI/*n*BuOH 2:1 at 110 °C for 10 min under air. Blue trace: UV channel, λ=254 nm; red trace: radioactivity channel. Abbreviations: p.c.i. – post column injection.

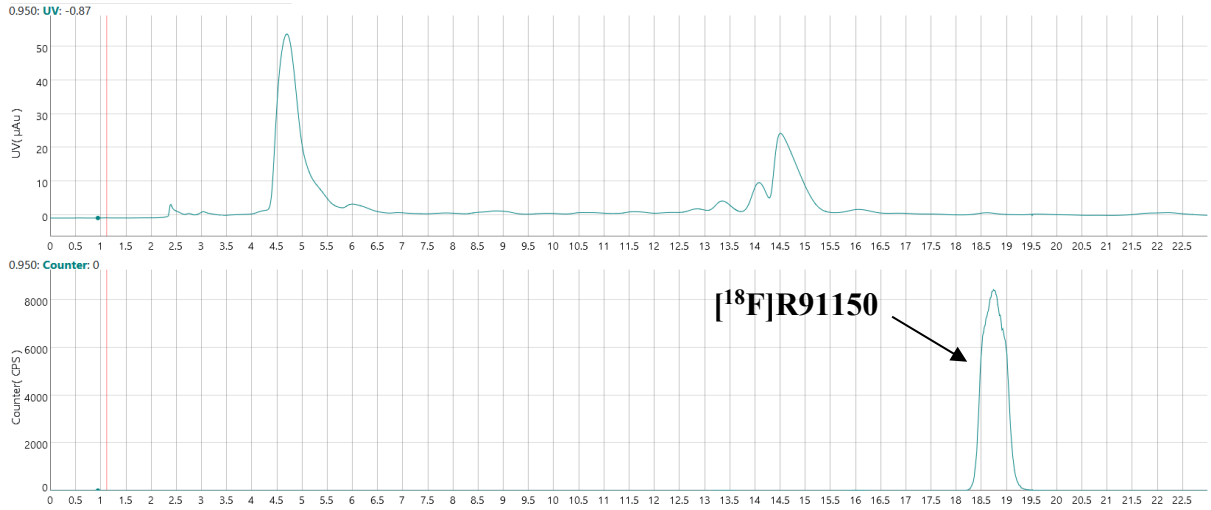

Figure S6: HPLC traces of purification of [^{18}F]R911150 by preparative HPLC (top: UV trace, λ=254 nm; bottom: radioactive trace).

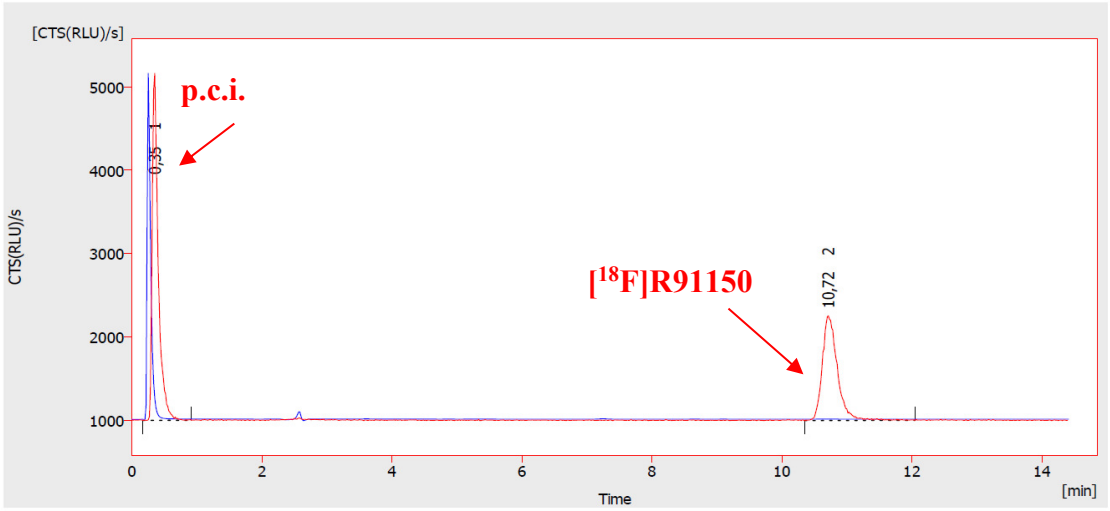

Result Table (Uncal - Data\alc-enhanced_1336_22_08_2023_[4 DMI][18F]R91150_opt_dominik_radio_purity - HERM)

	Reten. Time [min]	Area [CTS(RLU)/s.s]	Height [CTS(RLU)/s]	Area [%]
1	0,350	27032,000	4157,511	57,2
2	10,717	20196,000	1253,137	42,8
	Total	47228,000	5410,648	100,0

Figure S7: HPLC traces of the purified [^{18}F]R91150. Blue trace: UV channel, λ=254 nm; red trace: radioactivity channel. Abbreviations: p.c.i. – post column injection.

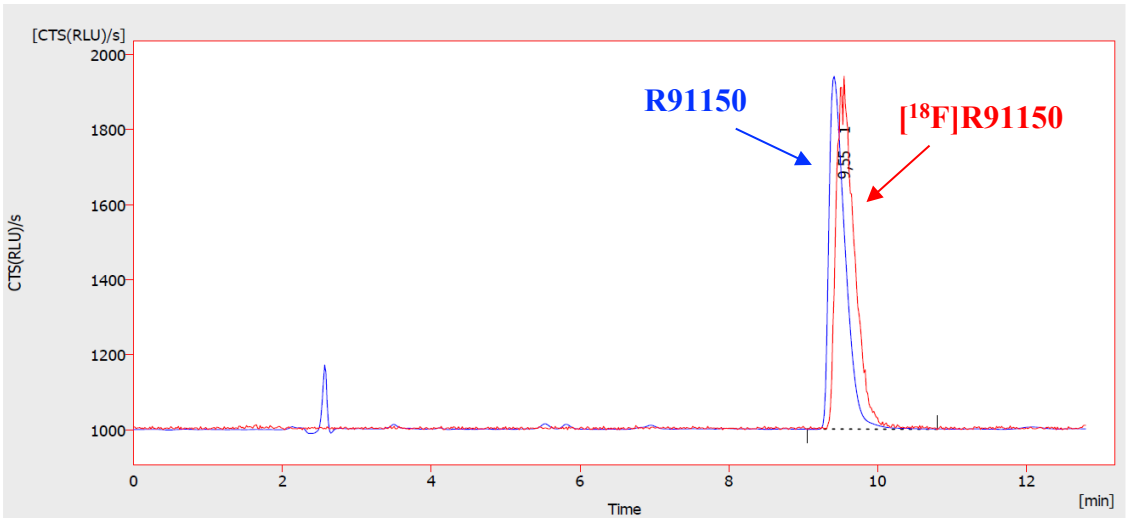

Result Table (Uncal - Data\alc-enhanced_1337_22_08_2023_[4 DMI][18F]R91150_opt_dominik_spike - HERM)

	Reten. Time [min]	Area [CTS(RLU)/s.s]	Height [CTS(RLU)/s]	Area [%]
1	9,550	16086,500	940,286	100,0
	Total	16086,500	940,286	100,0

Figure S8: HPLC traces of the purified [^{18}F]R91150 spiked with the non-radioactive reference compound R91150. Blue trace: UV channel, λ=254 nm; red trace: radioactivity channel. Abbreviations: p.c.i. – post column injection.

HPLC chromatograms of [^{18}F]R91150 prepared from Boc-protected precursor 10

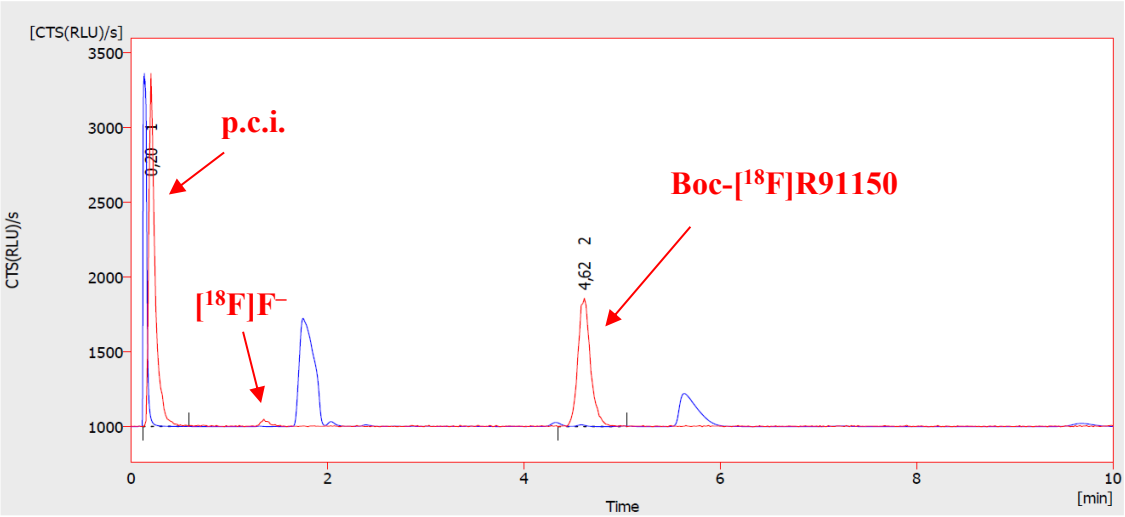

Result Table (Uncal - Data\alc-enhanced_1369_14_11_2023_[4 DMI][18F]R91150_boc_rcc - HERM)

	Reten. Time [min]	Area [CTS(RLU)/s.s]	Height [CTS(RLU)/s]	Area [%]
1	0,200	10446,000	2359,643	57,5
2	4,617	7709,000	857,619	42,5
	Total	18155,000	3217,262	100,0

Figure S9: HPLC traces of the crude Boc-[^{18}F]R91150 prepared from **10** using $Cu(4\text{-}PhPy)_4(ClO_4)_2$ in DMI/*n*BuOH 2:1 at 110 °C for 10 min under air. Blue trace: UV channel, λ=254 nm; red trace: radioactivity channel. Abbreviations: p.c.i. – post column injection.

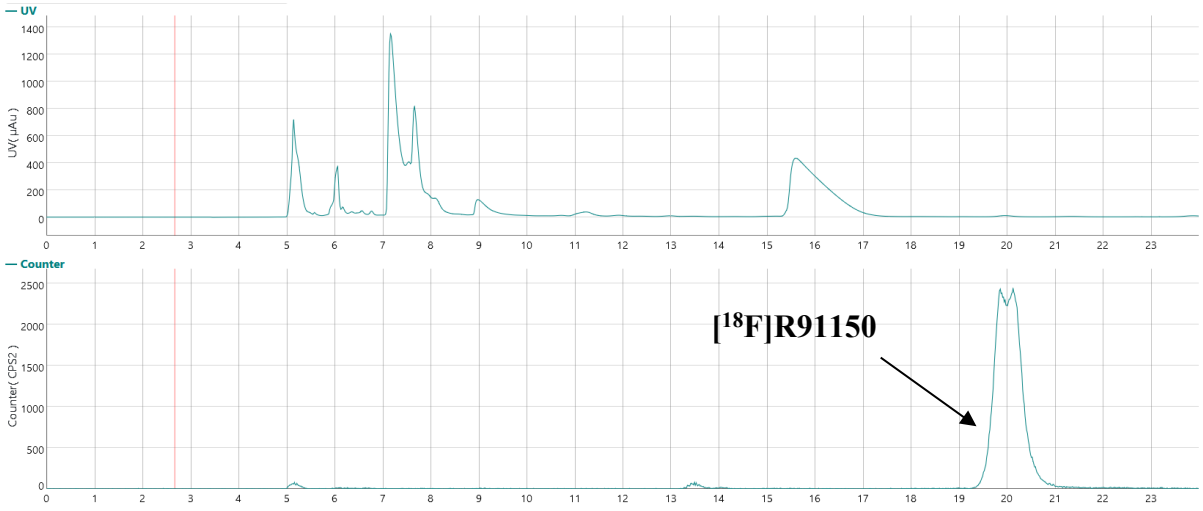

Figure S10: HPLC traces of purification of [^{18}F]R911150 by preparative HPLC (top: UV trace, λ=254 nm; bottom: radioactive trace).

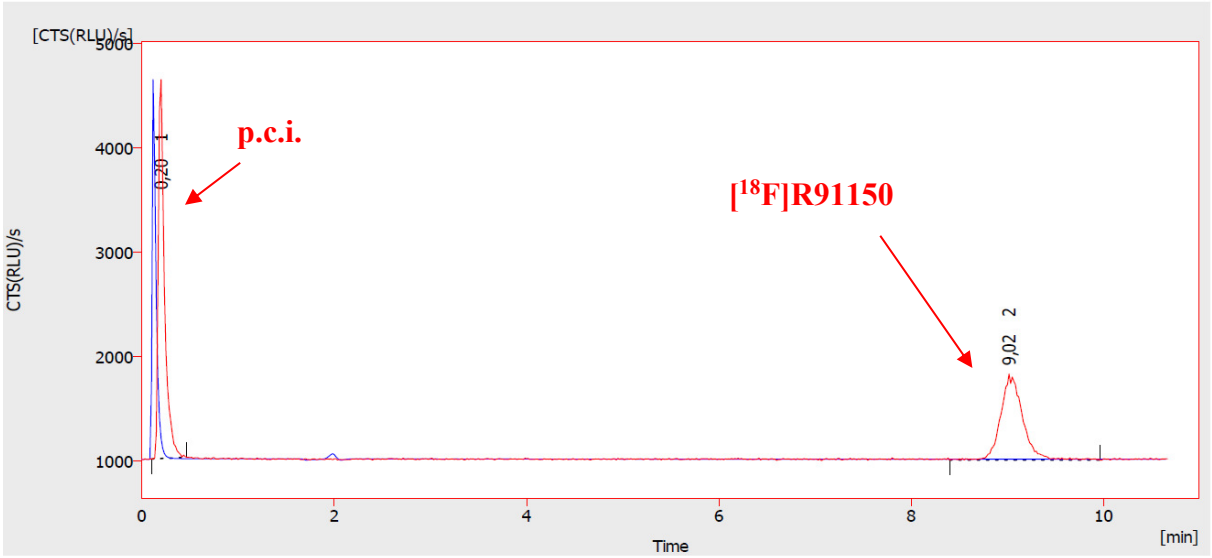

Result Table (Uncal - Data|alc-enhanced_1396_13_12_2023_[4 DMI][18F]R91150_MC18_radio_purity - HERM)

	Reten. Time [min]	Area [CTS(RLU)/s.s]	Height [CTS(RLU)/s]	Area [%]
1	0,200	16415,000	3633,909	55,6
2	9,017	13104,000	824,787	44,4
	Total	29519,000	4458,696	100,0

Figure S11: HPLC traces of the purified [^{18}F]R91150. Blue trace: UV channel, λ=254 nm; red trace: radioactivity channel. Abbreviations: p.c.i. – post column injection.

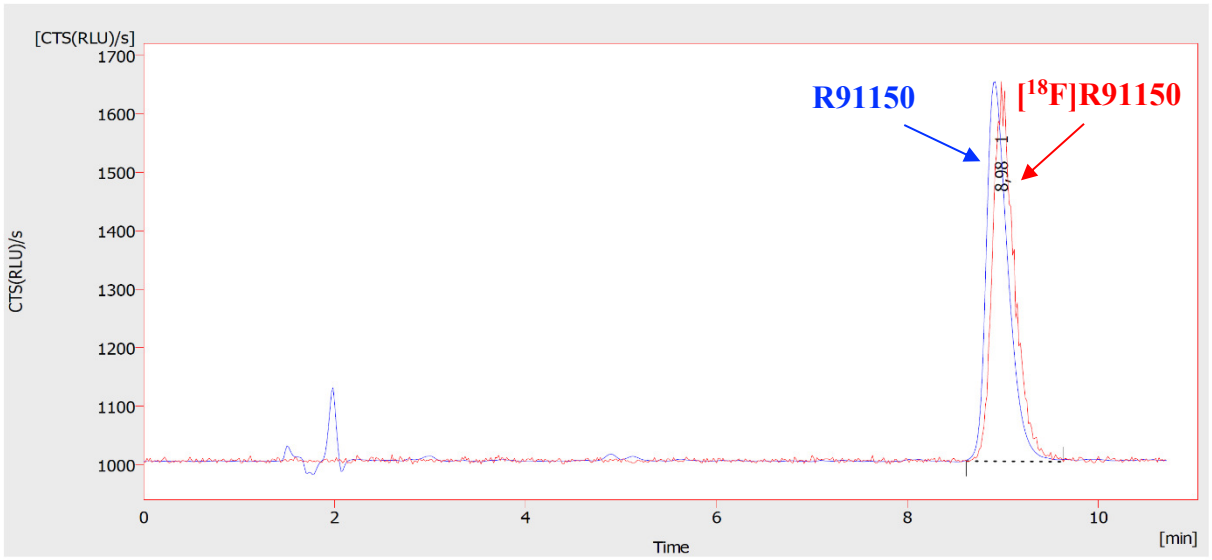

Result Table (Uncal - Data|alc-enhanced_1397_13_12_2023_[4 DMI][18F]R91150_MC18_spike - HERM)

	Reten. Time [min]	Area [CTS(RLU)/s.s]	Height [CTS(RLU)/s]	Area [%]
1	8,983	10154,500	649,361	100,0
	Total	10154,500	649,361	100,0

Figure S12: HPLC traces of the purified [^{18}F]R91150 spiked with the non-radioactive reference compound R91150. Blue trace: UV channel, λ=254 nm; red trace: radioactivity channel. Abbreviations: p.c.i. – post column injection.

3 In vivo µPET measurements

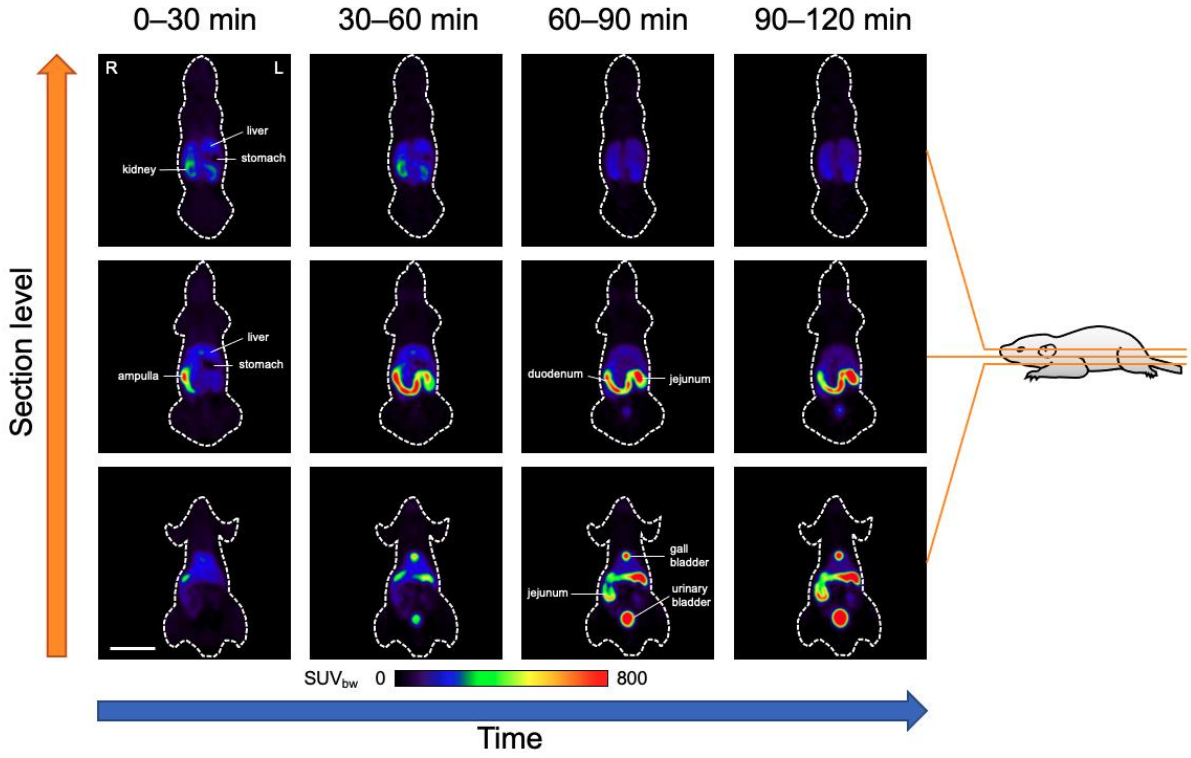

Figure S13: Hepatobiliary excretion of [^{18}F]R91150. Shown are 30 min time frames after tracer injection in one mouse, presented as horizontal sections of three different levels. The mouse's outline is indicated by the dashed white line. In the first frame of the second row, the ampulla is visible, where the bile duct opens into the duodenum. From there, the radioactive intestinal content moves forward through duodenum and jejunum. Radioactivity accumulates over time in the gall bladder and the urinary bladder as well. However, urinary radioactivity is much lower compared to other tracers with primarily renal excretion. Please note that the image orientation common for PET (i.e. dorsal view) has been flipped to match the ventral view with the mouse in supine position when observing a situs. Abbreviations: L - left, R - right. Scale bar: 20 mm

4 References

[1] S. Humpert, C. Hoffmann, F. Neumaier, B. D. Zlatopolskiy, B. Neumaier, *J Chromatogr B Analyt Technol Biomed Life Sci* **2023**, *1228*, DOI 10.1016/J.JCHROMB.2023.123847.